NEW OPTIMAL PWM STRATEGIES FOR A VSI INDUCTION MOTOR DRIVE

by

SHAKIR MAHMOUD ABDULRAHMAN

A doctoral thesis submitted in partial fulfilment of the requirement for the award of the degree of Doctor of Philosophy of the Loughborough University of Technology

Supervisor: Mr J.G. KETTLEBOROUGH

Department of Electronic and Electrical Engineering

to my father and mother

ACKNOWLEDGMENTS

I wish to express my gratitude for the assistance and helpful encouragement to my research supervisor Mr J.G. Kettleborough whose patience and technical guidance made this work possible.

I would like to thank my director of research Professor I.R. Smith whose valuable comments and advice greatly improved the contents of this thesis.

I would also like to thank Mr K. Gregory and Dr C.R. Fitton with whom I held extensive discussions on both technical and simulation problems encountered during the course of this research.

Last, but not least, I wish to express my gratitude to my wife for her patience and understanding throughout my study.

SYNOPSIS

The applications of robust squirrel-cage induction motors in variable speed inverter drive systems have increased considerably due to the availability of easily controlled semiconductor switching devices. One problem encountered in inverter drives is the non-sinusoidal nature of the supply voltage, which results in increased motor losses and harmful torque pulsations producing undesirable speed oscillations. The latter effects are negligible at high frequency operation, due to the damping effect of the rotor and load inertia. However, torque pulsations and speed ripple may be appreciable at low frequency, were they may result in abnormal wear of gear-teeth or torsional shaft failure. Hence, in applications where constant or precise speed control is important, eg; machine tool, antenna positioning, traction drives etc., it is essential to establish a method for determining the magnitudes of these torque pulsations and speed ripple, as a first stage in minimizing or eliminating them.

When a voltage source inverter is used in such applications, pulse width modulation (PWM) techniques are usually employed, whereby the quasi square waveshape is modulated so as to minimize or eliminate the low order harmonic voltage components and thereby reduce the torque pulsations. Recent investigations have shown that total elimination of low order components does not produce optimal efficiency or torque pulsations and speed ripple minimization. This thesis describes new PWM strategies which does not rely on complete elimination of low order harmonics, but on controlling the magnitude and phase of these components to achieve a smooth rotor motion.

Initially, a mathematical model for the inverter/induction motor drive was developed, based on numerical integration of the system differential equations. The changing topology of the inverter bridge was simulated using tensor techniques. Then an analytical method, based on harmonic equivalent circuit analysis was proposed for calculating the induction motor

pulsating torque components under steady-state operating conditions, in terms of stator and rotor current harmonics. The accuracy of this method was verified by comparing its results with those obtained from the mathematical model developed earlier. This provided an extremely rapid, numerically stable and efficient means for evaluating harmonic current and torque components with balanced non-sinusoidal applied voltages. This method was then used to formulate the torque performance function necessary to determine the new optimal PWM switching strategies.

Throughout the work, the predicted performance was extensively validated and supported by practical results obtained from an experimental rig specifically designed to drive the machine under different PWM techniques.

LIST OF PRINCIPAL SYMBOLS

a_n , b_n	Fourier coefficients of the nth-harmonic.
$C^b_{.m}$	Current transformation matrix.
E_b	Branch reference frame impressed voltage vector.
E_m	Mesh reference frame impressed voltage vector.
f_r	Rotor frequency.
f_s	Stator or modulating wave frequency.
f_t	Frequency of the carrier waveform.
h	Integer equal to 6 or multiple thereof.
$i^b_{A.B.C}$	Instantaneous branch currents of the stator phases A, B and C.
$i^b_{a.b.c}$	Instantaneous branch currents of the rotor phases a, b and c.
i^b_{dc}	Instantaneous branch current of the DC-link.
i^m_1 , i^m_2	Instantaneous mesh 1 and mesh 2 currents.
I^b	Branch reference frame current vector.
I^m	Mesh reference frame current vector.
I_s	Per-phase rms stator current.
I_r	Per-phase rms rotor current.
I'_r	Per-phase rms referred rotor current.
I_m	Per-phase rms magnetizing current.
I_{rms}	Total rms stator current.
$I_{s(n)}$	nth-harmonic component of the stator current.
$I_{r(n)}$	nth-harmonic component of the rotor current.
J	Moment of inertia.
K_{ws}	Stator winding factor.
K_{wr}	Rotor winding factor.
K_e	Excitation constant.
K_w	Windage constant.
K_v	Viscous friction constant.
K_1	1st-coefficient of Runge-Kutta 4th-order integration procedure.
K_2	2nd-coefficient of Runge-Kutta 4th-order integration procedure.

K_3	3rd-coefficient of Runge-Kutta 4th-order integration procedure.
K_4	4th-coefficient of Runge-Kutta 4th-order integration procedure.
L_b	Branch reference frame inductance matrix.
L_m	Mesh reference frame inductance matrix.
l_s	Per-phase stator leakage inductance.
l_r	Per-phase rotor leakage inductance.
l_m	Per-phase magnetizing inductance.
M	Modulation index.
N_s	Number of stator turns per phase.
N_r	Number of rotor turns per phase.
n_s	Synchronous speed.
n_r	Rotor speed.
p	Number of pairsof poles.
P_s	Per-phase stator power.
P_{Loss}	Per-phase rotor copper loss.
P_{mech}	Gross mechanical power.
R_s	Per-phase stator resistance.
R_r	Per-phase rotor resistance.
R_c	Per-phase core loss resistance.
R_b	Branch reference frame resistance matrix.
R_m	Mesh reference frame resistance matrix.
s	Slip.
s_{max}	Slip at maximum torque.
$T_{e\ max}$	Maximum torque.
$T_{e\ st}$	Starting torque.
T_m	Load torque.
T_f	Friction torque.
T_c	Coulomb friction torque.
TH_n	Width of the nth high level pulse.
TL_n	Width of the nth low level pulse.
T_t	Period of the carrier waveform.
T_e	Electromagnetic torque.
T_{e0}	Steady-state torque.
T_{eh}	hth-harmonic torque component magnitude.
t_{min}	Minimum switching time.
t_d	GTO gate-controlled delay time.

t_f	GTO gate-controlled fall time.
t_s	GTO gate-controlled storage time.
v_{AN}	Instantaneous phase A voltage.
v_{AB}	Instantaneous line voltage.
V_{dc}	DC-link voltage.
$V_{(n)}$	nth-component of rms phase voltage.
$V_{l(n)}$	nth-component of rms line voltage.
V_b	Branch reference frame voltage vector.
V_m	Mesh reference frame voltage vector.
V_s	Per-phase stator voltage drop.
X_s	Per-phase stator reactance.
X_m	Per-phase magnetizing reactance.
X_r'	Per-phase referred rotor reactance.
Z_i	Per-phase input impedance.
Z_b	Branch reference frame impedance matrix.
Z_m	Mesh reference frame impedance matrix.
ΔX	Integration step-length.
$\Delta\omega_m$	Peak-to-peak speed ripple.
$\Delta\theta_m$	Peak-to-peak positional error.
ΔT_e	Peak-to-peak torque pulsation.
ω_r	Rotor angular frequency.
ω_s	Stator (or modulating waveform) angular frequency.
ω_m	Mechanical angular speed of the rotor.
ω_t	Angular frequency of the carrier waveform.
α_m	Switching angle in radians.
p	Differential operator d/dt.
θ_e	Rotor electrical angular displacement.
$\theta_{s(n)}$	Phase angle of the nth stator current component.
$\theta_{r(n)}$	Phase angle of the nth rotor current component.
δ_h	Phase angle of the hth-harmonic torque component.

All other Symbols are defined as they appear.

CONTENTS

CHAPTER 1

INTRODUCTION

1.1 General Background

An increase in the number of applications requiring variable speed drives instigated the need for stable and versatile electrical machine and control schemes. During the 19th and early 20th centuries, and prior to the introduction of the mercury-arc rectifier, these requirements were traditionally met by the DC motor. In some applications, hazardous environments and frequent maintenance needs of the mechanical commutator, paved the way for the cage rotor AC motor. Various techniques were developed for both types of machine to provide continuous speed control over a wide range using, in all cases, auxiliary machines acting either as prime-movers or power supplies [1]. By the middle of this century, the development of semiconductor devices and their use in controlled rectifiers and static frequency changers had superseded the use of these auxiliary machines, and a new era of solid-state motor speed control techniques was evolving.

Speed control of a DC motor may be performed simply by controlling the armature voltage using a phase-controlled rectifier if the power supply is AC, or a DC-DC converter if it is DC. However, the complicated mechanical construction of the machine makes the overall scheme expensive. By contrast, AC motors require a variable frequency power supply and their speed control schemes are consequently more complicated. Nevertheless the induction motor, in particular its cage variant, has been widely used in industrial drives, due to the following major advantages it possesses over the DC motor:

(1) The cage rotor construction is both rugged and simple.
(2) The rotor inertia is lower than that of a DC machine and it can tolerate higher temperatures and over-speeds for longer periods.

(3) No brush-gear is necessary, which reduces the maintenance required.
(4) The power/weight ratio is about twice that of a DC motor.
(5) It is less expensive.

One of the most widely used methods of induction motor speed control uses the DC-link inverter. This can be either a voltage source inverter (VSI) or a current source inverter (CSI), both of which operate in the six-step or quasi-square wave (QSW) mode [2-5]. Although this is satisfactory for high operating frequencies, its low frequency implementation is characterised by significant low order harmonic voltage and/or current components, which have two major practical consequences. Firstly, they produce harmonic copper losses, reducing the overall efficiency and possibly causing overheating. Secondly, their resultant space harmonic mmfs produce negligible steady torque, but much larger pulsating harmonic torques. If the pulsating frequency is close to a resonant frequency of the rotating system, the resultant mechanical oscillations may unduly stress the rotating shaft and damage the connected assembly. Furthermore, the magnitudes of the resulting speed oscillations depend on the drive inertia and, in applications where precise and smooth rotor motion are essential, eg; machine tools, antenna positioning and traction drives they may reach an unacceptable level.

When a VSI is used in such applications, various pulse width modulation (PWM) strategies are employed. Generally speaking these are based on modulation of the basic 6-step voltage waveshape, with the object of reducing or eliminating low order harmonics to minimise the total harmonic losses and torque pulsations. The natural PWM strategy has been widely implemented using standard analogue techniques [6-10]. Developments in digital electronics and microprocessor control techniques, have greatly facilitated the implementation of more advanced PWM strategies such as the regular symmetrical, asymmetrical [10-15] and optimal PWM strategies [16-23].

Natural and regular PWM strategies have both been analysed using expressions based on a Fourier-series expansion of the modulation process [8,11,14]. These expressions provide relationships between the harmonic content of the PWM waveform and modulation parameters such as the frequency ratio, the modulation index and the sampling (switching) instants. The technique results in complex equations, requiring Bessel functions to derive the harmonic spectra expressions, which need a digital computer to determine the magnitudes of individual harmonics [15]. Optimal PWM strategies need extensive off-line computation to determine the switching angles which define the PWM waveform. However, once these have been obtained, simple Fourier-series dependent expressions are formed to determine the magnitudes of individual harmonics which led to the development of different techniques. In addition to selected harmonic elimination, these techniques have met specific operational requirements, such as the minimisation of harmonic distortion [20-22], torque pulsations and speed ripple [23].

The harmful effects of torque pulsations, such as mechanical resonance and speed ripple, become increasingly significant at low speed operation, where it may be necessary to eliminate an increasing number of voltage harmonics by using a higher number of pulses. Since the off-line computation of numerous switching angles for a conventional optimal PWM switching strategy is lengthy, natural or regular PWM strategies with a high switching frequency have sometimes been preferred in the past.

With the CSI, commutation constraints have restrained the implementation of PWM strategies with high pulse-numbers. Other modulation techniques based on the instantaneous control of either the DC-link current [24,25] or the stator current [26] were suggested to achieve lower torque pulsations and smooth rotor motion at low frequency operation. Nevertheless, optimal PWM strategies were implemented following certain modulation rules devised according to the power-circuit topology of the

CSI [24,27]. These rules however appear to be unnecessarily restrictive, and they have been revised to permit the implementation of various PWM patterns [28] which either eliminate low order harmonics from the stator current waveform or minimise its harmonic content [27-34]. Other optimal PWM strategies have emphasised the reduction of torque pulsations, rotor speed ripple and positional error [26,32-34].

Recent research on optimal PWM controlled CSI drives [26,30-34] has concluded that eliminating all harmonics below a given frequency over the whole speed range is not necessarily optimal, in terms of minimising torque pulsations, speed ripple or positional error. Indeed, when low order harmonic current components are eliminated high order components are significantly increased, which produce significant torque pulsations. Alternative PWM strategies minimise a weighting function for any performance criterion, perform the required optimization and reduce low order harmonic components without resulting in increased high order harmonics as experienced in the harmonic elimination case. Furthermore, since the torque waveform conforms to the current waveform pattern of a CSI, torque pulsations may be controlled by appropriate positioning of the switching angles to control the harmonics of the PWM current waveforms [32,34].

1.2 Stating the Problem

In certain AC traction drives, a VSI controlled induction motor is favoured [35,36], with an elimination optimal PWM strategy employed for most of the frequency range in preference to a natural or regular switching strategy for the following reasons:

(1) For a given pulse-number or switching frequency, the order of the first voltage harmonic remaining is almost double that when using natural or regular switching strategies.

(2) A higher fundamental voltage component is obtained before the minimum pulse width limit is reached, which is analogous to the pulse dropping technique for the other two strategies. At high frequencies, the optimal strategy thus provides better utilisation of the attainable DC-link voltage, extends the region of constant airgap flux and provides a smoother transition to the QSW mode of operation.

During low frequency operation, the higher switching frequency may however increase the inverter switching losses. The analytical simplicity of the optimal PWM strategy, and its ability to be defined for any practical performance criterion, make it appropriate for optimization studies on VSI drive systems. In contrast with the CSI, the voltage harmonic components produce reduced harmonic currents due to the motor harmonic input impedance. This has two consequences on the dynamic performance of the drive system. Firstly, their contribution to the production of torque pulsations is reduced, and secondly there is no direct conformity between the torque and current waveforms as is the case with the CSI.

1.3 Thesis Objective

This thesis describes an extensive investigation into a PWM voltage source inverter/induction motor drive, with special emphasis on improving the dynamic performance, especially at low speeds where torque pulsations produce uneven shaft rotation.

Using novel optimal PWM techniques, torque pulsation problems are to be minimized by mutual cancellation between harmonic torque components. Comparative evaluation of the drive performance obtained when using these techniques is to be made with that obtained using the conventional elimination optimal PWM technique.

1.4 Computer Aided Design and Analytical Methods

The simulation of drive systems using advanced mathematical modelling techniques provides a powerful tool in system design. Many studies have investigated the transient and steady-state performance of induction motor drives using both time and frequency-domain methods.

Time-domain methods require the numerical solution of sets of nonlinear differential equations representing the electrical and mechanical performance of the drive. The assembly of these equations requires logic checks at each time increment, to determine the conducting state of the inverter devices and the corresponding circuit topology. Some studies employed 2-axis machine models [37-42] due to their simplicity and low computational requirements, while others opted for the direct-phase model [43-47]. This latter model can account for the imperfections of an actual machine, which a 2-axis model cannot, with space harmonics in the airgap magnetic field and the effects of magnetic saturation being easily included. Furthermore, it is ideally suited to simulate the switching operation of the inverter devices.

The frequency-domain method has the merits of simplicity and efficiency in steady-state performance prediction [48-54]. It is based on a Fourier-series expansion of the inverter output voltage waveforms, in conjunction with the harmonic equivalent circuit of the induction motor. Each harmonic component is applied to a circuit whose frequency dependent parameters are adjusted according to the order of the input harmonic.

1.5 Thesis Organisation

Chapter 2 outlines the conventional equivalent circuit of the induction motor and its analytical equations for steady-state operation. It presents the theoretical concepts behind different methods of variable-speed operation, and introduces VSIs and CSIs with a brief comparison between the two types.

Chapter 3 surveys variable speed induction motor drives using a VSI with QSW and PWM switching modes. A detailed analysis and mathematical algorithms are presented for both regular and optimal PWM switching strategies. The chapter also describes an optimization process which eliminates particular inverter output voltage harmonics. Sets of switching angles are obtained for the elimination of successive pairs of harmonics. The contribution of both voltage and current harmonics to the motor losses, and the degradation of the mechanical dynamic performance, are explained.

Chapter 4 describes the experimental inverter/induction motor drive system used in the experimental work of the thesis. Emphasis is given to the switching characteristics and the gate drive circuit for the GTO thyristors used as switches in the inverter bridge. A unique digital technique is described, based on a look-up table for storing the inverter device switching patterns for any operating mode.

In chapter 5 tensor techniques are used in the development of a comprehensive mathematical model for a VSI/induction motor drive. Steady-state results obtained using this model are presented and compared with corresponding practical results.

Chapter 6 is concerned with the development of an analytical model based on conventional equivalent circuit analysis. An electromagnetic torque expression is derived, from which instantaneous torque and other weighing functions of speed ripple and positional error are obtained. Results from this

analysis are presented and verified by comparison with those obtained using the mathematical model developed in the previous chapter.

Chapter 7 describes new techniques by which the cancellation or minimisation of harmonic torque components is achieved, without eliminating completely either the voltage or current components responsible for them.

Chapter 8 compares results provided by both the comprehensive mathematical model and the frequency-domain model developed in chapters 5 and 6 respectively. It evaluates these using different performance indices between the strategies developed in the thesis and the conventional elimination strategy. It stresses the superiority of the new approach in reducing the extent of torque pulsations and speed ripple during low frequency operation, at the same time maintaining a low number of pulses.

Conclusions and suggestions for further work are given in chapter 9.

CHAPTER 2

3-PHASE INDUCTION MOTOR SPEED CONTROL

This chapter briefly describes the basic methods of induction motor speed control. The equivalent circuit which forms a fundamental building block for the analysis is described and results are presented for this circuit using the parameters given in appendix A.1.

2.1 Per-Phase Equivalent Circuit

The per-phase equivalent circuit of an induction motor under balanced steady-state conditions is shown in figure 2.1(a). The rotor frequency/speed relationship applied to this model is defined as

$$\omega_r = \omega_s - p\omega_m \qquad 2.1$$

where ω_r = angular frequency in the rotor circuit.
ω_s = angular frequency in the stator circuit.
ω_m = mechanical speed of rotation.
p = number of pair of poles.

The rotor slip with respect to the fundamental rotating field is defined as

$$s = \frac{\omega_r}{\omega_s} = \frac{\omega_s - p\omega_m}{\omega_s} \qquad 2.2$$

Assuming the stator and rotor windings have the same number of turns and winding arrangement

$$N_s K_{ws} = N_r K_{wr} \qquad 2.3$$

where N_s and N_r are respectively the effective number of stator and rotor turns per phase and K_{ws} and K_{wr} are their winding factors. The stator and rotor emfs are related by the equation

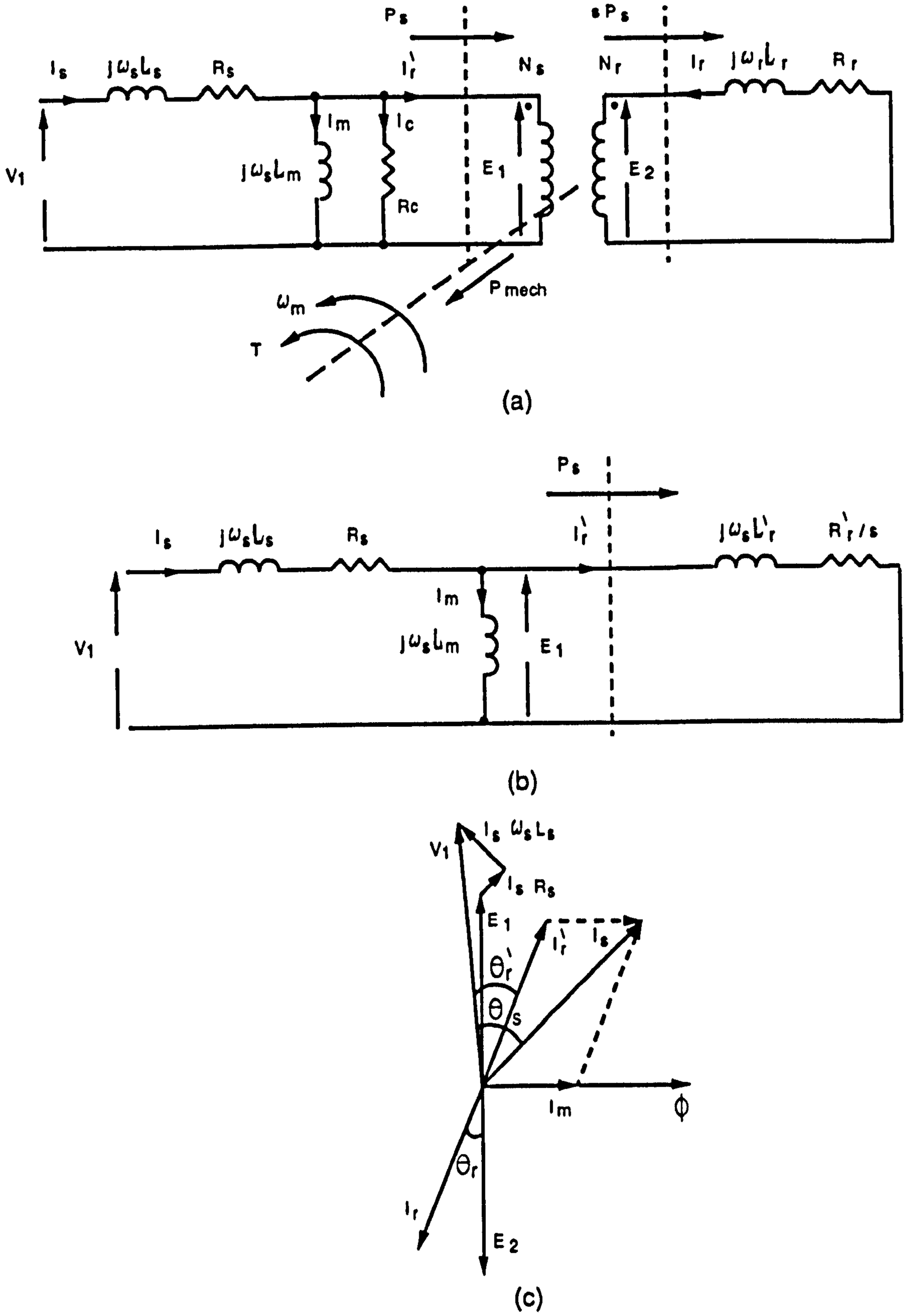

Figure 2.1 (a) Induction motor per-phase equivalent circuit
(b) Equivalent circuit referred to the stator neglecting stator iron loss
(c) Phasor diagram of the induction motor neglecting stator iron loss

$$\bar{E}_2 = s\bar{E}_1 \frac{N_r K_{wr}}{N_s K_{ws}} = s\bar{E}_1 \qquad 2.4$$

and the rotor current is given by

$$\bar{I}_r = \frac{\bar{E}_2}{R_r + js\omega_s l_r} \qquad 2.5$$

where R_r and l_r are the rotor winding resistance and leakage inductance per phase. The rotor current phase angle with respect to E_2 is

$$\theta_r = \tan^{-1} \frac{s\omega_s l_r}{R_r} \qquad 2.6$$

The stator current is given by

$$\bar{I}_s = \frac{\bar{V}_1 - \bar{E}_1}{R_s + j\omega_s l_s} \qquad 2.7$$

where $\bar{V}_1$ is the rms terminal phase voltage and R_s and l_s are the stator winding resistance and leakage inductance per phase. Substituting equation 2.4 in 2.5 and dividing throughout by s gives

$$\bar{I}_r = \frac{\bar{E}_1}{(R_r/s) + j\omega_s l_r} \qquad 2.8$$

This mathematical manipulation constrains the frequency of the rotor circuit to that of the supply frequency and the equivalent circuit resembles that of a single phase transformer, which is a first stage to joining the rotor and stator circuits directly.

The ideal transformer between the rotor and stator equivalent circuits shown in figure 2.1(a) is conveniently eliminated by referring the rotor circuit to the stator as shown in figure 2.1(b), where

$$I_r' = \frac{N_r K_{wr}}{N_s K_{ws}} I_r \quad .$$

$$\frac{R_r'}{s} = \left(\frac{N_s K_{ws}}{N_r K_{wr}}\right)^2 \frac{R_r}{s} \qquad 2.9$$

$$l_r' = \left(\frac{N_s K_{ws}}{N_r K_{wr}}\right)^2 l_r \quad .$$

The resistance R_c is included to account for iron losses and is used when calculating the values of other circuit parameters. Nevertheless, it is often omitted from the model, as shown in figure 2.1(b), since its value is sufficiently large to have little effect on calculations of the stator and rotor currents.

A phasor diagram representing the machine variables is shown in figure 2.1(c) where the magnetizing current I_m is taken as the reference phasor, with the stator back emf E_1 leading I_m by $90°$. The current I_m sets up the airgap magnetic flux and is maintained constant for a constant flux under different operating conditions, as is explained later. The current I_r' is the load component of the stator current which neutralizes the rotor mmf and lags E_1 by the rotor power factor angle θ_r. The stator current I_s is the phasor sum of I_m and I_r'.

The effective rotor resistance R_r'/s is split into the two components R_r' and $R_r'(1-s)/s$. This illustrates that the power transferred across the airgap or the input power to the rotor P_s comprises the sum of the rotor copper loss P_{loss} and the power available to do mechanical work P_{mech}. Thus

$$P_s = R_r' I_r'^2 + \frac{1-s}{s} R_r' I_r'^2 \qquad 2.10$$

where

$$P_{loss} = R_r' I_r'^2 \qquad 2.11$$

and

$$P_{mech} = \frac{1-s}{s} R_r' I_r'^2 \qquad 2.12$$

The electromagnetic torque T_e is related to the gross output mechanical power P_{mech} by

$$T_e \omega_m = 3\left(\frac{1-s}{s} R_r' I_r'^2\right) \qquad 2.13$$

Substituting for I_r' from equations 2.8 and 2.9 into equation 2.13 and re-arranging gives the electromagnetic torque as

$$T_e = \frac{3}{\omega_s} p s E_1^2 \frac{R_r'}{R_r'^2 + (s\omega_s l_r')^2} \qquad 2.14$$

This is the internal motor torque, which is greater than the useful shaft torque by the amount required to overcome the windage and transmission loss. For constant terminal voltage and frequency, and neglecting the stator voltage drops, E_1 is constant for all load conditions and the only variable in equation 2.14 is the slip s. The maximum torque and the slip at which this occurs may be determined by equating dT_e/ds to zero to give

$$s_{max} = \mp \frac{R_r'}{\omega_s l_r'} \qquad 2.15$$

where the positive and negative signs relate respectively to motor and generator operation. Substituting the value of $+s_{max}$ in equation 2.14 gives the maximum electromagnetic torque as

$$T_{e\,max} = 3 \frac{p}{2} \frac{E_1^2}{\omega_s^2 l_r'} \qquad 2.16$$

and setting $s = 1$ in equation 2.14 gives the starting torque as

$$T_{e,a} = \frac{3}{\omega_s} p E_1^2 \frac{R_r'}{R_r'^2 + (\omega_s l_r')^2} \quad 2.17$$

2.2 Induction Motor Speed Control

Induction motor speed control has long been seen as desirable and numerous methods of obtaining stepped or continuous speed change have been developed. The principles behind some of these are discussed briefly below.

2.2.1 Pole Changing

From equation 2.1 it is evident that changing the number of poles results in a change in the motor speed. This may be achieved by providing a squirrel cage machine with two stator windings arranged for different numbers of poles. Figure 2.2 shows one phase of a 4-pole winding, with two coils per phase. If the current in one coil is reversed, the mmf pattern results in a 2-pole distribution and a 2:1 change in the synchronous speed. Pole amplitude modulation [55] is a more versatile technique, whereby modulation of the amplitude of the mmf produced by each stator phase is used to produce mmf distributions with different pole numbers.

2.2.2 Rotor Resistance Variation

Equation 2.15 shows that if the rotor resistance is varied, the slip at which maximum torque occurs will change. To control speed by this method requires a wound rotor induction motor, in which additional resistance may be inserted in the rotor circuit as shown in figure 2.3(a). The effective rotor resistance may also be varied electronically either by an AC phase-controlled circuit or by a diode rectifier and a chopper. A family of torque-speed curves for various values of the rotor resistance is shown in figure 2.3(b). Stable operation occurs at the intersection of the motor torque and load torque curves.

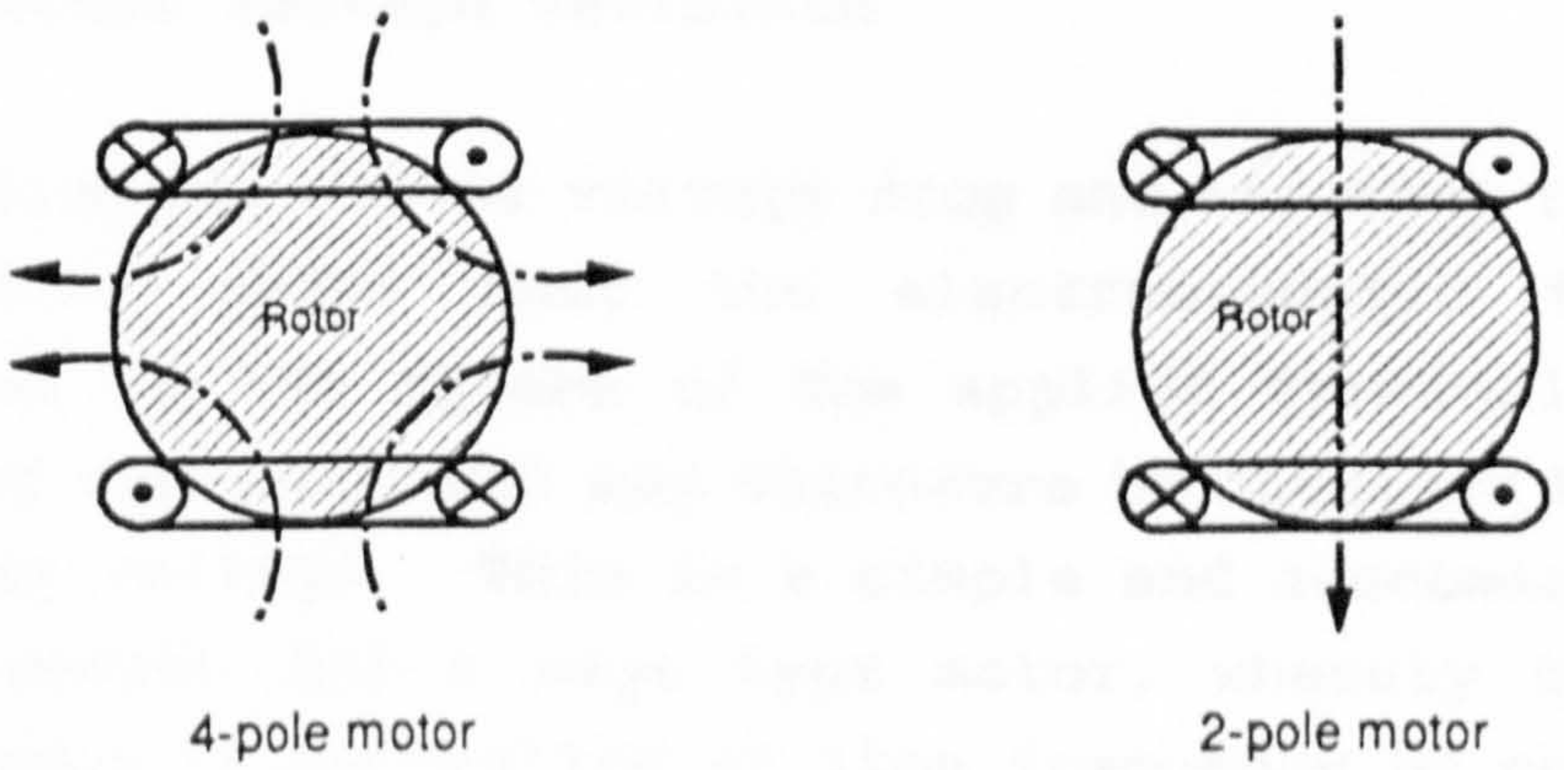

4-pole motor 2-pole motor

Fig 2-2 Pole Changing Winding

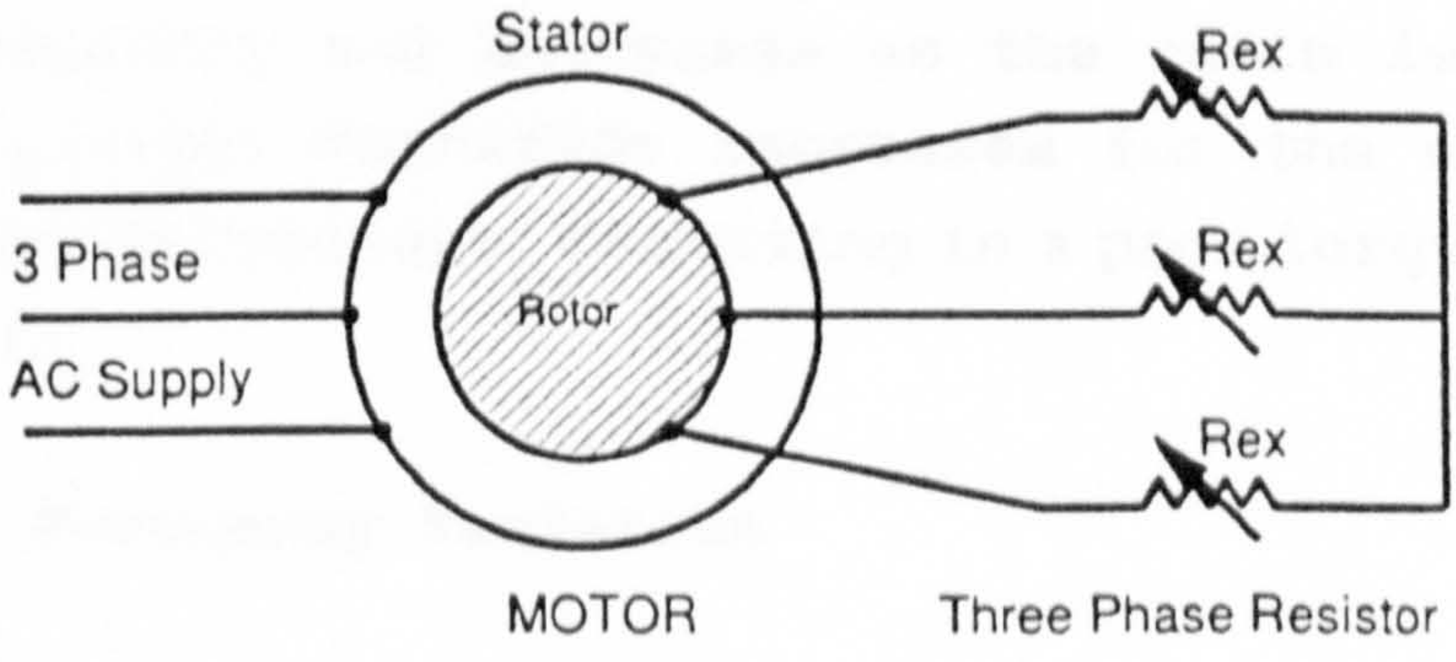

(a)

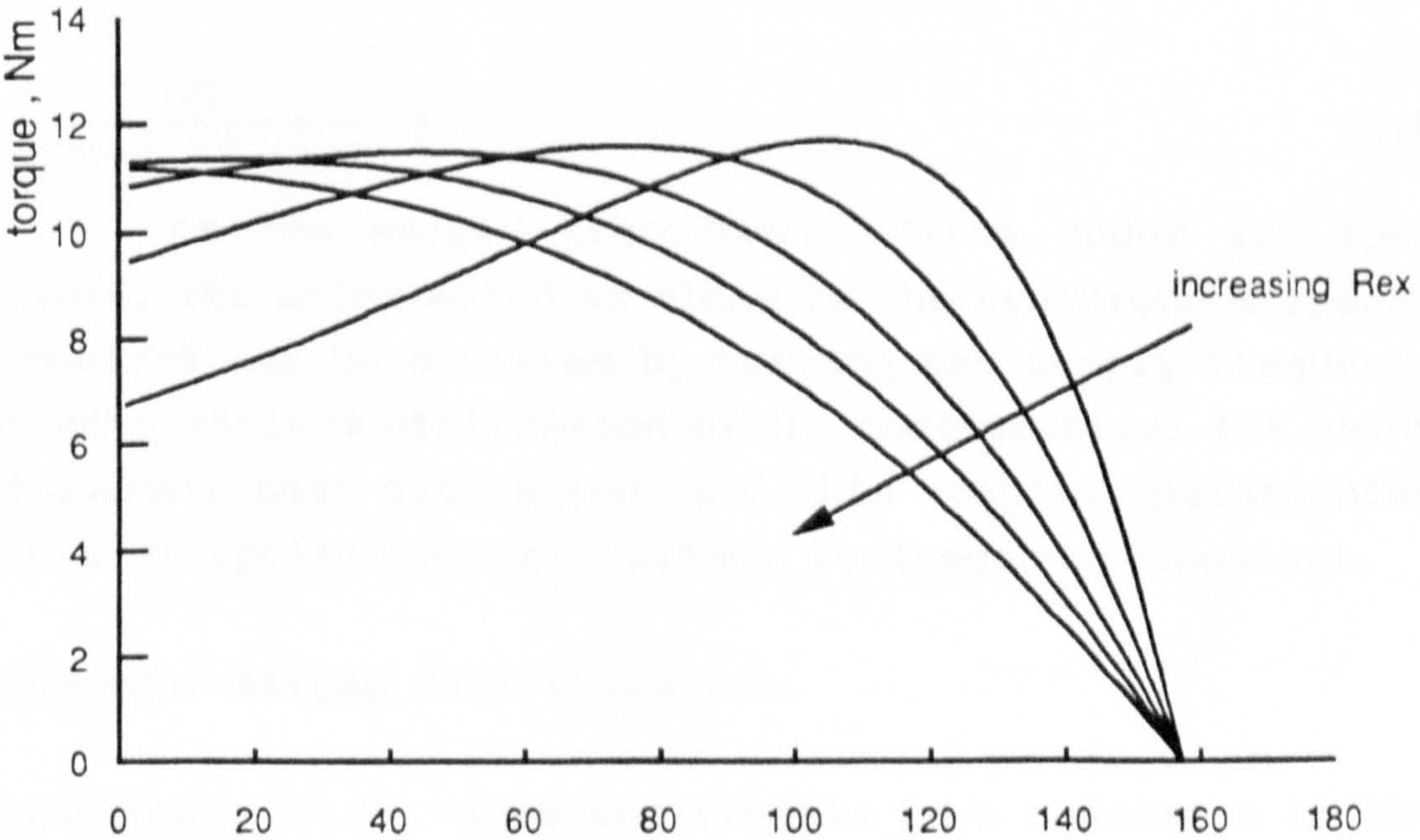

(b)

Figure 2.3 Speed control of wound-rotor induction motor
by variation of external rotor-circuit resistance
(a) External rotor-circuit resistance
(b) Torque-speed characteristics with variable rotor resistance

2.2.3 Terminal Voltage Variation

Neglecting the stator voltage drop and assuming that $E_1 = V_1$, equation 2.14 shows that the electromagnetic torque is proportional to the square of the applied terminal voltage. A measure of speed control may therefore be obtained by varying the terminal voltage. This is a simple and economical method of speed control for a cage type motor, whereby the stator supply voltage is controlled at line frequency by controlling the trigger angle of the AC controller shown in figure 2.4(a). The resulting torque-speed curves have the form shown in figure 2.4(b). The airgap flux is related to the ratio of stator voltage to frequency and decreases as the ratio is reduced. However, the current magnitude increases for the same value of torque at reduced voltage, resulting in a poor torque-current characteristic.

2.2.4 Supply Frequency Variation

The synchronous speed of an induction motor is given by

$$n_s = \frac{120}{number\ of\ poles} f_s \qquad 2.18$$

where f_s is the supply frequency. Since under all load conditions, the motor speed is close to the synchronous speed, speed control may be achieved by varying the supply frequency f_s. To give maximum utilization of the core material the motor should operate near saturation, and this requires maintaining the ratio of applied stator voltage to frequency constant.

2.3 Constant Airgap Flux Operation

Maintaining V_1/f_s constant results in a reduction in the airgap flux at low frequencies, due to the increased influence of the voltage drop in the stator resistance. The corresponding torque-speed characteristics shown in figure 2.5(a) illustrate the reduction in the maximum torque as the stator supply frequency is reduced.

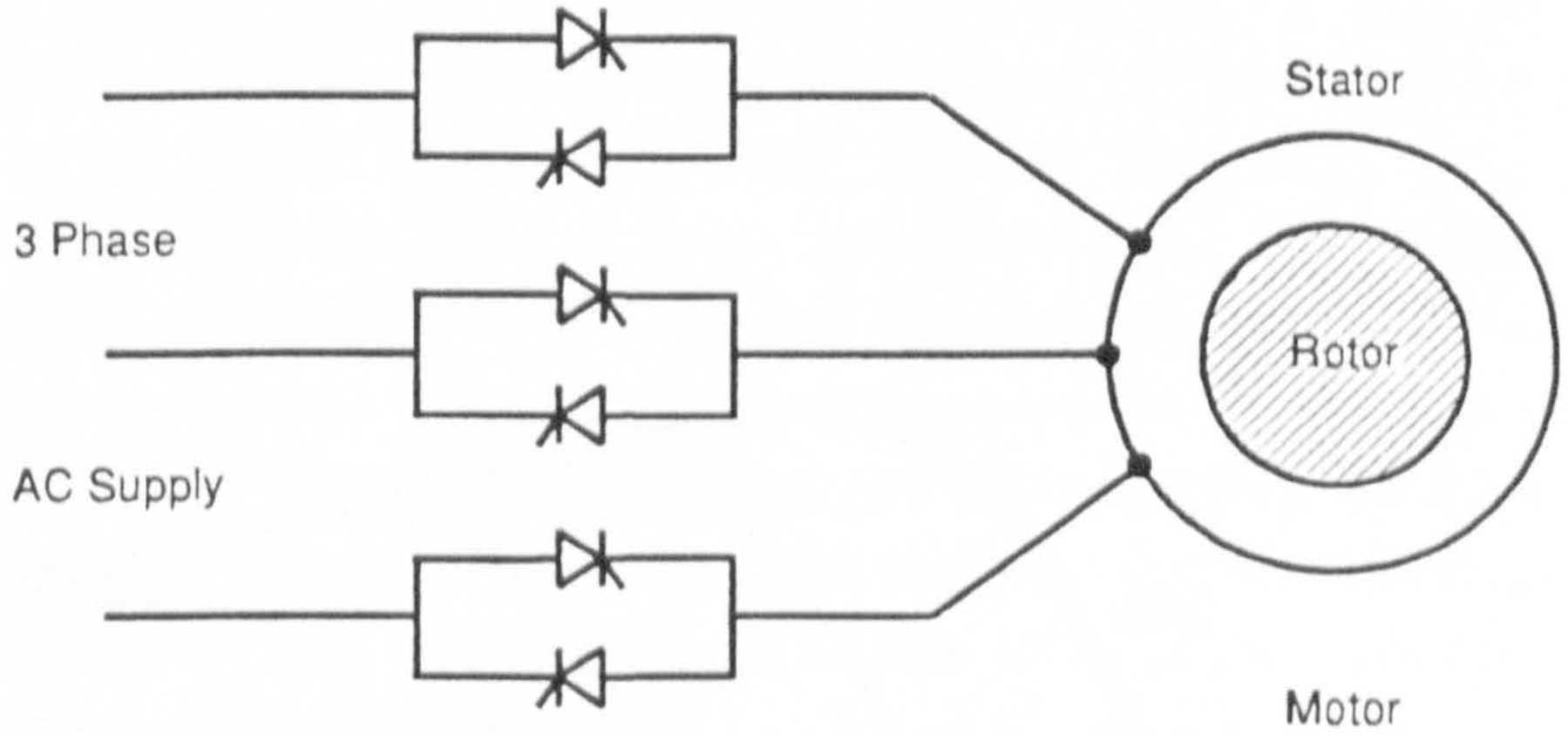

(a)

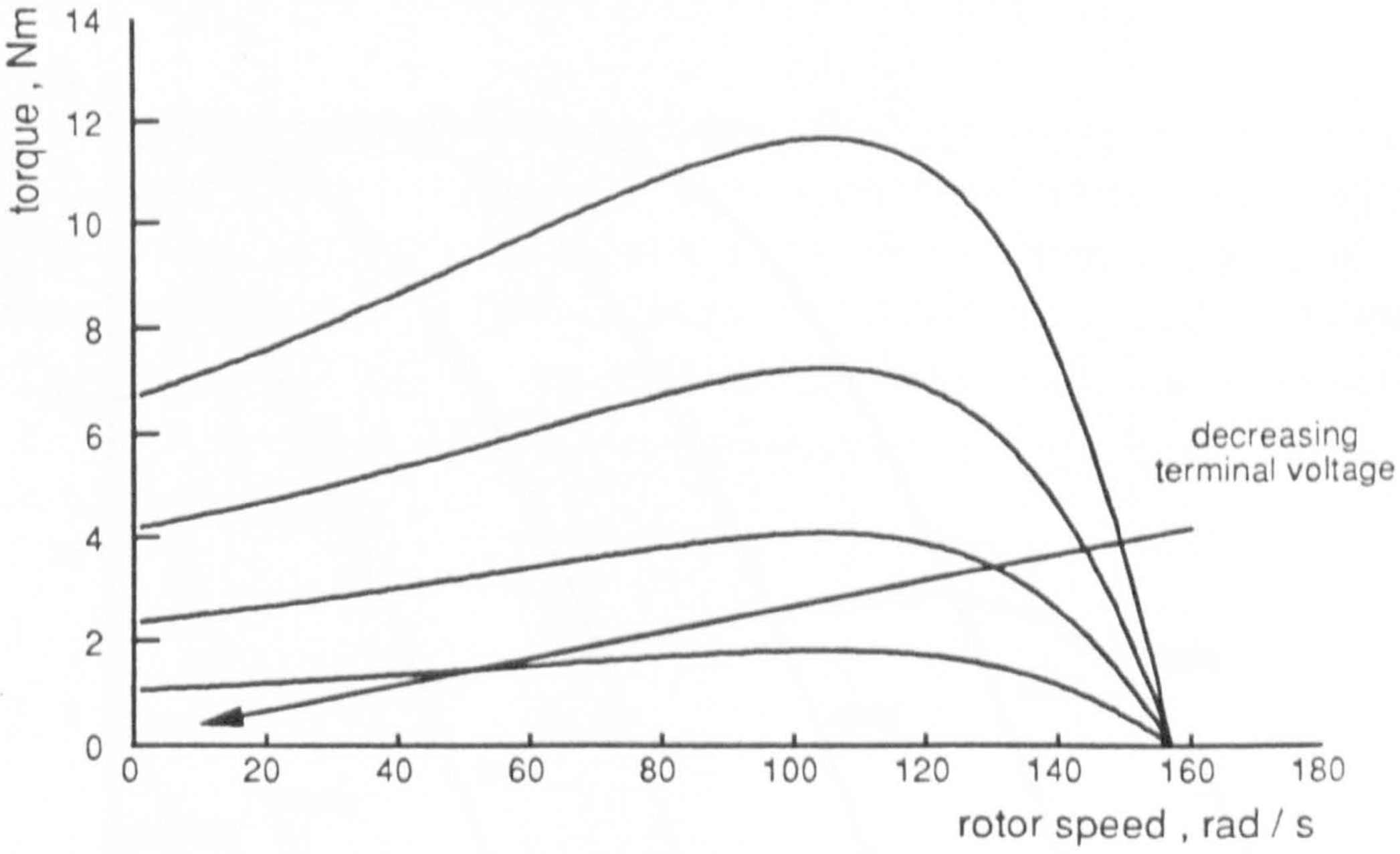

(b)

Figure 2.4 Speed control by variation of terminal voltage
(a) AC terminal voltage controller
(b) Torque-speed characteristics with terminal voltage variation

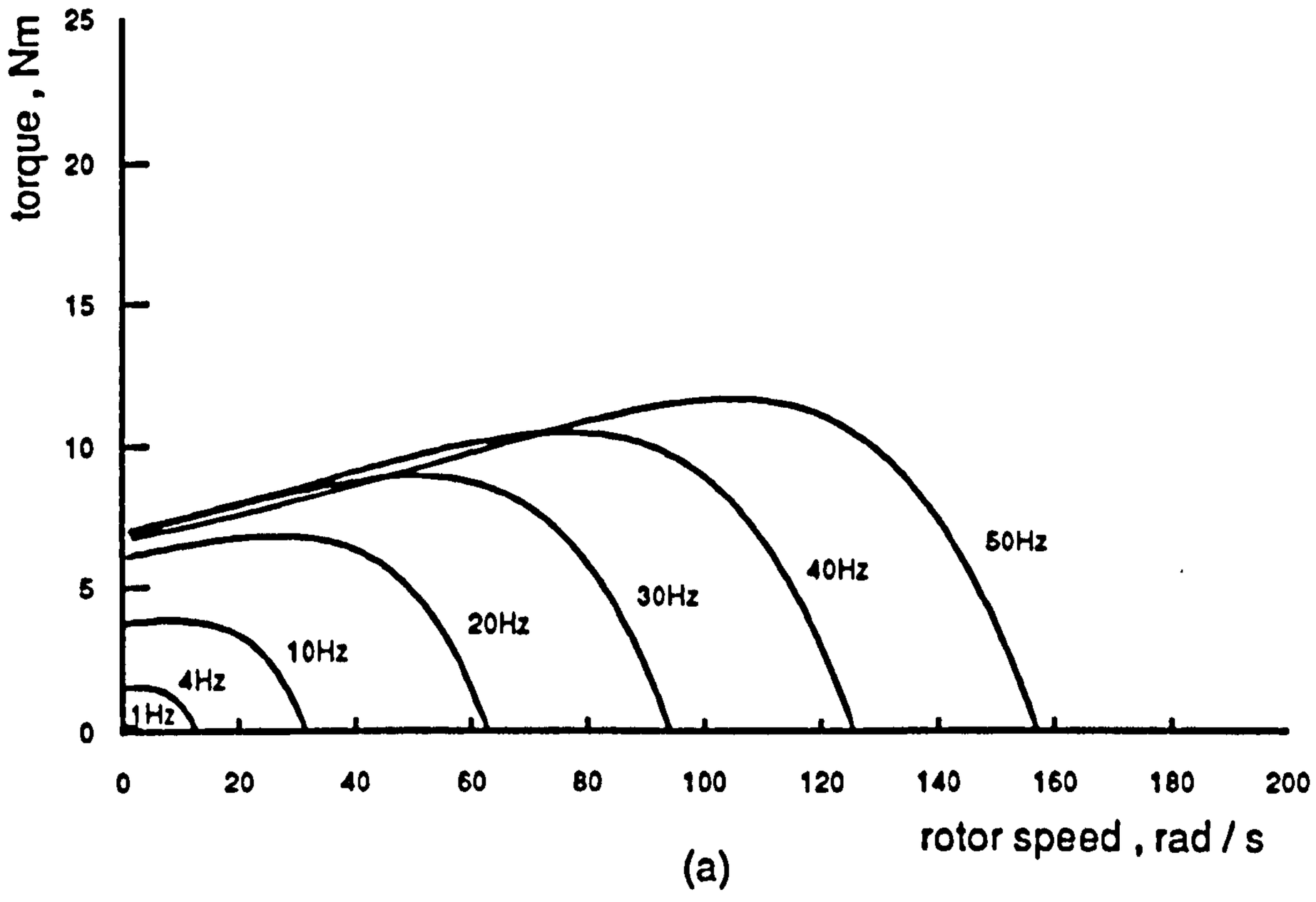

Figure 2.5 Torque-speed characteristics for variable-frequency operation of induction motor with
(a) Constant terminal-voltage / frequency ratio
(b) Constant airgap-voltage / frequency ratio

If the E_1/f_1 ratio is kept constant, I_m is constant at the value corresponding to full-load operation at rated voltage and frequency [56]. Equation 2.16 shows that the maximum torque and the product $s\omega$, at which it occurs are also constant, resulting in the parallel characteristics shown in the lower part of figure 2.5(b). Theoretically, the motor operating point may move over much of the plane bounded by the characteristics of this figure but, in practice, operation is restricted to conditions under which the stator current will not overheat the motor. During motor operation, the machines ability to provide rated load torque at low supply frequency is confined by the slope of the characteristics which represents the maximum slip-speed obtainable before the motor stalls or enters the generating quadrant. If the supply frequency increases above the rated value, the terminal voltage is held constant at the rated value and the ratio E_1/f_1 and consequently the maximum torque decreases. This corresponds to field weakening of a separately excited DC machine.

The required terminal voltage may be determined for different operating frequencies and load conditions by first calculating E_1 at rated terminal voltage and frequency under full-load conditions. The analysis below is based on the equivalent circuit shown in figure 2.1(b). Taking the rms terminal voltage as the reference phasor, the full-load stator current is obtained from

$$\bar{I}_1 = \frac{\bar{V}_1}{\bar{Z}_1} \qquad 2.19$$

where the input impedance $\bar{Z}_1$ is

$$\bar{Z}_1 = R_s + jX_s + \frac{jX_m((R_r'/s)+jX_r')}{(R_r'/s)+j(X_m+X_r')} \qquad 2.20$$

The phase angle of the stator current with respect to the terminal voltage V_1 is

$$\theta_s = - \tan^{-1} \frac{\Im Z_i}{\Re Z_i} \qquad 2.21$$

where $\Re Z_i$ and $\Im Z_i$ are respectively the real and imaginary parts of the input impedance. The stator voltage drop $\bar{V}_s$ is then calculated using

$$\bar{V}_s = \bar{I}_s \cdot (R_s + jX_s) \qquad 2.22$$

in which the magnetizing branch voltage $\bar{E}_1$ is given by

$$\bar{E}_1 = \bar{V}_1 - \bar{V}_s \qquad 2.23$$

The ratio E_1/f_s may now be calculated and fixed for use in obtaining the terminal voltage V_1 required for other operating frequencies or load conditions. At any other operating frequency f_s'' and slip s'', E_1'' is obtained from

$$E_1'' = \frac{E_1}{f_s} \cdot f_s'' \qquad 2.24$$

and is taken as the reference phasor when calculating the new stator current from

$$\bar{I}_s'' = \bar{E}_1'' \cdot \frac{(R_r'/s'') + j(X_m'' + X_r'')}{jX_m''((R_r'/s'') + jX_r'')} \qquad 2.25$$

in which all reactances have to be corrected for the new operating frequency. Using equations 2.22 and 2.23 the new terminal voltage $\bar{V}_1''$ may then be calculated. The stator current phase angle θ_s'' must be taken with respect to $\bar{V}_1''$ and not to $\bar{E}_1''$ as calculated from equation 2.25. The terminal voltage necessary to maintain a constant flux density is a function of the stator frequency f_s and the load. Curves of terminal voltage as a function of stator frequency are plotted

in figure 2.6, using the machine parameters given in appendix A.1, and the load dependent increase in terminal voltage is evident.

2.4 Frequency Converters

Of the methods mentioned above, only the variable frequency supply provides a continuous, efficient and wide range of speed control. The advent of power semiconductor devices has led to the development of static frequency changers specifically to provide this form of supply.

The cycloconverter converts the mains AC supply to a variable frequency lower than that of the supply, and consequently its implementation is restricted to low-frequency applications. The most common variable frequency drive employs a DC-link inverter, with the AC supply being first converted to DC by either a controlled or an uncontrolled rectifier and then inverted to produce a variable voltage, variable frequency supply. The basic switching action of the inverter normally results in non-sinusoidal output voltage and current waveforms rich in undesirable harmonics which degrade the motor performance. The two most common inverter types are termed current source and voltage source inverters.

2.4.1 Current Source Inverter

The current source inverter (CSI) is supplied from a variable voltage DC source, such as a phase-controlled rectifier as shown in figure 2.7, which is effectively converted to a current source by a large series inductance. The DC-link current I_{dc} is switched through a pair of conducting devices, one in each half of the inverter. Basically, each device conducts continuously for 120° of the cycle and the gate-drive firing pattern is shown in figure 2.8, together with typical phase current and voltage waveforms for an inductive load. The CSI is an adjustable-frequency current source whose output current is load independent.

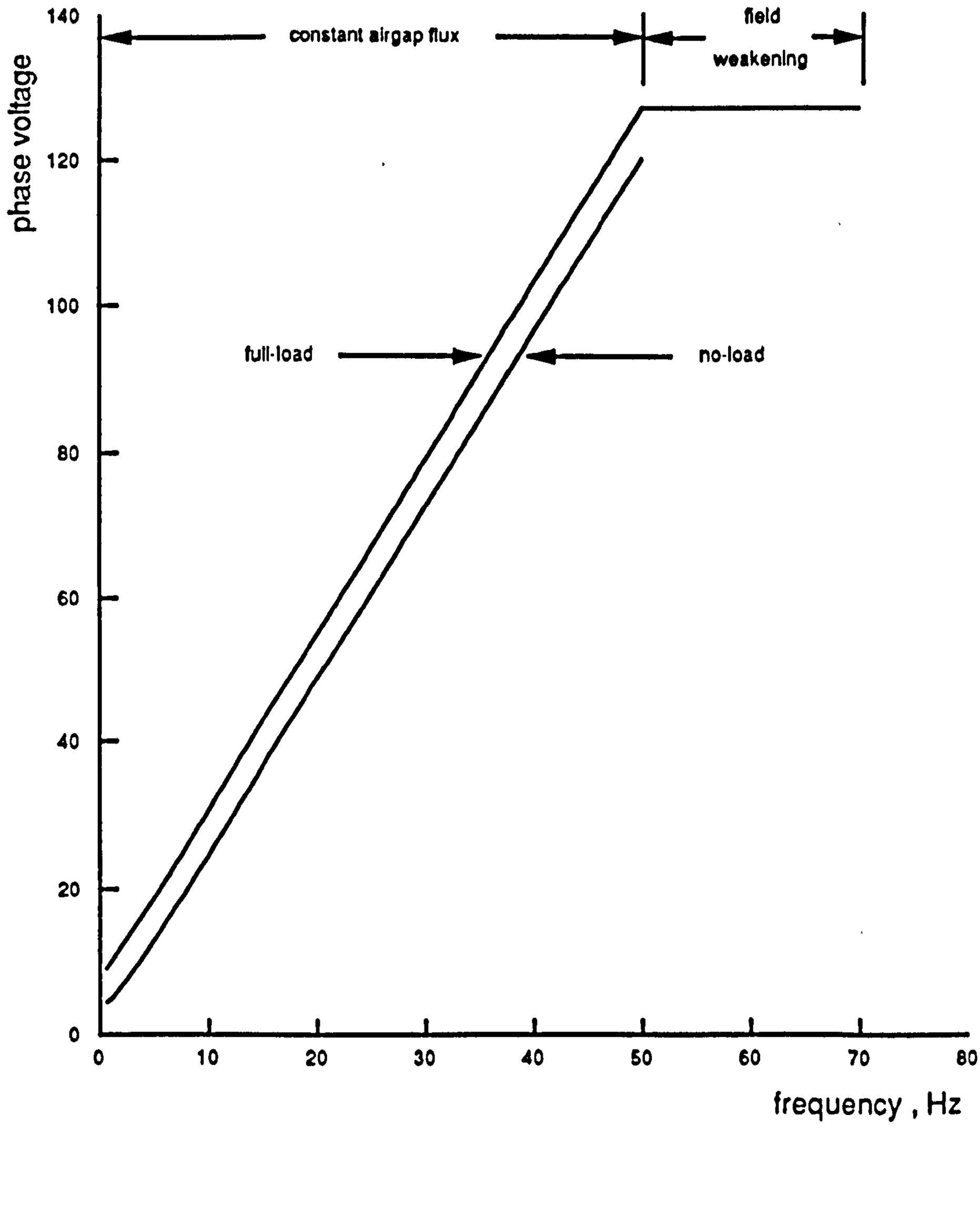

Figure 2.6 Phase-voltage / frequency characteristics during the constant airgap flux and field weakening regions.

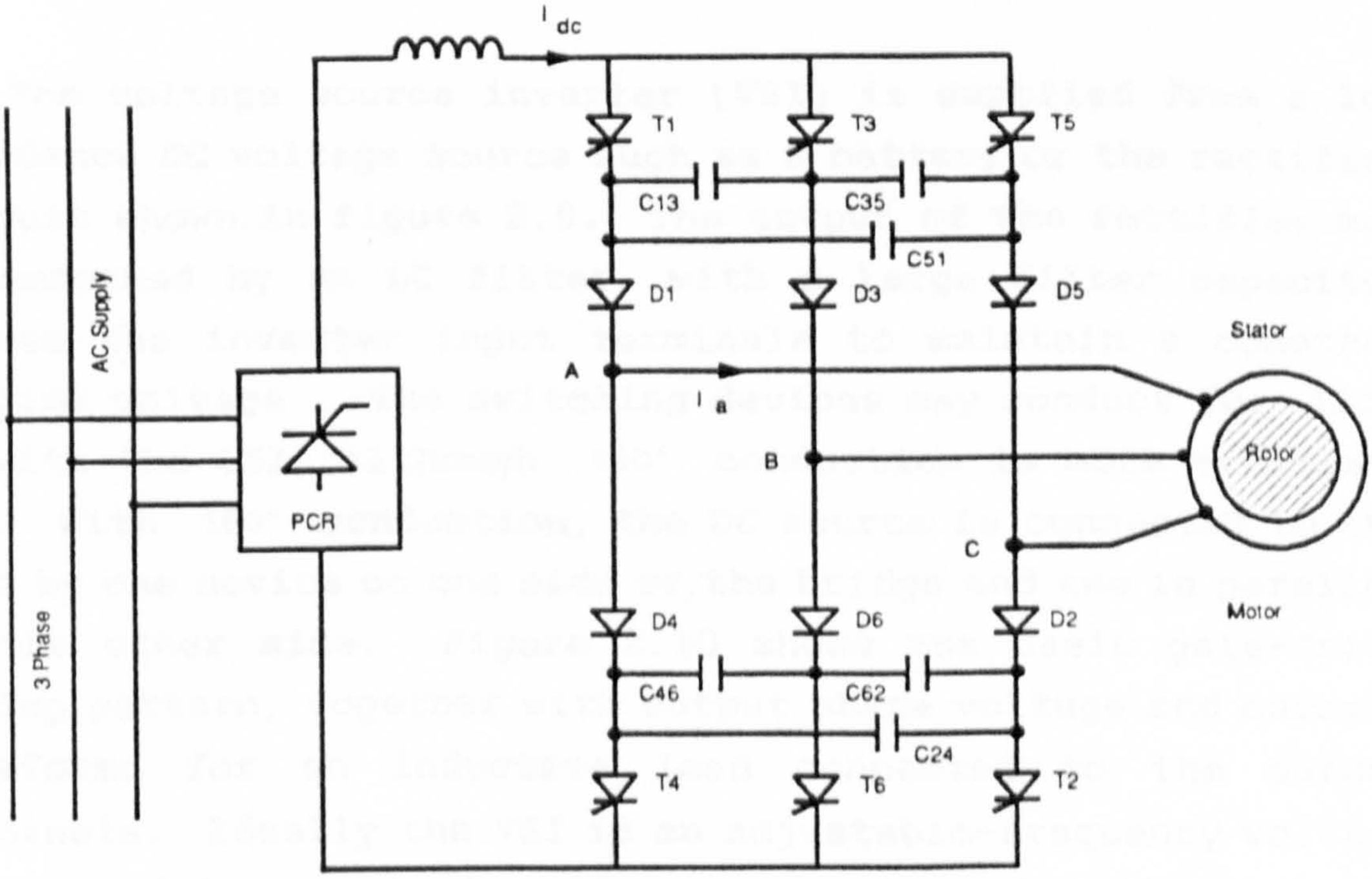

Figure 2.7 Phase controlled rectifier supplying a 3-phase CSI fed induction motor

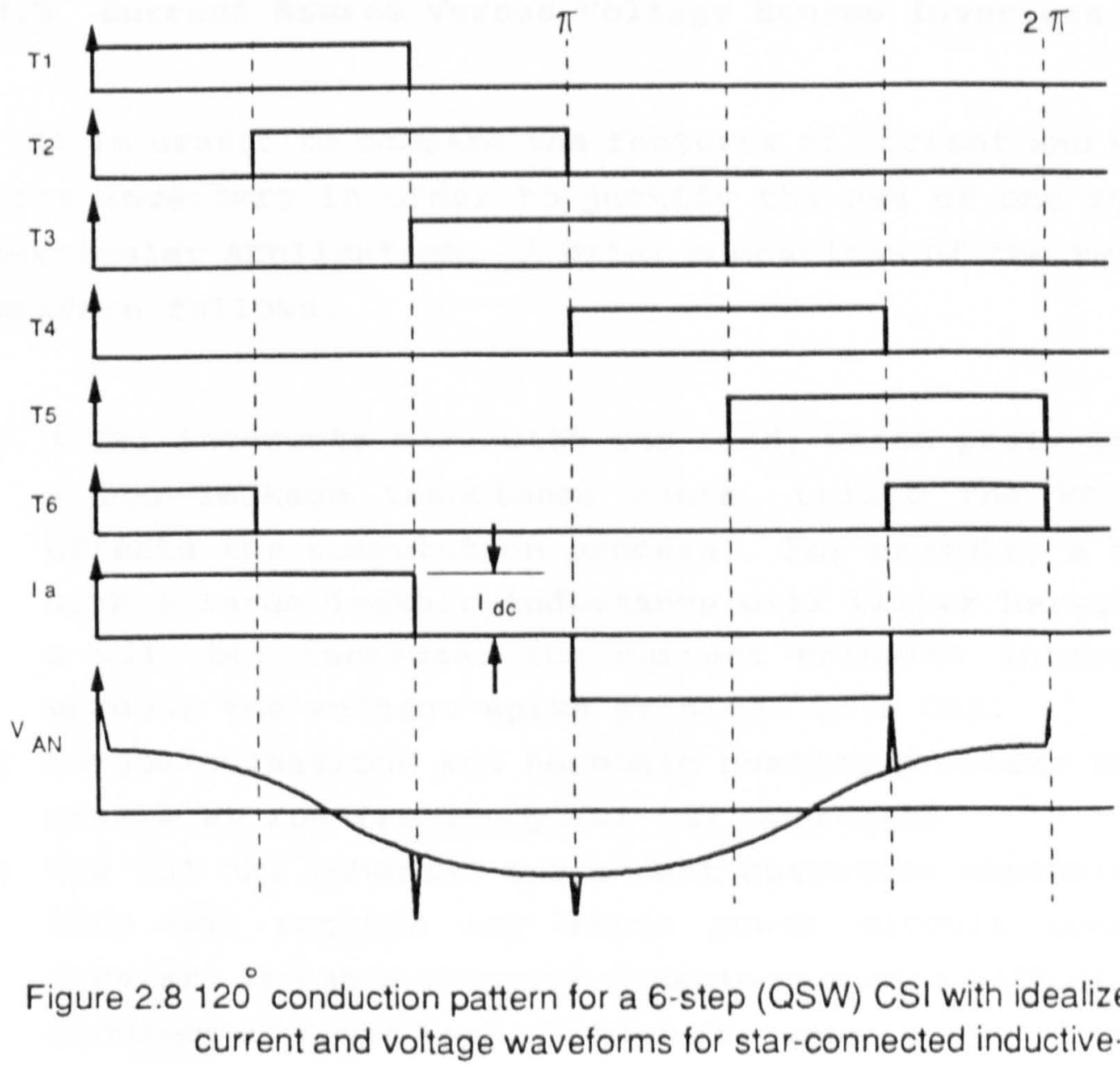

Figure 2.8 120° conduction pattern for a 6-step (QSW) CSI with idealized current and voltage waveforms for star-connected inductive-load

2.4.2 Voltage Source Inverter

The voltage source inverter (VSI) is supplied from a low impedance DC voltage source such as a battery or the rectifier circuit shown in figure 2.9. The output of the rectifier may be smoothed by an LC filter, with a large filter capacitor across the inverter input terminals to maintain a constant DC-link voltage . The switching devices may conduct for 120°, as with the CSI, although 180° conduction is more efficient [2]. With 180° conduction, the DC source is connected to the load by one device on one side of the bridge and two in parallel on the other side. Figure 2.10 shows the basic gate-drive firing pattern, together with output phase voltage and current waveforms for an inductive load connected to the output terminals. Ideally the VSI is an adjustable-frequency voltage source, with an output voltage which is independent of the load.

2.4.3 Current Source Versus Voltage Source Inverters

It is useful to compare the features of current and voltage source inverters in order to justify the use of one type for a particular application. A brief comparison of the two types therefore follows.

(a) A CSI interacts more with the load, which preferably has a low leakage inductance since, unlike the VSI, this effects the commutation process. For example, a machine with a large leakage inductance will filter harmonics in a VSI, but increases the current transfer interval and worsens the voltage spike problems in a CSI.
(b) Torque pulsations and harmonic heating problems are more severe at low frequency for CSI operation.
(c) The CSI has inherent 4-quadrant operation capability and does not require any extra power circuit component. However, it has a sluggish dynamic response with stability problems at light load and high frequency conditions making

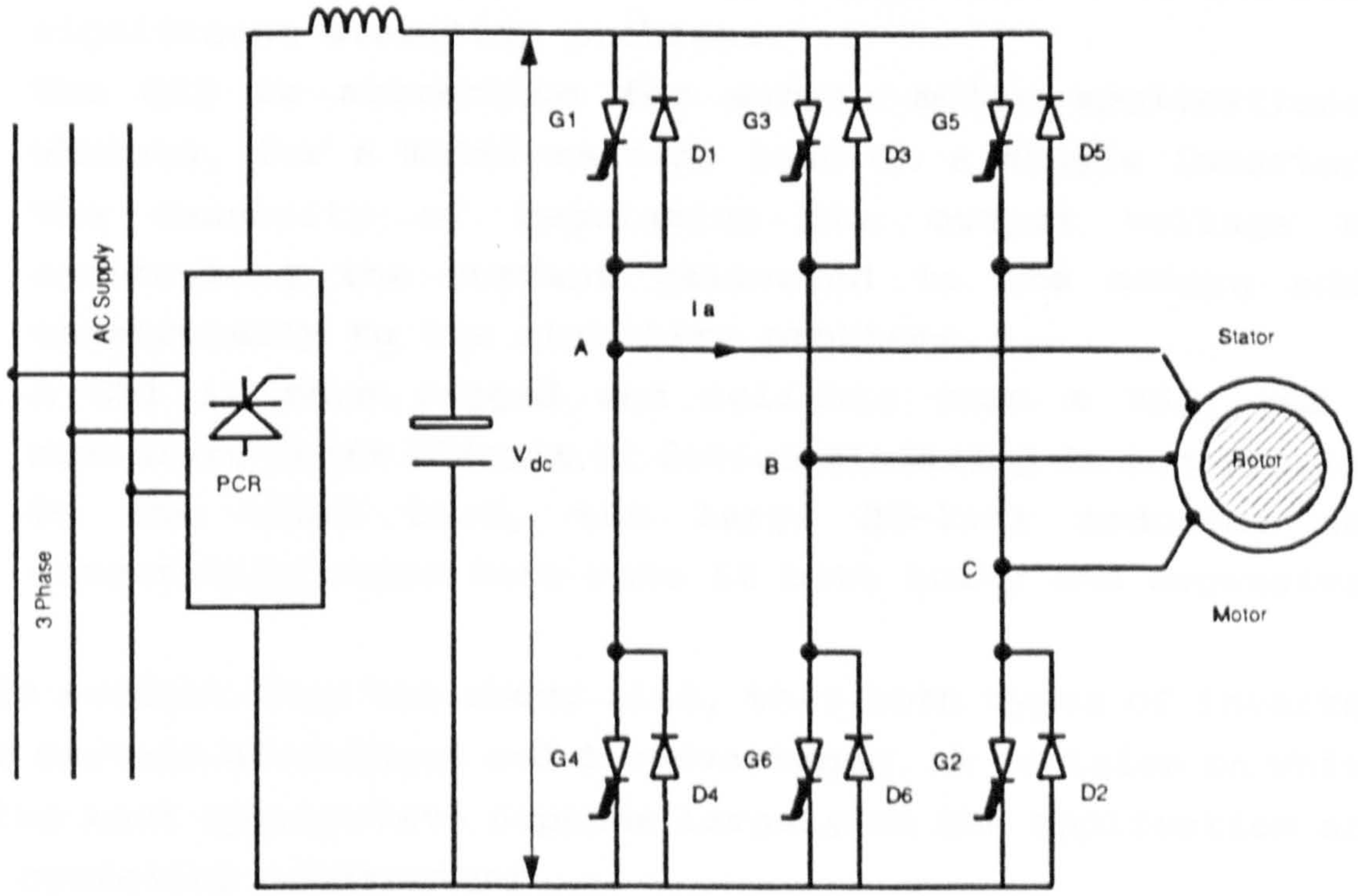

Figure 2.9 Phase controlled rectifier supplying a 3-phase VSI fed induction motor

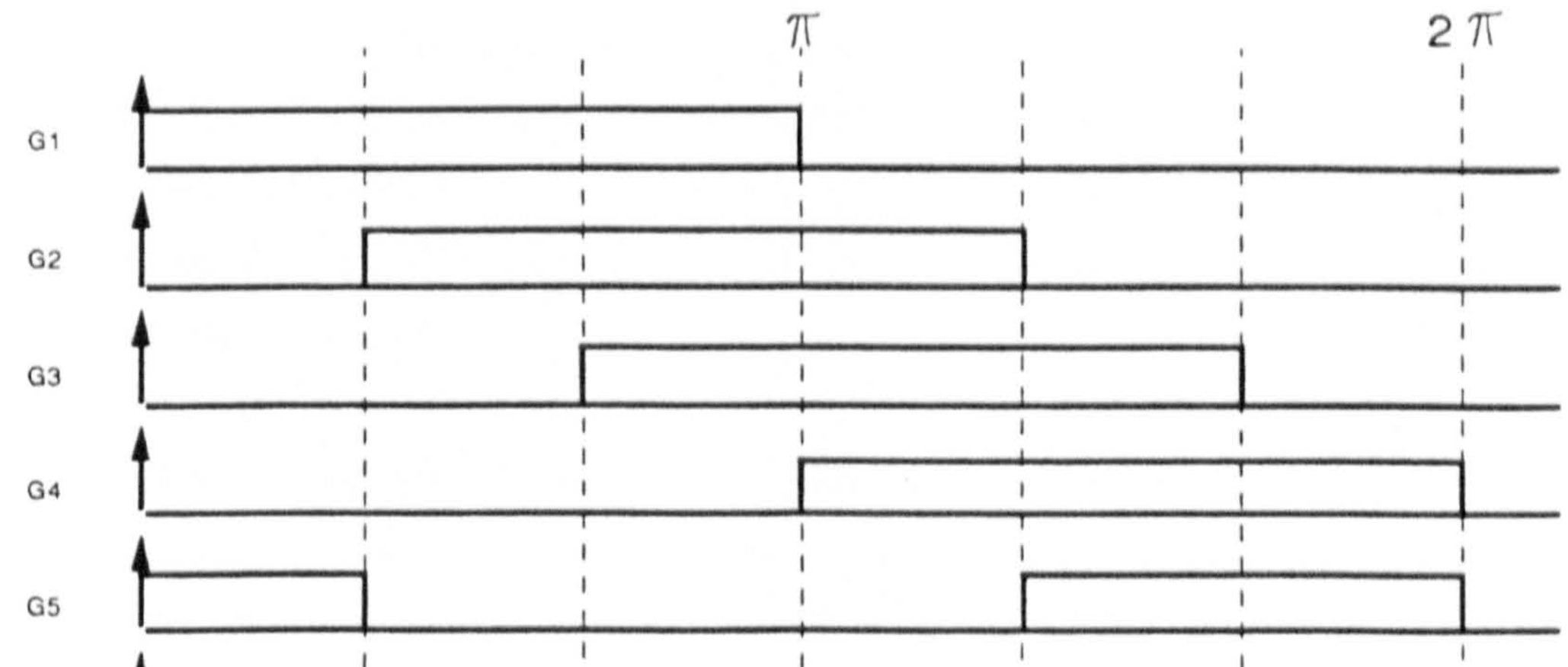

Figure 2.10 180 ^{o}conduction pattern for a 6-step (QSW) VSI with idealized voltage and current waveforms for star-connected inductive-load

closed loop operation essential. On the other hand, a VSI drive can be operated in open loop because of the less significant stability problems.

(d) The CSI is attractive for single motor applications, whereas, for a multi-machine load on a single inverter, the necessity of regulating the output voltage by controlling the current delivered to the motors adds considerably to the stability problems.

(e) A CSI is more rugged and reliable than a VSI, and a momentary short circuit or device misfiring is acceptable. On the other hand, the large DC-link inductor and commutating capacitors make it both bulky and expensive.

It is evident from the above list, that both types of inverter have certain advantages and disadvantages. A decision on which is the most appropriate depends largely on the application and the operating environment.

CHAPTER 3

VOLTAGE SOURCE INVERTER/INDUCTION MOTOR DRIVES

This chapter describes the operation of both QSW and PWM voltage source inverters. It presents a review of different PWM switching strategies, each with its own mathematical algorithm. Finally, it discusses the contribution made by voltage and current harmonic components in increasing the losses and in degrading the mechanical performance of the motor.

3.1 6-Step (QSW) Inverter Drive

Figure 2.9 illustrated the basic circuit configuration of a 3-phase VSI. The feedback or free-wheeling diodes provide reverse current paths such that, when a particular device is gated on, one output terminal and one input terminal are connected regardless of the direction of current. This is the topic of full discussion in chapter 5. In the analysis which follows, the presence of the rectifier and LC input filter of figure 2.9 is ignored. This enables the inverter to be regarded as fed from a DC supply voltage, leading to a simplified waveform analysis.

In the 6-step VSI, the gating signals result in 180° conduction for each switching device, as shown in figure 2.10 where the full cycle is divided into six separate modes. The conduction mode constraints define the output phase and line voltage waveforms. In the absence of a neutral current, and assuming a symmetrical 3-phase load such as an induction motor, the phase and line voltages may be determined. The Fourier-series representing these waveforms are respectively

$$v_{AN} = \frac{\sqrt{2}}{\pi} V_{dc}\left(\sin\omega t + \frac{1}{5}\sin 5\omega t + \frac{1}{7}\sin 7\omega t + \frac{1}{11}\sin 11\omega t + \frac{1}{13}\sin 13\omega t + \ldots\right) \quad 3.1$$

and

$$v_{AB} = \frac{\sqrt{6}}{\pi} V_{dc}\left(\sin\omega t - \frac{1}{5}\sin 5\omega t - \frac{1}{7}\sin 7\omega t + \frac{1}{11}\sin 11\omega t + \frac{1}{13}\sin 13\omega t - \ldots\right) \quad 3.2$$

where the origins of these two waveforms are chosen such that they are odd functions and consequently their Fourier-series expression contain sine terms only. Retaining only the fundamental components shows that the rms phase voltage $V_{(1)}$ and the line voltage $V_{l(1)}$ are related to the inverter DC-link voltage V_{dc} by

$$V_{(1)} = \frac{\sqrt{2}}{\pi} V_{dc} \quad 3.3$$

and

$$V_{l(1)} = \frac{\sqrt{6}}{\pi} V_{dc} \quad 3.4$$

Equations 3.1 and 3.2 indicate that the phase and line voltage waveforms contain only harmonics of order $6n\mp1$ (where n is a positive integer), whose magnitudes are inversely proportional to their order. The actual voltage waveshapes are slightly different from the ideal waveforms considered here, due to the commutation effects and internal voltage drops in the inverter circuit demonstrated later in chapter 5. The typical line-current waveform of figure 2.10 contains harmonics of sufficient magnitudes to cause significant additional heat losses in the machine, together with pronounced torque pulsations and speed ripple, particularly during low frequency operation.

The QSW inverter has been widely used for many years in adjustable-speed AC motor drives, with conventional thyristors being used together with a forced commutation circuit. Recently other semiconductor devices with a self turn-off capability, such as GTOs , power MOSFETs and transistors, have all become extensively used.

In induction motor drives, the inverter output voltage and frequency must both be controlled continuously to maintain the airgap flux constant, as discussed in chapter 2. Changing the inverter frequency is achieved by changing the frequency of the applied gate signals to the switching devices, but voltage control can only be obtained by changing the DC-link voltage using either a phase-controlled rectifier with a filter or a diode rectifier-chopper with a filter.

3.2 PWM Inverter Drives

The PWM inverter overcomes the problems associated with the QSW inverter by introducing intermediate switching instants into the basic QSW gate signal, such that lower order harmonic components are reduced or even eliminated from the output voltage waveform. The motor inductance can then effectively limit the remaining higher order harmonic components in the current waveform, thereby reducing machine losses and low speed torque pulsations and speed ripple. However, the number of switchings required per complete cycle is substantially higher than for a QSW inverter, and the inverter switching losses are consequently higher.

A PWM inverter can operate from a fixed voltage DC source, with the fundamental output frequency being controlled by varying the switching rate of the inverter devices and the output voltage by use of a PWM technique. Full frequency and voltage control is accomplished within the same power conversion stage. The inverter topology is the same as in figure 2.9,

with self-commutated power semiconductor devices being preferred since these can easily be turned on and off to provide any PWM profile.

Generally speaking, there are three different PWM switching strategies. The first, based on natural sampling, has been widely used because of its ease of implementation using analogue techniques. The second is regular sampling, considered to be advantageous following recent advances in electronic hardware and microprocessor-based techniques. The third, which is currently receiving considerable attention, employs optimized PWM switching techniques. These are based on the elimination of particular harmonics or the minimisation of certain performance criteria such as total harmonic distortion, torque pulsations or speed ripple.

3.2.1 Natural Switching Strategy

One basic method of generating sinusoidally distributed PWM switching waveforms is by electronically comparing the instantaneous amplitudes of a triangular (carrier) waveform and a sinusoidal (modulating) waveform. The switching edges of the width-modulated pulses are determined by the instantaneous intersections of the two waves as shown in figure 3.1, with the resultant pulse widths depending on the amplitude of the modulating wave at the instant switching occurs. It is evident from figure 3.1 that the centres of the pulses in the PWM wave are not uniformly spaced i.e $A \neq B$.

The switching waveforms for a 3-phase inverter are obtained from three sinusoidal modulating waves mutually displaced by $120°$, which are individually compared with a single symmetrical triangular carrier wave of fixed amplitude to produce identical switching patterns displaced by $120°$. The ratio of the modulating wave amplitude to that of the carrier defines the modulation index M , while the frequency ratio of the carrier

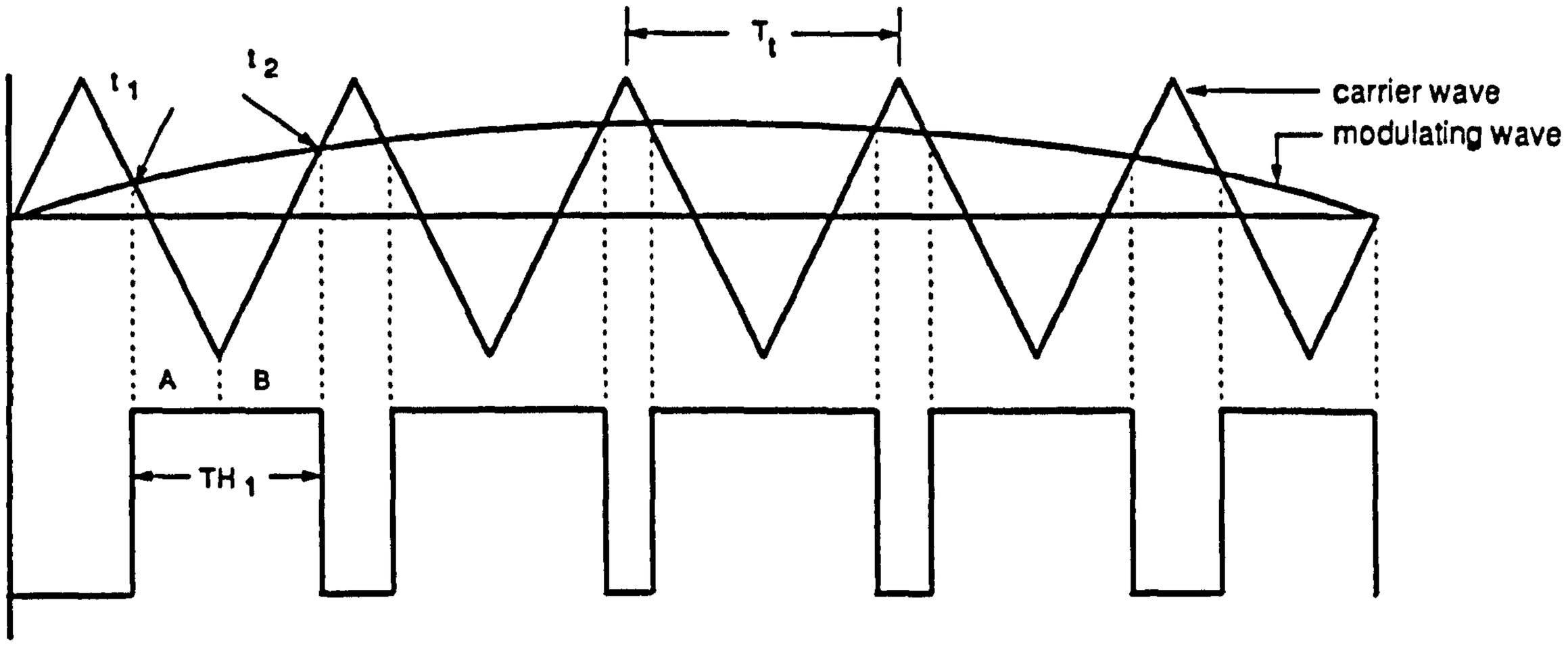

Figure 3.1 Half-cycle of natural PWM switcing strategy

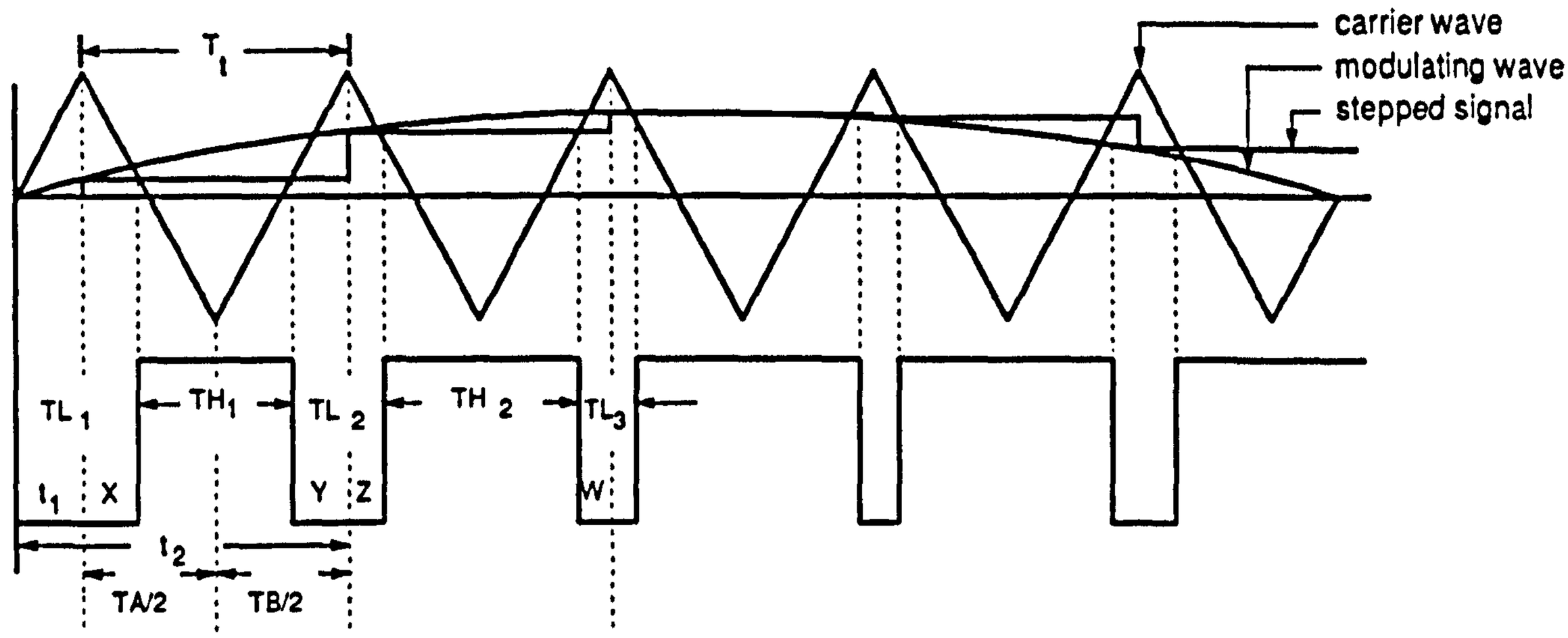

Figure 3.2 Half-cycle of symmetric regular PWM switching strategy

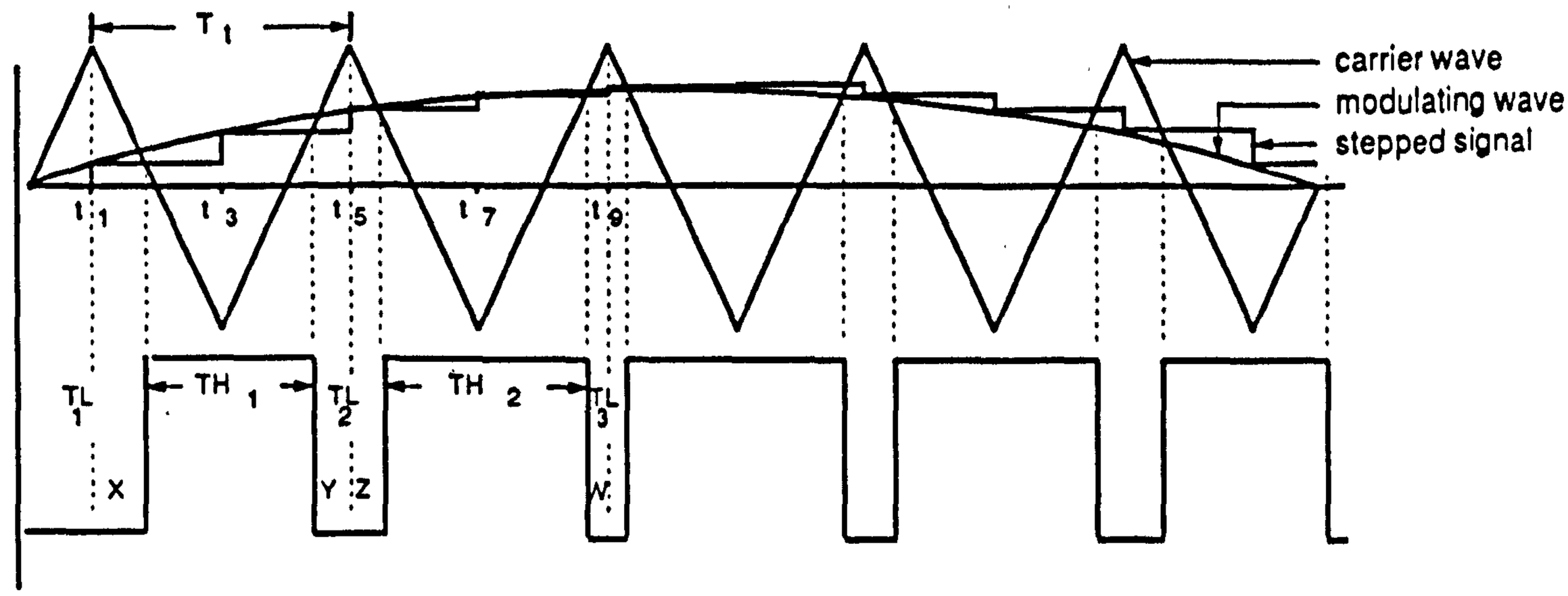

Figure 3.3 Half-cycle of asymmetric regular PWM switching strategy

to the modulating waveform gives the pulse number in the output PWM waveform. The width of the modulated pulses are defined by the transcendental equation

$$TH_1 = t_2 - t_1 = \frac{T_1}{2}\left(1 + \frac{M}{2}(\sin\omega_s t_1 + \sin\omega_s t_2)\right) \qquad 3.5$$

where ω_s is the angular frequency of the modulating wave.

Since output voltage control of an inverter is achieved by varying the amplitude of the modulating wave, output voltage and frequency control requires the generation of a set of 3-phase sinusoidal modulating voltages of adjustable amplitude and frequency . The fundamental output voltage of a natural PWM waveform is a maximum when the modulation index M is unity and the fundamental rms phase voltage component is [57]

$$V_{(1)} = M \frac{V_{dc}}{(2\sqrt{2})} \quad for \quad 0 \leq M < 1 \qquad 3.6$$

A comparison between equations 3.6 and 3.3 indicates that the maximum fundamental output voltage of a natural PWM inverter is less than that of a QSW inverter. As M approaches unity, the intervals between successive switching instants become very short near the positive and negative peaks of the modulating wave. They may in fact be less than the turn-off time of the semiconductor switches, implying that a device which has just been turned off must immediately be turned on again. A minimum time must thus be set, defining the shortest pulse duration, such that if the modulation scheme calls for a pulse width less than this, the pulse is dropped completely [58]. Increasing M above unity causes over-modulation, which improves the utilisation of the available DC-link. However, the modulating and the carrier waveforms fail to intersect and pulses are dropped in the output voltage waveform until a transition to QSW operation is accomplished.

Microprocessor implementation of the natural switching strategy requires a powerful arithmetic capability to solve equation 3.5 in real time [59]. Digital implementation may be performed by simulating the analogue process of natural sampling for a particular fundamental voltage, and storing the resultant PWM profile in a PROM accessed digitally or by microprocessor [60]. This process requires however a large memory space to store pulse widths for a wide range of output voltage and frequency.

3.2.2 Regular (Uniform) Switching Strategy

The regular switching strategy is based on comparing a triangular carrier wave with a stepped signal, obtained by sampling the sinusoidal modulating wave at regular instants. A sample-and-hold circuit operated at the carrier frequency is thus used to produce an amplitude modulated version of the modulating waveform. This signal is then compared with the carrier wave, to define points of intersection which determine the switching instants of the width-modulated pulses. As a result of this process the newly-formed stepped modulating signal has a constant amplitude while each sample is being taken, with the width of the pulses being proportional to the amplitude of the modulating waveform at uniformly spaced sampling times. Moreover, the sampling positions and their values can be defined clearly, i.e the pulses produced are predictable both in width and position, which is not the case with a natural switching strategy. There are two types of regular sampled PWM ; symmetric regular and asymmetric regular strategies.

3.2.2.1 Symmetric Regular Modulation

As illustrated in figure 3.2, the magnitude of the modulating waveform at a sampling instant t_1 is stored by a sample-and-hold circuit and kept at the same level until the next sampling instant t_2 , taken after a complete period of the carrier wave relative to the sampling instant t_1 . From

figure 3.2, the high level pulse width TH_1 is defined in terms of the sampled value of the modulating wave taken at time t_1 as

$$TH_1 = \frac{T_t}{2} (1 + M \sin \omega_s t_1) \qquad 3.7$$

where

$\omega_s = 2\pi f_s$

$T_t = \frac{1}{f_t}$ & $t_1 = \frac{T_t}{4}$

Similarly

$$TH_2 = \frac{T_t}{2} (1 + M \sin \omega_s t_2) \qquad 3.8$$

where

$t_2 = 5\frac{T_t}{4}$

In general

$$TH_{(j+1)} = \frac{T_t}{2} (1 + M \sin \omega_s t_{(j-1)}) \qquad 3.9$$

where

$$t_{(j+1)} = \frac{(4j+1)}{4} T_t \qquad j=0,1,2,\ldots,(R-1) \qquad 3.10$$

and R is the frequency ratio $= f_t / f_s$

Substituting for T_t and ω_s in equation 3.9

$$TH_{(j+1)} = \frac{1}{2Rf_s}\left(1 + M \sin \pi \frac{(4j + 1)}{2R} \right) \qquad 3.11$$

The low level pulse width TL_2 is calculated using the symmetrical sampling nature of regular modulation, since widths $TA/2$ and $TB/2$ are both equal to one-half the carrier period T_t and can be defined as

$$\frac{TA}{2} = X + \frac{TH_1}{2} \qquad \& \qquad \frac{TB}{2} = Y + \frac{TH_1}{2}$$

where

$$X = Y = \frac{T_t}{2} - \frac{TH_1}{2} \tag{3.12}$$

Similarly

$$W = Z = \frac{T_t}{2} - \frac{TH_2}{2} \tag{3.13}$$

From figure 3.2 it is clear that

$$TL_2 = Y + Z \tag{3.14}$$

Substituting Y and Z from equations 3.12 and 3.13 into equation 3.14 yields

$$TL_2 = T_t - \left(\frac{TH_1 + TH_2}{2}\right) \tag{3.15}$$

or, in general

$$TL_{(J+1)} = T_t - \left(\frac{TH_J + TH_{(J+1)}}{2}\right) \qquad J = 0,1,2,\ldots\ldots,(R-1) \tag{3.16}$$

where

$$TH_0 = \frac{T_t}{2}$$

Equation 3.11 is used to calculate the high level pulse widths, which are subsequently used to determine the low level pulse widths using equation 3.16. This forms a complete PWM pattern for one phase only, which is phase shifted by 120° and 240° to provide the remaining two phases.

3.2.2.2 Asymmetric Regular Modulation

With asymmetric regular modulation, each pulse edge is modulated by a different amount, as shown in figure 3.3. The leading and trailing edges of each pulse are determined using samples of the modulating signal at time instants t_1 and t_3. Each sample is held for one-half the period of the carrier wave to produce the stepped signal. The width of the resulting high level pulse is defined in terms of these sampling instants as

$$TH_1 = \frac{T_t}{2}\left(1 + \frac{M}{2}(\sin\omega_c t_1 + \sin\omega_c t_3)\right) \qquad 3.17$$

where

$$t_1 = \frac{T_t}{4} \quad \& \quad t_3 = 3\frac{T_t}{4}$$

Similarly

$$TH_2 = \frac{T_t}{2}\left(1 + \frac{M}{2}(\sin\omega_c t_5 + \sin\omega_c t_7)\right) \qquad 3.18$$

where

$$t_5 = 5\frac{T_t}{4} \quad \& \quad t_7 = 7\frac{T_t}{4}$$

In general

$$TH_{(j+1)} = \frac{T_t}{2}\left(1 + \frac{M}{2}(\sin\omega_c t_{(4j+1)} + \sin\omega_c t_{(4j-3)})\right) \qquad 3.19$$

where $j = 0, 1, 2, \ldots\ldots, (R-1)$

Substituting for T_t and ω_c in equation 3.19 gives

$$TH_{(j+1)} = \frac{1}{2Rf_c}\left(1 + \frac{M}{2}\left(\sin\pi\frac{(4j+1)}{2R} + \sin\pi\frac{(4j+3)}{2R}\right)\right) \qquad 3.20$$

In determining the low level pulse width TL_2 the intervals X and Y are calculated individually, since each pulse edge is modulated differently. Hence

$$T_t = X + TH_1 + Y$$

and substituting for TH_1 in equation 3.17 gives

$$T_t = X + \frac{T_t}{4} + \frac{T_t M}{4}\sin\omega_s t_1 + \frac{T_t}{4} + \frac{T_t M}{4}\sin\omega_s t_3 + Y \qquad 3.21$$

from which it can be deduced that

$$X = \frac{T_t}{4} - \frac{T_t M}{4}\sin\omega_s t_1 \quad and \quad Y = \frac{T_t}{4} - \frac{T_t M}{4}\sin\omega_s t_3$$

Similarly

$$Z = \frac{T_t}{4} - \frac{T_t M}{4}\sin\omega_s t_5 \quad and \quad W = \frac{T_t}{4} - \frac{T_t M}{4}\sin\omega_s t_7$$

The low level pulse width TL_2 can now be determined from

$$TL_2 = Y + Z$$

and substituting for Y and Z in this equation yields

$$TL_2 = \frac{T_t}{2}\left(1 - \frac{M}{2}(\sin\omega_s t_3 + \sin\omega_s t_5)\right) \qquad 3.22$$

Similarly

$$TL_3 = \frac{T_t}{2}\left(1 - \frac{M}{2}(\sin\omega_s t_7 + \sin\omega_s t_9)\right) \qquad 3.23$$

In general

$$TL_{(j+2)} = \frac{T_t}{2}\left(1 - \frac{M}{2}(\sin\omega_s t_{(4j+3)} + \sin\omega_s t_{(4j+5)})\right) \qquad 3.24$$

where $j = 0,1,2.....(R-2)$

$$TL_1 = \frac{T_t}{2}\left(1 - \frac{M}{2}\sin\omega_s t_1\right)$$

$$TL_{(R+1)} = \frac{T_t}{2}\left(1 - \frac{M}{2}\sin\omega_s t_{(4R-1)}\right)$$

Substituting for T_t and ω_s in equation 3.24 yields

$$TL_{(j+2)} = \frac{1}{2Rf_s}\left(1 - \frac{M}{2}\left(\sin\pi\frac{(4j+3)}{2R} + \sin\pi\frac{(4j+5)}{2R}\right)\right) \qquad 3.25$$

where $j = 0,1,2.....(R-2)$

$$TL_1 = \frac{1}{2Rf_s}\left(1 - \frac{M}{2}\sin\left(\frac{\pi}{2R}\right)\right)$$

$$TL_{(R+1)} = \frac{1}{2Rf_s}\left(1 - \frac{M}{2}\sin\left(\pi\frac{(4R-1)}{2R}\right)\right)$$

Equations 3.20 and 3.25 may be solved to calculate a complete PWM pattern for one phase only and by shifting this result by 120° and 240° the other two phase patterns are obtained.

A feature common to both natural and regular switching strategies is the possibility of varying the modulation index linearly with the frequency of the modulating wave. This technique provides a fundamental output voltage proportional to the output frequency, as is required for constant airgap flux operation of a motor. Moreover a 3-phase drive, working over a wide range of variable speeds, requires discrete-integer multiple-of-three values of the frequency ratio to eliminate any sub-harmonic or DC components in the inverter output waveforms [14], which requires locking of the carrier and modulating frequencies throughout the entire range of operation. This is however undesirable, since at high operating frequencies the carrier frequency is sufficiently high to cause excessive switching losses in the inverter, whereas at low frequencies the carrier frequency might not be high enough to

improve the machine performance. It is necessary therefore to change the frequency ratio whenever the carrier frequency become either too high or too low for satisfactory operation of the system. A number of pulses for this gear-changing process is illustrated in figure 3.4, with hysteresis included at each gear-change to prevent system oscillation [61,62].

Unlike the natural strategy, regular switching strategies are suitable for microprocessor implementation, since their mathematical algorithm is easier to solve in real time than is equation 3.5 for the natural strategy. Moreover it requires less memory space to store a small number of samples of the modulating waveform corresponding to the PWM pulse number. As for the regular switching strategy, it is important to note that, since more information about the modulating wave is contained in the asymmetric type, its harmonic spectrum is superior to that produced using the symmetric type. However, the number of calculations required to generate asymmetric PWM is twice that for symmetric PWM, extending the computation time for a microprocessor software based implementation.

In all these techniques, the most significant harmonics usually occur at $\omega_1 \mp 2\omega_c$ and $2\omega_1 \mp \omega_c$, , and they are normally accompanied by sidebands of order $\omega_1 \mp 4\omega_c$ and $2\omega_1 \mp 2\omega_c$. Significant harmonics may also appear with the symmetrical strategy at $2\omega_c$, $\omega_1 \mp \omega_c$ and $2\omega_1 \mp 4\omega_c$ [14,35,36].

3.2.3 Optimal Switching Strategy

In this strategy, the 2-level PWM voltage waveform shown in figure 3.5 is defined in terms of the set of switching angles α_m . If it is assumed that the periodic waveform has half-wave symmetry and unity amplitude then

$$f(\omega t) = - f(\omega t + \pi) \qquad 3.26$$

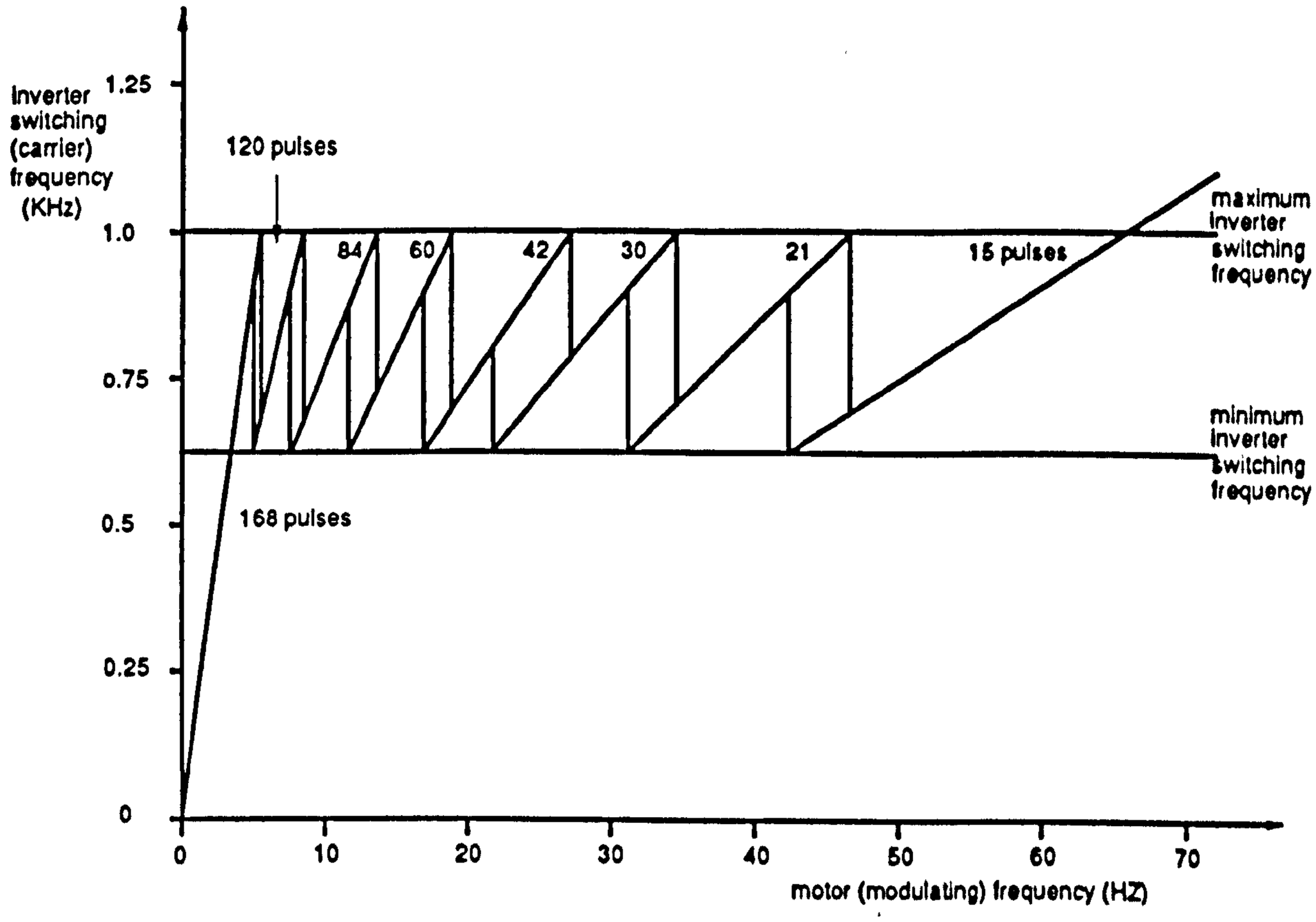

Figure 3.4 Gear-changing process

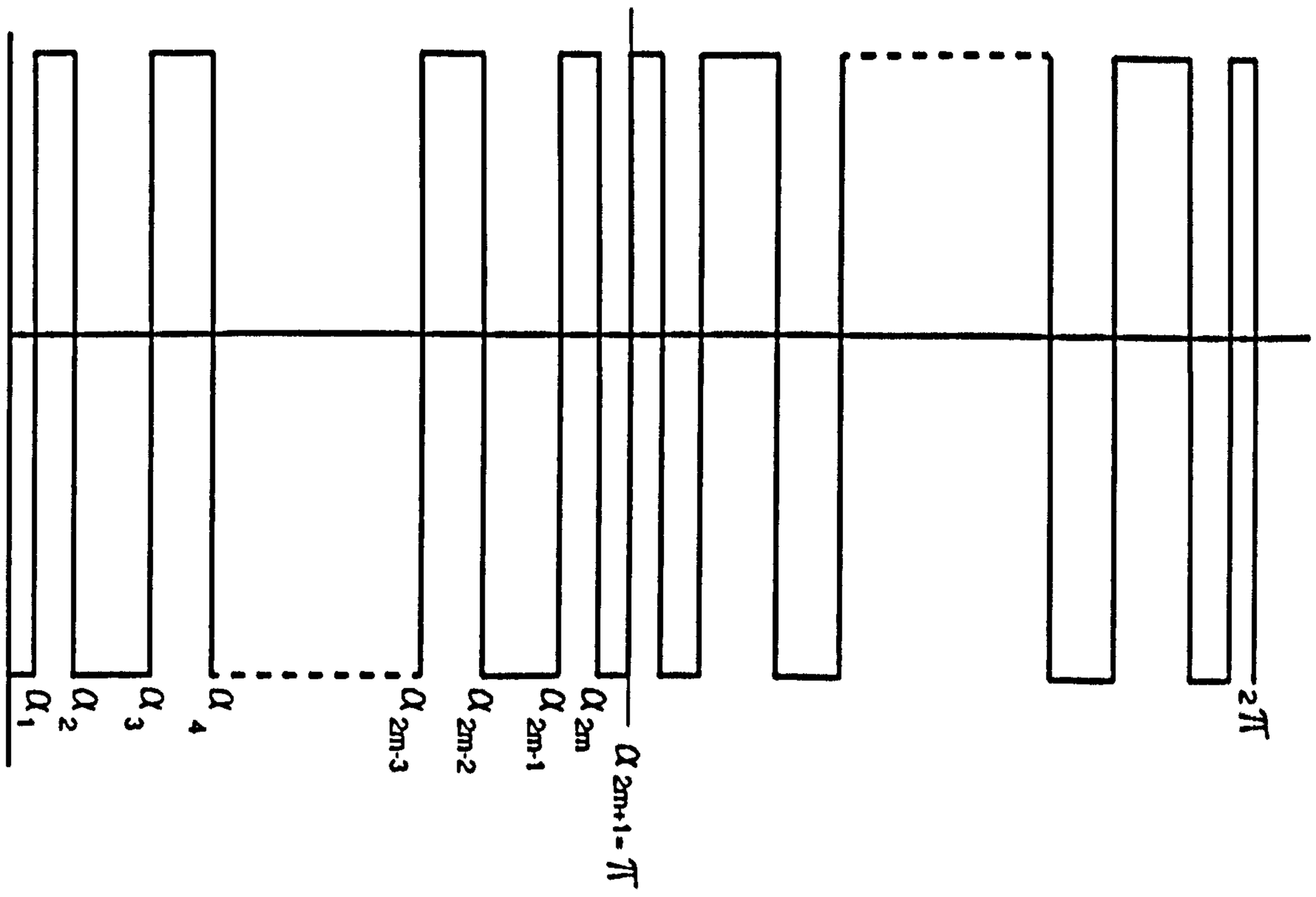

Figure 3.5 Generalized optimal PWM output waveform

where $f(\omega t)$ is a 2-state periodic function with m switching angles per half-cycle. The waveform can be represented by the Fourier-series

$$f(\omega t) = \sum_{n=1}^{\infty} a_n \sin(n\omega t) + b_n \cos(n\omega t) \qquad 3.27$$

where

$$a_n = \frac{1}{\pi}\int_0^{2\pi} f(\omega t)\sin(n\omega t)\, d\omega t \qquad 3.28$$

and

$$b_n = \frac{1}{\pi}\int_0^{2\pi} f(\omega t)\cos(n\omega t)\, d\omega t \qquad 3.29$$

Substituting for $f(\omega t)$ in 3.28 and using the half-wave symmetry property, then

$$a_n = \frac{2}{\pi}\sum_{i=0}^{2m}(-1)^i \int_{\alpha_i}^{\alpha_{i+1}} \sin(n\omega t)\, d\omega t \qquad 3.30$$

where

$\alpha_0 = 0$

$\alpha_{2m-1} = \pi$

$\alpha_0 < \alpha_1 < \alpha_2 < .... < \alpha_{(2m+1)}$

Evaluating equation 3.30

$$a_n = \frac{2}{n\pi}\left(1 - (-1)^n + 2\sum_{i=1}^{2m}(-1)^i \cos n\alpha_i\right) \qquad 3.31$$

Similarly

$$b_n = -\frac{4}{n\pi}\sum_{i=1}^{2m}(-1)^i \sin n\alpha_i \qquad 3.32$$

Utilizing the half-wave symmetry property of the waveform shows that $a_n = 0$ and $b_n = 0$ for even n. For odd n, equations 3.31 and 3.32 become

$$a_n = \frac{4}{n\pi}\left(1 + \sum_{i=1}^{2m} (-1)^i \cos n\alpha_i \right) \qquad 3.33$$

and

$$b_n = \frac{4}{n\pi}\left(- \sum_{i=1}^{2m} (-1)^i \sin n\alpha_i \right) \qquad 3.34$$

Due to the quarter-wave symmetry property of the waveform $b_n = 0$, and equation 3.33 reduces to

$$a_n = \frac{4}{n\pi}\left(1 + 2\sum_{i=1}^{m} (-1)^i \cos n\alpha_i \right) \qquad 3.35$$

Usually the design procedure for the calculation of switching angles α_1, α_2, ..., α_m is based upon a set of m equations, the first of which determines the fundamental rms phase voltage $V_{(1)}$

$$V_{(1)} = \frac{\sqrt{2}}{\pi} V_{dc}\left(1 + 2\sum_{i=1}^{m} (-1)^i \cos \alpha_i \right) \qquad 3.36$$

while the rest are devoted to the realization of a required optimization criteria, such as the elimination of $m-1$ harmonics,

$$V_{(5)} = \frac{\sqrt{2}}{5\pi} V_{dc}\left(1 + 2\sum_{i=1}^{m} (-1)^i \cos 5\alpha_i \right) = 0 \,.$$

$$V_{(7)} = \frac{\sqrt{2}}{7\pi} V_{dc}\left(1 + 2\sum_{i=1}^{m} (-1)^i \cos 7\alpha_i \right) = 0 \qquad 3.37$$

$$V_{(n)} = \frac{\sqrt{2}}{n\pi} V_{dc}\left(1 + 2\sum_{i=1}^{m} (-1)^i \cos n\alpha_i \right) = 0 \,.$$

Since the minimum pulse width requirements are to be satisfied, as discussed in section 3.2.1, the additional constraints on the unknown switching angles $\alpha_1,.....,\alpha_m$ per quarter-cycle in the PWM wave pattern are

$$\alpha_2 - \alpha_1 \geq t_{min}$$

$$\alpha_3 - \alpha_2 \geq t_{min}$$

$$- - - - - - - - - -$$

$$\alpha_i - \alpha_{i-1} \geq t_{min}$$

$$\pi/2 - \alpha_i \geq t_{min}$$

where all the switching angles must lie between t_{min} and $\pi/2$ when satisfying the above inequality constraints.

The switching angles can be selected to control the fundamental voltage component and optimize various performance criteria. The performance criteria can be classified as machine independent and machine dependent types. In VSI drives, voltage harmonic elimination or minimisation strategies belong to the first of these, while harmonic current distortion or torque pulsations and speed ripple minimisation belong to the second. Since equations 3.36 and 3.37 are both nonlinear and transcendental, their solution needs either an iterative numerical technique, such as the Newton-Raphson method, or a more complicated gradient search approach, such as Lagrange-Multipliers based on the Quasi-Newton method. This latter method produces accurate solutions and good convergence, provided that the initial guess for the switching angles is near a local minima. However, due to the periodicity of the trigonometric functions, several solutions for the equations may be obtained. For any desired number of switching angles, the harmonic spectra of the various solutions may be compared and the optimum solution selected.

Optimum PWM waveforms cannot be generated with analogue control circuitry, and the switching angles cannot be computed in real time. It is usual therefore to define a general PWM waveform in terms of a set of switching angles, then to determine these angles using a mainframe computer. The angles are subsequently pre-programmed into the microprocessor memory in the form of look-up table and used to generate PWM waveforms in real time [63]. Since in general the relationship between the switching angles and the fundamental of the PWM output voltage is non-linear, a large number of look-up tables are required, each corresponding to a discrete fundamental voltage level. Alternatively, some form of interpolation between tables can be used to produce a continuous fundamental voltage variation [36,64]. Another possible technique is to store a unique pattern of switching angles and to vary the fundamental voltage component by varying the DC-link voltage. In terms of the mathematical algorithm, this allows one more degree of freedom to be available for the optimization procedure. In other words m pre-determined harmonics can be eliminated using m switching angles [65]. This latter technique is employed in this thesis, and all the investigations and developments on optimized PWM switching strategies are based upon it.

Low order harmonics have the most pronounced harmful effect on machine performance and if they are eliminated, while the fundamental component is maximised, full utilization is obtained of the DC-link voltage. The optimization process is described in appendix A.2, where a PWM waveform containing 8 switching angles per quarter-cycle is considered for eliminating harmonic components up to the 25th. Table 3.1 shows sets of 2,4,6 and 8 switching angles computed to eliminate successive pairs of harmonic components up to the 25th, where the rms fundamental component for each set is given by

$$V_{(1)} = K \frac{\sqrt{2}}{\pi} V_{dc} \qquad 3.38$$

where K is a fundamental component factor obtained from the optimization procedure explained in appendix A.2.

TABLE 3.1
OPTIMIZATION SUBROUTINE SETS OF 2,4,6,8 SWITCHING ANGLES

MODE	K	α_1	α_2	α_3	α_4	α_5	α_6	α_7	α_8
PWM2	0.9330	0.2836	0.3852						
PWM4	0.9200	0.1841	0.2809	0.5394	0.5736				
PWM6	0.9140	0.1362	0.2212	0.4030	0.4474	0.6654	0.6807		
PWM8	0.9116	0.1081	0.1825	0.3213	0.3675	0.5323	0.5561	0.7409	0.7490

Comparing the expression for the rms fundamental component of equation 3.38, with that for QSW operation (equation 3.3), leads to the conclusion that for the same DC-link voltage the rms value of the fundamental phase voltage component is less with optimal PWM operation, due to the reduced voltage-time area per half-cycle. It is also clear from table 3.1 that, as additional notches are introduced in the basic QSW gate signal, the K value is reduced, thus reducing the magnitude of the fundamental voltage component for the same DC-link voltage.

3.3 Induction Motor Losses and Performance with Non-sinusoidal Supplies

The presence of time harmonics in the induction motor supply voltage results in currents that contain a fundamental and a series of harmonic components. One method for calculating the harmonic currents and the corresponding losses is to neglect magnetic saturation, so that the motor is regarded as a linear device to which the method of superposition can be applied. The motor behaviour is then analysed independently for the fundamental and for each harmonic component.

3.3.1 Motor Losses [50]

Additional losses in an AC motor with a non-sinusoidal supply are as follows

(a) Stator copper loss : This is proportional to the square of the rms current and is given by

$$P_{sc} = 3\ I_{rms}^2\ R_s \qquad 3.40$$

where

$$I_{rms} = \sqrt{I_{s(1)}^2 + \sum_{n=2}^{\infty} I_{s(n)}^2} \qquad 3.41$$

and $\sum_{n=2}^{\infty} I_{s(n)}^2$ is the total harmonic stator current content.

Substituting for I_{rms} in equation 3.40

$$P_{sc} = 3\ I_{s(1)}^2 R_s + 3\ \sum_{n=2}^{\infty} I_{s(n)}^2 R_s \qquad 3.42$$

where the second term represents the harmonic copper loss.

(b) Rotor copper loss : The backward rotating 5th-harmonic and the forward rotating 7th-harmonic mmfs both induce rotor currents of approximately six times the fundamental frequency. Similarly the 11th- and 13th-harmonics induce rotor currents of approximately twelve times the fundamental frequency. At these harmonic frequencies, the rotor resistance is much greater than its DC value due to the skin effect. Using Alger's correction curves [66], the rotor copper loss may be calculated independently for each harmonic as

$$P_{rc} = 3 \sum_{n} I_{r(n)}^2\ R_{r(n)} \quad , \quad n = 6, 12, 18, \ldots \qquad 3.43$$

where $I_{r(n)}$ is the nth-harmonic rotor current and $R_{r(n)}$ the corresponding rotor resistance corrected for skin effect.

(c) Harmonic core loss : The presence of mmf harmonics in the airgap causes negligible increase in the motor core loss. However, end-leakage and skew-leakage fluxes, which normally contribute to the stray load loss, produce a significant core loss at harmonic frequencies which may approach the harmonic copper losses.

3.3.2 Torque Pulsations and Speed Ripple

MMF harmonics in the airgap result in both steady and pulsating torques at the motor shaft. Steady torques are developed by the interaction between harmonic airgap fluxes and harmonic rotor currents of the same order, and they usually have negligible effect on the motor operation. Pulsating torque components arise from interactions between harmonic airgap fluxes and rotor currents of different orders, as explained in chapter 6. Pulsating torques cause an undesirable speed ripple, especially at low speed, where the motor may cog if the rotor and load inertia is insufficient to minimise this effect.

3.4 Conclusion

This chapter has described the three main PWM strategies, and stated the mathematical algorithm representing each type. It can be concluded that optimal PWM strategies may be arranged to produce switching instants in the PWM voltage waveforms which optimize some specified performance criteria. This is in direct contrast to the natural or regular PWM strategies, which are based on the comparison of a modulating and a carrier wave and are not therefore directly related to any particular performance criteria. Moreover, for a given pulse-number, the order of the first uneliminated harmonic component in the optimal strategy is almost double that for a natural or regular sampled PWM techniques [35,36], which results in a far superior voltage waveform harmonic spectrum.

CHAPTER 4

EXPERIMENTAL OPEN-LOOP DRIVE SYSTEM CONTROL

An open-loop induction motor drive system comprising a variable voltage DC-link supplying a 3-phase bridge inverter was designed and built in support of the theoretical work in the thesis. The drive comprises a phase-controlled thyristor bridge rectifier and a GTO-thyristor inverter bridge, together with a PWM gate-drive signal generator. It was provided with over-current protection and regeneration control circuits as well as a soft-start/stop module to implement the start, acceleration, deceleration and stop techniques essential to the safe operation of the drive. A block diagram of the system is shown in figure 4.1, and a detailed description is available elsewhere [67]. This chapter describes briefly the 3-phase GTO-thyristor inverter bridge. A unique digital technique for generation of a 3-phase PWM switching pattern is explained, and a digital system for speed and torque monitoring is described. This was specifically designed and built to measure the fluctuation of the instantaneous speed around its average value, from which an analogue signal may be obtained which is related to the torque pulsations.

4.1 GTOs in Inverter/Induction Motor Drives

The GTO-thyristor is a 3-terminal, 4-layer p-n-p-n semiconductor switch, which combines the most desirable characteristics of the bipolar transistor and the conventional thyristor. It incorporates the fast switching and gate drive simplicity of the transistor with the ability of the thyristor to pass high forward current when turned on and to block high forward voltage when turned off.

Figure 4.2 shows the basic circuit configuration for the inverter, with the three upper devices connected to individual motor phases. These are switched at the high voltage levels

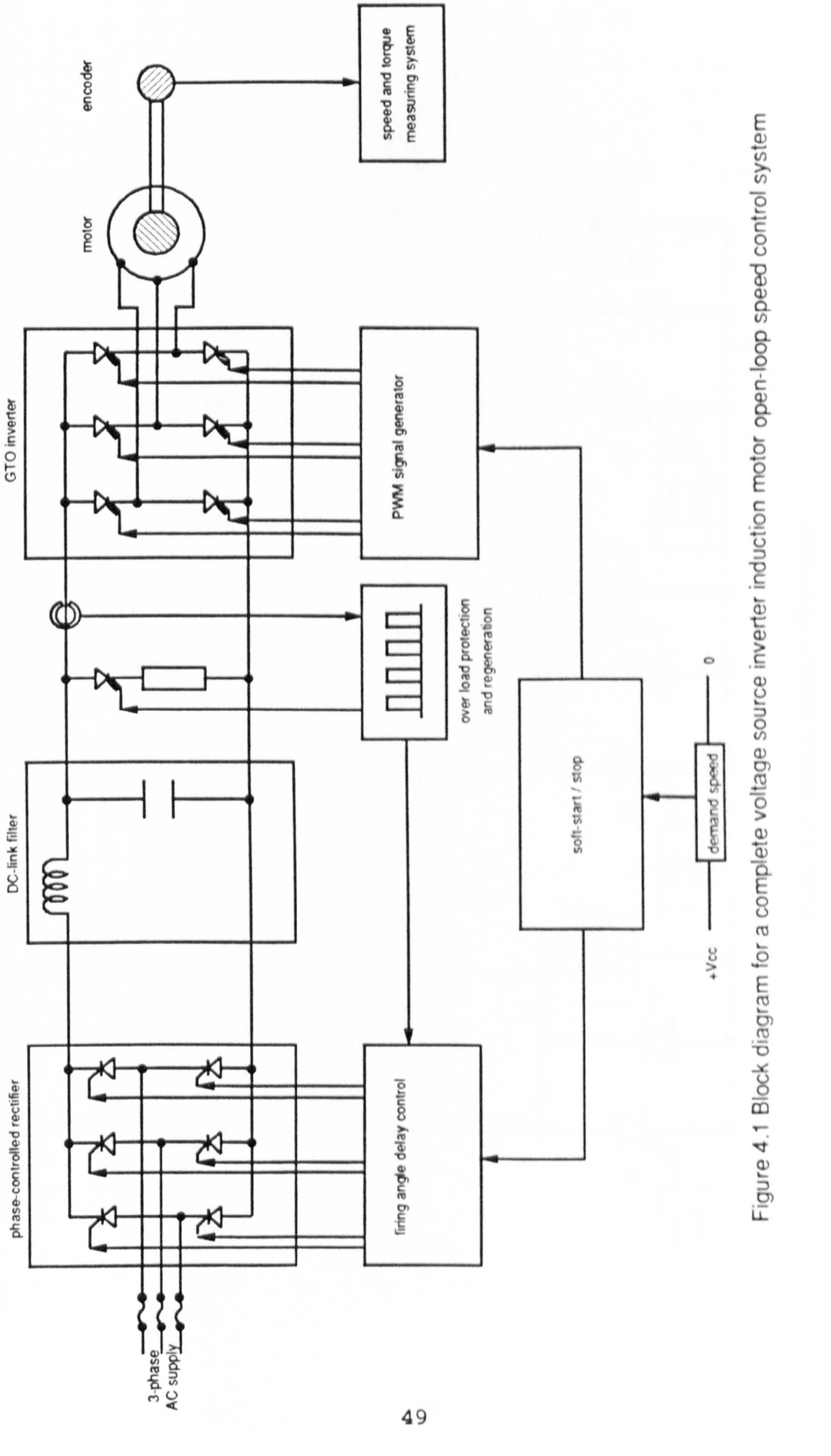

Figure 4.1 Block diagram for a complete voltage source inverter induction motor open-loop speed control system

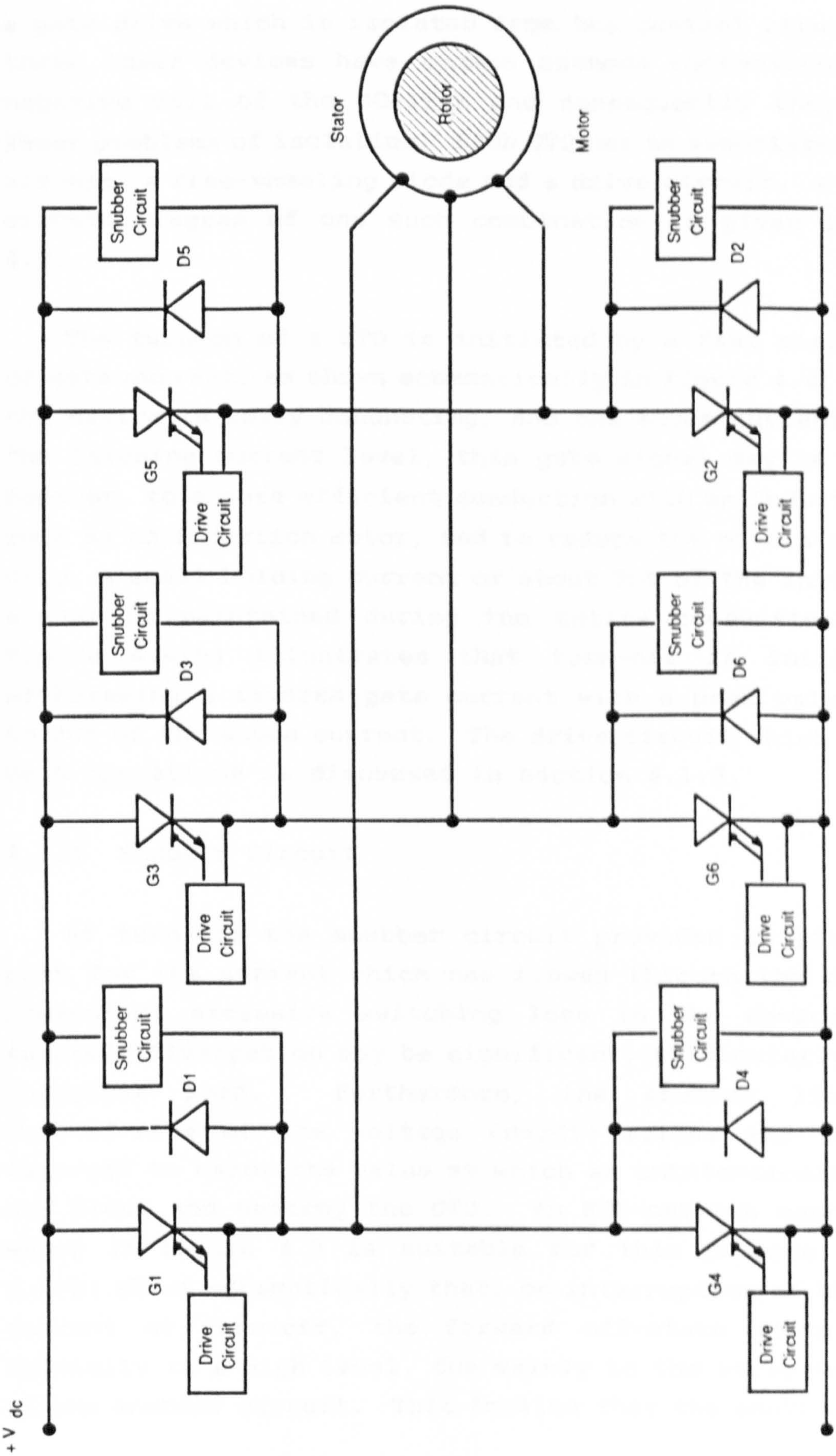

Figure 4.2 3-phase bridge GTO inverter

of the output waveform and it is essential therefore to have a gate drive which is isolated from the control circuit. The three lower devices have common cathode connections to the negative rail of the DC-link and consequently they present fewer problems of isolation. Each GTO has an associated snubber circuit, a free-wheeling diode and a drive circuit. A complete circuit diagram of one such combination is given in figure 4.3.

The turn-on of a GTO is initiated by a fast rising pulse of gate current, as shown schematically in figure 4.4(a). When the device is fully conducting, and the anode current exceeds the latching current level, this gate signal may be removed. However, to ensure efficient conduction with an inductive load such as an induction motor, and to reduce the on-state voltage drop, a small holding current of about 30% of the initial gate signal is maintained during the entire conduction period. Figure 4.4(b) illustrates that turn-off is initiated by withdrawing a reverse gate current with a peak value of 25% to 30% of the anode current. The drive circuit which achieves both operations is discussed in section 4.1.3.

4.1.1 Snubber Circuit

At turn-off the snubber circuit provides an alternative path for the current which has flowed through the GTO, thus preventing excessive switching loss in the device. This turn-off dissipation may be significant, particularly with an inductive load. Furthermore, the snubber limits the rate-of-rise of the voltage (dv/dt) across the device at turn-off to below the value at which an unintentional turn-on may occur and destroy the GTO. An RCD-network connected as shown in figure 4.3 is suitable for this purpose. Figure 4.4(b) shows schematically that, on interruption of the device current at turn-off, the forward off-state voltage jumps initially to a high level, due mainly to the stray inductance of the snubber circuit. This implies that the snubber circuit

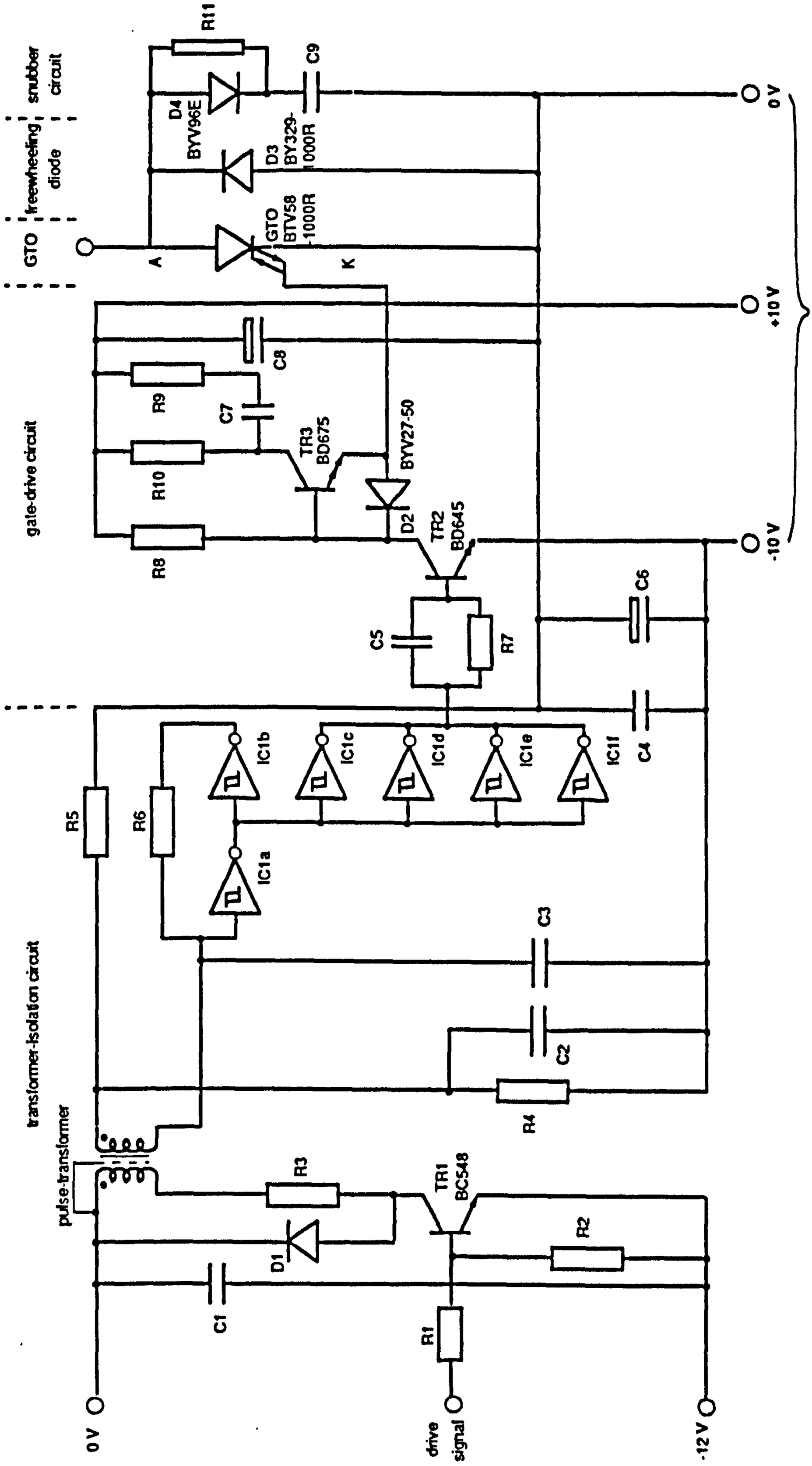

Figure 4.3 Transformer isolated gate-drive circuit for GTO thyristor

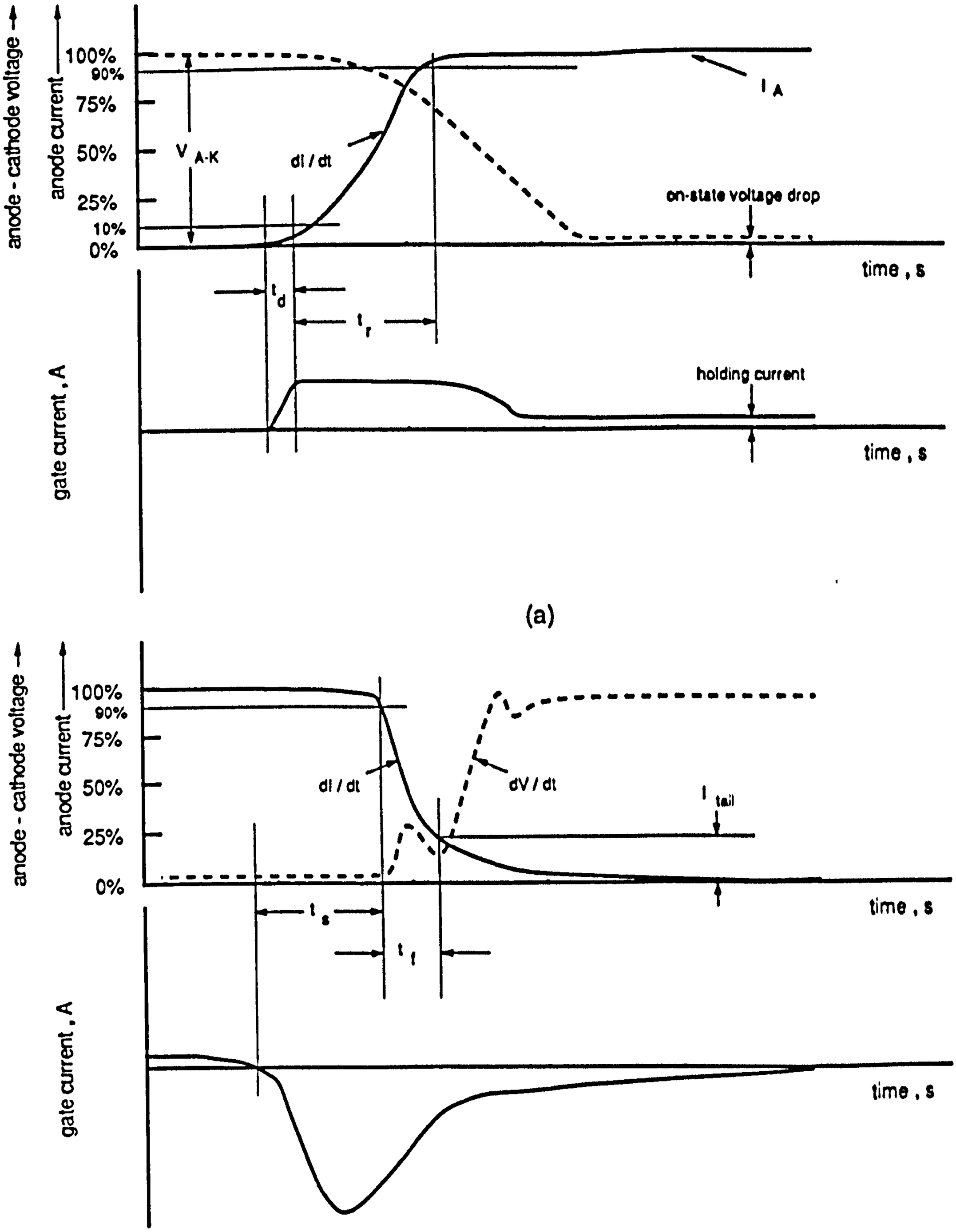

Figure 4.4 Schematic representation of (a) turn-on (b) turn-off process of GTO with RCD-snubber circuit

must be connected as near as possible to the GTO terminals. The energy stored in capacitor C9 during turn-off is dissipated in resistor R11 during the next turn-on period.

4.1.2 Free-wheeling Diode

If the load is inductive, as is the case with an induction motor, the inverse parallel free-wheeling diode D3 across the GTO carries the load current after turn-off of the opposite GTO in the inverter arm, until this reduces to zero. A detailed discussion on its operation is given in the next chapter.

4.1.3 Isolated Gate-Drive Circuit

The GTO gate-drive circuit is required to provide a positive on-gate current and a negative off-gate current. These requirements are met by the dual-polarity isolated switched-mode power supply shown in figure 4.3 [68]. Isolation of the control circuit from the power circuit is achieved by a low impedance pulse transformer, whose secondary voltage is a differentiated version of the primary waveform. The Schmitt-trigger circuit IC1a and IC1b in the (HEF40106B) IC restores the sharp edges of this signal, which is then buffered by IC1c to IC1f and applied to transistor TR2. When TR2 is turned off, TR3 conducts. This transistor is connected in series with network R9, C7 and R10, which provides the initial positive gate-current pulse to turn-on the GTO. The GTO is turned off when TR2 conducts, and gate-current is extracted via diode D2 into the smoothing capacitor C6 connected to the -12V isolated supply. The multiple-output isolated power supply for this drive circuit is described elsewhere [68].

4.1.4 Delayed Switching Characteristics

When a GTO is either turned on or turned off there is a delay before the new stable state is reached. A minimum turn-on duration should be sustained before attempting to turn-off the GTO, to ensure a better distribution of the on-state current

over the conducting cathode regions. Figure 4.4(a) shows that this duration includes the delay time of the gate current t_d and the rise time of the on-state current t_r. When the device is turned off the on-state current does not fall immediately, but reduces gradually as a result of the delay characteristics. Figure 4.4(b) illustrates that this delay consists of two intervals. Firstly, the gate controlled storage time t_s during which the anode current continues in its normal trend, and secondly the fall time t_f when it starts decreasing rapidly to I_{tail} which is defined as the tail current. To reduce t_s the stray inductance of the GTO gate circuit during turn-off must be kept to a minimum, to ensure fast pull-out of the gate current. These time intervals are usually provided in the data sheet for specified conditions.

The two complementary GTOs in the same arm of the inverter bridge must not be turned on simultaneously, otherwise a short circuit of the DC-link will occur. This implies that a fixed time delay should be introduced into their gate-drive signals. This delay is referred to as the non-overlapping time and is slightly longer than either the on and the off delay times.

4.2 Soft-Start/Stop

The rate at which the motor speed can be changed is limited by the drive inertia and the motor torque. If the stator frequency is increased there is a lag in the rotor speed response and the slip becomes large, with correspondingly large stator currents. If the frequency is decreased, the slip becomes negative, and the rotational energy which is returned to the DC-link increases the link voltage.

The function of the soft-start/stop module is to co-ordinate the rate of increase/decrease of the motor supply frequency with the acceleration/deceleration performance characteristics of the drive system in the low-slip region. A simplified circuit diagram is shown in figure 4.5, the details of which are in [69]. The motor speed is determined by the potentiometer

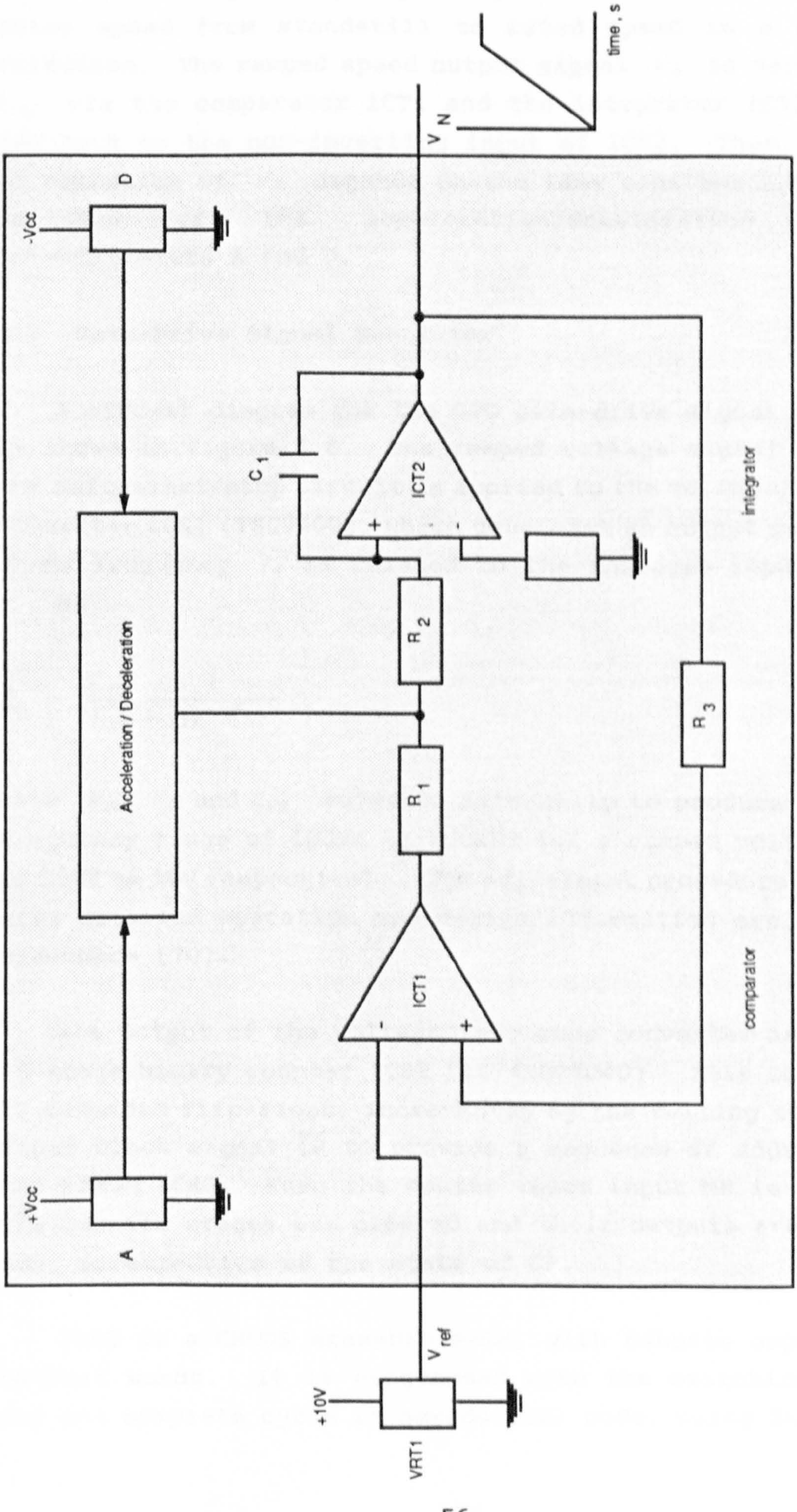

Figure 4.5 Soft-start / stop simplified circuit diagram

VRT1, whose output V_{ref} may change from 0 to +10V to vary the motor speed from standstill to rated speed in a clockwise direction. The ramped speed output signal V_N is derived from V_{ref} via the comparator ICT1 and the integrator ICT2. It is fed back to the non-inverting input of ICT2. Thus, the rate of variation of V_N depends on the time constant C_1R_2 and the settings of the acceleration/deceleration limiting potentiometers A and D.

4.3 Gate-Drive Signal Generator

A circuit diagram for the GTO gate-drive signal generator is shown in figure 4.6. The ramped voltage signal V_N from the soft-start/stop circuit is applied to the voltage/frequency converter ICS1 (TSC9400), which generates an output pulse train whose frequency f_o is related to the analogue input voltage V_N by

$$f_o = \frac{V_N}{R_{S3}} \frac{1}{V_{REF} C_{SS}} \qquad 4.1$$

with R_{S3}, V_N and C_{SS} adjusted externally to produce an output frequency range of 100Hz to 100kHz for a ramped voltage range of 10mV to 10V respectively. The adjustment procedure, together with detailed operation and design information are explained elsewhere [70].

The output of the voltage/frequency converter is fed to a 12-stage binary counter ICS2 (IC74HCT4040). This consists of 12 cascaded flip-flops, incremented by the falling edge of the input clock signal $\overline{CP}$ to provide a sequence of addresses for the EPROM ICS3. When the master reset input MR is high, all the counter stages are cleared and their outputs are reset to low, irrespective of the state of $\overline{CP}$.

ICS3 is a CHMOS erasable PROM, with 64kbits organized as 8k-8bit words. It is programmed with the switching pattern for one complete cycle in hexadecimal code, using 2k words as

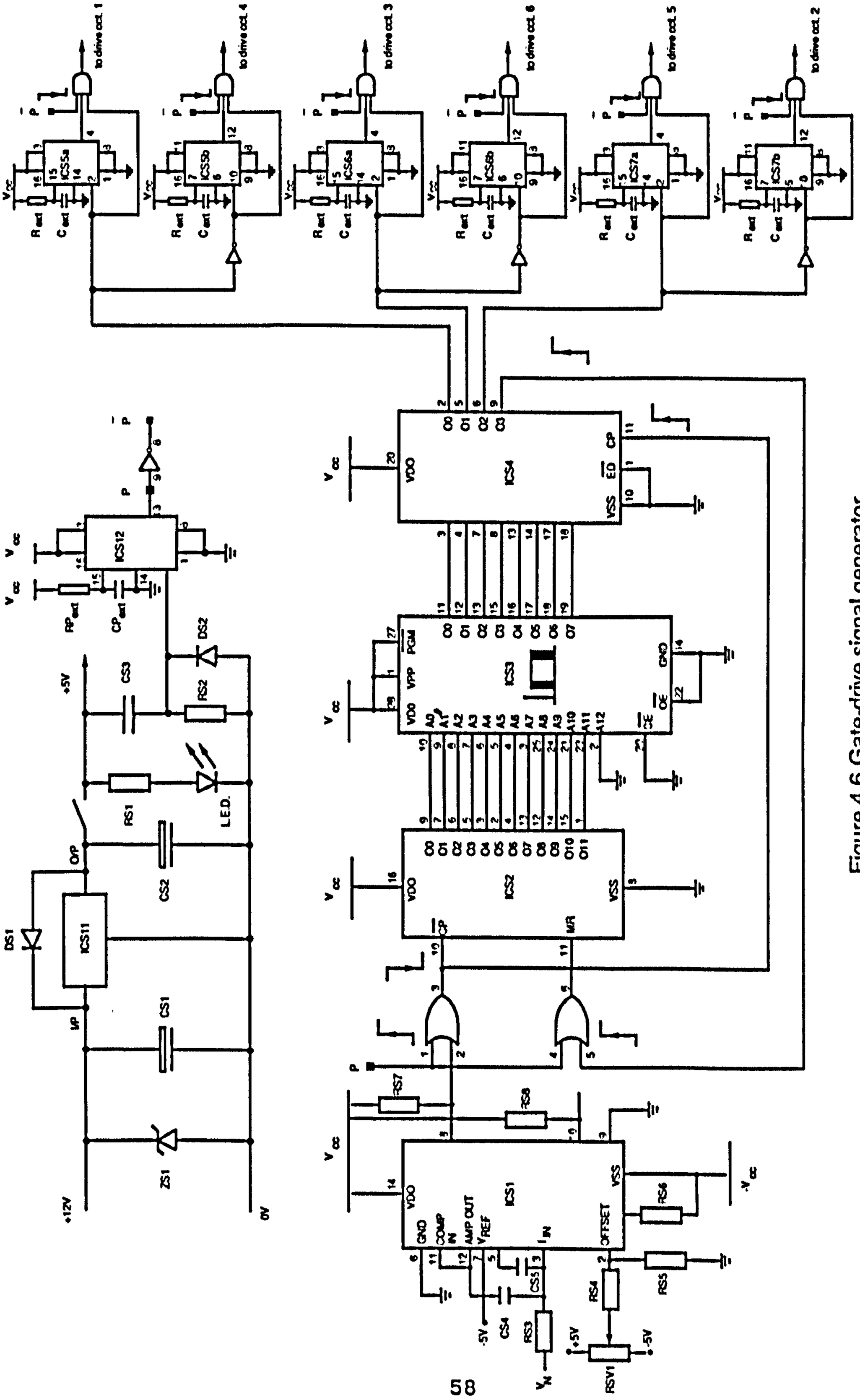

Figure 4.6 Gate-drive signal generator

explained below. $\overline{CE}$ is the power control used for device selection and $\overline{OE}$ the output enable control used to gate data from the output. Both $\overline{CE}$ and $\overline{OE}$ are grounded to ensure that the stored data which has been addressed by ICS2 is always available at the outputs O0 to O7 connected to ICS4.

ICS4 is an octal D-type flip-flop (IC74HCT374) used to latch the data at its output while the EPROM is delivering new data. This consists of 8 positive edge triggered D-type flip-flops operating from the clock CP, which also drives ICS2. When CP goes high, the input data D0 to D7 appears at the output; when it goes low, the output retains the data. As long as CP is low the input can change without affecting the output, until the arrival of the next pulse. The first three least significant bits of ICS4, output O0 to O2, define the conduction state of the three upper GTOs as either on (1) or off (0). The fourth bit on O3 is always low (0), while the switching code during a cycle is being accessed. At the end of one complete cycle, a high pulse on O3 is used to reset ICS2 enabling a new counting process to start for another cycle.

A 10μs non-overlapping time-delay is introduced between complementary output signals, to prevent a short circuit of the DC-link. This is achieved by applying the output signals of ICS4 to the three dual monostable multivibrators ICS5, ICS6 and ICS7, which generate the time delays in the trigger pulses. Figure 4.7 illustrates this operation schematically.

4.4 EPROM Programming

The implementation of the QSW mode or any of the optimal PWM modes is achieved using a look-up table technique. This involves mapping the pulse patterns for GTOs 1,3 and 5, as shown in figures 4.8(a) and (b) for the QSW and PWM2 modes of operation respectively. By doing this the 120° phase-shift between the three inverter phases is obtained, and phase balancing is achieved without the need for complex circuitry.

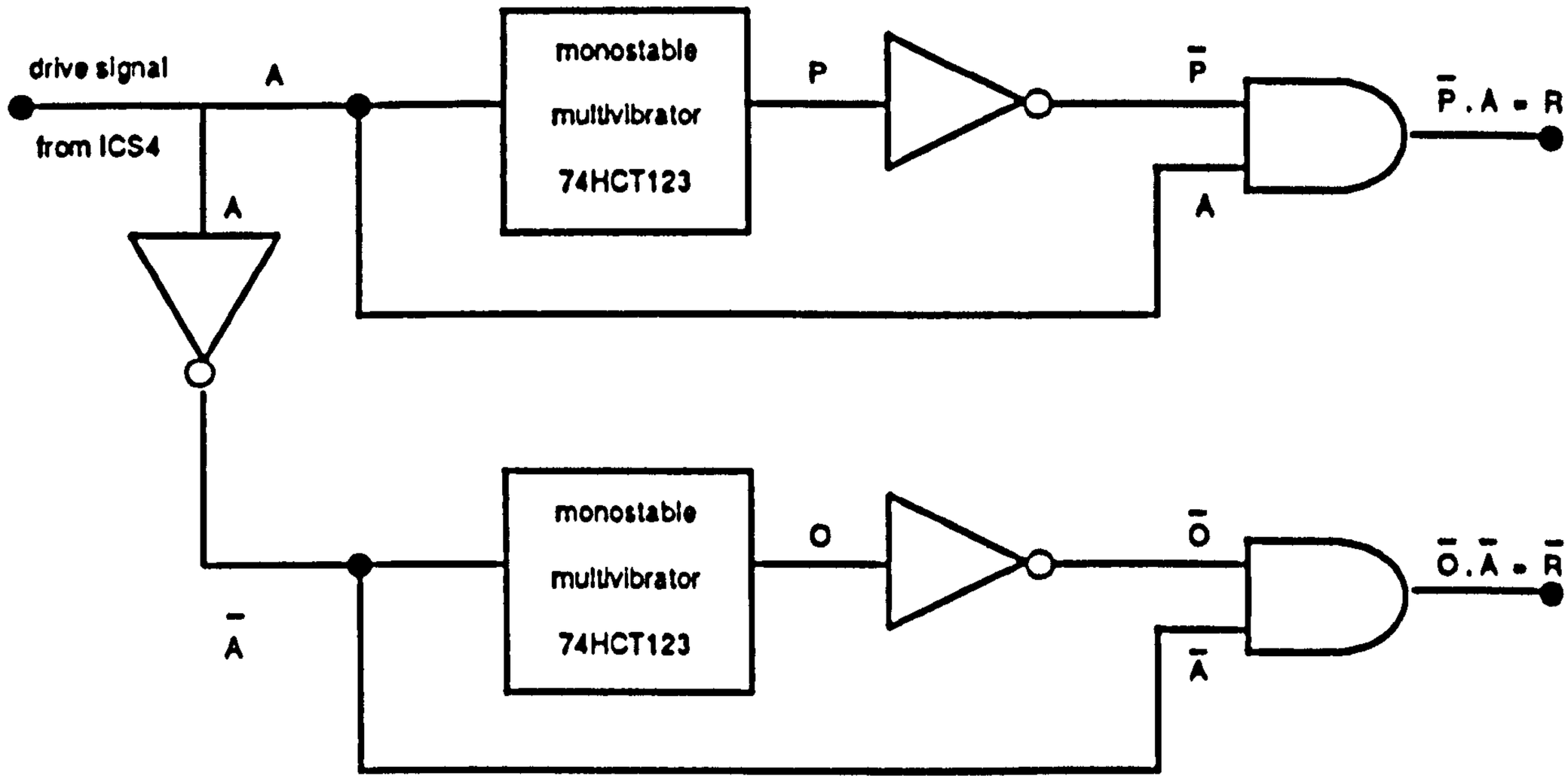

(a)

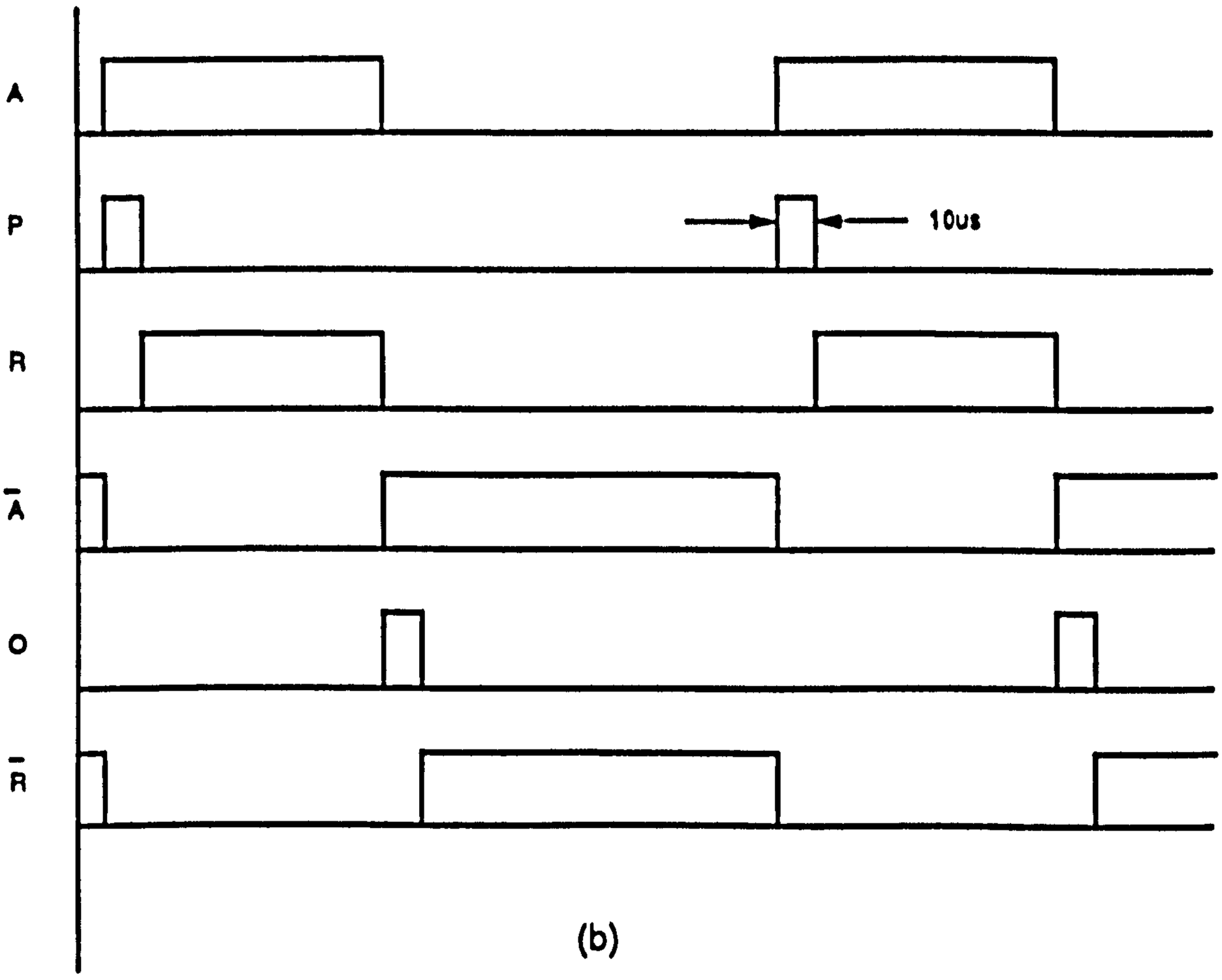

(b)

Figure 4.7 (a) Block diagram of circuit producing non-overlapping time delay in GTO1 and GTO4 energising phase A in the inverter bridge
(b) Waveforms at different stages in (a)

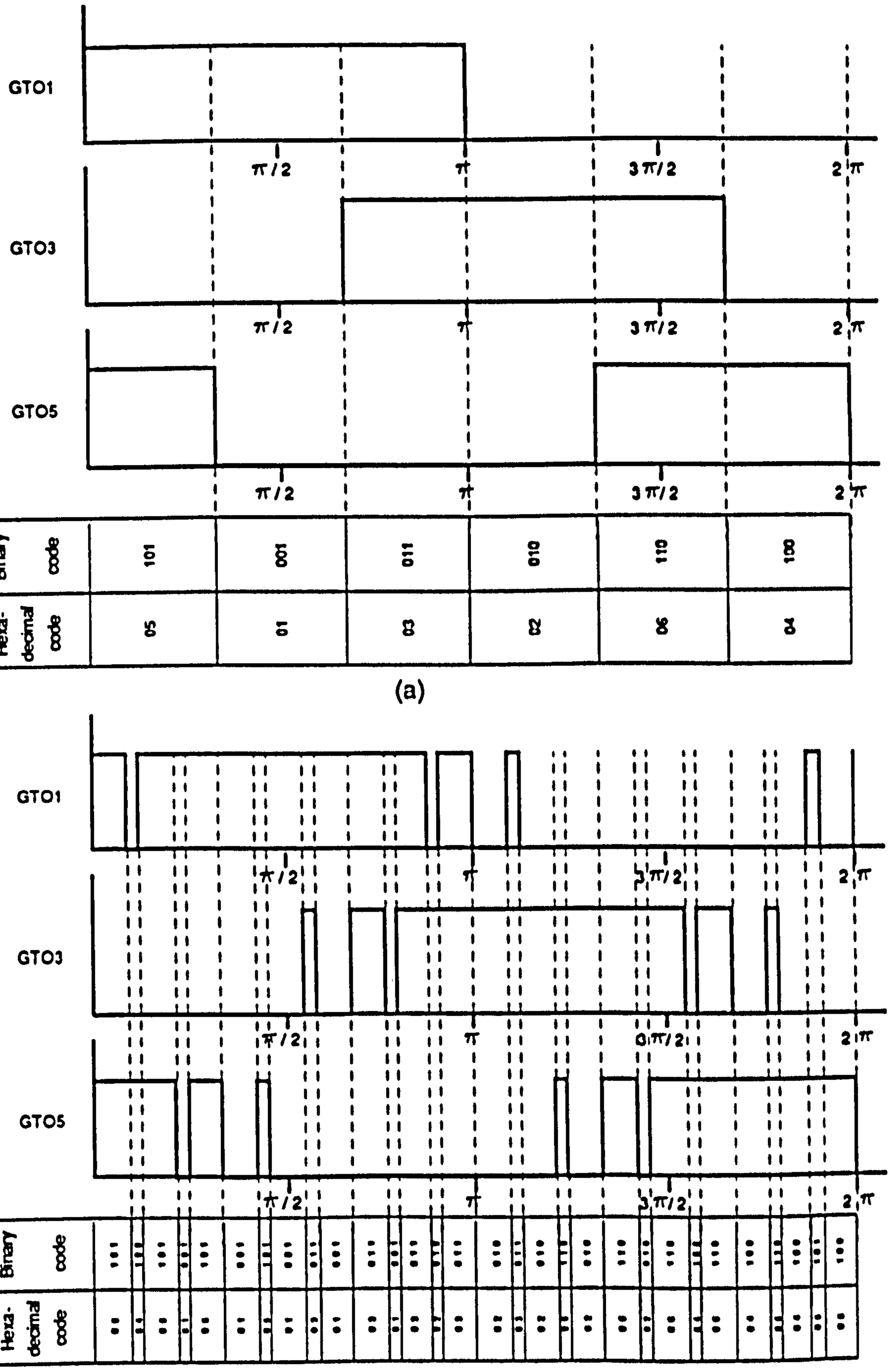

Binary code	101	001	011	010	110	100
Hexa-decimal code	05	01	03	02	06	04

(a)

(b)

Figure 4.8 Mapping of pulse-width durations for GTO1 , GTO3 and GTO5 , with the binary and hexadecimal codes representing their conduction patterns for (a) QSW and (b) PWM2 operating inverter modes

Irrespective of the pulse pattern, each switching instant α_i is defined as an angle with respect to the initial point of the cycle (which is zero radians). The pulse-width durations ΔP_n , are calculated in radians from

$$\Delta P_n = \alpha_{i-1} - \alpha_i \qquad 4.2$$

These pulse-width durations need to be transformed to integer numbers to be loaded into the EPROM. The number of words needed to be loaded into the EPROM to express the conduction pattern during these pulse durations is

$$W'_n = \frac{f_{o(max.)}}{f_{s(max.)}} \qquad 4.3$$

where $f_{o(max)} = 100kHz$ is the maximum clock frequency produced by the voltage/frequency converter and $f_{s(max)} = 50Hz$ is the maximum inverter output frequency. Hence $W'_n = 2000$ words define the switching pattern for one complete cycle, each of which corresponds to 0.0001π radians. The number of words NW_n in each pulse duration ΔP_n is

$$NW_n = \frac{\Delta P_n}{0.0001\pi} \qquad 4.4$$

The dimensionless numbers calculated from equation 4.4 are rounded to the nearest integer and stored in the EPROM memory in the form of a look-up table, shown in tables 4.1 and 4.2 for the QSW and PWM2 operating modes respectively.

4.5 Rotor Speed Measuring and Monitoring System

A principle objective of this thesis is to minimise the effect of torque pulsations in producing dangerous stresses and unsmooth angular motion of the rotor shaft, especially during low frequency operation. To accomplish this, a transducer is needed which accurately and instantaneously measures the speed response of the rotor shaft. An incremental

Table 4.1
Switching Pattern Hexadecimal Code for QSW Mode

ADD.	00	01	02	03	04	05	06	07	08	09	0A	0B	0C	0D	0E	0F
0000	05	05	05	05	05	05	05	05	05	05	05	05	05	05	05	05
0010	05	05	05	05	05	05	05	05	05	05	05	05	05	05	05	05
0020	05	05	05	05	05	05	05	05	05	05	05	05	05	05	05	05
0030	05	05	05	05	05	05	05	05	05	05	05	05	05	05	05	05
0040	05	05	05	05	05	05	05	05	05	05	05	05	05	05	05	05
0050	05	05	05	05	05	05	05	05	05	05	05	05	05	05	05	05
0060	05	05	05	05	05	05	05	05	05	05	05	05	05	05	05	05
0070	05	05	05	05	05	05	05	05	05	05	05	05	05	05	05	05
0080	05	05	05	05	05	05	05	05	05	05	05	05	05	05	05	05
0090	05	05	05	05	05	05	05	05	05	05	05	05	05	05	05	05
00A0	05	05	05	05	05	05	05	05	05	05	05	05	05	05	05	05
00B0	05	05	05	05	05	05	05	05	05	05	05	05	05	05	05	05
00C0	05	05	05	05	05	05	05	05	05	05	05	05	05	05	05	05
00D0	05	05	05	05	05	05	05	05	05	05	05	05	05	05	05	05
00E0	05	05	05	05	05	05	05	05	05	05	05	05	05	05	05	05
00F0	05	05	05	05	05	05	05	05	05	05	05	05	05	05	05	05
0100	05	05	05	05	05	05	05	05	05	05	05	05	05	05	05	05
0110	05	05	05	05	05	05	05	05	05	05	05	05	05	05	05	05
0120	05	05	05	05	05	05	05	05	05	05	05	05	05	05	05	05
0130	05	05	05	05	05	05	05	05	05	05	05	05	05	05	05	05
0140	05	05	05	05	05	05	05	05	05	05	05	05	01	01	01	
0150	01	01	01	01	01	01	01	01	01	01	01	01	01	01	01	01
0160	01	01	01	01	01	01	01	01	01	01	01	01	01	01	01	01
0170	01	01	01	01	01	01	01	01	01	01	01	01	01	01	01	01
0180	01	01	01	01	01	01	01	01	01	01	01	01	01	01	01	01
0190	01	01	01	01	01	01	01	01	01	01	01	01	01	01	01	01
01A0	01	01	01	01	01	01	01	01	01	01	01	01	01	01	01	01
01B0	01	01	01	01	01	01	01	01	01	01	01	01	01	01	01	01
01C0	01	01	01	01	01	01	01	01	01	01	01	01	01	01	01	01
01D0	01	01	01	01	01	01	01	01	01	01	01	01	01	01	01	01
01E0	01	01	01	01	01	01	01	01	01	01	01	01	01	01	01	01
01F0	01	01	01	01	01	01	01	01	01	01	01	01	01	01	01	01
0200	01	01	01	01	01	01	01	01	01	01	01	01	01	01	01	01
0210	01	01	01	01	01	01	01	01	01	01	01	01	01	01	01	01
0220	01	01	01	01	01	01	01	01	01	01	01	01	01	01	01	01
0230	01	01	01	01	01	01	01	01	01	01	01	01	01	01	01	01
0240	01	01	01	01	01	01	01	01	01	01	01	01	01	01	01	01
0250	01	01	01	01	01	01	01	01	01	01	01	01	01	01	01	01
0260	01	01	01	01	01	01	01	01	01	01	01	01	01	01	01	01
0270	01	01	01	01	01	01	01	01	01	01	01	01	01	01	01	01
0280	01	01	01	01	01	01	01	01	01	01	01	01	01	01	01	01
0290	01	01	01	01	01	01	01	01	01	01	01	03	03	03	03	03
02A0	03	03	03	03	03	03	03	03	03	03	03	03	03	03	03	03
02B0	03	03	03	03	03	03	03	03	03	03	03	03	03	03	03	03
02C0	03	03	03	03	03	03	03	03	03	03	03	03	03	03	03	03
02D0	03	03	03	03	03	03	03	03	03	03	03	03	03	03	03	03
02E0	03	03	03	03	03	03	03	03	03	03	03	03	03	03	03	03
02F0	03	03	03	03	03	03	03	03	03	03	03	03	03	03	03	03
0300	03	03	03	03	03	03	03	03	03	03	03	03	03	03	03	03
0310	03	03	03	03	03	03	03	03	03	03	03	03	03	03	03	03
0320	03	03	03	03	03	03	03	03	03	03	03	03	03	03	03	03
0330	03	03	03	03	03	03	03	03	03	03	03	03	03	03	03	03
0340	03	03	03	03	03	03	03	03	03	03	03	03	03	03	03	03
0350	03	03	03	03	03	03	03	03	03	03	03	03	03	03	03	03
0360	03	03	03	03	03	03	03	03	03	03	03	03	03	03	03	03
0370	03	03	03	03	03	03	03	03	03	03	03	03	03	03	03	03
0380	03	03	03	03	03	03	03	03	03	03	03	03	03	03	03	03
0390	03	03	03	03	03	03	03	03	03	03	03	03	03	03	03	03
03A0	03	03	03	03	03	03	03	03	03	03	03	03	03	03	03	03
03B0	03	03	03	03	03	03	03	03	03	03	03	03	03	03	03	03
03C0	03	03	03	03	03	03	03	03	03	03	03	03	03	03	03	03
03D0	03	03	03	03	03	03	03	03	03	03	03	03	03	03	03	03
03E0	03	03	03	03	03	03	03	03								

ADD.	00	01	02	03	04	05	06	07	08	09	0A	0B	0C	0D	0E	0F
03E0													02	02	02	02
03F0	02	02	02	02	02	02	02	02	02	02	02	02	02	02	02	02
0400	02	02	02	02	02	02	02	02	02	02	02	02	02	02	02	02
0410	02	02	02	02	02	02	02	02	02	02	02	02	02	02	02	02
0420	02	02	02	02	02	02	02	02	02	02	02	02	02	02	02	02
0430	02	02	02	02	02	02	02	02	02	02	02	02	02	02	02	02
0440	02	02	02	02	02	02	02	02	02	02	02	02	02	02	02	02
0450	02	02	02	02	02	02	02	02	02	02	02	02	02	02	02	02
0460	02	02	02	02	02	02	02	02	02	02	02	02	02	02	02	02
0470	02	02	02	02	02	02	02	02	02	02	02	02	02	02	02	02
0480	02	02	02	02	02	02	02	02	02	02	02	02	02	02	02	02
0490	02	02	02	02	02	02	02	02	02	02	02	02	02	02	02	02
04A0	02	02	02	02	02	02	02	02	02	02	02	02	02	02	02	02
04B0	02	02	02	02	02	02	02	02	02	02	02	02	02	02	02	02
04C0	02	02	02	02	02	02	02	02	02	02	02	02	02	02	02	02
04D0	02	02	02	02	02	02	02	02	02	02	02	02	02	02	02	02
04E0	02	02	02	02	02	02	02	02	02	02	02	02	02	02	02	02
04F0	02	02	02	02	02	02	02	02	02	02	02	02	02	02	02	02
0500	02	02	02	02	02	02	02	02	02	02	02	02	02	02	02	02
0510	02	02	02	02	02	02	02	02	02	02	02	02	02	02	02	02
0520	02	02	02	02	02	02	02	02	02	02	02	02	02	02	02	02
0530	02	02	02	02	02	06	06	06	06	06	06	06	06	06	06	06
0540	06	06	06	06	06	06	06	06	06	06	06	06	06	06	06	06
0550	06	06	06	06	06	06	06	06	06	06	06	06	06	06	06	06
0560	06	06	06	06	06	06	06	06	06	06	06	06	06	06	06	06
0570	06	06	06	06	06	06	06	06	06	06	06	06	06	06	06	06
0580	06	06	06	06	06	06	06	06	06	06	06	06	06	06	06	06
0590	06	06	06	06	06	06	06	06	06	06	06	06	06	06	06	06
05A0	06	06	06	06	06	06	06	06	06	06	06	06	06	06	06	06
05B0	06	06	06	06	06	06	06	06	06	06	06	06	06	06	06	06
05C0	06	06	06	06	06	06	06	06	06	06	06	06	06	06	06	06
05D0	06	06	06	06	06	06	06	06	06	06	06	06	06	06	06	06
05E0	06	06	06	06	06	06	06	06	06	06	06	06	06	06	06	06
05F0	06	06	06	06	06	06	06	06	06	06	06	06	06	06	06	06
0600	06	06	06	06	06	06	06	06	06	06	06	06	06	06	06	06
0610	06	06	06	06	06	06	06	06	06	06	06	06	06	06	06	06
0620	06	06	06	06	06	06	06	06	06	06	06	06	06	06	06	06
0630	06	06	06	06	06	06	06	06	06	06	06	06	06	06	06	06
0640	06	06	06	06	06	06	06	06	06	06	06	06	06	06	06	06
0650	06	06	06	06	06	06	06	06	06	06	06	06	06	06	06	06
0660	06	06	06	06	06	06	06	06	06	06	06	06	06	06	06	06
0670	06	06	06	06	06	06	06	06	06	06	06	06	06	06	06	06
0680	06	06	06	04	04	04	04	04	04	04	04	04	04	04	04	04
0690	04	04	04	04	04	04	04	04	04	04	04	04	04	04	04	04
06A0	04	04	04	04	04	04	04	04	04	04	04	04	04	04	04	04
06B0	04	04	04	04	04	04	04	04	04	04	04	04	04	04	04	04
06C0	04	04	04	04	04	04	04	04	04	04	04	04	04	04	04	04
06D0	04	04	04	04	04	04	04	04	04	04	04	04	04	04	04	04
06E0	04	04	04	04	04	04	04	04	04	04	04	04	04	04	04	04
06F0	04	04	04	04	04	04	04	04	04	04	04	04	04	04	04	04
0700	04	04	04	04	04	04	04	04	04	04	04	04	04	04	04	04
0710	04	04	04	04	04	04	04	04	04	04	04	04	04	04	04	04
0720	04	04	04	04	04	04	04	04	04	04	04	04	04	04	04	04
0730	04	04	04	04	04	04	04	04	04	04	04	04	04	04	04	04
0740	04	04	04	04	04	04	04	04	04	04	04	04	04	04	04	04
0750	04	04	04	04	04	04	04	04	04	04	04	04	04	04	04	04
0760	04	04	04	04	04	04	04	04	04	04	04	04	04	04	04	04
0770	04	04	04	04	04	04	04	04	04	04	04	04	04	04	04	04
0780	04	04	04	04	04	04	04	04	04	04	04	04	04	04	04	04
0790	04	04	04	04	04	04	04	04	04	04	04	04	04	04	04	04
07A0	04	04	04	04	04	04	04	04	04	04	04	04	04	04	04	04
07B0	04	04	04	04	04	04	04	04	04	04	04	04	04	04	04	04
07C0	04	04	04	04	04	04	04	04	04	04	04	04	04	04	04	04
07D0	0C															

Table 4.2
Switching Pattern Hexadecimal Code for PWM2 Optimal Mode

ADD.	00	01	02	03	04	05	06	07	08	09	0A	0B	0C	0D	0E	0F
0000	05	05	05	05	05	05	05	05	05	05	05	05	05	05	05	05
0010	05	05	05	05	05	05	05	05	05	05	05	05	05	05	05	05
0020	05	05	05	05	05	05	05	05	05	05	05	05	05	05	05	05
0030	05	05	05	05	05	05	05	05	05	05	05	05	05	05	05	05
0040	05	05	05	05	05	05	05	05	05	05	05	05	05	05	05	05
0050	05	05	05	05	05	05	05	05	05	05	04	04	04	04	04	04
0060	04	04	04	04	04	04	04	04	04	04	04	04	04	04	04	04
0070	04	04	04	04	04	04	04	04	04	04	05	05	05	05	05	05
0080	05	05	05	05	05	05	05	05	05	05	05	05	05	05	05	05
0090	05	05	05	05	05	05	05	05	05	05	05	05	05	05	05	05
00A0	05	05	05	05	05	05	05	05	05	05	05	05	05	05	05	05
00B0	05	05	05	05	05	05	05	05	05	05	05	05	05	05	05	05
00C0	05	05	05	05	05	05	05	05	05	05	05	05	05	05	05	05
00D0	05	05	01	01	01	01	01	01	01	01	01	01	01	01	01	01
00E0	01	01	01	01	01	01	01	01	01	01	01	01	01	01	01	01
00F0	01	01	01	05	05	05	05	05	05	05	05	05	05	05	05	05
0100	05	05	05	05	05	05	05	05	05	05	05	05	05	05	05	05
0110	05	05	05	05	05	05	05	05	05	05	05	05	05	05	05	05
0120	05	05	05	05	05	05	05	05	05	05	05	05	05	05	05	05
0130	05	05	05	05	05	05	05	05	05	05	05	05	05	05	05	05
0140	05	05	05	05	05	05	05	05	05	05	05	05	05	01	01	01
0150	01	01	01	01	01	01	01	01	01	01	01	01	01	01	01	01
0160	01	01	01	01	01	01	01	01	01	01	01	01	01	01	01	01
0170	01	01	01	01	01	01	01	01	01	01	01	01	01	01	01	01
0180	01	01	01	01	01	01	01	01	01	01	01	01	01	01	01	01
0190	01	01	01	01	01	01	01	01	01	01	01	01	01	01	01	01
01A0	01	01	01	01	01	01	01	05	05	05	05	05	05	05	05	05
01B0	05	05	05	05	05	05	05	05	05	05	05	05	05	05	05	05
01C0	05	05	05	05	05	05	05	05	01	01	01	01	01	01	01	01
01D0	01	01	01	01	01	01	01	01	01	01	01	01	01	01	01	01
01E0	01	01	01	01	01	01	01	01	01	01	01	01	01	01	01	01
01F0	01	01	01	01	01	01	01	01	01	01	01	01	01	01	01	01
0200	01	01	01	01	01	01	01	01	01	01	01	01	01	01	01	01
0210	01	01	01	01	01	01	01	01	01	01	01	01	01	01	01	01
0220	03	03	03	03	03	03	03	03	03	03	03	03	03	03	03	03
0230	03	03	03	03	03	03	03	03	03	03	03	03	03	03	03	03
0240	03	01	01	01	01	01	01	01	01	01	01	01	01	01	01	01
0250	01	01	01	01	01	01	01	01	01	01	01	01	01	01	01	01
0260	01	01	01	01	01	01	01	01	01	01	01	01	01	01	01	01
0270	01	01	01	01	01	01	01	01	01	01	01	01	01	01	01	01
0280	01	01	01	01	01	01	01	01	01	01	01	01	01	01	01	01
0290	01	01	01	01	01	01	01	01	01	01	03	03	03	03	03	03
02A0	03	03	03	03	03	03	03	03	03	03	03	03	03	03	03	03
02B0	03	03	03	03	03	03	03	03	03	03	03	03	03	03	03	03
02C0	03	03	03	03	03	03	03	03	03	03	03	03	03	03	03	03
02D0	03	03	03	03	03	03	03	03	03	03	03	03	03	03	03	03
02E0	03	03	03	03	03	03	03	03	03	03	03	03	03	03	03	03
02F0	03	03	03	03	03	01	01	01	01	01	01	01	01	01	01	01
0300	01	01	01	01	01	01	01	01	01	01	01	01	01	01	01	01
0310	01	01	01	01	01	03	03	03	03	03	03	03	03	03	03	03
0320	03	03	03	03	03	03	03	03	03	03	03	03	03	03	03	03
0330	03	03	03	03	03	03	03	03	03	03	03	03	03	03	03	03
0340	03	03	03	03	03	03	03	03	03	03	03	03	03	03	03	03
0350	03	03	03	03	03	03	03	03	03	03	03	03	03	03	03	03
0360	03	03	03	03	03	03	03	03	03	03	03	03	03	02	02	02
0370	02	02	02	02	02	02	02	02	02	02	02	02	02	02	02	02
0380	02	02	02	02	02	02	02	02	02	02	02	02	02	02	03	03
0390	03	03	03	03	03	03	03	03	03	03	03	03	03	03	03	03
03A0	03	03	03	03	03	03	03	03	03	03	03	03	03	03	03	03
03B0	03	03	03	03	03	03	03	03	03	03	03	03	03	03	03	03
03C0	03	03	03	03	03	03	03	03	03	03	03	03	03	03	03	03
03D0	03	03	03	03	03	03	03	03	03	03	03	03	03	03	03	03
03E0	03	03	03	03	03	03	03	03								

ADD.	00	01	02	03	04	05	06	07	08	09	0A	0B	0C	0D	0E	0F
03E0									02	02	02	02	02	02	02	02
03F0	02	02	02	02	02	02	02	02	02	02	02	02	02	02	02	02
0400	02	02	02	02	02	02	02	02	02	02	02	02	02	02	02	02
0410	02	02	02	02	02	02	02	02	02	02	02	02	02	02	02	02
0420	02	02	02	02	02	02	02	02	02	02	02	02	02	02	02	02
0430	02	02	02	02	02	02	02	02	02	02	02	02	02	02	02	02
0440	02	02	03	03	03	03	03	03	03	03	03	03	03	03	03	03
0450	03	03	03	03	03	03	03	03	03	03	03	03	03	03	03	03
0460	03	03	02	02	02	02	02	02	02	02	02	02	02	02	02	02
0470	02	02	02	02	02	02	02	02	02	02	02	02	02	02	02	02
0480	02	02	02	02	02	02	02	02	02	02	02	02	02	02	02	02
0490	02	02	02	02	02	02	02	02	02	02	02	02	02	02	02	02
04A0	02	02	02	02	02	02	02	02	02	02	02	02	02	02	02	02
04B0	02	02	02	02	02	02	02	02	02	02	06	06	06	06	06	06
04C0	06	06	06	06	06	06	06	06	06	06	06	06	06	06	06	06
04D0	06	06	06	06	06	06	06	06	06	06	06	06	02	02	02	02
04E0	02	02	02	02	02	02	02	02	02	02	02	02	02	02	02	02
04F0	02	02	02	02	02	02	02	02	02	02	02	02	02	02	02	02
0500	02	02	02	02	02	02	02	02	02	02	02	02	02	02	02	02
0510	02	02	02	02	02	02	02	02	02	02	02	02	02	02	02	02
0520	02	02	02	02	02	02	02	02	02	02	02	02	02	02	02	02
0530	02	02	02	02	02	06	06	06	06	06	06	06	06	06	06	06
0540	06	06	06	06	06	06	06	06	06	06	06	06	06	06	06	06
0550	06	06	06	06	06	06	06	06	06	06	06	06	06	06	06	06
0560	06	06	06	06	06	06	06	06	06	06	06	06	06	06	06	06
0570	06	06	06	06	06	06	06	06	06	06	06	06	06	06	06	06
0580	06	06	06	06	06	06	06	06	06	06	06	06	06	06	06	02
0590	02	02	02	02	02	02	02	02	02	02	02	02	02	02	02	02
05A0	02	02	02	02	02	02	02	02	02	02	02	02	02	02	02	02
05B0	06	06	06	06	06	06	06	06	06	06	06	06	06	06	06	06
05C0	06	06	06	06	06	06	06	06	06	06	06	06	06	06	06	06
05D0	06	06	06	06	06	06	06	06	06	06	06	06	06	06	06	06
05E0	06	06	06	06	06	06	06	06	06	06	06	06	06	06	06	06
05F0	06	06	06	06	06	06	06	06	06	06	06	06	06	06	06	06
0600	06	06	06	06	06	06	06	06	04	04	04	04	04	04	04	04
0610	04	04	04	04	04	04	04	04	04	04	04	04	04	04	04	04
0620	04	04	04	04	04	04	04	04	04	06	06	06	06	06	06	06
0630	06	06	06	06	06	06	06	06	06	06	06	06	06	06	06	06
0640	06	06	06	06	06	06	06	06	06	06	06	06	06	06	06	06
0650	06	06	06	06	06	06	06	06	06	06	06	06	06	06	06	06
0660	06	06	06	06	06	06	06	06	06	06	06	06	06	06	06	06
0670	06	06	06	06	06	06	06	06	06	06	06	06	06	06	06	06
0680	06	06	06	04	04	04	04	04	04	04	04	04	04	04	04	04
0690	04	04	04	04	04	04	04	04	04	04	04	04	04	04	04	04
06A0	04	04	04	04	04	04	04	04	04	04	04	04	04	04	04	04
06B0	04	04	04	04	04	04	04	04	04	04	04	04	04	04	04	04
06C0	04	04	04	04	04	04	04	04	04	04	04	04	04	04	04	04
06D0	04	04	04	04	04	04	04	04	04	04	04	04	04	06	06	06
06E0	06	06	06	06	06	06	06	06	06	06	06	06	06	06	06	06
06F0	06	06	06	06	06	06	06	06	06	06	06	06	06	04	04	04
0700	04	04	04	04	04	04	04	04	04	04	04	04	04	04	04	04
0710	04	04	04	04	04	04	04	04	04	04	04	04	04	04	04	04
0720	04	04	04	04	04	04	04	04	04	04	04	04	04	04	04	04
0730	04	04	04	04	04	04	04	04	04	04	04	04	04	04	04	04
0740	04	04	04	04	04	04	04	04	04	04	04	04	04	04	04	04
0750	04	04	04	04	04	05	05	05	05	05	05	05	05	05	05	05
0760	05	05	05	05	05	05	05	05	05	05	05	05	05	05	05	05
0770	05	05	05	05	05	05	04	04	04	04	04	04	04	04	04	04
0780	04	04	04	04	04	04	04	04	04	04	04	04	04	04	04	04
0790	04	04	04	04	04	04	04	04	04	04	04	04	04	04	04	04
07A0	04	04	04	04	04	04	04	04	04	04	04	04	04	04	04	04
07B0	04	04	04	04	04	04	04	04	04	04	04	04	04	04	04	04
07C0	04	04	04	04	04	04	04	04	04	04	04	04	04	04	04	04
07D0	0C															

shaft encoder was used, which produces a train of pulses at a rate directly proportional to the instantaneous angular velocity. This is applied to a frequency/voltage converter connected as in figure 4.9, with the output voltage signal being related to the input frequency $f_{encoder}$ by

$$V_{out} = [\ V_{REF}\ C_5 \cdot R_9\ ]\ f_{encoder} \qquad 4.5$$

with V_{REF}, C_5 and R_9 adjusted externally. The output signal inevitably contains a superimposed ripple, and this is minimised using the circuit shown in figure 4.9. This ripple eliminator circuit has unity DC gain and operates on the principle of matching the gain of the positively amplified ripple via the lower path and the negatively amplified ripple via the upper path. Thus, when both paths have the same gain, complete ripple cancellation is achieved.

A digital technique is implemented to calibrate the analogue output signal and to obtain accurate speed measurement over the full speed range. This technique is designated as a constant time resolver [71], since it involves the counting, in successive scaled equal intervals, of the number of pulses that are enclosed. The encoder used in this work produces N = 1250 pulses per revolution of its rotor shaft. If the rotor speed is ω_m rpm, the encoder output pulse frequency is

$$f_{encoder} = N\ \omega_m / 60 \qquad 4.6$$

and the pulse duration $T_{encoder}$ is

$$T_{encoder} = \frac{60}{\omega_m\ N} \qquad 4.7$$

For a minimum rotor speed of 1rpm, a maximum pulse-duration of 48ms is produced. This represents the width of the time interval which encloses a number of encoder pulses equal to the rotor speed in rpm.

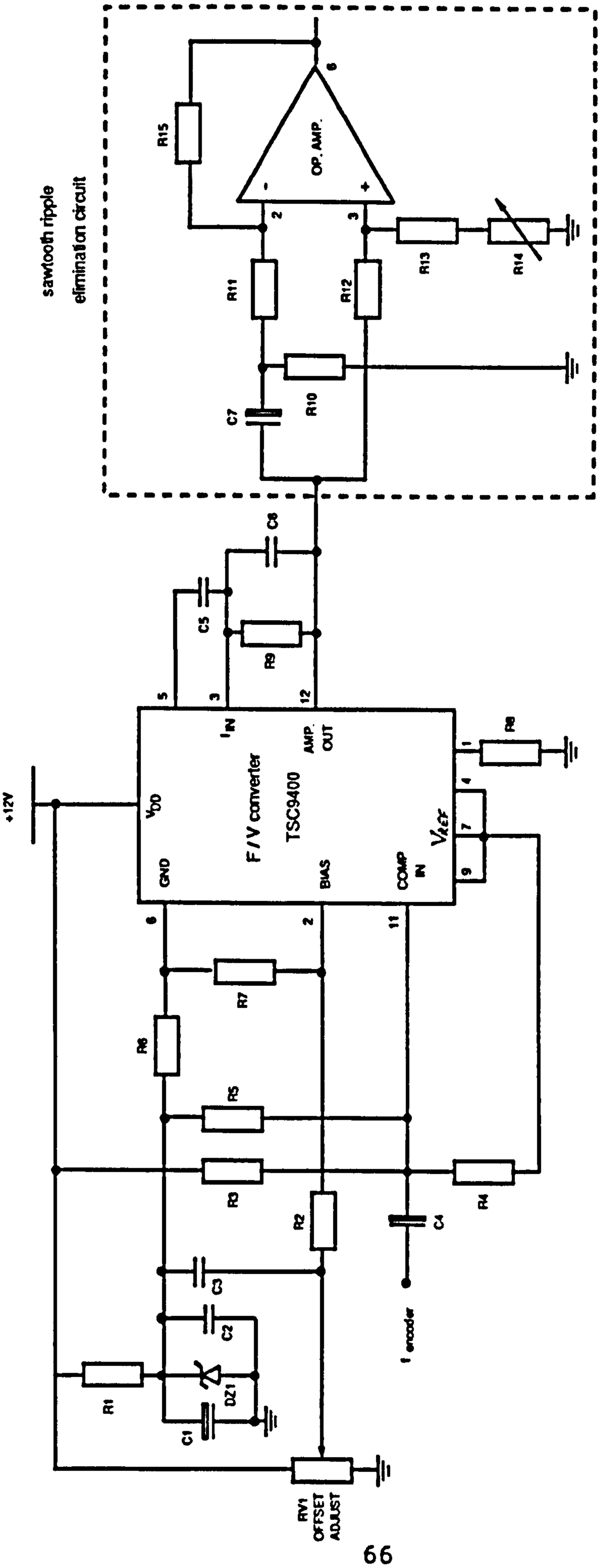

Figure 4.9 Analogue speed and ripple detection circuit

Figure 4.10 shows the digital system designed specifically to determine the motor speed. The pulse duration of 48ms is achieved using the astable multivibrator IC1 to generate a clock signal A of 18.4Hz (i.e. a periodic time of 54.4ms). This is applied to the monostable multivibrator IC2, with a proper selection of R_{ext} and C_{ext} providing a counting signal B of 48ms duration. This signal is gated with the encoder output, using an AND gate to produce an output pulse train C within the duration of the gating signal.

IC3 is a CMOS L.C.D. counter/decoder/driver, which counts the number of pulses within the prescribed duration of the gating signal B. At the end of this signal, IC3 provides outputs suitable for driving a conventional four-digit by seven segment L.C.D. display. IC3 will increment on the falling edge of the signal at the count input. At the end of each counting period the output data latched at the driver are updated when a low level pulse is applied at the store pin 34. At the end of the store pulse, a further pulse resets the counter when it is received at pin 33. These two pulses are generated by a dual monostable multivibrator IC4. IC4a is triggered by the falling edge of gating signal B and produces store pulse D, while IC4b is triggered by the falling edge of pulse D and produces the reset pulse E.

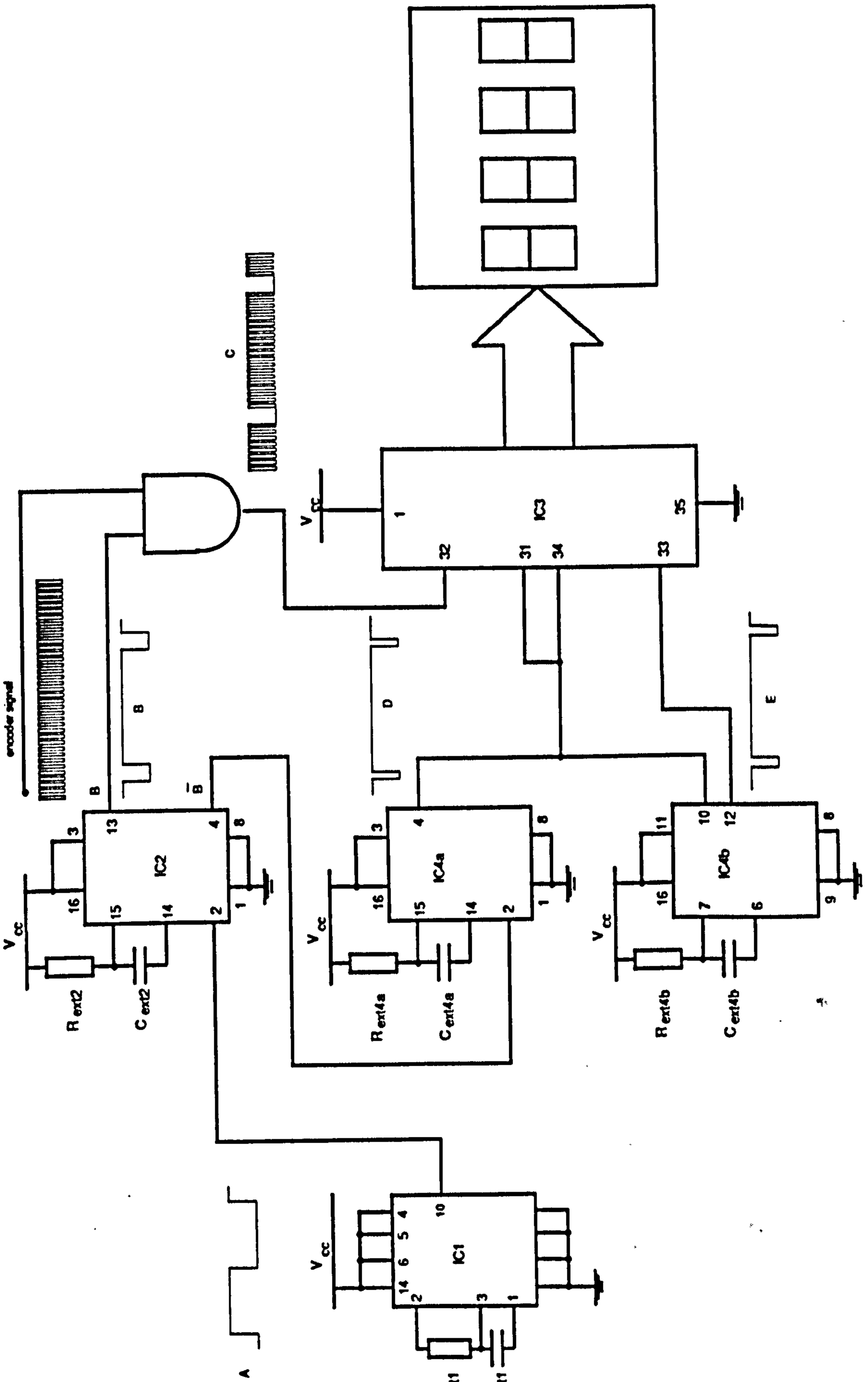

Figure 4.10 Digital speed measurement system

CHAPTER 5

MATHEMATICAL MODELLING OF VOLTAGE SOURCE INVERTER/INDUCTION MOTOR DRIVE SYSTEM

This chapter describes a computer model for a VSI/Induction motor drive system, which enables a thorough investigation of QSW and various PWM strategies to be undertaken. Due to the greater flexibility and accuracy of prediction, the model uses direct-phase reference frame machine equations in preference to those in d,q or $\alpha.\beta$ reference frames. The analysis uses tensor techniques to simulate the switching operation of the inverter semiconductor devices, specifying some of their physical constraints so that the model reflects the practical system as closely as possible. A detailed description of the program structure shows how the model handles changing circuit topologies for any operating mode. The choice of numerical integration and Fourier analysis methods according to the model requirements are explained. Finally, computed results which illustrate the machine dynamics in terms of voltage, current, torque and speed are presented, and these are compared wherever possible with practical results.

5.1 Voltage Source Inverter/Induction Motor Model

The drive system of figure 5.1 shows star-connected stator and rotor windings and the analysis below is based upon the following assumptions :

(1) The inverter is fed from an infinitely stiff voltage source.
(2) A GTO is turned on when a firing pulse is applied to its gate, developing a forward voltage drop when conducting. When turned off, it behaves as an ideal open switch.
(3) The motor has an ideal cylindrical rotor and a uniform airgap.
(4) Magnetic saturation, hysteresis and eddy current effects are neglected.
(5) The stator and rotor windings are symmetrical.

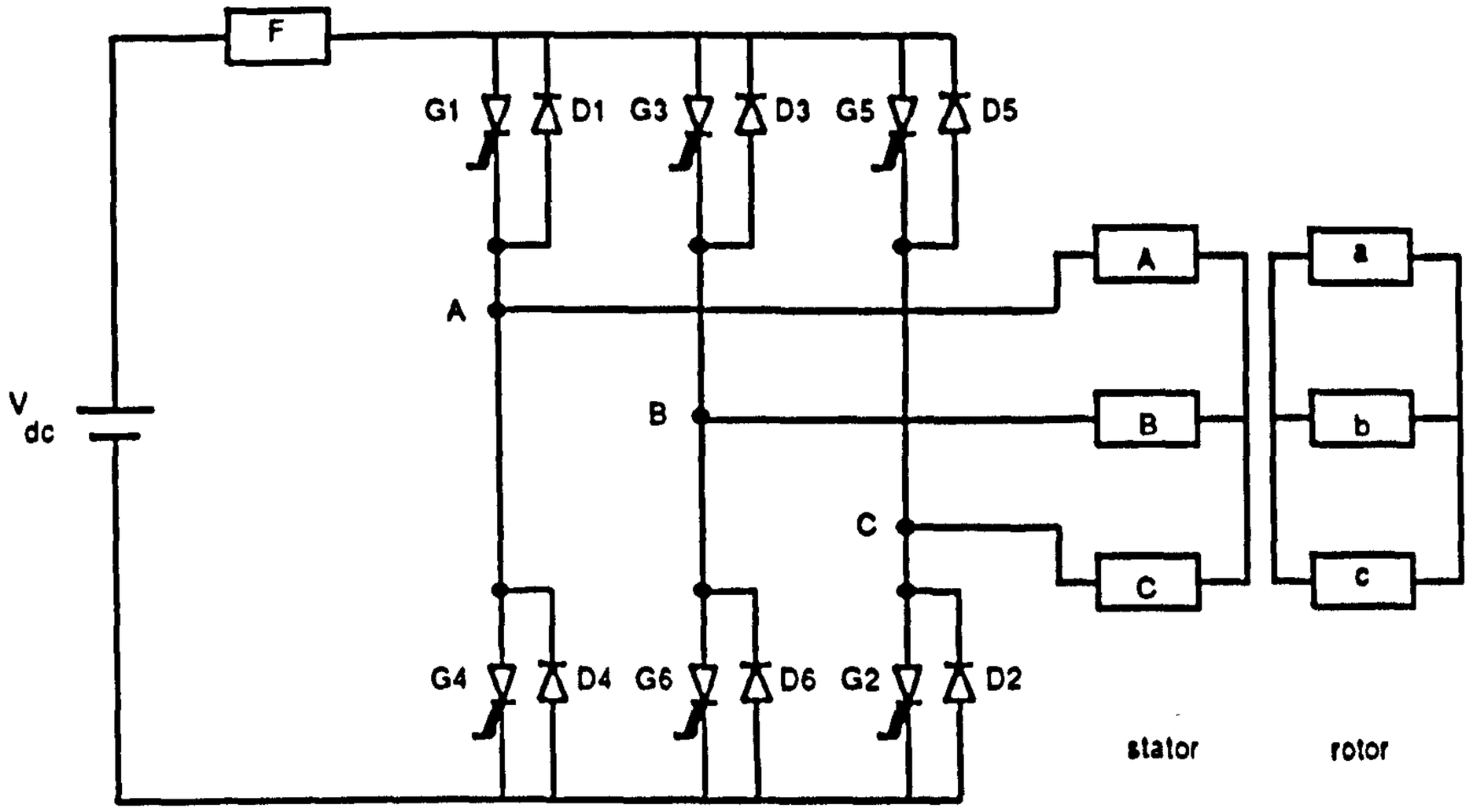

Figure 5.1 Voltage source inverter / induction motor drive

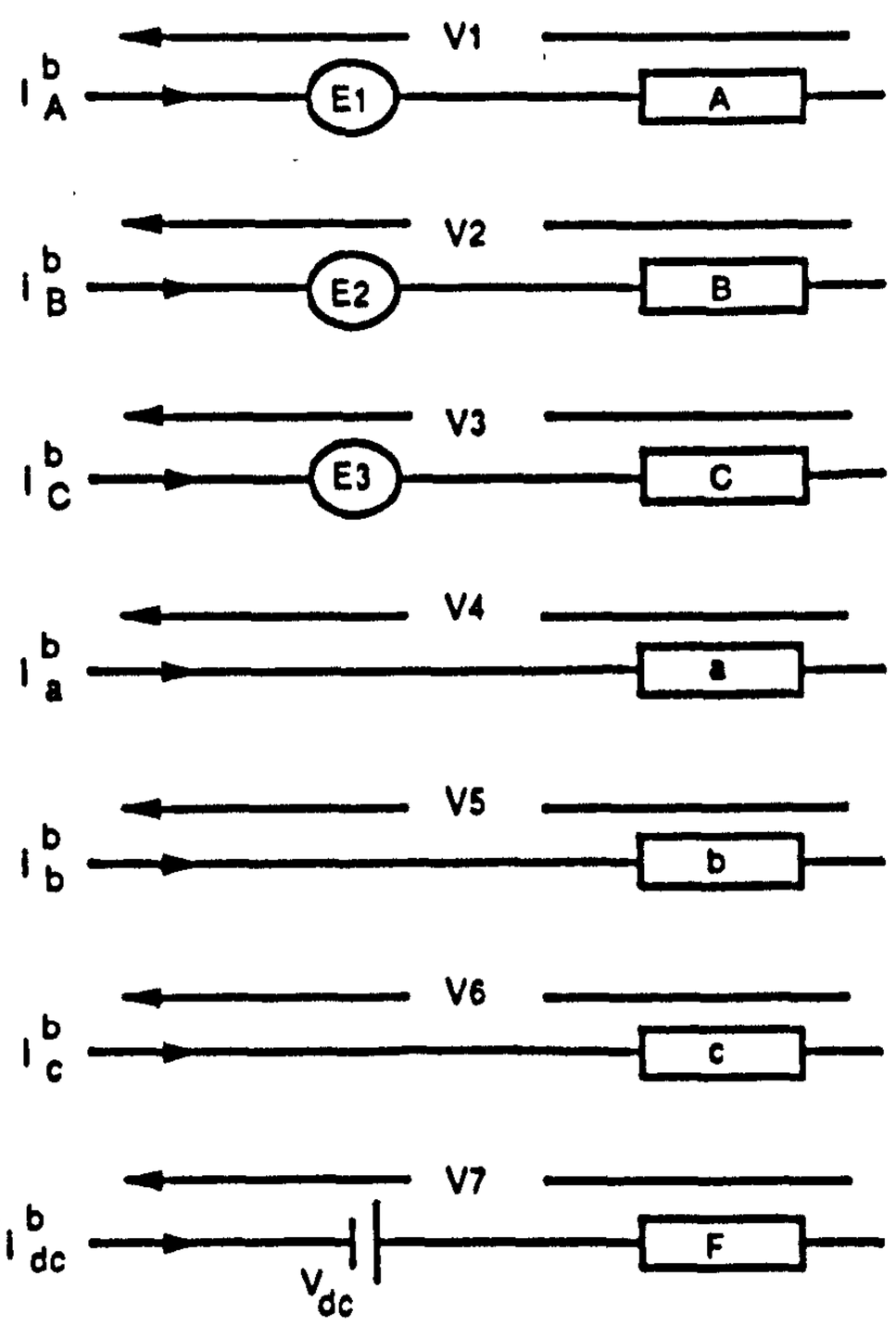

Figure 5.2 Branch (primitive) reference frame

(6) The mutual inductances between any stator and rotor windings are cosine functions of the rotor electrical angle.

Three inverter devices are on at any time during a 180° , with the constraint that, to prevent a short circuit of the DC-link, no two devices in the same arm are conducting. There are therefore six possible switch combinations usually associated with QSW and PWM operation modes, corresponding to six different circuit topologies. Moreover, since the motor current lags the voltage, operation of the free-wheeling diodes is considered in conjunction with that of the GTOs.

5.2 Tensor Analysis

In order to simulate the inverter operation the program requires a logic check at each time increment, both to determine the conducting devices forming each circuit topology and to set up the system equations. The development of tensor techniques in modelling static circuits [72-73] has led to an elegant and superior method of dealing with periodic varying circuit topologies and this technique is employed here. The automatic assembly of the mesh differential equations relevant to the changing pattern of switching devices requires the definition of branch (or primitive) and mesh reference frames.

5.2.1 Branch and Mesh Reference Frames

The branch network for the inverter/induction motor system can be developed by disconnecting all stator and rotor windings and removing all connections between circuit elements forming the inverter. Assuming that each parallel diode/GTO may be represented by resistor would require the addition of six branches defining the inverter, thereby complicating the program unnecessarily and increasing the computation time [74]. A simpler representation is obtained by adding the forward voltage drops of the conducting devices to the relevant branch voltage sources F_1 . F_2 & F_3 as shown in figure 5.2. When this is done the matrix differential equation relating to the branch reference frame is as given in equation 5.1,

$$
\begin{vmatrix} E_1+0 \\ E_2+0 \\ E_3+0 \\ 0 \\ 0 \\ 0 \\ 0 \\ E_T \end{vmatrix} = \begin{vmatrix} R_s+\rho L_{ss} & \rho M_s & \rho M_s & \rho M_{sr}\cos\theta_e & \rho M_{sr}\cos\left(\theta_e+\frac{2\pi}{3}\right) & \rho M_{sr}\cos\left(\theta_e-\frac{2\pi}{3}\right) & 0 \\ \rho M_s & R_s+\rho L_{ss} & \rho M_s & \rho M_{sr}\cos\left(\theta_e-\frac{2\pi}{3}\right) & \rho M_{sr}\cos\theta_e & \rho M_{sr}\cos\left(\theta_e+\frac{2\pi}{3}\right) & 0 \\ \rho M_s & \rho M_s & R_s+\rho L_{ss} & \rho M_{sr}\cos\left(\theta_e+\frac{2\pi}{3}\right) & \rho M_{sr}\cos\left(\theta_e-\frac{2\pi}{3}\right) & \rho M_{sr}\cos\theta_e & 0 \\ \rho M_{sr}\cos\theta_e & \rho M_{sr}\cos\left(\theta_e-\frac{2\pi}{3}\right) & \rho M_{sr}\cos\left(\theta_e+\frac{2\pi}{3}\right) & R_r+\rho L_{rr} & \rho M_r & \rho M_r & 0 \\ \rho M_{sr}\cos\left(\theta_e+\frac{2\pi}{3}\right) & \rho M_{sr}\cos\theta_e & \rho M_{sr}\cos\left(\theta_e-\frac{2\pi}{3}\right) & \rho M_r & R_r+\rho L_{rr} & \rho M_r & 0 \\ \rho M_{sr}\cos\left(\theta_e-\frac{2\pi}{3}\right) & \rho M_{sr}\cos\left(\theta_e+\frac{2\pi}{3}\right) & \rho M_{sr}\cos\theta_e & \rho M_r & \rho M_r & R_r+\rho L_{rr} & 0 \\ 0 & 0 & 0 & 0 & 0 & 0 & R_{dc}+\rho L_{dc} \end{vmatrix} \cdot \begin{vmatrix} i_A \\ i_B \\ i_C \\ i_a \\ i_b \\ i_c \\ i_{dc} \end{vmatrix}
$$

5.1

Using Happ's notation [75], equation 5.1 may be written in the abbreviated form

$$V_b + E_b = Z_b I^b = \left(R_b + \rho\theta_e \frac{\partial L_b}{\partial \theta_e}\right) I^b + L_b \rho I^b \qquad 5.2$$

where ρ is the differential operator d/dt and θ_e the rotor electrical angle. R_b is a 7x7 resistance matrix containing diagonal terms only and L_b and $\partial L_b/\partial\theta_e$ are respectively a 7x7 inductance matrix and its rate-of-change, I^b a 7x1 branch current vector, V_b a 7x1 branch voltage vector and E_b the 7x1 vector of source voltages within the branches. E_1, E_2, E_3 are the voltage drops across the conducting devices in the inverter arms connected to phases A,B,C respectively, and E_7 is the DC-link voltage. R_{dc} and L_{dc} represent the source impedance shown as F in figure 5.1 and are substituted as 0.0 in the analysis. The parameters of equation 5.1 are derived from the equivalent circuit parameters and are given in appendix A.1.

The mesh reference frame is concerned with the mesh equations formed when the inverter switching elements connect the motor phases to the DC source. As explained earlier, the drive operation can be represented by the six different circuit topologies shown in figures 5.3(a) to (f), where each topology is defined by four meshes. The abbreviated form of the matrix differential equation defining the system meshes is

$$V_m + E_m = Z_m I^m = \left(R_m + \rho\theta_e \frac{\partial L_m}{\partial \theta_e}\right) I^m + L_m \rho I^m \qquad 5.3$$

where

E_m is a 4x1 mesh voltage vector.

$V_m = 0$ (null vector) according to Kirchhoff's voltage law.

I^m a 4x1 mesh current vector.

R_m a 4x4 mesh resistance matrix.

L_m a 4x4 mesh inductance matrix.

branch \ mesh	m_{i1}	m_{i2}	m_{i3}	m_{i4}
i_{bA}	1	1	0	0
i_{bB}	0	-1	0	0
i_{bC}	-1	0	0	0
i_{ba}	0	0	-1	-1
i_{bb}	0	0	0	1
i_{bc}	0	0	1	0
i_{bf}	1	0	0	0

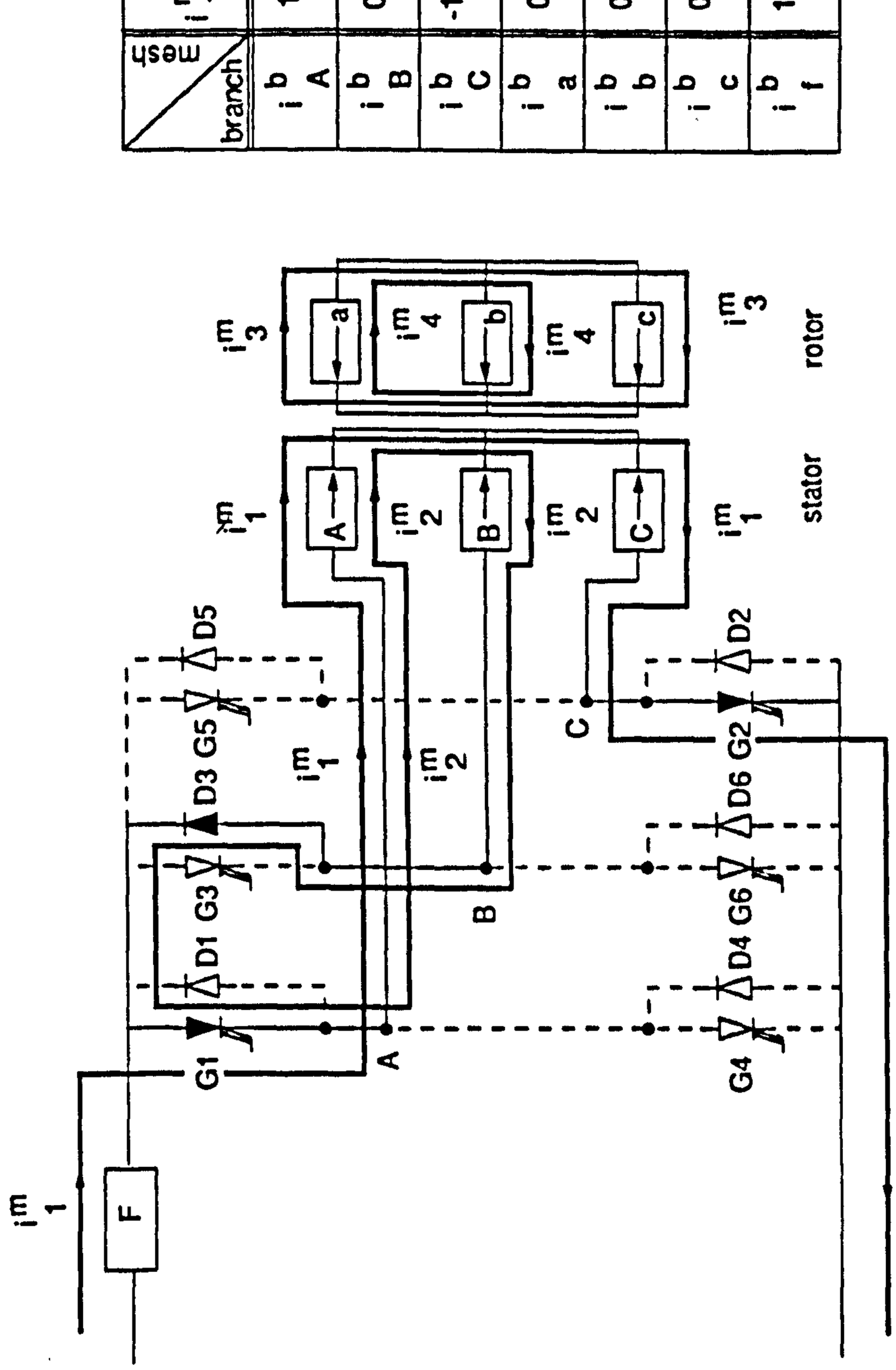

Figure 5.3 (a) Typical circuit topology and current transformation matrix when GTOs 1 2 3 are fired and diode 3 is conducting

branch \ mesh	i^m_1	i^m_2	i^m_3	i^m_4
i^b_A	0	1	0	0
i^b_B	1	-1	0	0
i^b_C	-1	0	0	0
i^b_a	0	0	-1	-1
i^b_b	0	0	0	1
i^b_c	0	0	1	0
i^b_f	1	0	0	0

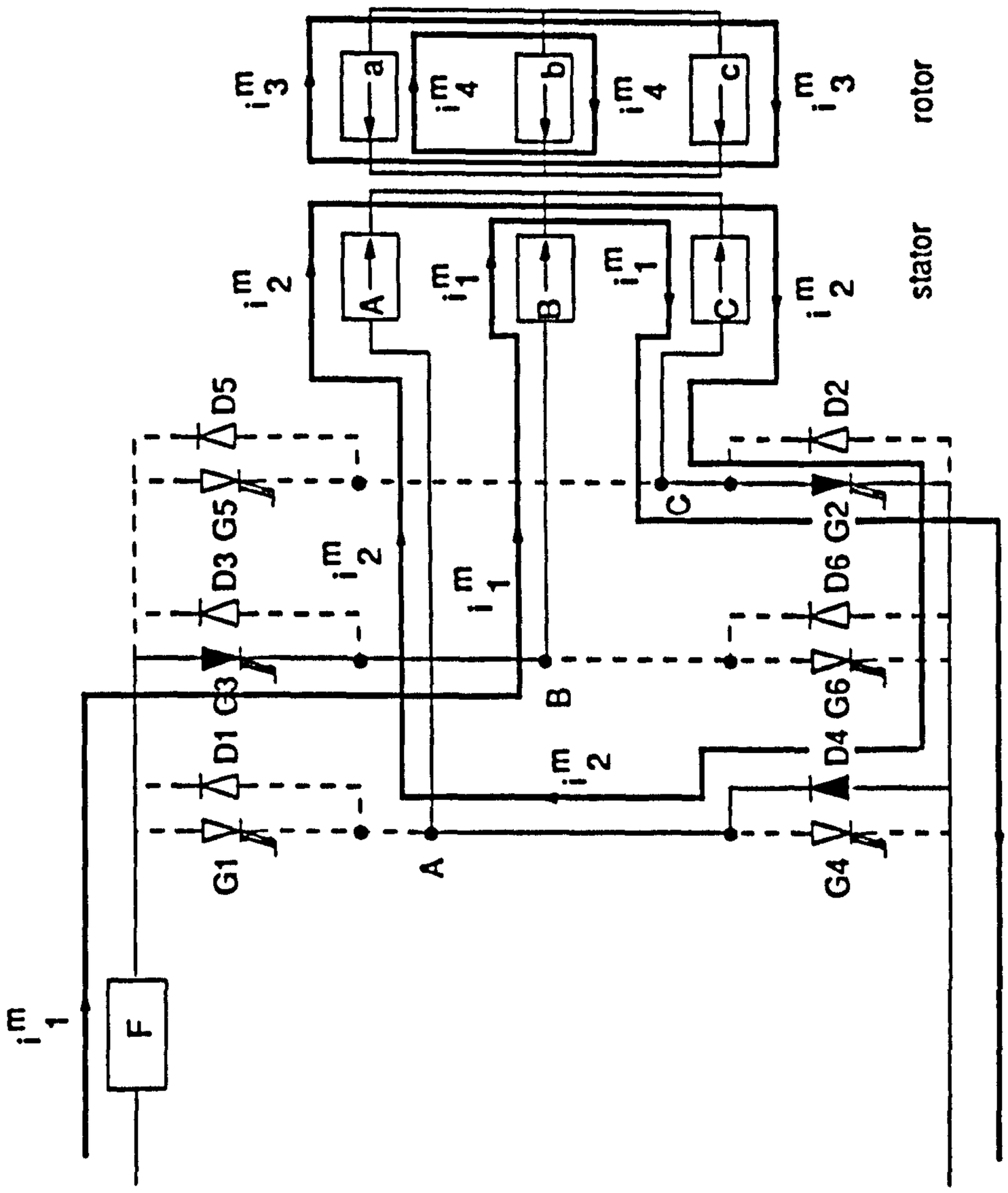

Figure 5.3 (b) Typical circuit topology and current transformation matrix when GTOs 2 3 4 are fired and diode 4 is conducting

branch \ mesh	i_1^m	i_2^m	i_3^m	i_4^m
i_A^b	-1	0	0	0
i_B^b	1	1	0	0
i_C^b	0	-1	0	0
i_a^b	0	0	-1	-1
i_b^b	0	0	0	1
i_c^b	0	0	1	0
i_f^b	1	0	0	0

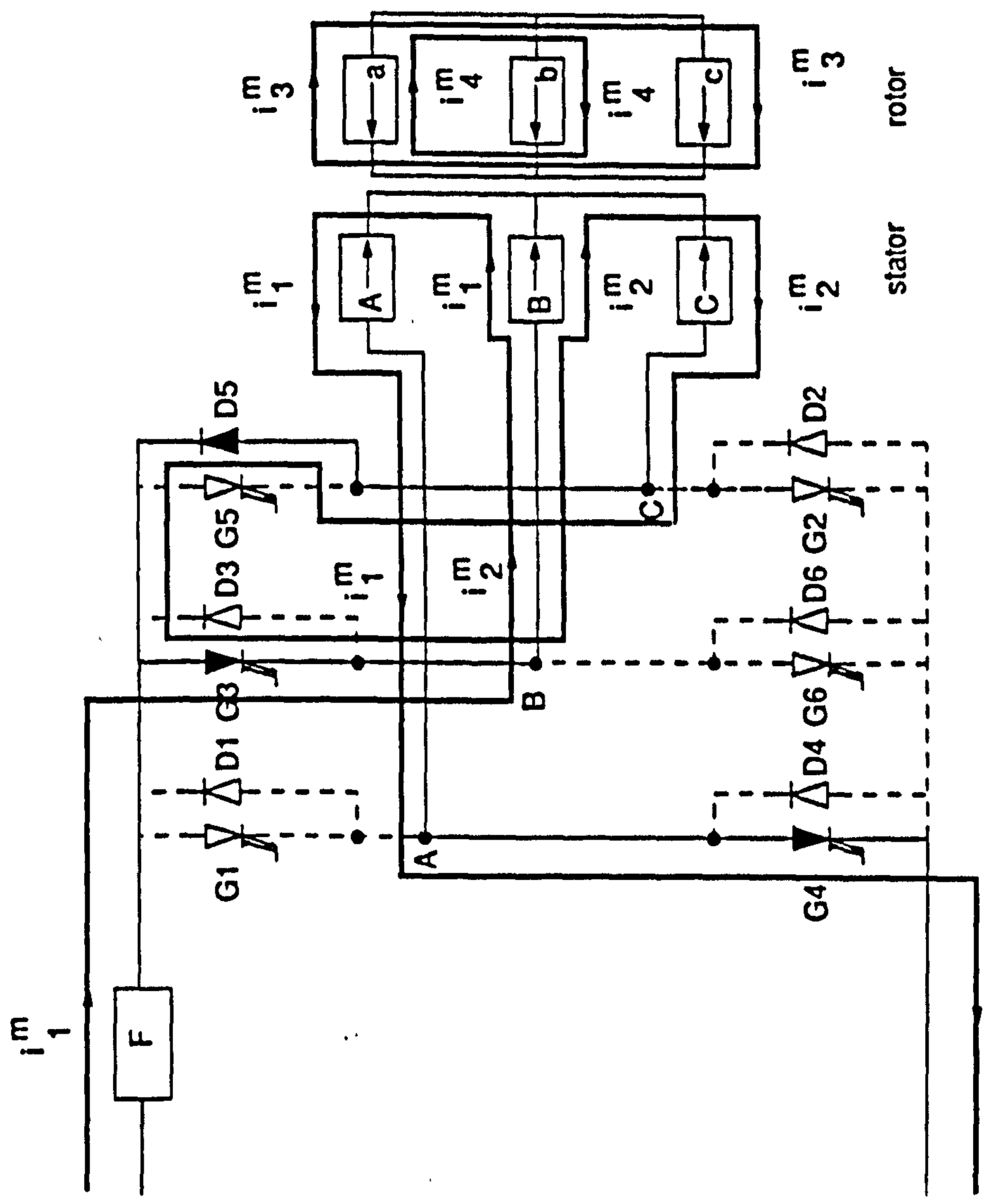

Figure 5.3 (c) Typical circuit topology and current transformation matrix when GTOs 3 4 5 are fired and diode 5 is conducting

mesh / branch	i^m_1	i^m_2	i^m_3	i^m_4
i_{bA}	-1	-1	0	0
i_{bB}	0	1	0	0
i_{bC}	1	0	0	0
i_{ba}	0	0	-1	-1
i_{bb}	0	0	0	1
i_{bc}	0	0	1	0
i_{bf}	1	0	0	0

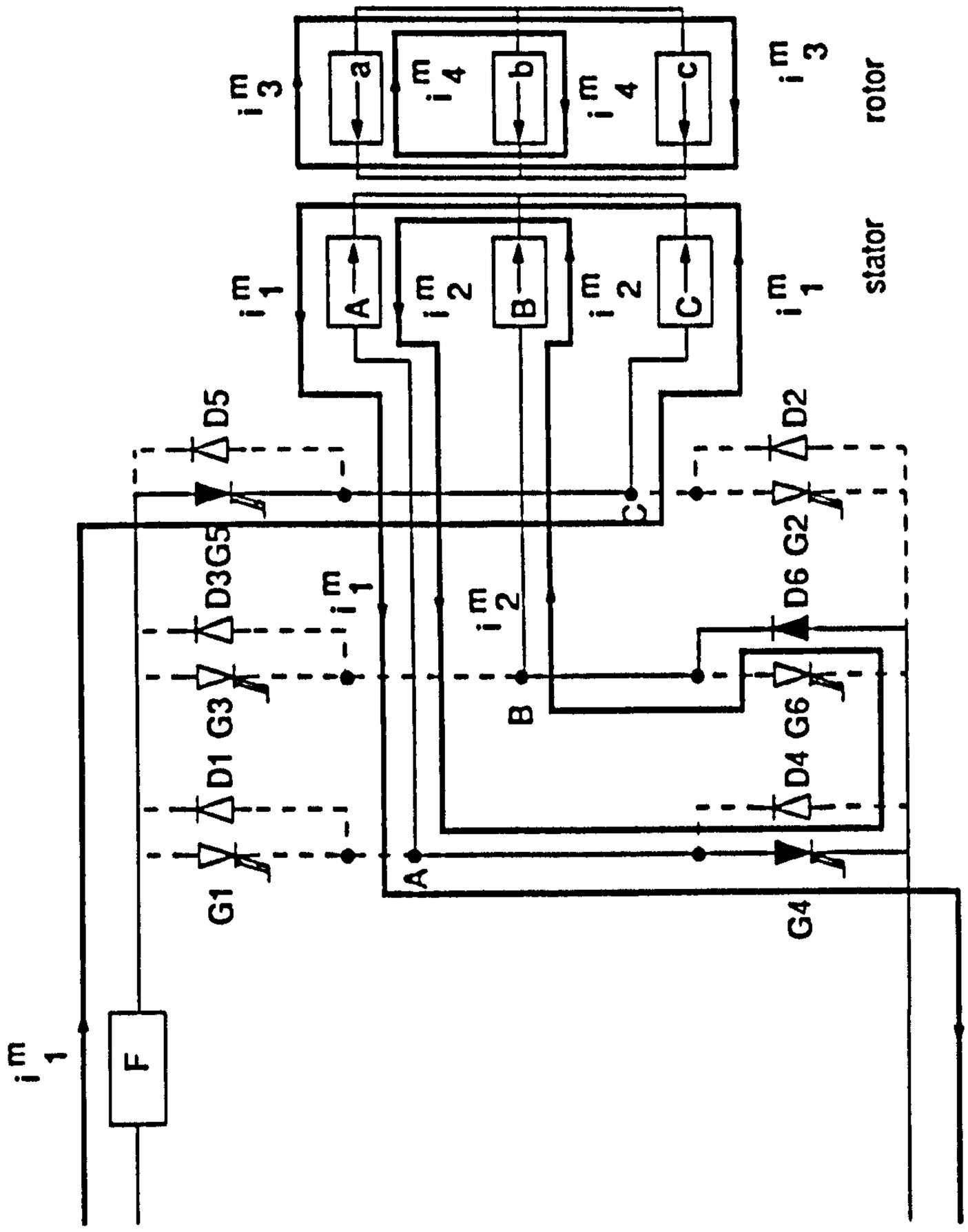

Figure 5.3 (d) Typical circuit topology and current transformation matrix when GTOs 4 5 6 are fired and diode 6 is conducting

mesh / branch	i_{m1}	i_{m2}	i_{m3}	i_{m4}
i_{bA}	0	-1	0	0
i_{bB}	-1	0	0	0
i_{bC}	1	1	0	0
i_{ba}	0	0	-1	-1
i_{bb}	0	0	-1	1
i_{bc}	0	0	1	0
i_{bf}	1	0	0	0

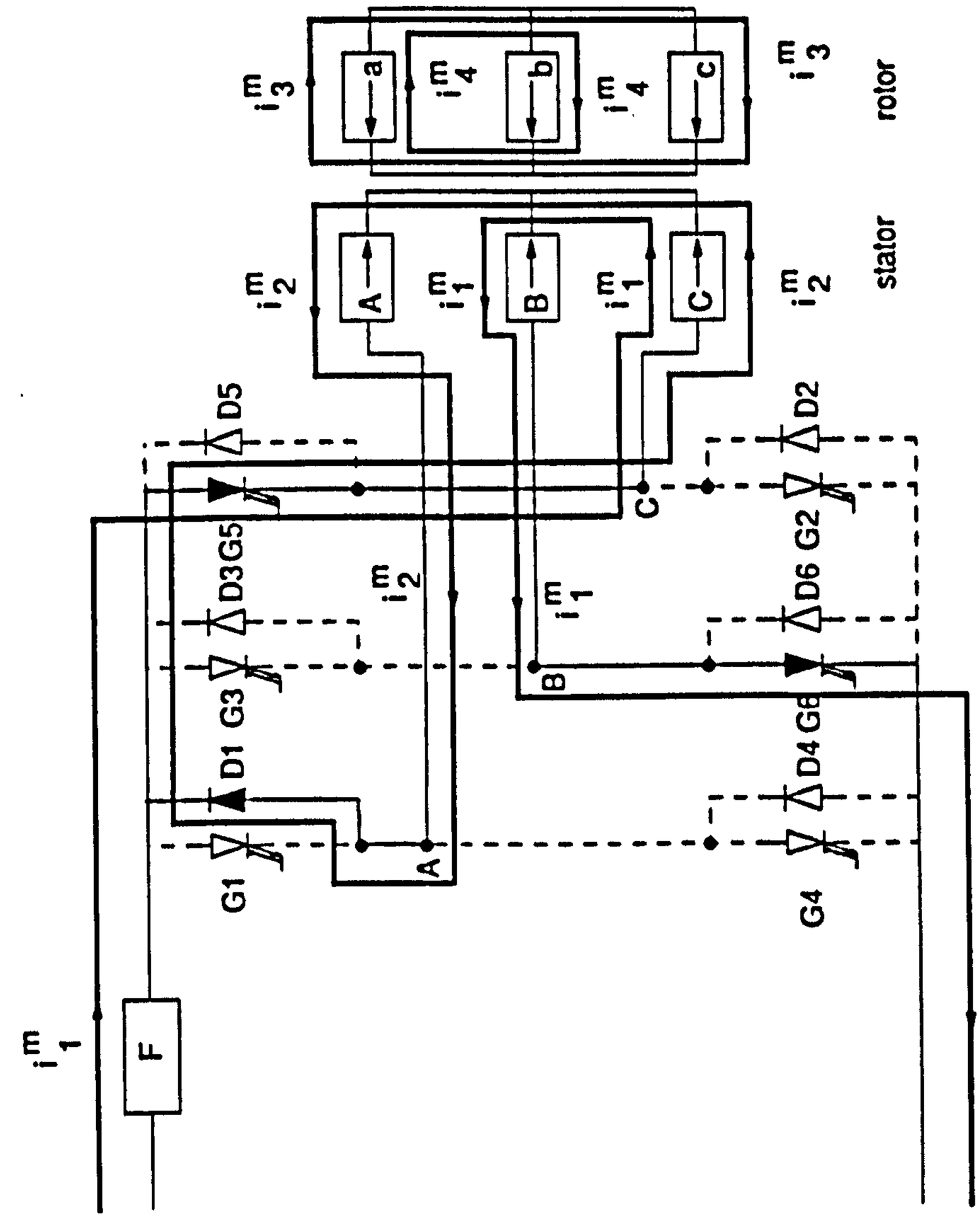

Figure 5.3 (e) Typical circuit topology and current transformation matrix when GTOs 5 6 1 are fired and diode 1 is conducting

branch \ mesh	i_1^m	i_2^m	i_3^m	i_4^m
i_A^b	1	0	0	0
i_B^b	-1	0	0	-1
i_C^b	0	0	1	1
i_a^b	0	0	0	-1
i_b^b	0	0	0	1
i_c^b	0	0	1	0
i_f^b	1	0	0	0

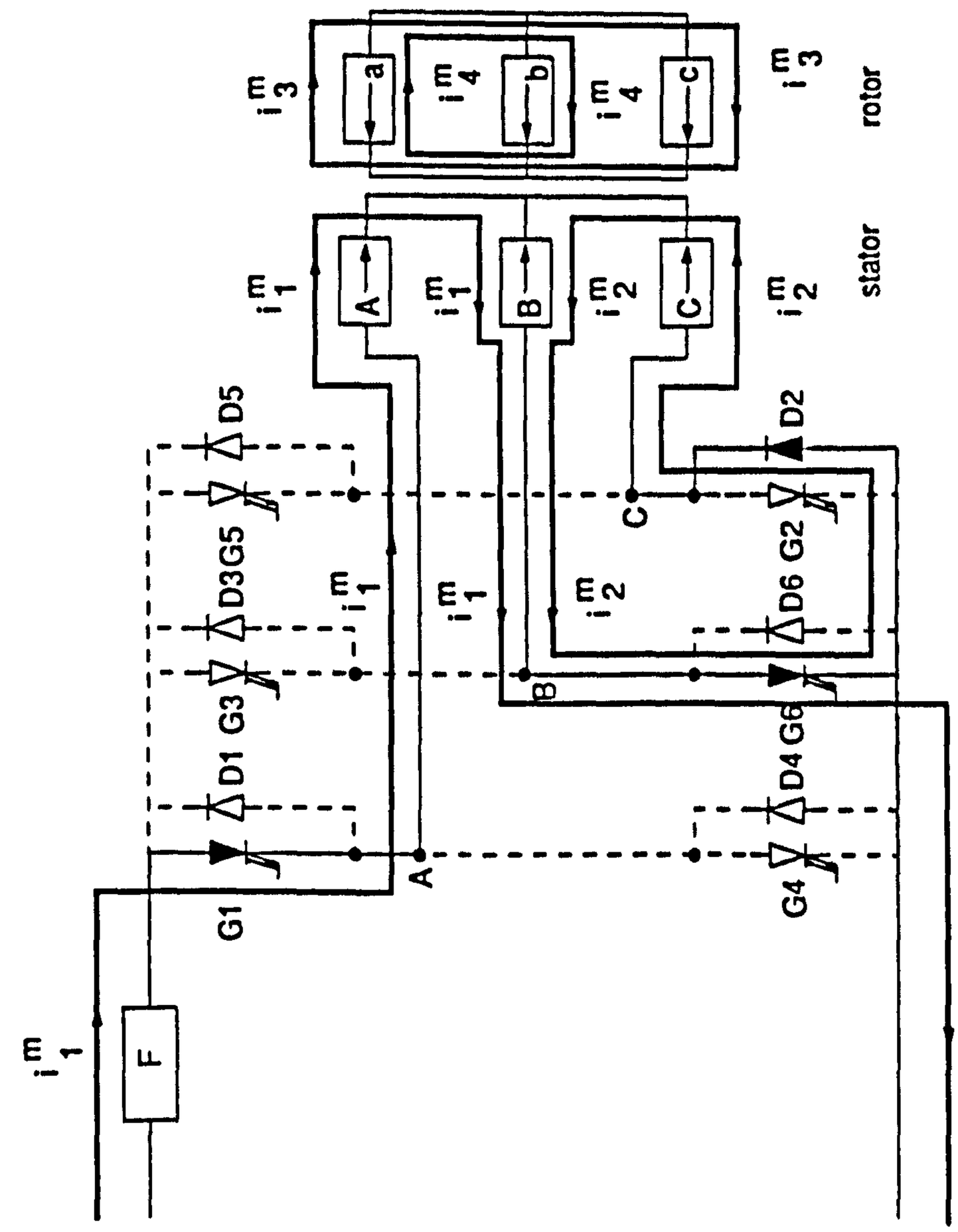

Figure 5.3 (f) Typical circuit topology and current transformation matrix when GTOs 6 1 2 are fired and diode 2 is conducting

5.2.2 Branch/Mesh Transformation

The transformation between branch and mesh reference frames may be demonstrated by comparing the branch and mesh currents of figures 5.2 and 5.3(a), thus

$$i_A^b = i_1^m + i_2^m$$

$$i_B^b = -i_2^m$$

$$i_C^b = -i_1^m$$

$$i_a^b = -i_3^m - i_4^m$$

$$i_b^b = i_4^m$$

$$i_c^b = i_3^m$$

$$i_{dc}^b = i_1^m$$

In matrix form

$$\begin{bmatrix} i_A^b \\ i_B^b \\ i_C^b \\ i_a^b \\ i_b^b \\ i_c^b \\ i_{dc}^b \end{bmatrix} = \begin{bmatrix} 1 & 1 & 0 & 0 \\ 0 & -1 & 0 & 0 \\ -1 & 0 & 0 & 0 \\ 0 & 0 & -1 & -1 \\ 0 & 0 & 0 & 1 \\ 0 & 0 & 1 & 0 \\ 1 & 0 & 0 & 0 \end{bmatrix} \cdot \begin{bmatrix} i_1^m \\ i_2^m \\ i_3^m \\ i_4^m \end{bmatrix}$$

and in abbreviated form

$$I^b = C_{.m}^b I^m \qquad 5.4$$

where $C_{.m}^b$ is the current transformation matrix between the two reference frames. This transformation maintains both real and reactive power invariance [76] and hence

$$V_{.b} I^b = V_{.m} I^m \qquad 5.5$$

where $V_{.b}$ and $V_{.m}$ are respectively the transpose vectors of V_b and V_m . The voltage transformation is derived by substituting equation 5.4 in 5.5 to give

$$V_{.b}C^{b}_{.m}I^{m} = V_{.m}I^{m} \qquad 5.6$$

on re-arranging,

$$(V_{.b}C^{b}_{.m} - V_{.m})I^{m} = 0 \qquad 5.7$$

Assuming a non-trivial solution $I^{m} \neq 0$ implies that

$$V_{.m} = V_{.b}C^{b}_{.m} \qquad 5.8$$

which transposes to

$$V_{m} = C^{.b}_{m}V_{b} \qquad 5.9$$

where $C^{.b}_{m}$ is the transpose of $C^{b}_{.m}$. Similarly

$$E_{m} = C^{.b}_{m.}E_{b} \qquad 5.10$$

Adding equations 5.9 and 5.10 gives

$$V_{m} + E_{m} = C^{.b}_{m}(V_{b} + E_{b}) \qquad 5.11$$

Substituting in equation 5.11 for $(V_b + E_b)$ and I^b from equations 5.2 and 5.4 respectively gives

$$V_{m} + E_{m} = C^{.b}_{m}\left(R_{b}C^{b}_{.m}I^{m} + L_{b}C^{b}_{.m}\rho I^{m} + \rho 0_{.}\frac{\partial L_{b}}{\partial \theta_{.}}C^{b}_{.m}I^{m} \right) \qquad 5.12$$

Comparing equations 5.12 and 5.2 yields the following equations for the resistance and inductance transformation

$$R_m = C_m^{\cdot b} R_b C_{\cdot m}^b \qquad 5.13$$

$$L_m = C_m^{\cdot b} L_b C_{\cdot m}^b \qquad 5.14$$

$$\frac{\partial L_m}{\partial \theta_e} = C_m^{\cdot b} \frac{\partial L_b}{\partial \theta_e} C_{\cdot m}^b \qquad 5.15$$

5.2.3 System Equations and Solution Organization

Equation 5.3 may be formed and re-arranged in state variable form as

$$p I^m = L_m^{-1} \left[E_m - \left(R_m + p\theta_e \frac{\partial L_m}{\partial \theta_e} \right) I^m \right] \qquad 5.16$$

The mechanical equations representing the system dynamics are [76,77]

$$T_e = \frac{p}{2} I^{\cdot m} \frac{\partial L_m}{\partial \theta_e} I^m \qquad 5.17$$

$$p\omega_m = \frac{(T_e - T_m - T_f)}{J} \qquad 5.18$$

and

$$p\theta_e = p\omega_m \qquad 5.19$$

where T_e is the electromagnetic torque, p the number of pairs of poles, ω_m the mechanical rotor speed, T_m the mechanical load torque, J the combined inertia of the motor and load and T_f the friction torque, is composed of several components and may be approximated as [78]

$$T_f = T_c + K_v \omega_m + K_w \omega_m^2 \qquad 5.20$$

where T_c is the Coulomb friction torque, K_v is the viscous constant, and K_w is the windage constant. These components were obtained experimentally and are given in appendix A.1 together with the mechanically coupled load torque T_m .

The elements of the current transformation matrix $C^b_{.m}$ of equation 5.4 vary, as shown in figure 5.3, according to the changing circuit topology. The first and second (varying) columns of $C^b_{.m}$ define two dynamic meshes, l^m_1 and l^m_2 , formed when three conducting devices connect the stator phases to the DC-link under different conduction patterns. The third and fourth (invariant) columns of $C^b_{.m}$ define two permanent meshes formed by the star-connected rotor windings.

To solve numerically the system equations 5.16 to 5.19, a step-by-step integration routine is used, in which the first two columns of $C^b_{.m}$ are updated whenever a change in circuit topology is detected. To simplify this process, a technique was used [79] in which a master matrix is formed, as shown in figure 5.4, containing all possible branch-mesh permutations of stator meshes.

5.2.4 Voltage Drops in Conducting Devices

At the beginning of each integration step, the existing circuit topology and the direction of the branch currents obtained from the previous step provide sufficient information for the conducting device to be identified as either a GTO or a diode. The static conduction characteristics for the GTOs and the free-wheeling diodes considered in this thesis are shown in figure 5.5. Each conducting device develops a voltage drop, which could be adequately represented by a reverse connected voltage source with a series resistance. Practical values for these were found by fitting a bi-linear function to each characteristic, and choosing a common current value for both devices at which the transition from one slope to the

branch \ mesh	i^m_1	i^m_2	i^m_1	i^m_2	i^m_1	i^m_2	i^m_1	i^m_2	i^m_1	i^m_2	i^m_1	i^m_2
i^b_A	0	1	-1	0	-1	-1	0	-1	1	0	1	1
i^b_B	1	0	1	1	0	1	-1	0	-1	-1	0	-1
i^b_C	-1	-1	0	-1	1	0	1	1	0	1	-1	0
i^b_a	0	0	0	0	0	0	0	0	0	0	0	0
i^b_b	0	0	0	0	0	0	0	0	0	0	0	0
i^b_c	0	0	0	0	0	0	0	0	0	0	0	0
i^b_{dc}	1	0	1	0	1	0	1	0	1	0	1	0
GTO's switching mode	2 3 4		3 4 5		4 5 6		5 6 1		6 1 2		1 2 3	

Figure 5.4 Master matrix

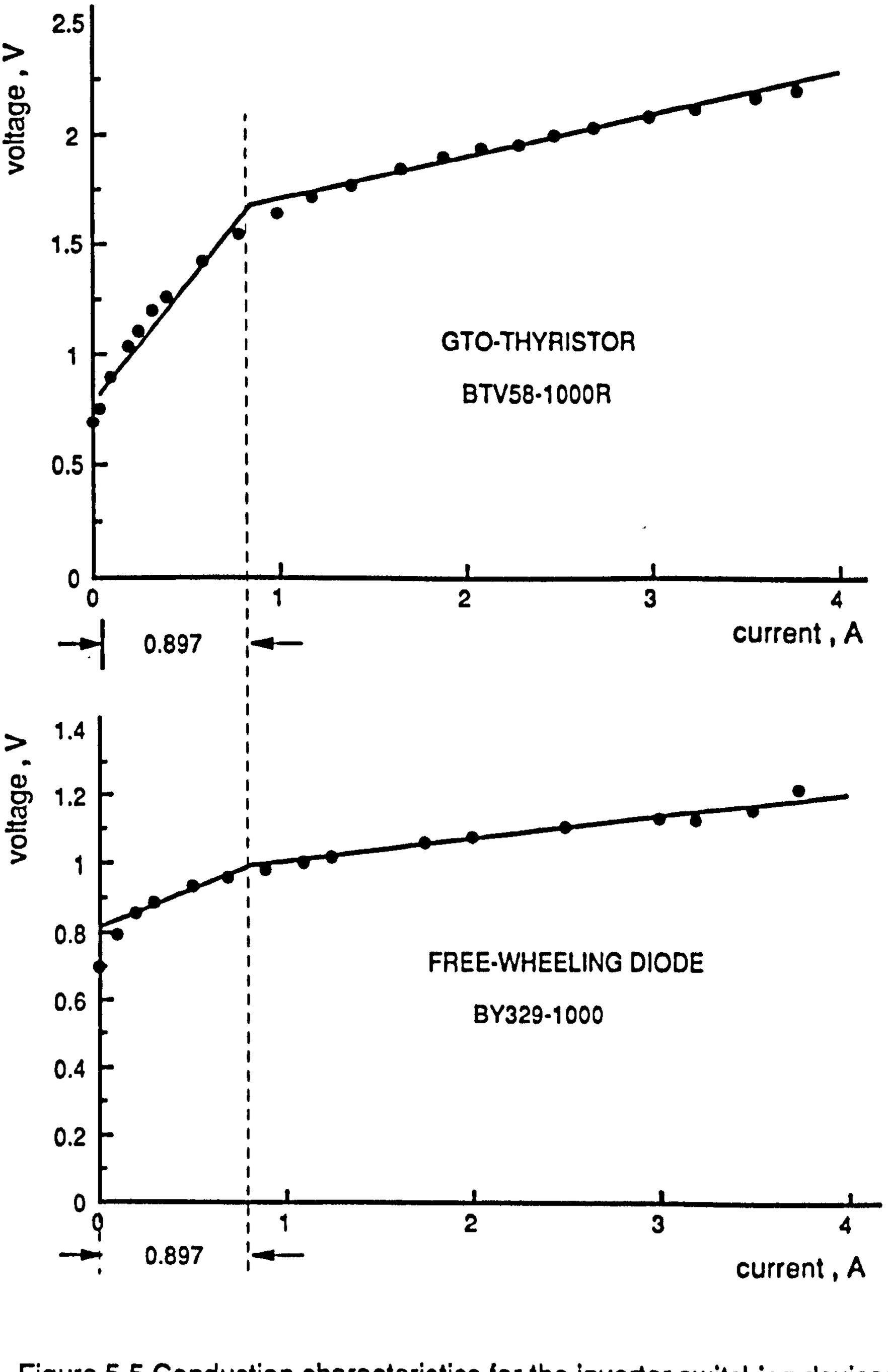

Figure 5.5 Conduction characteristics for the inverter switching devices

other occurs. It was found by this process that the voltage drop across any conducting device may be calculated instantaneously from the equations

$$E_{GTO} = 0.78 + 0.970 i_n^b \quad , \quad for \ \ i_n^b \le 0.897\,A$$
$$= 1.65 + 0.195 i_n^b \quad , \quad for \ \ i_n^b > 0.897\,A \qquad 5.21$$

and

$$E_{DIODE} = 0.82 + 0.200 i_n^b \quad , \quad for \ \ i_n^b \le 0.897\,A$$
$$= 1.00 + 0.064 i_n^b \quad , \quad for \ \ i_n^b > 0.897\,A \qquad 5.22$$

where i_n^b is the instantaneous stator branch current.

5.2.5 Switching Pattern Determination

For a QSW drive, the firing pattern is as shown in figure 2.10, where each device conducts continuously for $180°$. For quarter-wave symmetrical optimal PWM modes, the pattern may be generated by following a number of off-line switching angles $\alpha_{(m)}$ as follows. At an operating frequency f_s, the switching instants for the first quarter-cycle are

$$t_{(i)} = \frac{\alpha_{(i)}}{2\pi f_s} \quad , \ i = 1, \ldots\ldots, m \qquad 5.23$$

and for the second quarter-cycle

$$t_{(i+m)} = \frac{1}{2f_s} - \frac{\alpha_{(j)}}{2\pi f_s} \quad , \ i = 1, \ldots\ldots, m \qquad 5.24$$
$$j = m, m-1, \ldots, 1$$

The switching instant at π is

$$t_{(2m+1)} = \frac{1}{2f_s} \qquad 5.25$$

The second half of the cycle may be generated using the half-wave symmetry property. Hence for the third quarter-cycle

$$t_{(2m+i+1)} = \frac{1}{2f_s} + \frac{\alpha_{(i)}}{2\pi f_s} \quad , \; i = 1, \ldots\ldots, m \qquad 5.26$$

and the fourth quarter-cycle

$$t_{(3m+i+1)} = \frac{1}{f_s} - \frac{\alpha_{(j)}}{2\pi f_s} \quad , \; i = 1, \ldots\ldots, m \qquad 5.27$$

$$j = m, m-1, \ldots, 1$$

The switching instant at 2π is

$$t_{(4m+2)} = \frac{1}{f_s} \qquad 5.28$$

Assuming these instants relate to GTO1, those for GTO3 and GTO5 may be obtained by introducing 120° and 240° phase shifts, while those for GTOs 4, 6 and 2 are mirror images of their counterparts. A complete switching pattern with two switching angles per quarter-cycle is shown in figure 5.6.

5.3 Program Procedure

A computer program was written to solve equations 5.16 to 5.19, using a step-by-step numerical integration routine with a logic check at each step to determine the conducting state of every device and to update C_m^o if necessary. A flow chart of the program is shown in figure 5.7 and the basic procedure describing its operation is as follows

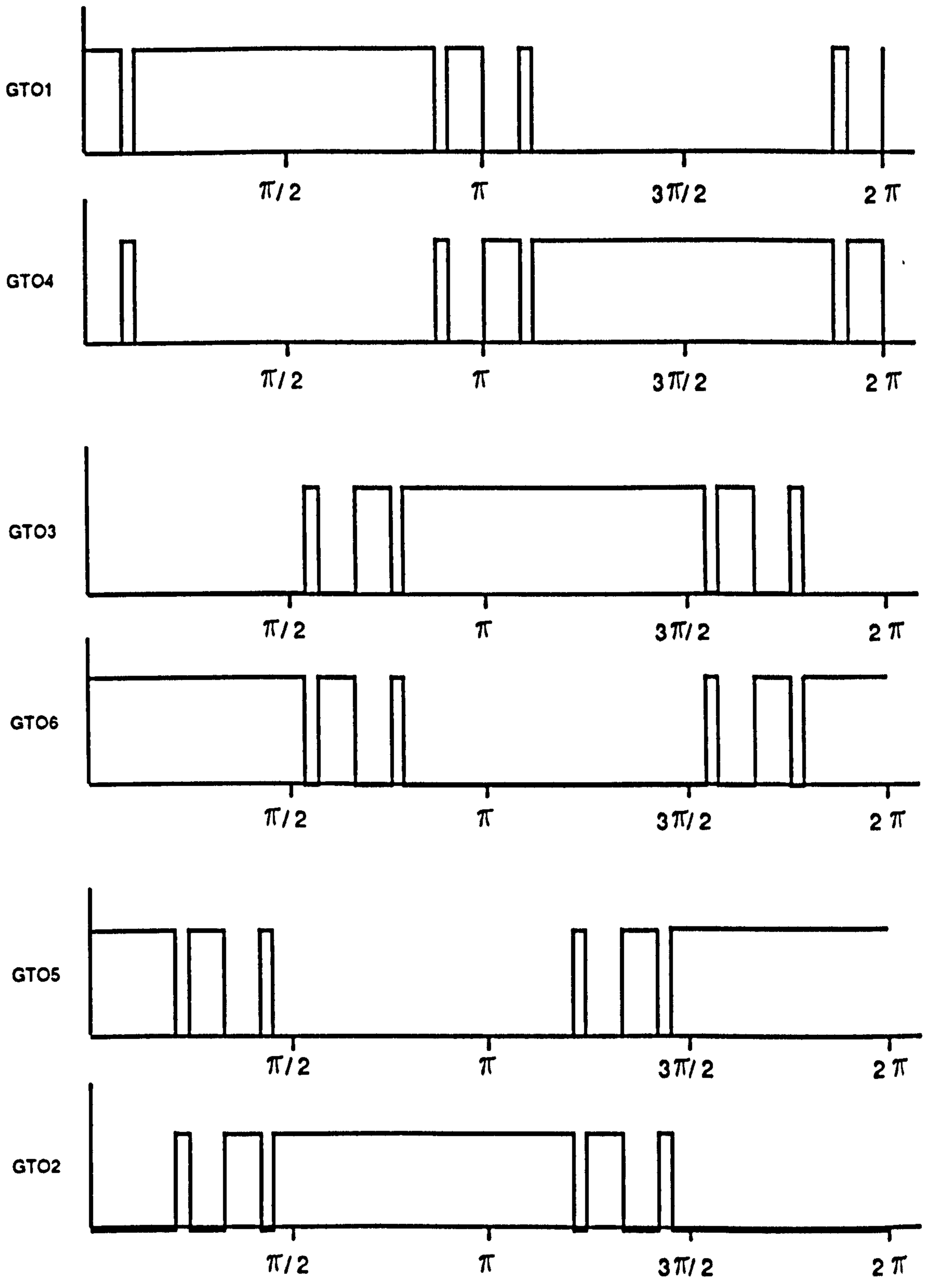

Figure 5.6 Typical switching pattern for all GTOs , generated using two switching angles per quarter-cycle for PWM2 operating mode

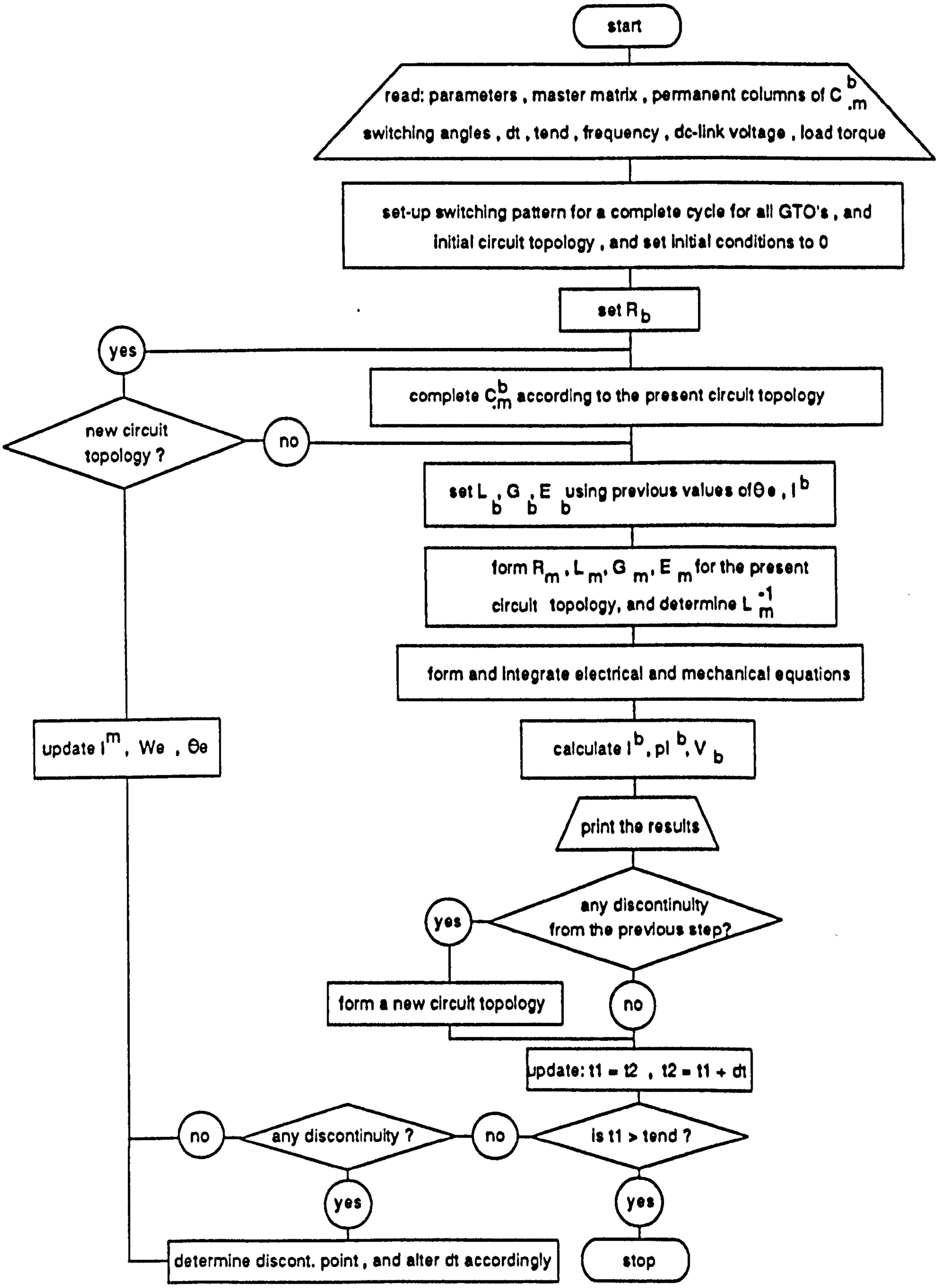

Figure 5.7 Inverter / induction motor program flow-chart

(a) After reading the machine parameters and initial conditions, the firing pattern for all GTOs is set individually, as explained in section 5.2.5.

(b) The elements of the R_b matrix are time independent, and therefore need to be formed once only at the beginning of the program.

(c) From the existing circuit topology, which must initially be defined, C^b_m and its transpose are formed.

(d) The elements of the L_b and $\partial L_b/\partial\theta_e$ matrices depend on the rotor angle θ_e and are determined at every stage of the integration. The voltage drops across the conducting devices are calculated as explained in section 5.2.4 and substituted as the voltage source components in the stator branch reference frame of figure 5.2.

(e) The E_m vector and R_m , L_m , $\partial L_m/\partial\theta_e$ matrices are formed, using equations 5.10, 5.13-15, and L_m is inverted.

(f) The information obtained from previous steps allows the state variable equation 5.16 to be formed and integrated, together with equations 5.18 and 5.19, to give the new mesh current vector I^m , its derivative pI^m , the rotor mechanical speed ω_m , and the electrical angle of rotation θ_e .

(g) The branch current vector I^b and its derivative pI^b are obtained using equation 5.4. These are used to calculate the branch voltages using equation 5.2.

Operations (d) to (g) are repeated for each time step after updating all branch and mesh currents, the rotor speed ω_m and the angle θ_e . At the end of each integration step, the inverter devices are tested for any change in their conduction state for the next integration step. If detected, these are treated as discontinuities and the program proceeds as follows;

(1) The time between the start of the step and the discontinuity point is determined.

(2) Operations (d) to (g) are performed, with the system equations integrated from the start of the step to the point of the discontinuity.

(3) A new current transformation matrix $C^b_{.m}$ is assembled according to the new circuit topology.

(4) The stator mesh currents are re-defined at discontinuities, according to the new circuit topology, and it is necessary to update them according to their new definition such that branch currents are consistent during the discontinuity. Assuming

$$[I^b]^- = [C^b_{.m}]^- \ [I^m]^- \qquad 5.29$$

is the relation between branch and mesh currents before the discontinuity, and

$$[I^b]^+ = [C^b_{.m}]^+ \ [I^m]^+ \qquad 5.30$$

is the relation between them after the discontinuity. Equating 5.29 and 5.30 results in

$$[C^b_{.m}]^\dagger \ [I^m]^+ = [C^b_{.m}]^- \ [I^m]^- \qquad 5.31$$

The matrix $C^b_{.m}$ is not square and is therefore singular. It cannot be inverted and solving equation 5.31 for $[I^m]^+$ is not possible. Alternatively, the branch currents can be re-arranged individually; for example, the state of branch currents before the discontinuity in figure 5.3(a) was such that

$$[i^b_A]^- = [i^m_1]^- + [i^m_2]^-$$

$$[i^b_B]^- = -[i^m_2]^-$$

$$[i^b_C]^- = -[i^m_1]^-$$

and after the discontinuity consideration of the currents of figure 5.3(b) shows that

$$[i_A^b]^+ = [i_2^m]^+$$

$$[i_B^b]^+ = [i_1^m]^+$$

$$[i_C^b]^+ = -[i_1^m]^+ - [i_2^m]^- \quad .$$

It is now possible, by using equation 5.31 for any branch current, to find the relationship between the mesh currents before and after the discontinuity,

$$[i_1^m]^+ = -[i_2^m]^-$$

$$[i_2^m]^+ = [i_1^m]^- + [i_2^m]^- \quad .$$

$[i_1^m]^+$ and $[i_2^m]^+$ can now be used as the initial values for stator mesh currents at the discontinuity point.

(5) Operations (c) to (g) are repeated from the point of discontinuity to the end of a new complete step.

(6) The inverter is tested for any further discontinuities during (5). If any is detected, operations (1) to (5) are repeated. If not, the program proceeds with operations (d) to (g) over the next step.

5.3.1 Numerical Integration Methods [80]

Single-step techniques, such as the Runge-Kutta, Euler and modified Euler methods, can begin the solution by the provision of only the initial conditions at each subsequent step using only information from the previous step. The integration is performed by extrapolating from the value of the function at the beginning of the step to obtain a value at the end of the step, with the ability to perform the next integration step with a different step size.

Of the single-step methods available, the 4th-order Runge-Kutta method was chosen, due to its computational efficiency and high accuracy. This method evaluates four values of the function during a step and uses a weighted average

of these to determine the value of the function at the end of the step. The mathematical algorithm of this method as applied to the solution of the first order differential equation $pY = f(X, Y)$ is

$$Y_{n+1} = Y_n + \frac{1}{6}(K_1 + 2K_2 + 2K_3 + K_4) \qquad 5.32$$

where

$$\begin{aligned} K_1 &= \Delta X\, f(X_n \ , \ Y_n) \\ K_2 &= \Delta X\, f\left(X_n + \frac{\Delta X}{2} \ , \ Y_n + \frac{K_1}{2}\right) \\ K_3 &= \Delta X\, f\left(X_n + \frac{\Delta X}{2} \ , \ Y_n + \frac{K_2}{2}\right) \\ K_4 &= \Delta X\, f(X_n + \Delta X \ , \ Y_n + K_3) \end{aligned} \qquad 5.33$$

and ΔX is the integration step-length.

5.3.2 Fourier Analysis

The mathematical model included a Fourier analysis algorithm which determines the harmonic contents of both the inverter output voltage and current waveforms and the torque and speed of the machine once steady-state conditions are achieved. In the present application the waveforms to be analysed are defined over a full time period $T = 2\pi/\omega$, by a series of Y ordinate values at known values of t as shown in figure 5.8. Since these ordinates are not necessarily equispaced (as described earlier), the integration required to determine the Fourier coefficients may be performed most easily by summing all the trapezoidal areas. Using this technique the Fourier coefficients are given by

$$a_n = \frac{2}{T}\sum_{m=1}^{(-1)} \frac{1}{2}(Y_m \cos n\omega t_m + Y_{m-1} \cos n\omega t_{m-1})(t_{m-1} - t_m) \qquad 5.34$$

and

$$b_n = \frac{2}{T}\sum_{m=1}^{(-1)} \frac{1}{2}(Y_m \sin n\omega t_m + Y_{m-1} \sin n\omega t_{m-1})(t_{m-1} - t_m) \qquad 5.35$$

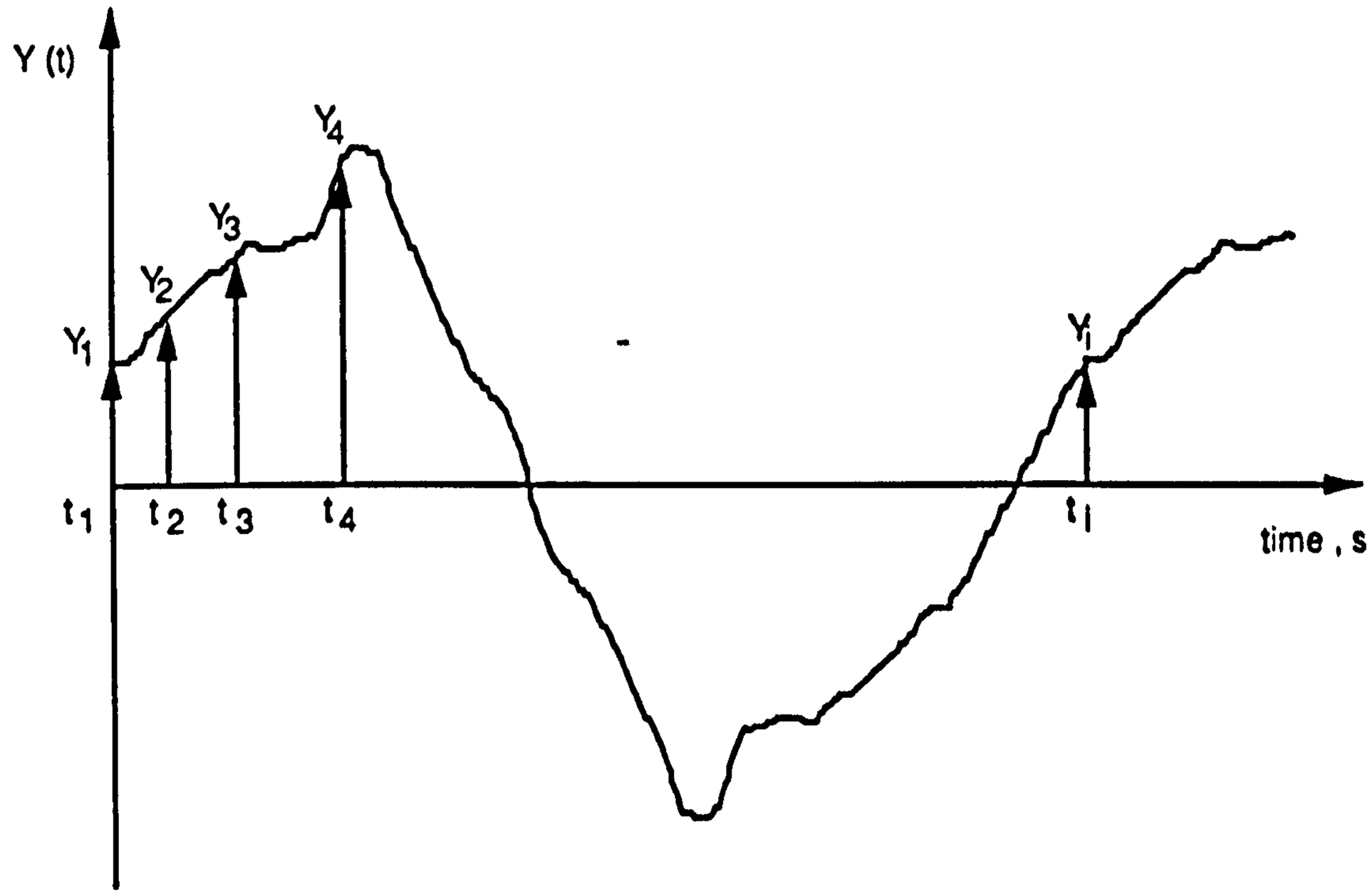

Figure 5.8 Typical example of an arbitrary waveform defined by its Y ordinates at known values of (t)

where m is the ordinate number and i the number of ordinates in a complete cycle. From these equations, the peak value of the nth-harmonic F_n and its phase-angle θ_n may be calculated from

$$F_n = \sqrt{a_n^2 + b_n^2} \qquad 5.36$$

and

$$\theta_n = \tan^{-1}\frac{a_n}{b_n} \qquad 5.37$$

It is obvious from figure 5.8 that, replacing a curve by a straight line, may introduce large errors. To ensure sufficient accuracy, it is therefore necessary to use a short step-length in the simulation model, thereby providing sufficient points for use in the Fourier analysis program. It was found that 10000 points/cycle provided enough information for acceptable accuracy in the results, where step-length values ranged from $100\mu s$ at 1Hz to $2\mu s$ at 50Hz operating frequency.

5.4 Experimental Set-Up

The experimental drive system described in chapter 4 consists of a GTO-thyristor inverter driving the 0.56kW squirrel-cage induction motor whose parameters are given in appendix A.1. The motor drive-end was coupled to a swinging-frame DC dynamometer, with a strain-gauge torque transducer mounted on its stator which was locked to limit its movement. Regardless of whether QSW or PWM modulation techniques were under investigation, sufficient mechanical disturbance was present, to distort the measurement of instantaneous torque pulsations, and consequently, this arrangement was only used for the measurement of average torque.

An incremental shaft encoder was coupled to the non-drive end of the motor shaft. The resulting digital signal was applied to a frequency/voltage converter whose analogue output provided a measure of the instantaneous rotor speed. The AC component of this signal was differentiated, to provide an

analogue signal proportional to the acceleration torque. It was found in practice that to obtain a reasonably meaningful measurement of speed ripple, it was necessary to operate the machine at a stator frequency below 4Hz, where the ripple is relatively large and can be measured with reasonable accuracy. However, when the pulse number is increased in the PWM operation mode, the rotor speed ripple is correspondingly reduced and experimental measurement is made more difficult even at very low operating frequencies. An external DC source was used to supply the inverter with a link voltage which was adjusted manually to suit different frequencies and load requirements.

5.5 Computed And Experimental Results

This section presents results describing the drive operation using waveforms obtained from the theoretical model. Computed and experimental waveforms are compared and the characteristics at different operating conditions are considered. It is important to note that the theoretical model can produce results showing the machine dynamics during transient and steady-state conditions at any desired operating frequency. However, the following results are intended to highlight typical practical effects during low frequency steady-state operation. Particular emphasis is given to frequencies below 5Hz, where the instantaneous torque pulsation can produce significant speed variations particularly during QSW operation.

5.5.1 Basic Drive Operation

To explain the drive system operation, and to demonstrate the capability of the computer model in dealing with varying circuit topologies, figure 5.9 shows phase voltage and current waveforms for a 4Hz QSW drive under both no-load and full-load conditions. Following the defined timing instants, t_1 is the time at which GTO4 is turned off and GTO1 is turned on, thereby connecting phase A to the positive DC rail. Since the phase current I_A is negative, it must be carried by diode D1

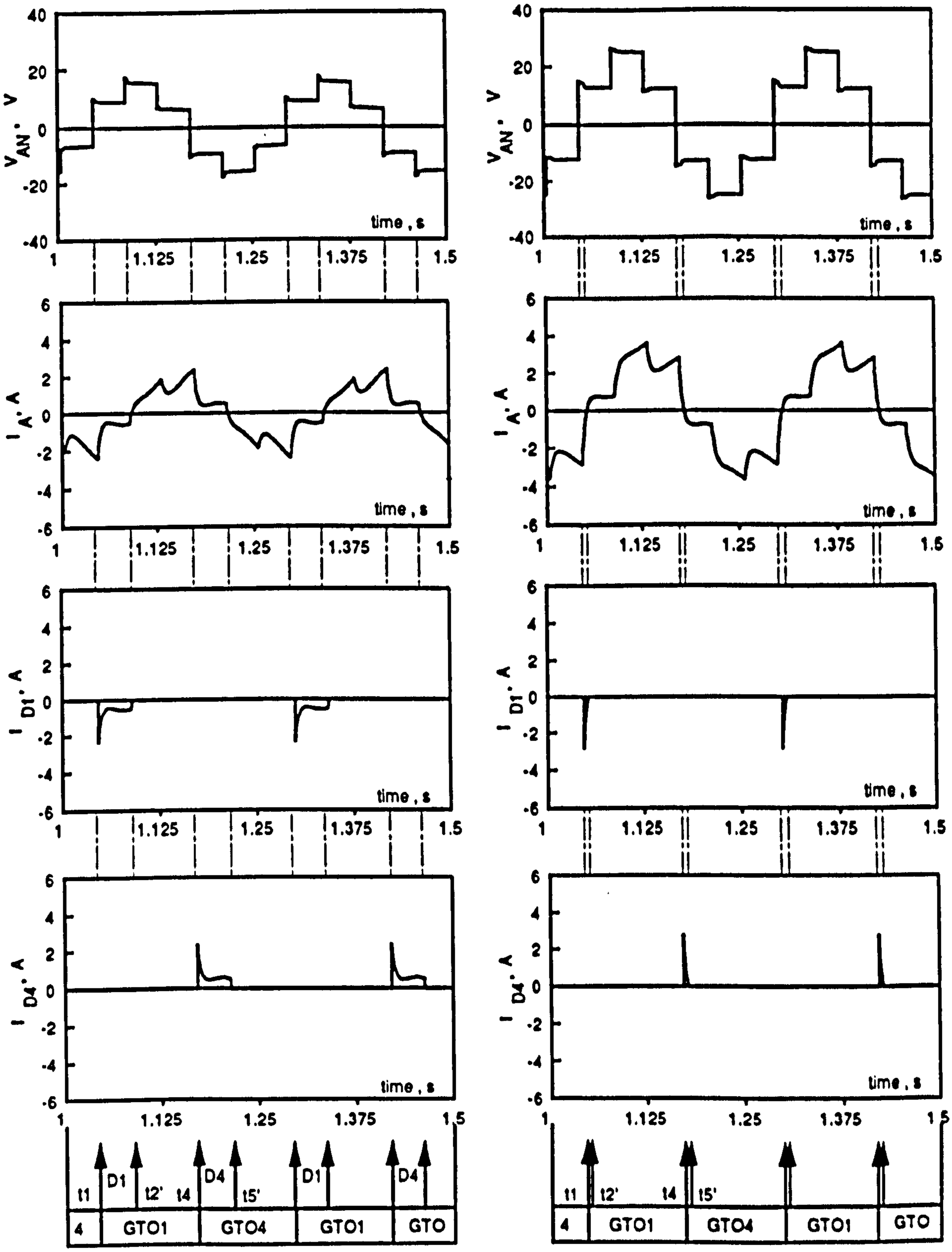

Figure 5.9 Phase voltage and current waveforms , with the current in the free-wheeling diodes for QSW inverter driving star-connected induction motor operating at 4Hz frequency with (a) Unloaded motor (b) Fully-loaded motor

circulating through GTO5 phase C and phase A, as shown in figure 5.3(e). Although GTO1 is not conducting during the time (t_1-t_2') , a continuous gating signal is maintained for the full 180° from t_1 to t_4 , so that when I_A reverses at t_2' GTO1 starts to conduct. Figure 5.9(b) illustrates that the time (t_1-t_2') is load dependent.

Figure 5.10 shows the DC-link current and the currents through all six free-wheeling diodes for a complete cycle, under the same operating conditions as those of figure 5.9(a). It illustrates the mechanism of energy feedback through the inverter to the DC-link side. It is clear that the circulating current in diode D1 lasts for more than 60° , during which GTO5 is turned off and GTO2 is turned on. This allows the return of inductive load current, which signifies stored energy, to the DC supply via diodes D1 and D2 for a time (t_2-t_2') .

The effect of the voltage drops across the conducting devices on the voltage waveshapes is clear in the 3-phase voltage waveforms of figure 5.11(a). The dotted line waveforms represent the ideal voltage waveshape, assuming that the inverter devices are ideal switches. Figure 5.11(b) shows all possible circuit topologies for each time indicated in figure 5.11(a), with equations defining the stator phase voltages in terms of the branch voltages $V'_s(1), V'_s(2), V'_s(3)$ and the forward voltage drops across each conducting device. Both waveforms were obtained under the same conditions as figure 5.9(a) with a DC-link voltage of 23.7V calculated from

$$V'_{dc} = \frac{\pi}{\sqrt{2}} V'_{(1)} \qquad 5.38$$

The fundamental phase voltage $V'_{(1)}$ required to provide constant airgap flux is 10.66V for this condition. It was found that distortion of the ideal voltage waveform reduced this figure to 9.98V, emphasizing the need to boost the link voltage to 25.30V to compensate for the device voltage drops and to maintain a constant airgap flux. In the same way, the DC-link

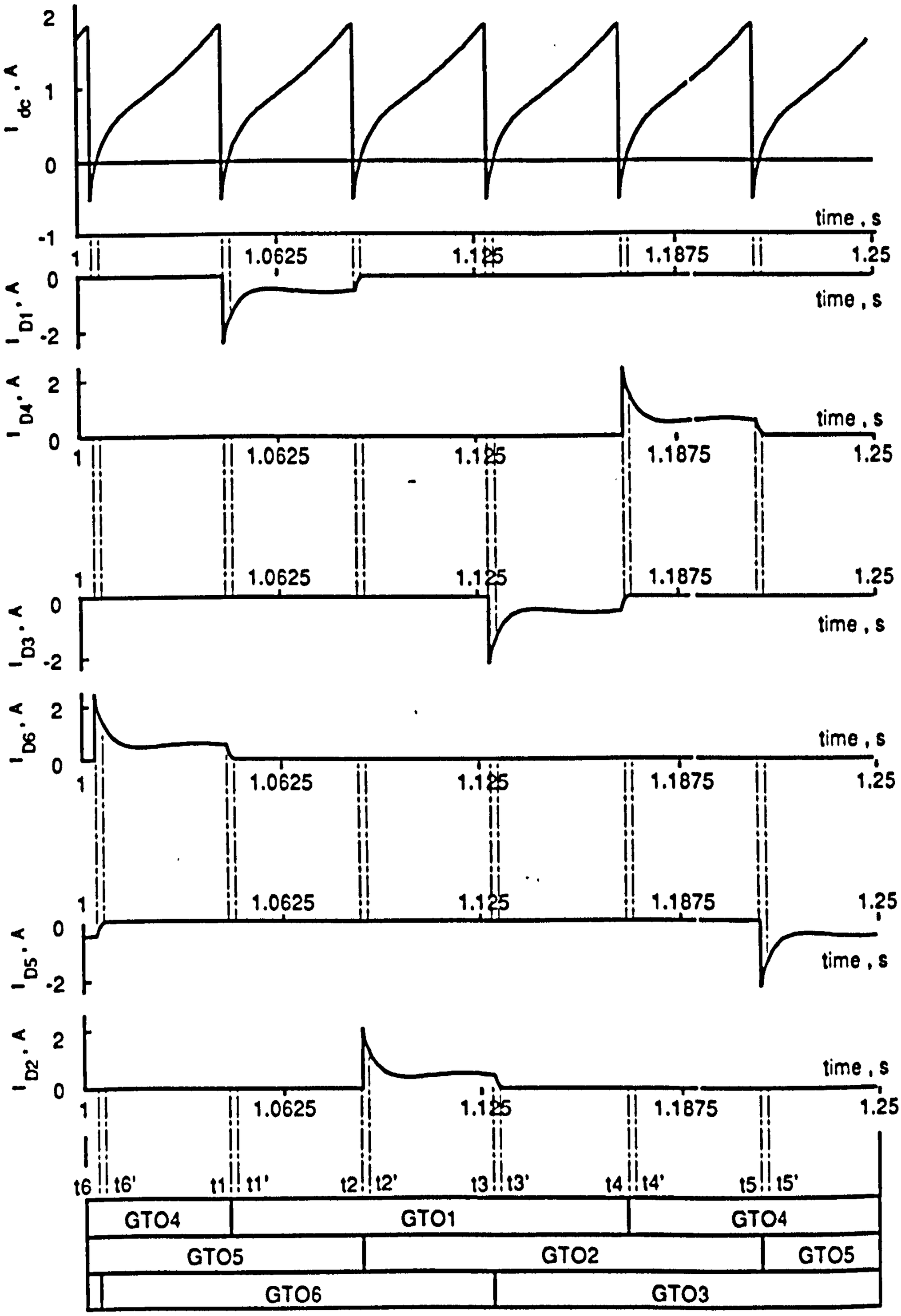

Figure 5.10 DC-link and free-wheeling diode currents for , 4Hz , no-load QSW operation mode

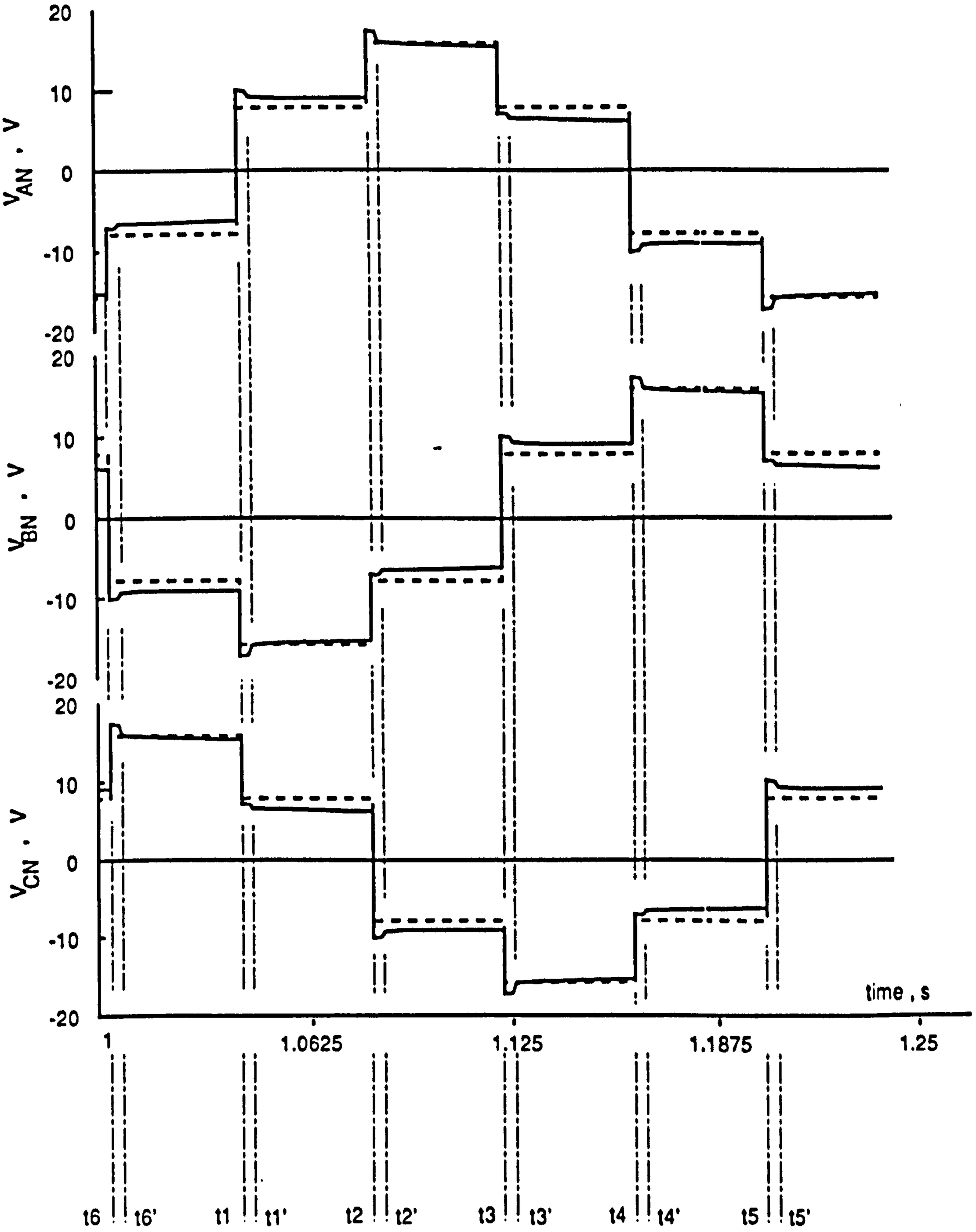

Figure 5.11 (a) Ideal and actual voltage waveforms , illustrating the effect of inverter devices voltage drops , at 4Hz , no-load , QSW mode

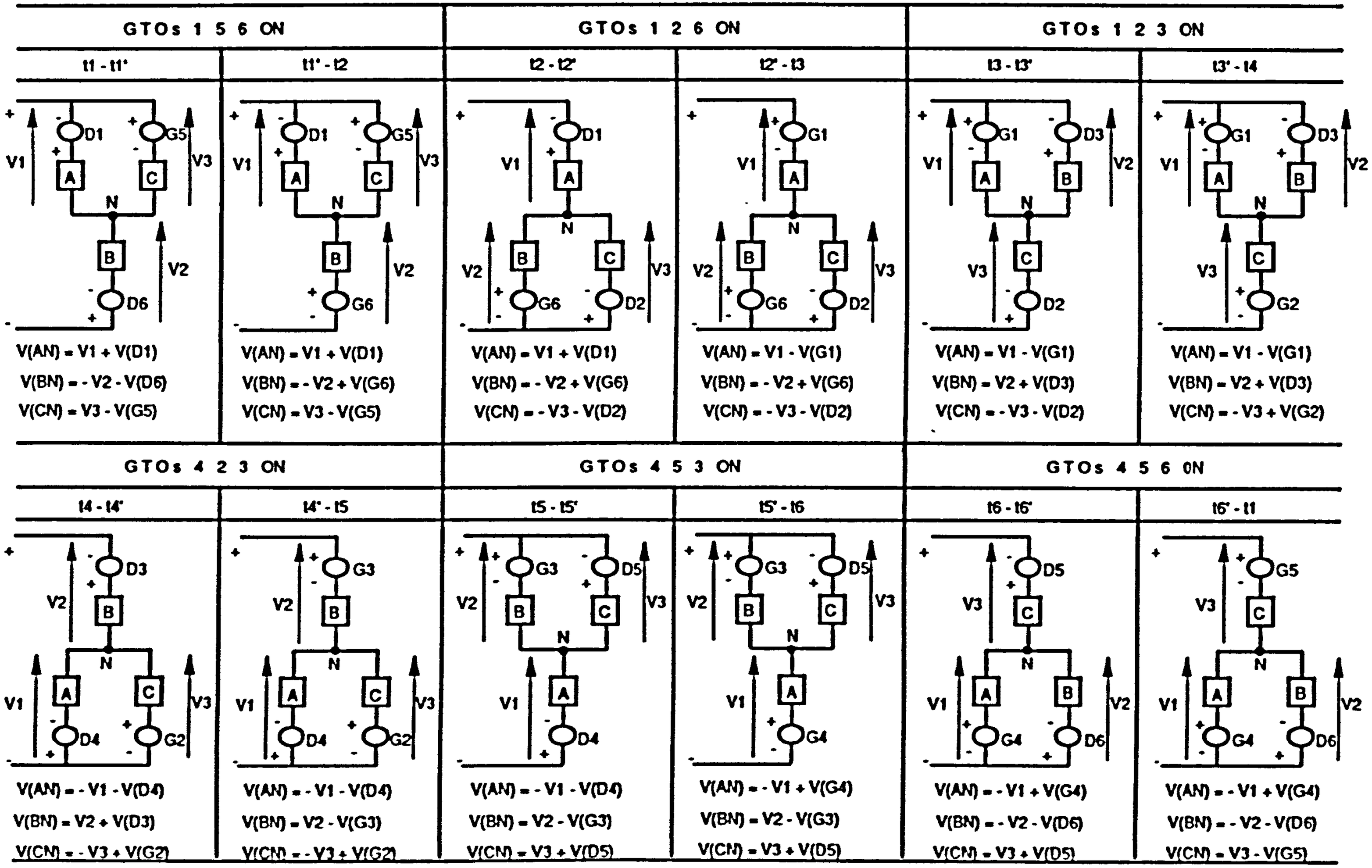

Figure 5.11 (b) Drive circuit configurations during the specified time periods of figure 5.11 (a)

voltage required at full-load for the same frequency is 41.3V for a fundamental phase voltage of 16.47V, instead of the 36.6V provided by equation 5.38. The precise amount of DC-link voltage compensation for this voltage drop depends on the instantaneous current carried by each GTO and free-wheeling diode in the inverter circuit, which varies according to the load condition and switching profile. Its average value is found to be between 2V and 5V from no-load up to full-load operation of the machine, which represents a significant proportion of the DC-link voltage at low operating frequencies. The compensation process may be simplified by boosting the DC-link voltage by an average value of 3.5V under all load and operating frequency conditions.

5.5.2 Discussion Of Results

Computed and experimental results for 1Hz no-load operation are shown in figures 5.12 to 5.16, for QSW and harmonic elimination PWM operation with 2,4,6 and 8 switching angles per quarter-cycle. Comparison of these results shows good agreement between computed and experimental line voltage and current waveforms and harmonic spectra for all operating modes. There is however some discrepancy between the computed and practical speed and acceleration torque waveforms, especially with high pulse PWM operation, with the sharp edges in both computed waveforms being more rounded in the practical ones. This is due mainly to the limited sensitivity of the encoder to small deviations of speed and the poor response time of the frequency/voltage converter to a change in the input frequency. Both effects result in a reduction in the high order components of the measured waveforms.

Figures 5.12(a) and (b) show the line voltage and stator current waveforms and their harmonic spectra for QSW operation. The reduction in the fundamental component due to device voltage drops was compensated for by boosting the DC-link voltage to 14.1V, rather than the uncompensated figure of 10.6V calculated from

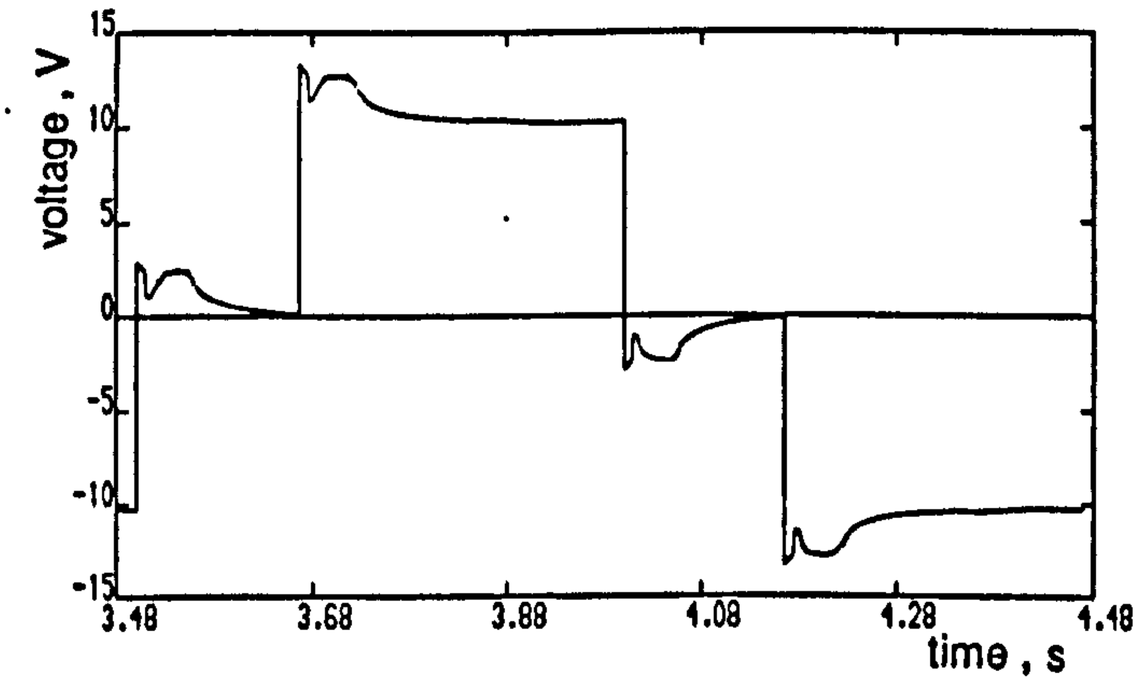

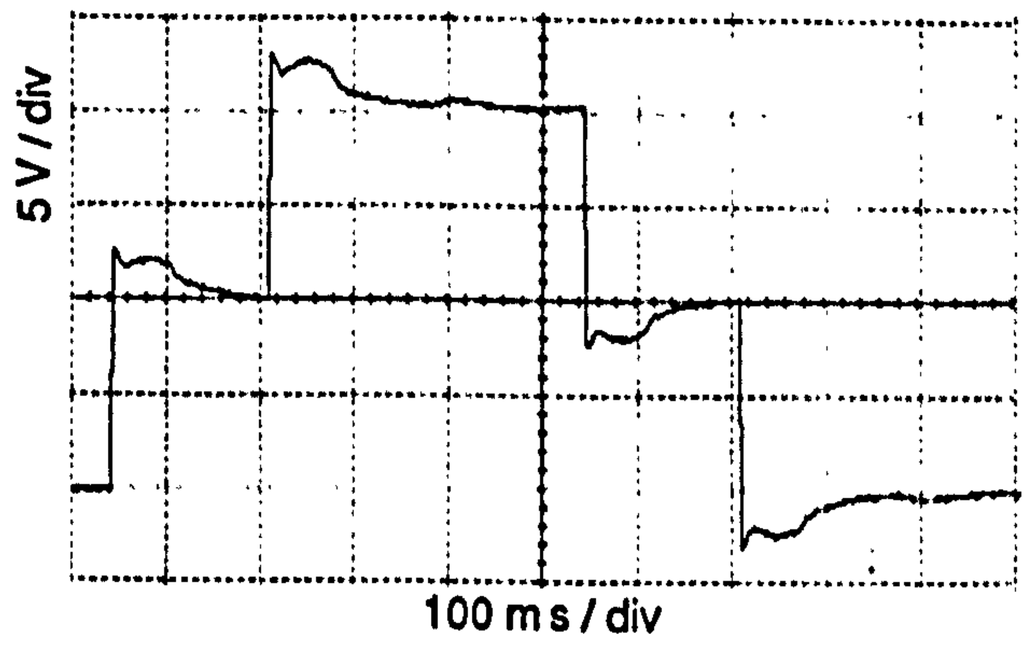

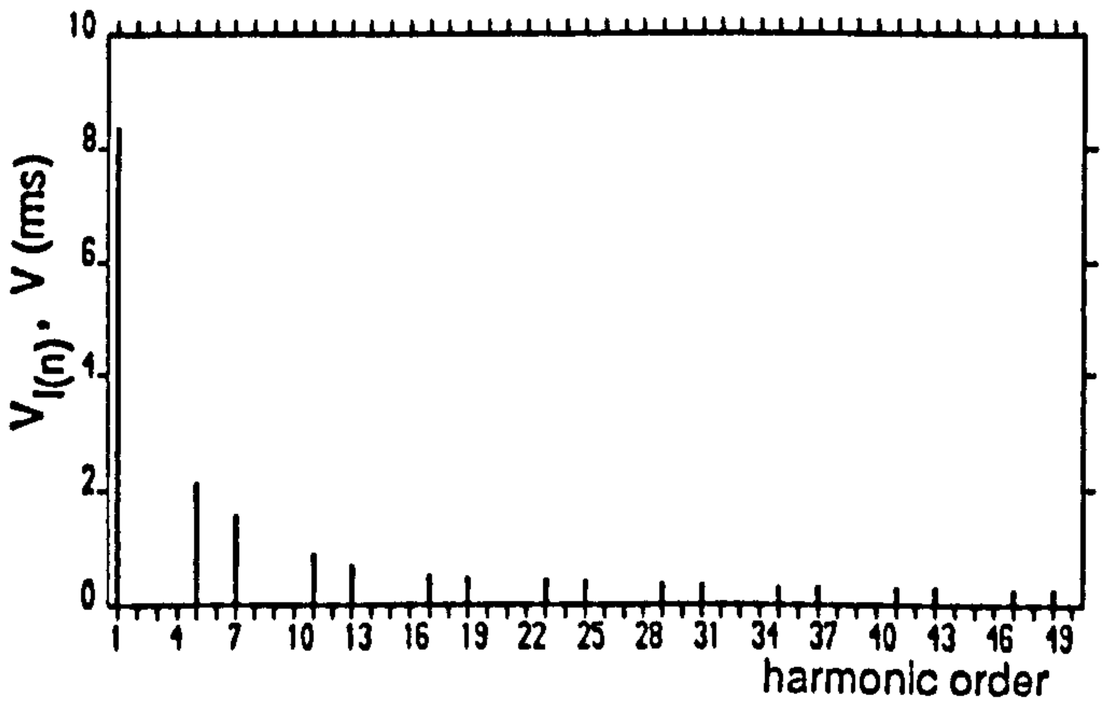

(a)

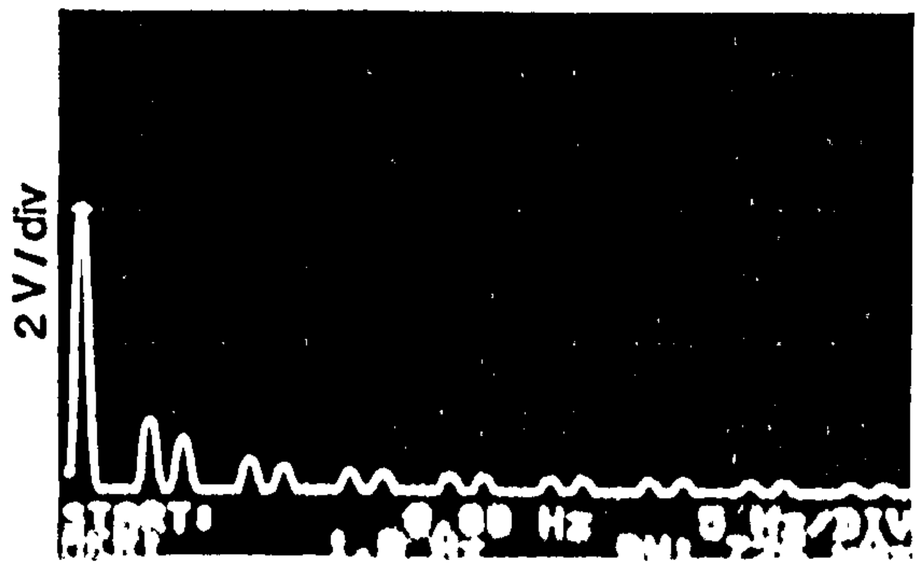

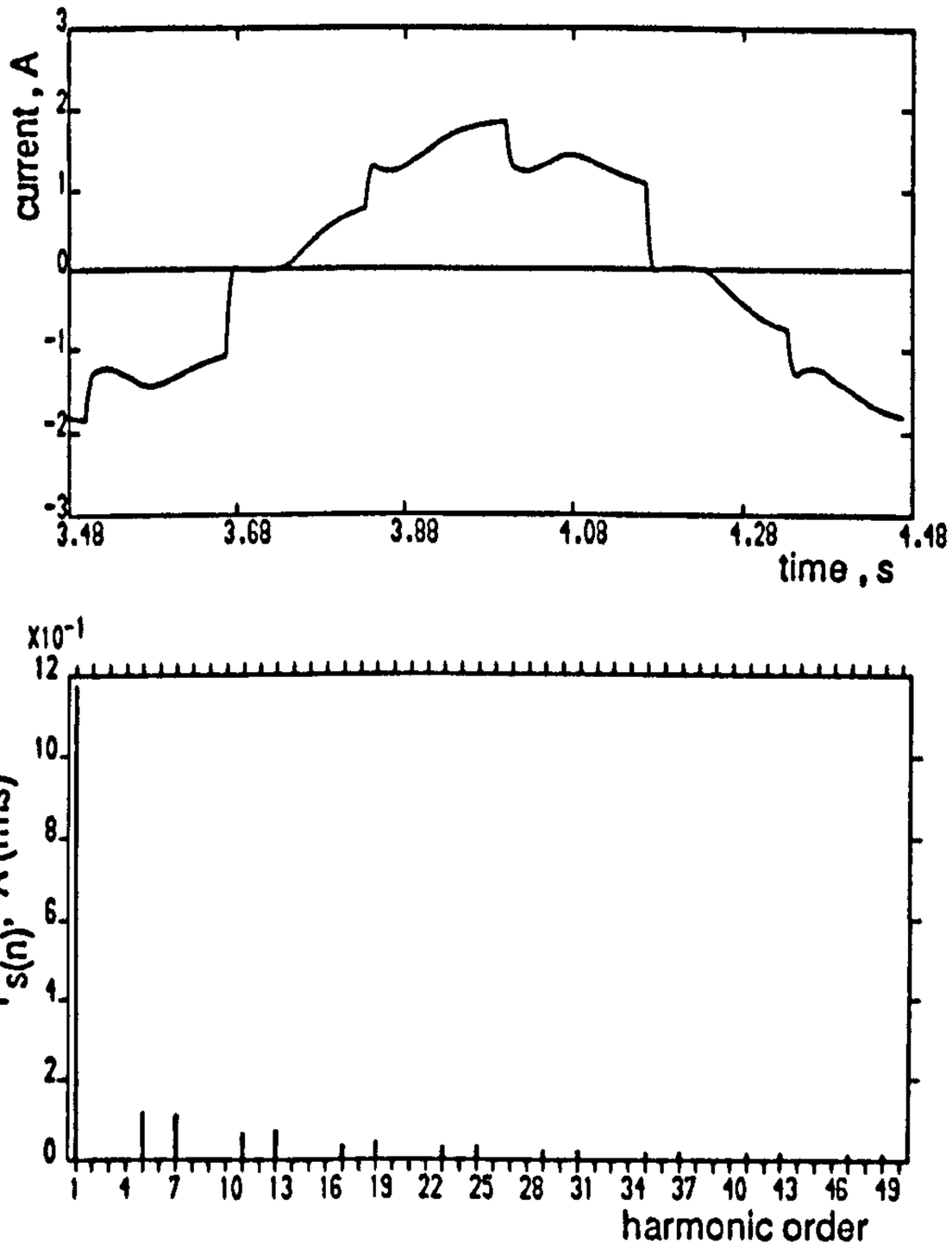

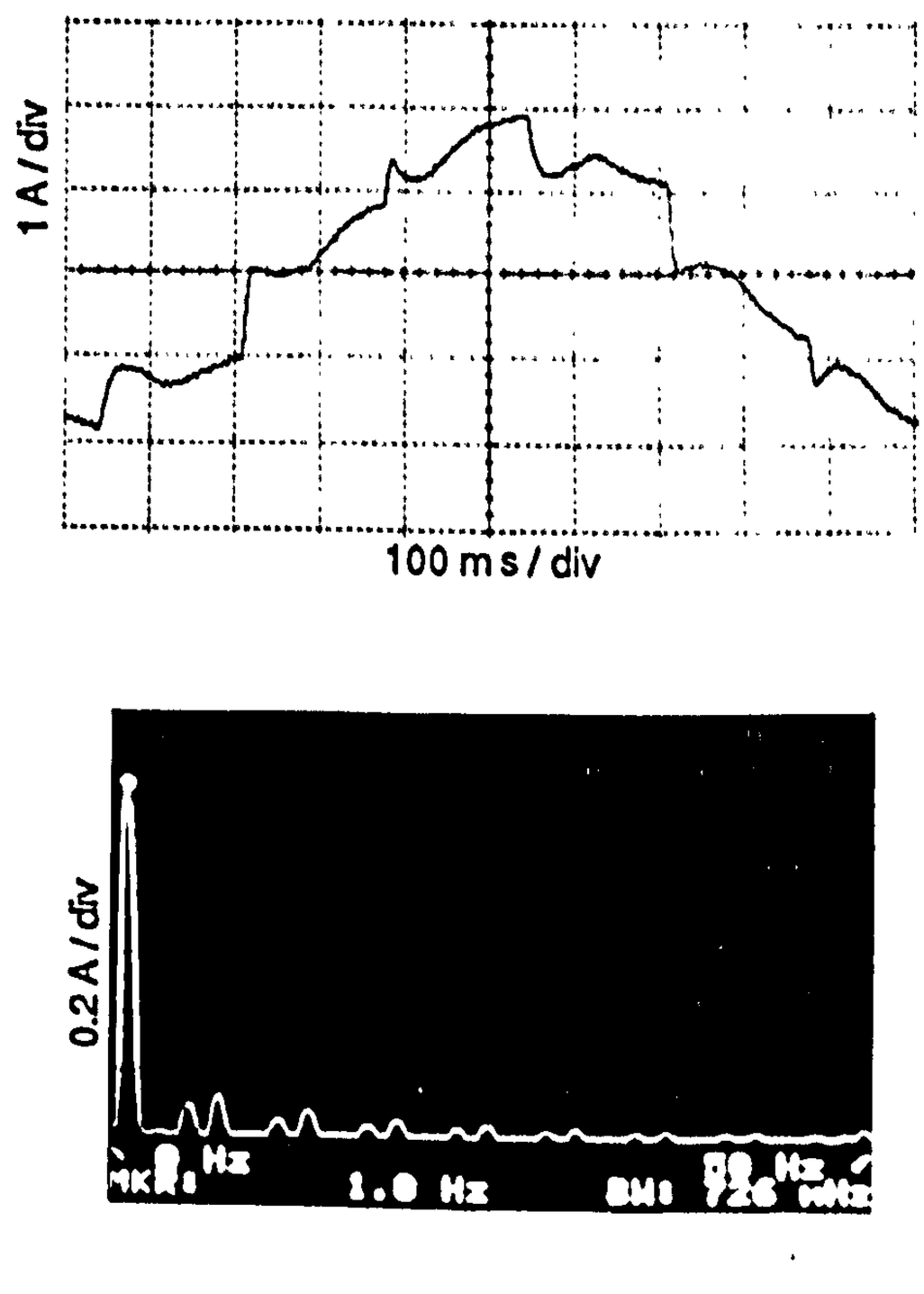

(b)

Figure 5.12 Computed and experimental results for QSW mode
1Hz stator frequency , no-load operation
(a) Line voltage and spectrum
(b) Stator current and spectrum

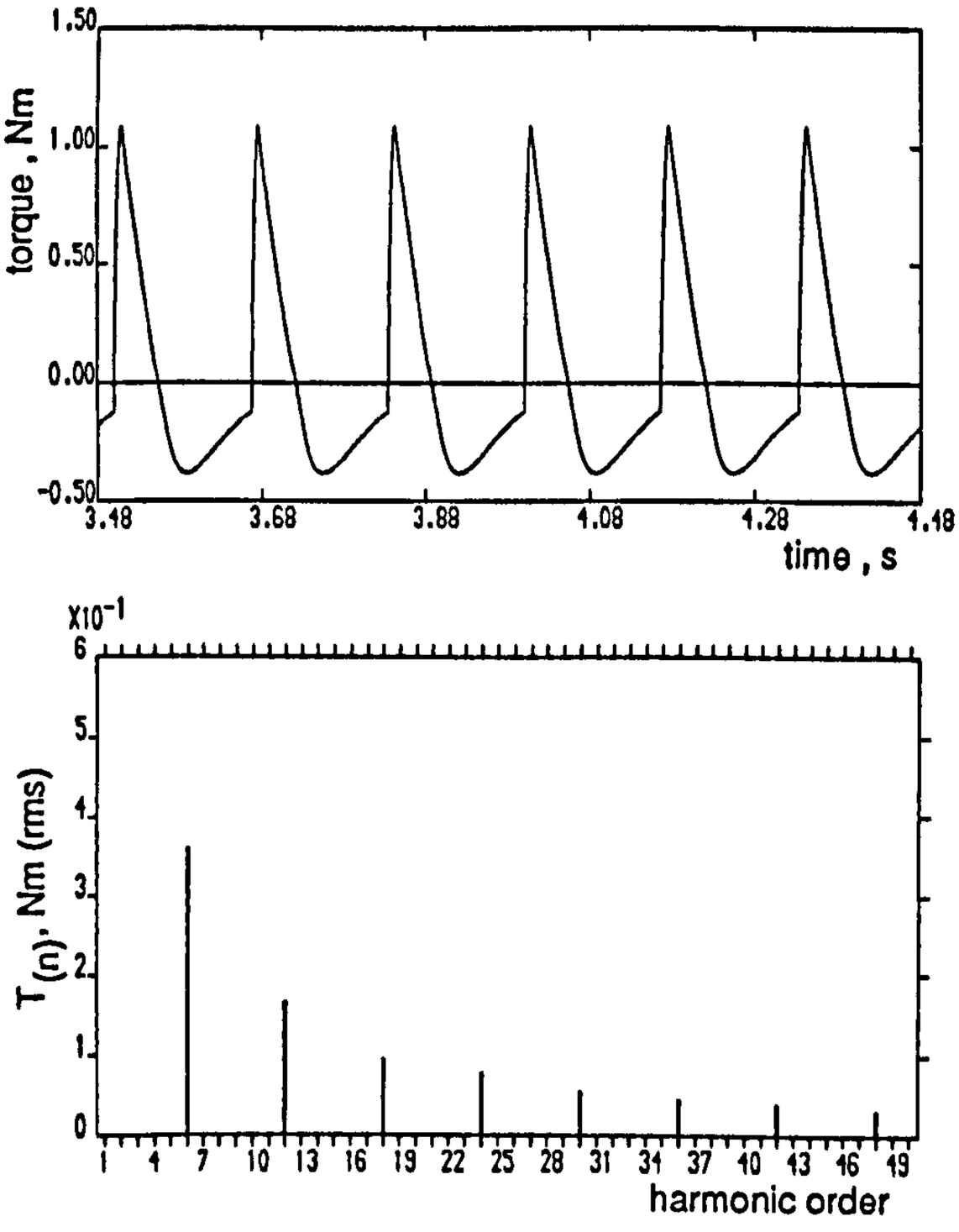

(c)

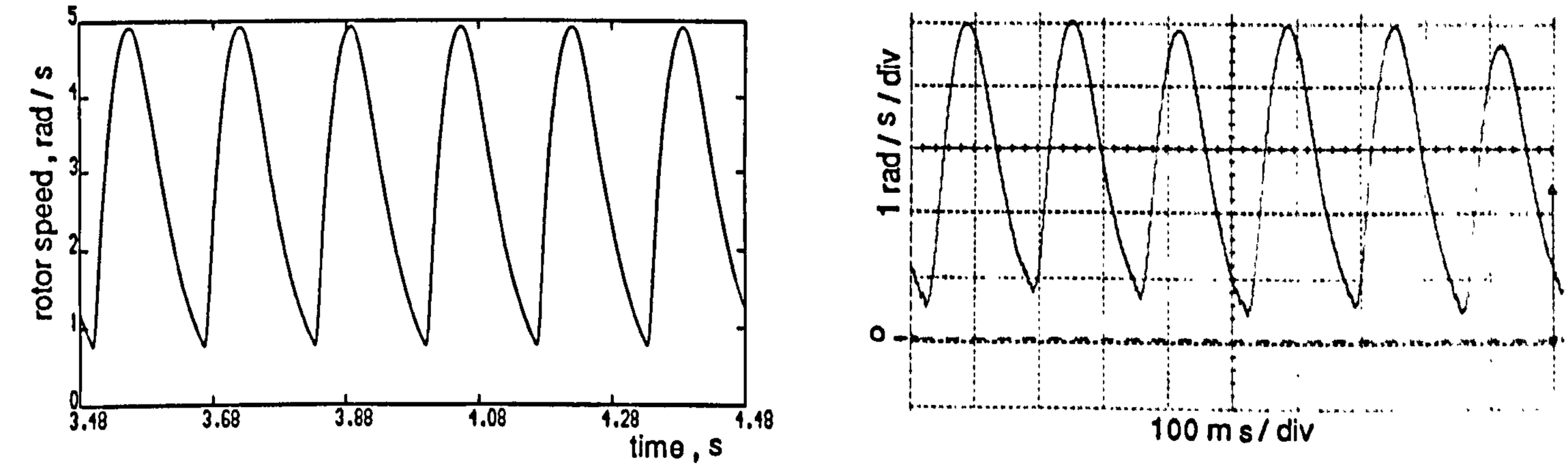

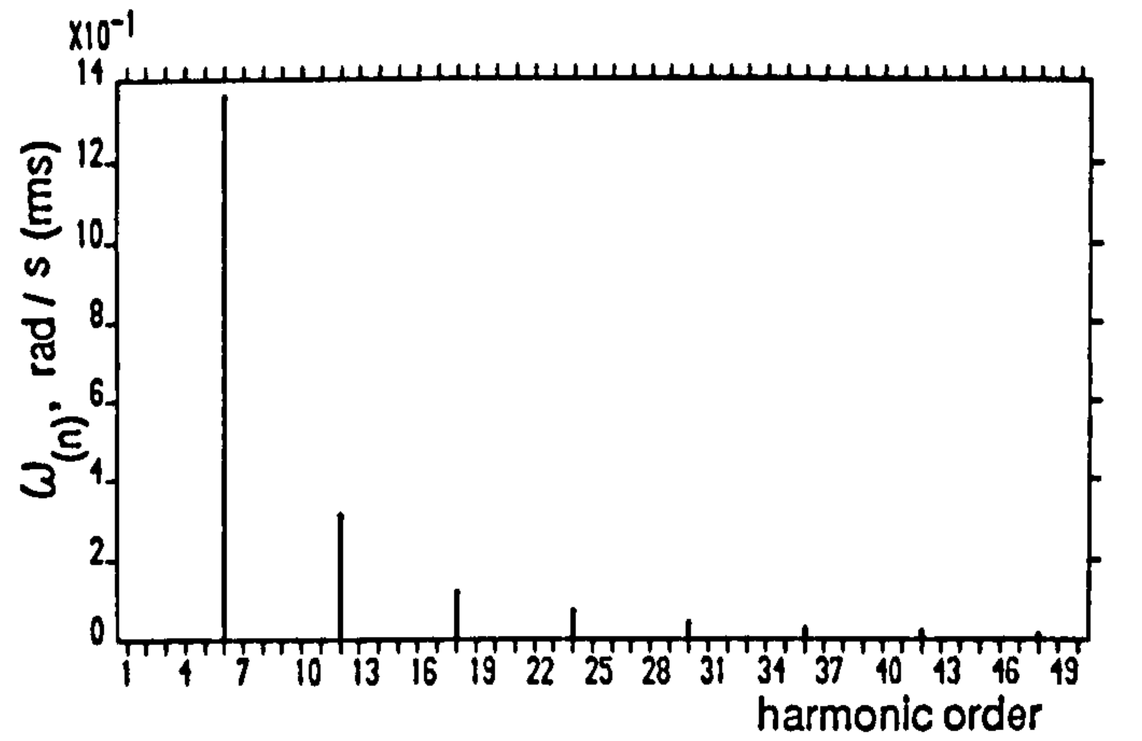

(d)

Figure 5.12 continued (c) Acceleration torque and spectrum
(d) Rotor speed and spectrum

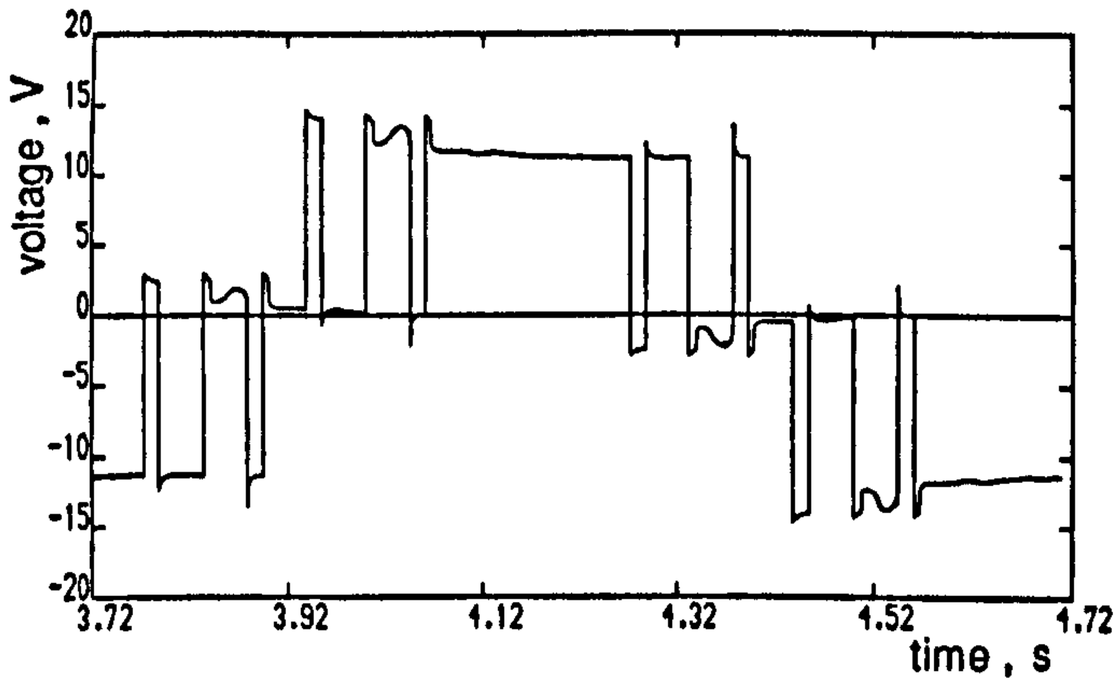

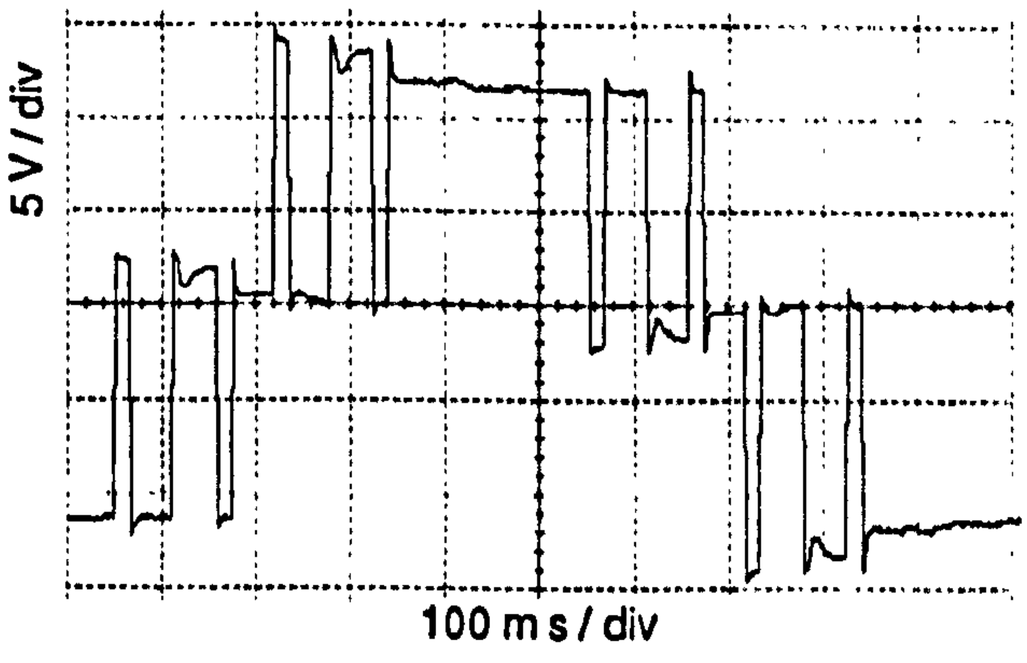

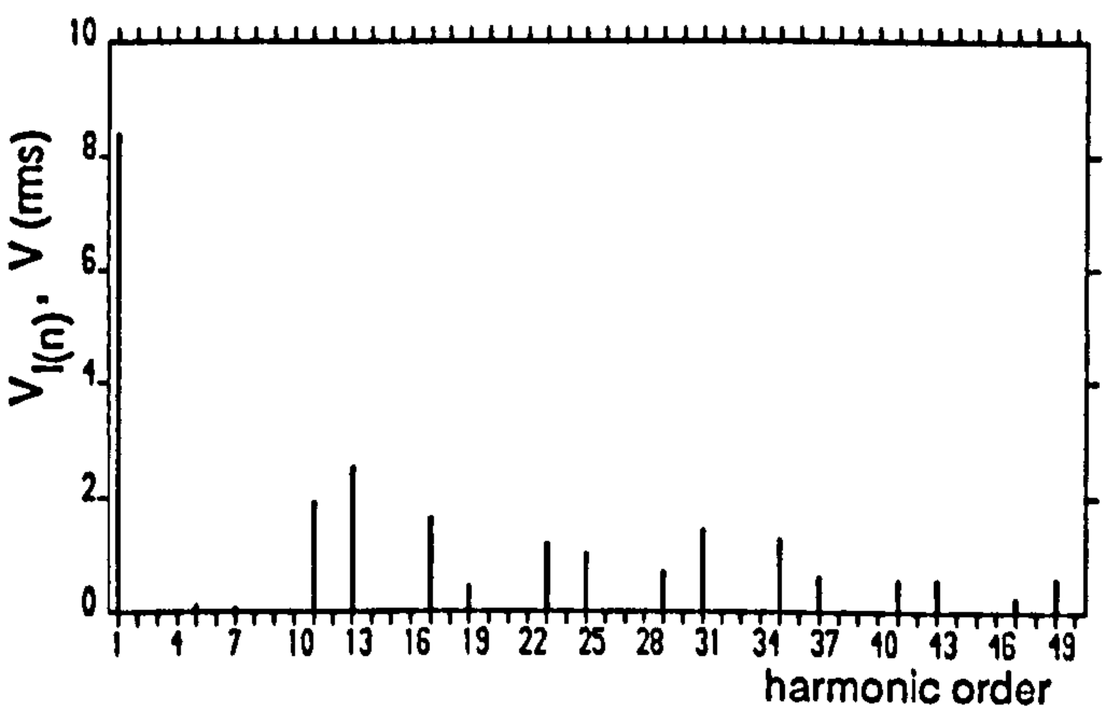

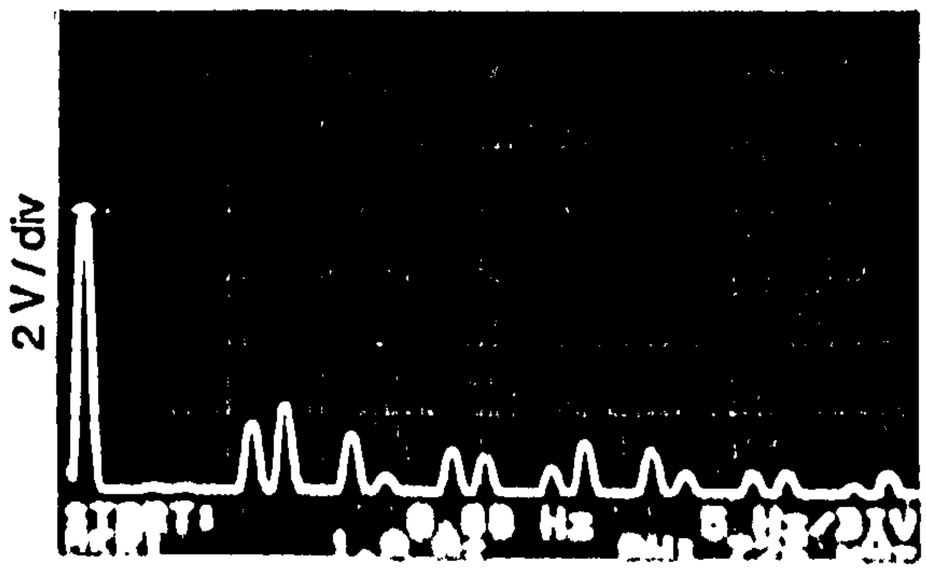

(a)

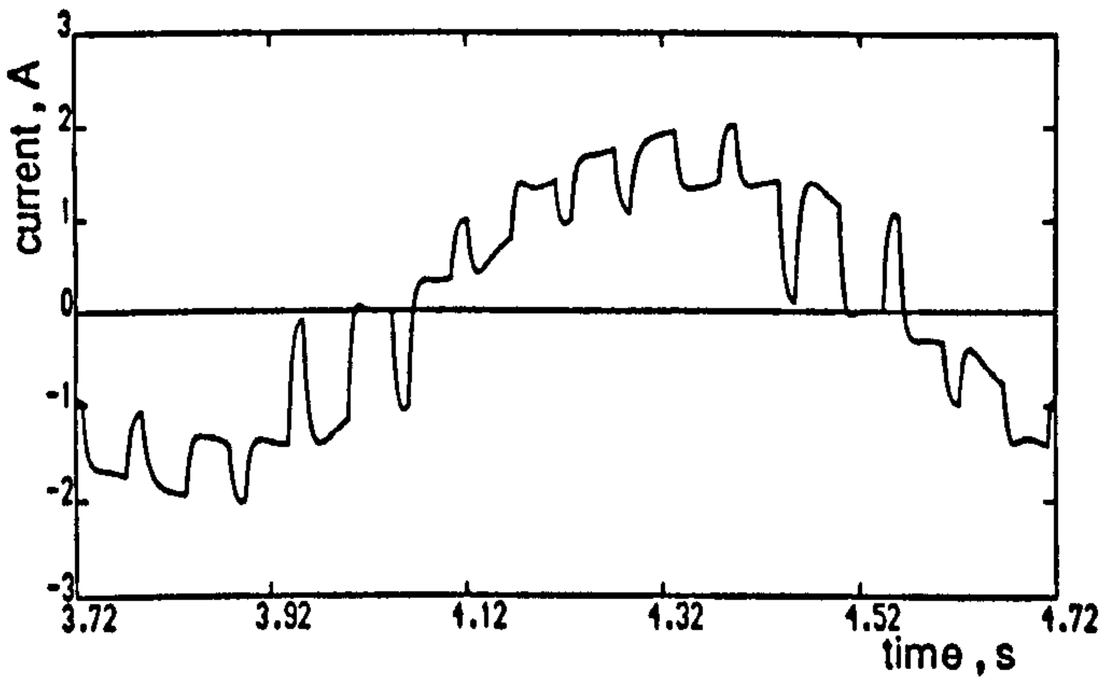

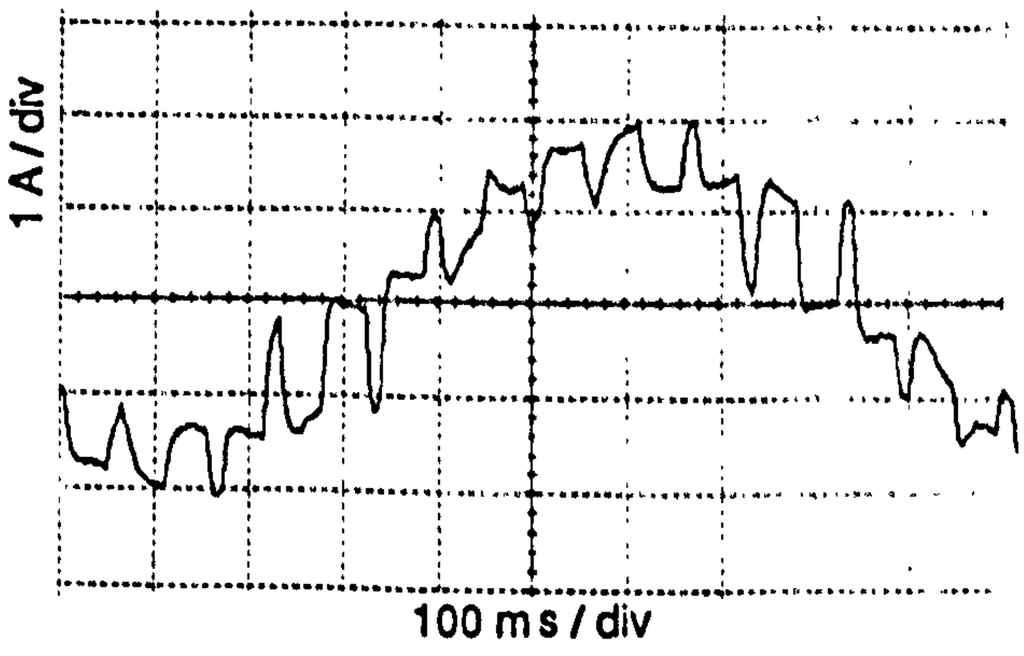

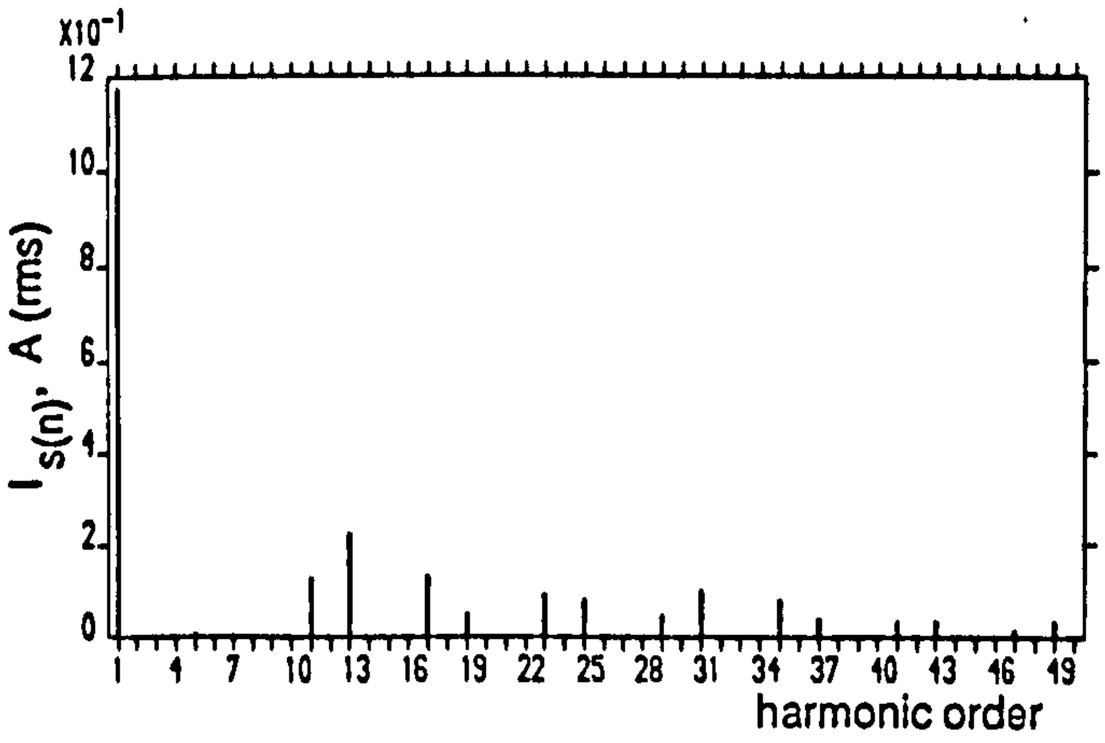

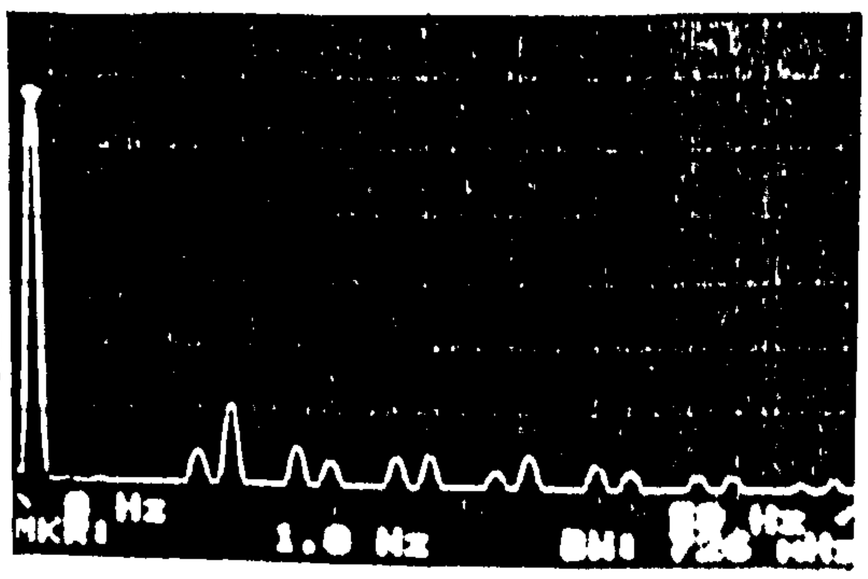

(b)

Figure 5.13 Computed and experimental results for PWM2 elimination mode at 1Hz stator frequency , no-load operation
(a) Line voltage and spectrum
(b) Stator current and spectrum

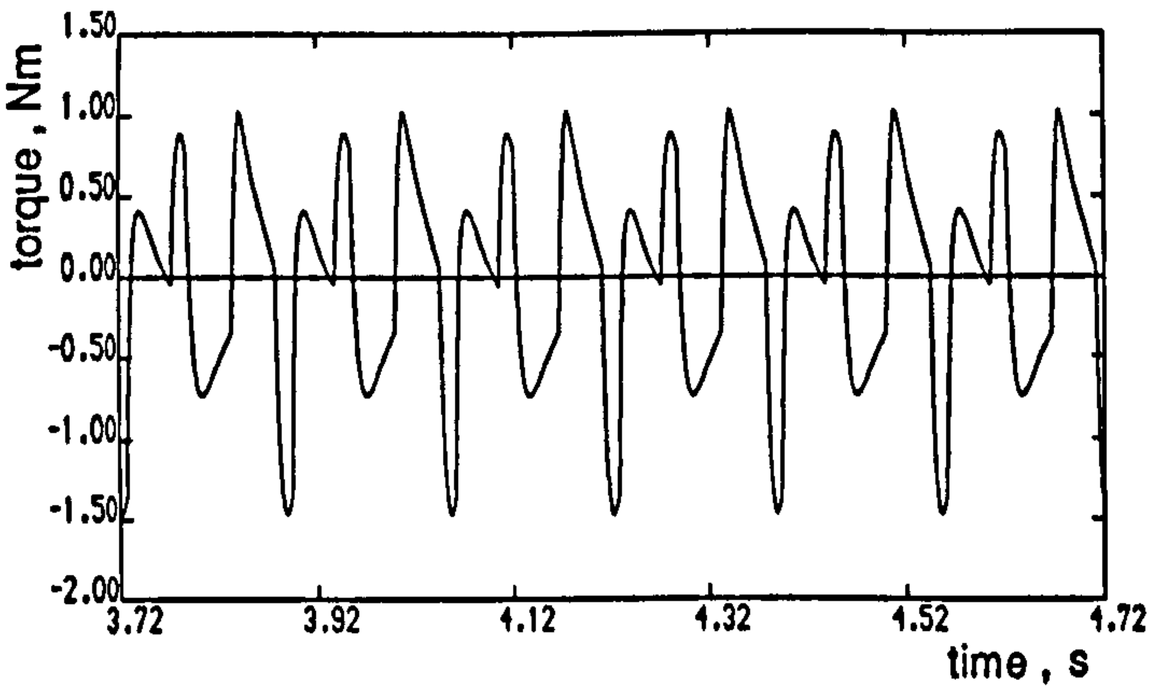

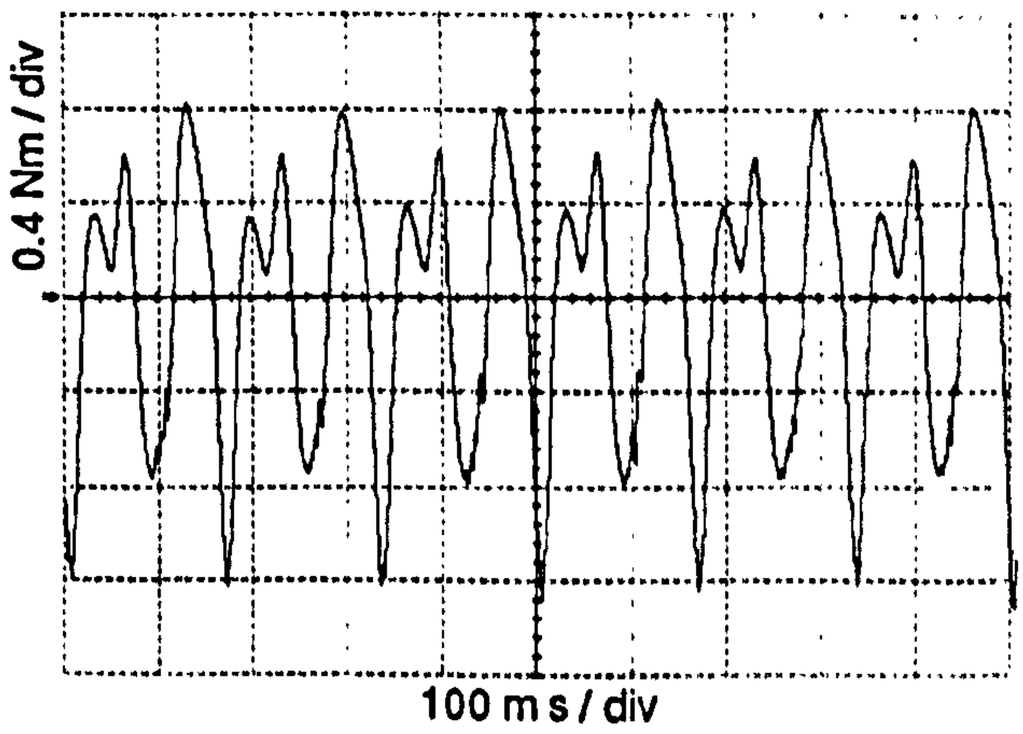

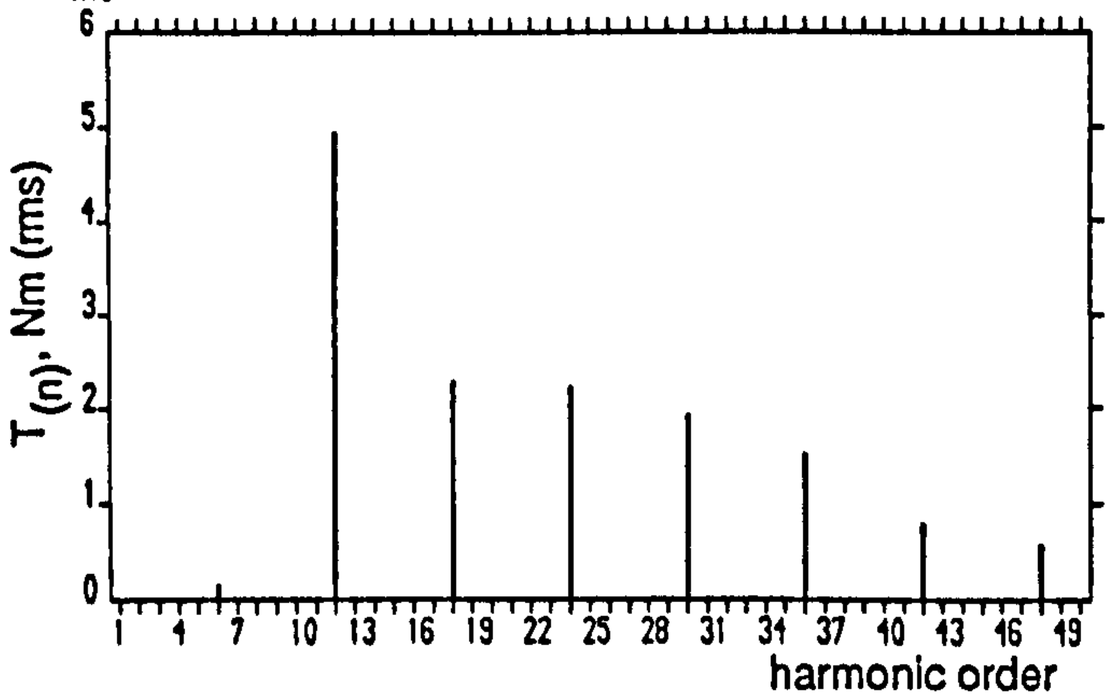

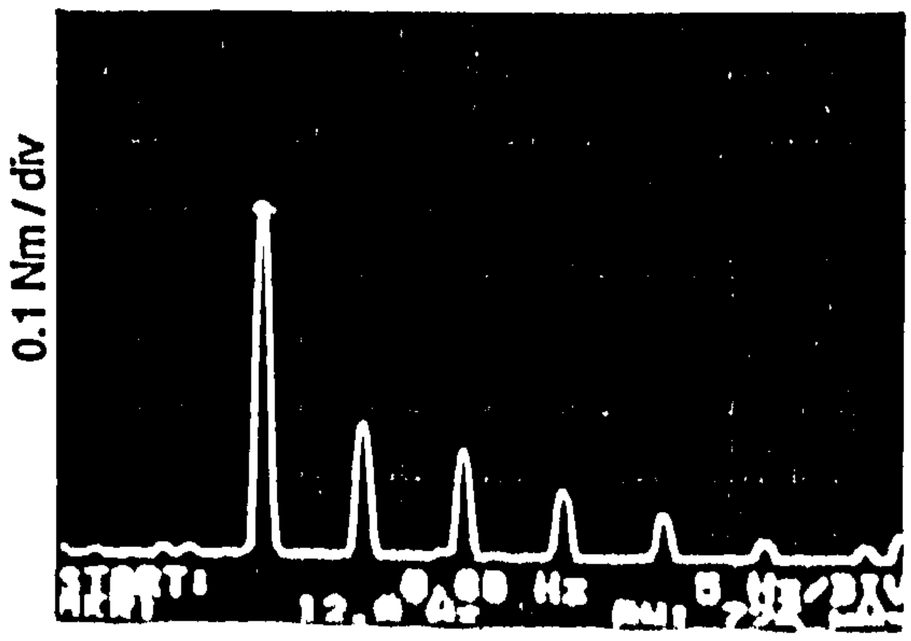

(c)

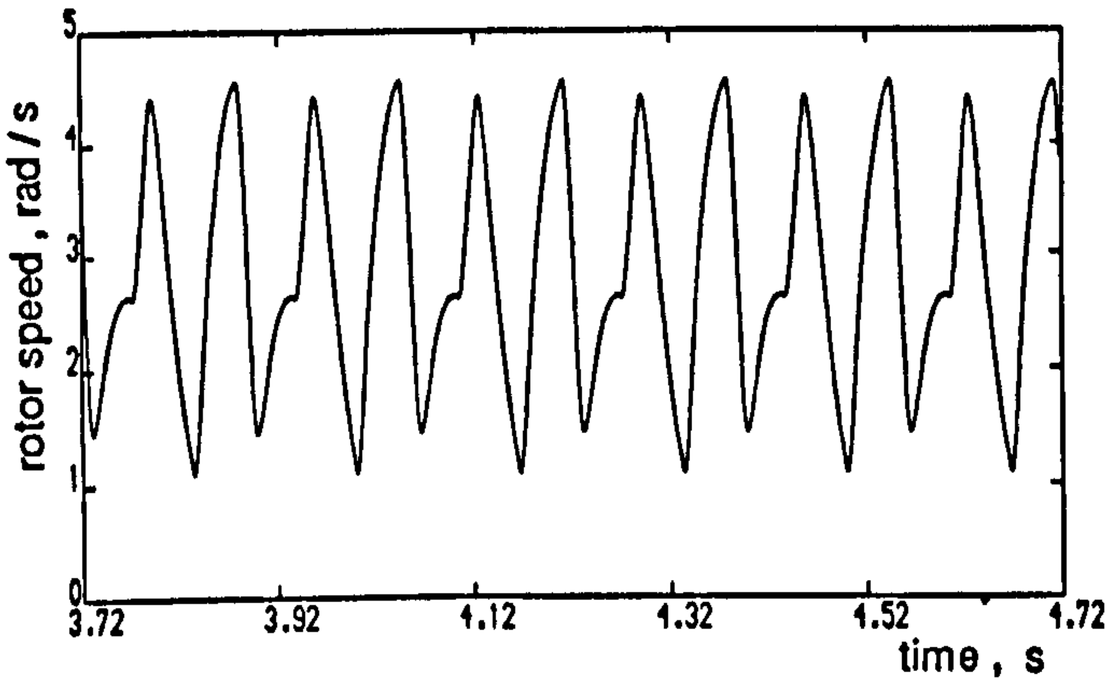

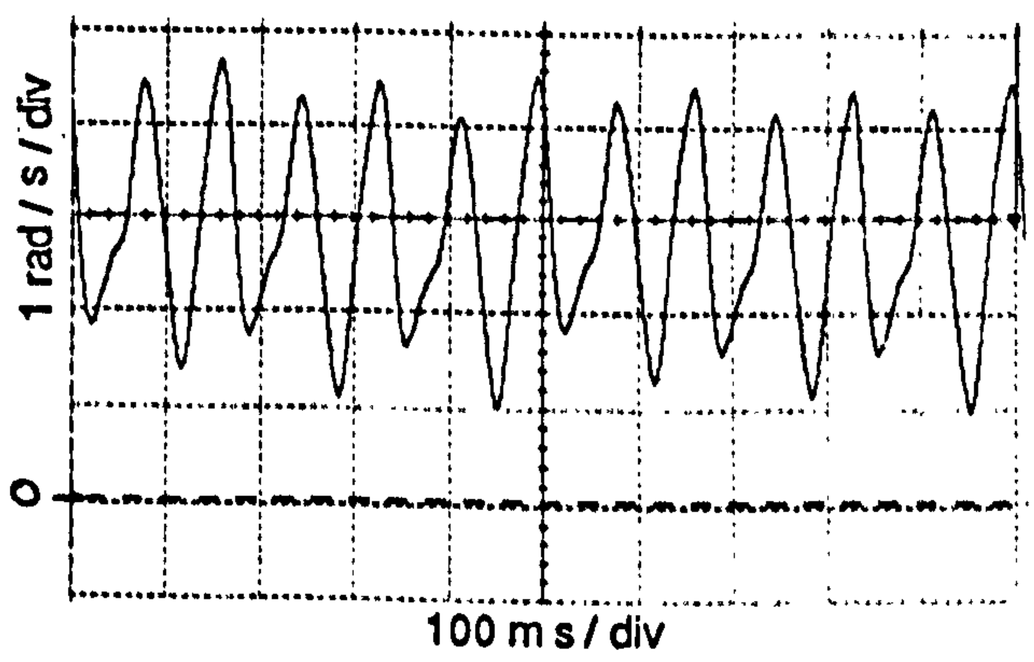

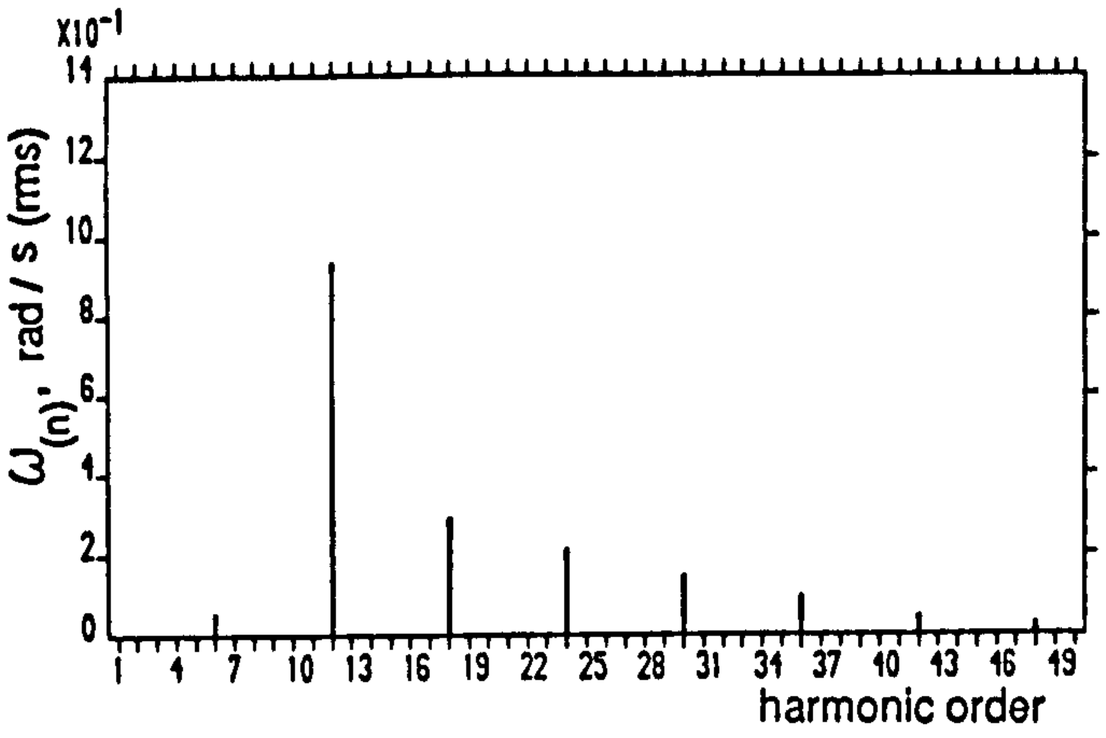

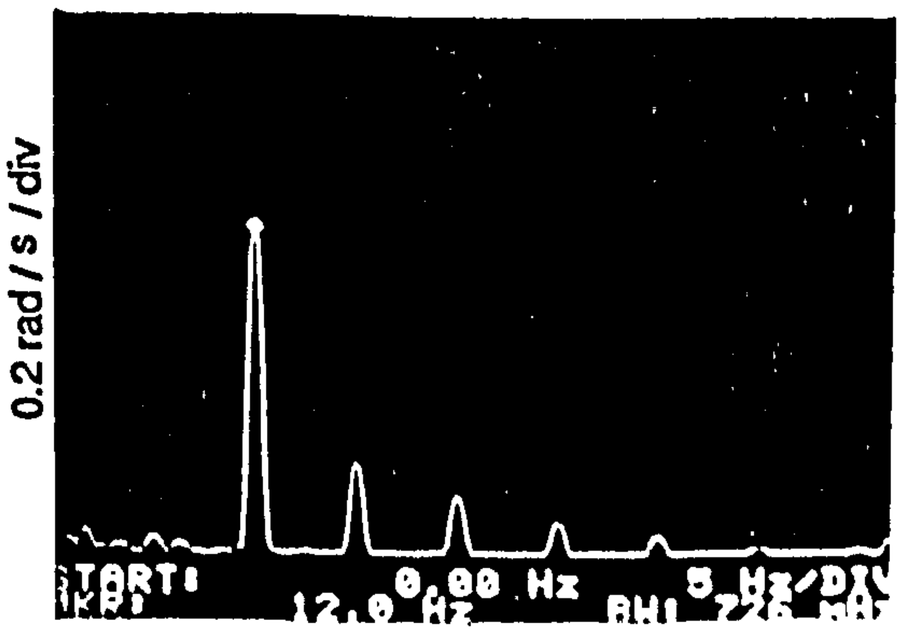

(d)

Figure 5.13 continued (c) Acceleration torque and spectrum
(d) Rotor speed and spectrum

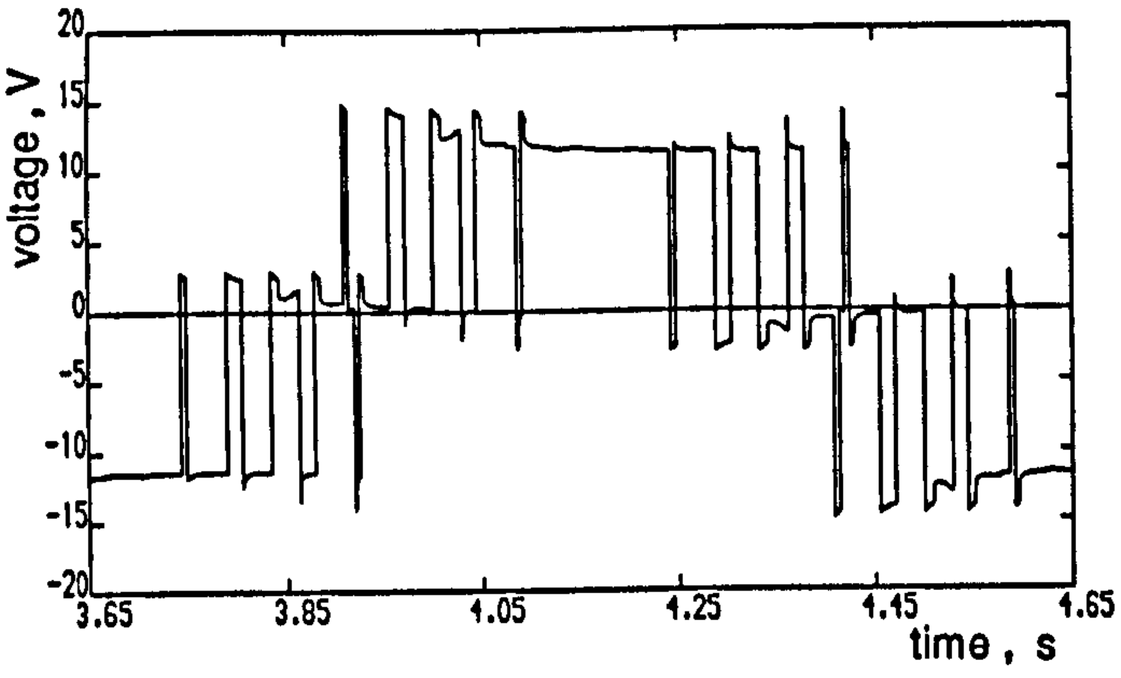

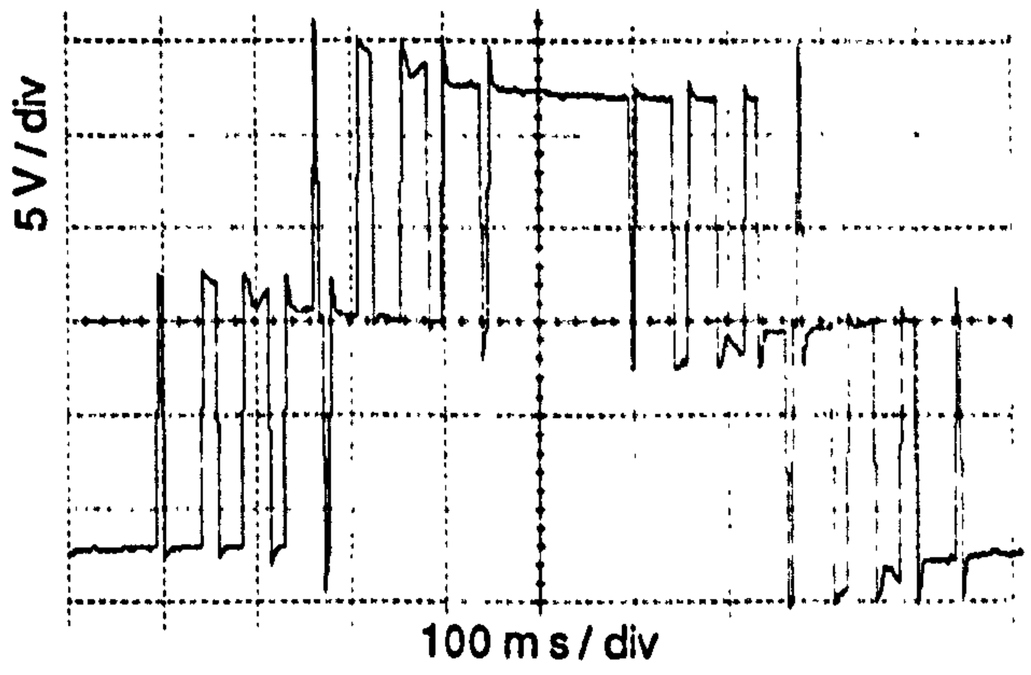

(a)

(b)

Figure 5.14 Computed and experimental results for PWM4 elimination mode at 1Hz stator frequency , no-load operation
(a) Line voltage and spectrum
(b) Stator current and spectrum

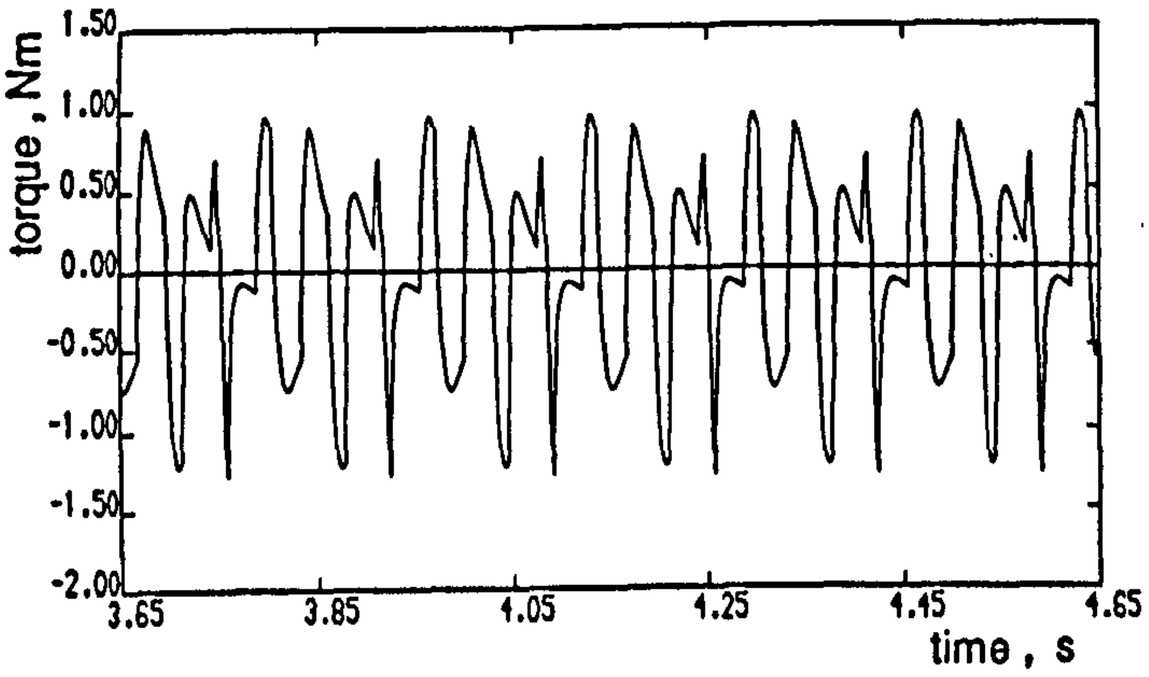

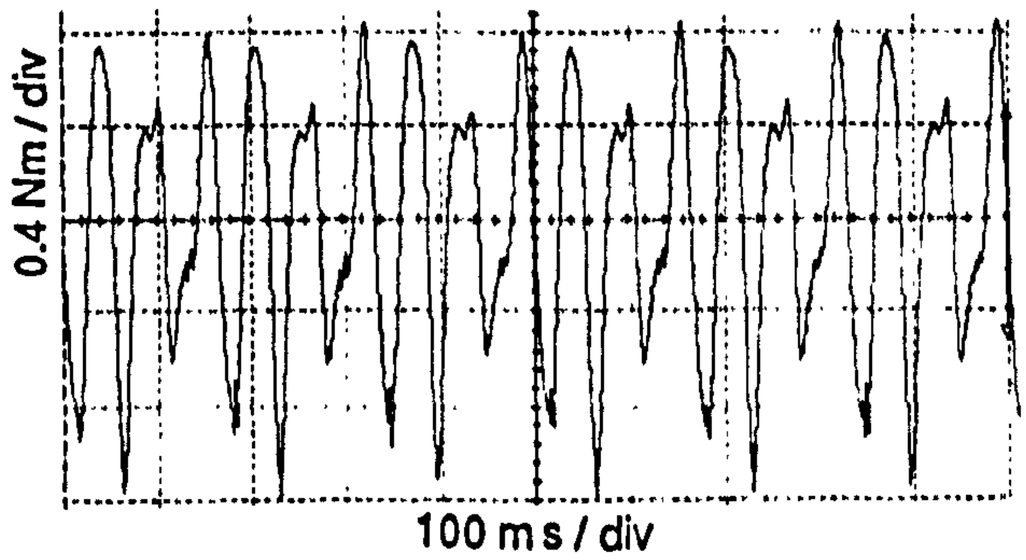

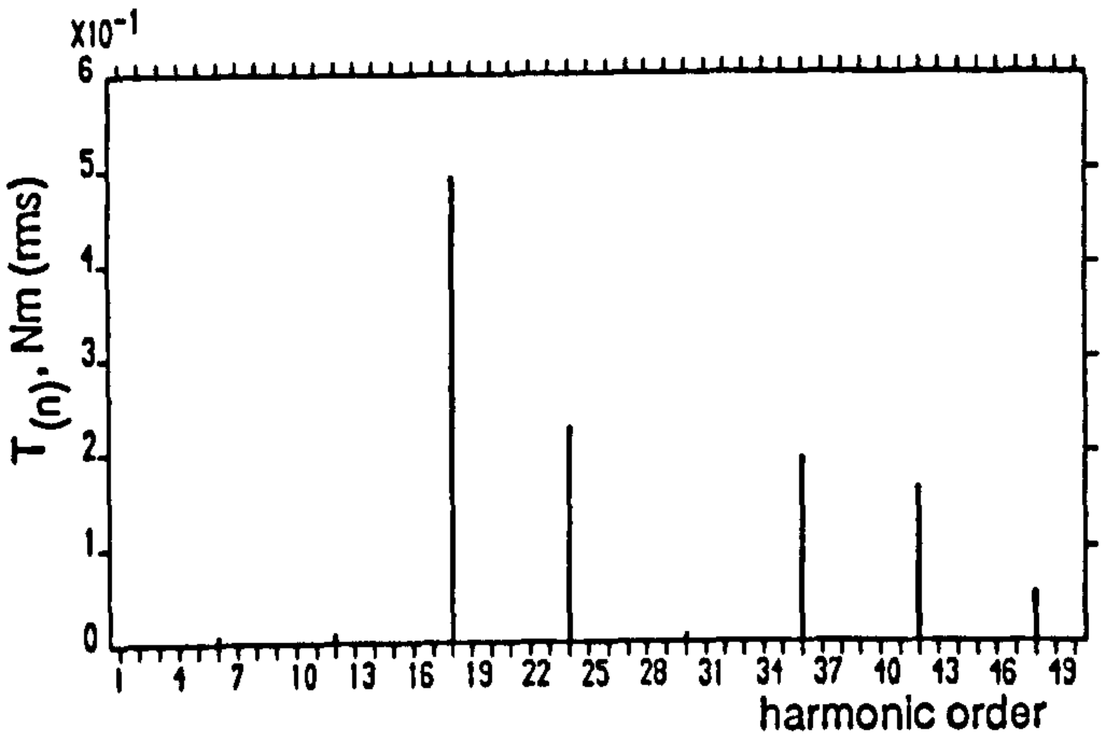

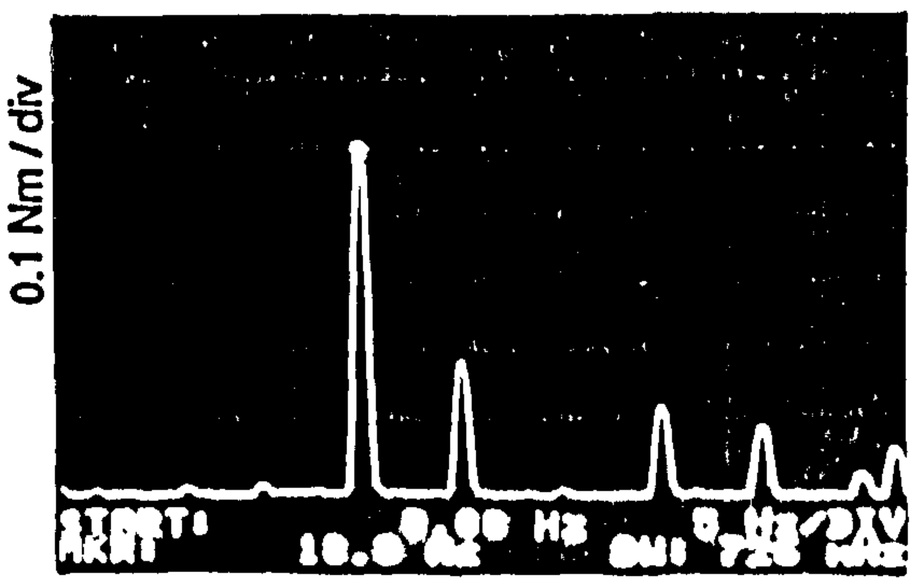

(c)

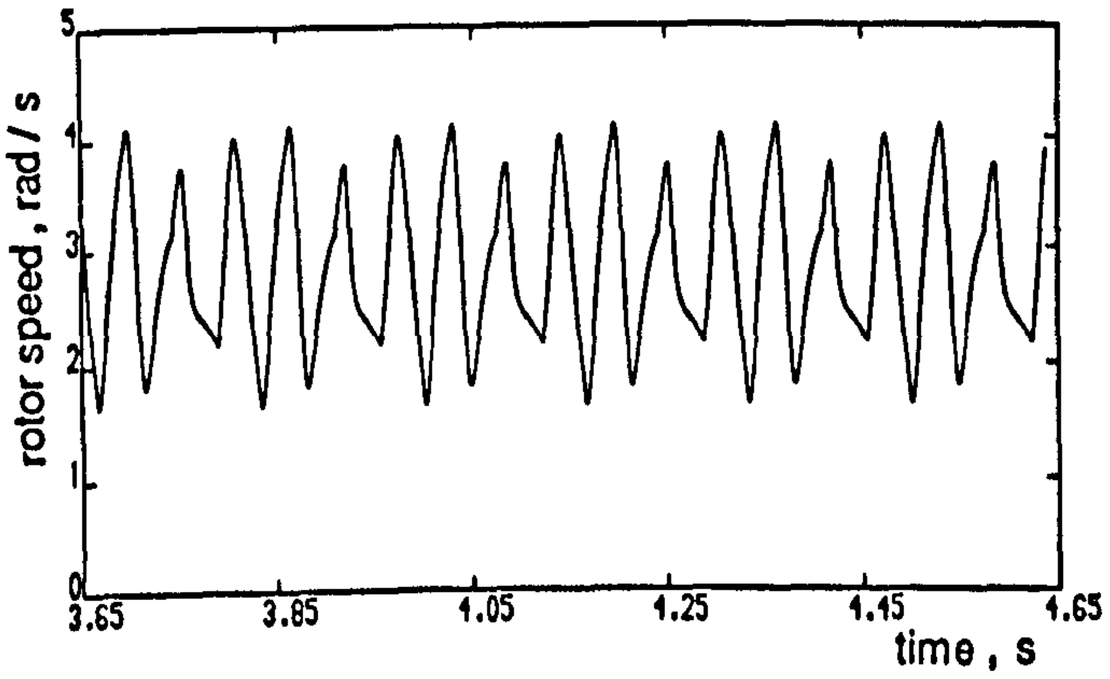

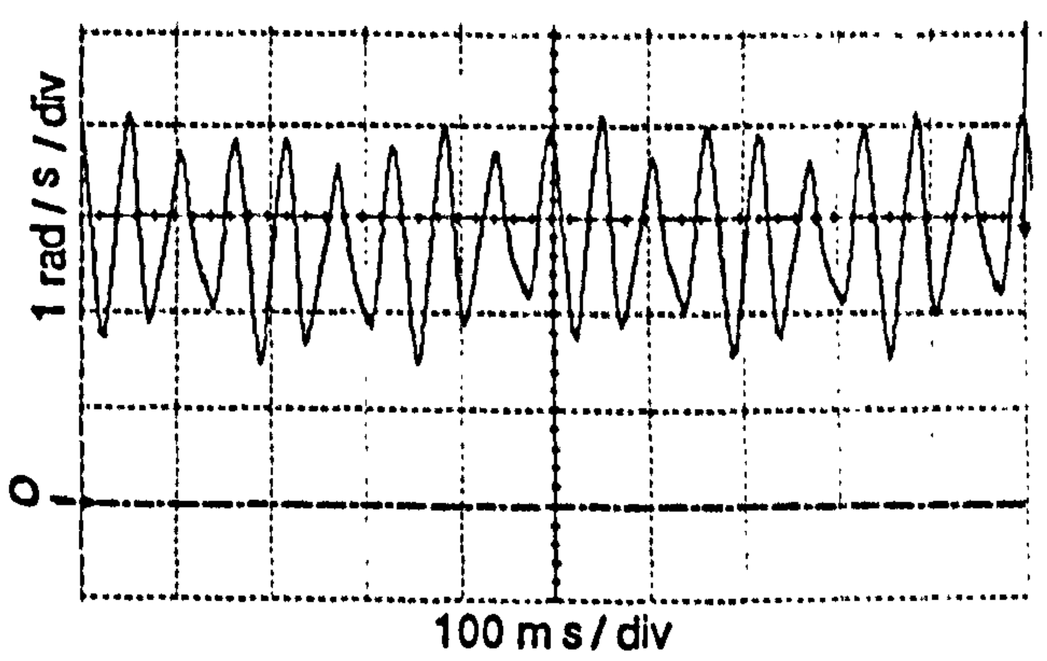

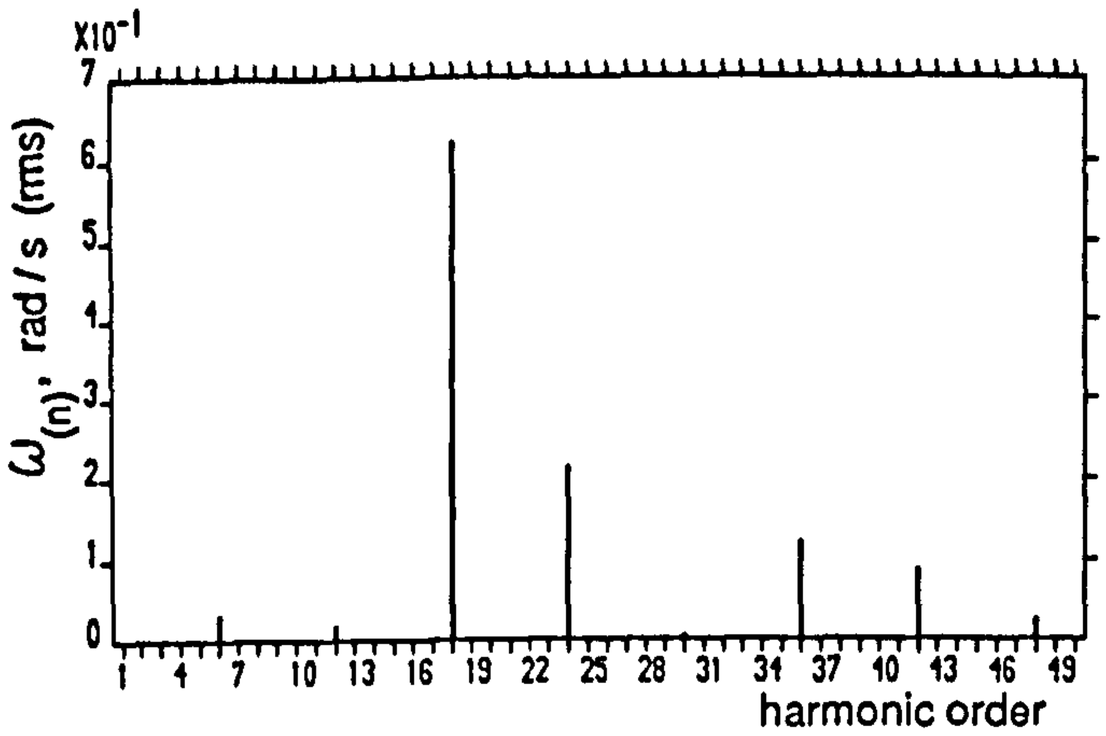

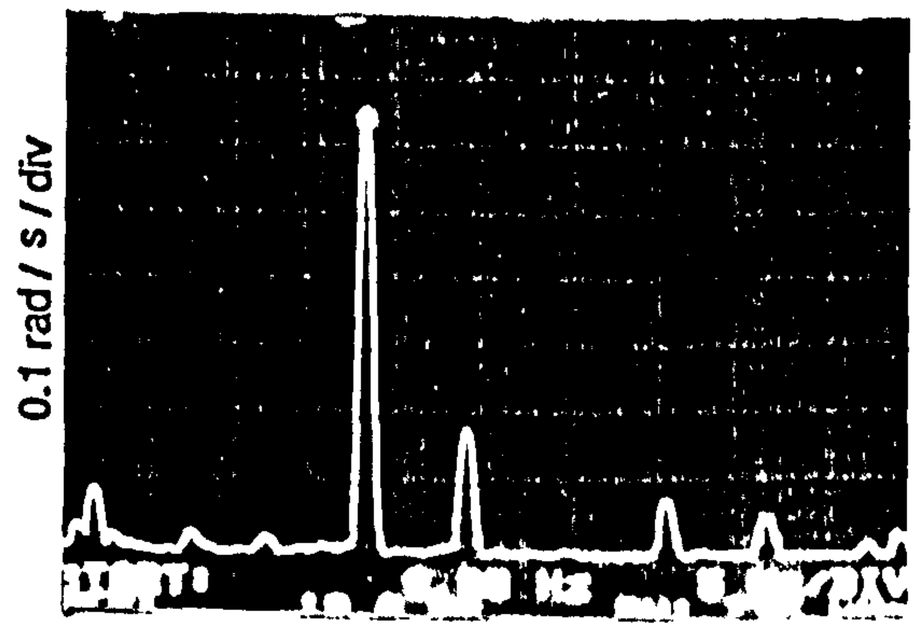

(d)

Figure 5.14 continued (c) Acceleration torque and spectrum
(d) Rotor speed and spectrum

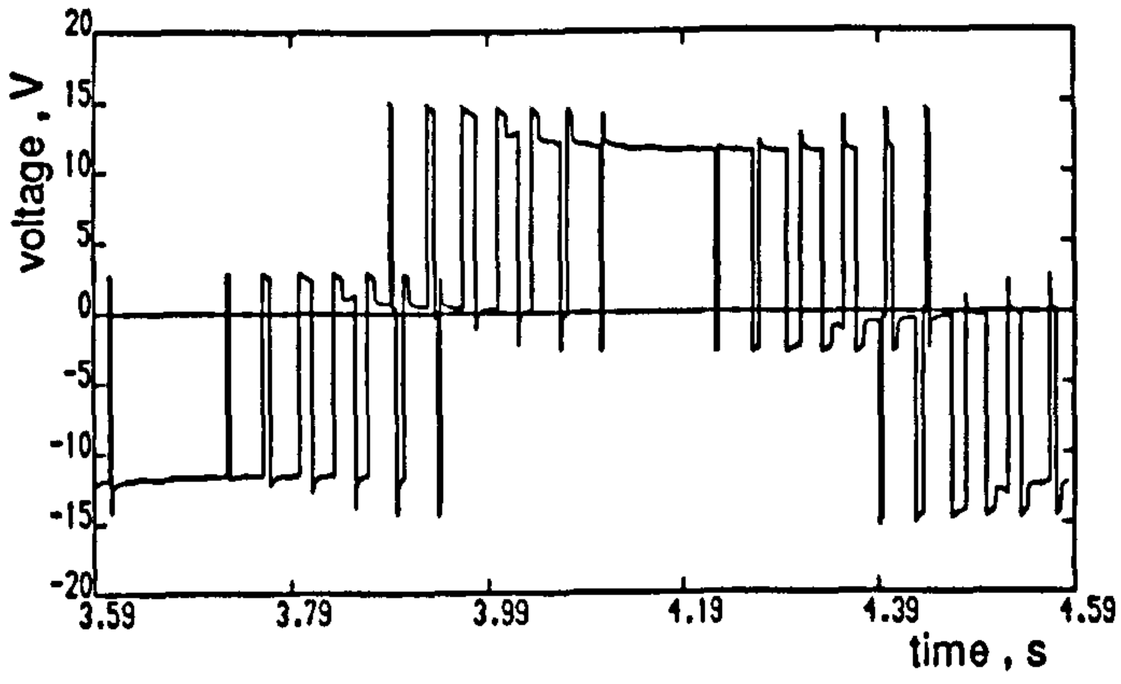

(a)

(b)

Figure 5.15 Computed and experimental results for PWM6 elimination mode at 1Hz stator frequency , no-load operation
(a) Line voltage and spectrum
(b) Stator current and spectrum

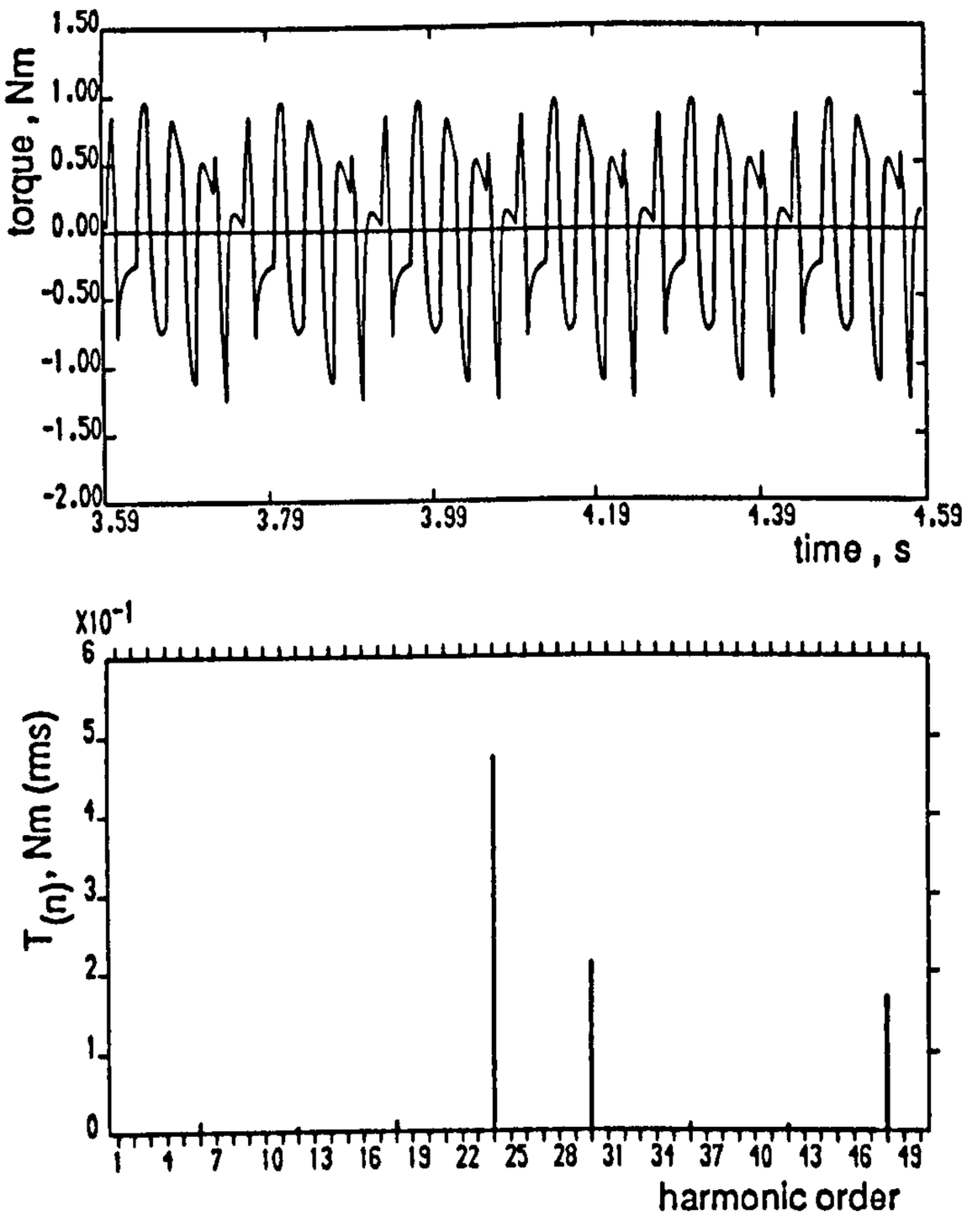

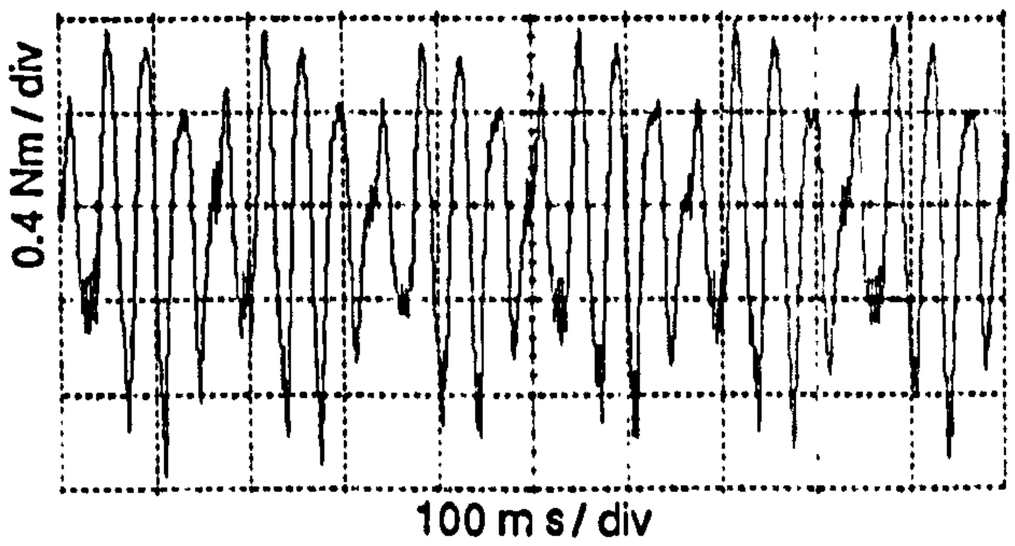

(c)

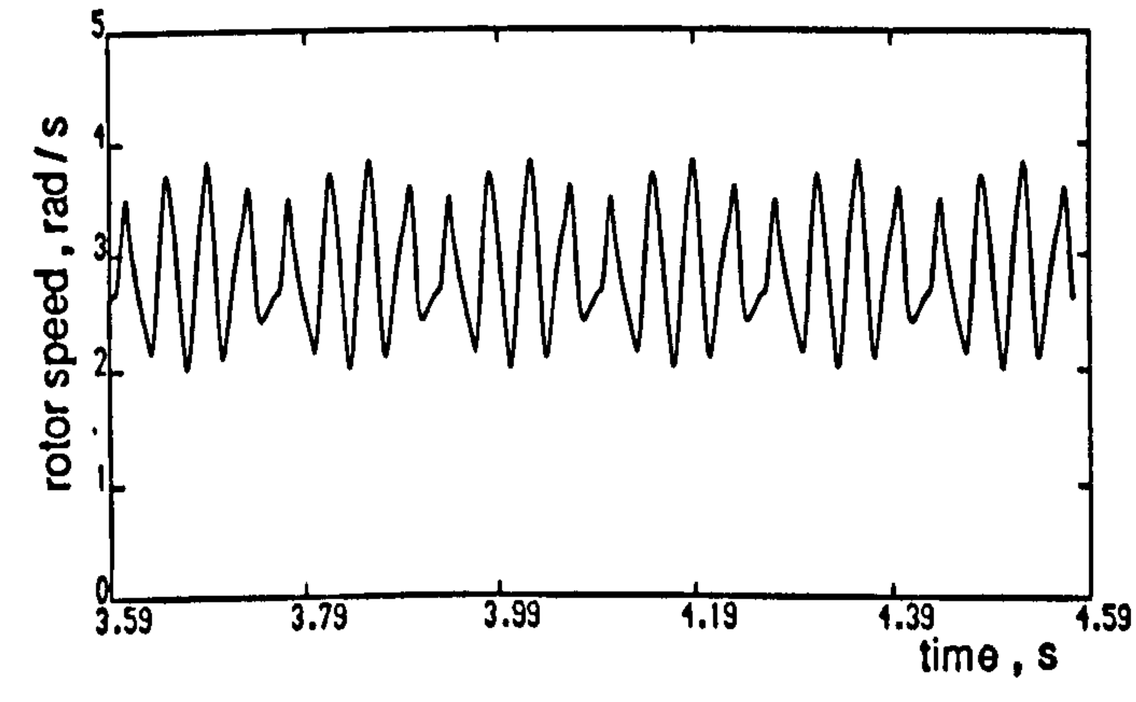

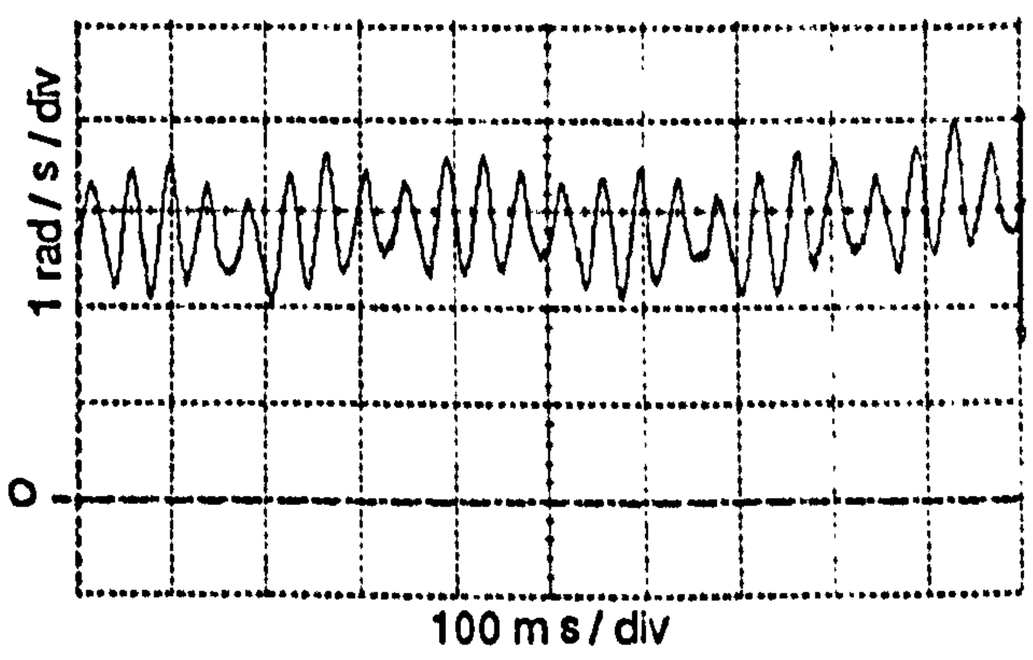

(d)

Figure 5.15 continued (c) Acceleration torque and spectrum
(d) Rotor speed and spectrum

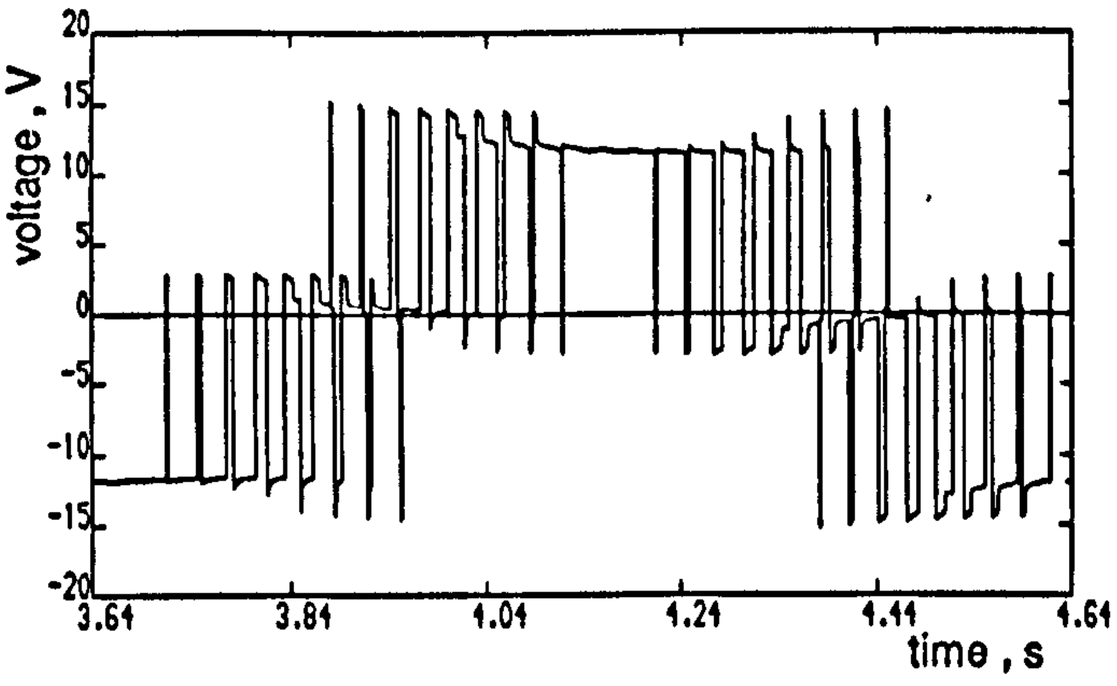

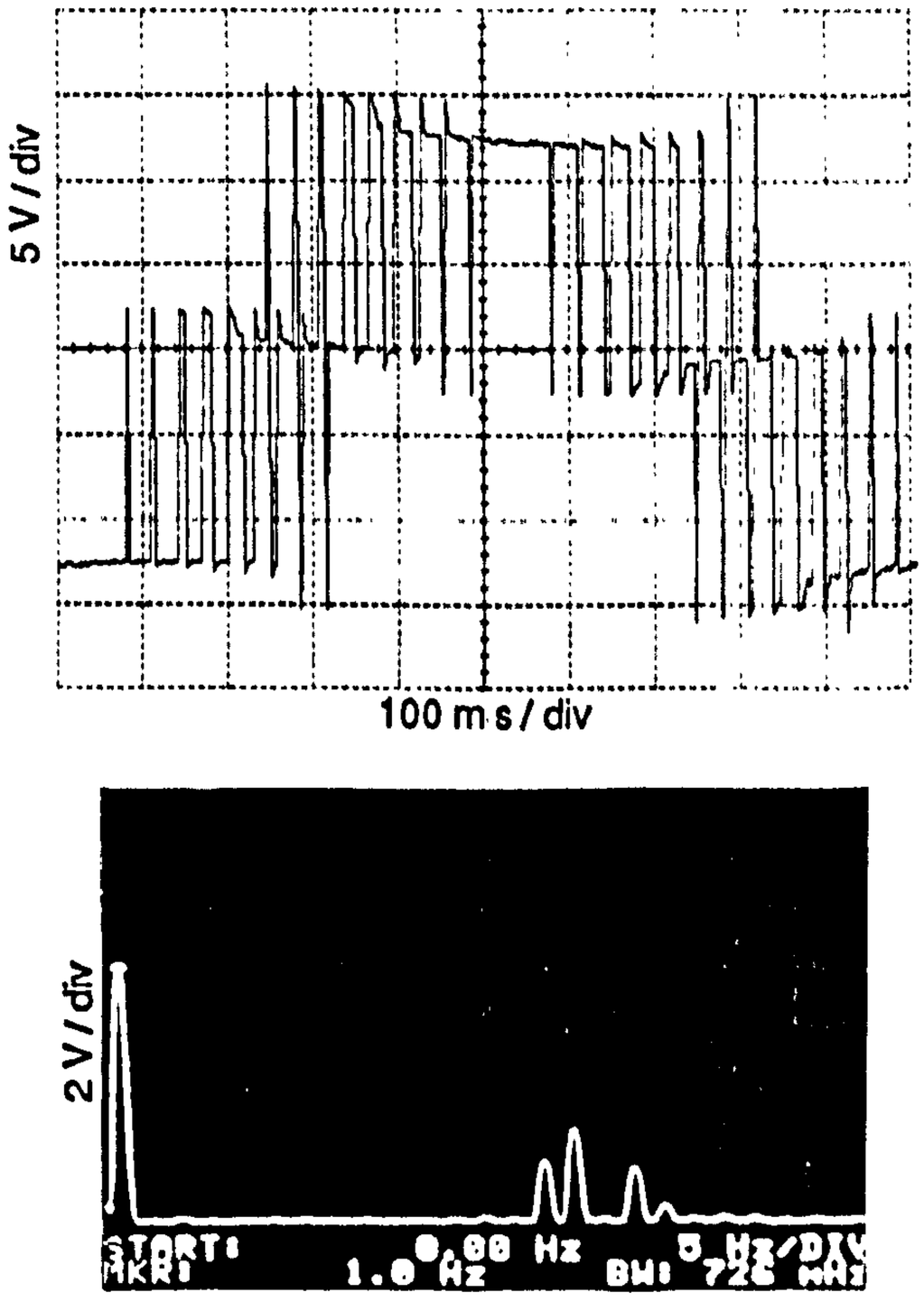

(a)

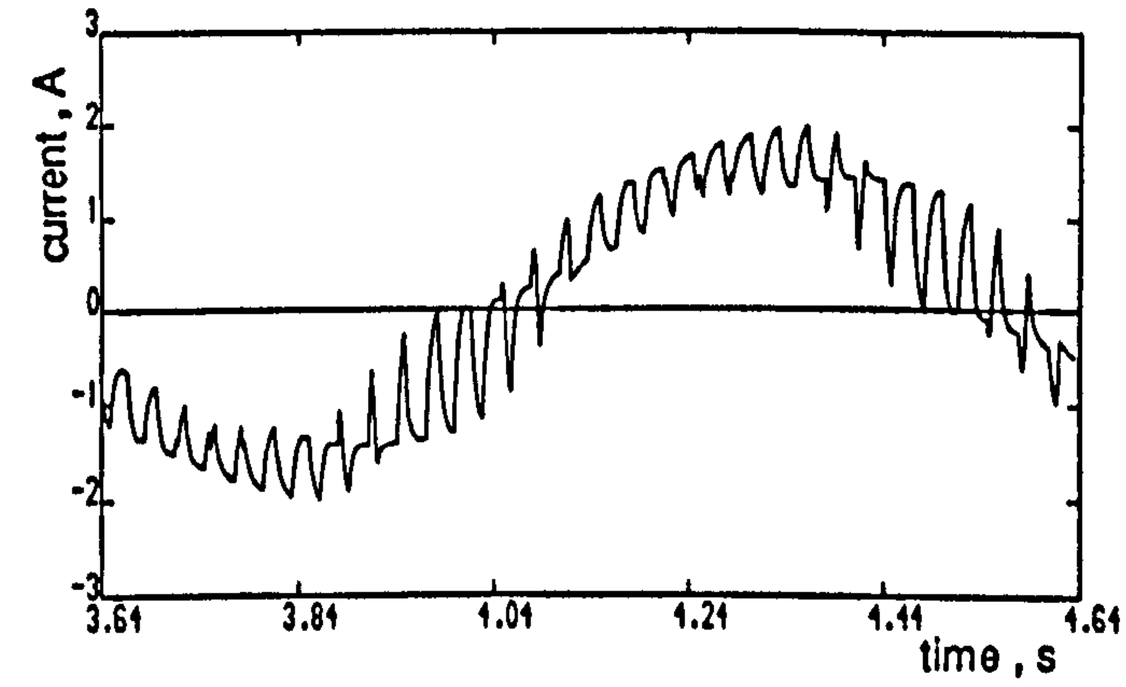

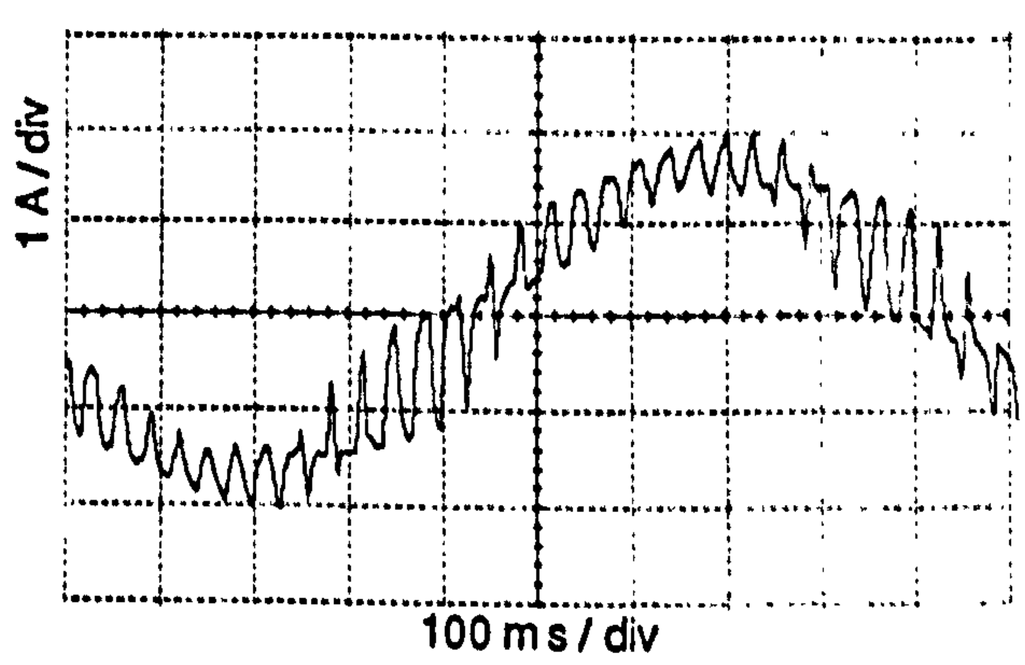

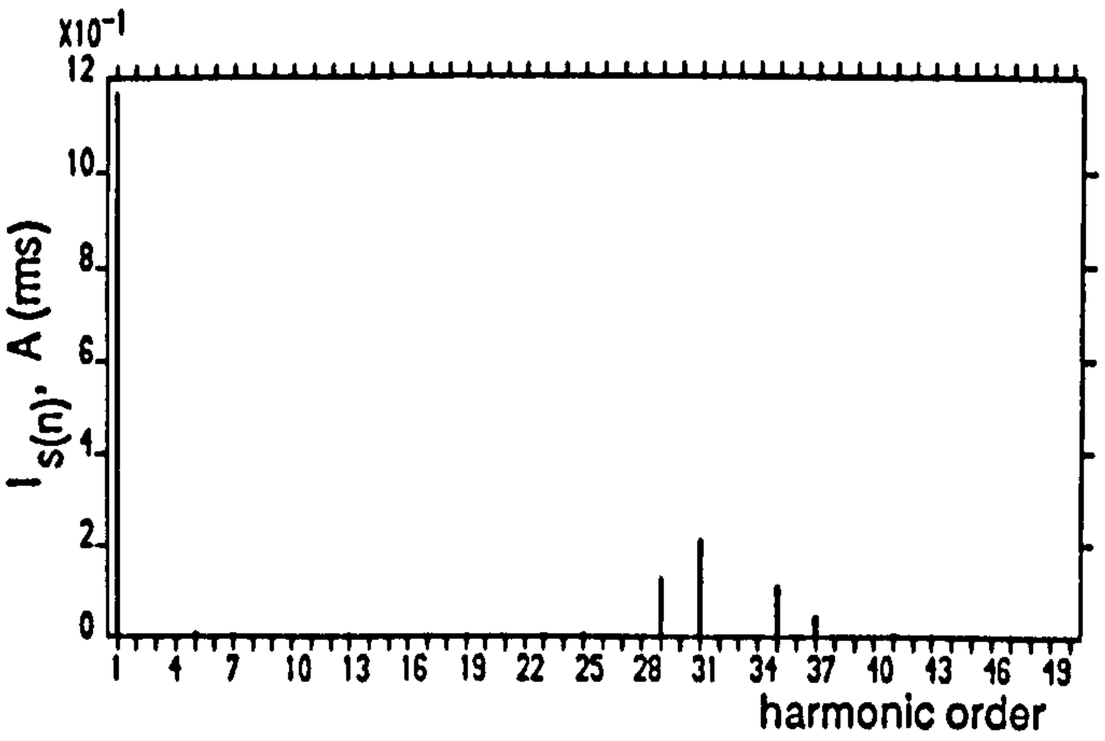

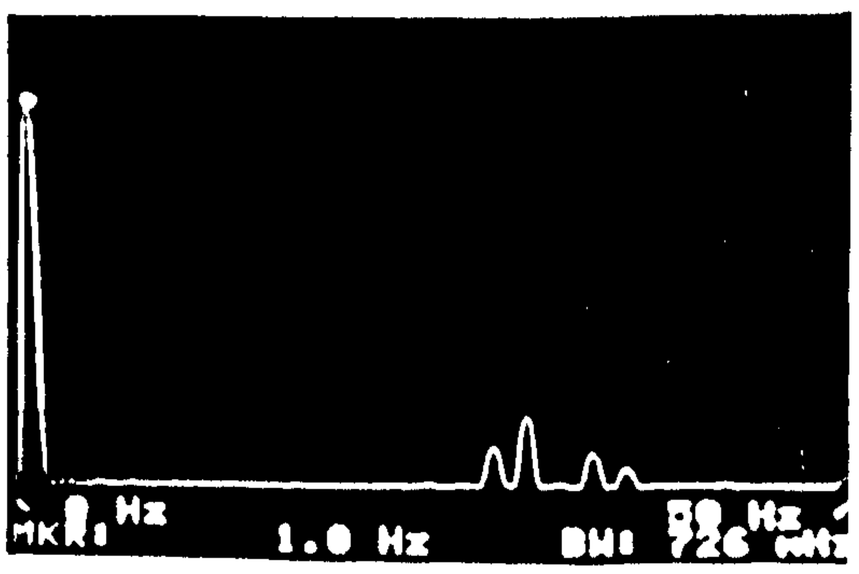

(b)

Figure 5.16 Computed and experimental results for PWM8 elimination mode at 1Hz stator frequency , no-load operation
(a) Line voltage and spectrum
(b) Stator current and spectrum

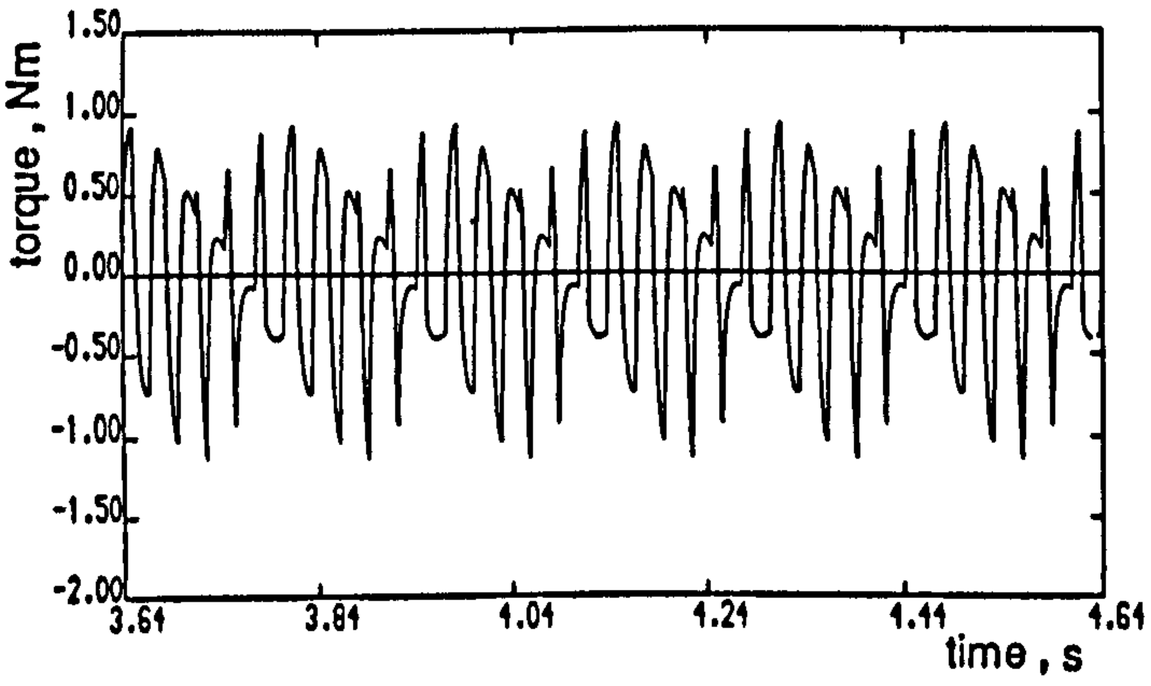

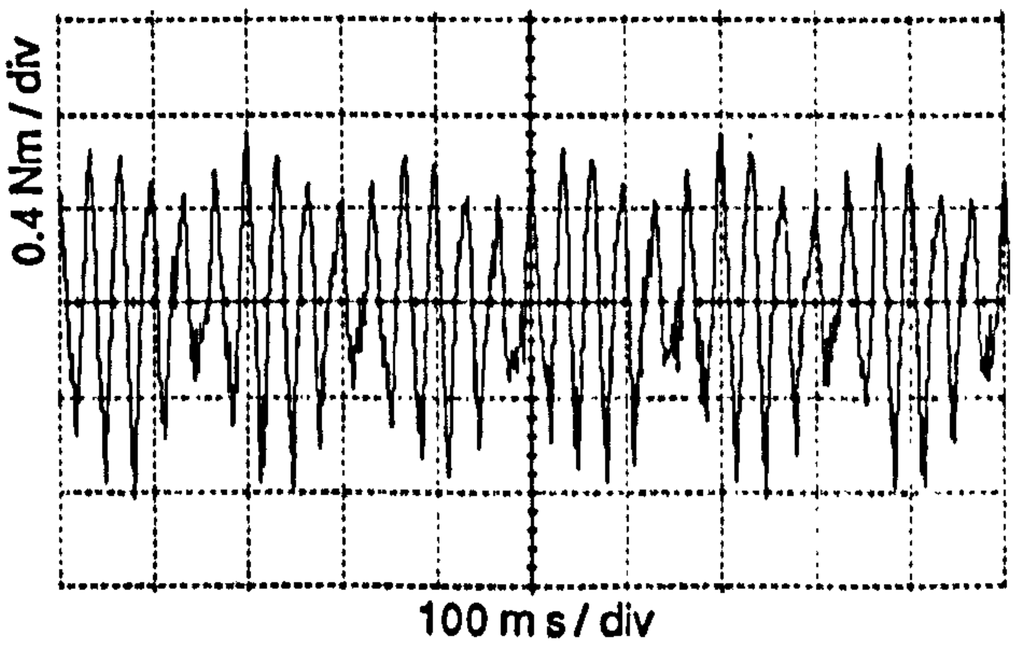

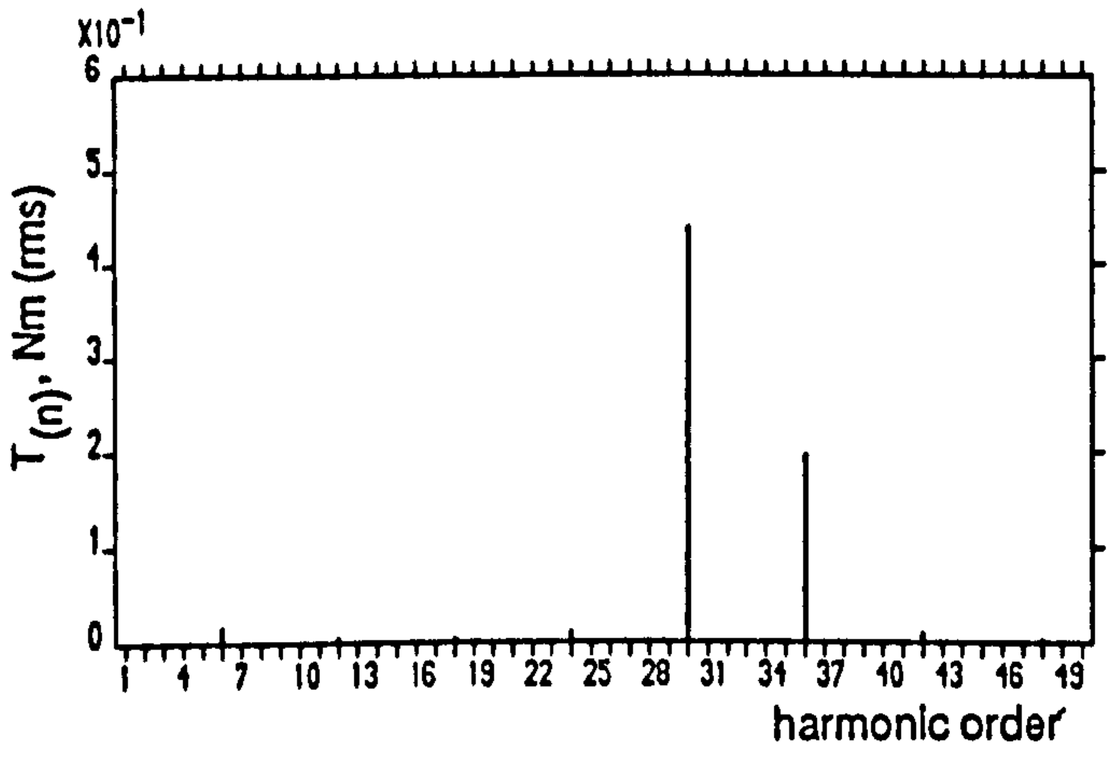

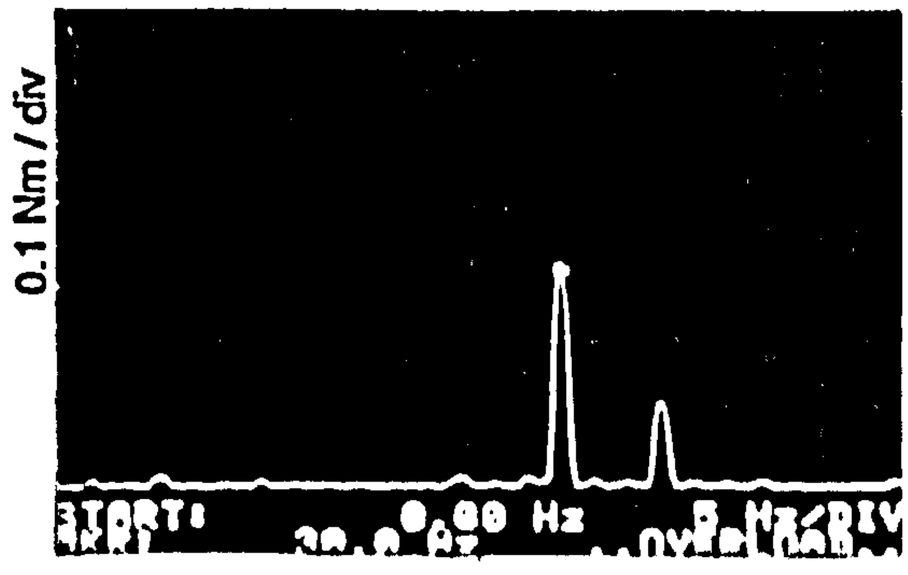

(c)

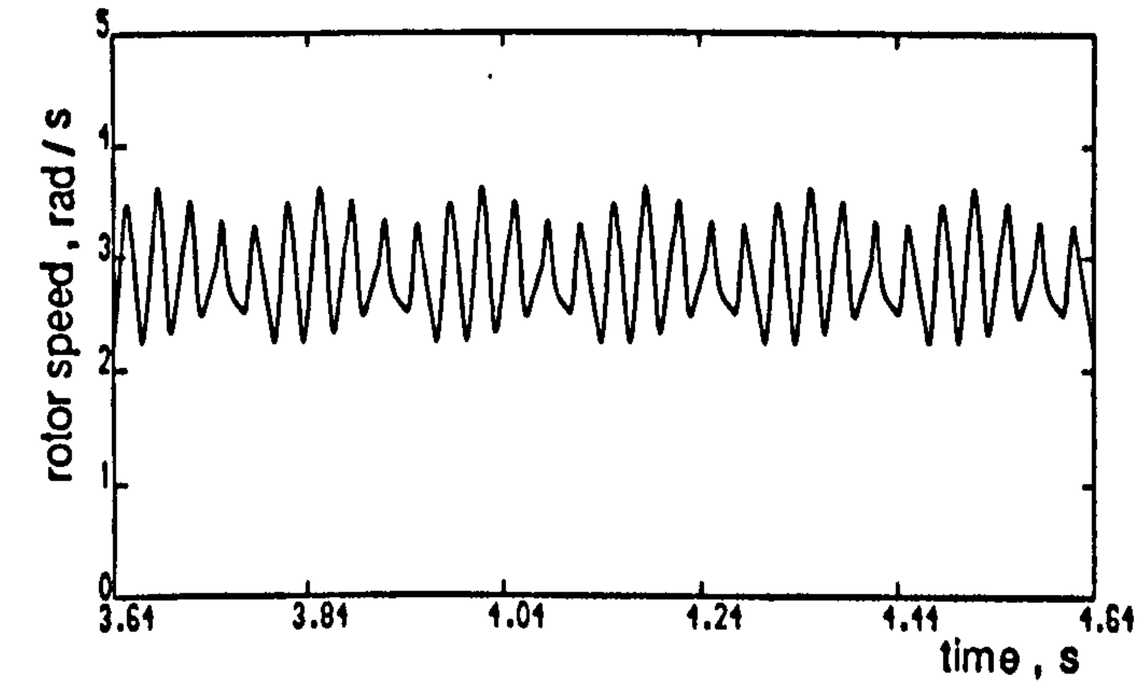

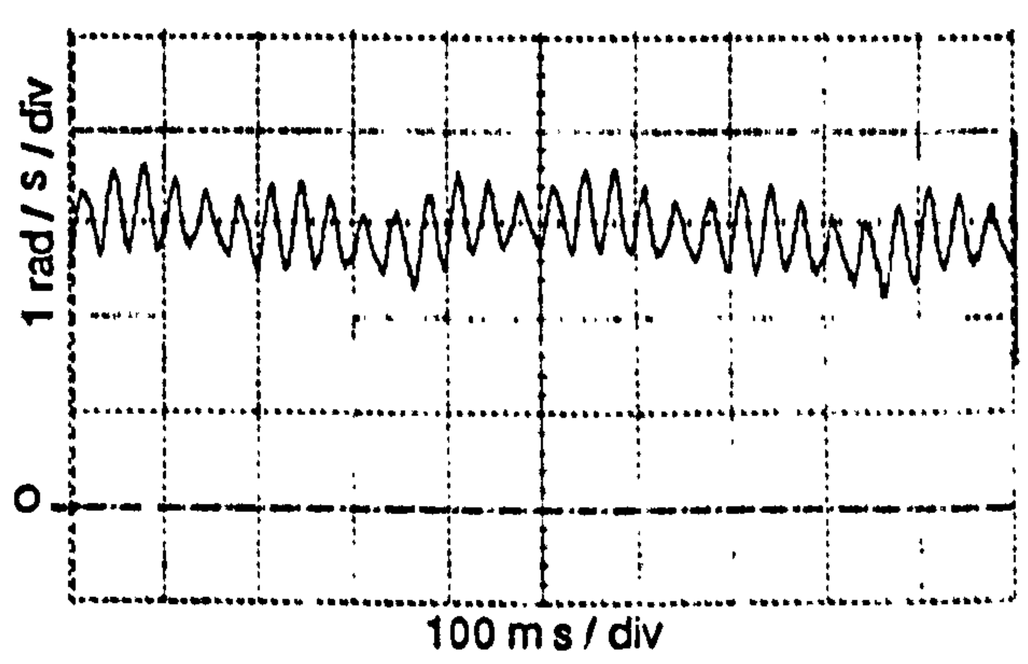

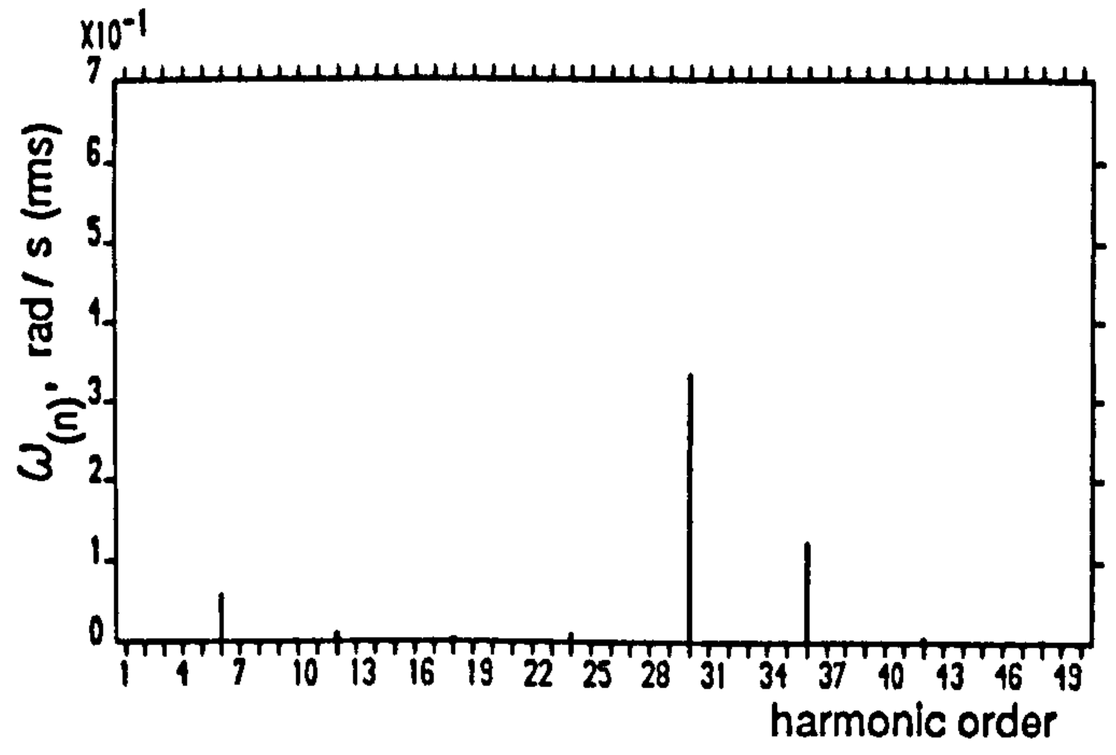

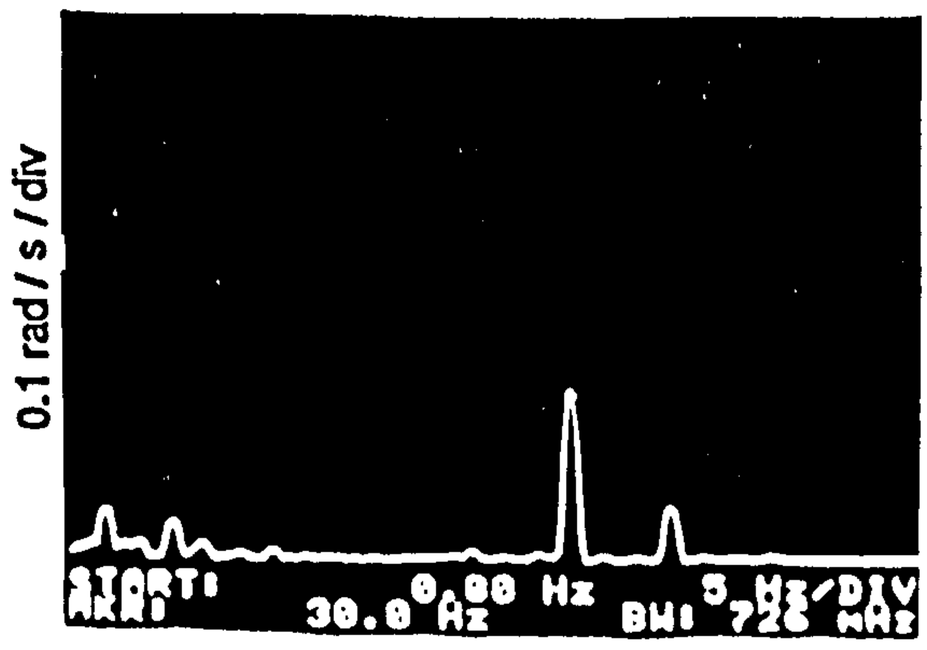

(d)

Figure 5.16 continued (c) Acceleration torque and spectrum
(d) Rotor speed and spectrum

$$V_{dc} = \frac{\pi}{\sqrt{6}} V_{l(1)} \qquad 5.39$$

where $V_{l(1)} = 8.3V$ is the fundamental line voltage component required for constant airgap flux. The current waveform has an rms fundamental component of 1.18A. Evidently all even components in both harmonic spectra are absent, and the remaining odd non-triplen components decrease in magnitude with increasing harmonic order.

The computed acceleration torque waveform of figure 5.12(c) has a peak-to-peak value of 1.47Nm, while figure 5.12(d) shows the average speed to be 2.83rad/s with a peak-to-peak value of 4.15rad/s. The harmonic spectra of these waveforms show that both contain harmonics of order six and multiples thereof, with magnitudes decreasing with increasing harmonic order. The low order 6th- and 12th- torque and speed harmonics are thus of principle concern in the design of a PWM strategy to provide smooth machine operation.

Figures 5.13(a) and (b) show respectively the line voltage and current waveforms, together with their respective harmonic spectra for PWM operation using two switching angles to eliminate the 5th- and 7th-harmonic voltage components. The required DC-link voltage including the inverter drop compensation is 14.9V. This compares with 11.4V calculated for an ideal voltage waveform from

$$V_{dc} = \frac{\pi}{K\sqrt{6}} V_{l(1)} \qquad 5.40$$

where $K = 0.933$ for this PWM mode, is obtained from the optimization process, and is the fundamental component factor given in table 3.1. The line voltage waveform has five pulses per half-cycle for 5th- and 7th-harmonic elimination. Comparing figures 5.13(a) and (b) with figures 5.12(a) and (b), it is clear that when low order harmonic elimination is achieved, the high order components are increased. Figure 5.13(c) shows

that, although the 6th-harmonic acceleration torque component is significantly reduced, the remaining 12th- and 18th-harmonic components are increased respectively from 0.17Nm and 0.10Nm for QSW to 0.50Nm and 0.23Nm for PWM2 operating mode. Similar behaviour of the other higher order harmonics results in a peak-to-peak acceleration torque of 2.48Nm. Nevertheless, figure 5.13(d) shows that, since the contribution of the remaining high order torque components to speed ripple production is more effectively damped by the motor and load inertia, a peak-to-peak ripple of 3.46rad/s is achieved, a reduction of approximately 16.6% compared with QSW operation.

Figures 5.14 to 5.16 show that, by increasing the number of switching angles per quarter-cycle to 4, 6 and 8, to eliminate additional successive pairs of higher harmonic components up to and including the 25th, the PWM line voltage waveforms contain 9, 13 and 17 pulses per half-cycle respectively. The respective DC-link voltages are 15.1V, 15.2V and 15.2V, calculated using equation 5.40 and fundamental component factors (from table 3.1) of 0.92, 0.914 and 0.9116, including compensation. Inspection of the voltage and current waveforms in these figures confirms that elimination of successive pairs of harmonic components is almost complete. The small residues are due to distortion of the voltage waveform by the inverter voltage drops, and the accuracy with which the switching instants are sampled and stored in a look-up table.

The peak-to-peak torque pulsation magnitudes in figures 5.14(c), 5.15(c) and 5.16(c) of 2.26Nm, 2.20Nm and 2.04Nm respectively, are still higher than the peak-to-peak torque pulsation for the QSW mode, despite the significant successive reduction in the 12th, 18th- and the 24th-harmonic torque components. This again can be attributed to the increase in the remaining high order components, whose contribution to speed ripple production is attenuated more effectively by the motor and load inertia. The resulting smoother rotor motion as the PWM pulse number is increased has a peak-to-peak speed ripple of 2.46rad/s, 1.83rad/s and 1.36rad/s respectively.

The fundamental and 2nd-harmonic components present in the practical speed spectra become significant with PWM operation, when a high pulse number and a minimum speed ripple are achieved. It was observed that mechanical misalignment between the coupled shafts contribute to the production of the fundamental component of speed ripple. Moreover, any imbalance in the machine windings produces a 2nd-harmonic component of rotor speed as demonstrated in figure 5.17, computed under the same operating conditions as figure 5.16 but with a *5% resistance imbalance in the stator winding resistance.

To demonstrate the effect of loading on the drive performance, figures 5.18 and 5.19 present computed and experimental waveforms for QSW operation at 4Hz under no-load and full-load conditions. The fundamental current at no-load is 1.18A for a DC-link voltage of 25.3V and at full-load 2.3A for a DC-link voltage of 41.3V (3.95Nm load applied at the motor shaft), with both values adjusted to compensate for inverter voltage drops. Figures 5.20(a) and (b) show computed and practical waveforms for the rotor speed for both load conditions. Computed results show a peak-to-peak speed ripple of 1.01rad/s about an average speed of 12.24rad/s at no-load and 0.78rad/s about an average speed of 4.74rad/s at full-load. The average speed dropped by the slip-speed , corresponding to full-load operation. The reduction in the peak-to-peak speed ripple is due to the damping and additional inertia of the load, which reduced the computed peak-to-peak torque pulsations from 1.27Nm at no-load to 1.02Nm at full-load as illustrated respectively in figures 5.21(a) and (b).

Figures 5.22 to 5.25 show computed and experimental line voltage and current waveforms, with current harmonic spectra, for 4Hz full-load harmonic elimination PWM with 2,4,6 and 8 switching angles per quarter-cycle respectively. The harmonic spectra for each current waveform shows the same fundamental current component of 2.3A, with elimination taking place of successive pairs of harmonic components up to the 25th.

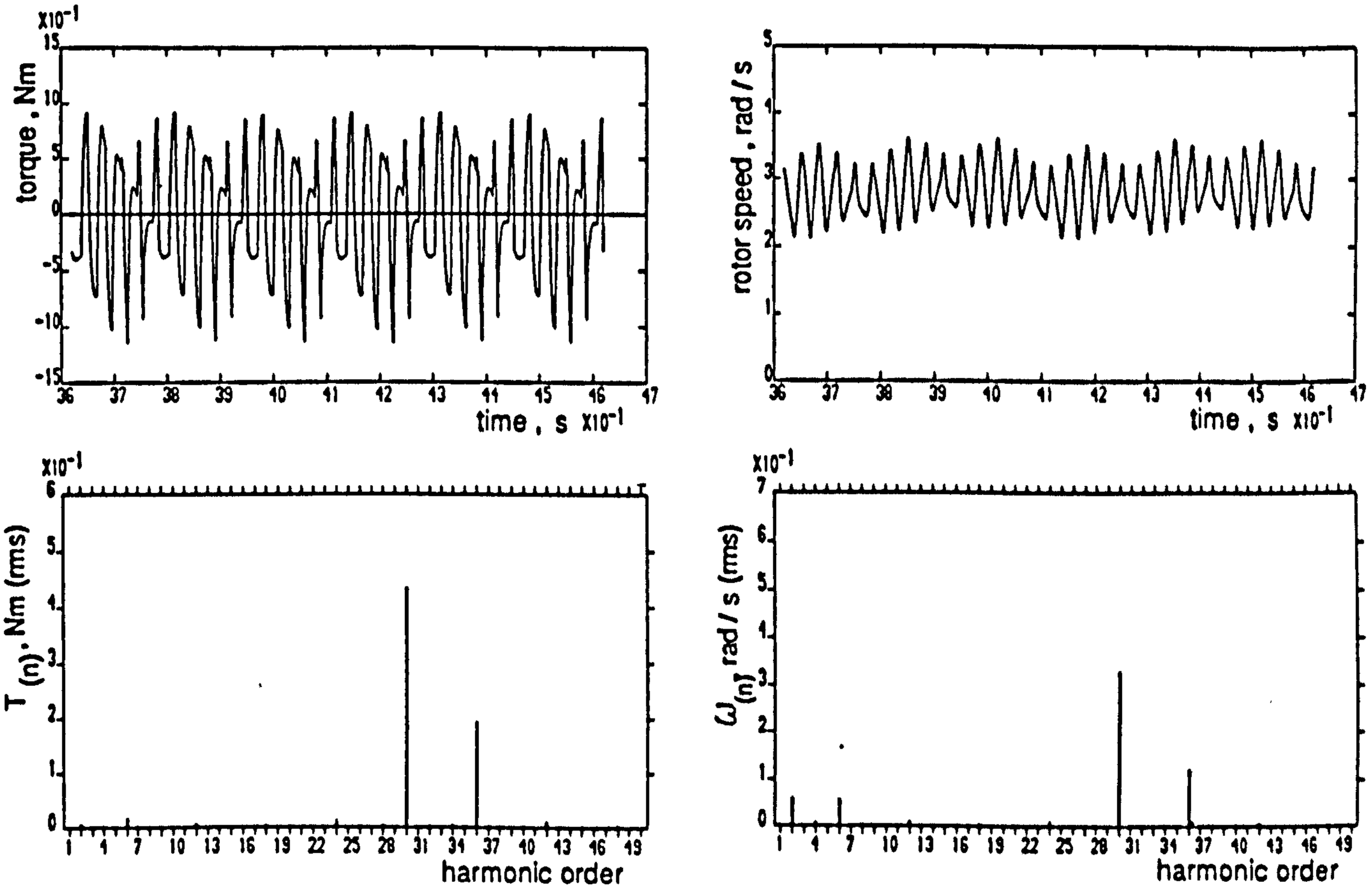

Figure 5.17 Computed acceleration torque and rotor speed and their spectra for PWM8 elimination mode , at 1Hz no-load operation with unbalanced machine windings

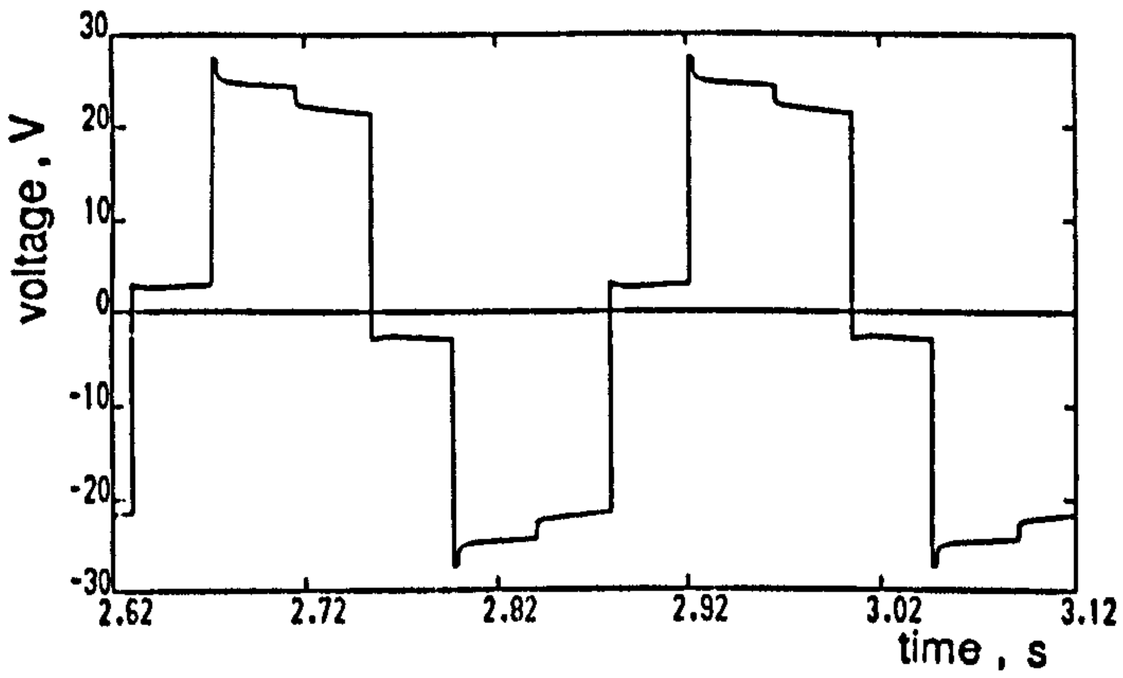

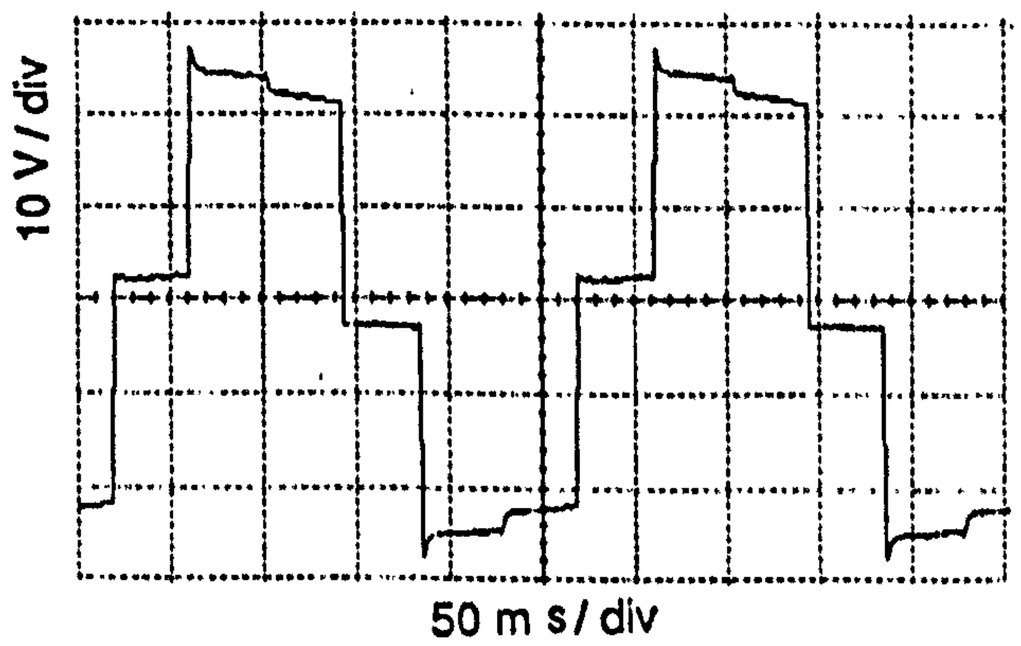

(a)

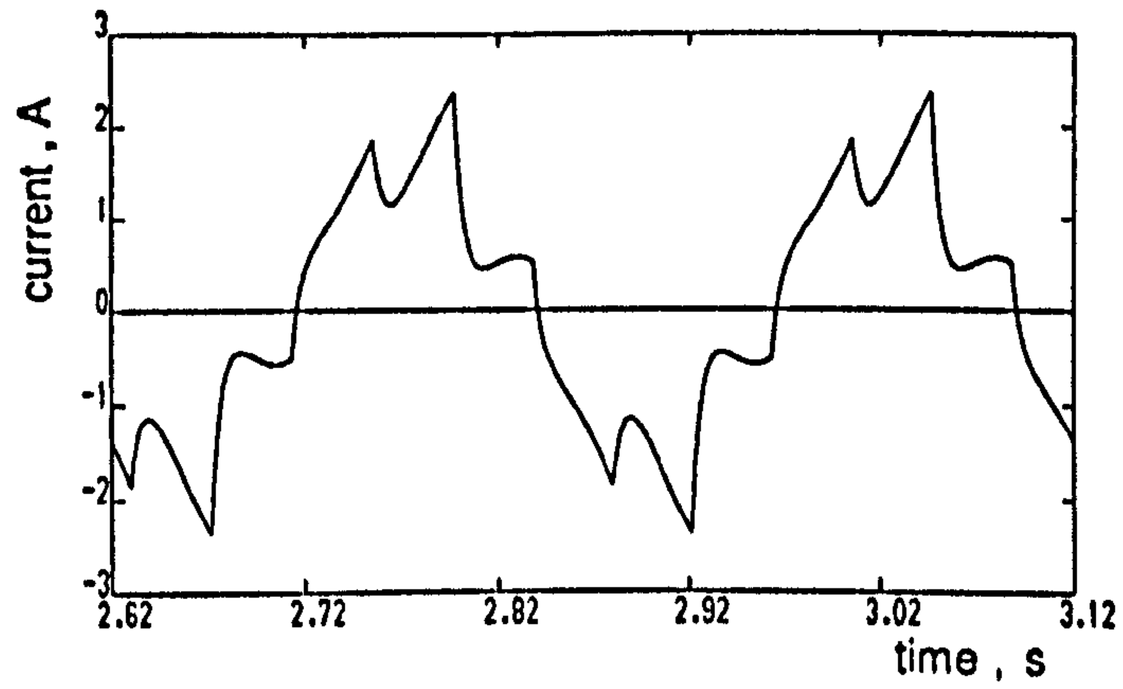

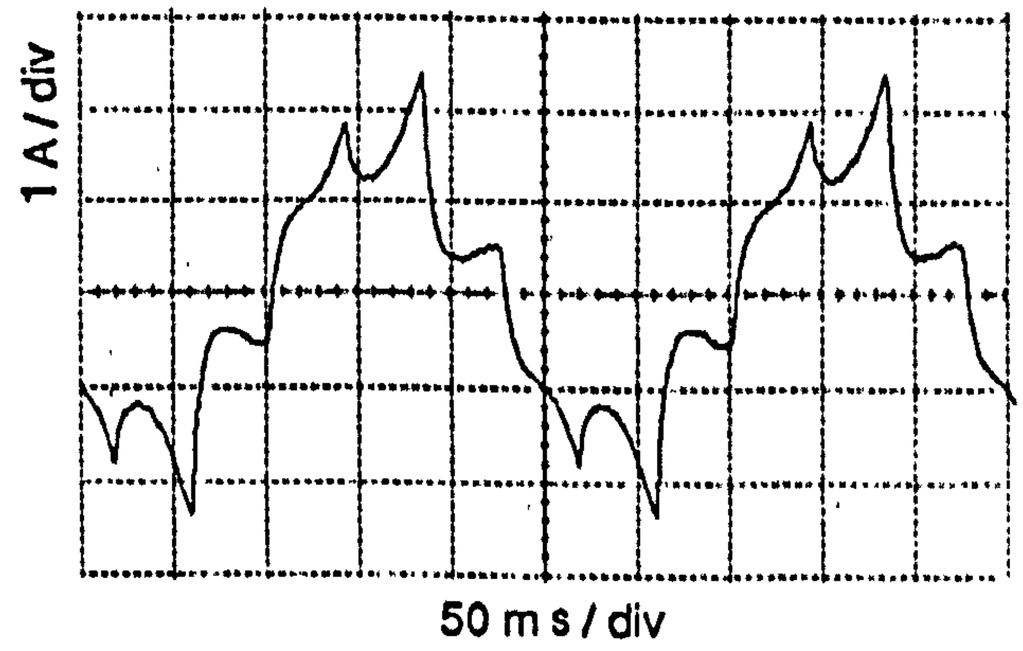

(b)

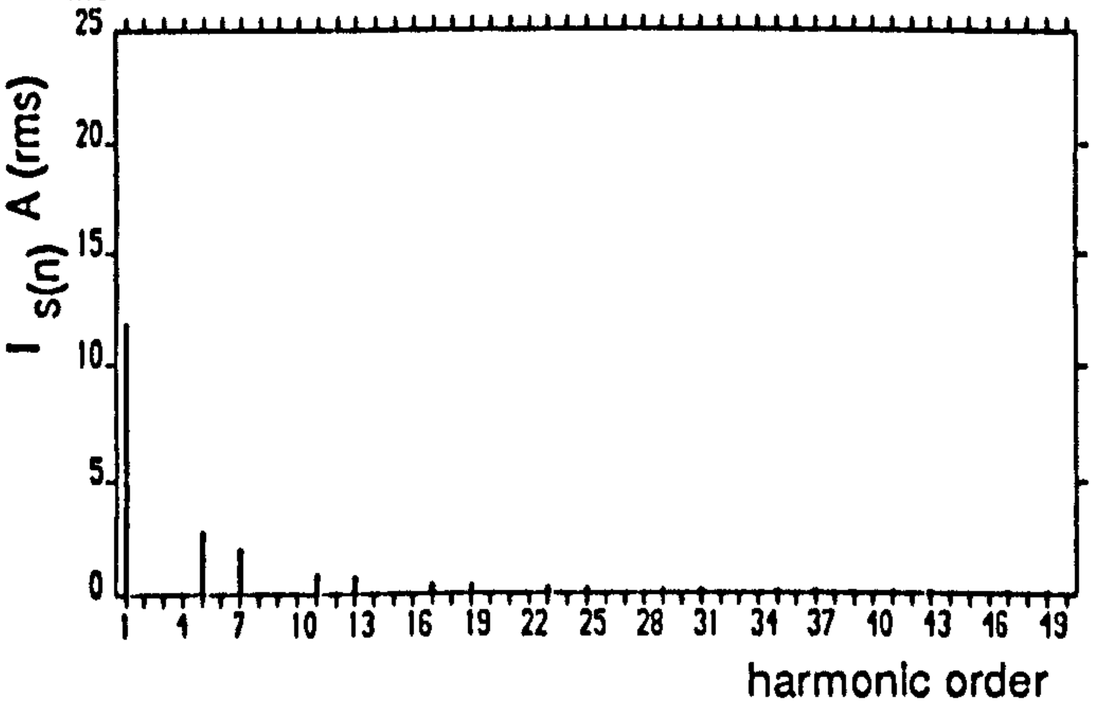

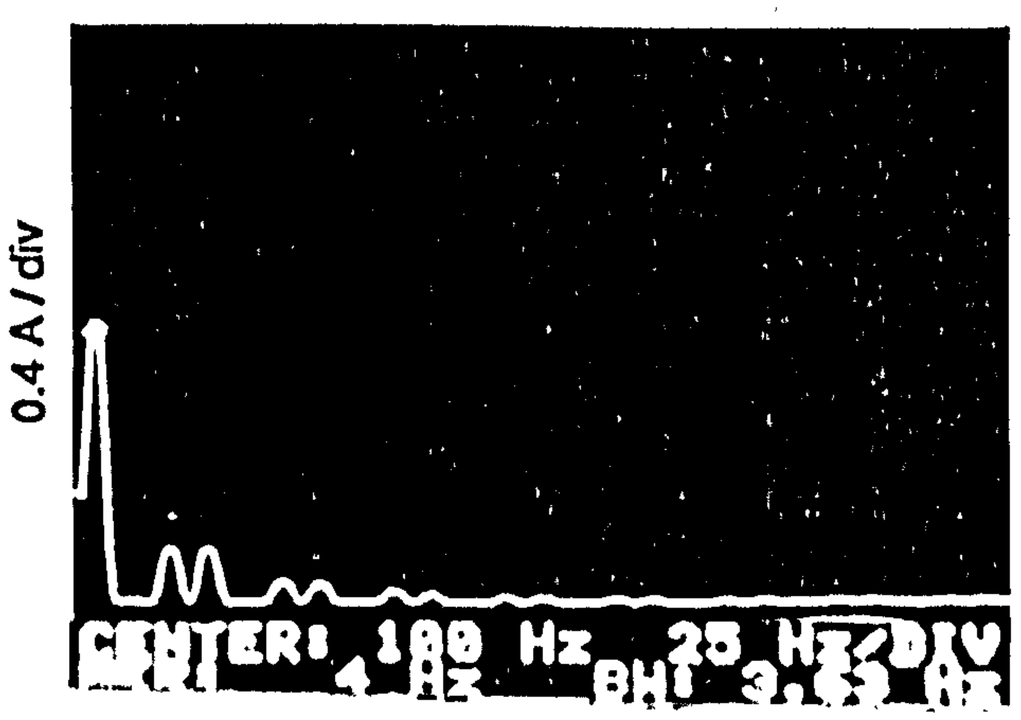

(c)

Figure 5.18 Computed and experimental results for QSW mode

4Hz stator frequency , no-load operation

(a) Line voltage

(b) Stator current

(c)Stator current spectrum

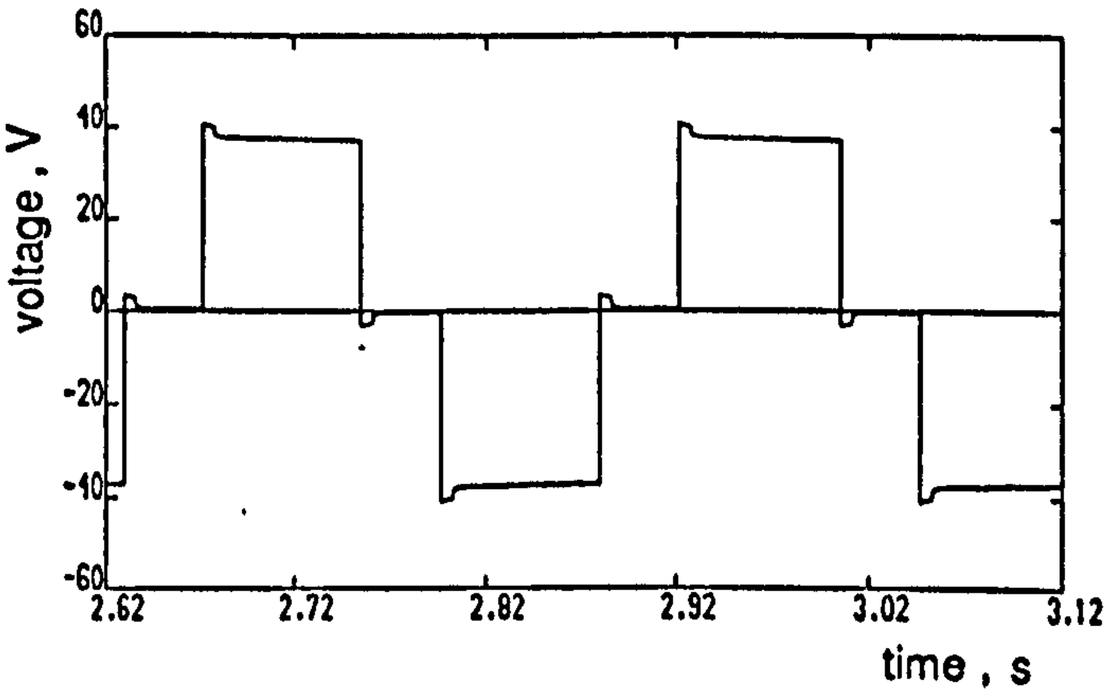

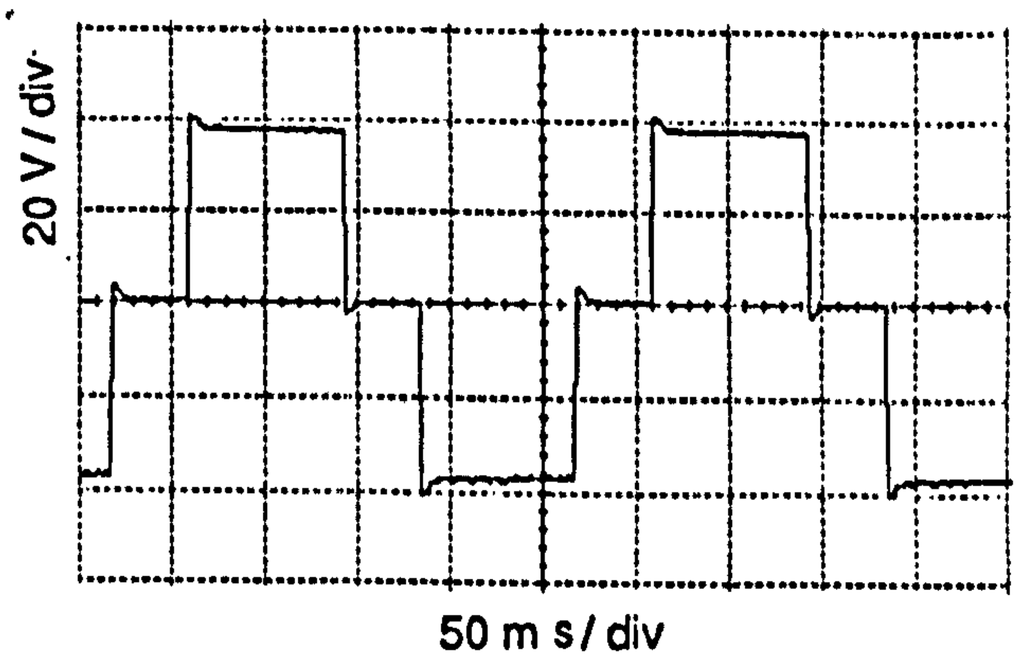

(a)

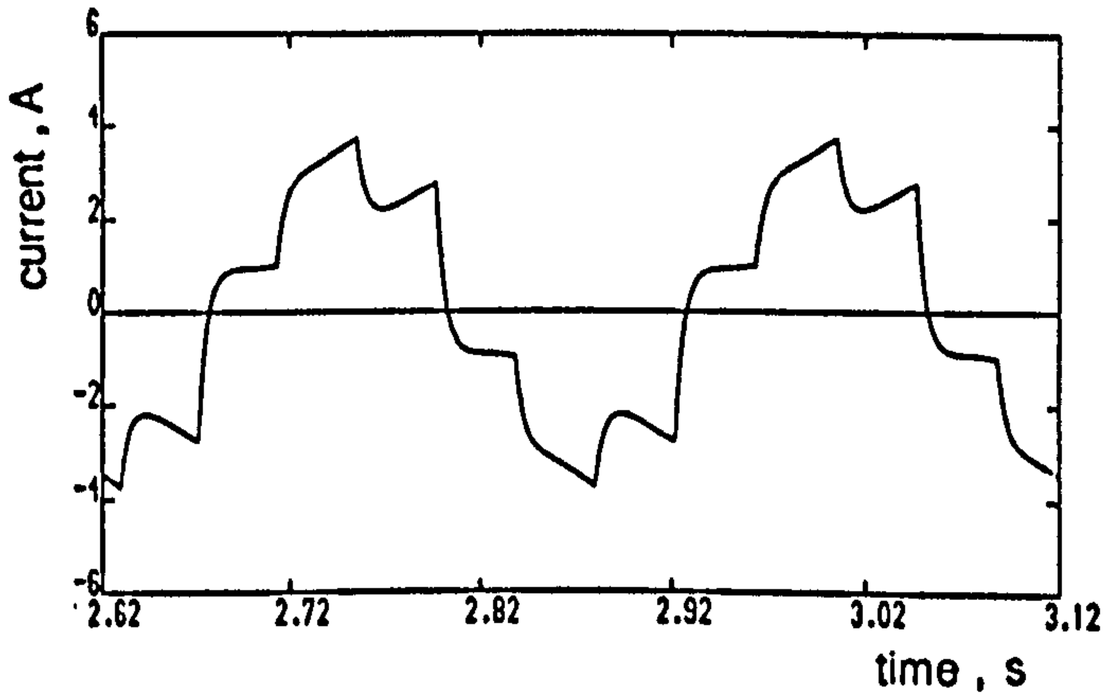

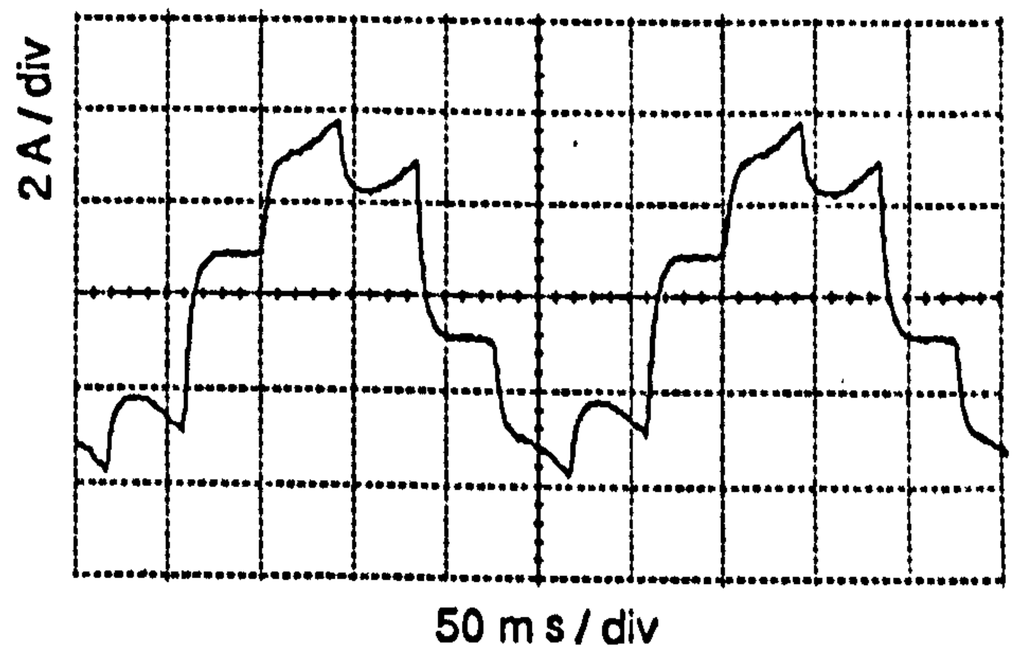

(b)

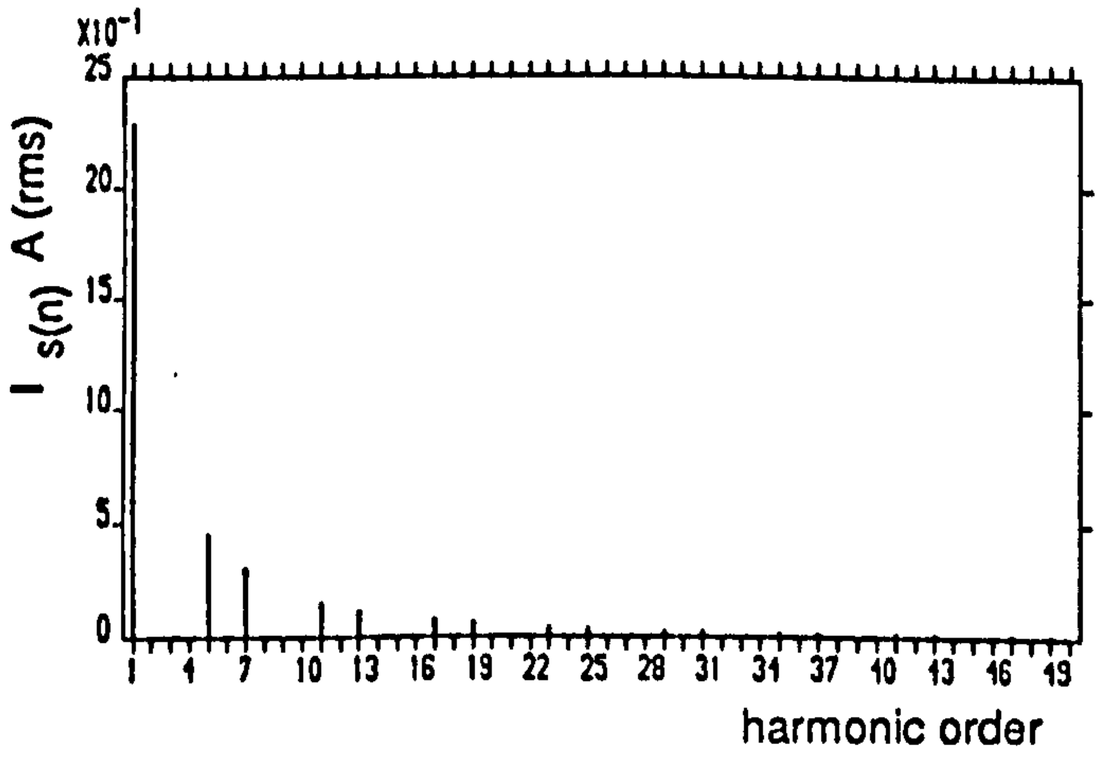

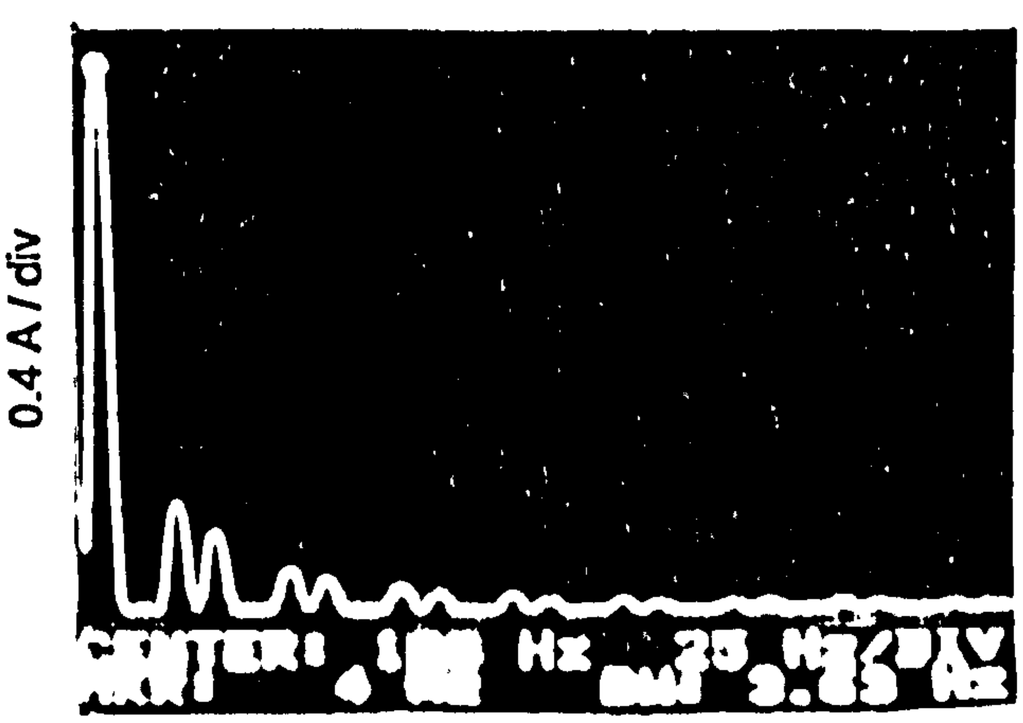

(c)

Figure 5.19 Computed and experimental results for QSW mode

4Hz stator frequency , full-load operation

(a) Line voltage

(b) Stator current

(c)Stator current spectrum

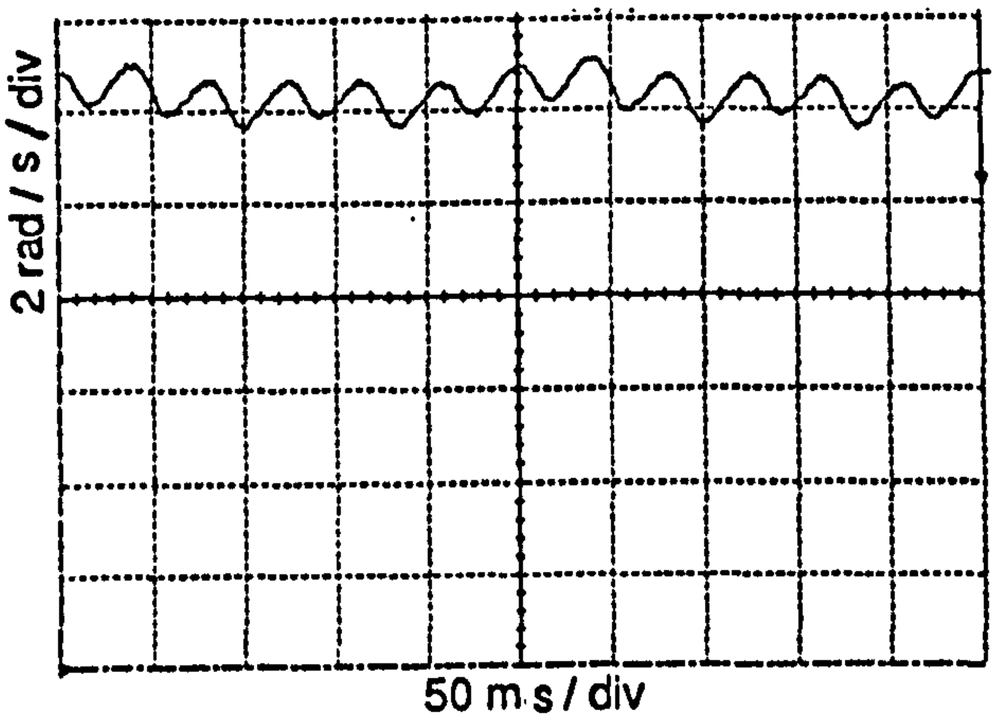

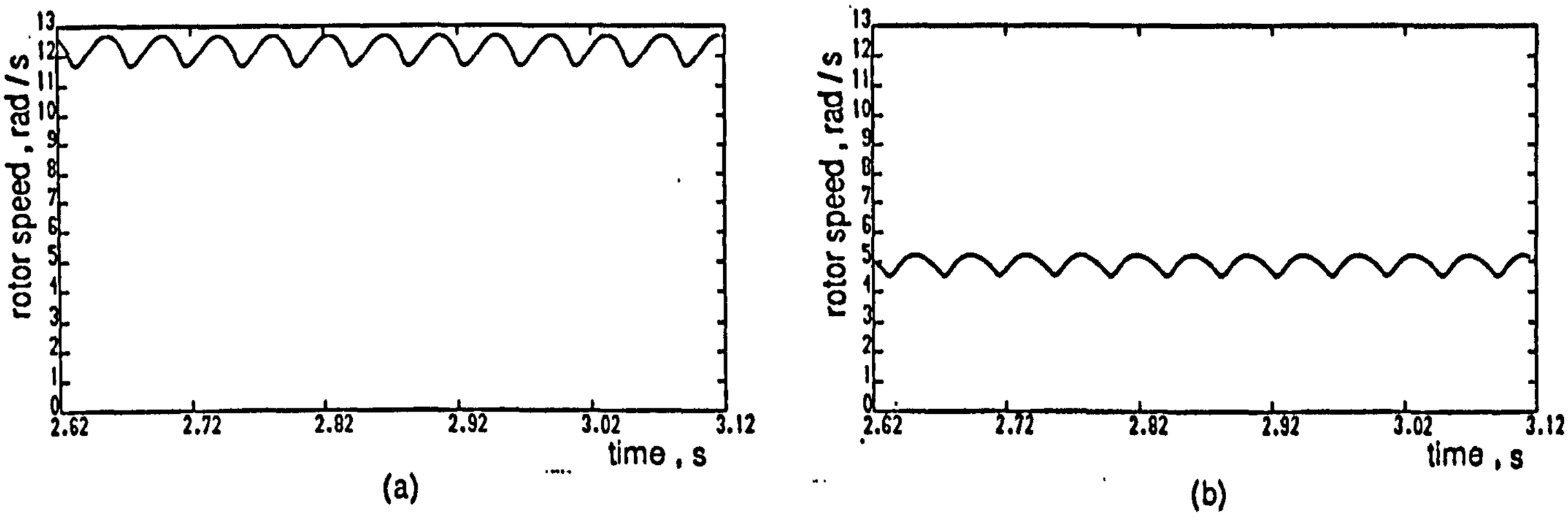

Figure 5.20 Computed and experimental rotor speed for QSW mode 4Hz stator frequency (a) No-load (b)Full-load

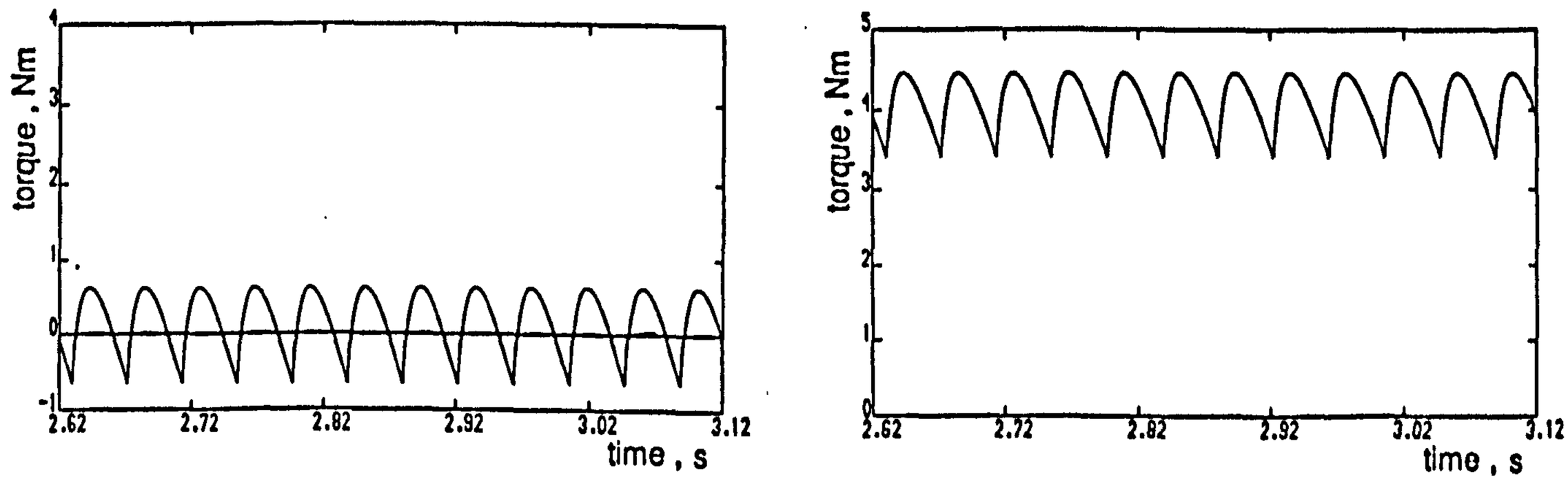

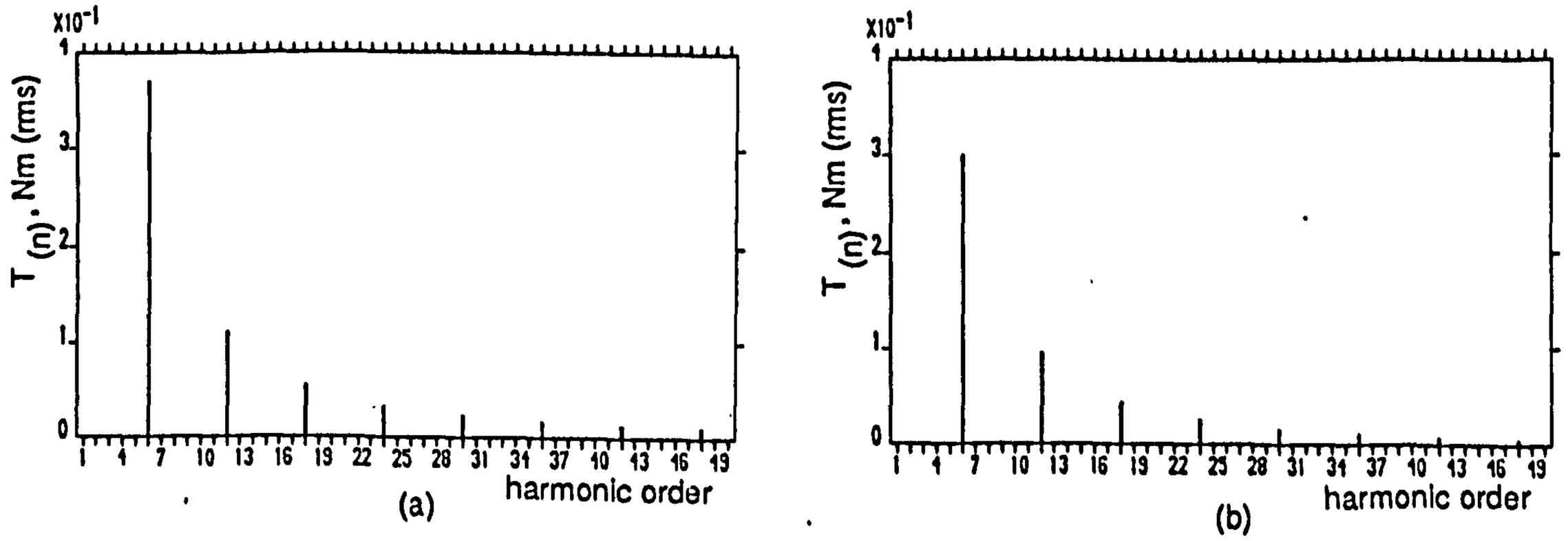

Figure 5.21 Computed electromagnetic torque and its harmonic spectrum for QSW , 4Hz stator frequency (a)No-load (b)Full-load

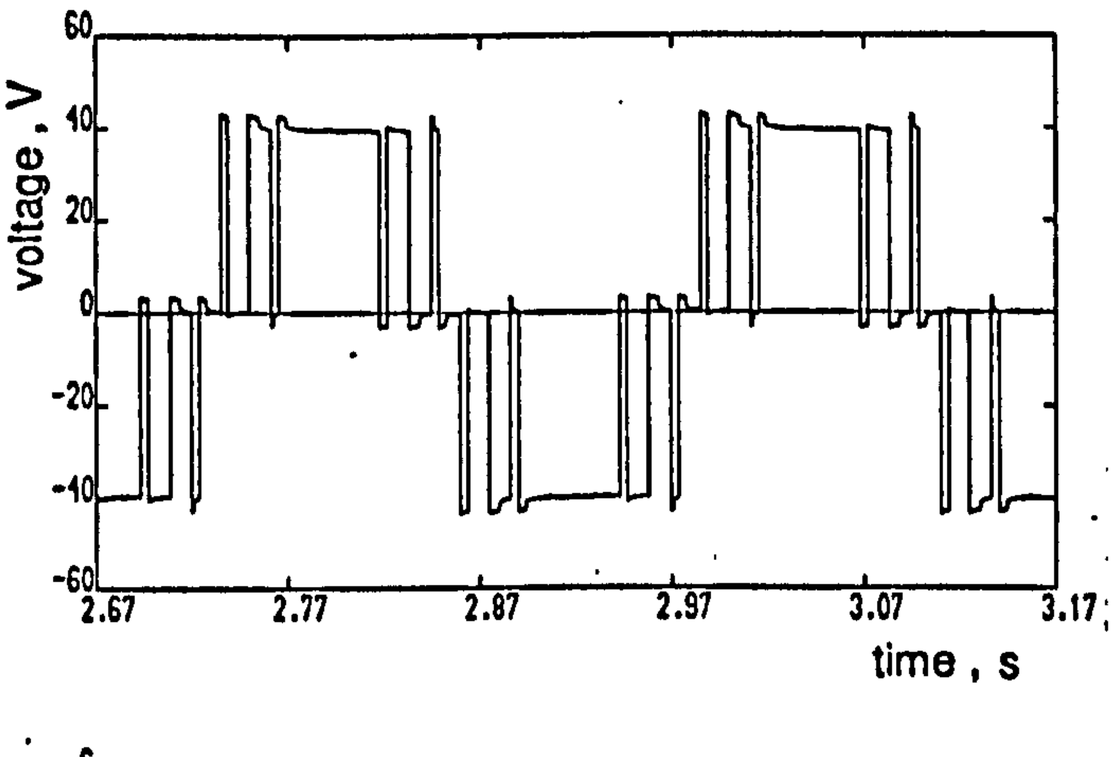

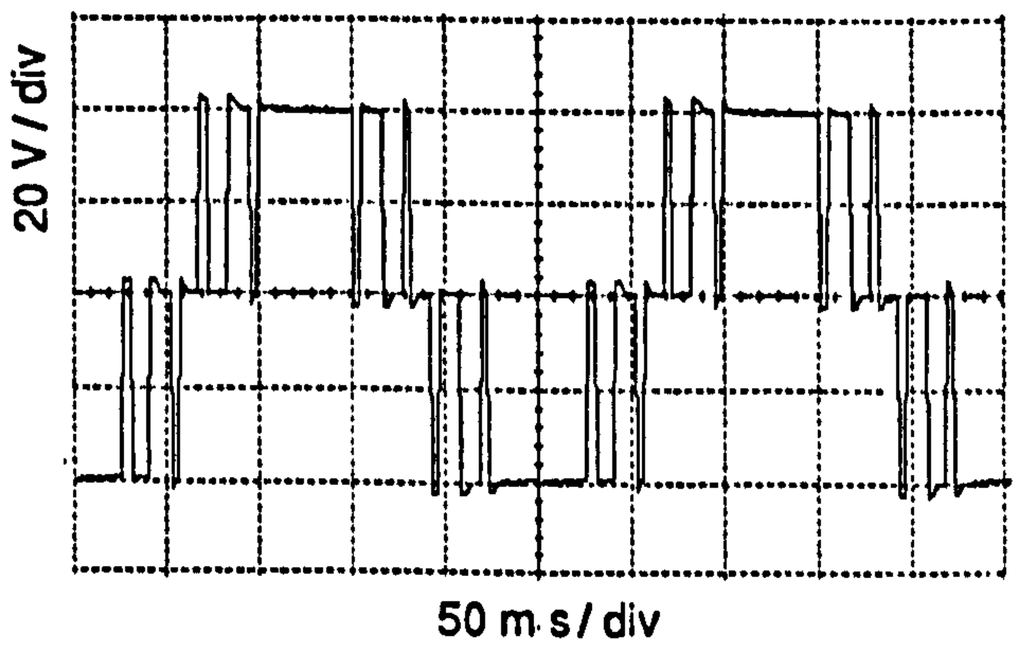

(a)

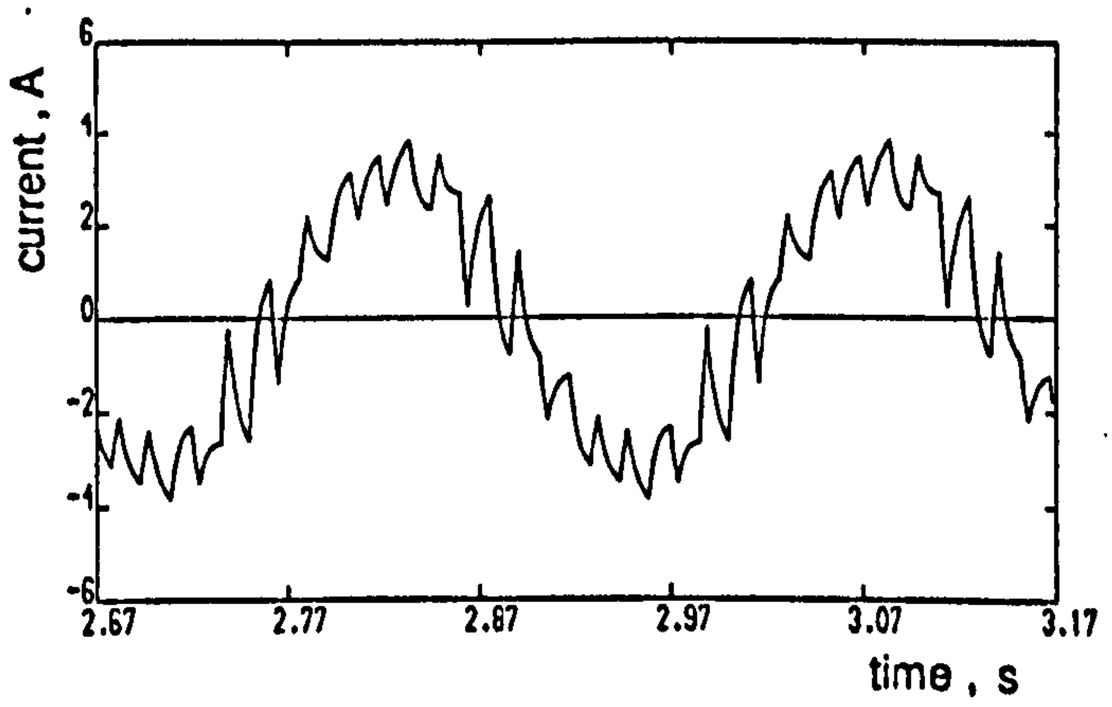

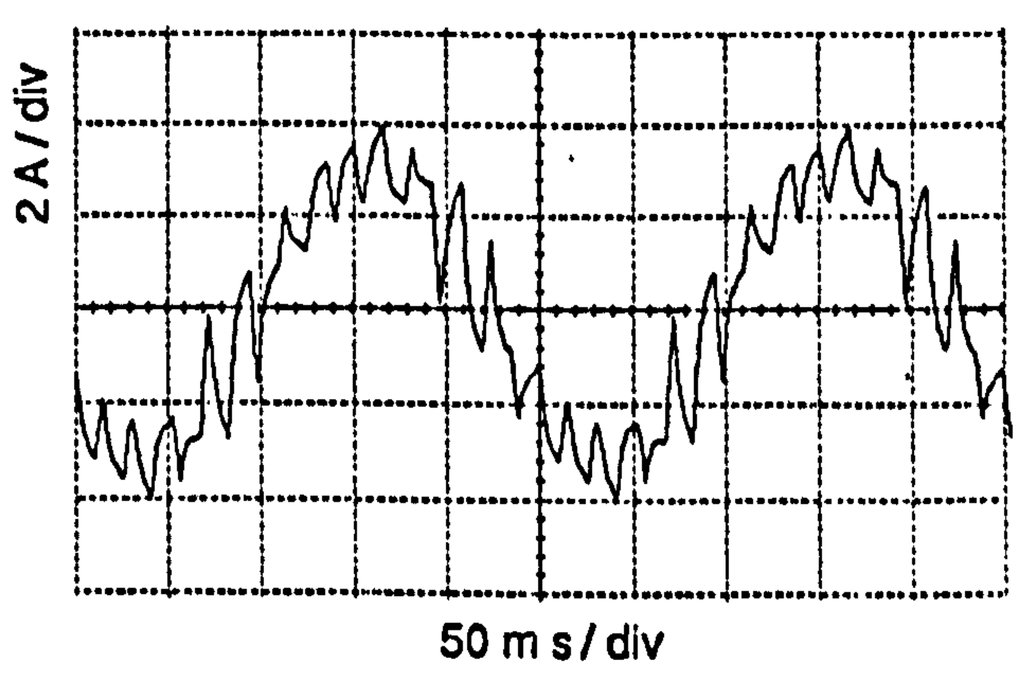

(b)

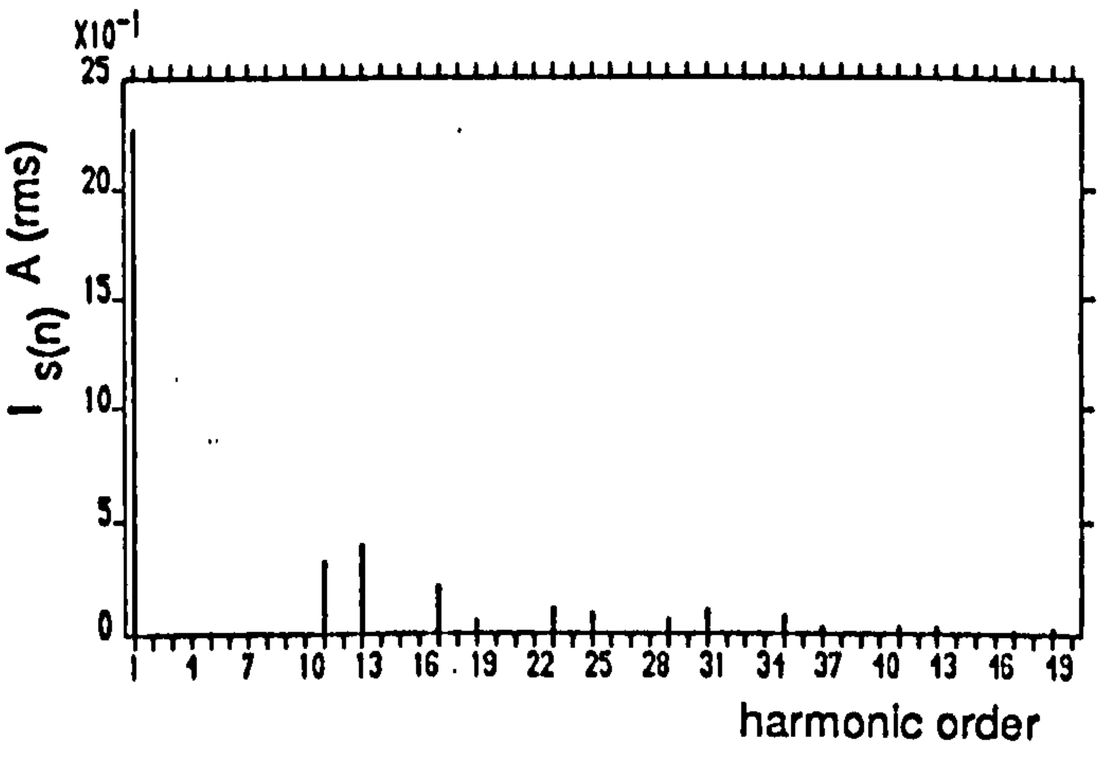

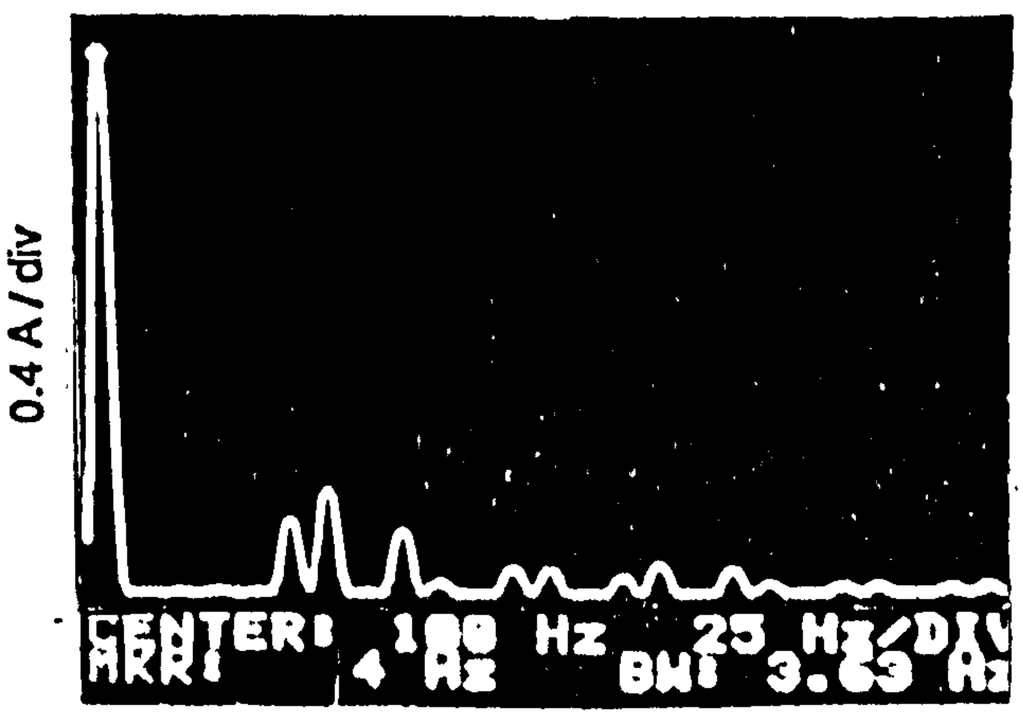

(c)

Figure 5.22 Computed and experimental results for PWM2 elimination mode

4Hz stator frequency , full-load operation

(a) Line voltage

(b) Stator current

(c)Stator current spectrum

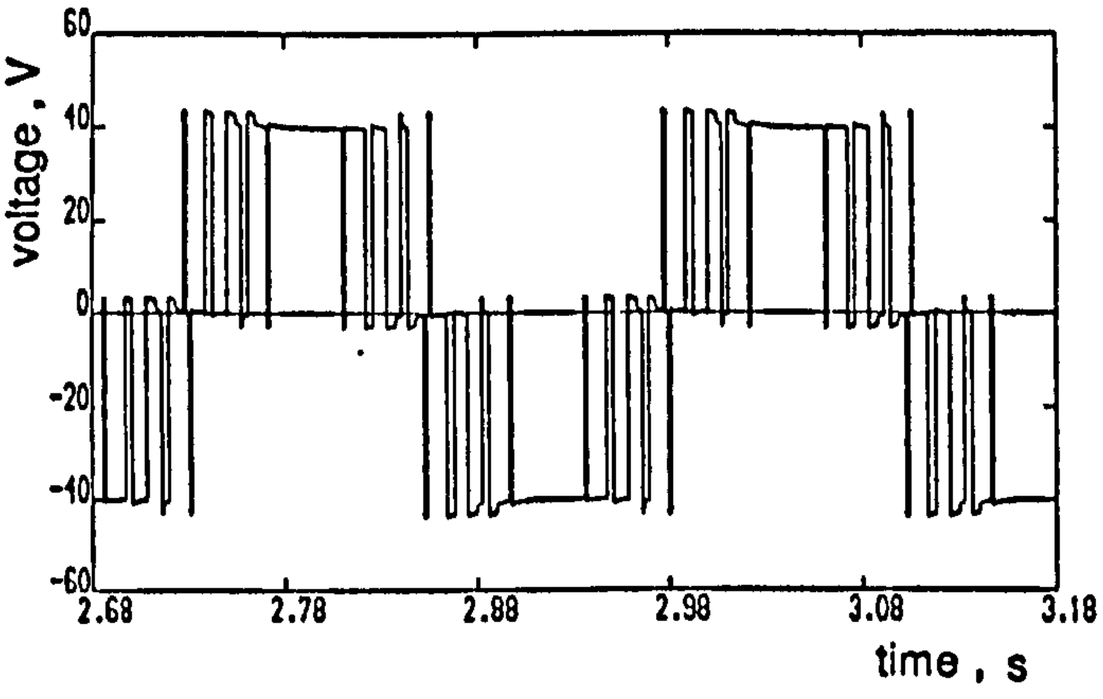

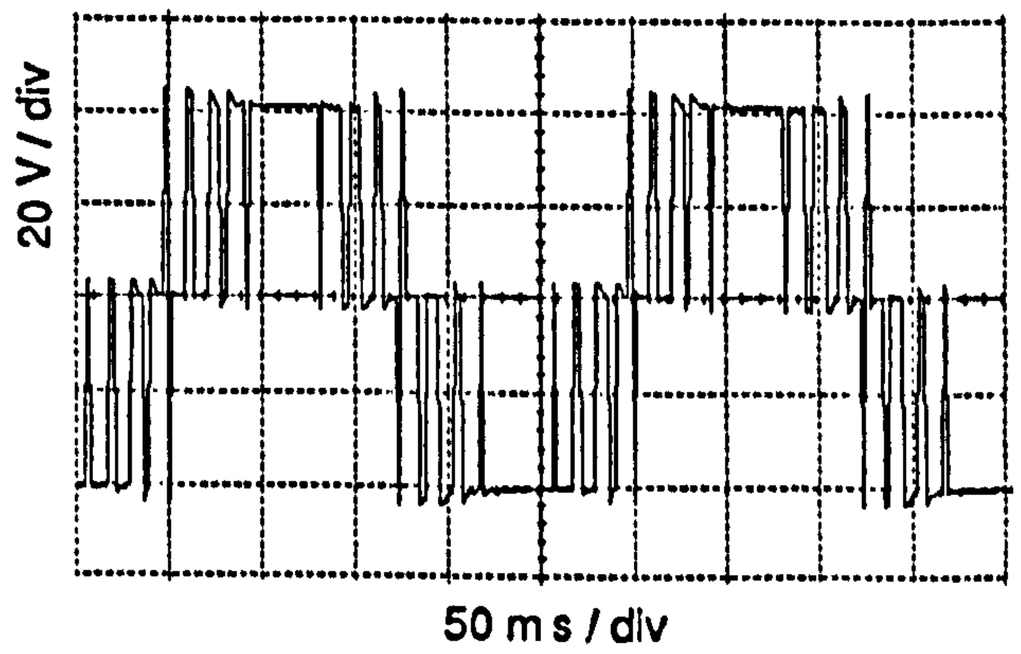

(a)

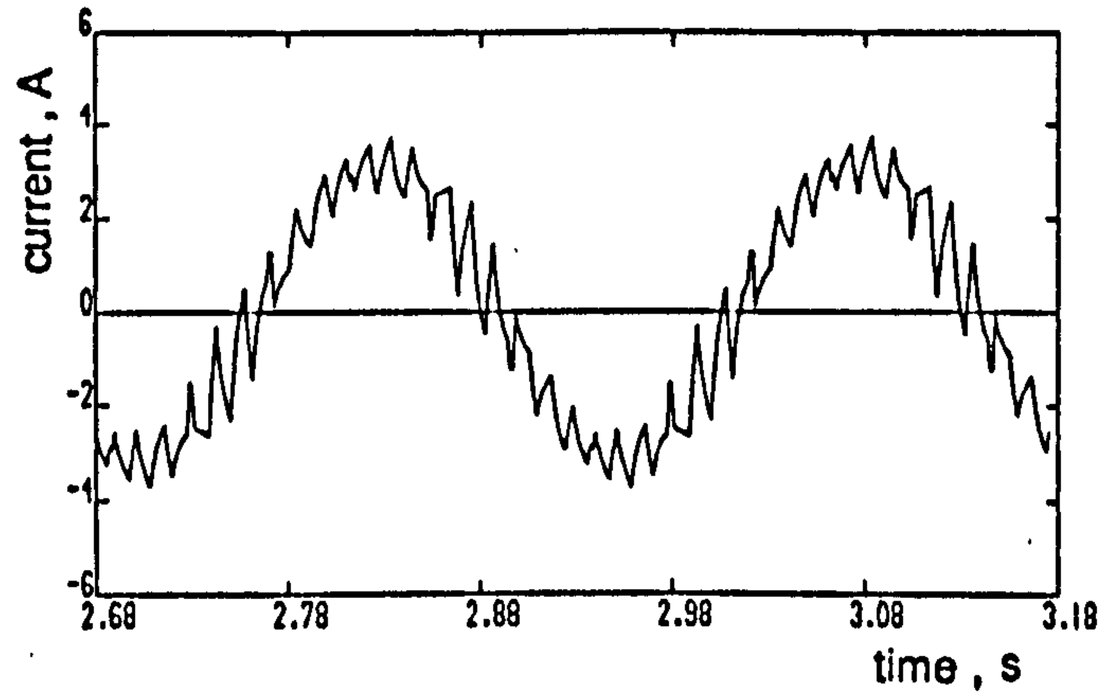

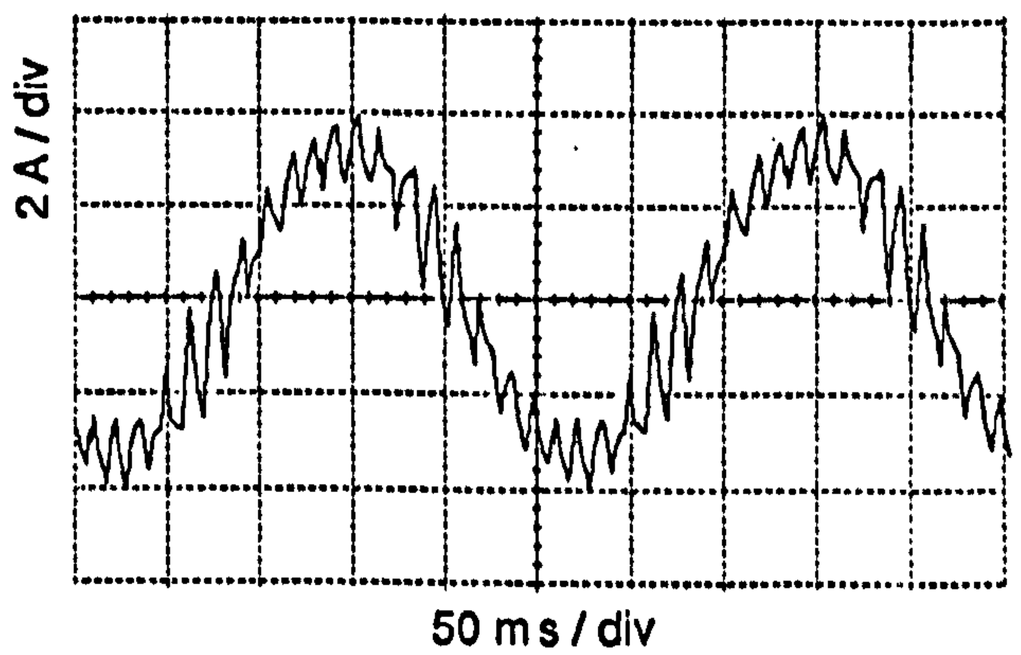

(b)

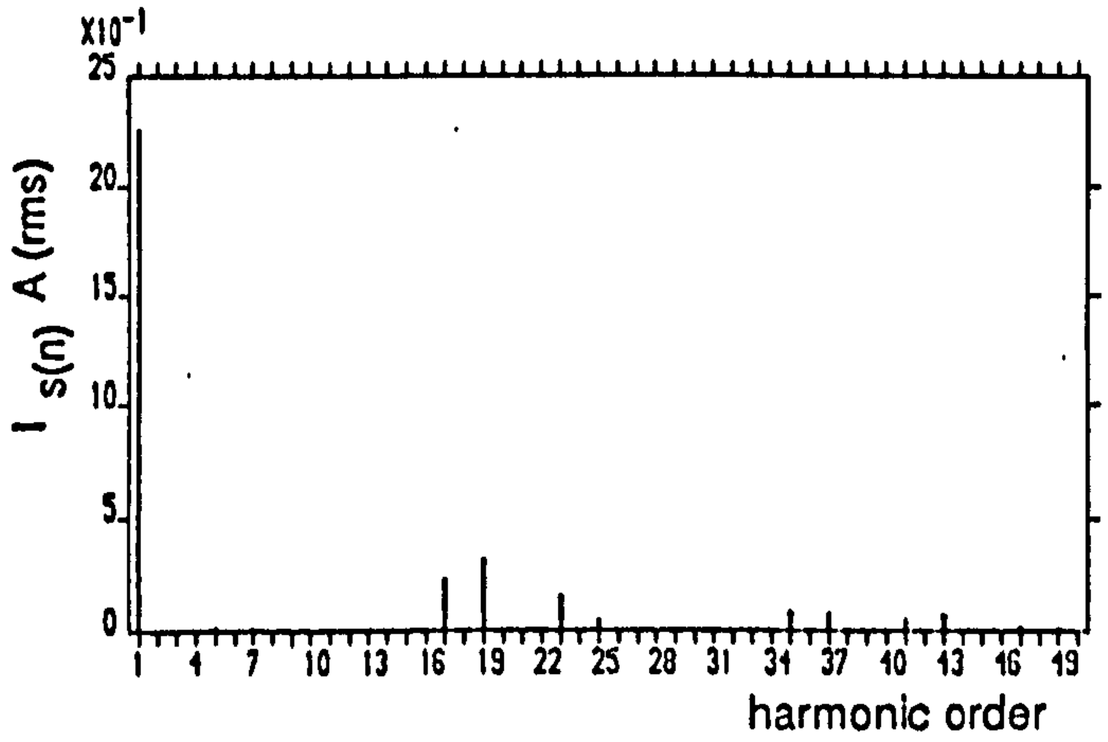

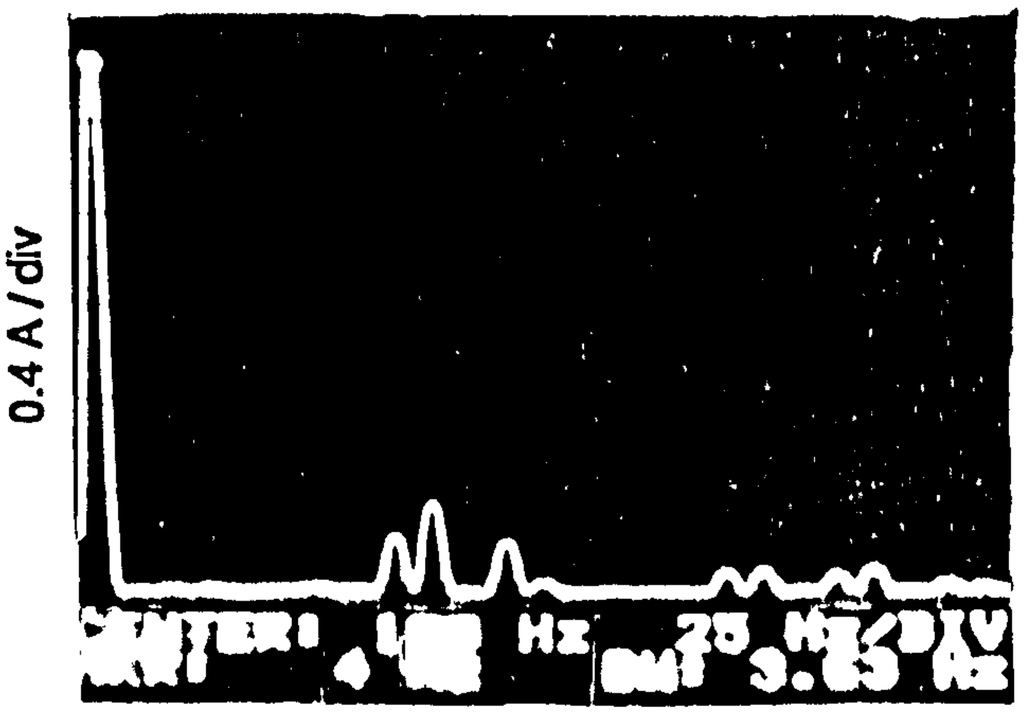

(c)

Figure 5 .23 Computed and experimental results for PWM4 elimination mode 4Hz stator frequency , full-load operation

(a) Line voltage

(b) Stator current

(c) Stator current spectrum

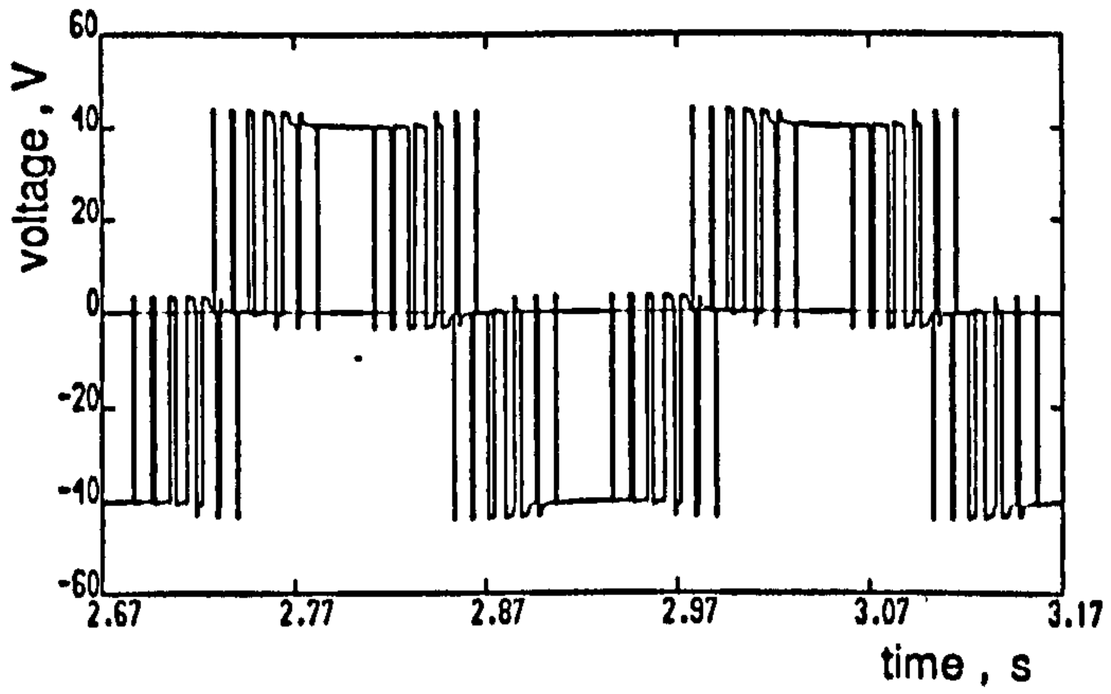

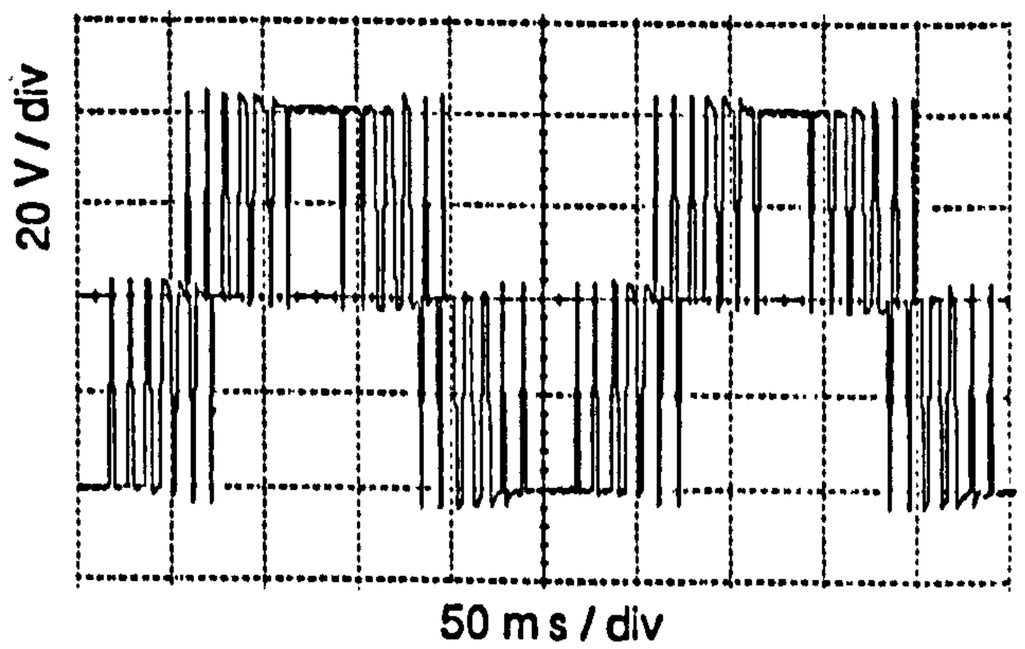

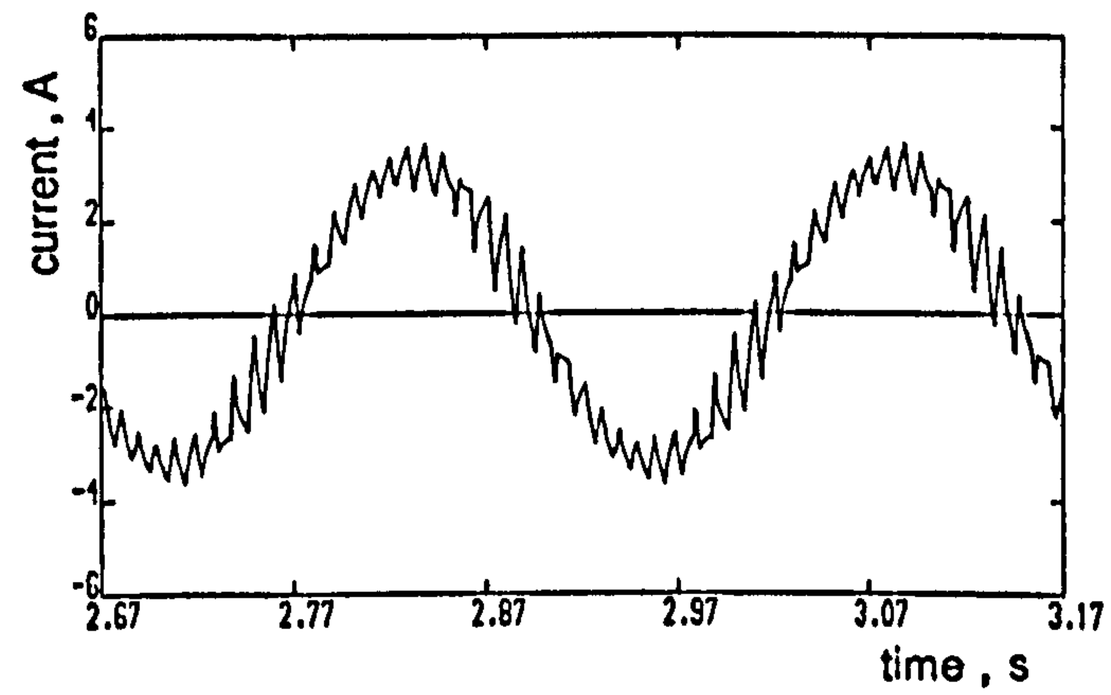

(a)

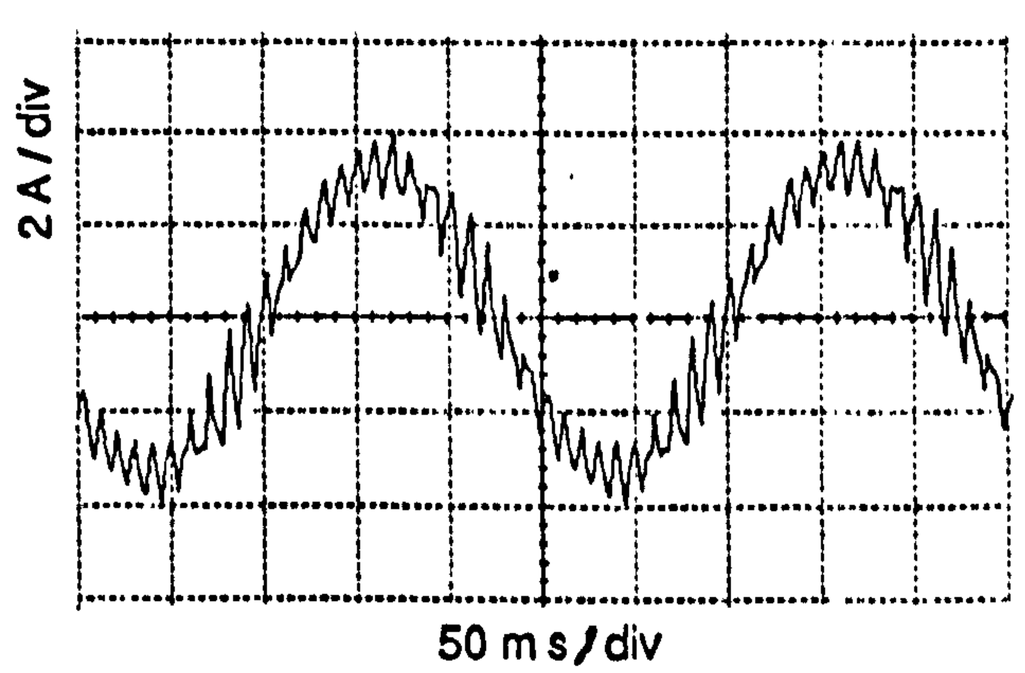

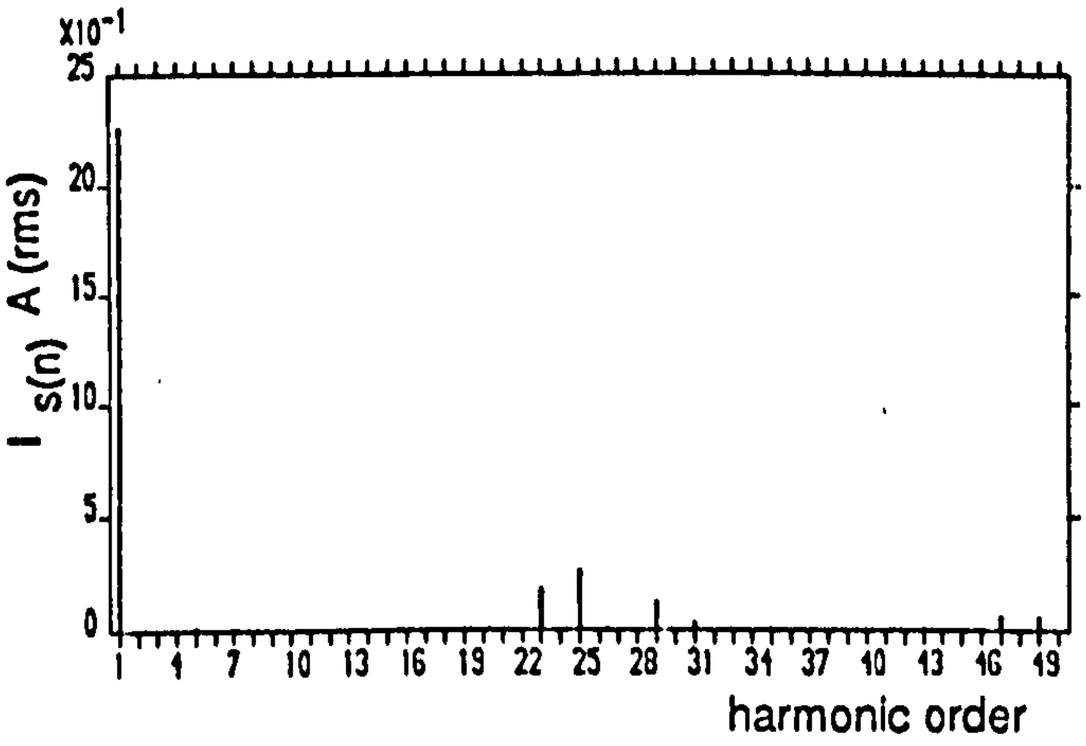

(b)

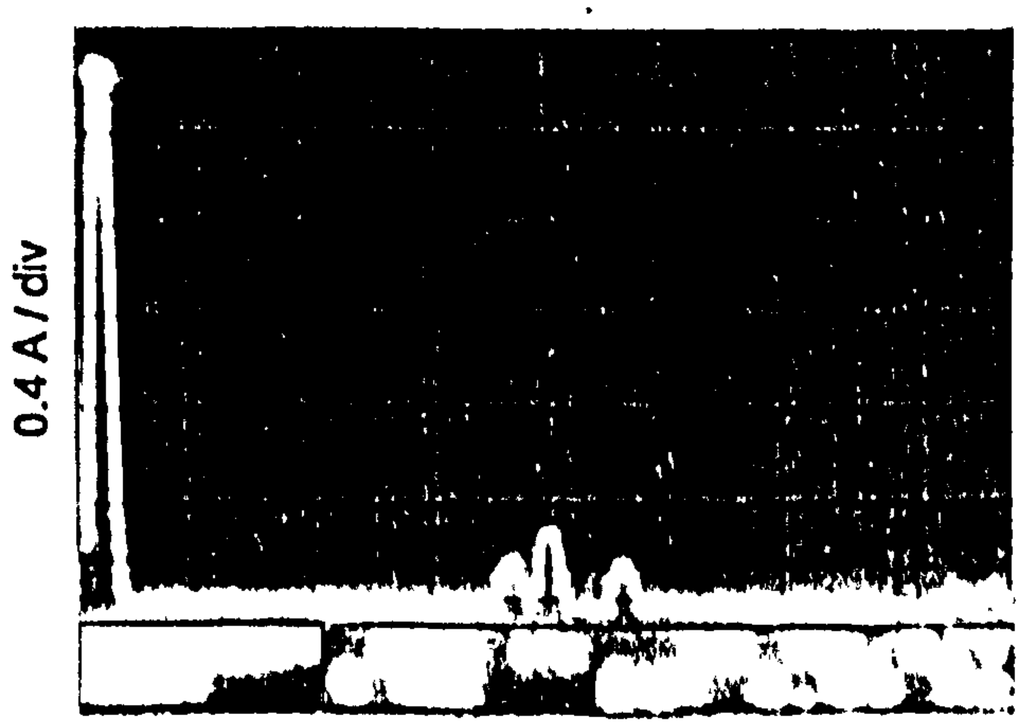

(c)

Figure 5.24 Computed and experimental results for PWM6 elimination mode 4Hz stator frequency , full-load operation

(a) Line voltage

(b) Stator current

(c)Stator current spectrum

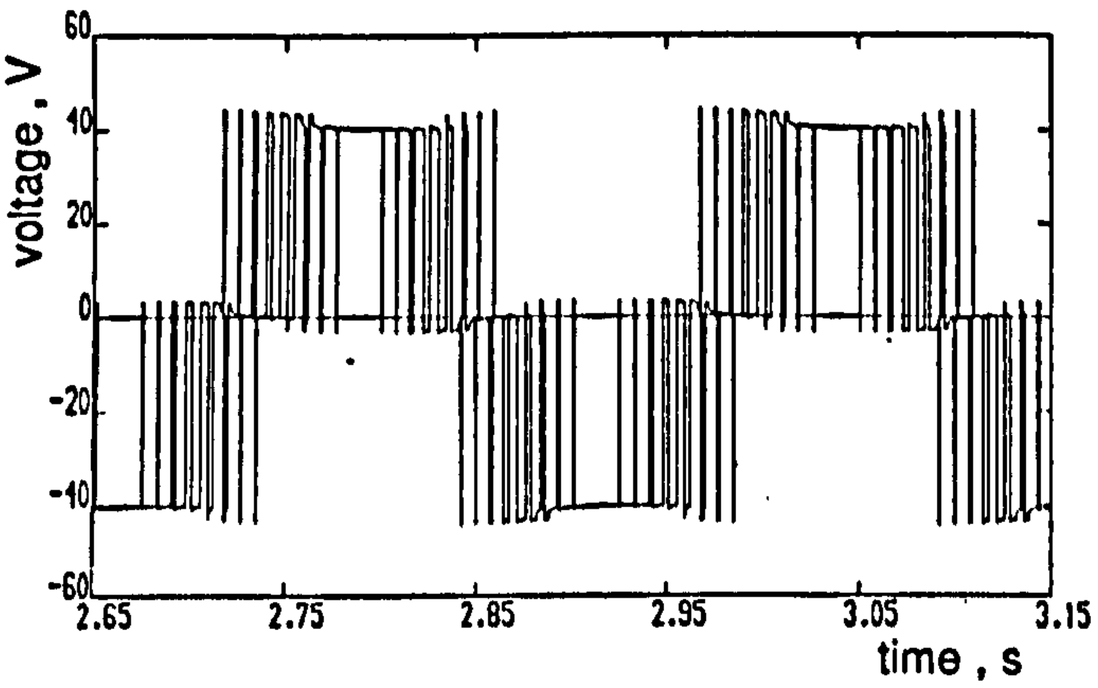

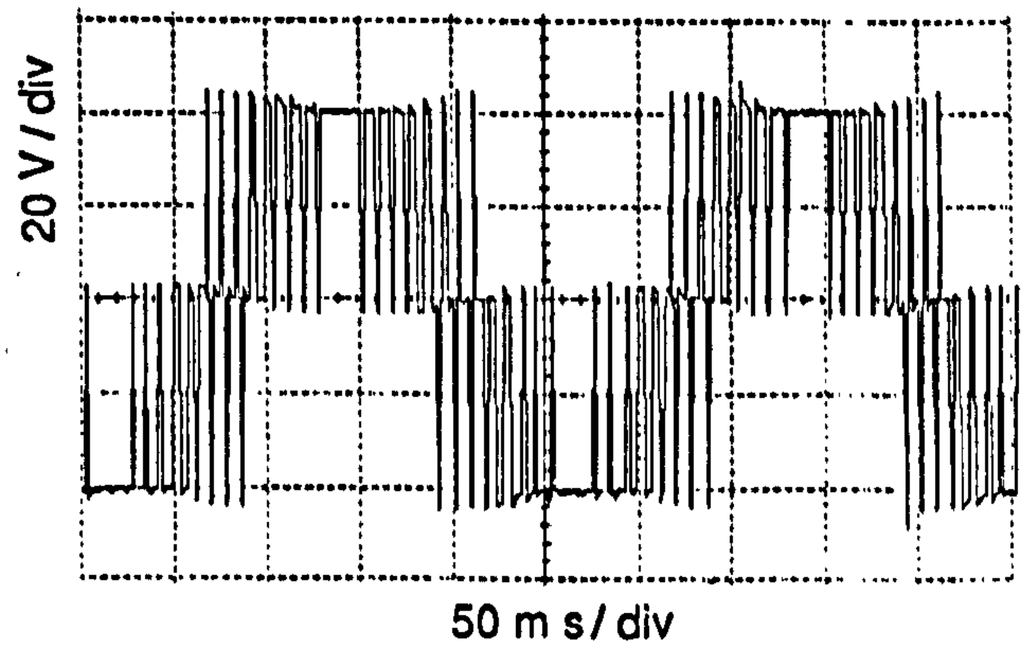

(a)

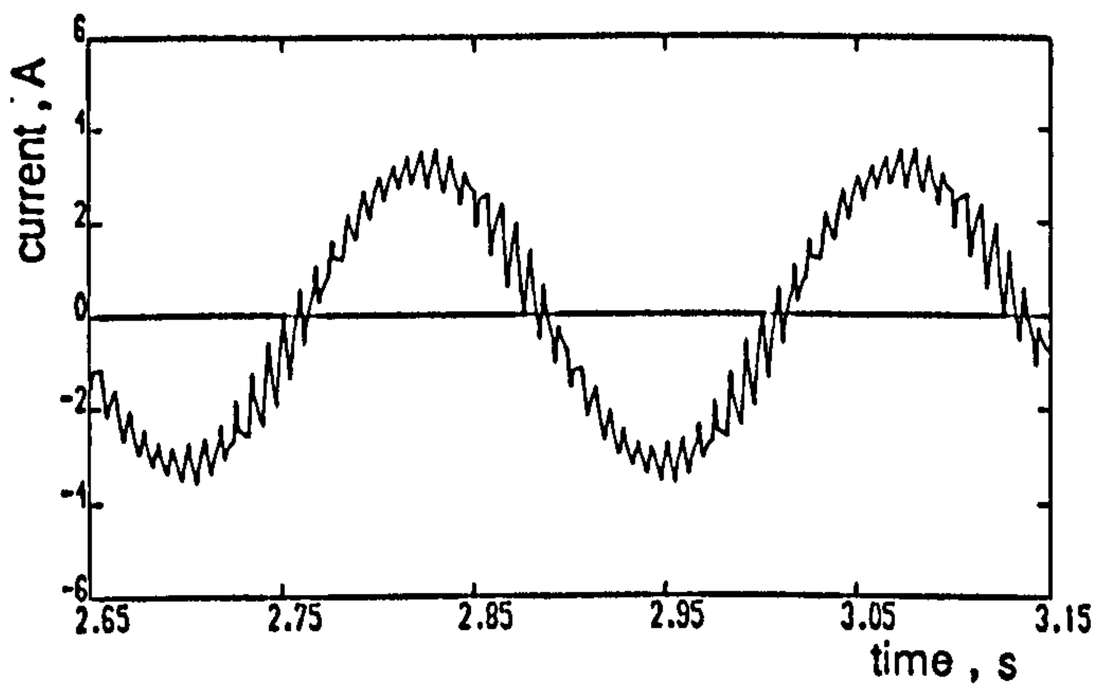

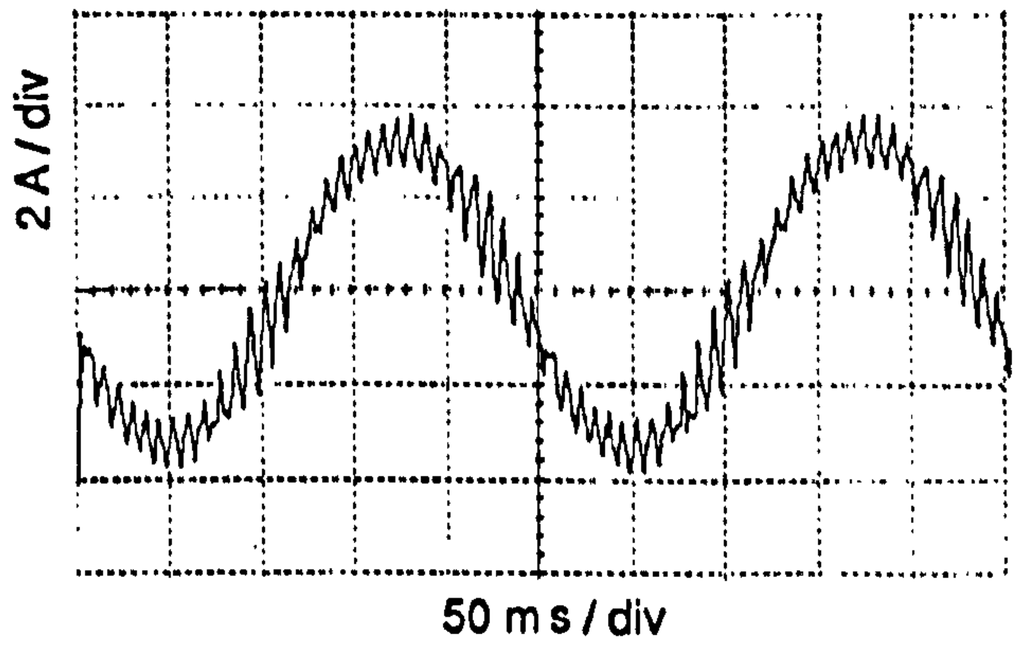

(b)

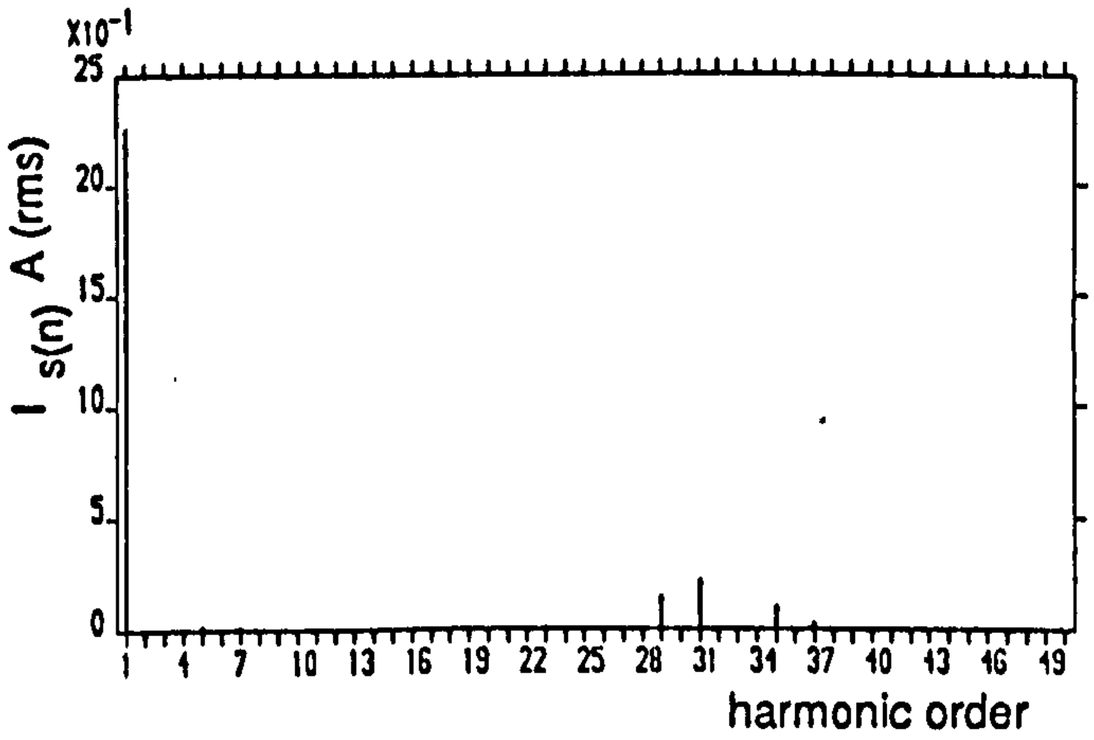

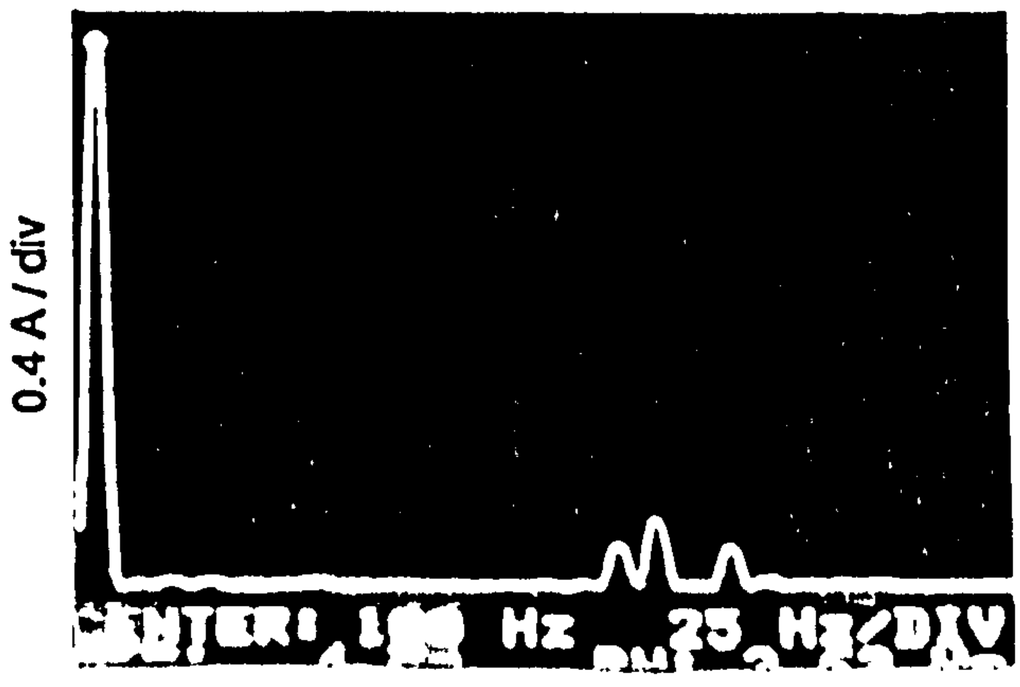

(c)

Figure 5.25 Computed and experimental results for PWM8 elimination mode 4Hz stator frequency , full-load operation

(a) Line voltage

(b) Stator current

(c) Stator current spectrum

Observation of these figures demonstrates close correlation between computed and experimental waveforms and provides further confirmation and validation of the computer model.

Figures 5.26(a) to (d) show computed electromagnetic torque and rotor speed ripple waveforms with each pulse number. The peak-to-peak torque pulsations and speed ripple magnitudes listed in table 5.1 provide a clear comparison between QSW and the different PWM modes.

Table 5.1

Operating Mode	Torque peak-to-peak - Nm	Speed peak-to-peak rad/s
QSW	1.02	0.78
PWM2	1.73	0.53
PWM4	1.28	0.28
PWM6	1.15	0.20
PWM8	0.98	0.15

The table emphasizes that eliminating low order harmonic components may result in an increase in the remaining high order components and produce high peak-to-peak torque pulsations. However, since their effect in producing speed ripple is highly attenuated, the peak-to-peak speed ripple decreases with increasing pulse number. Experimental rotor speed waveforms for PWM operation at this frequency are not included, due to the limited definition of the analogue speed signal. It is noted however that these where confirmed earlier for the case of 4Hz QSW operation (figure 5.20) and 1Hz no-load condition (figures 5.12 to 5.16).

On loading the machine, other limitations were encountered in measuring the speed ripple at frequencies below 2Hz, when the slip-speed increases and the average speed drops virtually to zero. At some point, when the speed ripple is large,

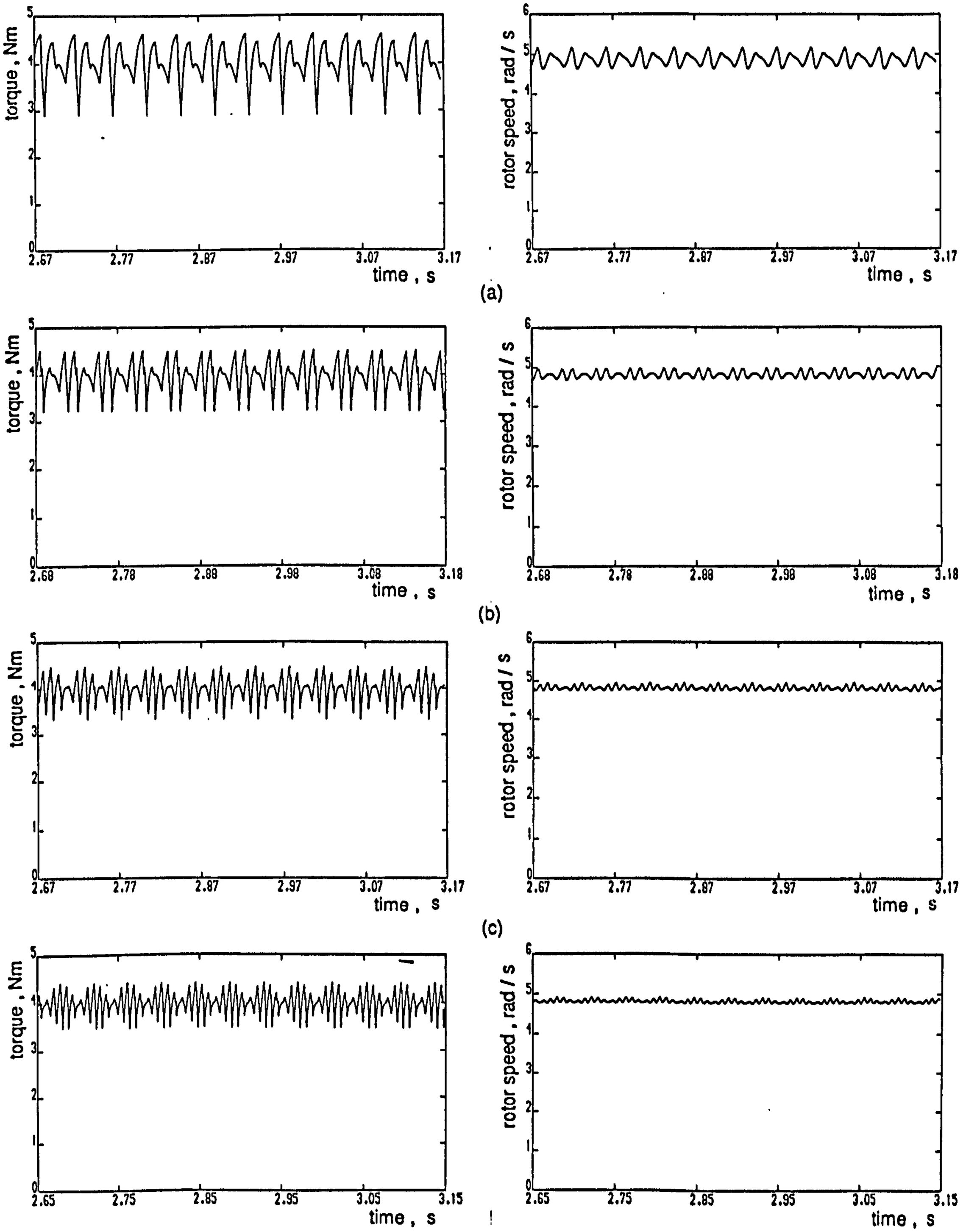

Figure 5.26 Computed electromagnetic torque and rotor speed
for 4Hz , full-load , PWM elimination
(a) PWM2 (b) PWM4 (c) PWM6 (d) PWM8 modes

especially during QSW operation, part of the speed ripple is in the reverse direction of rotation. The measuring circuit described in chapter 4 was designed to provide an analogue signal relative to the rotor shaft speed in the forward direction of rotation. Hence it is only possible to obtain a unidirectional speed analogue signal which resulted in a reflection of the negative part of the speed ripple.

To verify this fact, computed and experimental results are presented in figures 5.27 and 5.28. Figure 5.27(a) shows, for 1Hz operation, the computed electromagnetic torque with an average load torque of 0.8Nm. The computed rotor speed in figure 5.27(b) demonstrates a drop in the average speed from 2.83rad/s, with a superimposed peak-to-peak ripple of 4.15rad/s at no-load to 1.55rad/s on-load with a superimposed peak-to-peak ripple of 3.77rad/s, of which 0.42rad/s is in the reverse direction of rotation. Figure 5.27(c) shows the computed modulus of the rotor speed, which agrees well with what obtained experimentally in figure 5.27(d). For further confirmation, results are presented in figure 5.28 for the same operating frequency but an increased load. Figure 5.28(a) shows the computed electromagnetic torque with an average load torque of 1.42Nm. Figure 5.28(b) shows the computed rotor speed with an average of 0.29rad/s and a superimposed ripple of 3.32rad/s, of which 1.33rad/s is negative. Figure 5.28(c) shows the computed modulus of rotor speed, while the experimental waveform is as shown in figure 5.28(d).

5.6 Conclusion

This chapter has described the development of a versatile mathematical model for a VSI/induction motor drive. The model is capable of readily handling a wide range of pulsed waveforms, allowing the effect of any proposed PWM strategy to be studied on a computer before practical implementation. The operational modes investigated, and the results presented, were chosen principally for ease of presentation and experimental confirmation, and to provide a basis for confirming the validity

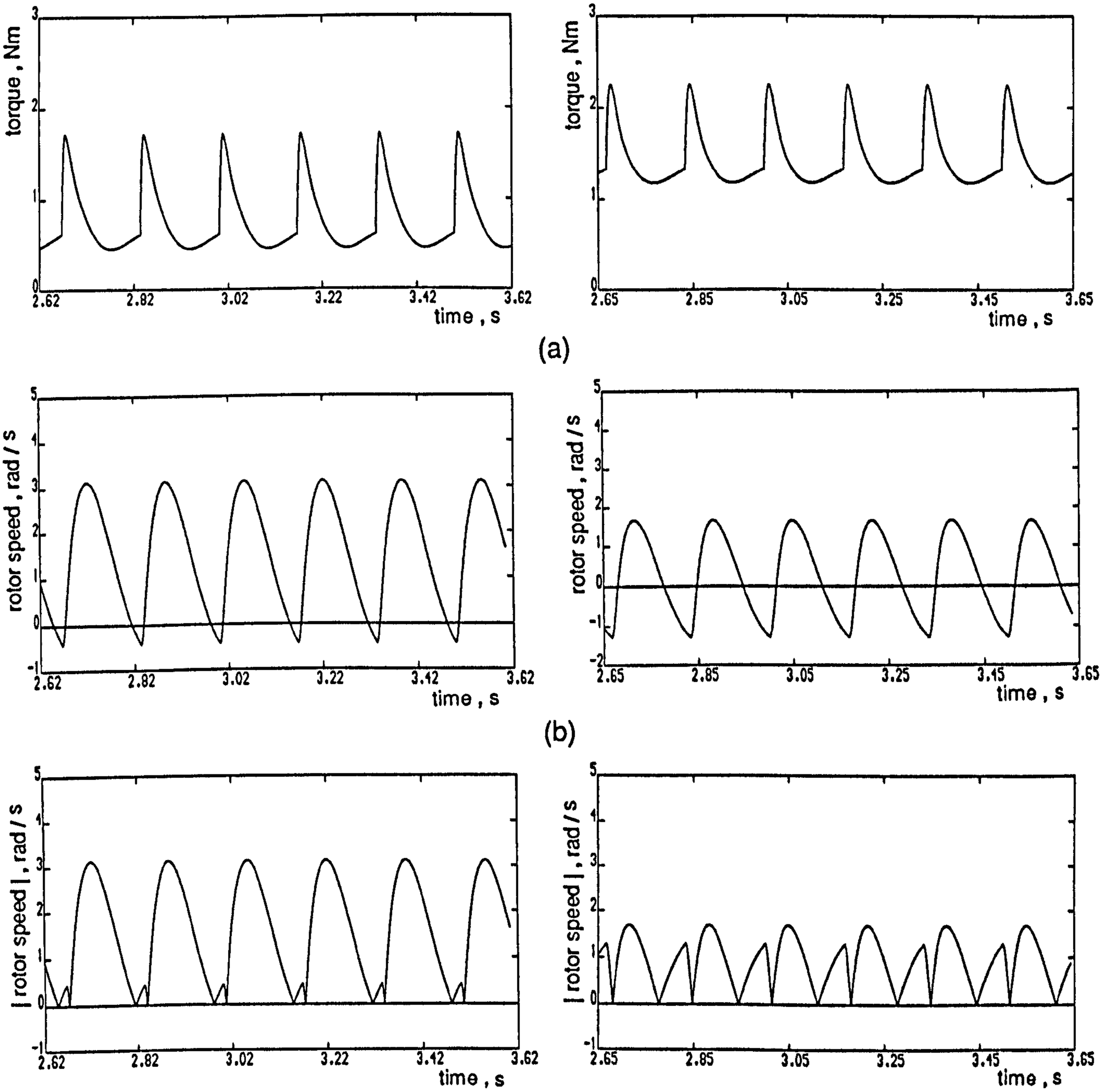

Figure 5.27

Figure 5.28

Torque and speed responce at 1Hz , QSW operation mode with 0.8 Nm load 1.42 Nm load

(a) Computed electromagnetic torque
(b) Computed actual rotor speed
(c) Computed modulus of rotor speed
(d) Experimental rotor speed

and accuracy of the computer modelling techniques used. Comparison of computed and experimental results confirmed the validity and accuracy of the computer model. These results highlight that simulation provides a powerful tool for investigating and studying the dynamic performance of the machine, especially when experimental limitations may lead to wrong judgment.

CHAPTER 6

A NEW APPROACH TO CONVENTIONAL STEADY-STATE ANALYSIS WITH NON-SINUSOIDAL SUPPLIES

This chapter extends the use of the induction motor equivalent circuit analysis of chapter 2 to cover non-sinusoidal supply voltages, with a detailed analysis being demonstrated using both QSW and PWM operational modes. An analytical torque equation is proposed, which is used for further investigations into the dynamic performance of optimal PWM voltage source inverter drives.

6.1 Methods Of Analysis

The optimal PWM switching strategies designed specifically to eliminate low order harmonic components in the inverter output voltage waveform are machine independent. The optimization method described in section 3.2.3 performs the optimization procedure, by iteratively processing equations defining the fundamental and harmonic components to maximize the former and to equate the latter to zero. There are however other performance criteria which can be optimised; for example the harmonic current content, or the level of torque pulsations or speed ripple could be minimized. Since these are all defined as machine performance requirements, they are therefore dependent on the operating conditions.

A fast and accurate system model is required to perform wide ranging investigations into the effects of using optimal PWM control techniques on the steady-state motor performance. The method requires rapid and efficient computation of the switching angles, especially when numerical minimisation techniques are involved, to minimize a performance criterion objective function which is interactive with the machine parameters and operating conditions.

The time-domain solution described in Chapter 5 is inappropriate for use with optimization techniques, due to its complicated and excessively long computation requirements. Frequency-domain methods, using Fourier analysis, are usually employed to obtain the harmonic content of the VSI output voltage waveshape. These harmonics are applied to harmonic equivalent circuits for the motor, to determine the corresponding current components. The motor torque is then calculated from the interaction and superposition of harmonic current components. This approach has been used for efficiency and machine loss optimization [22] and has proved to be computationally efficient, reasonably accurate and suitable for use with any minimisation process.

6.2 Inverter Voltage Waveform Representation

In a VSI drive, the non-sinusoidal output voltage during steady-state operation may be resolved into fundamental and harmonic components. Assuming ideal voltage waveforms, possessing both quarter and half-wave symmetry, the general Fourier-series representation of the phase voltages contains only sine terms and is

$$v_{AN} = \sqrt{2}\{V_{(1)}\sin\omega_s t + V_{(5)}\sin 5\omega_s t + V_{(7)}\sin 7\omega_s t + \ldots.\}$$

$$v_{BN} = \sqrt{2}\{V_{(1)}\sin\left(\omega_s t - \frac{2\pi}{3}\right) + V_{(5)}\sin\left(5\omega_s t + \frac{2\pi}{3}\right) + V_{(7)}\sin\left(7\omega_s t - \frac{2\pi}{3}\right) + \ldots.\} \quad 6.1$$

$$v_{CN} = \sqrt{2}\{V_{(1)}\sin\left(\omega_s t + \frac{2\pi}{3}\right) + V_{(5)}\sin\left(5\omega_s t - \frac{2\pi}{3}\right) + V_{(7)}\sin\left(7\omega_s t + \frac{2\pi}{3}\right) + \ldots.\}$$

where ω_s is the fundamental angular frequency of the supply and $V_{(n)}$ the rms value of the nth phase voltage harmonic. These equations demonstrate that the 5th-harmonic component $V_{(5)}$ has a negative phase sequence and the 7th-harmonic component $V_{(7)}$ a positive phase sequence. As explained in chapter 3, the magnitudes of the phase voltage components for a 6-step phase voltage waveshape are inversely proportional to their order and are given by

$$V_{(n)} = \frac{\sqrt{2}}{n\pi} V_{dc} \qquad 6.2$$

For any optimal PWM mode, with quarter-wave symmetry, the magnitudes follow the general expression in terms of the switching angles given by

$$V_{(n)} = \frac{\sqrt{2}}{n\pi} V_{dc} \left(1 + 2 \sum_{i=1}^{m} (-1)^i \cos n\alpha_i \right) \qquad 6.3$$

where V_{dc} is the DC-link voltage and m the number of switching angles α_i per quarter-cycle.

6.3 Harmonic Equivalent Circuit Analysis

Equivalent circuit analysis is usually applied to steady-state operating conditions with constant speed and sinusoidal excitation. To use this approach, in analysing the performance of an inverter driven induction motor, each harmonic component of the supply voltage (equation 6.1) must be applied to an equivalent circuit in which both reactance components and slip are appropriately scaled, as shown in figure 6.1. Since rotor speed is related to the fundamental frequency only, the rotor slip s at the nth-harmonic is

$$s(n) = \frac{n\omega_s \mp p\omega_m}{n\omega_s} \qquad 6.4$$

where the negative and positive signs relate to forward and backward rotating fields respectively. Substituting from equation 2.2 in equation 6.4 and simplifying yields

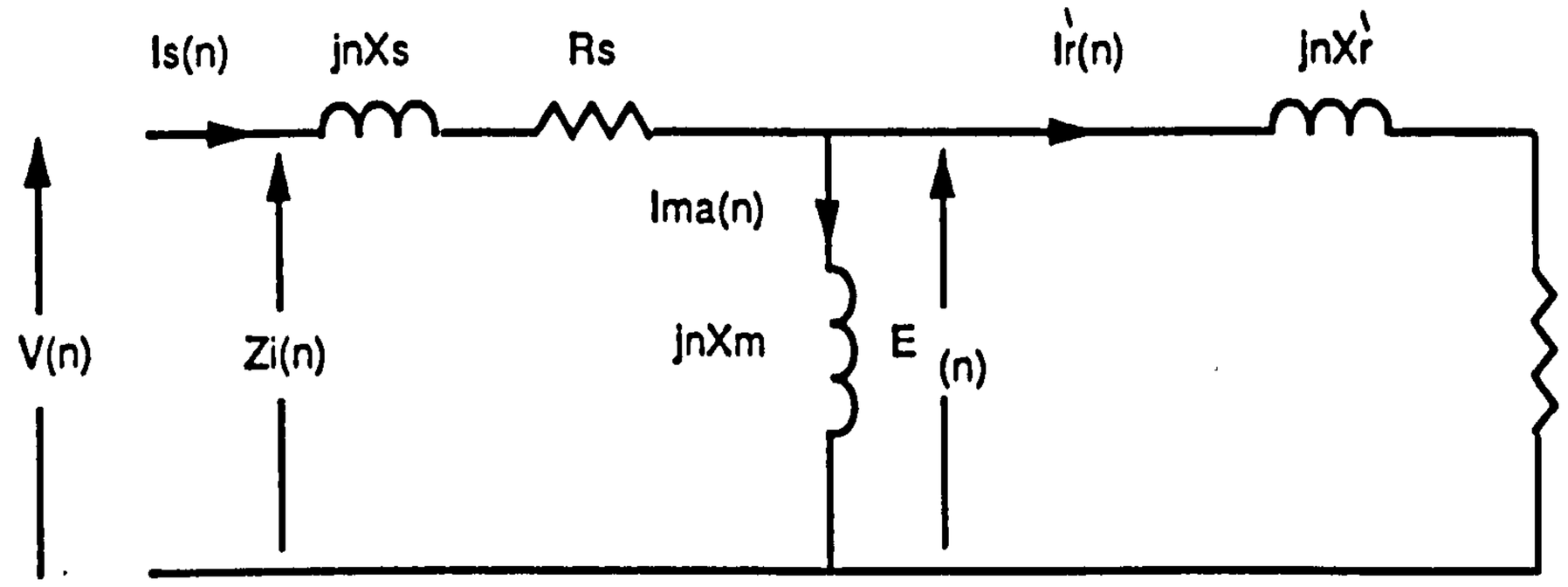

Figure 6.1 Per-phase harmonic equivalent circuit of the induction motor

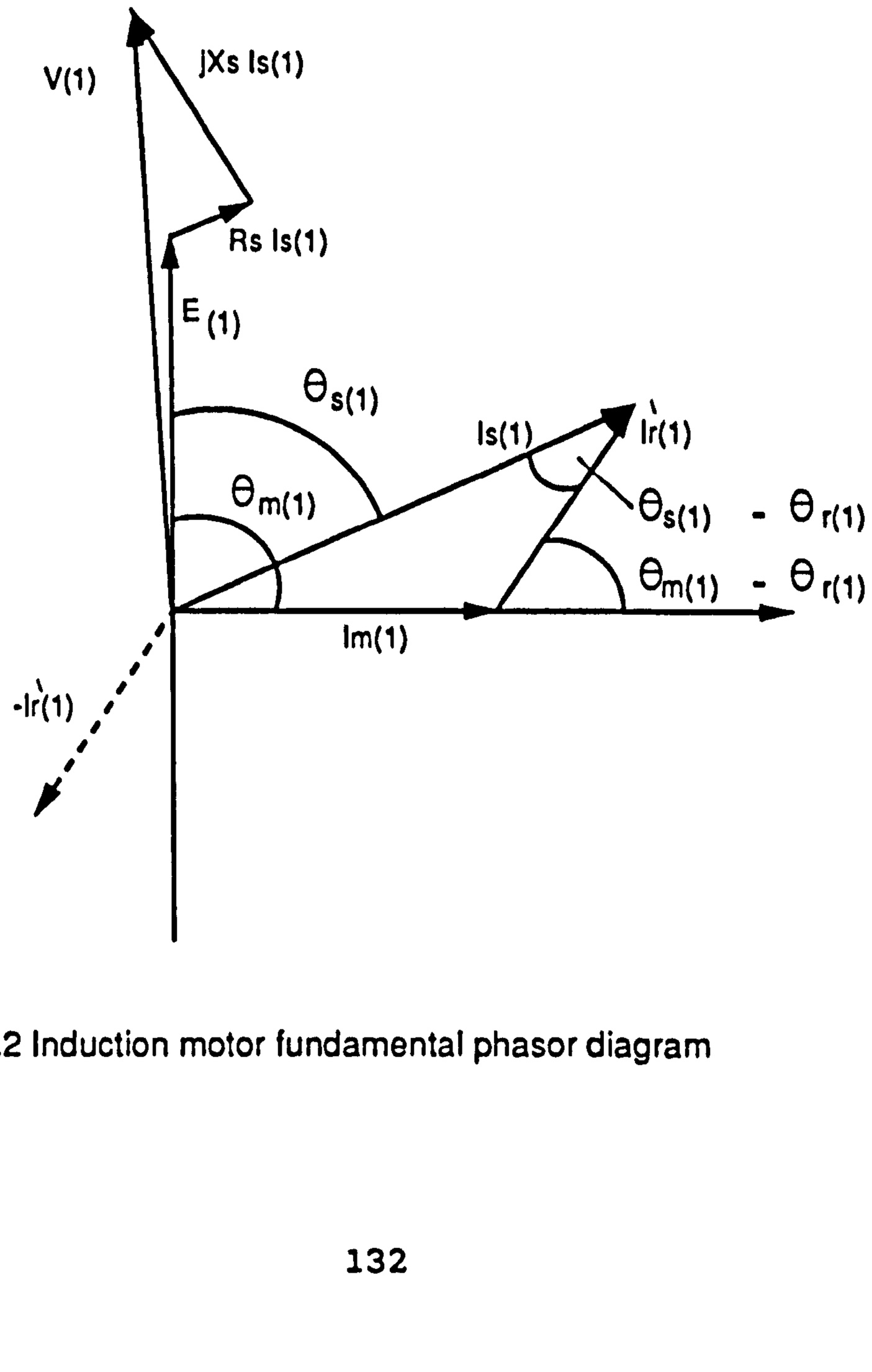

Figure 6.2 Induction motor fundamental phasor diagram

$$s(n) = \frac{(n-1)+s(1)}{n} \qquad ,n=1,7,13,19,\ldots \quad .$$

for forward rotating fields, and

$$s(n) = \frac{(n+1)-s(1)}{n} \qquad ,n=5,11,17,\ldots \quad .$$

for backward rotating fields, and $s(1)$ is the fundamental slip.

6.3.1 Harmonic Equivalent Circuit Considerations

Two main factors effect the equivalent circuit parameters due to the presence of time harmonic components. Firstly, the harmonics result in increased saturation of the leakage flux paths, due to the greater peak value of the non-sinusoidal current waveform, and thus reduce both the magnetizing and leakage inductances. Secondly, skin effect can be a significant factor in increasing the stator and rotor resistances, particularly if the rotor has a deep bar construction. Although precise calculation of the machine parameters is important in predicting the machine performance, it involves excessive complication and was not adopted in the present equivalent circuit analysis.

On the other hand, certain important approximations are often used in equivalent circuit analysis. For example, the resistive components may be neglected in comparison with the reactive components at harmonic frequencies, and the shunt magnetizing reactance branch may be omitted if its value is much greater than the rotor leakage reactance. These approximations are not valid at low frequencies (below about 10Hz), where the stator and rotor winding resistances are significant when compared with the reactances, and they are therefore not used in the present analysis.

6.3.2 Harmonic Current Representation

Applying the voltage waveforms of equation 6.1 to the machine terminals results in stator currents i_{sA} , i_{sB} and i_{sC} whose half-wave symmetrical waveforms can be expressed by the Fourier-series

$$\begin{aligned}
i_{sA} &= \sqrt{2}\{I_{s(1)}\sin(\omega_s t + \theta_{s(1)}) \\
&\quad + I_{s(5)}\sin(5\omega_s t + \theta_{s(5)}) + I_{s(7)}\sin(7\omega_s t + \theta_{s(7)}) + ..\} \\
i_{sB} &= \sqrt{2}\{I_{s(1)}\sin\left(\omega_s t + \theta_{s(1)} - \frac{2\pi}{3}\right) \\
&\quad + I_{s(5)}\sin\left(5\omega_s t + \theta_{s(5)} + \frac{2\pi}{3}\right) + I_{s(7)}\sin\left(7\omega_s t + \theta_{s(7)} - \frac{2\pi}{3}\right) + ..\} \\
i_{sC} &= \sqrt{2}\{I_{s(1)}\sin\left(\omega_s t + \theta_{s(1)} + \frac{2\pi}{3}\right) \\
&\quad + I_{s(5)}\sin\left(5\omega_s t + \theta_{s(5)} - \frac{2\pi}{3}\right) + I_{s(7)}\sin\left(7\omega_s t + \theta_{s(7)} + \frac{2\pi}{3}\right) + ..\}
\end{aligned} \qquad 6.5$$

where $I_{s(n)}$ is the rms value of the nth stator current component and $\theta_{s(n)}$ its phase angle with respect to the corresponding phase voltage component. Each stator current component produces an airgap mmf, rotating either forward or backward according to the phase sequence of the component which produces it. This in turn induces currents i_{ra} , i_{rb} and i_{rc} in the rotor at a harmonic slip frequency $(n\omega_s \mp p\omega_m)$ which may be defined as

$$i_{ra} = \sqrt{2}\{I_{r(1)}\sin(\omega_s t - p\omega_m t + \theta_{r(1)}) + I_{r(5)}\sin(5\omega_s t + p\omega_m t + \theta_{r(5)}) + I_{r(7)}\sin(7\omega_s t - p\omega_m t + \theta_{r(7)}) + ..\}$$

$$i_{rb} = \sqrt{2}\{I_{r(1)}\sin\left(\omega_s t - p\omega_m t + \theta_{r(1)} - \frac{2\pi}{3}\right) + I_{r(5)}\sin\left(5\omega_s t + p\omega_m t + \theta_{r(5)} + \frac{2\pi}{3}\right) + I_{r(7)}\sin\left(7\omega_s t - p\omega_m t + \theta_{r(7)} - \frac{2\pi}{3}\right) + \cdots\} \quad 6.6$$

$$i_{rc} = \sqrt{2}\{I_{r(1)}\sin\left(\omega_s t - p\omega_m t + \theta_{r(1)} + \frac{2\pi}{3}\right) + I_{r(5)}\sin\left(5\omega_s t + p\omega_m t + \theta_{r(5)} - \frac{2\pi}{3}\right) + I_{r(7)}\sin\left(7\omega_s t - p\omega_m t + \theta_{r(7)} + \frac{2\pi}{3}\right) + ..\}$$

where $I_{r(n)}$ is the rms value of the nth rotor current component and $\theta_{r(n)}$ its phase angle with respect to the corresponding phase voltage.

Individual harmonic current components and their phase angles may be obtained from a harmonic equivalent circuit, using the procedure explained in chapter 2 for fundamental component analysis. The stator nth-harmonic current component is obtained from

$$\bar{I}_{s(n)} = \frac{\bar{V}_{(n)}}{\bar{Z}_{i(n)}} \quad 6.7$$

where the input impedance of the nth-harmonic equivalent circuit $\bar{Z}_{i(n)}$ is

$$\bar{Z}_{i(n)} = R_s + jnX_s + \frac{jnX_m(R_r'/s(n) + jnX_r')}{R_r'/s(n) + jn(X_m + X_r')} \quad 6.8$$

and the phase angle is

$$\theta_{s(n)} = -\tan^{-1}\frac{\Im Z_{i(n)}}{\Re Z_{i(n)}} \quad 6.9$$

The referred rotor nth-harmonic current component $I_{r(n)}'$, and its phase angle $\theta_{r(n)}'$ are

$$\bar{I}'_{r(n)} = \bar{I}_{s(n)} \cdot \frac{jnX_m}{R'_r/s(n) + jn(X_m + X'_r)} \qquad 6.10$$

and

$$\theta'_{r(n)} = \tan^{-1}\frac{\Im I'_{r(n)}}{\Re I'_{r(n)}} \qquad 6.11$$

respectively.

It is emphasised here that the currents of equation 6.6 are the actual slip frequency rotor current components, whereas the referred rotor current components calculated using equation 6.10 are stator frequency harmonics, with their phase angles reflected by 180° following the relation $\theta_{r(n)} = \theta'_{r(n)} - 180°$ defined in figure 2.1(c).

6.4 Correlation between Current Components in Torque Production

To illustrate the interaction between the fundamental current components in producing constant steady torque, equation 2.13 may be re-arranged according to the fundamental phasor diagram shown in figure 6.2, and written as [77]

$$T_e = 3p\, l_m\, I_{m(1)}\, I'_{r(1)} \sin(\phi_{m(1)} - \phi_{r(1)}) \qquad 6.12$$

or

$$T_e = 3p\, l_m\, I_{s(1)}\, I'_{r(1)} \sin(\phi_{s(1)} - \phi_{r(1)}) \qquad 6.13$$

where l_m is the magnetizing branch inductance, and $\phi_{s(1)}$, $\phi_{r(1)}$, $\phi_{m(1)}$ are the stator, rotor and magnetizing current phase angles with the stator generated emf $E_{(1)}$, taken as the reference phasor. These equations express the electromagnetic torque of the motor either in terms of the fundamental components of the magnetizing and referred rotor currents $I_{m(1)}$ and $I'_{r(1)}$, or the stator and referred rotor currents $I_{s(1)}$ and $I'_{r(1)}$, and the sine of the angle between them.

Current time phasors represent, to a certain scale, mmf space phasors, and equations 6.12 and 6.13 reveal that the torque is proportional to either the product of the mutual

airgap flux and rotor mmf, or the stator and rotor mmfs and the sine of the angle between them. Since these phasor components are of the same harmonic order, they rotate at the same speed and the angle between them remains constant. Only constant torque is produced by their interaction, which applies also when considering components of a higher, but equal, harmonic order. Torque pulsations are produced when airgap flux or stator mmf at one frequency interacts with rotor mmf at another frequency, and the angle between them varies as the difference between the speeds of the two rotating space phasors.

6.4.1 Analytical Equation for Electromagnetic Torque

Having established the basic principles of torque production, it is important to define the relationship between current and torque harmonic components. Equation 5.17 defines the electromagnetic torque in the mesh reference frame. Due to power invariance, the equation may be defined in the branch reference frame as

$$T_e = \frac{p}{2} I^{abc} \frac{\partial L_{abc}}{\partial \theta_e} I^{abc} \qquad 6.14$$

in terms of the instantaneous machine currents and the 6x6 rate-of-change of the inductance matrix $\partial L_{abc}/\partial \theta_e$ given as

$$\frac{\partial L_b}{\partial \theta_e} = -M_{sr}\begin{bmatrix} 0.0 & 0.0 & 0.0 & \sin(\theta_e) & \sin\left(\theta_e+\frac{2\pi}{3}\right) & \sin\left(\theta_e-\frac{2\pi}{3}\right) \\ 0.0 & 0.0 & 0.0 & \sin\left(\theta_e-\frac{2\pi}{3}\right) & \sin(\theta_e) & \sin\left(\theta_e+\frac{2\pi}{3}\right) \\ 0.0 & 0.0 & 0.0 & \sin\left(\theta_e+\frac{2\pi}{3}\right) & \sin\left(\theta_e-\frac{2\pi}{3}\right) & \sin(\theta_e) \\ \sin(\theta_e) & \sin\left(\theta_e-\frac{2\pi}{3}\right) & \sin\left(\theta_e+\frac{2\pi}{3}\right) & 0.0 & 0.0 & 0.0 \\ \sin\left(\theta_e+\frac{2\pi}{3}\right) & \sin(\theta_e) & \sin\left(\theta_e-\frac{2\pi}{3}\right) & 0.0 & 0.0 & 0.0 \\ \sin\left(\theta_e-\frac{2\pi}{3}\right) & \sin\left(\theta_e+\frac{2\pi}{3}\right) & \sin(\theta_e) & 0.0 & 0.0 & 0.0 \end{bmatrix}$$

After simplification, equation 6.14 becomes

$$T_e = -pM_{sr}\{(i_{sA}i_{ra}+i_{sB}i_{rb}+i_{sC}i_{rc})\sin\theta_e + (i_{sA}i_{rb}+i_{sB}i_{rc}+i_{sC}i_{ra})\sin\left(\theta_e+\frac{2\pi}{3}\right) + (i_{sA}i_{rc}+i_{sB}i_{ra}+i_{sC}i_{rb})\sin\left(\theta_e-\frac{2\pi}{3}\right)\} \quad 6.16$$

where $M_{sr} = (2/3)l_m$ as defined in appendix A.1.

Equations 6.13 and 6.16 are similar in that they both express the torque in terms of stator and rotor currents. However, equation 6.16 is non-linear due to the presence of the rotor electrical angle θ_e . This may be defined in terms of speed which is assumed constant during steady-state operation by

$$\theta_e = \int_0^t p\omega_m \, dt = p\omega_m t \quad 6.17$$

Substituting equation 6.17 for θ_e results in

$$T_e = -p\left(\frac{2}{3}l_m\right)\{(i_{sA}i_{ra}+i_{sB}i_{rb}+i_{sC}i_{rc})\sin(p\omega_m t) + (i_{sA}i_{rb}+i_{sB}i_{rc}+i_{sC}i_{ra})\sin\left(p\omega_m t+\frac{2\pi}{3}\right) + (i_{sA}i_{rc}+i_{sB}i_{ra}+i_{sC}i_{rb})\sin\left(p\omega_m t-\frac{2\pi}{3}\right)\} \quad 6.18$$

Following the manipulation of appendix A.3, equations 6.5 and 6.6 are substituted in equation 6.18 to give the following general expression

$$T_e = 3pl_m \sum_{ks} \sum_{kr} \{ I_{s(ksf)} I_{r(krf)} \sin((ksf - krf)\omega_s t + \theta_{s(ksf)} - \theta_{r(krf)})$$

$$- I_{s(ksb)} I_{r(krb)} \sin((ksb - krb)\omega_s t + \theta_{s(ksb)} - \theta_{r(krb)})$$

$$+ I_{s(ksb)} I_{r(krf)} \sin((ksb + krf)\omega_s t + \theta_{s(ksb)} + \theta_{r(krf)})$$

$$- I_{s(ksf)} I_{r(krb)} \sin((ksf + krb)\omega_s t + \theta_{s(ksf)} + \theta_{r(krb)}) \} \qquad 6.19$$

where

$ksf, krf = 6m + 1$ is the order of current components which induce forward rotating magnetic fields, $m = 0.1.2.3,\ldots$.

$ksb, krb = 6m - 1$ is the order of current components which induce backward rotating magnetic fields, $m = 1.2.3,\ldots$.

Equation 6.19 provides the amplitude and phase angle of individual harmonic torque components and accounts for all possible interactions between forward and backward stator and rotor harmonic components. When substituting $ksf = krf = 1$, the first term gives the constant torque produced by the interaction between the stator and rotor fundamental mmf field components which is the same as equation 6.13. In general, when $ksf = krf$ and $ksb = krb$, the first and second terms gives the constant torque components, and when $ksf \neq krf$ and $ksb \neq krb$ harmonic torque components are obtained.

6.4.2 Calculation of Harmonic Torque Components

The general torque expression defined by equation 6.19 may be re-arranged as

$$T_e = \sum_{k = ks = kr} [T_{e0}]_k + \sum_h T_{eh} \sin(h\omega_s t + \delta_h) \qquad 6.20$$

where T_{e0} is the constant torque produced when $ksf = krf$ and $ksb = krb$, h is the order of the harmonic torque component (equal to 6 or multiples thereof) and δ_h the phase angle of the hth torque harmonic. The total harmonic torque of a given order h may be obtained by phasor addition of the individual torque components having that order.

Table 6.1 shows the constant torque components obtained using equation 6.19 for a 4Hz QSW mode and full load operation. It is evident from the table that constant torques produced by components, other than the fundamental, are negligible.

TABLE 6.1

HARMONIC CURRENT COMPONENTS AND CONSTANT TORQUE PRODUCED BY INTERACTION OF THEIR RESPECTIVE MMF FIELDS

ks	kr	$I_{s(s)} \angle\theta_{s(s)}$	$I_{r(s)} \angle\theta_{r(s)}$	T_o
1	1	2.2545 ∠-22.59	1.8239 ∠-171.13	+3.9384
5	5	0.4431 ∠-35.14	0.4194 ∠148.97	-2.418e-02
7	7	0.2695 ∠-42.48	0.2553 ∠140.82	+7.218e-03
11	11	0.1361 ∠-55.72	0.1290 ∠126.26	-1.079e-03
13	13	0.1016 ∠-59.28	0.0963 ∠122.45	+5.418e-04
17	17	0.0633 ∠-65.97	0.0601 ∠115.29	-1.535e-04
19	19	0.0514 ∠-67.87	0.0488 ∠113.35	+9.408e-05
23	23	0.0360 ∠-71.68	0.0342 ∠109.25	-3.664e-05
25	25	0.0307 ∠-72.83	0.0291 ∠108.05	+2.518e-05

Tables 6.2 and 6.3 demonstrate the procedure by which equations 6.19 and 6.20 are used to calculate the 6th- and 12th-harmonic torque components and their phase angles. It is evident that the harmonic torque components resulting from the interaction of fundamental and harmonics of stator and rotor mmf fields are large, while those due to harmonic fields alone are sufficiently small to be neglected.

TABLE 6.2
PEAK AMPLITUDE AND PHASE ANGLE OF THE 6TH-HARMONIC TORQUE COMPONENT

ks	*kr*	$T_{.6}\ \angle\delta_6°$	*Summation of* $T_{.6}\ \angle\delta_6$	
1	5	-1.734 ∠126.38	0.801 ∠-112.11	0.370 ∠-66.41
5	1	1.482 ∠-206.20		
1	7	-1.055 ∠163.39	0.603 ∠41.88	
7	1	0.901 ∠128.62		
5	11	0.105 ∠161.30	0.011 ∠-112.42	0.007 ∠115.02
11	5	-0.105 ∠-204.69		
7	13	-0.048 ∠164.93	0.004 ∠71.87	
13	7	0.047 ∠-200.08		
11	17	0.015 ∠171.01	8.3e-04 ∠-102.64	3.7e-04 ∠-102.22
17	11	-0.015 ∠-192.17		
13	19	-0.009 ∠172.58	4.6e-04 ∠77.02	
19	13	0.009 ∠-190.32		

TABLE 6.3
PEAK AMPLITUDE AND PHASE ANGLE OF THE 12TH-HARMONIC TORQUE COMPONENT

ks	*kr*	$T_{.12}\ \angle\delta_{12}$	*Summation of* $T_{.12}\ \angle\delta_{12}$	
1	11	-0.533 ∠103.61	0.263 ∠-134.95	0.10 ∠-82.1
11	1	0.455 ∠-226.82		
1	13	-0.398 ∠145.04	0.218 ∠23.67	
13	1	0.340 ∠111.82		
5	7	0.207 ∠105.70	0.003 ∠20.10	0.003 ∠-86.20
7	5	-0.207 ∠106.49		
5	17	0.049 ∠150.39	0.004 ∠-123.53	
17	5	-0.049 ∠-214.94		
7	19	-0.024 ∠155.78	0.002 ∠63.55	1.6e-03 ∠52.61
19	7	0.024 ∠-208.67		
11	23	0.008 ∠164.97	4.2e-04 ∠-70.85	
23	11	-0.008 ∠-197.88		

6.5 Comparison between Direct-Phase and Conventional Analysis Models

A computer program was written to predict the steady-state performance of the machine under non-sinusoidal excitation. To maintain constant airgap flux, the $E_{(1)}/f$ ratio was determined according to the analysis presented in chapter 2 and fixed for any frequency and load during the constant torque regime. After specifying the frequency and load condition, the program proceeds to calculate the required fundamental terminal voltage component. For any operating mode (QSW or optimal PWM), the DC-link voltage is determined using equations 3.3 and 3.38, from which the other harmonic components are obtained using equations 6.2 or 6.3. Each component is applied separately to a frequency-scaled harmonic equivalent circuit, to determine the stator and rotor harmonic current components and their phase angles. These are substituted in equation 6.19, to calculate the average and harmonic torque components. Superposition, according to equation 6.20, yields the torque value at any given time. The period of one output cycle is divided into 10000 equal intervals and the torque value calculated at every time instant to ensure a fair comparison with results obtained from the direct-phase model.

6.5.1 CPU Time

Figures 6.3(a) to (c) show torque waveforms for a PWM voltage pattern with two switching angles per quarter-cycle and the same operating conditions as figure 5.13. They were obtained using harmonic superposition of the first 50, 100 and 200 harmonics respectively. The corresponding CPU times required for these results are 39s , 68s and 134s respectively, compared with the 378s needed for the direct-phase model to reach steady-state and to provide one complete cycle of steady-state waveform.

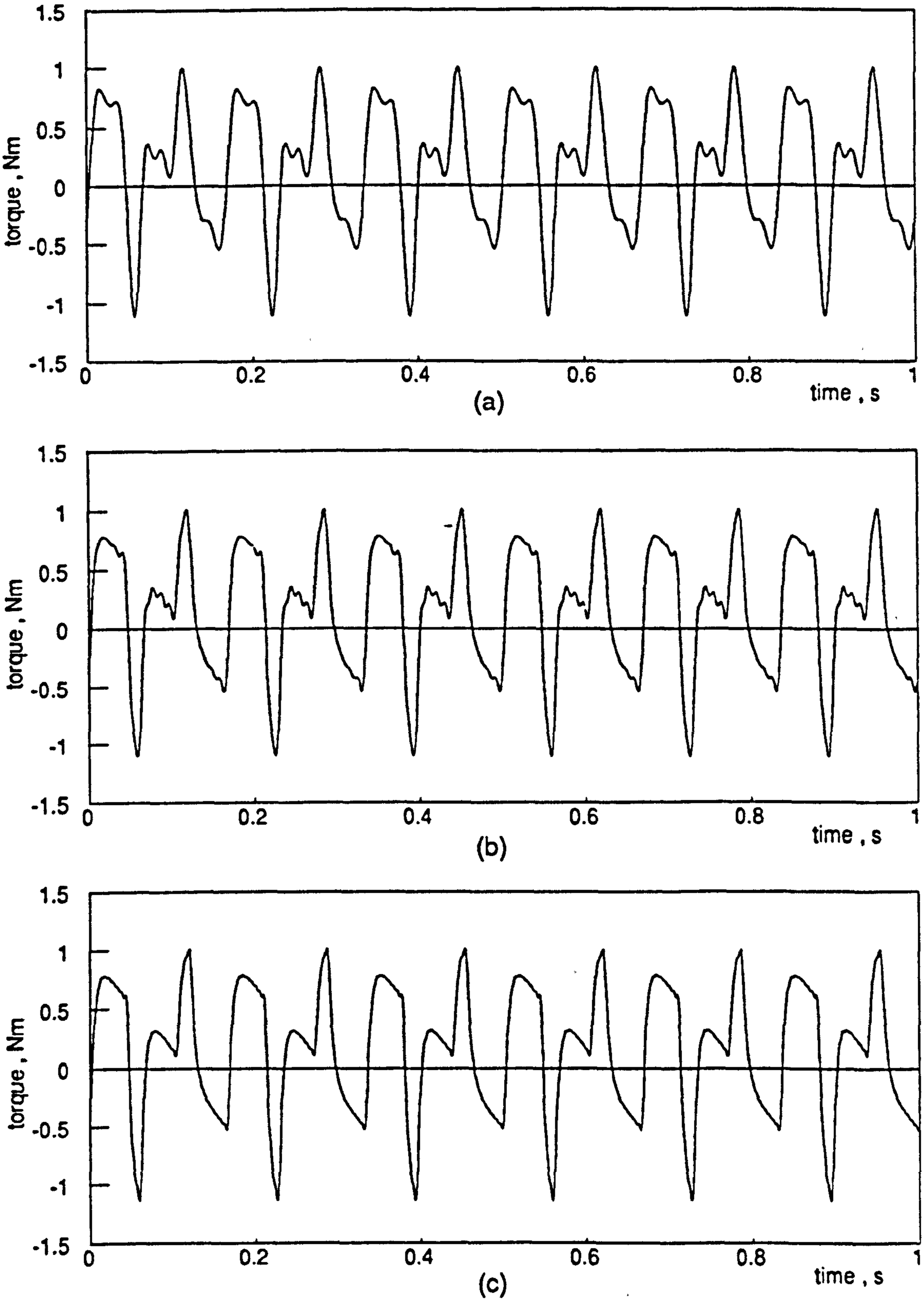

Figure 6.3 Electromagnetic torque waveforms obtained from the frequency-domain model for PWM2 mode inverter driving unloaded motor at 1Hz stator frequency
(a) 50 harmonics (b) 100 harmonics (c) 200 harmonics , are included

Comparison of the no-load condition waveforms of figure 6.3 with those given earlier in figure 5.13, reveals that 200 harmonics are necessary to achieve an acceptable degree of accuracy, and this extends considerably the computation time. This problem does not exist with a direct-phase model, where all the harmonic components are inherently accounted for in the time description of the waveform. However, on loading the motor, more CPU time is needed for the direct-phase model to reach steady-state. Comparing CPU times for both models indicates that frequency-domain analysis, even when 200 harmonics are included, provides at least a 64.5% saving in CPU time.

6.5.2 Waveform Accuracy

The effect on the waveform accuracy of the number of harmonics considered is not as severe with a QSW waveforms since, in this case, the higher order harmonics have smaller magnitudes and their contribution to the torque waveform is small. Figures 6.4(a) to (c) show the torque waveform for a QSW case, obtained using the frequency-domain model under the same conditions as those of figure 6.3.

The equations describing the frequency-domain analysis were linearized to permit superposition, by assuming a constant steady-state rotor speed. It was demonstrated in chapter 5 that torque harmonics produce speed oscillations, and although their effect is insignificant for a high frequency or PWM pulse number, it may nevertheless become appreciable for a lower operating frequency or PWM pulse number.

Figures 6.5(a) to (c) show torque waveforms, with the solid and dotted traces illustrating respectively results from the frequency-domain and the direct-phase models. The discrepancy between the traces is particularly significant for the QSW 1Hz operation shown in figure 6.5(a), where the speed ripple is noticeable, as was also shown earlier in figure 5.12(d). With the elimination of low order harmonics and the reduction of

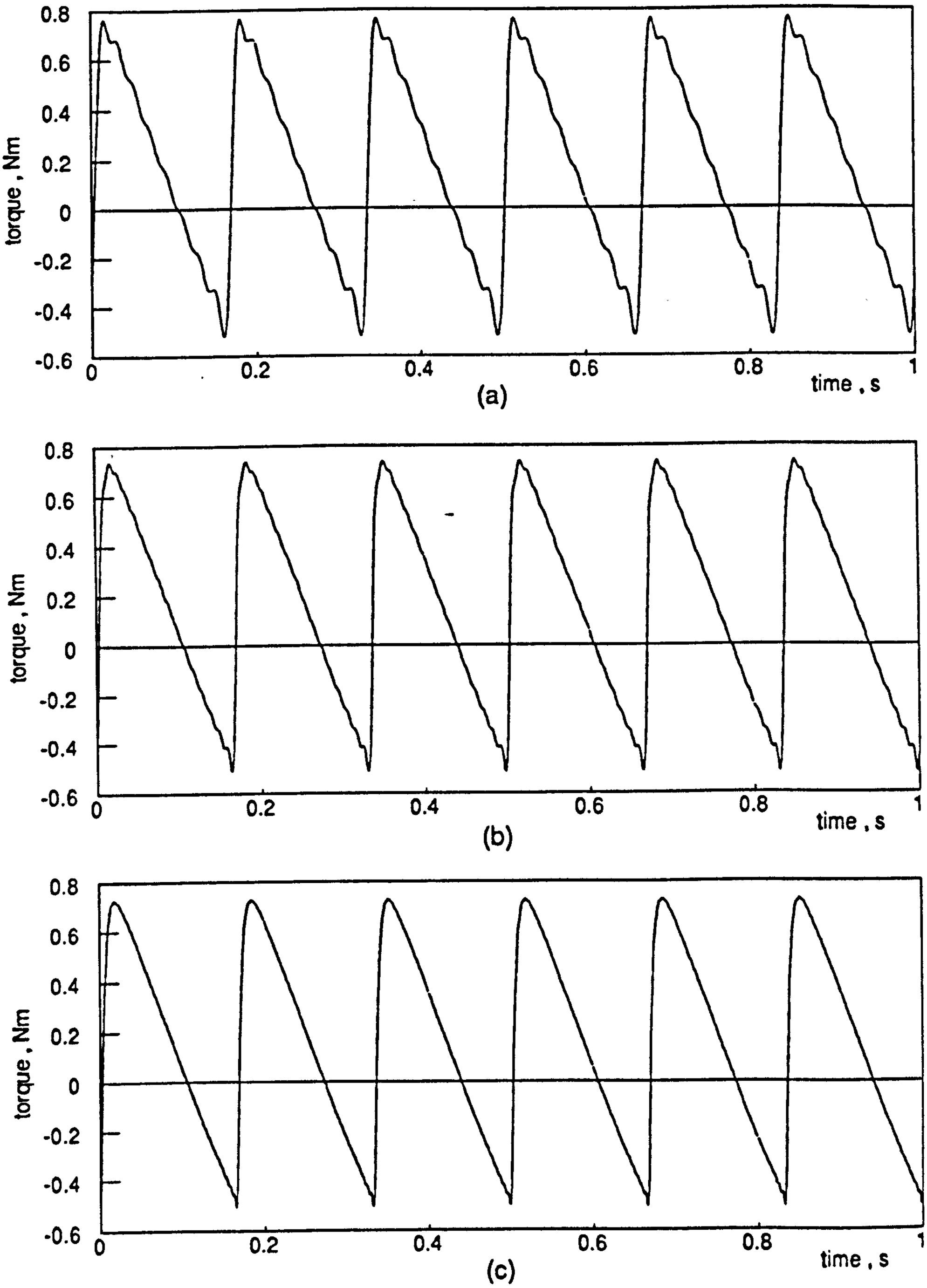

Figure 6.4 Electromagnetic torque waveforms obtained from the frequency-domain model for a QSW mode inverter driving unloaded motor at 1Hz stator frequency (a) 50 harmonics (b) 100 harmonics (c) 200 harmonics , are included

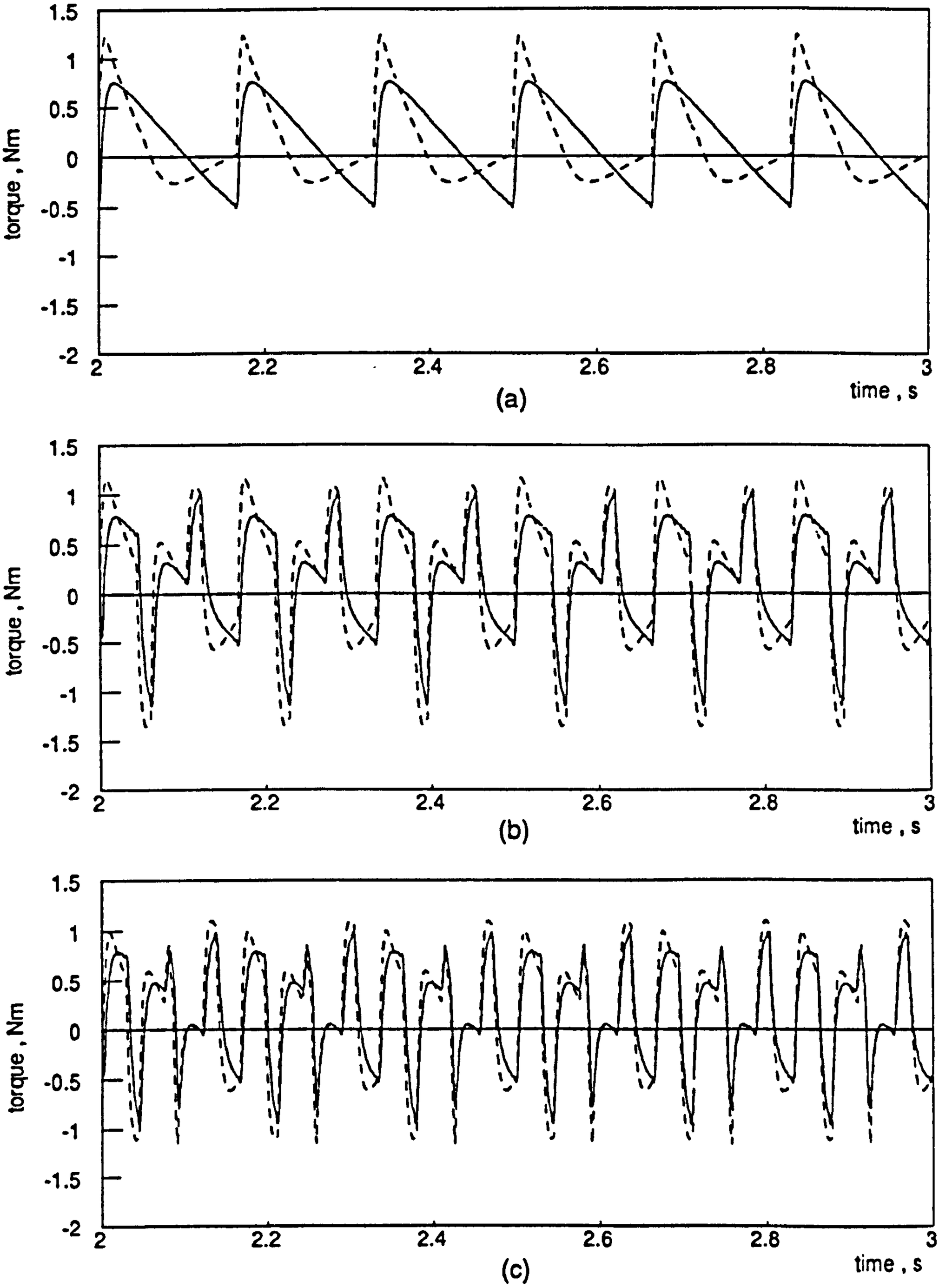

Figure 6.5 Computed electromagnetic torque from direct-phase model (dotted line) frequency-domain model (continuous line) for 1Hz frequency, no-load operation (a) QSW operation mode (b) PWM2 (c) PWM4 elimination strategy modes

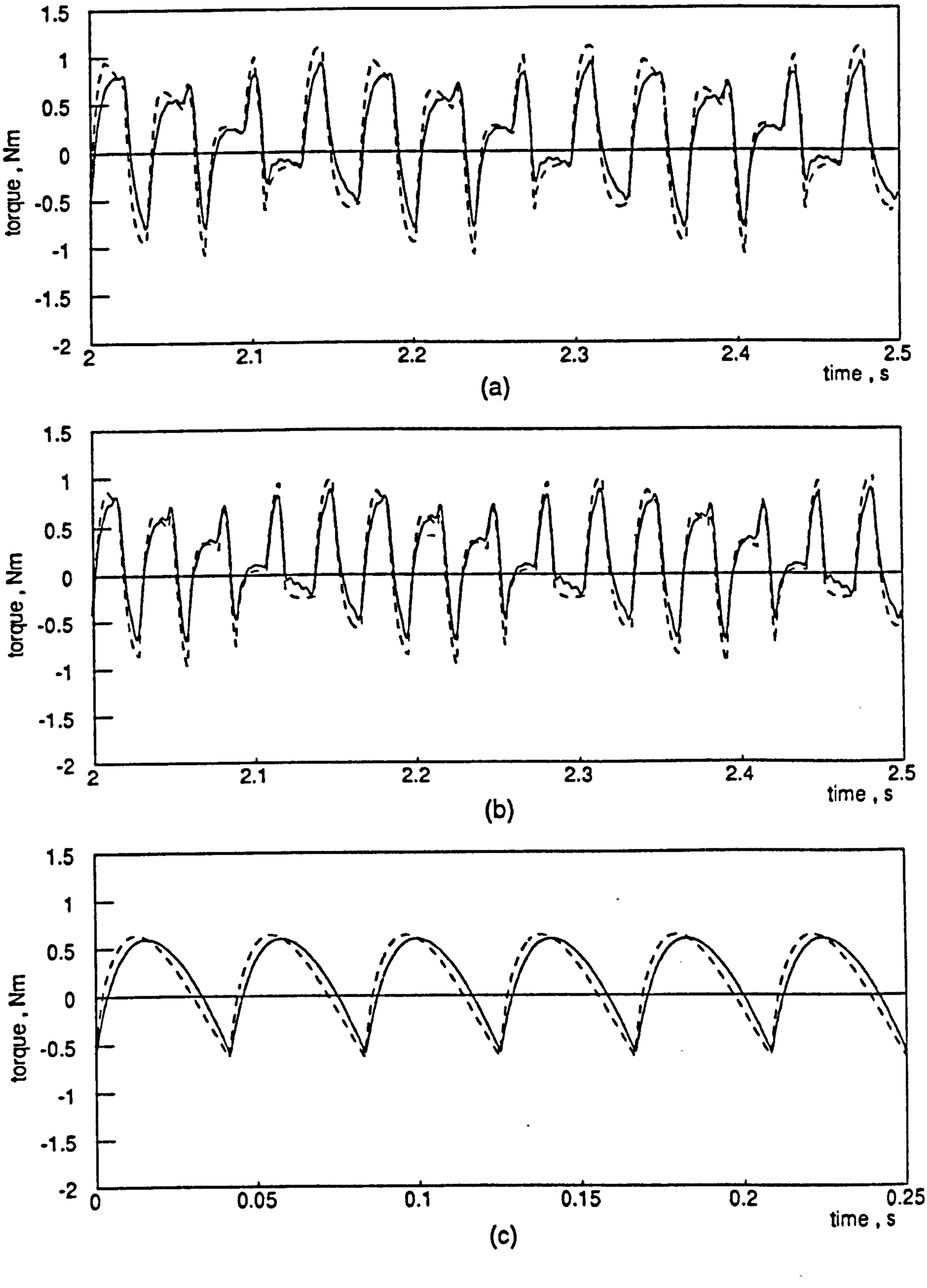

Figure 6.6 Computed electromagnetic torque from direct-phase model (dotted line) frequency-domain model (continuous line) no-load operation (a) PWM6 and (b) PWM8 elimination strategy modes displaying half-cycle at 1Hz frequency (c) QSW mode operating at 4Hz frequency

speed deviation around its average value, the constant speed assumption becomes closer to reality. This results in a closer correspondence between the two traces, as shown in figures 6.5(b) and (c), representing PWM modes with two and four switching angles per quarter-cycle respectively. Figures 6.6(a) and (b) with six and eight switching angles per quarter-cycle, show even better correlation. Figure 6.6(c) shows the torque waveform for 4Hz QSW operation which, when compared with figure 6.5(a), provides further confirmation that a higher operating frequency results in a reduced speed ripple, and consequently a reduced error in the frequency-domain model.

The discrepancies between harmonic torque components as predicted using the two models are assessed in table 6.4. These results, obtained for the same operating conditions as figures 6.5 and 6.6, show good agreement and verify that the frequency-domain model predicts the machine performance with an acceptable accuracy. An increase in the remaining harmonics is evident when the low order ones are eliminated, as verified earlier.

TABLE 6.4

Harm. order	6		12		18		24	
mode	*direct phase*	*freq. dom.*	*direct phase*	*freq. dom.*	*direct phase*	*freq. dom.*	*direct phase*	*freq. dom.*
1Hz QSW	0.388	0.329	0.170	0.148	0.100	0.091	0.066	0.061
PWM2	0.018	0.000	0.500	0.416	0.230	0.195	0.210	0.168
PWM4	0.016	0.000	0.015	0.000	0.490	0.410	0.210	0.182
PWM6	0.014	0.000	0.010	0.000	0.015	0.000	0.460	0.392
PWM8	0.018	0.000	0.005	0.000	0.003	0.000	0.010	0.000
4Hz QSW	0.379	0.330	0.102	0.100	0.055	0.044	0.035	0.030

TABLE 6.4 continued

Harm. order	30		36		42		48	
mode	*direct phase*	*freq. dom.*	*direct phase*	*freq. dom.*	*direct phase*	*freq. dom.*	*direct phase*	*freq. dom.*
1Hz QSW	0.051	0.044	0.039	0.034	0.029	0.026	0.028	0.021
PWM2	0.180	0.153	0.150	0.111	0.080	0.063	0.067	0.042
PWM4	0.008	0.004	0.197	0.155	0.166	0.130	0.048	0.032
PWM6	0.198	0.154	0.008	0.003	0.008	0.005	0.160	0.133
PWM8	0.410	0.360	0.190	0.140	0.006	0.003	0.004	0.002
4Hz QSW	0.026	0.020	0.019	0.015	0.018	0.0088	0.008	0.006

6.6 Speed Ripple and Positional Error Analytical Expressions

The torque expression of equation 6.19 was derived assuming the speed to remain constant during steady-state operation. Nevertheless, its accuracy of prediction permits the derivation of an analytical expression for speed ripple, which in turn provides a qualitative factor for the harmonic torque components. Substituting for T_f , T_e and T_m , from equations 5.20, 6.20 and A.1.5 respectively, in equation 5.18, and neglecting the windage losses which form a negligible proportion of the total mechanical losses, yields

$$p\omega_m = \left(\frac{1}{J}\right)\left[\sum_{k=ks=kr}[T_{e0}]_k + \sum_h T_{eh}\sin(h\omega_s t + \delta_h)\right.$$
$$\left. -\left(\frac{K_\phi V_T + K_\phi^2 \omega_m}{R}\right) - (T_c + K_v\omega_m)\right] \qquad 6.21$$

Previous authors [32-34] neglected also viscous and transmission losses when deriving a speed ripple expression. This is however not the case in the present work, since these losses are seen as providing additional damping on the speed

ripple and generalise the analysis for different types of load. An analytical expression for the speed ripple is obtained by removing the mean value of torque from equation 6.21, which enables the speed ripple function to be written as

$$p\Delta\omega_m = \left(\frac{1}{J}\right)\left[\sum_h T_{eh}\sin(h\omega_s t+\delta_h)-\left(\frac{K_\phi^2+K_v R}{R}\right)\Delta\omega_m\right] \qquad 6.22$$

which may be re-arranged as

$$p\Delta\omega_m+\alpha\Delta\omega_m = \left(\frac{1}{J}\right)\sum_h T_{eh}\sin(h\omega_s t+\delta_h) \qquad 6.23$$

where

$$\alpha = \frac{K_\phi^2+K_v R}{RJ}$$

Use of an integration factor $e^{\alpha t}$ reduces equation 6.23 to

$$\Delta\omega_m e^{\alpha t} = \left(\frac{1}{J}\right)\int_0^t \sum_h T_{eh}\sin(h\omega_s t+\delta_h)e^{\alpha t}\,dt \qquad 6.24$$

and after integrating the right-hand side of equation 6.24 twice by parts and re-arranging

$$\Delta\omega_m = \frac{1}{J(\alpha^2+h^2\omega_s^2)}\left[\sum_h \alpha T_{eh}\sin(h\omega_s t+\delta_h)\right.$$
$$\left.-\sum_h h\omega_s T_{eh}\cos(h\omega_s t+\delta_h)\right] \qquad 6.25$$

since the constant of integration is irrelevant to the peak-to-peak speed ripple function. This equation may be solved, to obtain the variation of ω_m between the lowest and highest value.

During steady-state sinusoidal operation, the rotor angular position increases linearly with time, but with an inverter

drive, the speed ripple causes the rotor to experience periodic deviations from a true linear response. This positional error may be expressed as the integral of the rotor speed ripple

$$\Delta\theta_m = \int_0^t \Delta\omega_m \, dt \qquad 6.26$$

Substituting equation 6.25 into equation 6.26 and integrating yields

$$\Delta\theta_m = -\frac{1}{J(a^2+h^2\omega_s^2)} \left[\sum_h \frac{a}{h\omega_s} T_{eh}\cos(h\omega_s t+\delta_h) + \sum_h T_{eh}\sin(h\omega_s t+\delta_h)\right] \qquad 6.27$$

where the integration constant is again suppressed. Equations 6.25 and 6.27 provide simple analytical expressions for $\Delta\omega_m$ and $\Delta\theta_m$, in terms of the harmonic torque components and their phase angles.

Figure 6.7 shows speed ripple waveforms obtained using equation 6.25, and corresponding to the operating conditions of figures 5.12 to 5.16. With the exception of the QSW mode, and as the pulse number increases for the PWM modes, these frequency-domain results show improved correspondence with those obtained from the direct-phase model and the experimental results presented in Chapter 5. Figures 6.8 and 6.9 show positional error waveforms obtained using respectively equation 6.27 of the frequency-domain model and the direct-phase model. They indicate a good correlation and verify the mathematical manipulation followed in deriving equations 6.25 and 6.27.

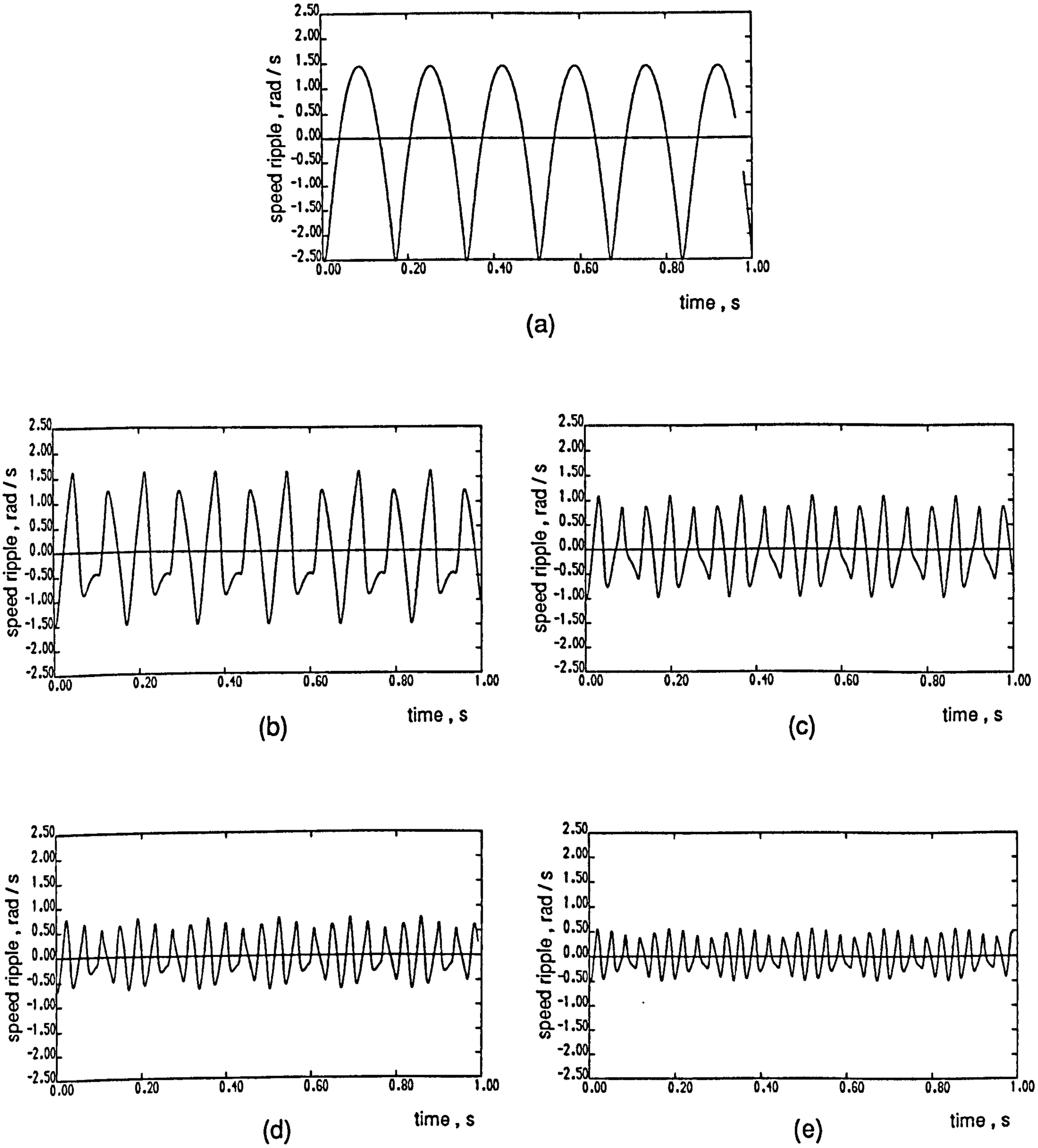

Figure 6.7Speed ripple waveforms obtained using the frequency-domain model for 1 Hz , no-load operation , for: (a) QSW (b) PWM2 (c) PWM4 (d) PWM6 (e) PWM8

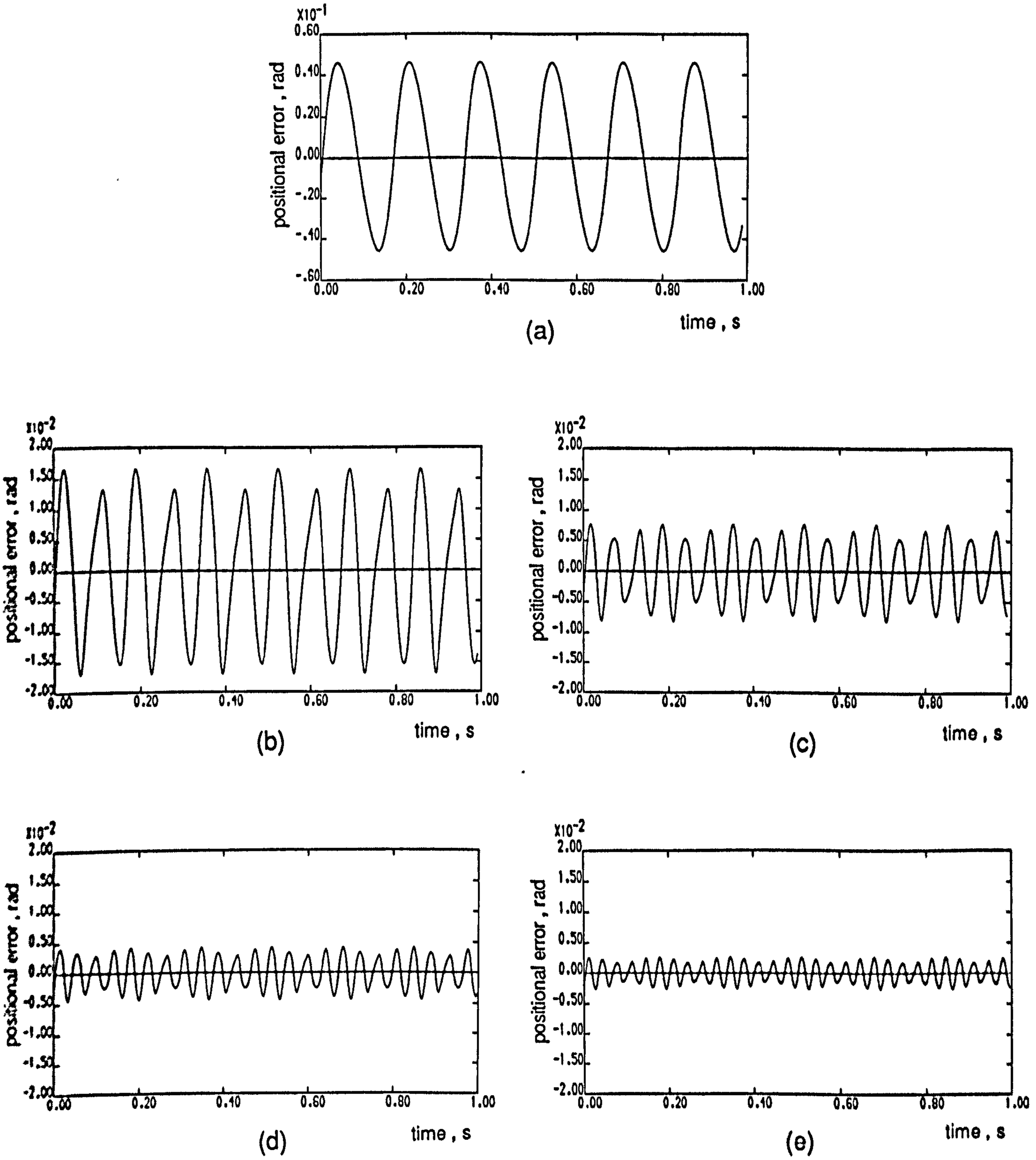

Figure 6.8 Positional error waveforms obtained using the frequency-domain model for 1 Hz , no-load operation , for: (a) QSW
(b) PWM2 (c) PWM4
(d) PWM6 (e) PWM8

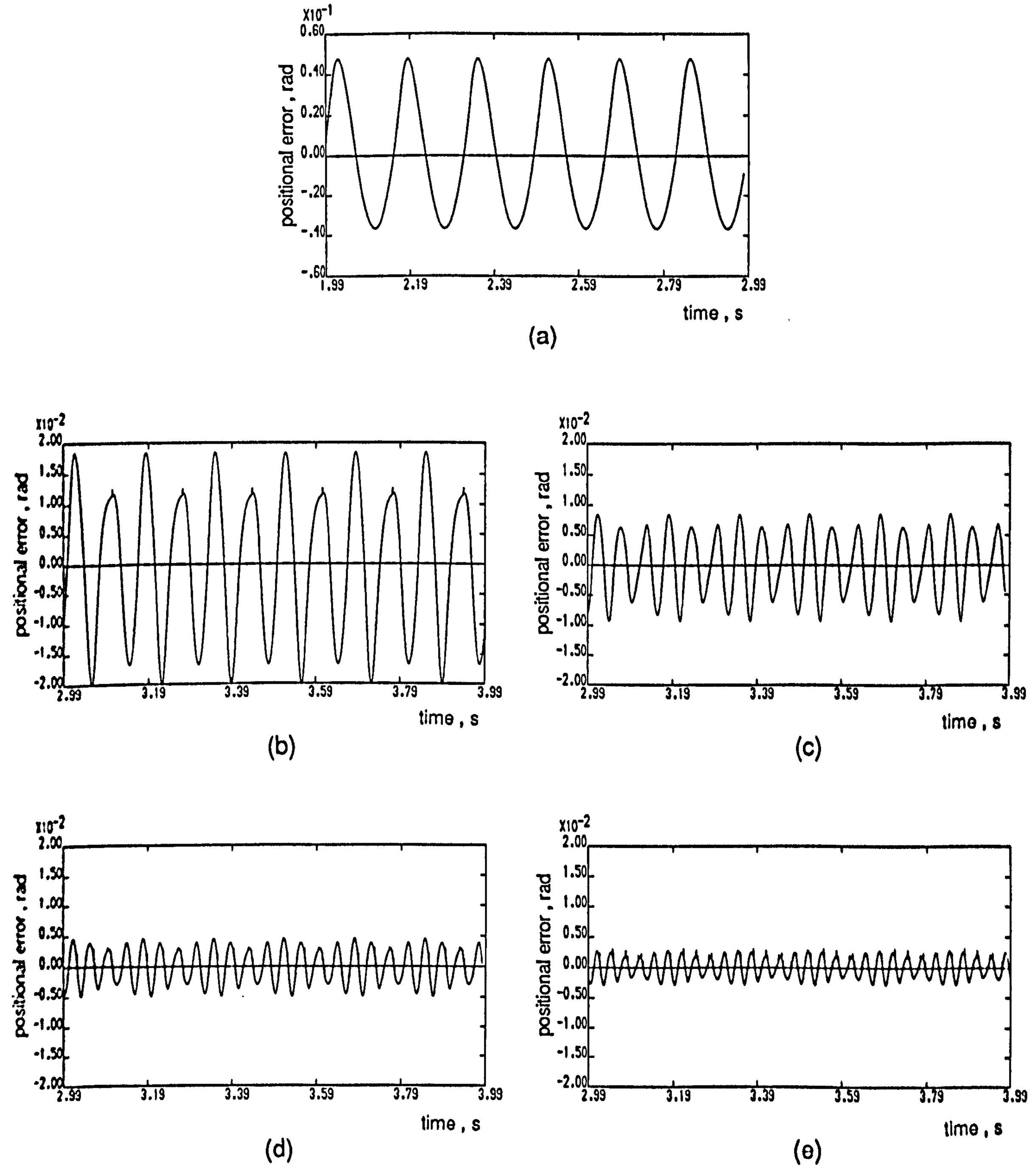

Figure 6.9 Positional error waveforms obtained using the direct-phase model for 1 Hz , no-load operation , for: (a) QSW (b) PWM2 (c) PWM4 (d) PWM6 (e) PWM8

6.7 Performance Criteria

In the following sections different performance indices are defined and investigated, based on the analysis outlined in the previous sections. Each of these criteria could form a design requirement for a certain application, and a specific PWM strategy may be designed in each case.

6.7.1 Total Harmonic Current Distortion

Motor efficiency may be regarded as an important performance index, when designing a PWM strategy to minimize the machine harmonic losses. Efficiency optimization has often placed an emphasis on minimizing copper losses [83], which proved to give near optimam results for other types of harmonic losses [48]. A simplistic method of assessing copper losses for different operating modes is based on the sum of the rms values of the stator harmonic current components, with the total harmonic current distortion factor (THD) defined by

$$THD = \frac{\sqrt{\sum_{n=2}^{l} I_{s(n)}^2}}{I_{s(1)}} \cdot 100\% \qquad 6.28$$

where l is the highest harmonic order under consideration.

Figure 6.10 shows the variation of harmonic distortion with frequency, as predicted for no-load operation using both frequency-domain and direct-phase models. The figure illustrates that, in the frequency range (20-50)Hz, harmonic distortion appears to be constant for each of the modes considered. Moreover, it indicates that the QSW mode has the highest harmonic distortion, which decreases as successive pairs of low order harmonic components are eliminated with the PWM modes. Below 20Hz, the harmonic distortion begins to decrease for the QSW mode, with a more rapid decrease below 10Hz, until at 5Hz it becomes even lower than other PWM modes. This behaviour may be attributed to the variation of motor input impedance with frequency and interaction with the terminal

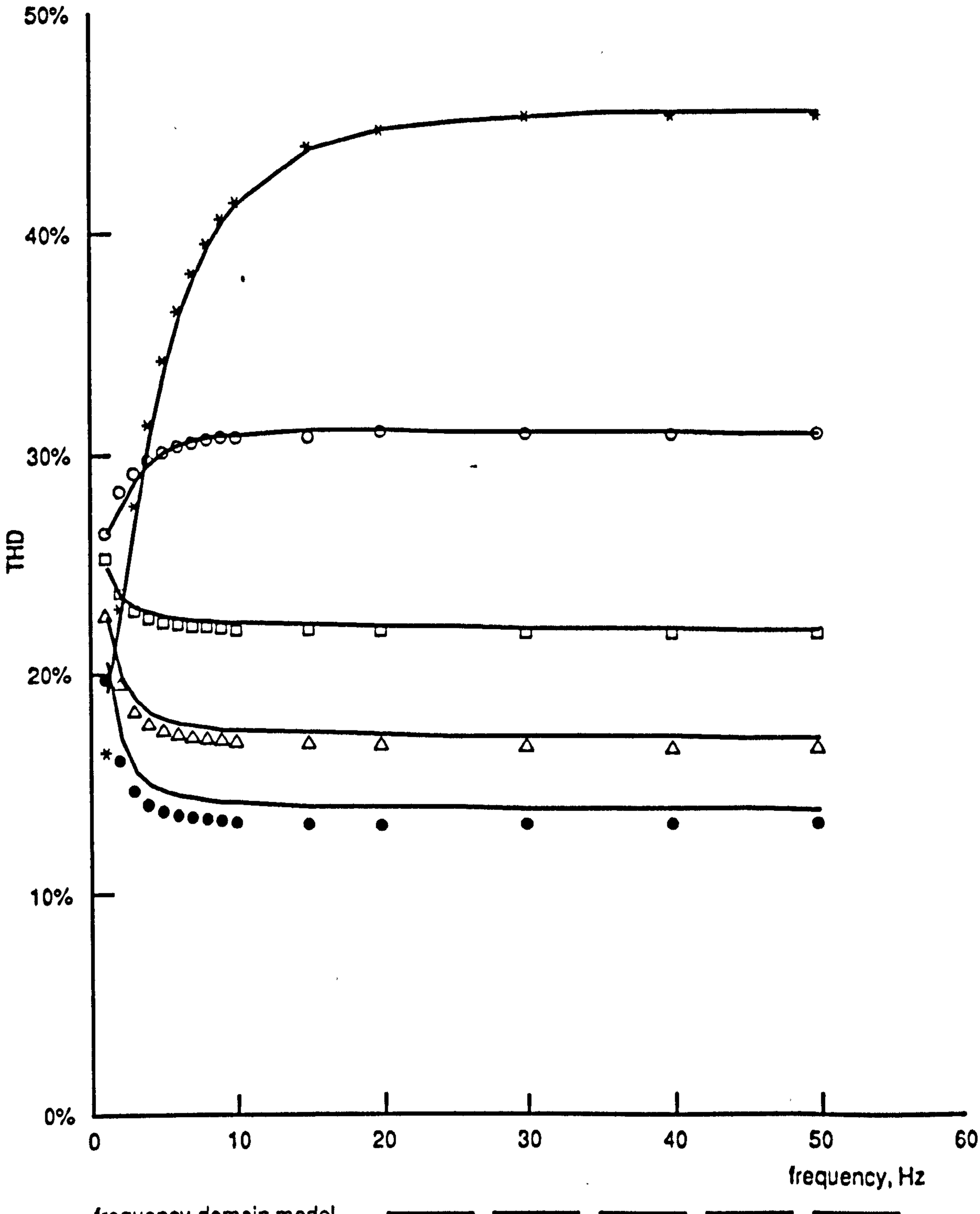

Figure 6.10 Harmonic distortion against operating frequency , no-load operation

voltage. The input impedance, given by equation 6.8, depends on a moderately constant resistive component and a reactive component decreasing with frequency, while the terminal voltage decreases with frequency even with the voltage boost at low frequencies shown earlier in figure 2.6 . As the frequency is reduced, the contribution of the reactive part becomes progressively less significant, leaving the magnitude of the input impedance depending mainly on a constant resistive component. The decreasing terminal voltage produces reduced low order harmonic current components at low frequencies, which result in a lower distortion factor. When the machine is loaded, the fundamental current component increases without a significant increase in the harmonic components. This results in a reduced distortion factor for all modes of operation, as shown in figure 6.11 for the full-load operating condition.

Moreover, it may be concluded from figures 6.10 and 6.11 that the increase in the remaining harmonic voltage and current components when the low order voltage components are eliminated is more pronounced at low frequency operation, since high order current components are increasingly attenuated by the reactive part of the machine input impedance as the input frequency is increased.

6.7.2 Torque Pulsations

At low operating frequencies, the increased magnitudes of the remaining high order harmonic torque components may excite high frequency mechanical resonances unnoticeable in quasi-square wave operation. If the application prohibits the use of a damping coupling, the small damping present in the rotor shaft may be insufficient to reduce the order and magnitude of these resonances and dangerous stresses may arise leading to possible torsional shaft failure.

It has been demonstrated that harmonic torque components are induced by interaction between stator and rotor current

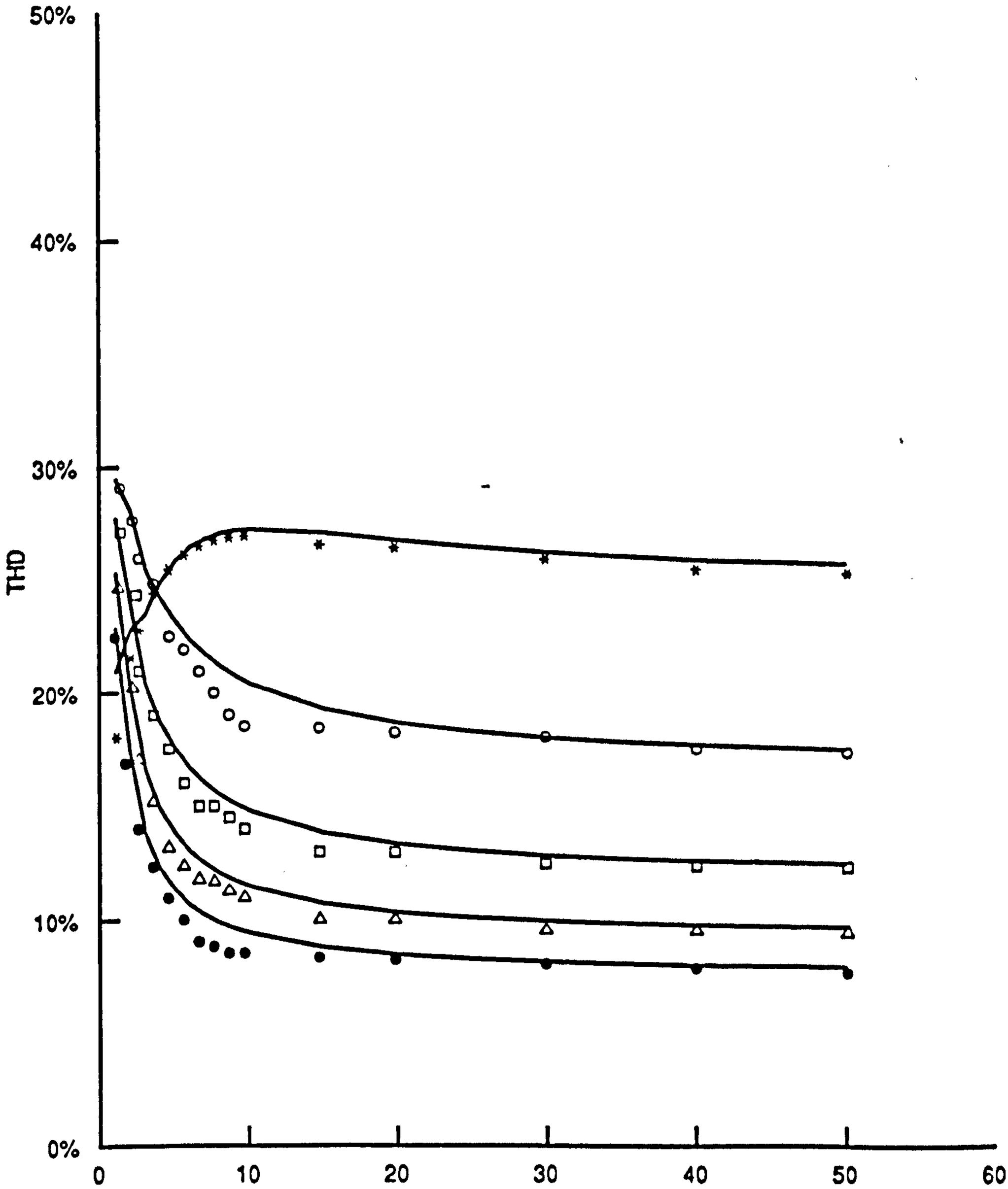

Figure 6.11 Harmonic distortion against operating frequency full-load operation

components of different orders. To understand the characteristics of the resultant harmonic torque, each component must be analysed in terms of the current harmonics which produced it. Figures 6.12(a) and (b) show respectively the phasor representation of the 6th-harmonic torque components and their phasor sum, as produced by the group of currents (1,5) and (1,7) for no load conditions and over the operating frequency range 1Hz-50Hz. It illustrates how the phasor locus of each component, which is determined by the phase angles of current harmonics, depends on the operating frequency. At low frequencies, the 6th-harmonic torque components are small, but their phasor sum produces an enhanced resultant. As the frequency increases the harmonic magnitudes also increase, but their phasor sum remains approximately unchanged due to mutual cancellation of harmonic torques of the same order.

The effect of mutual cancellation can be confirmed by considering the higher harmonic torque components over the same range of operating frequencies. This is demonstrated in figures 6.13(a) and (b), which illustrate the phasor representation of the 12th-harmonic torque components. As the operating frequency increases, the components of figure 6.13(a) mutually cancel, producing only the resultant shown in figure 6.13(b), even though their individual amplitudes are large.

The peak-to-peak value of torque pulsation provides an approximate assessment of the quality of a torque waveform which contain significant high order components, since these will produce higher sharp edges. Figure 6.14 shows the variation of peak-to-peak torque pulsation with frequency for different modes of operation under no-load conditions. It shows that, below a 2Hz operating frequency, the torque pulsation is lower for the QSW mode than any other mode of PWM elimination strategy, as confirmed earlier. As the frequency and the pulse number increase, the PWM modes show a better performance in terms of this criteria, which can be attributed to the progressive mutual cancellation of high order harmonic torque components. Figures 6.15(a) to (e) illustrate the behaviour of a group of

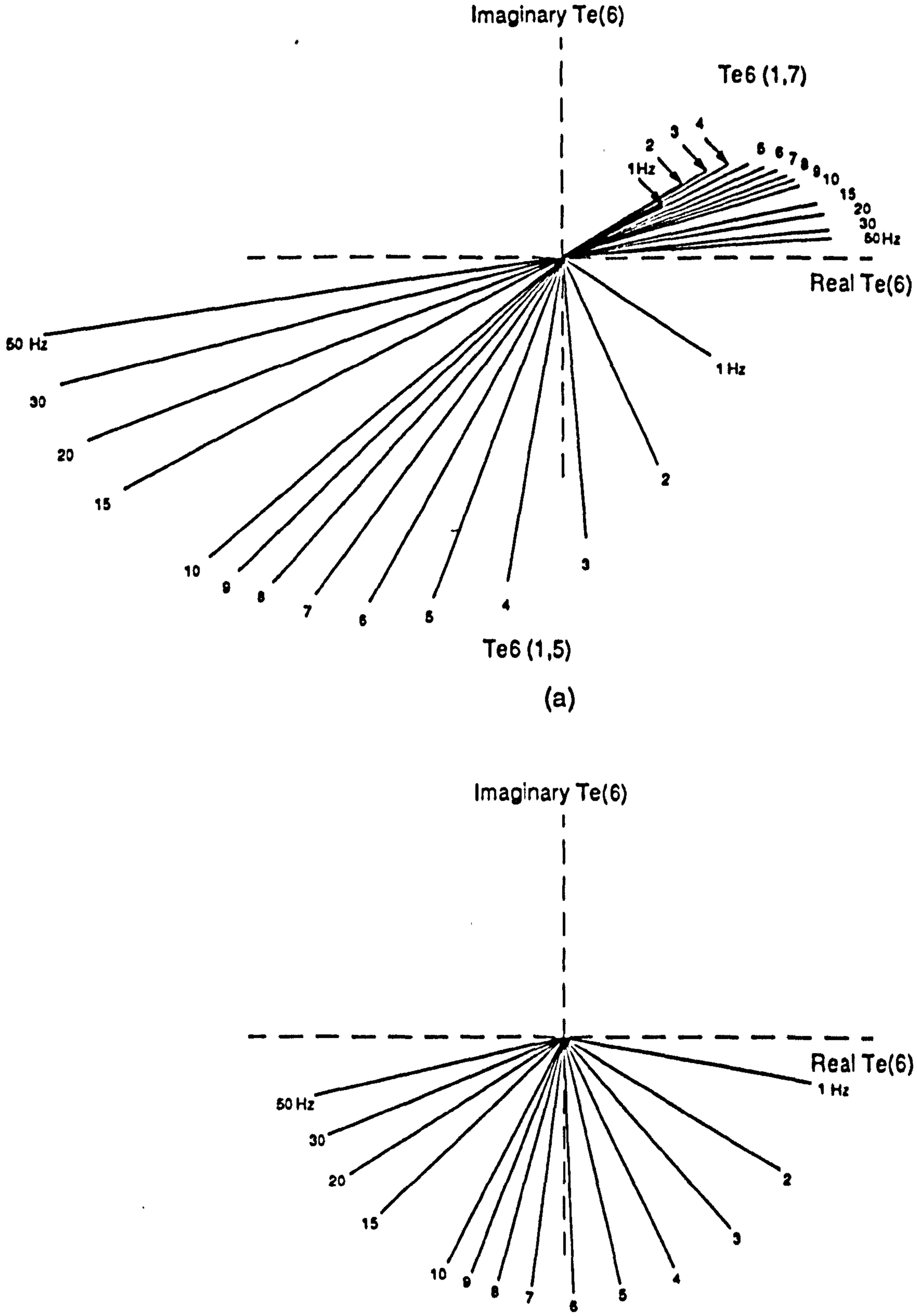

Figure 6.12 (a) Phasor representation of the 6th harmonic torque components
(b) Resultant 6th harmonic torque component
for a QSW mode , no-load operation

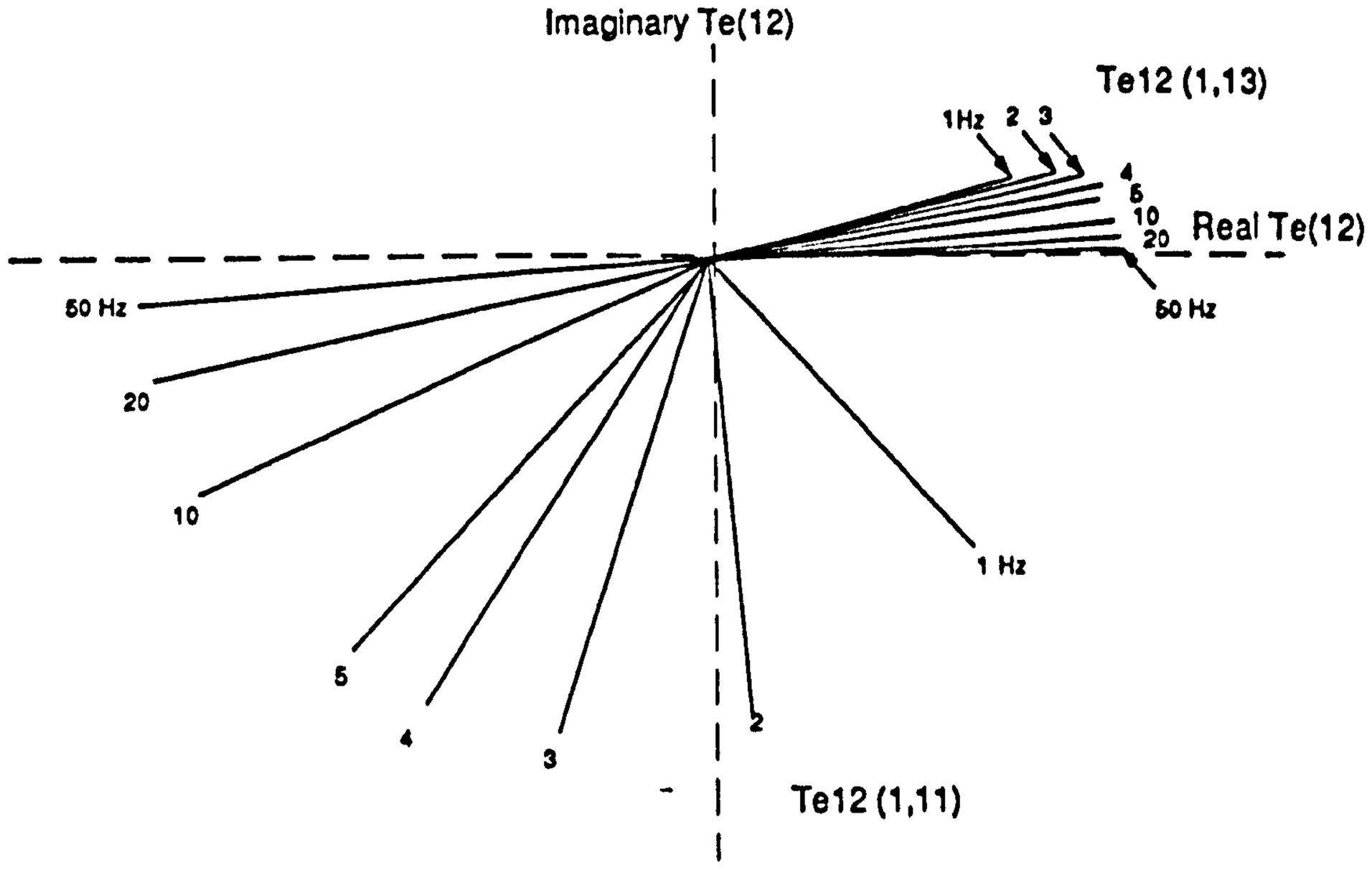

(a)

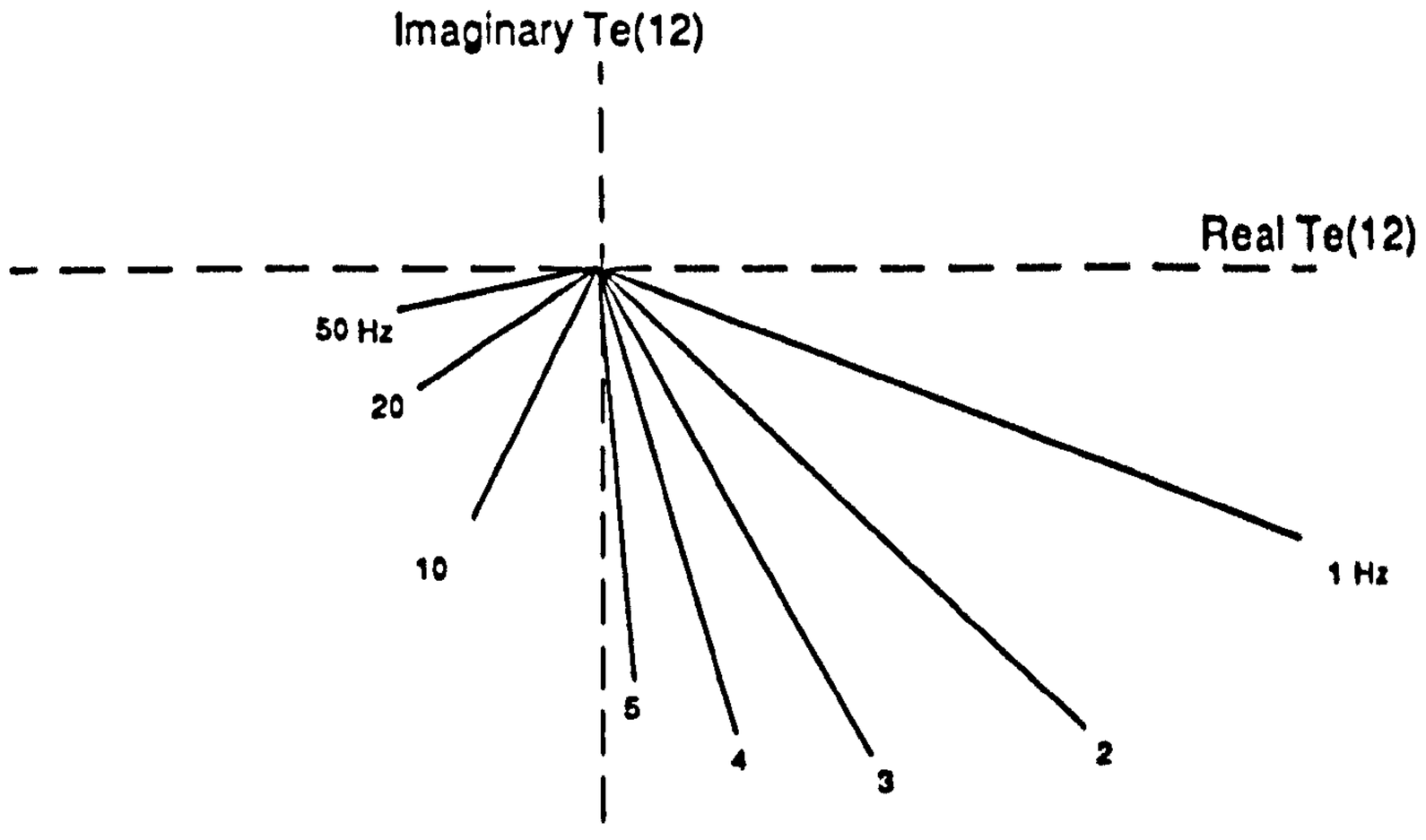

(b)

Figure 6.13 (a) Phasor representation of the 12th harmonic torque components
(b) Resultant 12th harmonic torque components
for a QSW mode , no-load operation

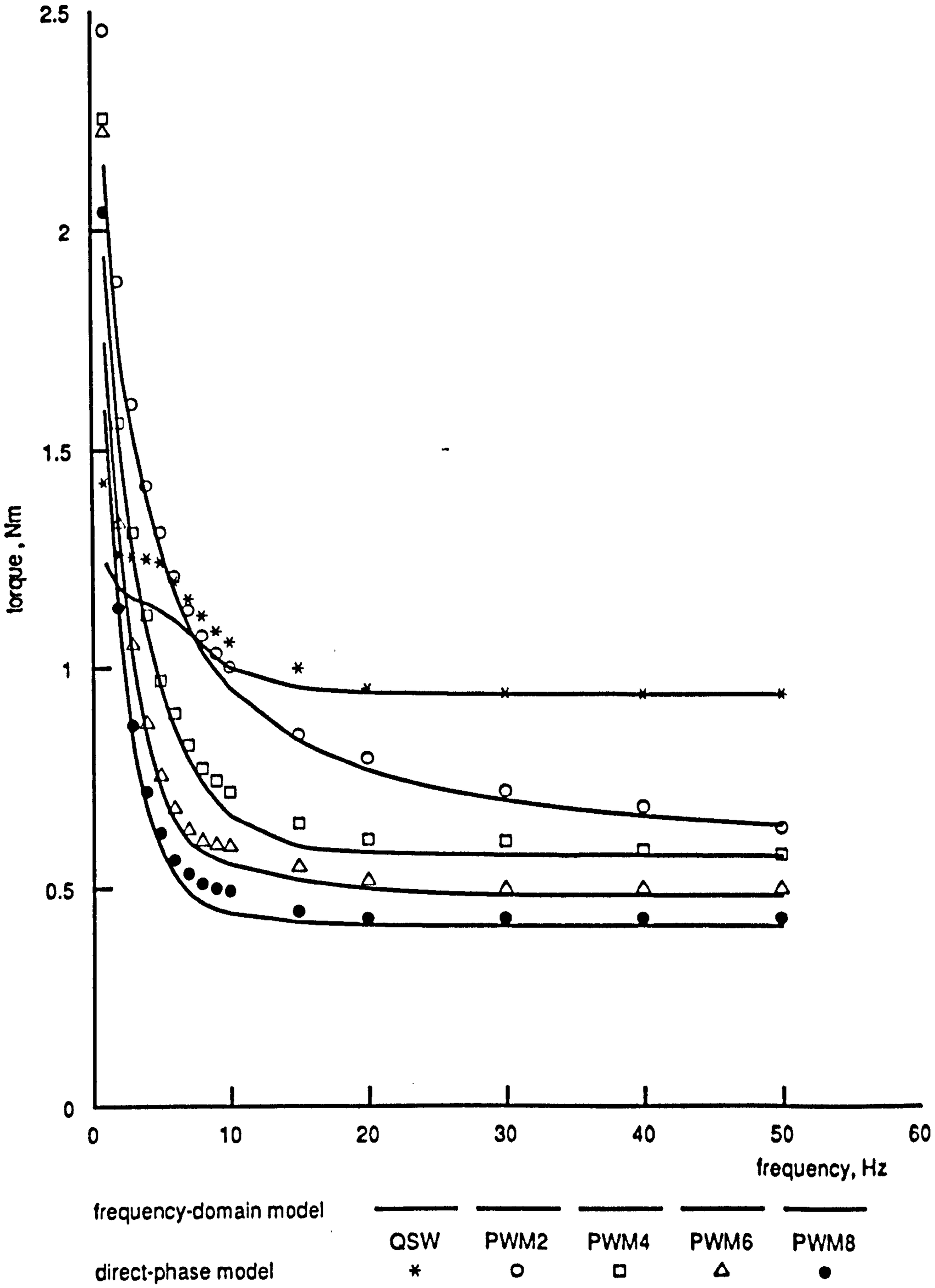

Figure 6.14 Peak-to-peak torque pulsation against operating frequency for no-load operating condition

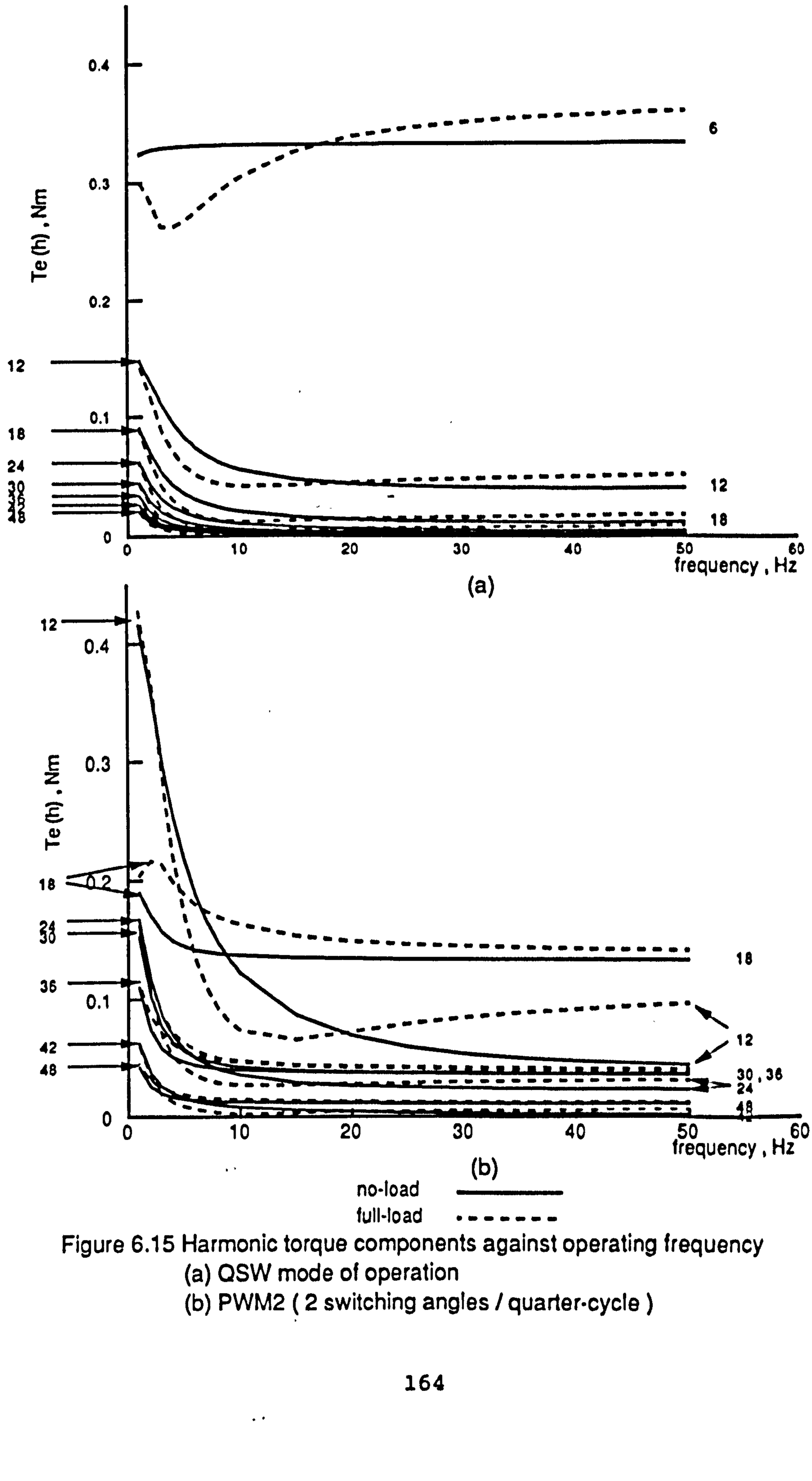

Figure 6.15 Harmonic torque components against operating frequency
(a) QSW mode of operation
(b) PWM2 (2 switching angles / quarter-cycle)

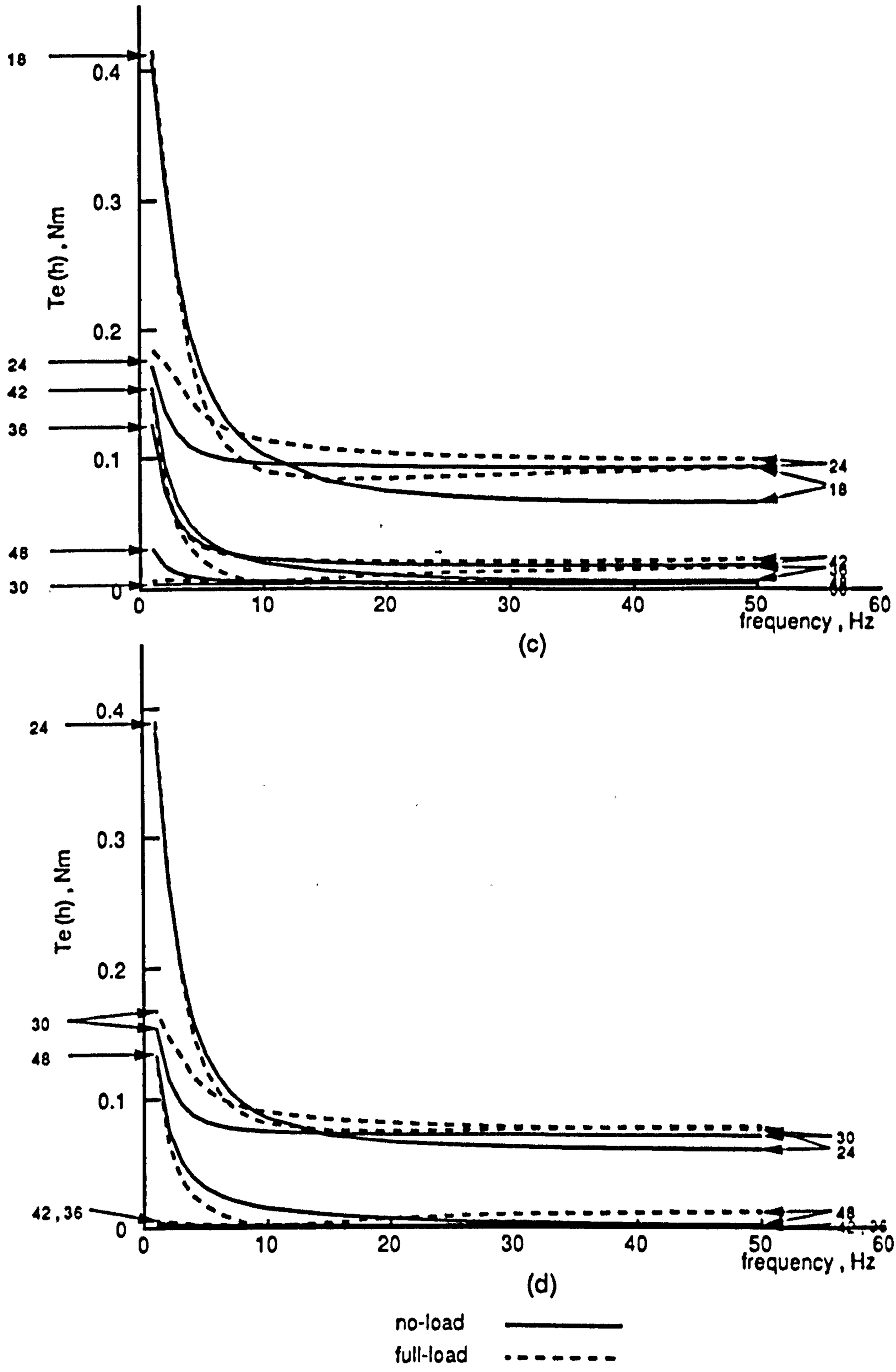

Figure 6.15 continued (c) PWM4 (4 switching angles / quarter-cycle)
(d) PWM6 (6 switching angles / quarter-cycle)

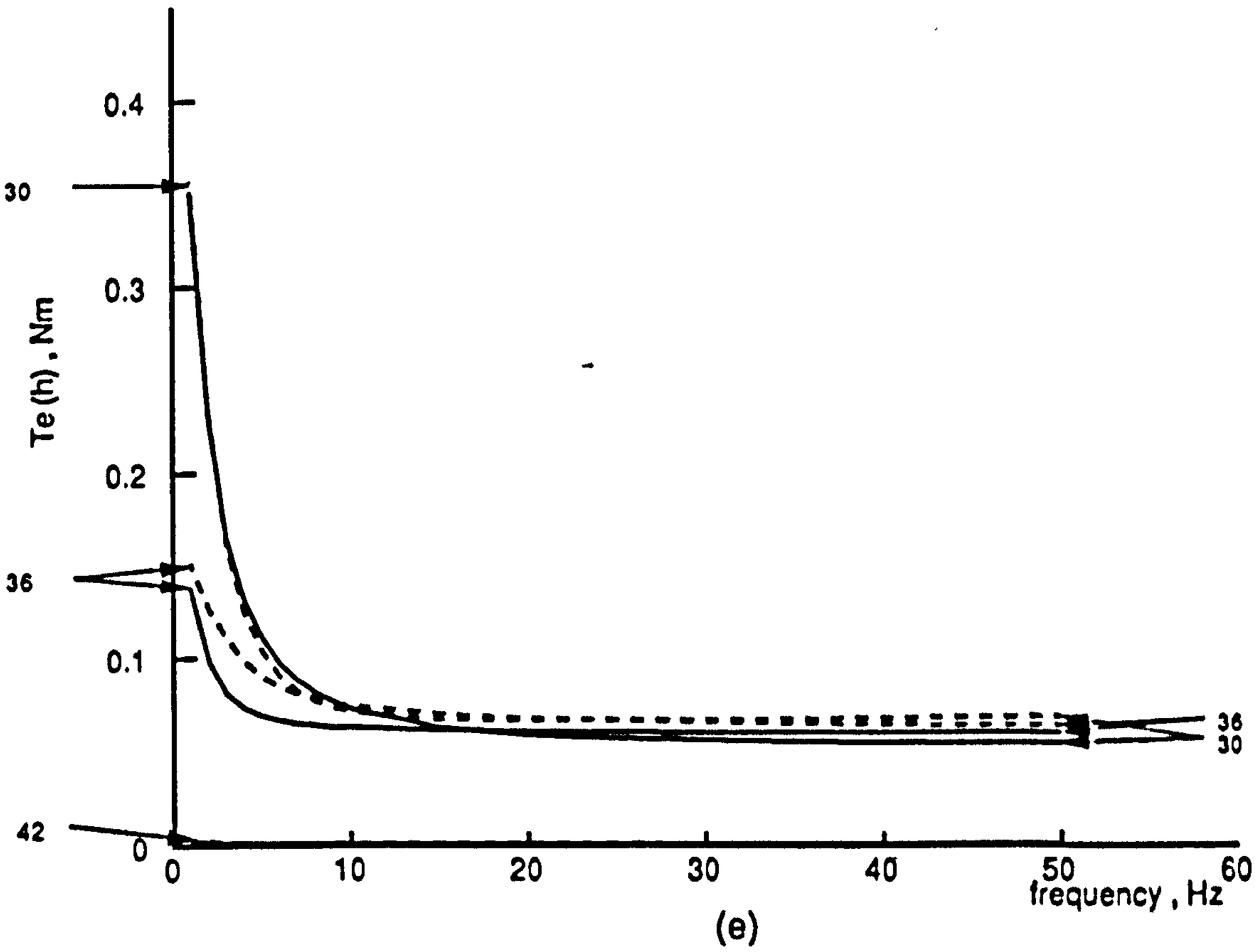

Figure 6.15 continued (e) PWM8 (8 switching angles / quarter-cycle)

these harmonic torque components, and these confirm that at low operating frequencies the remaining harmonic torque components are significantly increased, when compared with the QSW mode, and thus produce higher torque pulsations. As the frequency is increased, high order harmonic torque components decrease, resulting in a reduced torque pulsations.

On loading the machine, the fundamental stator current increases together with the harmonic components, although figure 6.11 shows that the increase in the latter is to a much reduced extent. This results in the slight increase in the torque pulsations evident in figure 6.16.

6.7.3 Speed Ripple and Positional Error

In applications such as machine tool, traction and mill drives, antenna positioning, robotics, etc. rotor speed ripple or positional error represents a design requirement. These features were expressed previously in equations 6.25 and 6.27 and minimisation of these equations with respect to α_i provides a PWM profile which reduces $\Delta\omega_m$ and $\Delta\theta_m$ respectively. This may be achieved by rearranging the equations in terms of the phase voltage harmonics expressed in terms of the undetermined switching angles. This approach is however inefficient and time consuming, since it is necessary to access the subroutine which calculates the peak-to-peak magnitude of each function during the course of numerical minimisation. The problem becomes more severe as the PWM pulse number is increased. To simplify the process, the number of harmonic components considered in the definition of each function may be limited. Moreover, by observing torque, speed and positional error waveforms it can be deduced that one-sixth of a cycle contains sufficient information about the waveform for the minimisation process to be applied.

Figures 6.17 and 6.18 show respectively the variations of $\Delta\omega_m$ and $\Delta\theta_m$ with frequency, for both QSW and PWM modes of operation, computed (for no-load operation) using both models.

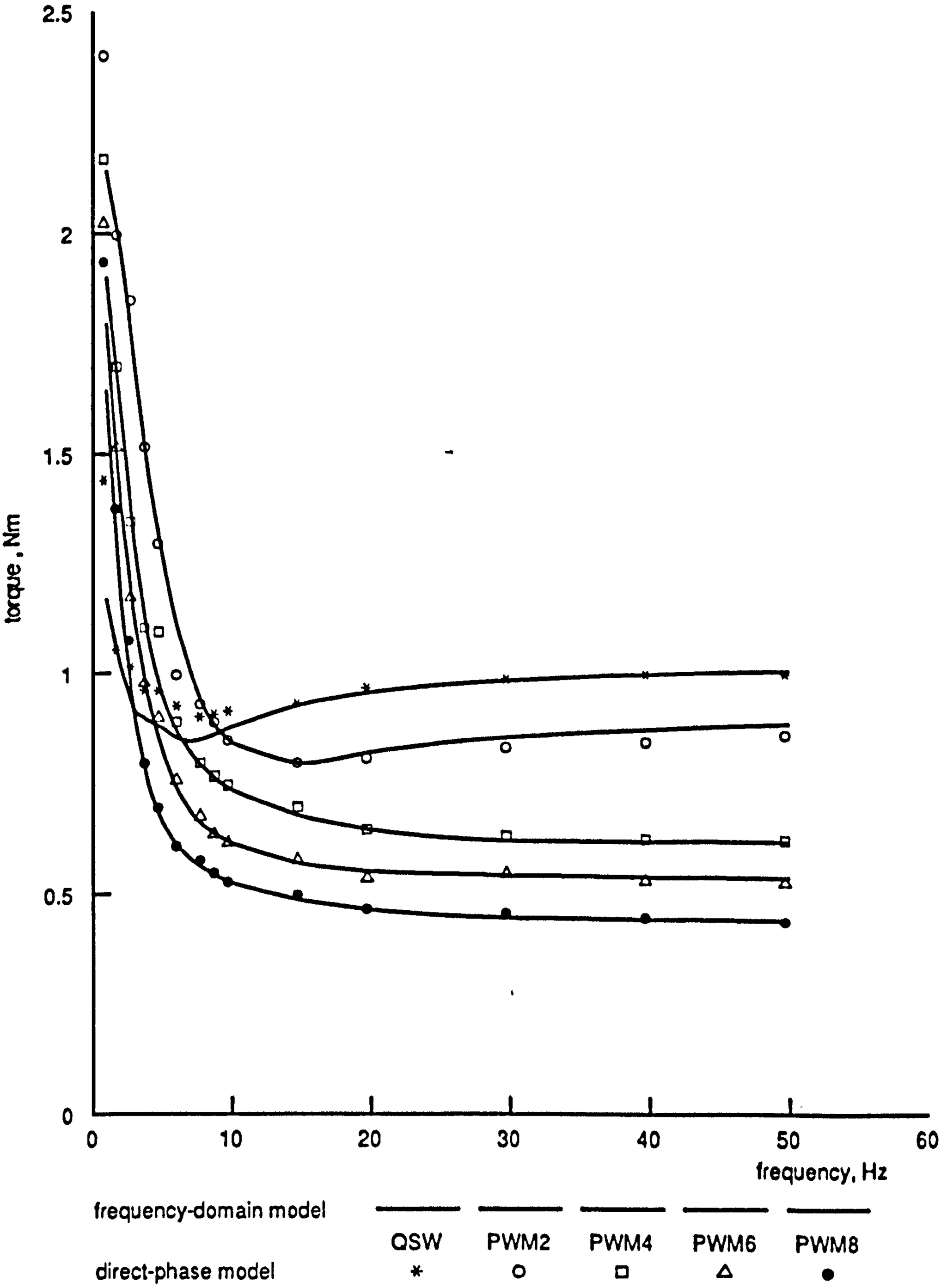

Figure 6.16 Peak-to-peak torque pulsation against operating frequency for full-load operating condition

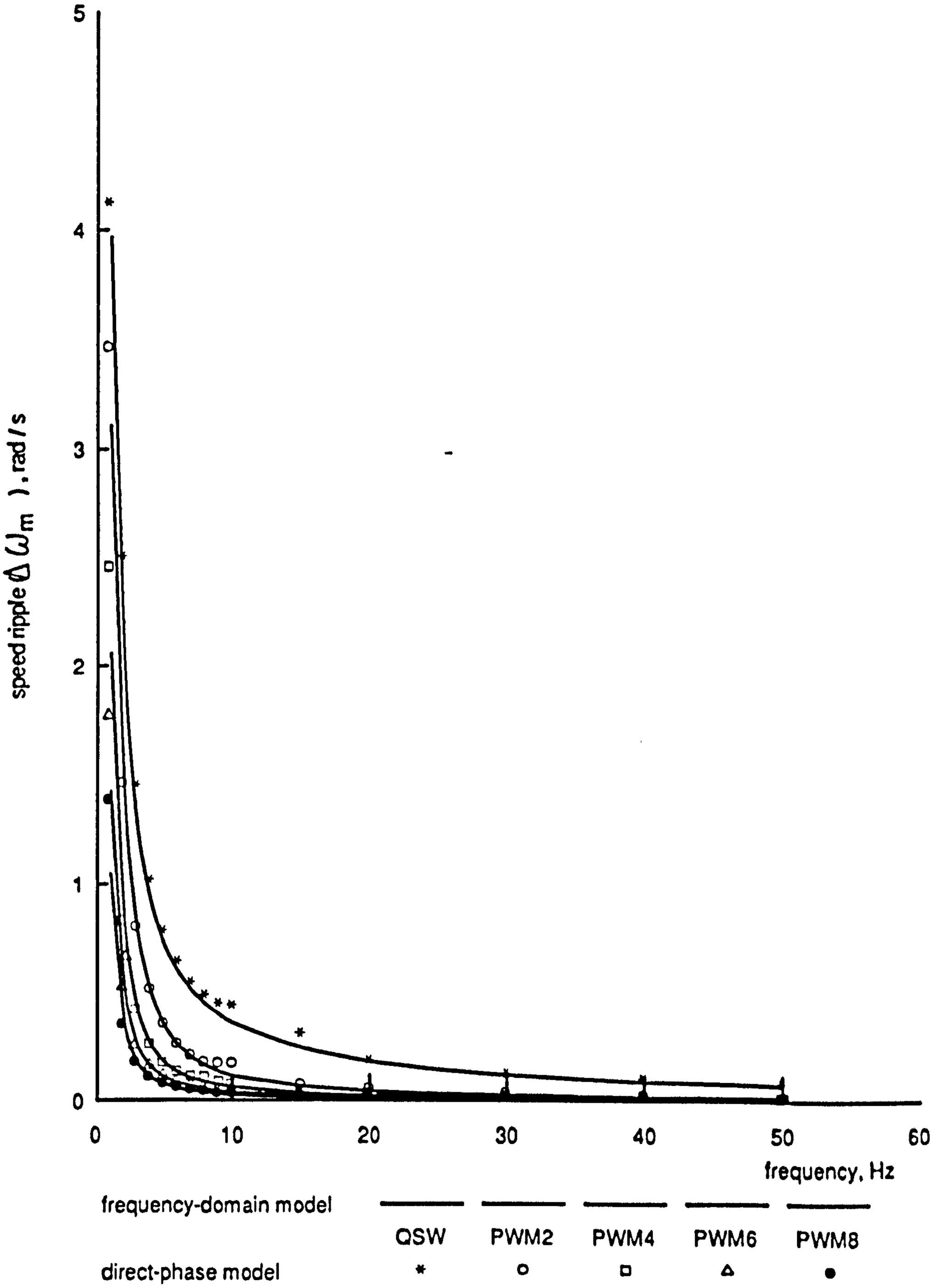

Figure 6.17 Peak-to-peak speed ripple against operating frequency for no-load operation

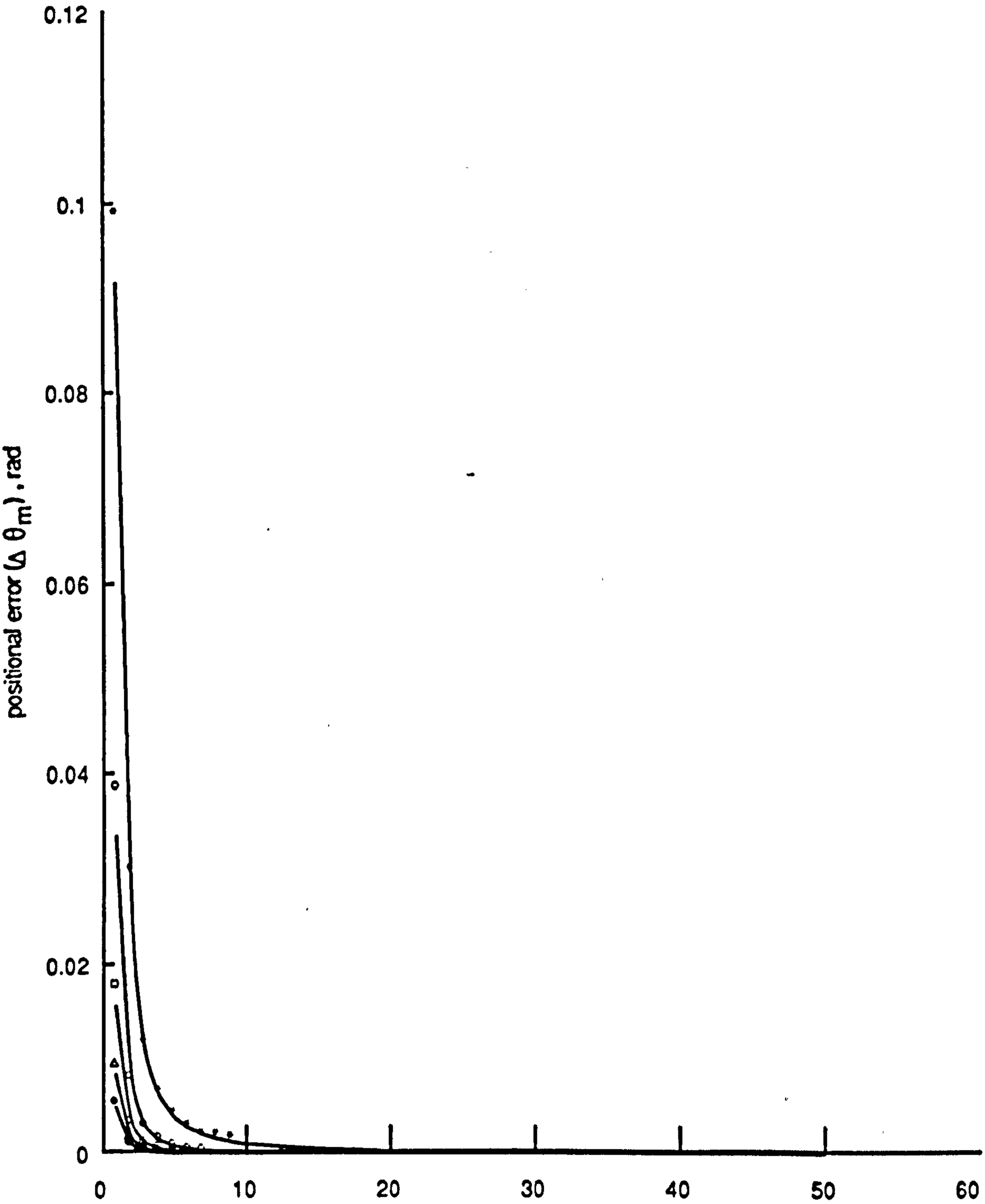

Figure 6.18 Peak-to-peak positional error against operating frequency for no-load operation

These figures illustrate the effect of increasing the operating frequency on the damping and provide a qualitative measure of the extent to which the two factors could be tolerated for any application.

6.8 Conclusion

This chapter has demonstrated the necessity to consider pairs of harmonic voltage components, which produce corresponding current components whose magnitudes and phase angles play an important role in harmonic torque production. It has verified that a frequency-domain model based on the familiar induction motor equivalent circuit may be used as an efficient and fast alternative to the comprehensive time-domain analysis represented by the direct-phase model, provided that certain assumptions that govern its implementation are sufficiently valid for the conditions being considered. At low operating frequencies, low order harmonics suffer from large errors which contribute to some discrepancies in the analysis. Eliminating these will result in closer correlation between results from the two models.

The performance of the harmonic elimination PWM strategy used to remove the low order harmonic voltage components may be examined with the aid of figures 6.17 and 6.18, which show that a worthwhile improvement is obtained in terms of both reduced speed ripple and rotor positional error throughout the operating frequency range. Figures 6.10, 6.11, 6.14 and 6.16 demonstrate that at low frequency, the harmonic losses and torque pulsations for the PWM modes are worse than for the QSW mode, especially for a low pulse number per half-cycle. Using a higher pulse number improves the machine performance, but this requires a better resolution for storing the PWM pattern in a look-up table and incurs higher switching losses in the inverter. Also, it becomes increasingly difficult to obtain an optimal solution as the pulse number is increased.

Higher torque pulsations at low operating frequencies are due to increased magnitudes of the remaining high order torque components. The operating frequency provides a further damping

factor to these components, reducing their magnitudes at higher frequency operation. Hence it is at low operating frequencies where these components are to be treated to minimize their harmful effect.

CHAPTER 7

NEW OPTIMAL PWM STRATEGIES

In this chapter, new strategies are proposed which minimize the harmful effects of torque pulsations without the total elimination of current harmonics. Their implementation with a VSI is unique, as opposed to the usual and more straightforward implementation when using a CSI. Theoretical results are presented, together with practical verification obtained using the experimental system described in chapter 4.

7.1 Harmonic Minimisation Strategies

Harmonic minimisation strategies are dependent on the motor operating conditions, whereas elimination strategies are not. Whether the harmonic losses or the torque pulsations is the performance criterion to be optimized, both are functions of the slip frequency or the phase angle between the current components. These strategies may be derived with a quarter-wave symmetrical PWM voltage switching pattern, similar to the elimination strategy. This produces voltage waveforms whose Fourier series components have either zero or 180° phase displacement. Consequently, the phase angles of the harmonic current components are determined solely by the operating conditions of the machine, and the torque harmonics are reduced only by minimisation of the harmonic current magnitudes. The following sections are devoted to the development of new PWM strategies which manipulate the phase angles and/or the magnitudes of the individual current components, to achieve mutual cancellation between the torque components in an attempt to improve the drive dynamics.

7.2 Harmonic Current Control Techniques

Torque components of order 6n are produced predominantly by the interaction between currents of harmonic orders 1,6n-1 and 1,6n+1. For any quarter-wave symmetrical periodic voltage

waveform, the phase angle between these components increases with operating frequency, as demonstrated for the QSW mode in figures 6.12 and 6.13. For this operating mode, figure 7.1 shows the variation of the phase angle with frequency, at no-load and full-load operating conditions for the 6th, 12th, 18th- and 24th-harmonics. It illustrates that, as the frequency falls below about 10Hz, the phase angle decreases rapidly, resulting in an increased magnitude of the resultant components. At low frequency, cancellation between torque components of the same order may be achieved by equating their magnitudes and re-adjusting their phase angle to $180°$. The phase angle of the torque component depends on the phase angles of the stator and rotor current components with respect to the terminal voltage component. Adjustment of the torque components' phase angles requires easing the quarter-wave symmetry property of the voltage pattern to half-wave symmetry only, so that the harmonic voltage component phasors are no longer mutually in phase or anti-phase at $t = 0$.

At higher operating frequencies and load conditions, the phase angle approaches $180°$, and the resultant torque components consequently have lower magnitudes. It is proposed that, at high frequency, equating only the magnitudes of these components, while maintaining the quarter-wave symmetry property of the voltage pattern, will result in a significant decrease in the resultant torque components.

Both techniques are described in detail below.

7.3 Half-Wave Symmetrical Strategy

Cancellation between torque components of the same order can be achieved by magnitude and phase adjustment of the individual harmonic current components, with equation 6.19 providing the mathematical basis for this mechanism.

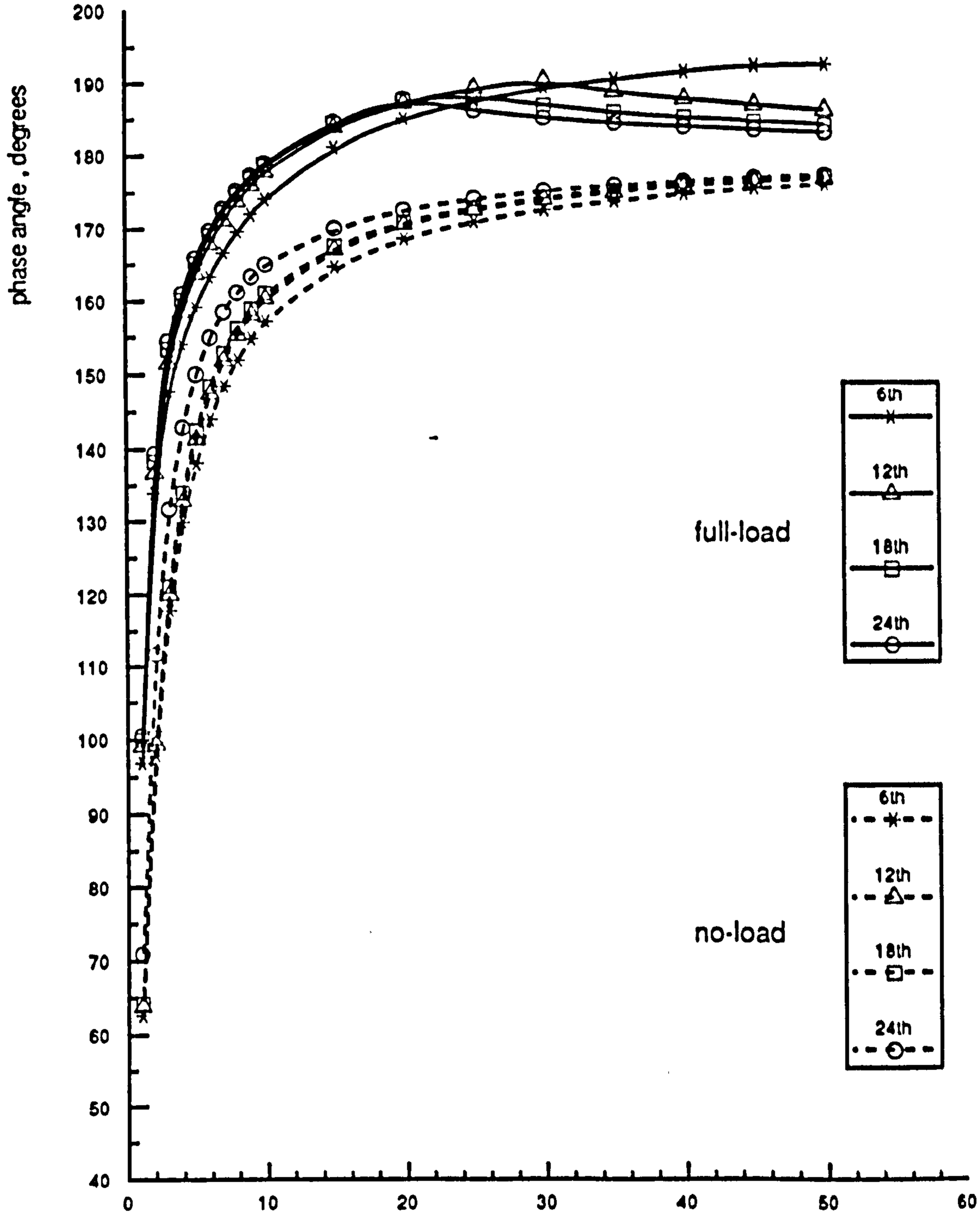

Figure 7.1 Phase angle between harmonic torque components of the same order against operating frequency for quarter-wave symmetrical QSW modes of operation

7.3.1 Solution Organization

The Fourier coefficients for a half-wave symmetrical PWM voltage pattern with α_m switching angles per half-cycle are

$$a_{(n)} = \frac{\sqrt{2}}{(n\pi)} V_{dc} \left(1 + \sum_{(i=1)}^{m} (-1)^i \cos n(\alpha_i) \right) \qquad 7.1$$

and

$$b_{(n)} = \frac{\sqrt{2}}{(n\pi)} V_{dc} \left(- \sum_{(i=1)}^{m} (-1)^i \sin n(\alpha_i) \right) \qquad 7.2$$

where n is the harmonic order, m the number of switching angles per half-cycle and V_{dc} the DC-link voltage. The nth-harmonic component has the rms value

$$V_{(n)} = \sqrt{a^2_{(n)} + b^2_{(n)}} \qquad 7.3$$

and the phase angle calculated in a 4-quadrant plane with real and imaginary axes is

$$\begin{aligned} \Psi_{(n)} &= \tan^{-1} \frac{a_{(n)}}{b_{(n)}} && \text{for } b_{(n)} > 0 \\ &= \tan^{-1} \frac{abs(b_{(n)})}{a_{(n)}} + \frac{\pi}{2} && \text{for } b_{(n)} \leq 0 \ , \ a_{(n)} > 0 \\ &= -\tan^{-1} abs\left(\frac{b_{(n)}}{a_{(n)}}\right) - \frac{\pi}{2} && \text{for } b_{(n)} \leq 0 \ , \ a_{(n)} < 0 \end{aligned} \qquad 7.4$$

The rms components of the stator current may be obtained using equation 6.7, while their phase angles with respect to the reference real axis are obtained using equation 6.9 written as

$$\theta_{s(n)} = \Psi_{(n)} - \tan^{-1} \frac{\Im Z_{i(n)}}{\Re Z_{i(n)}} \qquad 7.5$$

The rotor current components and their phase angles can be obtained using equations 6.10 and 6.11. This procedure interprets the stator and rotor current components with their phase angles in terms of unknown switching instants, whose determination is obtained iteratively during the progression of the optimization process described in the next section.

7.3.2 Mathematical Techniques and Optimization Approach

By analogy with the conventional elimination PWM strategy, the design procedure involves considerations of a set of m equations. The first of these ensures a fundamental voltage component expressed by the equation

$$V_{(1)} = \sqrt{a_{(1)}^2 + b_{(1)}^2} \qquad 7.6$$

while the rest are devoted to providing cancellation of harmonic torque components of the same order. This may be achieved using equation 6.19 as follows.

At a certain frequency and load condition, interaction between current components of order (1,6n-1) produces a harmonic torque component

$$T_e(1,6n-1) = 3pl_m[I_{s(6n-1)}I_{r(1)}\sin(6n\omega_s t + \theta_{s(6n-1)} + \theta_{r(1)}) - I_{s(1)}I_{r(6n-1)}\sin(6n\omega_s t + \theta_{s(1)} + \theta_{r(6n-1)})] \qquad 7.7$$

which comprises two rotating time phasors, one produced by the currents $I_{s(6n-1)}$ and $I_{r(1)}$, and the other by the currents $I_{s(1)}$ and $I_{r(6n-1)}$. Both phasors rotate in an anti-clockwise direction. From figures 6.12 and 6.13, each component may be resolved into real (cosine terms) and imaginary (sine terms) parts as

$$\Re T_e(1,6n-1) = 3pl_m[I_{s(6n-1)}I_{r(1)}\cos(\theta_{s(6n-1)} + \theta_{r(1)}) - I_{s(1)}I_{r(6n-1)}\cos(\theta_{s(1)} + \theta_{r(6n-1)})] \qquad 7.8$$

$$\Im T_e(1,6n-1) = 3pl_m[I_{s(6n-1)}I_{r(1)}\sin(\theta_{s(6n-1)}+\theta_{r(1)}) - I_{s(1)}I_{r(6n-1)}\sin(\theta_{s(1)}+\theta_{r(6n-1)})] \quad 7.9$$

Interaction between current components of order (1,6n+1) yields

$$T_e(1,6n+1) = 3pl_m[I_{s(6n+1)}I_{r(1)}\sin(6n\omega_s t+\theta_{s(6n+1)}-\theta_{r(1)}) + I_{s(1)}I_{r(6n+1)}\sin(-6n\omega_s t+\theta_{s(1)}-\theta_{r(6n+1)})] \quad 7.10$$

illustrating that the currents $I_{s(6n+1)}$ and $I_{r(1)}$ produce an anti-clockwise rotating time phasor, while $I_{s(1)}$ and $I_{r(6n+1)}$ produce a clockwise rotating time phasor. Mutual cancellation can only be achieved if all phasors rotate in the same direction. Thus equation 7.10 may be re-written as

$$T_e(1,6n+1) = 3pl_m[I_{s(6n+1)}I_{r(1)}\sin(6n\omega_s t+\theta_{s(6n+1)}-\theta_{r(1)}) - I_{s(1)}I_{r(6n+1)}\sin(6n\omega_s t-\theta_{s(1)}+\theta_{r(6n+1)})] \quad 7.11$$

with the real and imaginary parts being

$$\Re T_e(1,6n+1) = 3pl_m[I_{s(6n+1)}I_{r(1)}\cos(\theta_{s(6n+1)}-\theta_{r(1)}) - I_{s(1)}I_{r(6n+1)}\cos(-\theta_{s(1)}+\theta_{r(6n-1)})] \quad 7.12$$

$$\Im T_e(1,6n+1) = 3pl_m[I_{s(6n+1)}I_{r(1)}\sin(\theta_{s(6n-1)}-\theta_{r(1)}) - I_{s(1)}I_{r(6n+1)}\sin(-\theta_{s(1)}+\theta_{r(6n+1)})] \quad 7.13$$

Cancellation between $T_e(1,6n-1)$ and $T_e(1,6n+1)$ is achieved if

$$\Re T_e(1,6n-1) = -\Re T_e(1,6n+1)$$

$$\Im T_e(1,6n-1) = -\Im T_e(1,6n+1)$$

Substituting equations 7.8 , 7.9 , 7.12 and 7.13 into these relationships, re-arranging and setting to zero results in

$$cc(n) = 3p\,l_m[\,.I_{s(6n-1)}I_{r(1)}\cos(\theta_{s(6n-1)} + \theta_{r(1)})$$
$$- I_{s(1)}I_{r(6n-1)}\cos(\theta_{s(1)} + \theta_{r(6n-1)})$$
$$+ I_{s(6n+1)}I_{r(1)}\cos(\theta_{s(6n+1)} - \theta_{r(1)})$$
$$- I_{s(1)}I_{r(6n+1)}\cos(-\theta_{s(1)} + \theta_{r(6n-1)})] = 0 \qquad 7.14$$

$$cc(n+1) = 3p\,l_m[\,.I_{s(6n-1)}I_{r(1)}\sin(\theta_{s(6n-1)} + \theta_{r(1)})$$
$$- I_{s(1)}I_{r(6n-1)}\sin(\theta_{s(1)} + \theta_{r(6n-1)})$$
$$+ I_{s(6n+1)}I_{r(1)}\sin(\theta_{s(6n+1)} - \theta_{r(1)})$$
$$- I_{s(1)}I_{r(6n+1)}\sin(-\theta_{s(1)} + \theta_{r(6n+1)})] = 0$$

where $cc(n)$ and $cc(n+1)$ are the nth and (n+1)th equality constrains imposed on the optimization process.

To satisfy both the minimum pulse-width requirement and the half-wave symmetry property of the PWM pattern, the additional inequality constraint imposed on any number of unknown switching angles per half-cycle is

$$t_{min} < \alpha_1 < \alpha_2 < \alpha_3 <.....< \alpha_m < \pi$$

7.3.3 Optimization Results

When cancellation is performed on one torque component, three equations are involved; one for setting the fundamental component factor and two for real and imaginary component cancellation. Since the magnitude of the fundamental component is controlled via the DC-link, the solution requires at least two switching angles ($m = 2$), corresponding to three pulses per half-cycle in the line voltage waveform, compared with five pulses per half-cycle required by an elimination strategy with quarter-wave symmetry. As m is increased by two, cancellation can be performed on one further torque component. Thus, with $m = 8$, the line voltage waveform will have nine pulses per half-cycle, compared with seventeen for the elimination strategy, and four consecutive torque components

can be cancelled. This indicates that the switching losses in the inverter are likely to be approximately 50% lower than with the elimination strategy. An example for cancellation of the 6th-harmonic torque component using two switching angles per half-cycle is given in appendix A.4.

Table 7.1 shows sets of 2,4,6 and 8 switching angles per half-cycle, corresponding to 3,5,7 and 9 pulses per half-cycle in the line voltage waveform. Each set produces a PWM pattern designed to provide successive cancellation of the 6th, 12th, 18th and 24th torque components for 1Hz operation at no-load. These sets will be denoted as type A PWMT, to distinguish them from the elimination strategy.

TABLE 7.1

OPTIMIZATION SUBROUTINE SETS OF 2,4,6,8 SWITCHING ANGLES PER HALF-CYCLE , TYPE A

MODE	K	α_1	α_2	α_3	α_4	α_5	α_6	α_7	α_8
PWMT2	0.9680	0.2111	0.3634						
PWMT4	0.9593	0.1143	0.2667	0.4601	0.5369				
PWMT6	0.9557	0.0724	0.2106	0.3340	0.4250	0.5928	0.6393		
PWMT8	0.9540	0.0502	0.1741	0.2605	0.3514	0.4687	0.5296	0.6759	0.7071

A fair comparison may be made with the elimination strategy, if the number of switching angles per half-cycle is doubled, so that the line voltage waveform has the same number of pulses per half-cycle as the quarter-wave symmetrical elimination strategy. This demonstrates the practical feasibility of implementing a high pulse-number strategy for low frequency operation of the drive. Hence, using 4,8,12 and 16 switching angles per half-cycle produces 5,9,13 and 17 pulses per half-cycle in the line voltage waveform. Table 7.2 shows sets of switching angles denoted as type B PWMT, for 1Hz no-load operation.

TABLE 7.2
OPTIMIZATION SUBROUTINE SETS OF 4,8,12,16 SWITCHING ANGLES PER HALF-CYCLE , TYPE B

MODE	K	α_1	α_2	α_3	α_4	α_5	α_6	α_7	α_8
PWMT4	0.9659	0.1257	0.1970	0.3090	0.4154				
PWMT8	0.9577	0.0716	0.1516	0.1916	0.2449	0.3064	0.3696	0.5279	0.5884
PWMT12	0.9543	0.0390	0.1313	0.1853	0.2583	0.2961	0.3307	0.4157	0.4795
PWMT16	0.9535	0.0378	0.1203	0.1391	0.1727	0.2104	0.2583	0.2872	0.3015

TABLE 7.2 continued

MODE	K	α_9	α_{10}	α_{11}	α_{12}	α_{13}	α_{14}	α_{15}	α_{16}
PWMT12	0.9543	0.5642	0.5818	0.6745	0.7057				
PWMT16	0.9535	0.3351	0.3844	0.4389	0.4628	0.5336	0.5761	0.7095	0.7357

7.3.4 Switching Pattern Generation

Based on the half-wave symmetry property of the PWM switching pattern, the switching instants $t_{(i)}$ for switching angles $\alpha_{(i)}$ are determined as follows.

At an operating frequency f_s, the switching instants for the first half-cycle are

$$t_{(i)} = \frac{\alpha_{(i)}}{2\pi f_s} \quad , \quad i = 1, \ldots\ldots, m \qquad 7.15$$

and the switching instant at π is

$$t_{(m+1)} = \frac{1}{2f_s} \qquad 7.16$$

Using the half-wave symmetry property, the switching instants for the second half of the cycle are

$$t_{(i+m+1)} = \frac{1}{2f_s} + \frac{\alpha_{(i)}}{2\pi f_s} \quad , \quad i = 1, \ldots\ldots, m \qquad 7.17$$

and the switching instant at 2π is

$$t_{(2m+2)} = \frac{1}{f_s} \qquad 7.18$$

By introducing phase shifts of $2\pi/3$ and $4\pi/3$ into the above equations, switching instants for the three GTOs in the same half of the inverter bridge are determined. Those for the other half are mirror images of the ones obtained above. Figure 7.2 demonstrates an example of the switching pattern generated using the PWMT2 set with the two switching angles given in table 7.1.

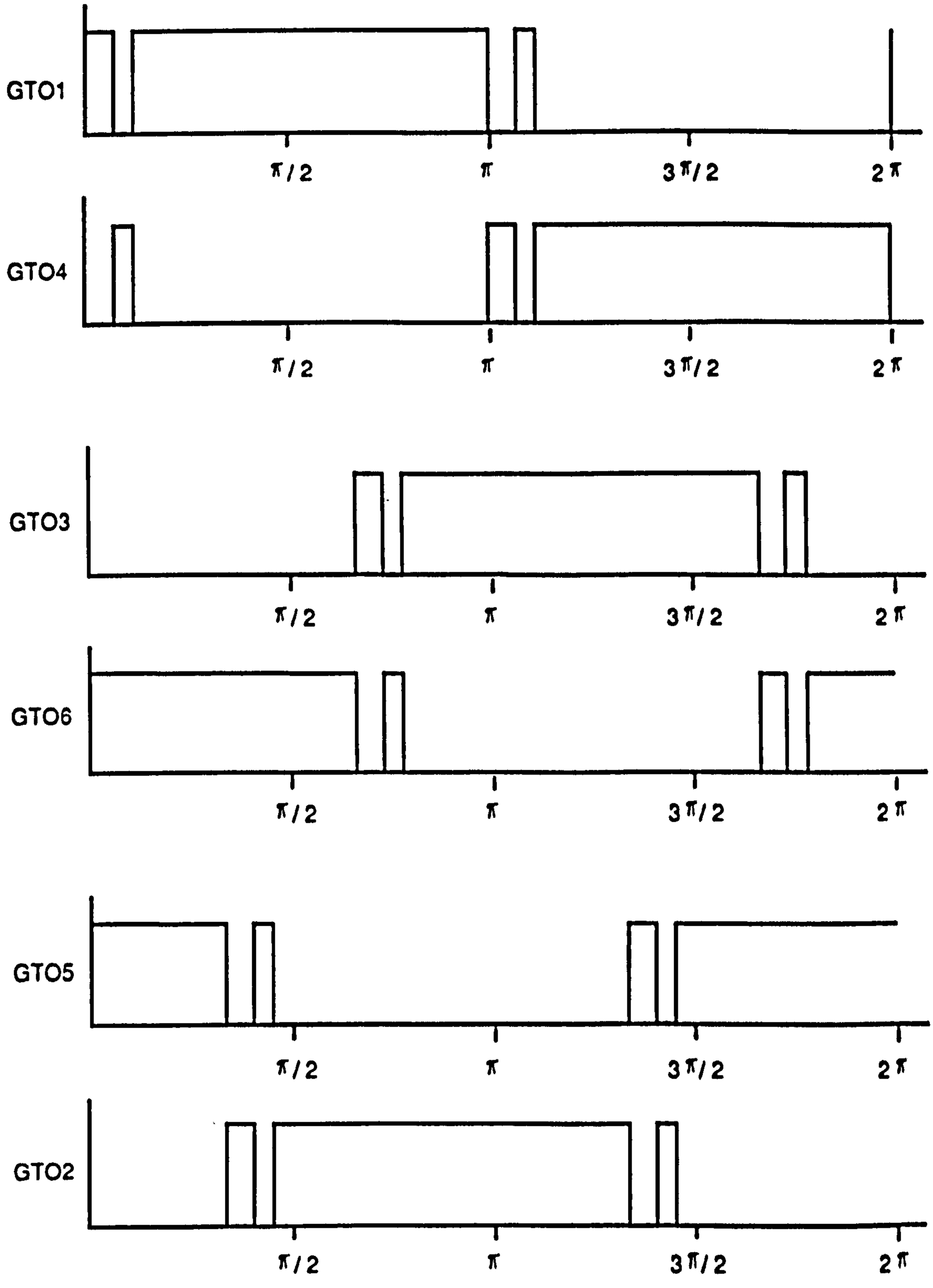

Figure 7.2 Typical switching pattern for all GTOs , generated using two switching angles / half-cycle for PWMT2 operating mode

7.4 Computed and Experimental Results

Computed and experimental results are presented in this section to verify the two versions of the PWM strategy developed in section 7.3 and the mathematical techniques involved in their derivation. The computed results were obtained using the direct-phase model and are confirmed by experiment. All results refer to an inverter frequency of 1Hz, with the motor unloaded.

The results for a type A strategy with two switching angles per half-cycle are presented in figure 7.3. Figure 7.3(a) shows the line voltage waveform having three pulses per half-cycle, obtained using a DC-link voltage of 14.5V calculated from equation 5.40 and including inverter voltage drop compensation. The waveform clearly does not possess quarter-wave symmetry. Figure 7.3(b) shows the corresponding current waveform, together with its harmonic spectrum, which illustrates that, although the 5th- and 7th-harmonic current components are not eliminated completely, their magnitudes are less than in the QSW case of figure 5.12(b). Comparing this spectrum with that in figure 5.13(b) for the PWM2 mode, when the 5th and 7th components were completely eliminated, illustrates a more uniform distribution in terms of the magnitudes of successive pairs of harmonic current components. This results in a significant reduction in the magnitude of the 6th-harmonic torque component and a redistribution of the remaining harmonic torque content. When compared with the elimination strategy, the 12th-harmonic torque component reduces from 0.50Nm with the PWM2 mode to 0.39Nm with the PWMT2 mode, as shown in figure 7.3(c). The 18th-harmonic component increases from 0.23Nm for the PWM2 mode to 0.36Nm for the PWMT2 mode, while all other higher harmonic torque components show smaller magnitudes than in the PWM2 mode. Compared with the QSW mode, the 6th-harmonic torque component is significantly minimized, with the small residual magnitude arising due to;

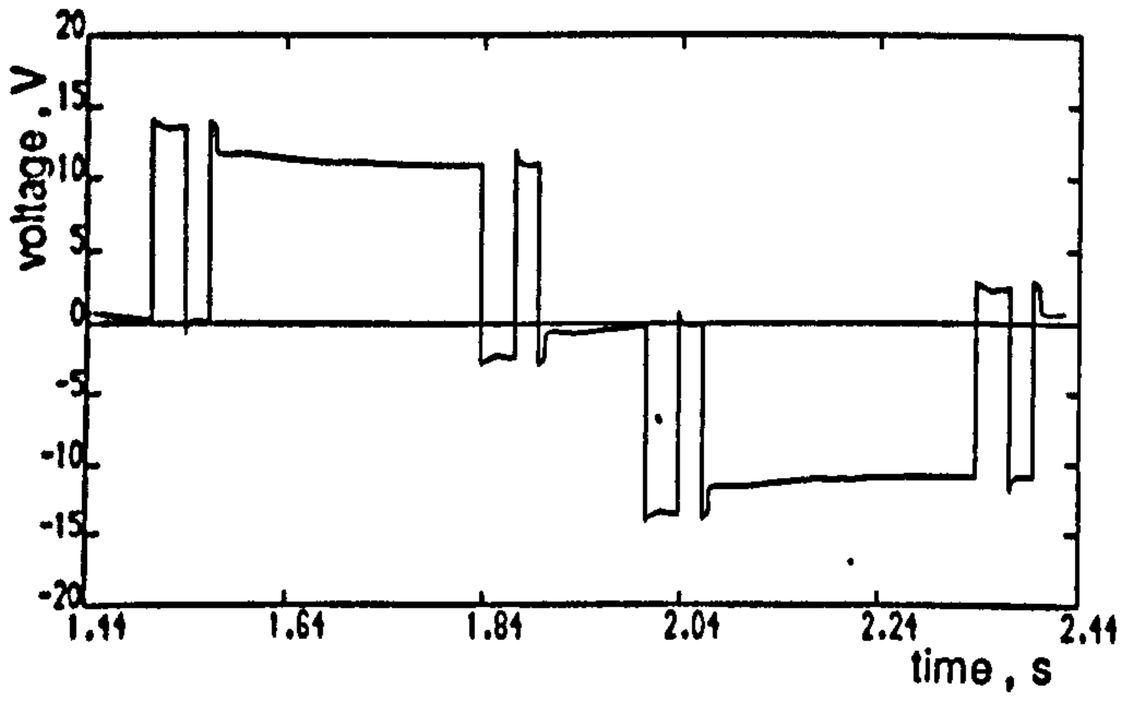

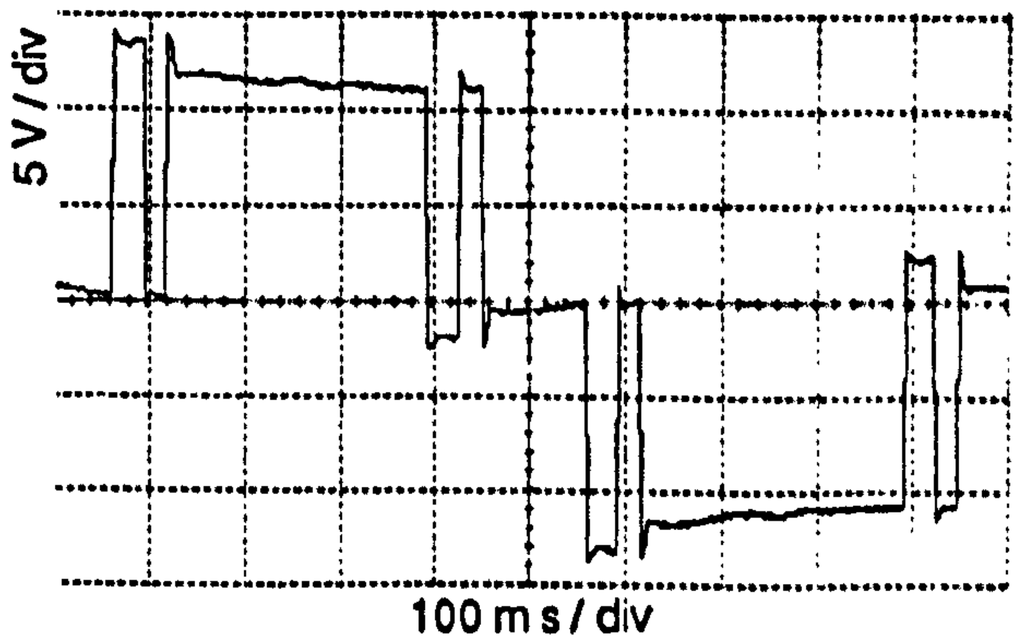

(a)

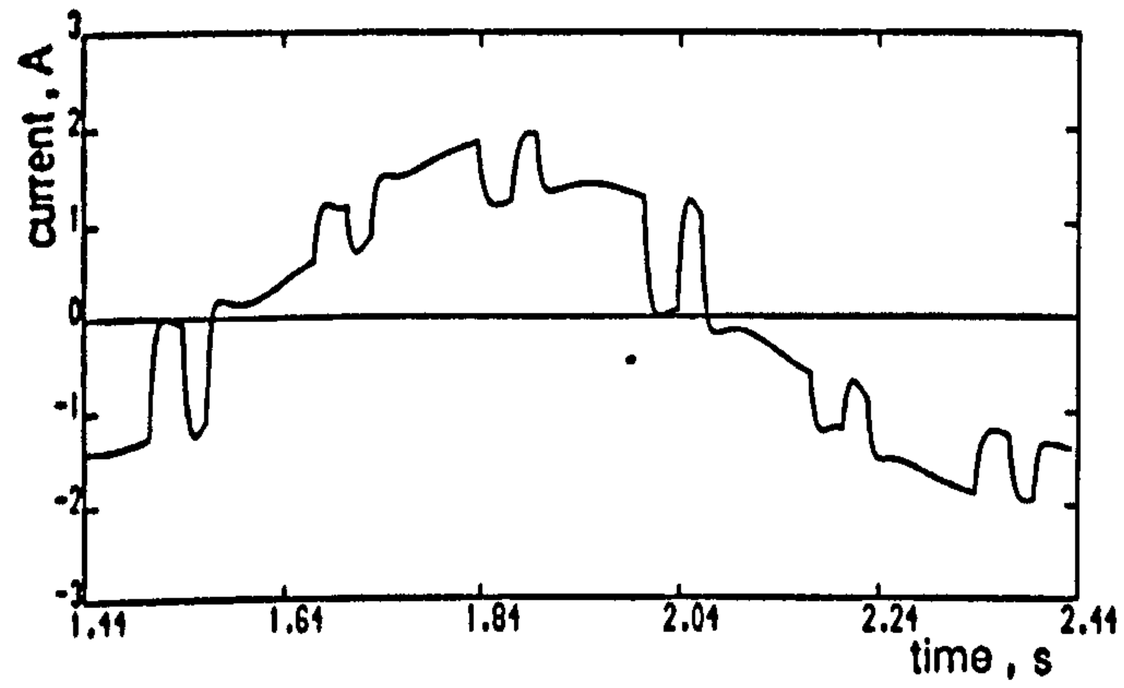

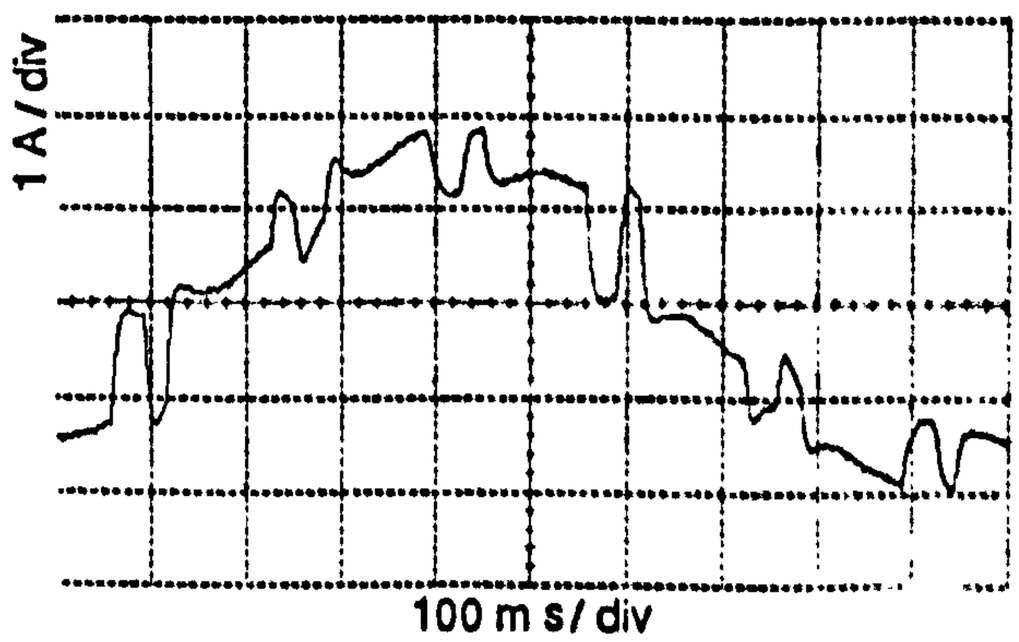

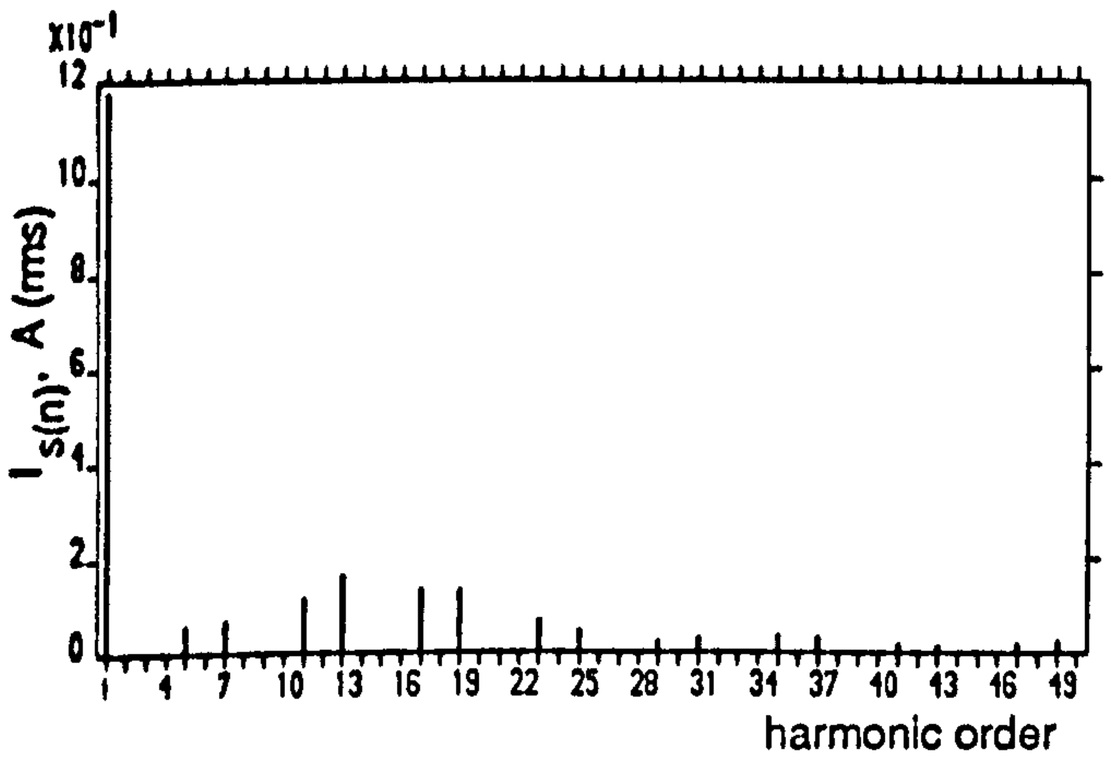

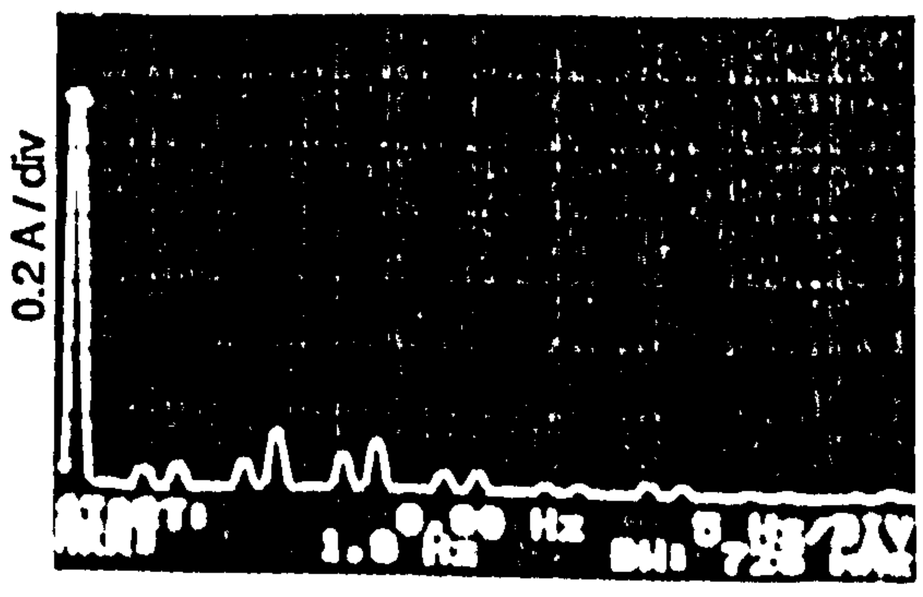

(b)

Figure 7.3 Computed and experimental results for type A PWMT2 half-wave symmetrical strategy at 1Hz stator frequency no-load operating condition
(a) Line voltage
(b) Stator current and spectrum

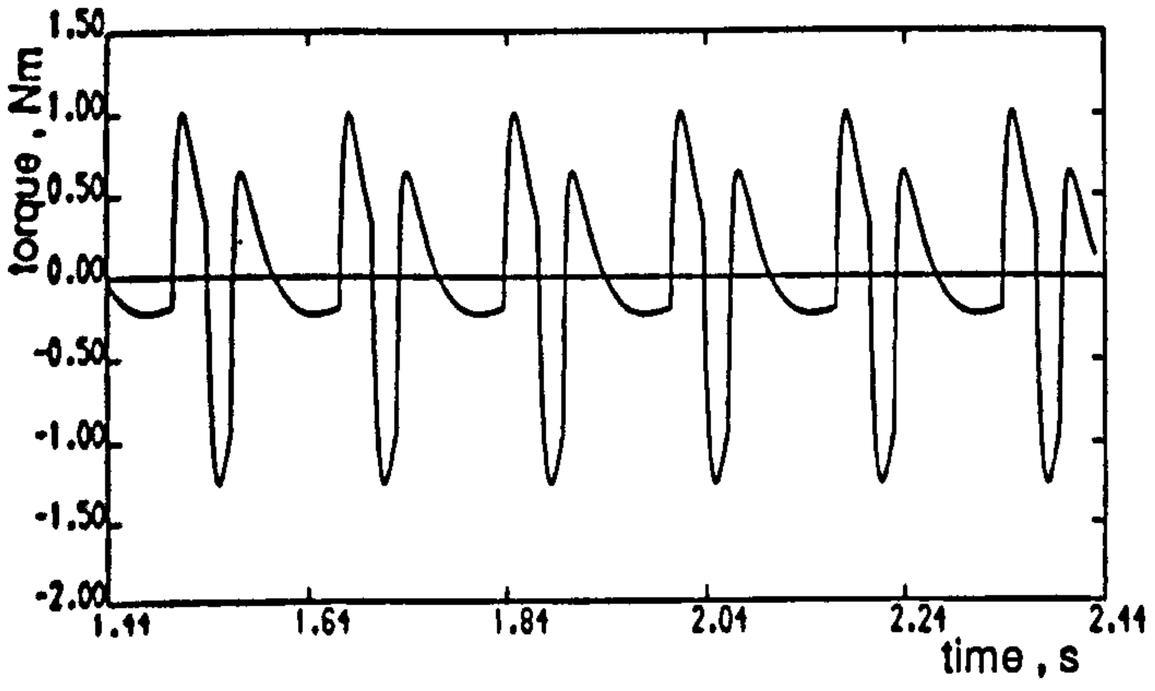

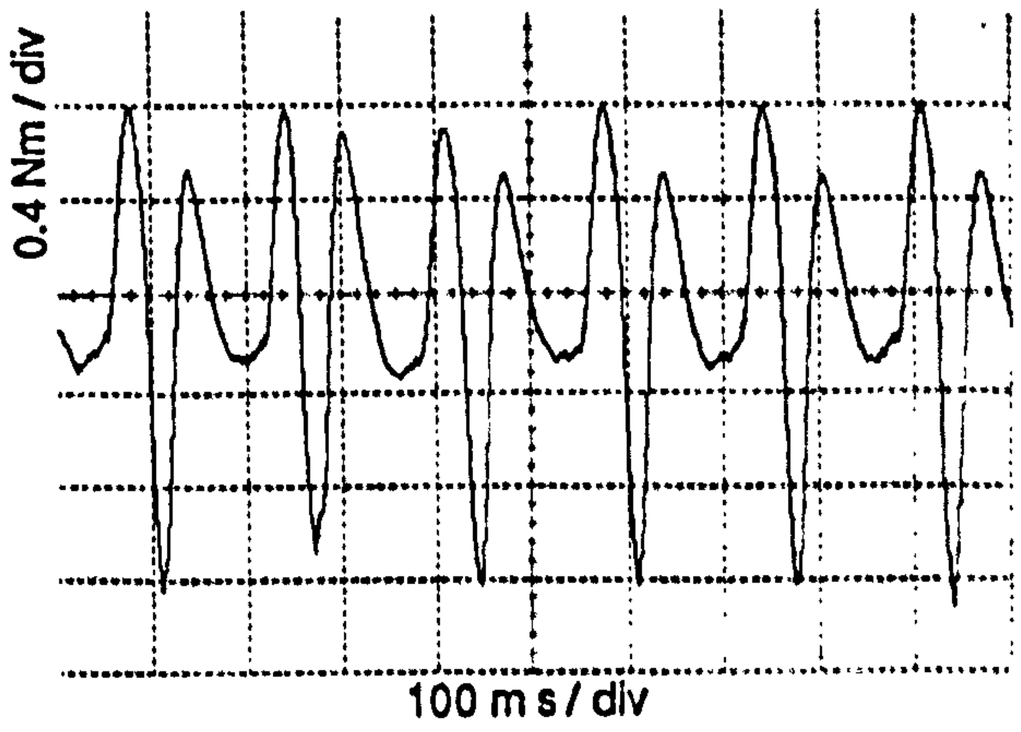

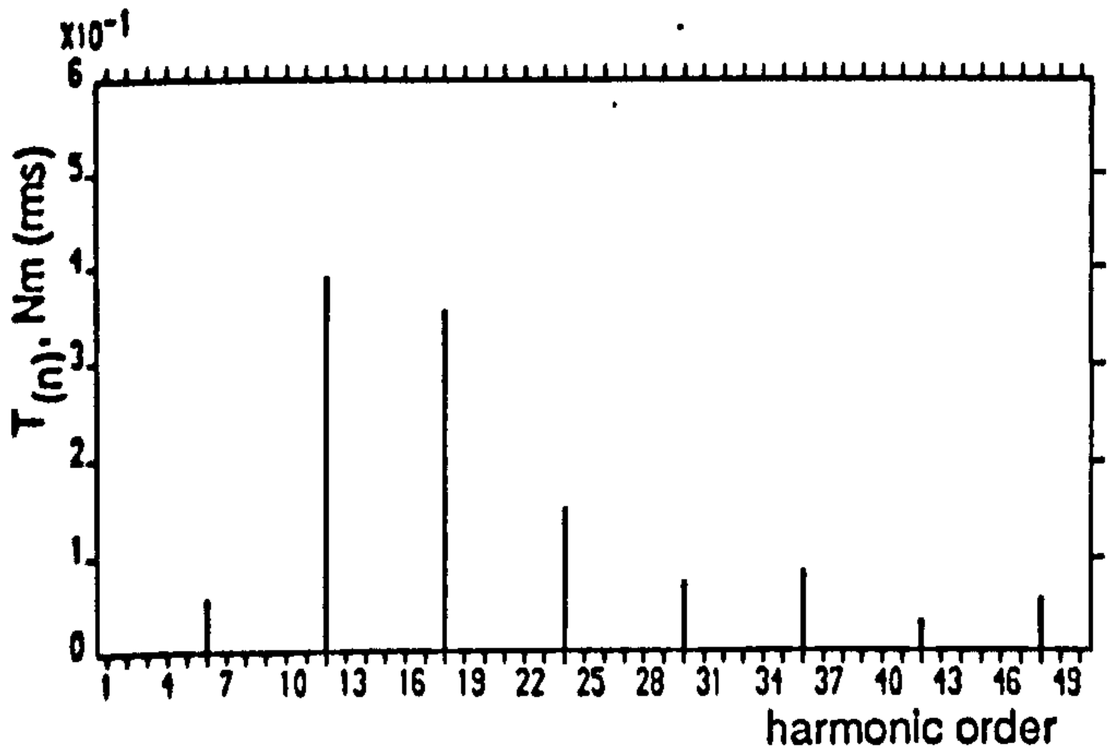

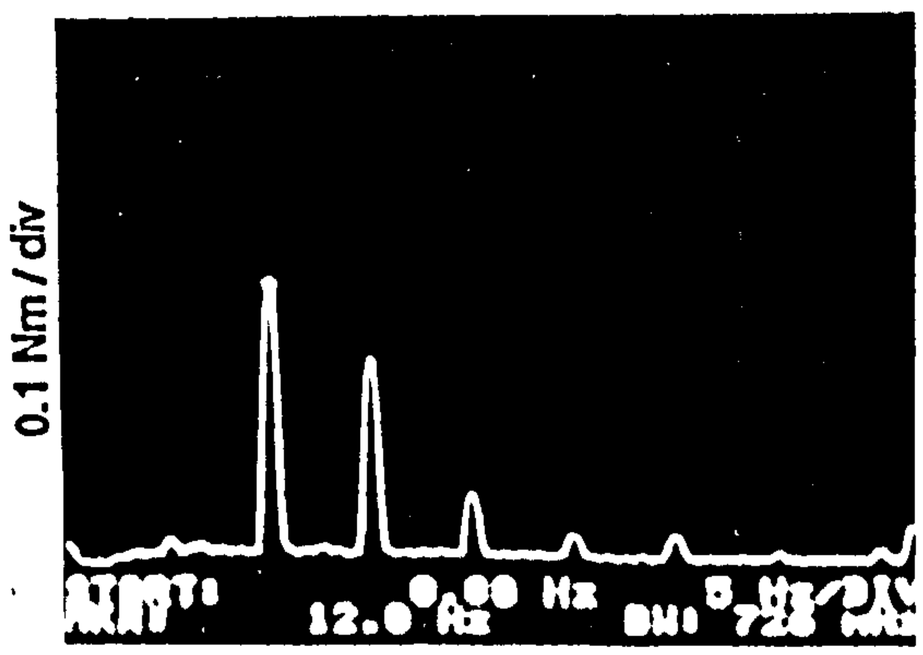

(c)

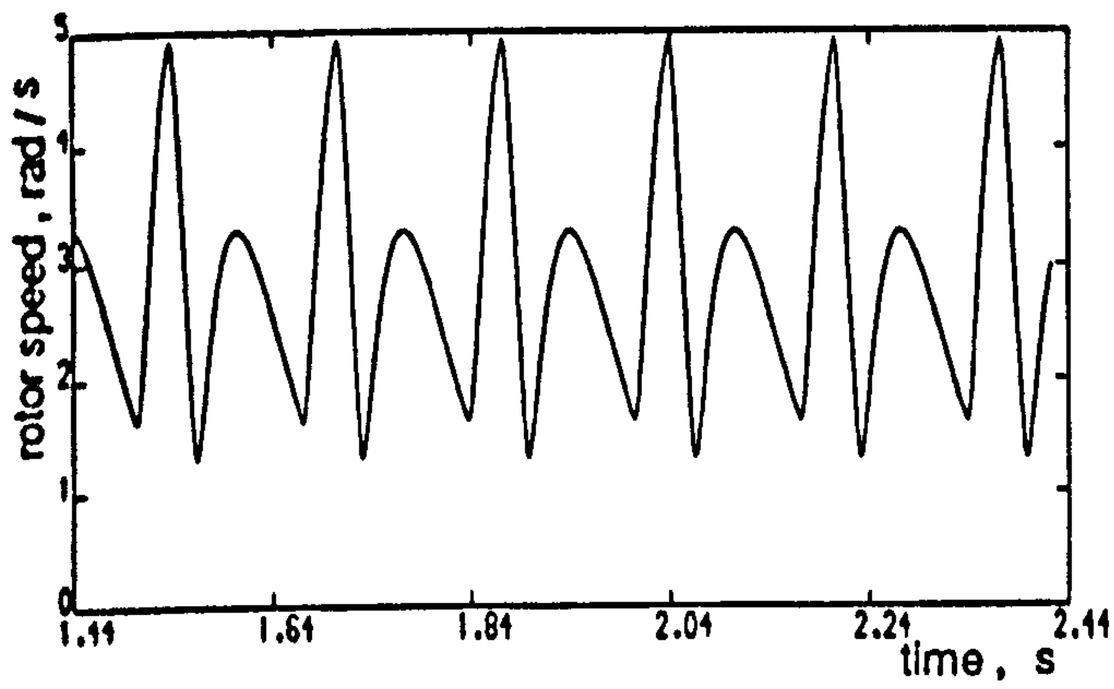

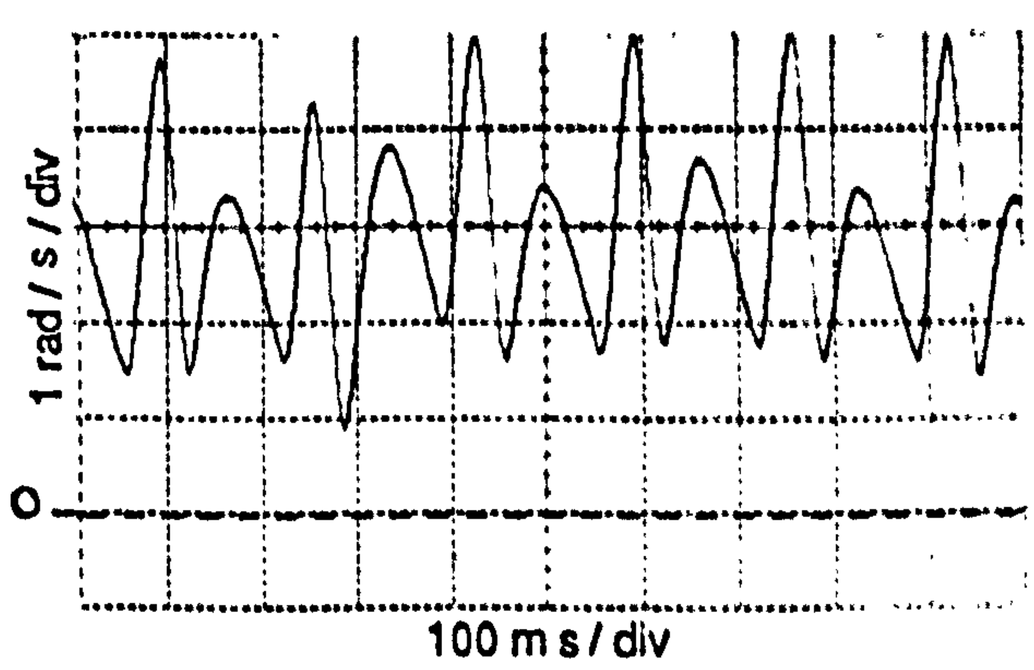

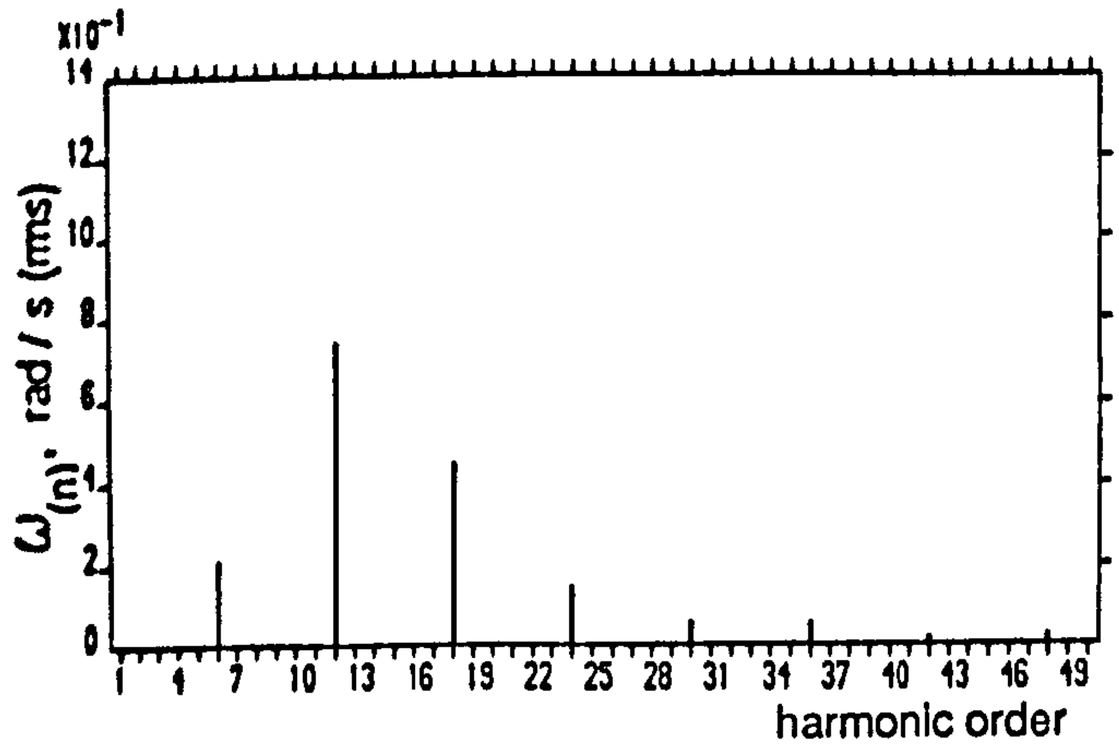

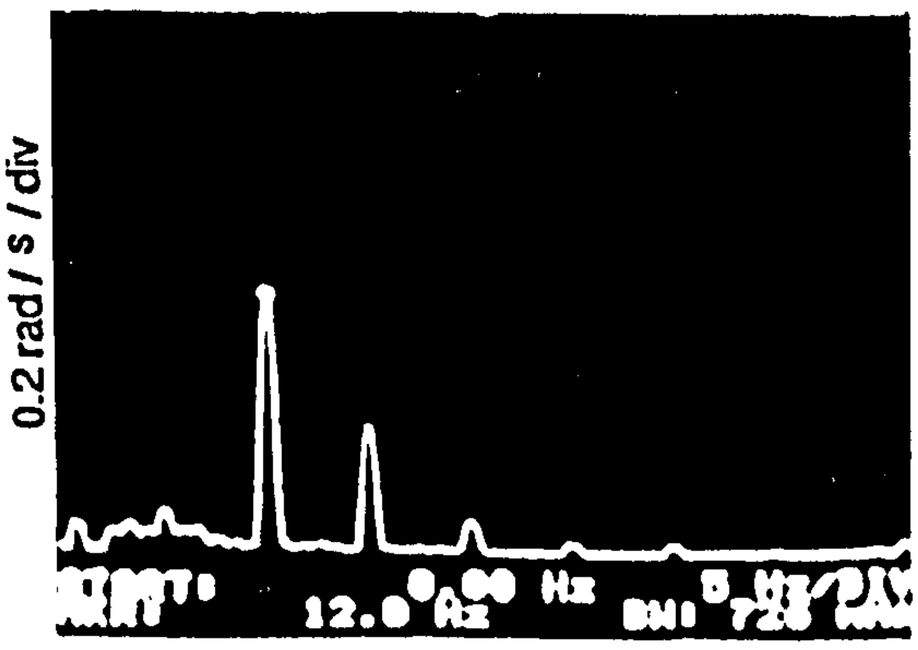

(d)

Figure 7.3 continued (c) Acceleration torque and spectrum
(d) Rotor speed and spectrum

(1) The constant speed assumption made in the frequency-domain analysis and used in the optimization process for switching angle determination.
(2) The distortion imposed on the terminal voltage waveform by voltage drops in the inverter devices.
(3) The contribution of harmonic-harmonic interaction in producing the 6th-harmonic torque component, which was not accounted for in the optimization process.

The computed acceleration torque waveform shown in figure 7.3(c) has a peak-to-peak value of 2.26Nm, while figure 7.3(d) shows that, at an average speed of 2.83rad/s, the superimposed peak-to-peak ripple is 3.63rad/s.

Figures 7.4 to 7.6 show the drive performance when the cancellation process is extended to higher order torque components. Figure 7.4(a) shows the PWMT4 mode line voltage waveform with five pulses per half-cycle for a DC-link voltage of 14.6V. The corresponding stator current waveform and its harmonic spectra are shown in figure 7.4 (b). Again, the voltage switching pattern does not possess quarter-wave symmetry, and the 5th , 7th and 11th , 13th-harmonic current components are still present, with each pair having approximately the same magnitude. The magnitudes of the higher order harmonic current components have a better distribution than for the elimination PWM4 mode of figure 5.14(b). Figure 7.4(c) illustrates that the 6th- and 12th-harmonic torque components experience a great reduction. The remaining higher order torque components are less than those appearing in figure 5.14(c) for the quarter-wave symmetrical PWM4 mode, with the exception of the 24th-and the 48th-harmonics. Figures 7.4(c) and (d) demonstrate that both torque pulsations and speed ripple decrease as additional pulses are introduced in the PWM pattern and more torque components are cancelled.

Figures 7.5(a) to (d) and 7.6(a) to (d) show results for PWMT6 and PWMT8 modes of operation, with three and four pairs of low order harmonic current components being considered

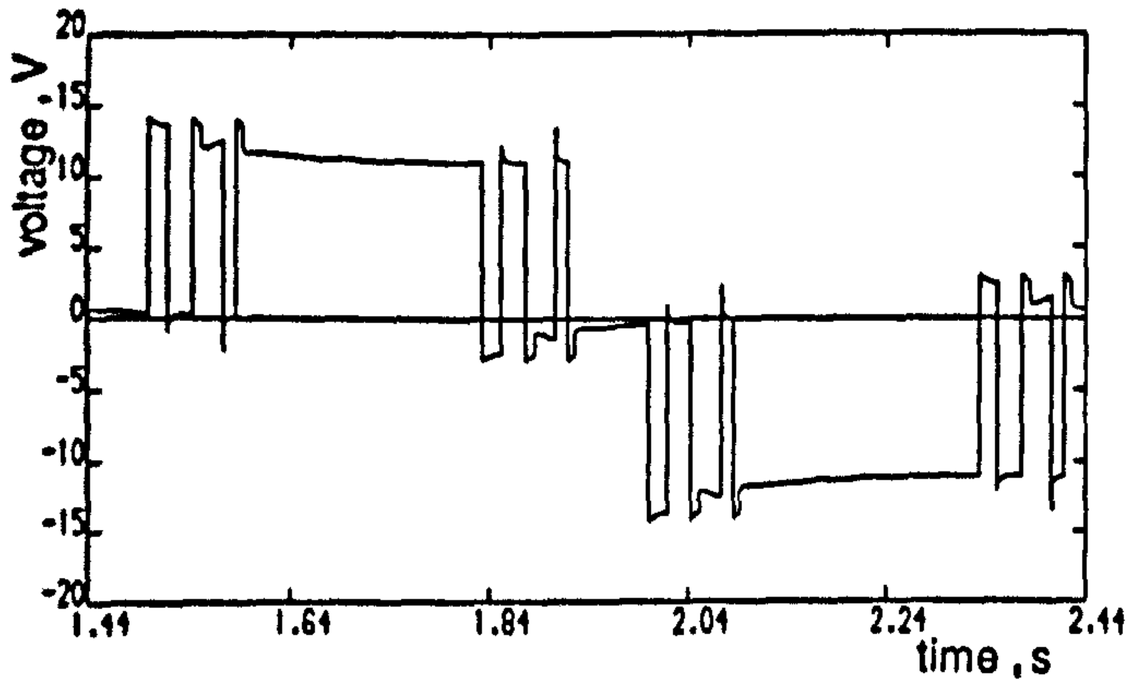

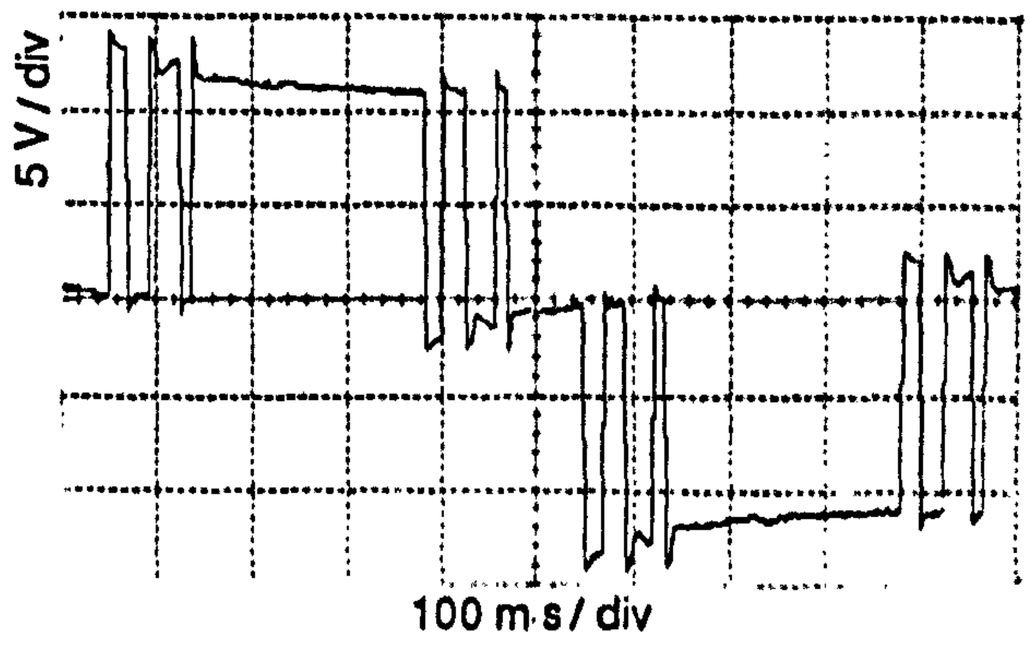

(a)

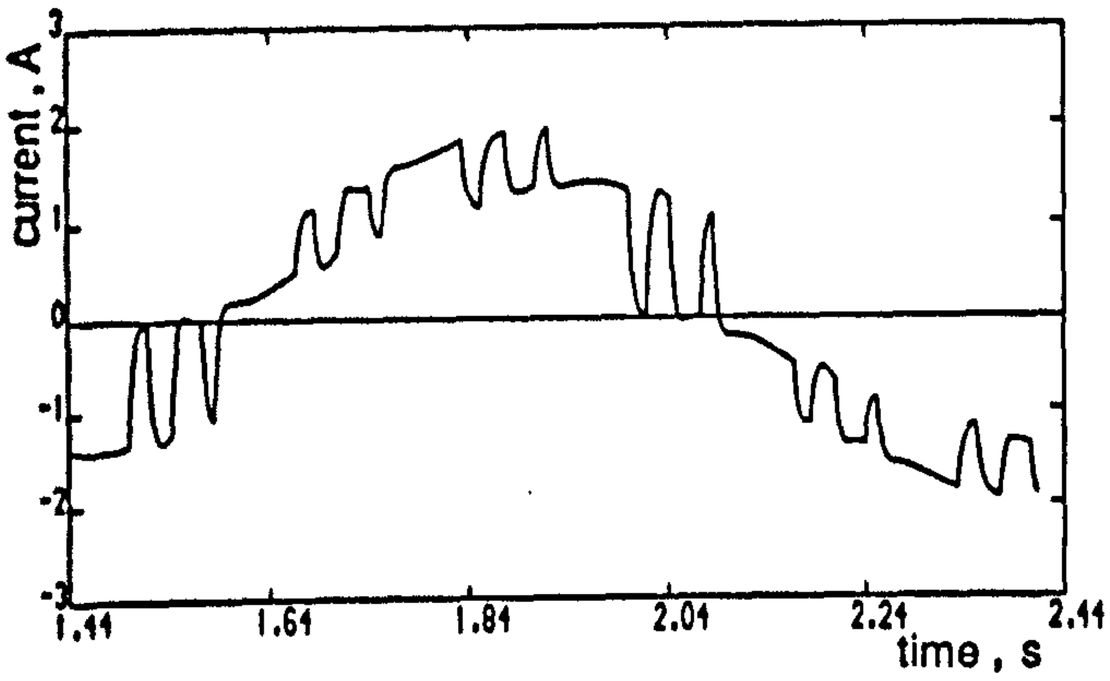

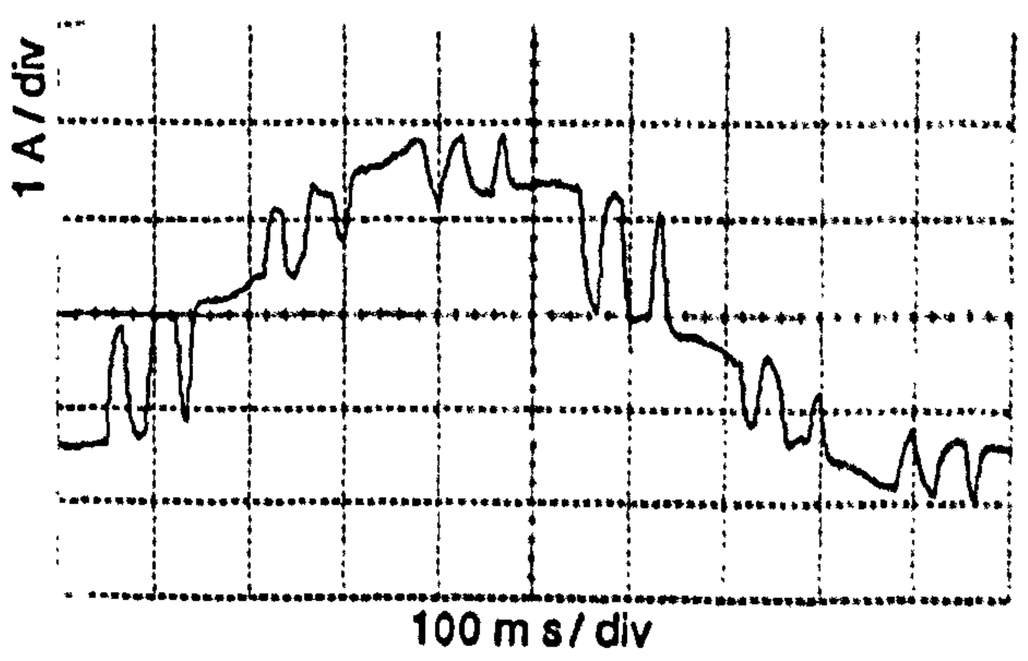

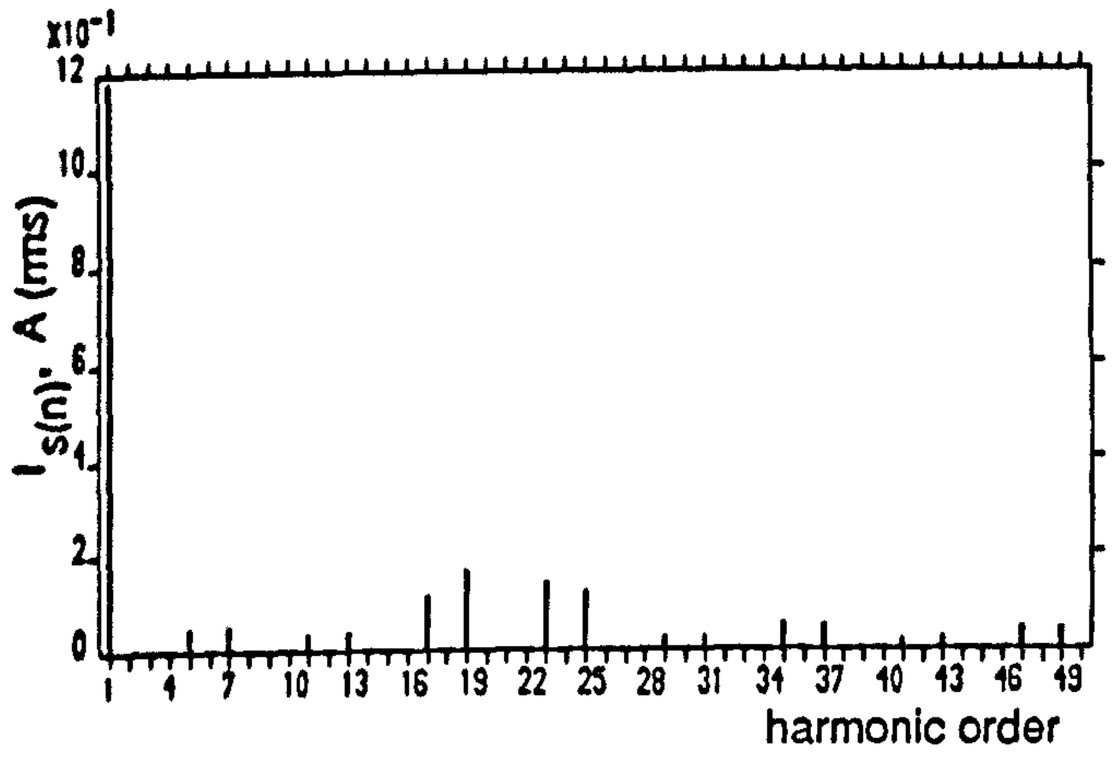

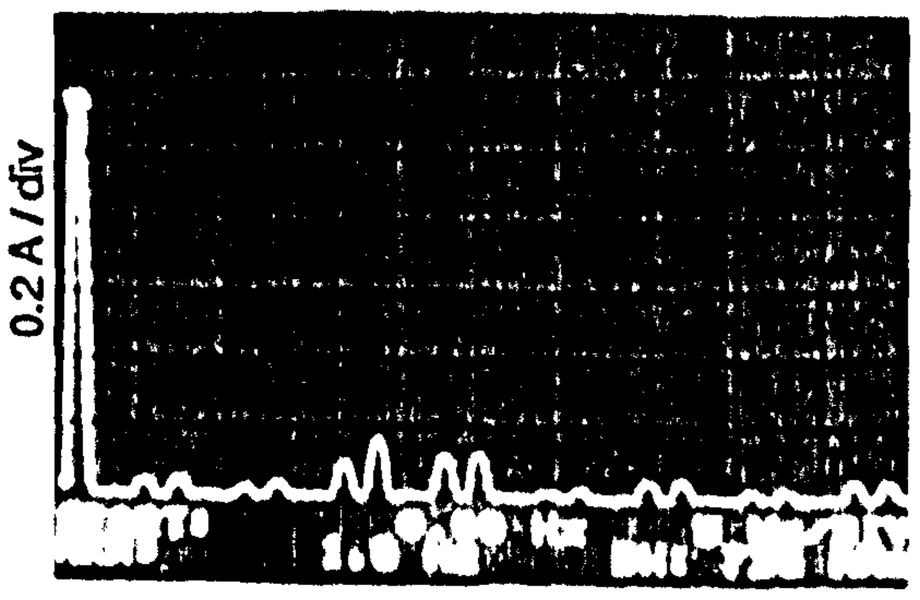

(b)

Figure 7.4 Computed and experimental results for type A PWMT4 half-wave symmetrical strategy at 1Hz stator frequency no-load operating condition
(a) Line voltage
(b) Stator current and spectrum

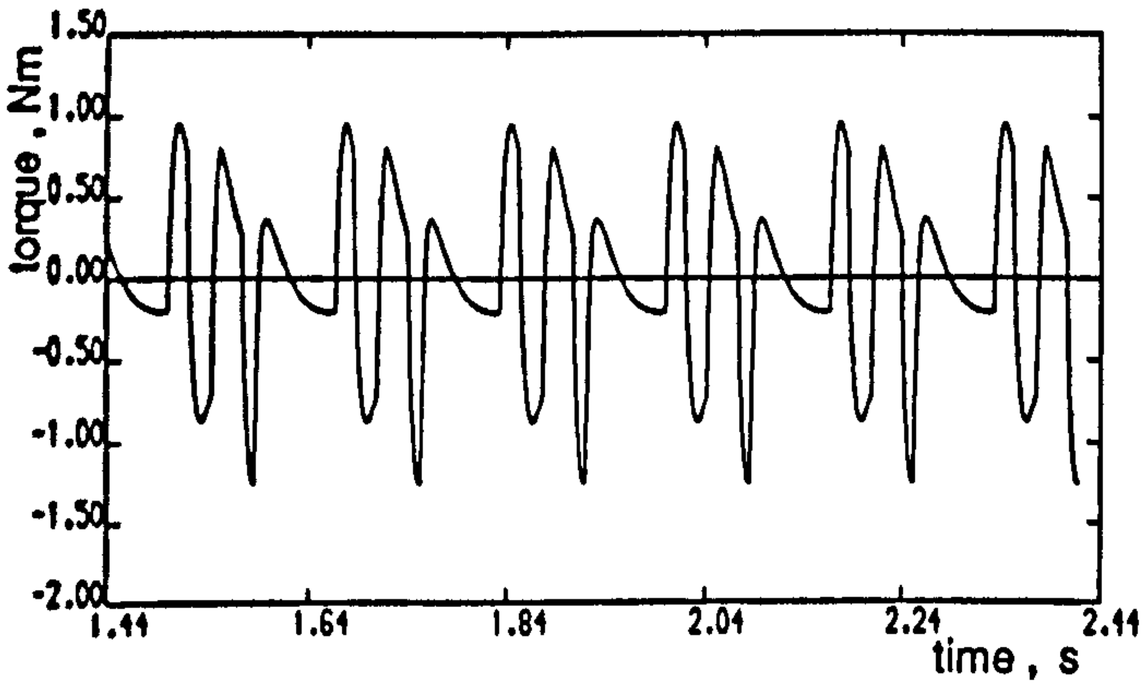

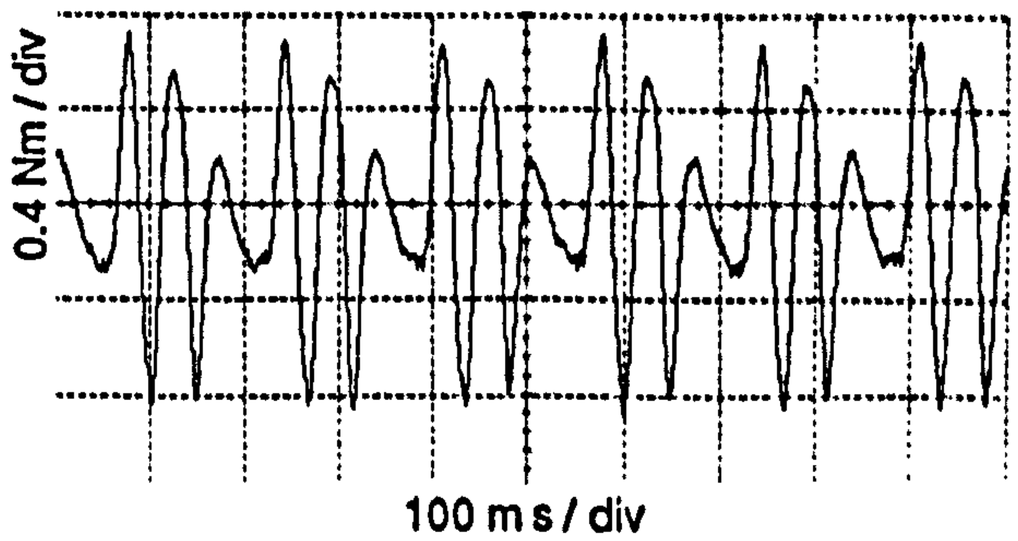

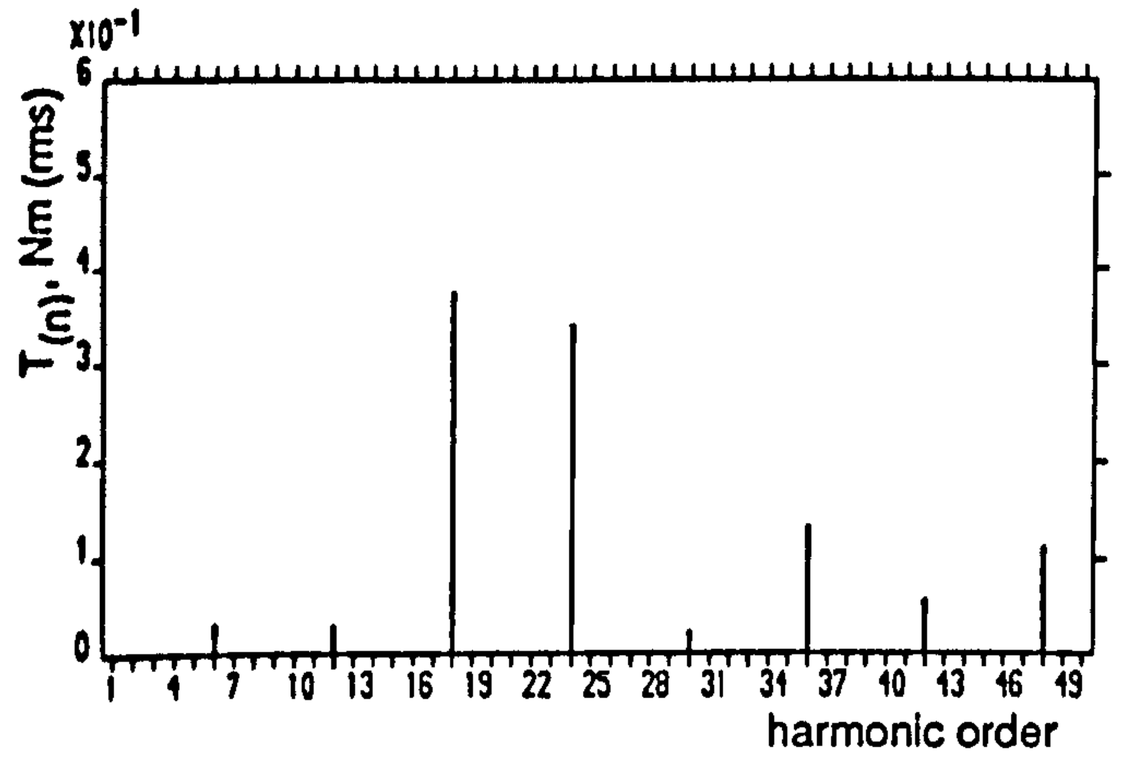

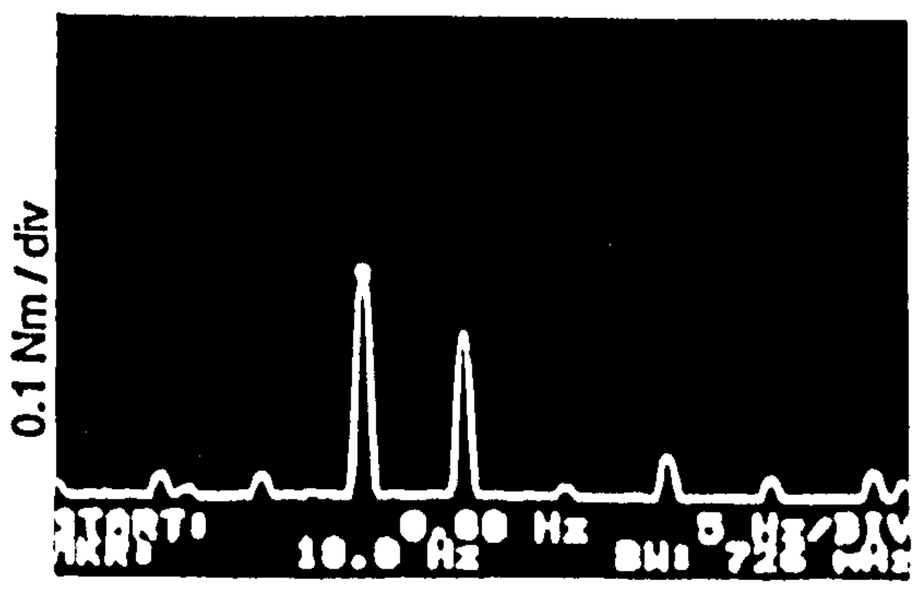

(c)

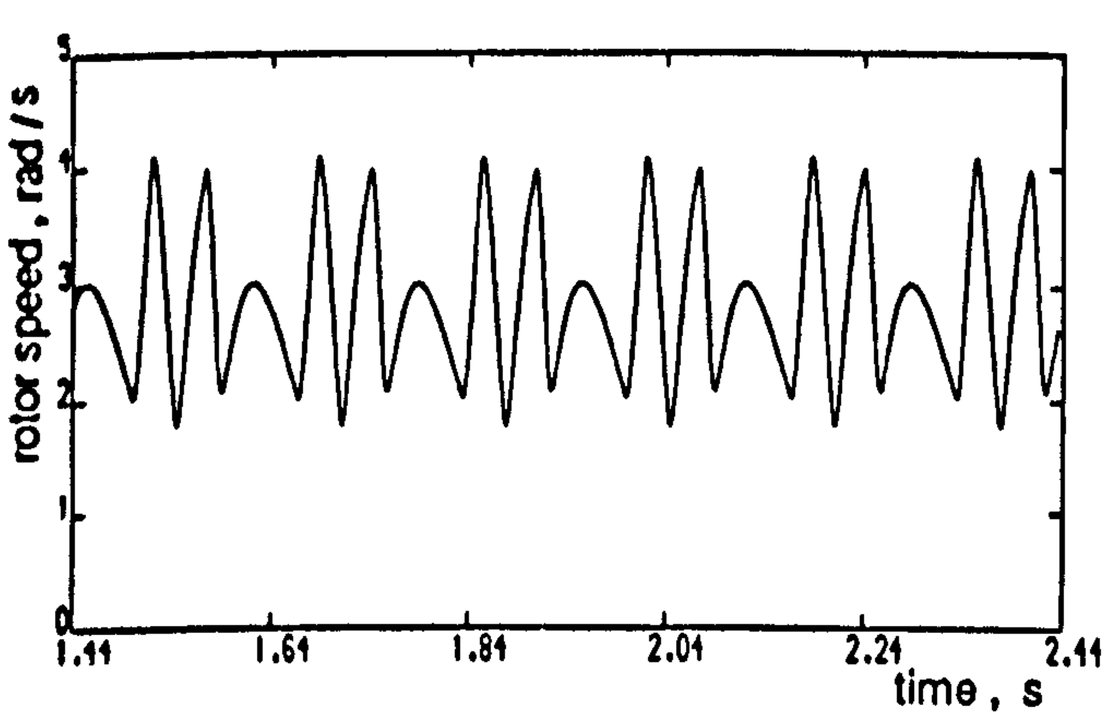

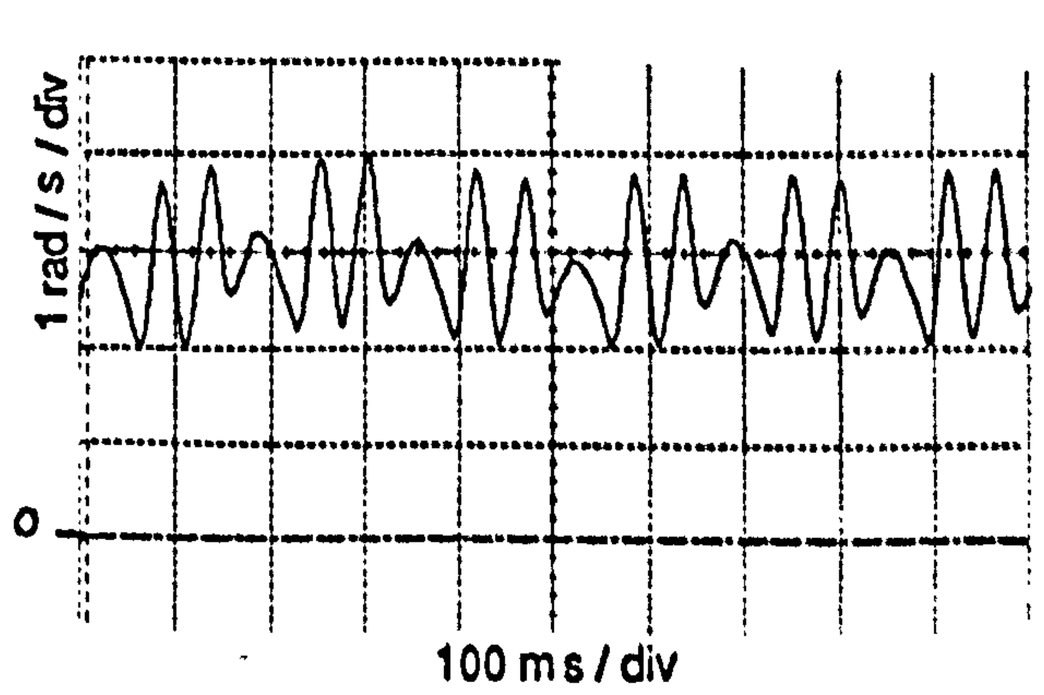

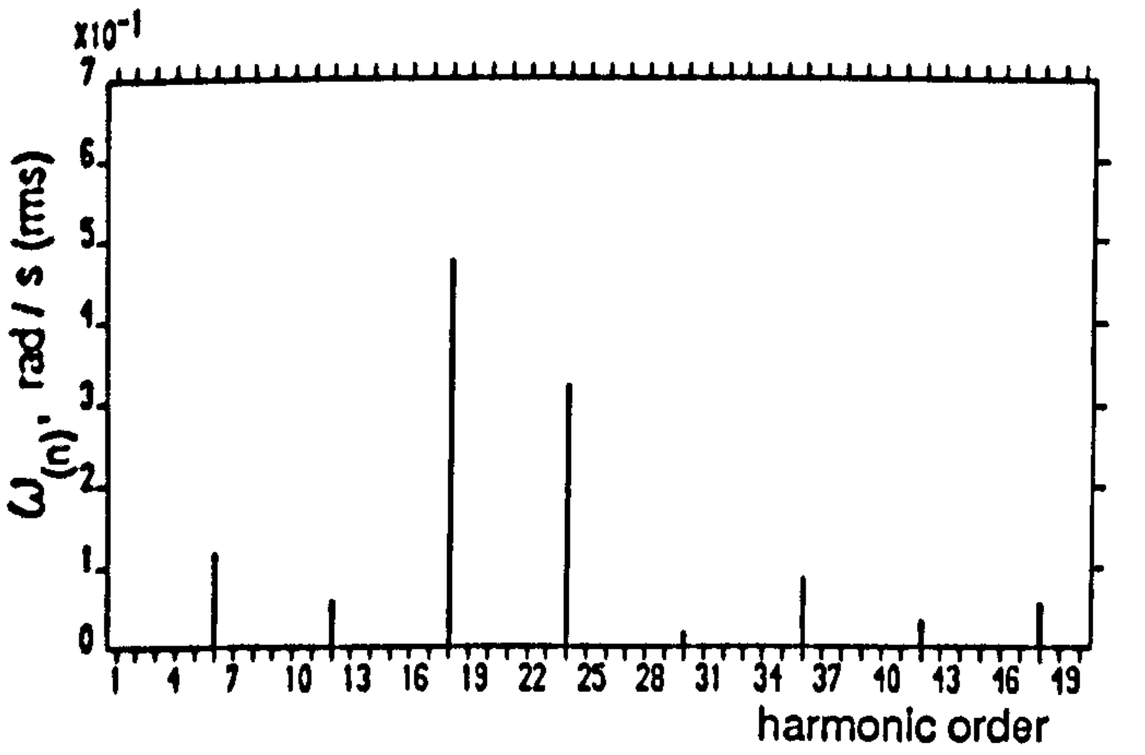

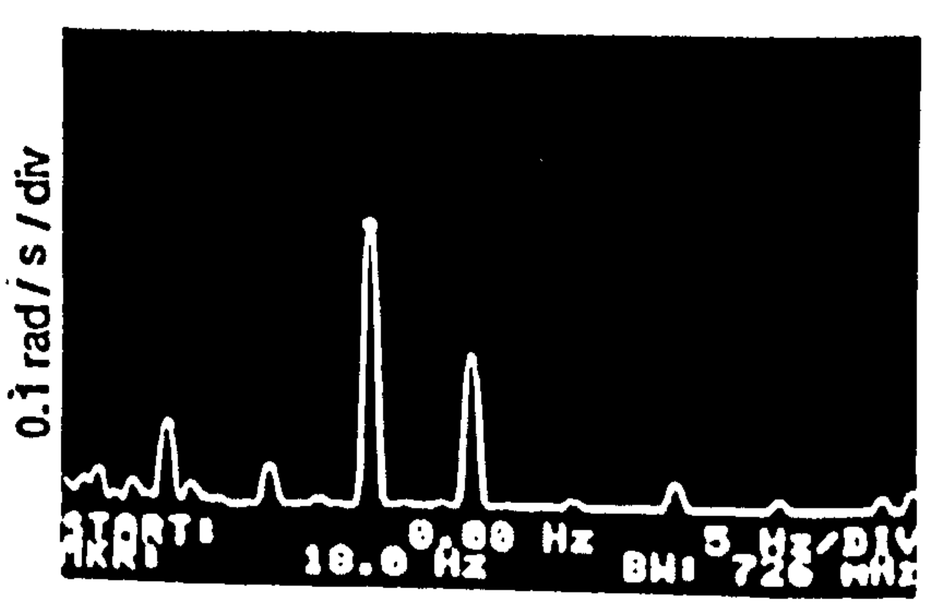

(d)

Figure 7.4 continued (c) Acceleration torque and spectrum
(d) Rotor speed and spectrum

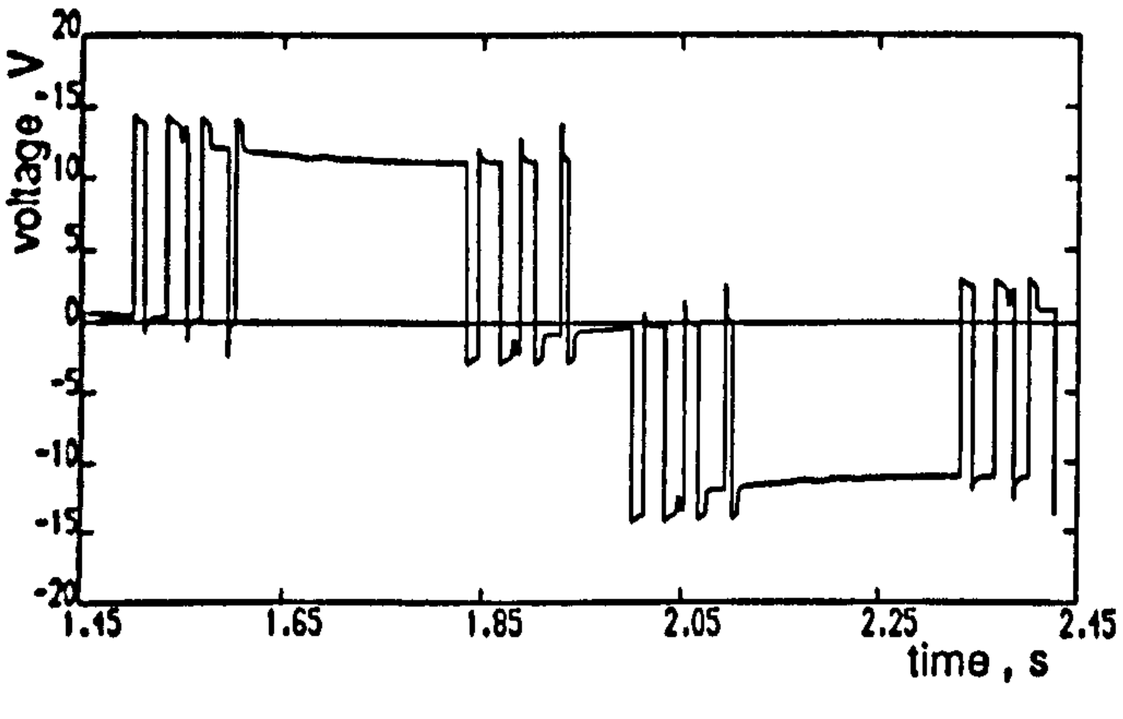

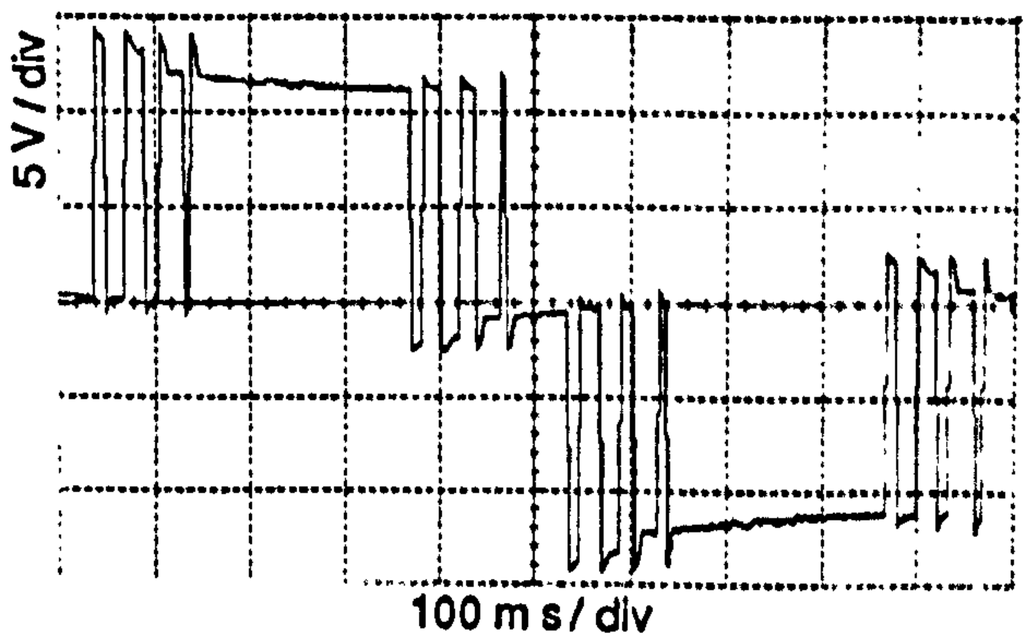

(a)

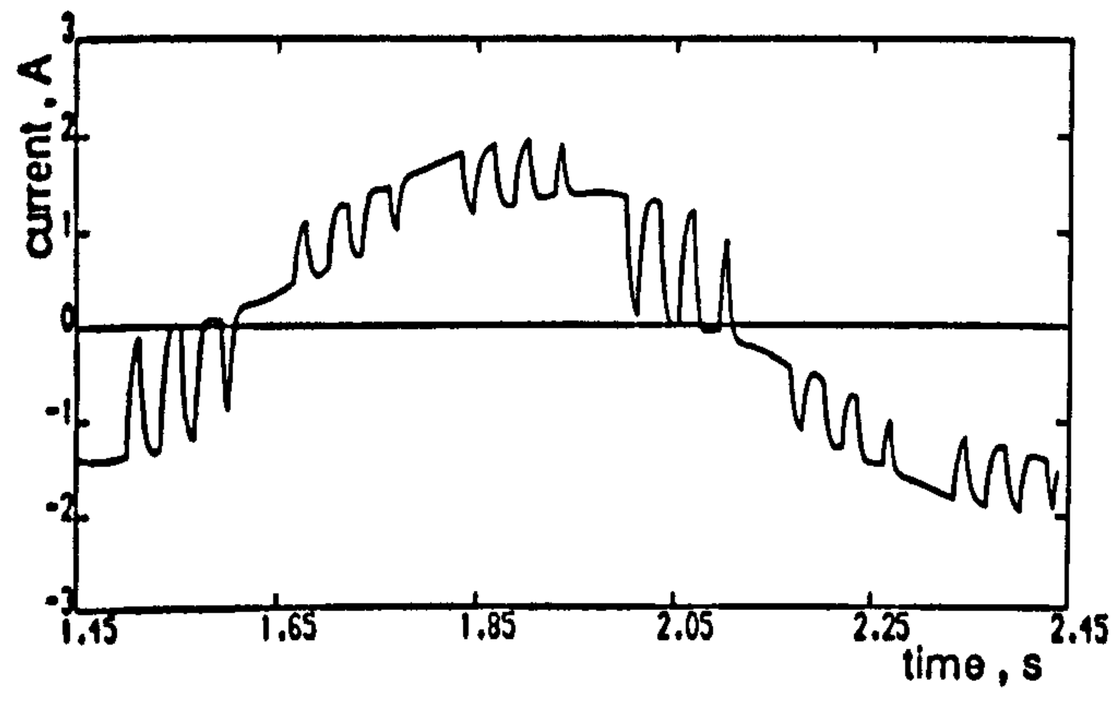

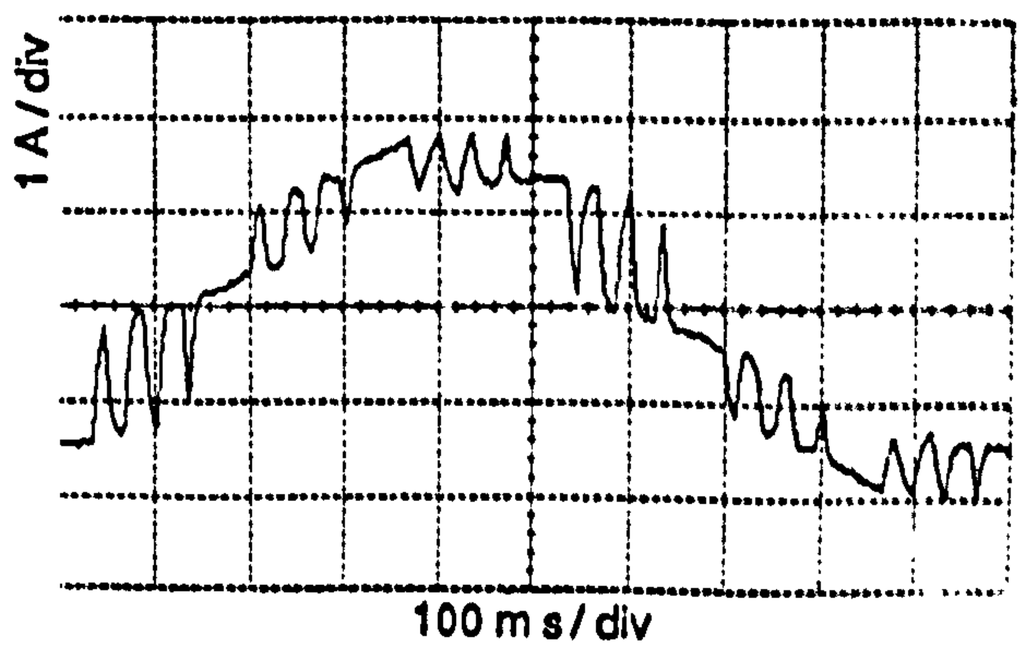

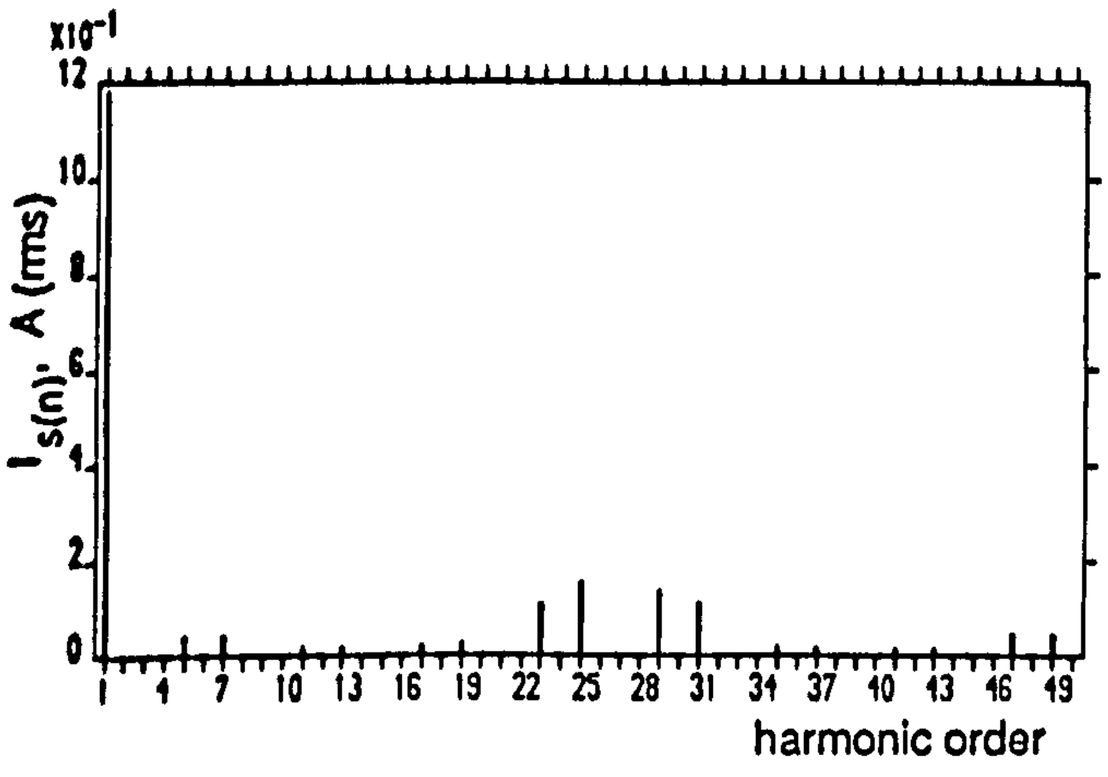

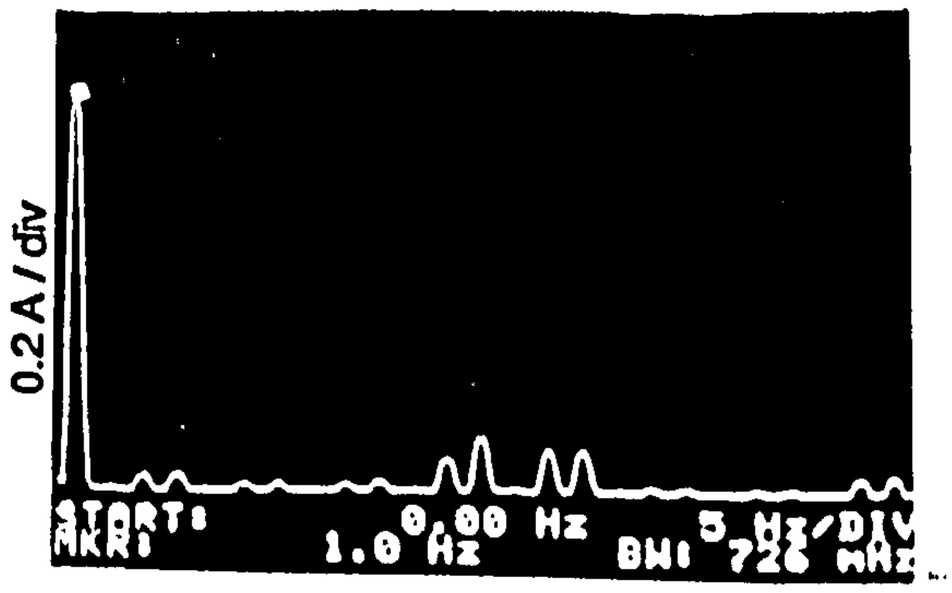

(b)

Figure 7.5 Computed and experimental results for type A PWMT6 half-wave symmetrical strategy at 1 Hz stator frequency no-load operating condition
(a) Line voltage
(b) Stator current and spectrum

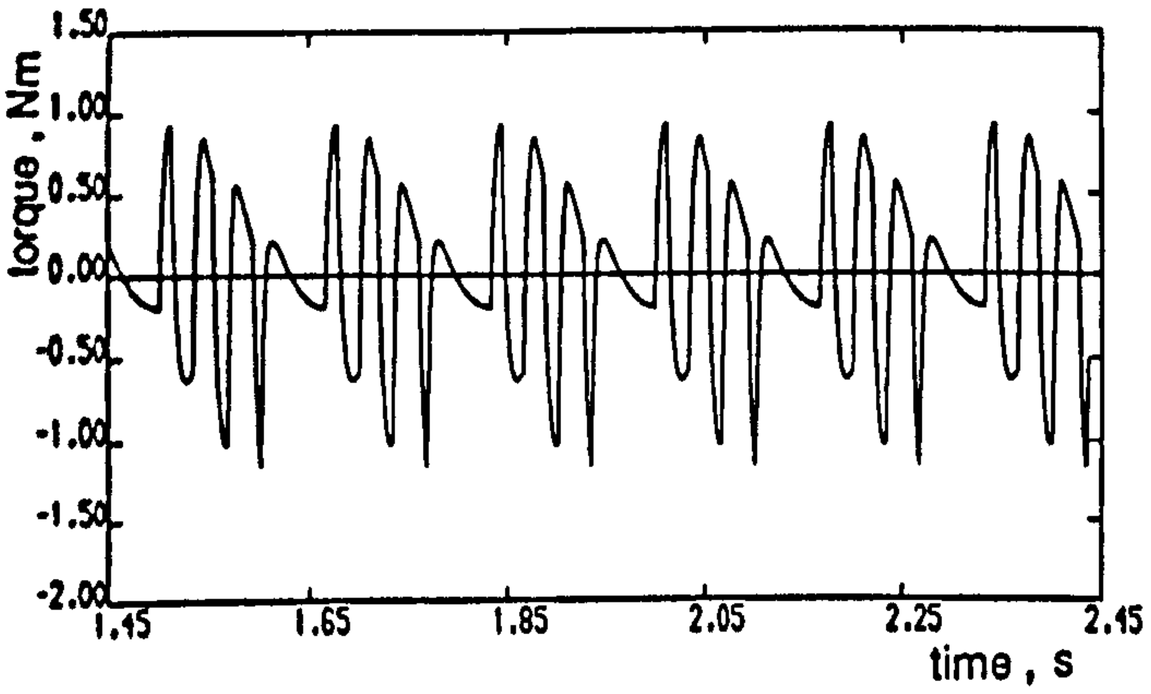

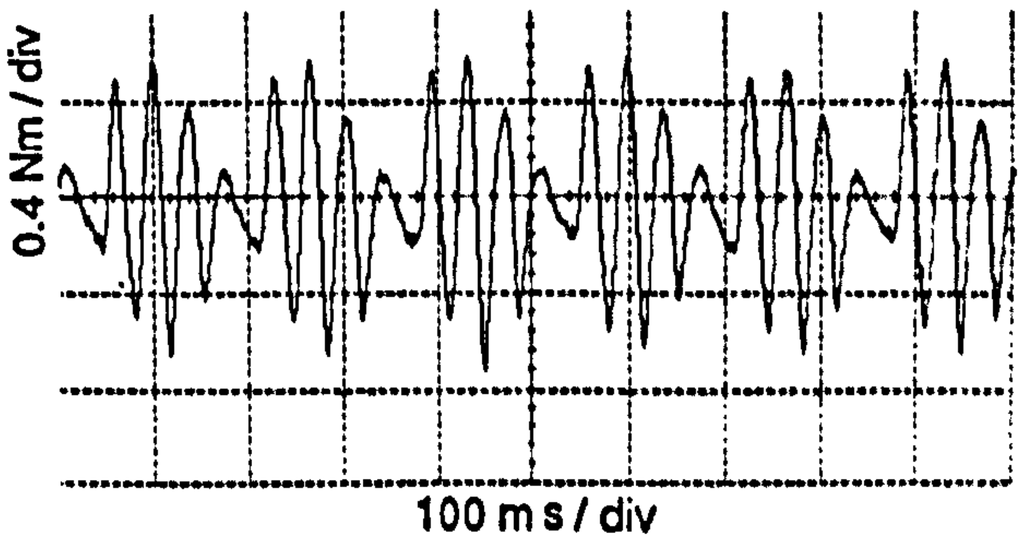

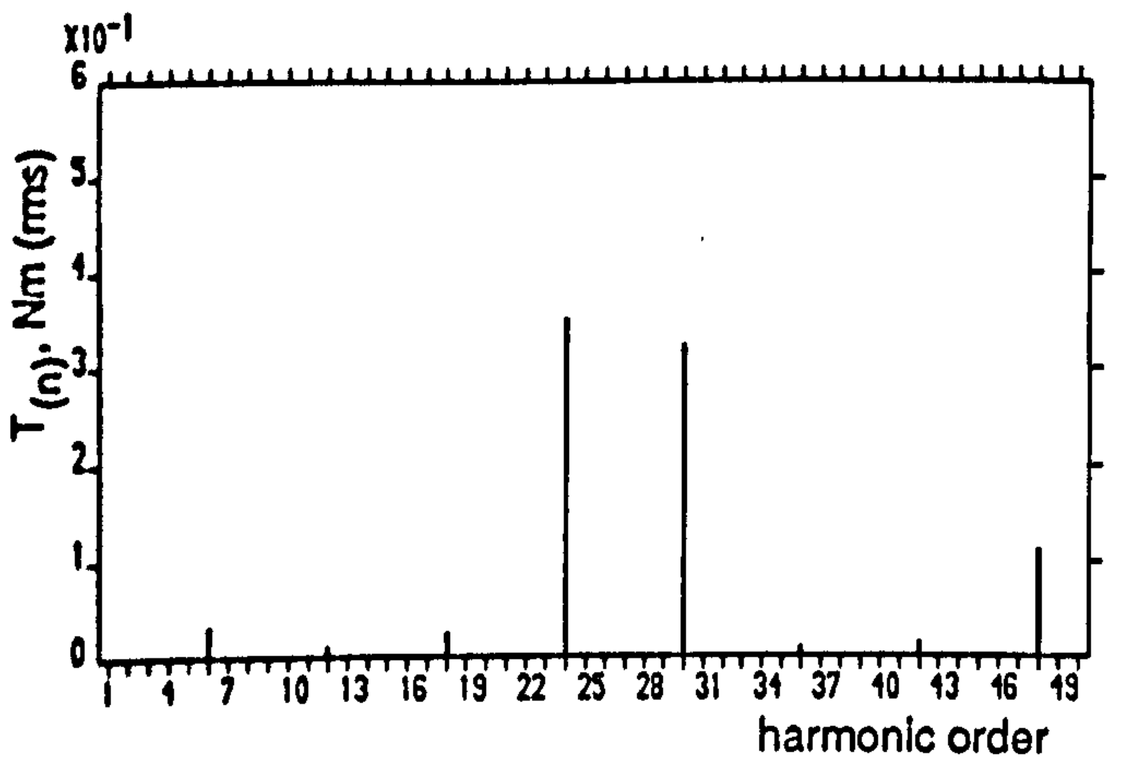

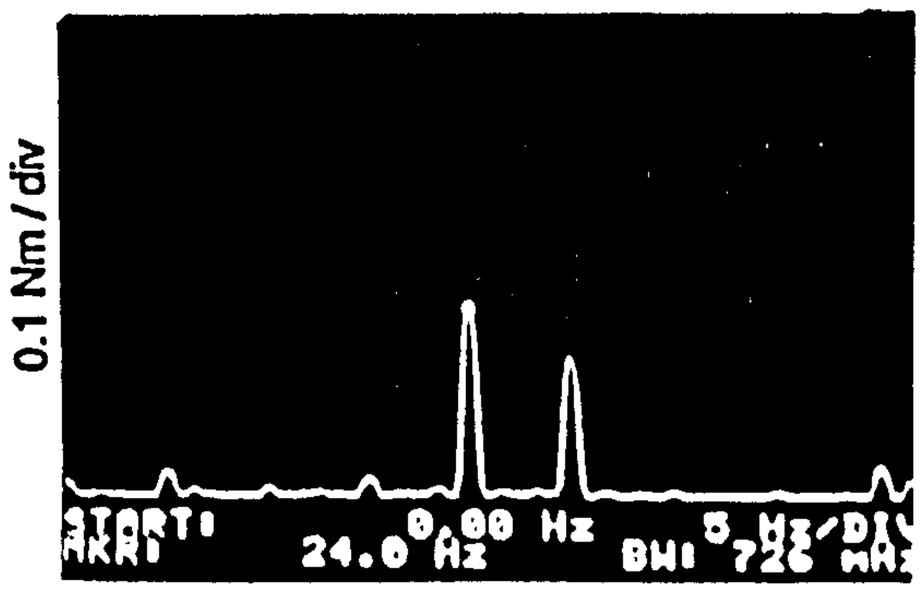

(c)

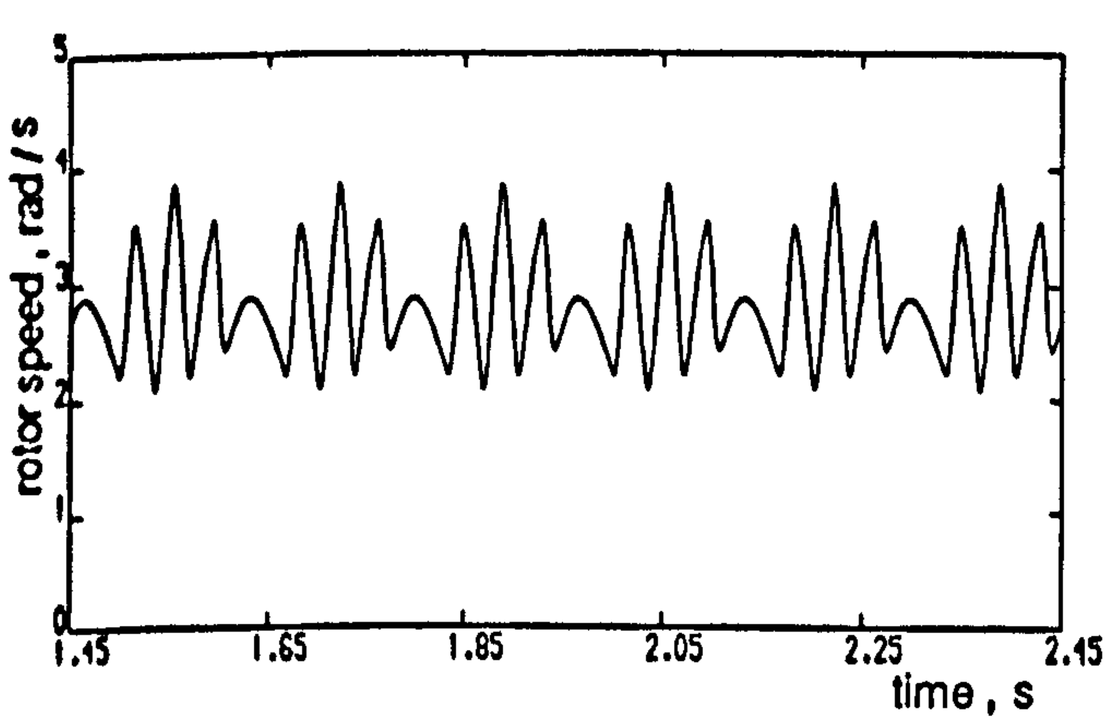

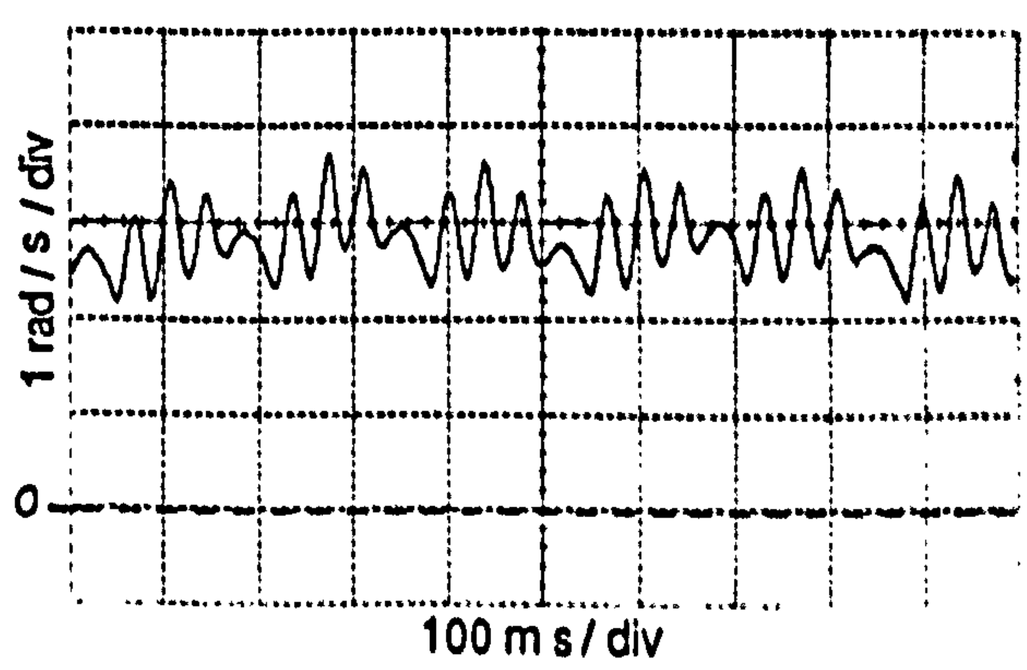

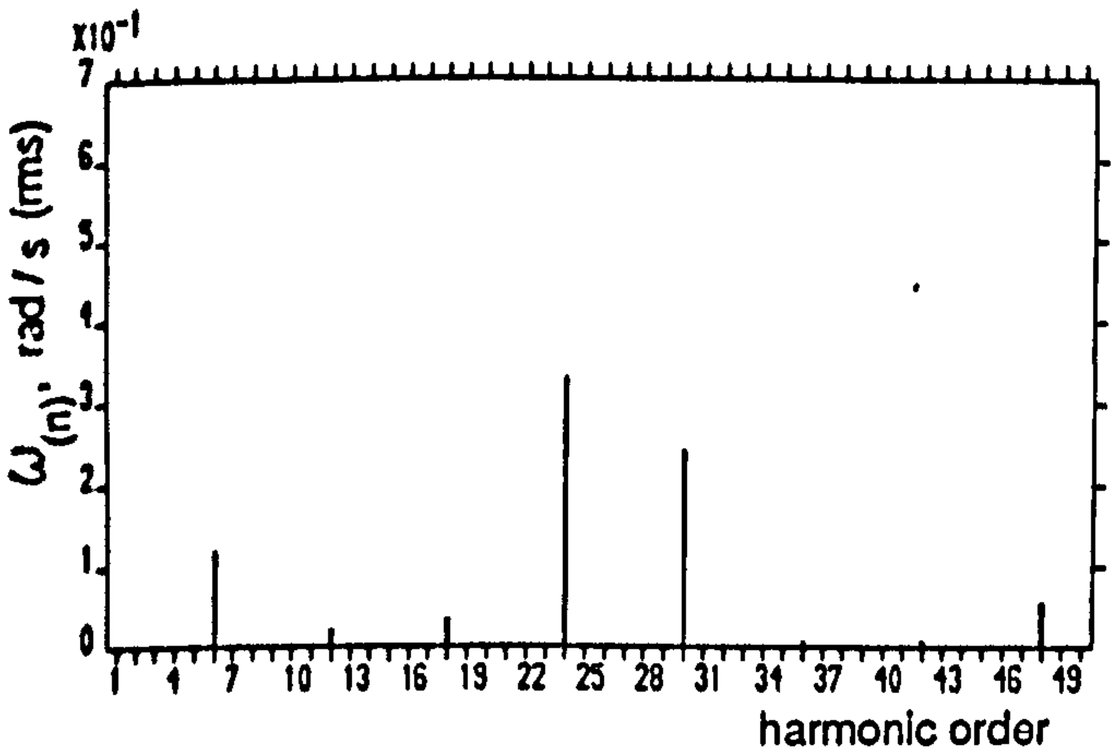

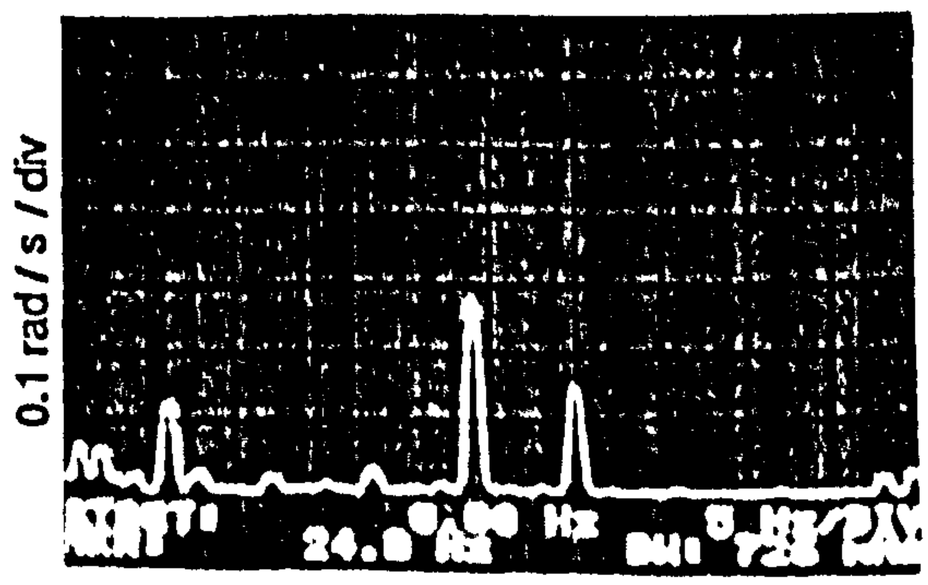

(d)

Figure 7.5 continued (c) Acceleration torque and spectrum
(d) Rotor speed and spectrum

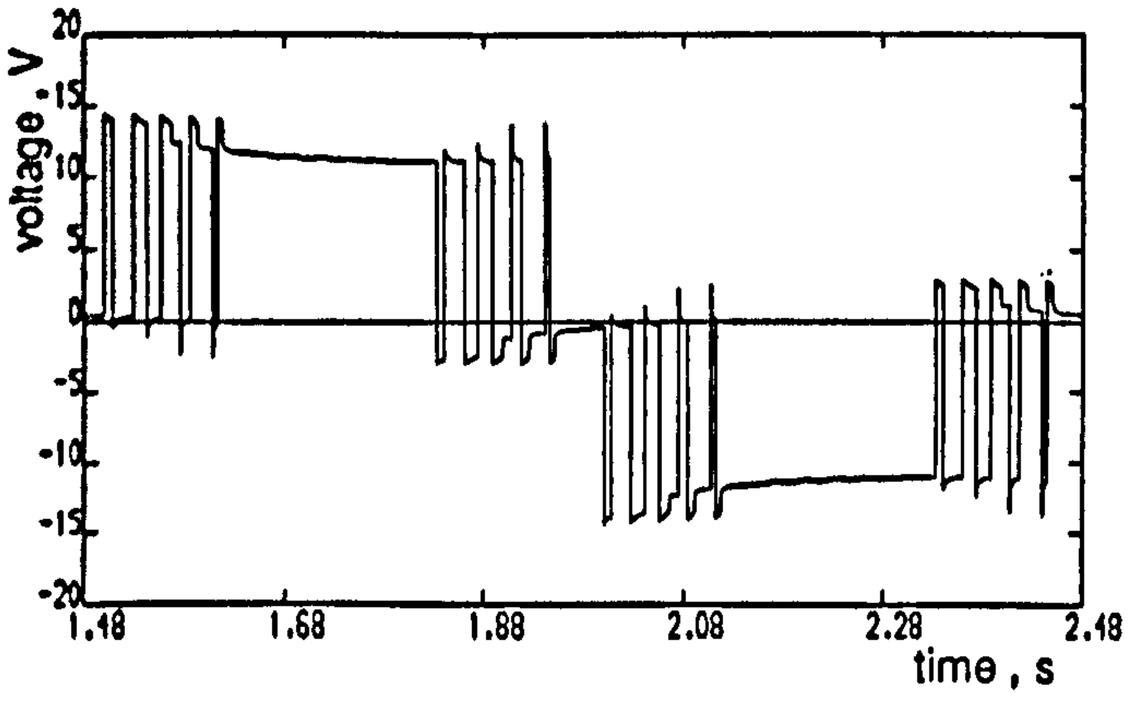

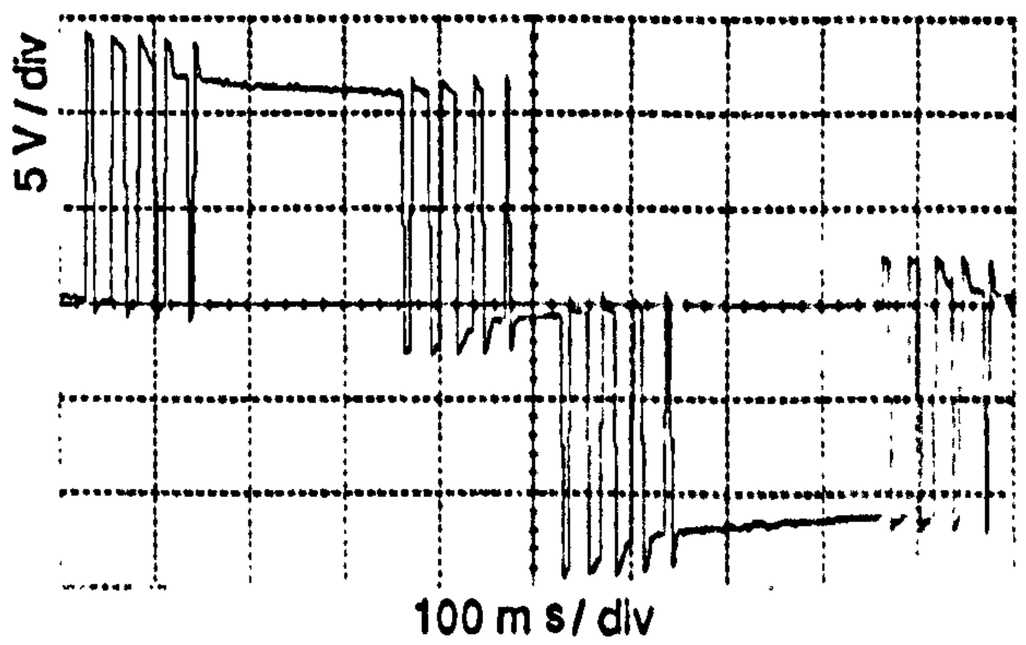

(a)

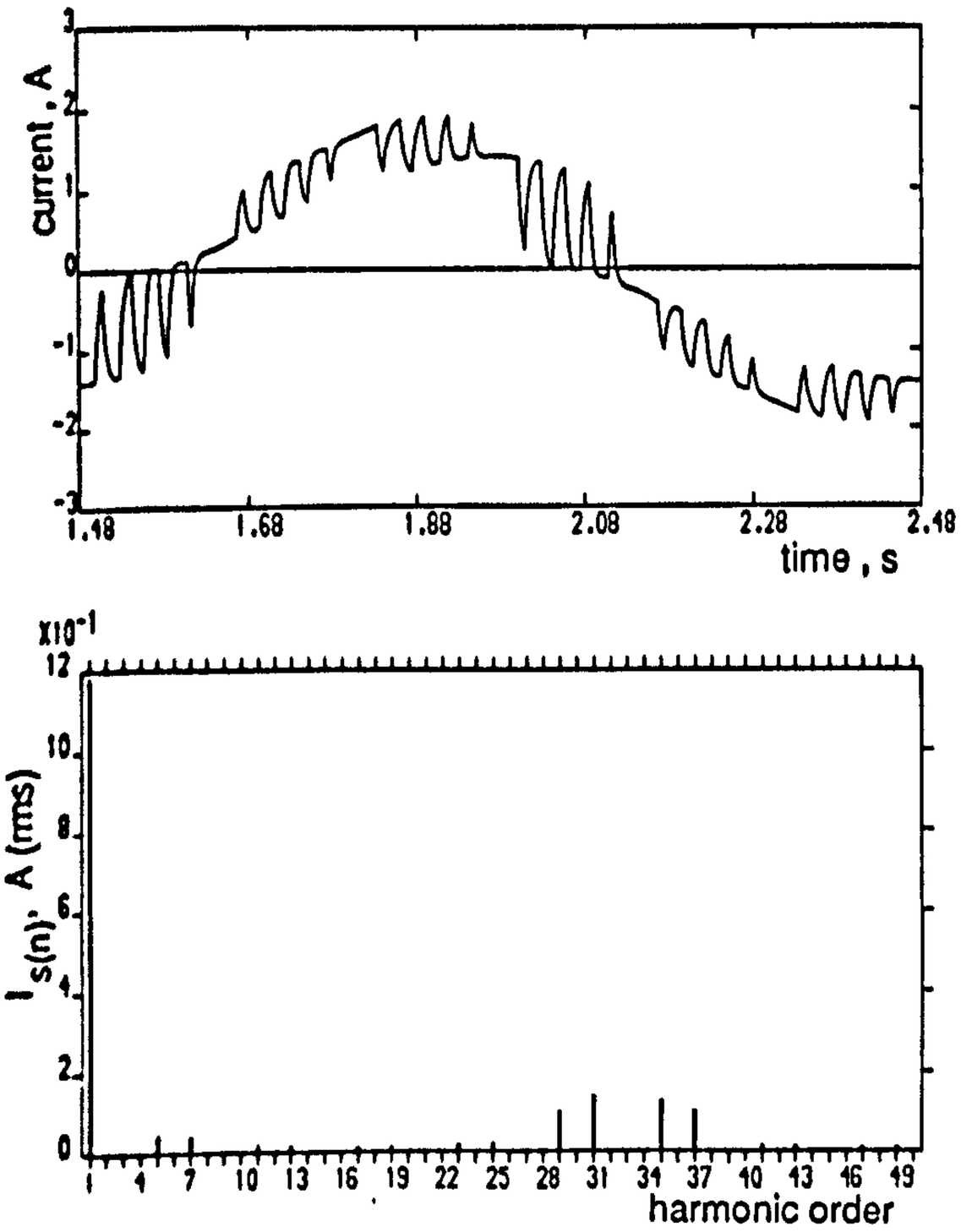

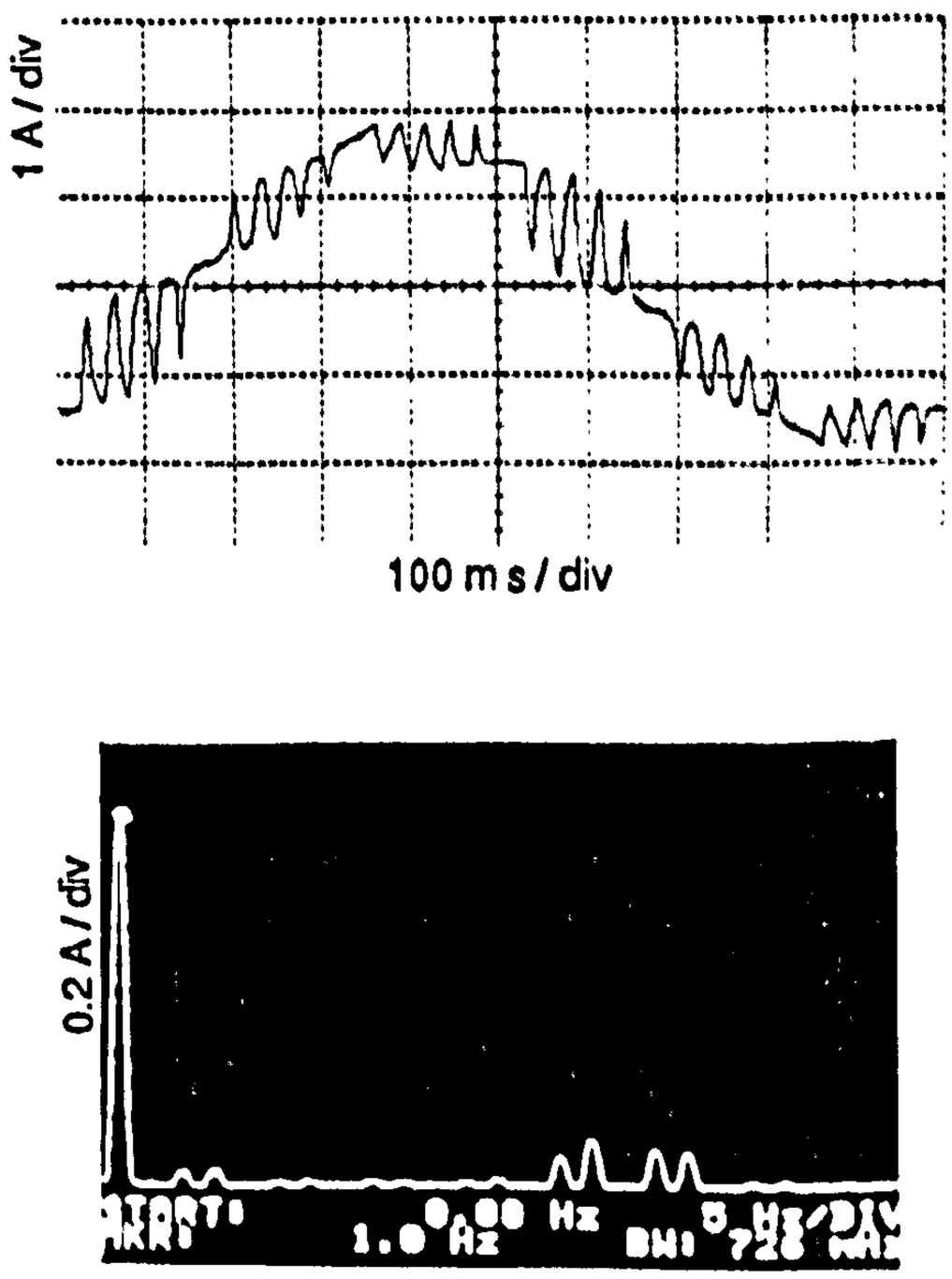

(b)

Figure 7.6 Computed and experimental results for type A PWMT8 half-wave symmetrical strategy at 1Hz stator frequency no-load operating condition
(a) Line voltage
(b) Stator current and spectrum

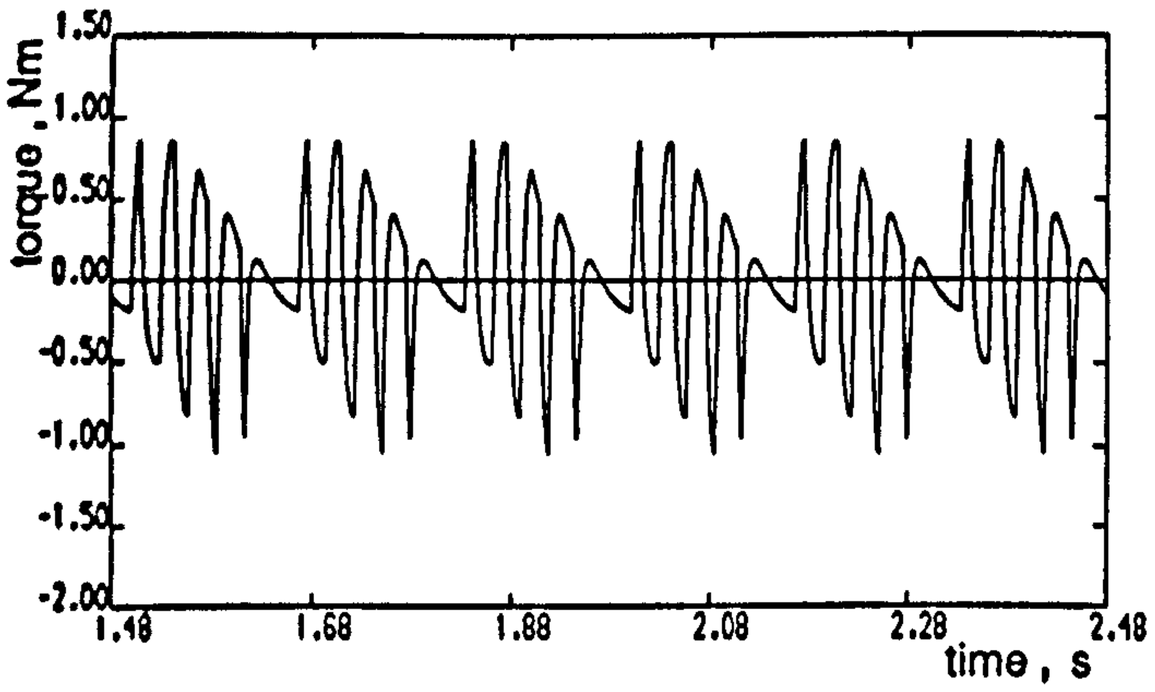

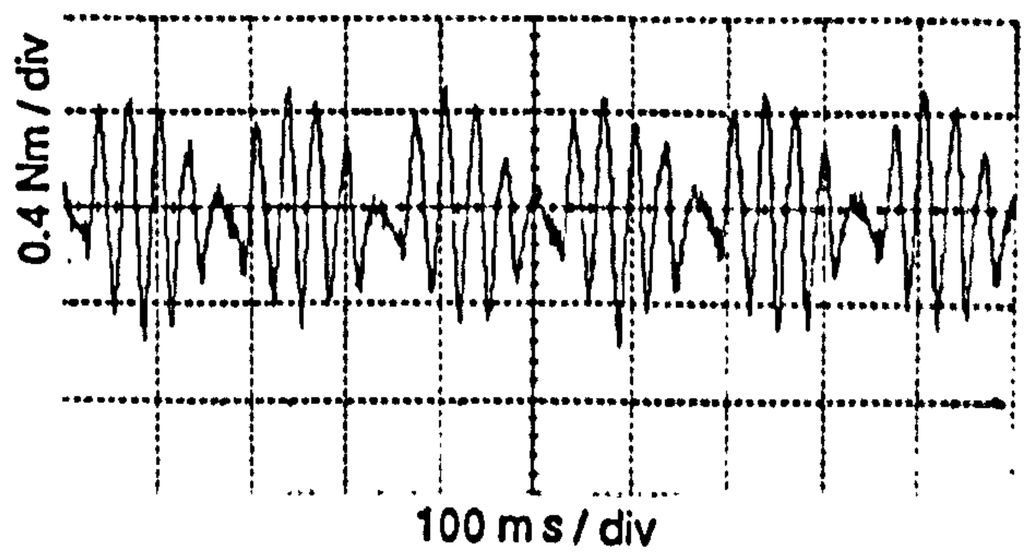

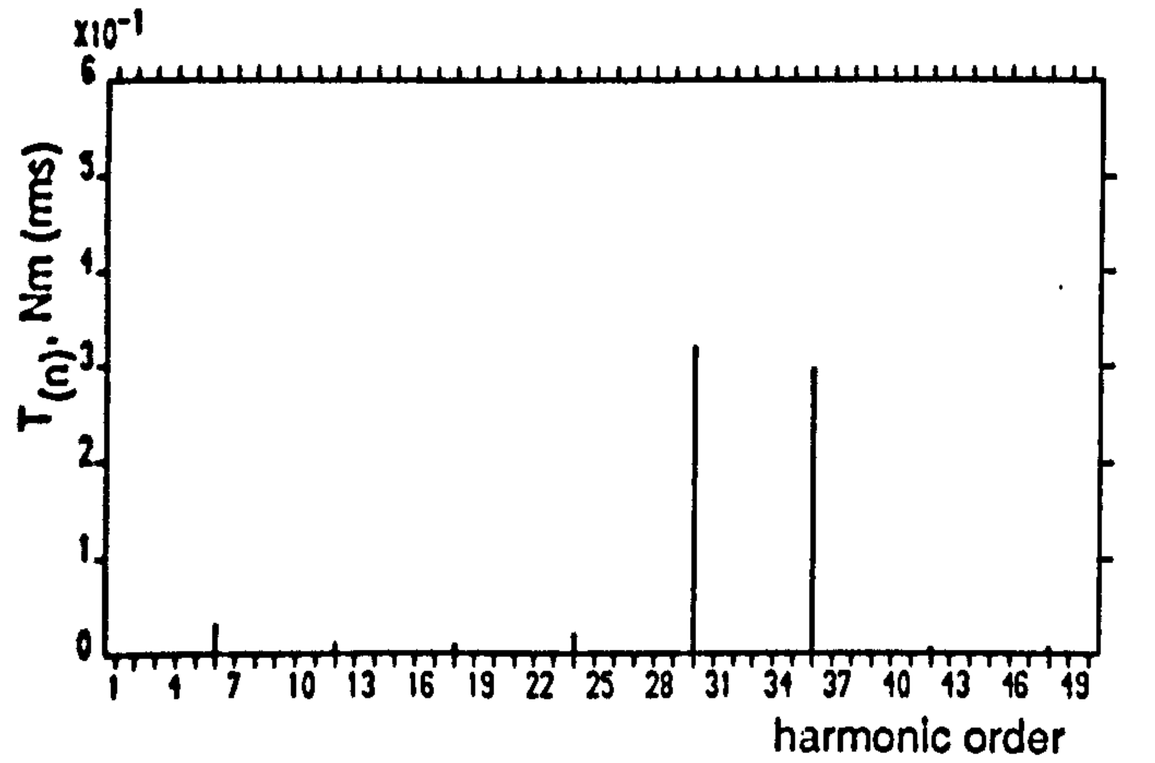

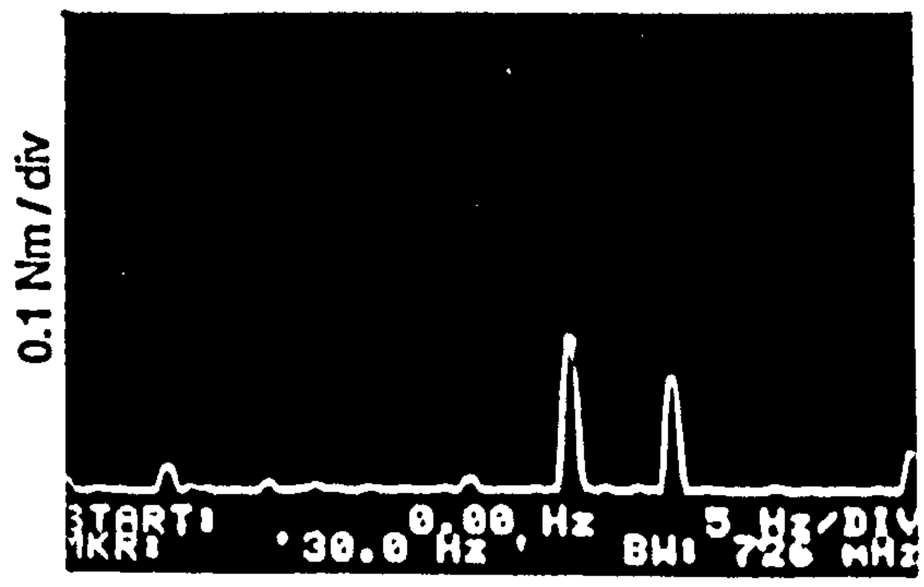

(c)

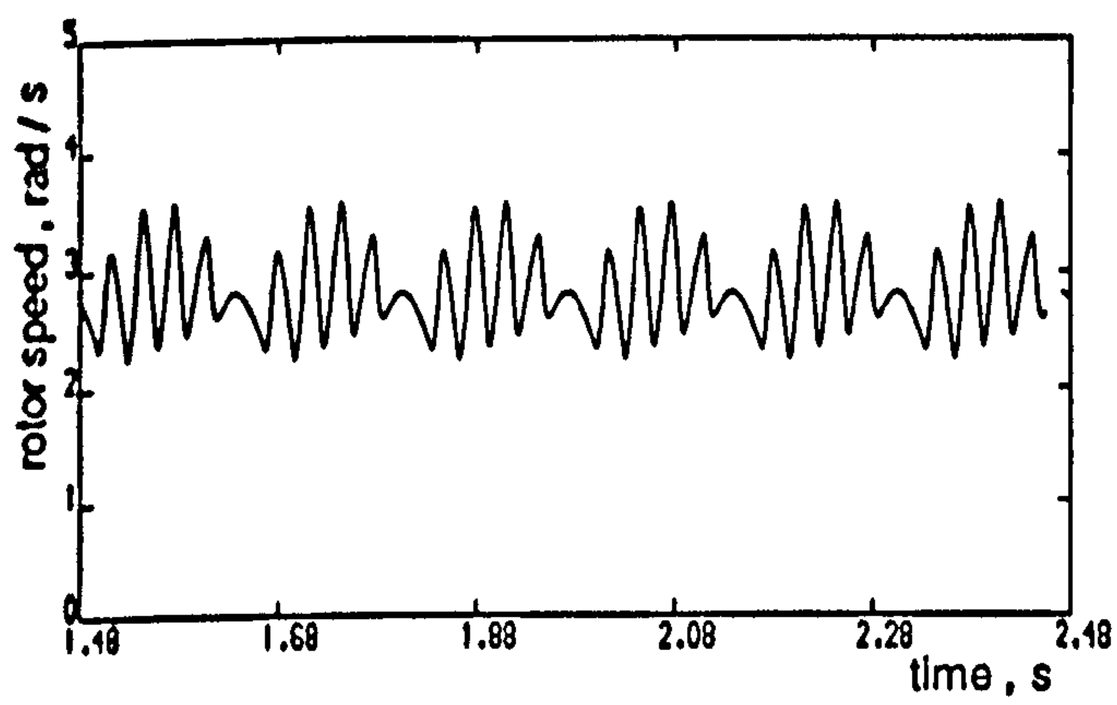

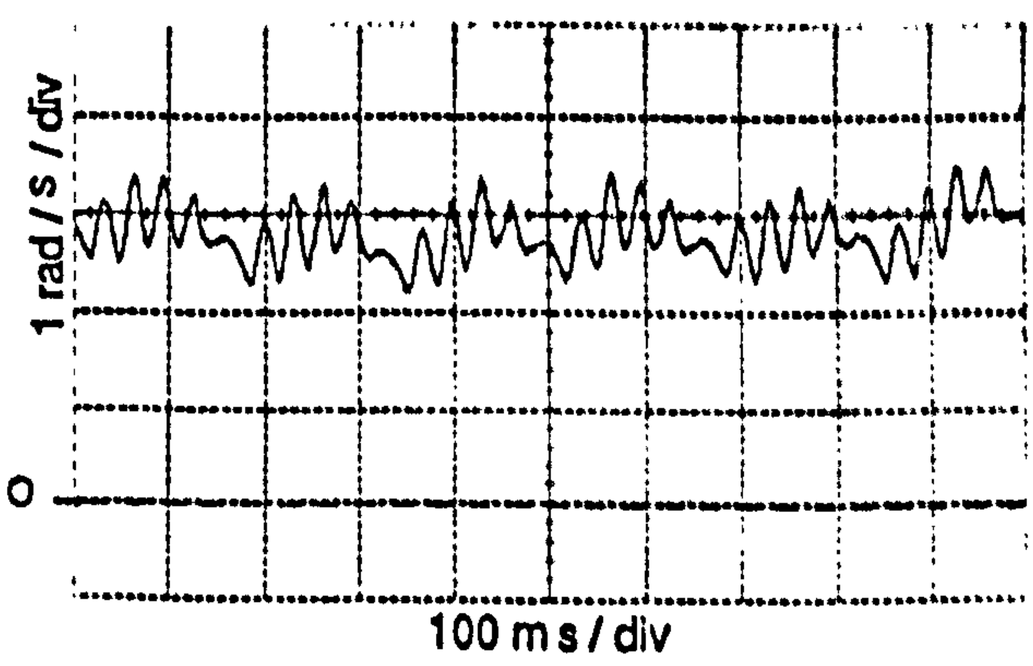

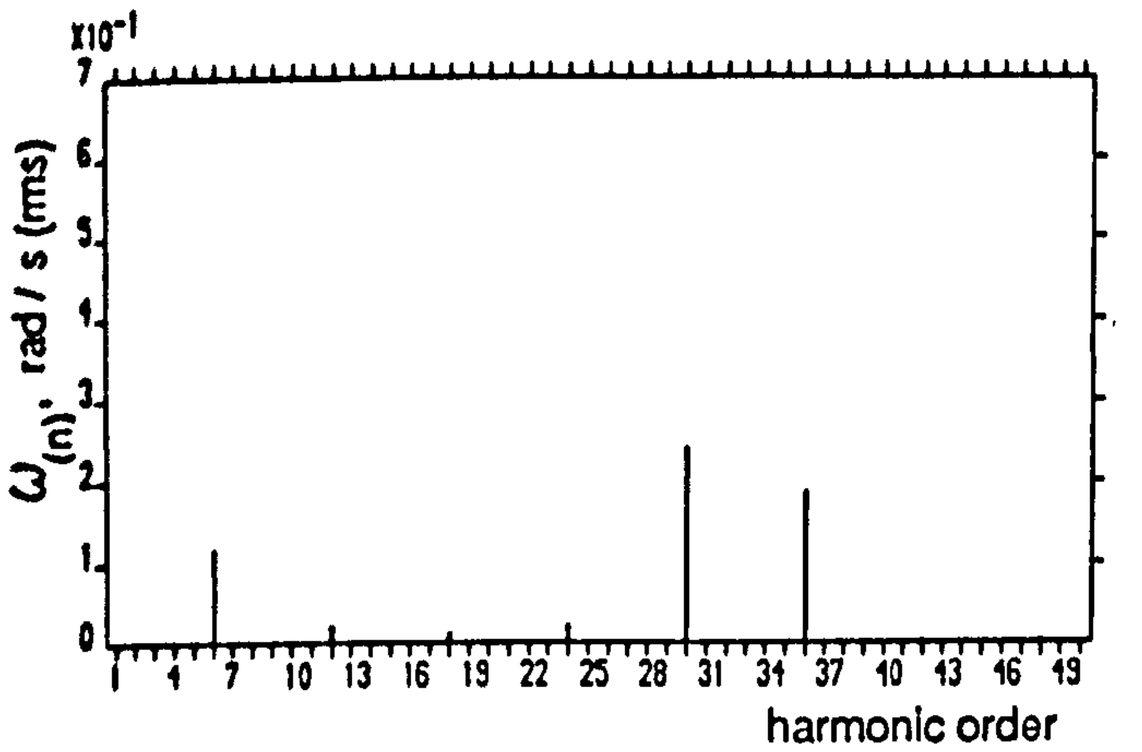

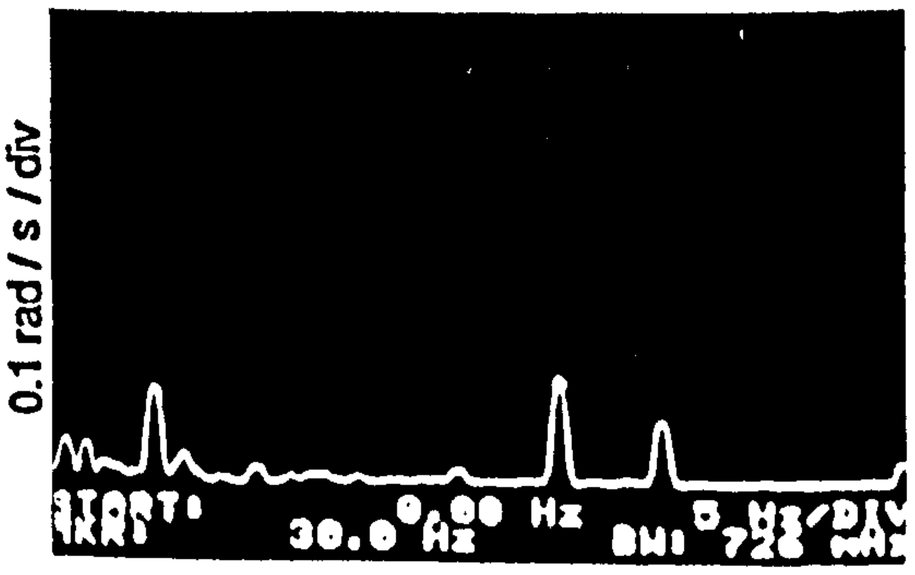

(d)

Figure 7.6 continued (c) Acceleration torque and spectrum
(d) Rotor speed and spectrum

respectively. In each mode, the first three and four low order torque components are considerably reduced by the cancellation process. A redistribution of the high order harmonic magnitudes is still evident when compared with figures 5.15 and 5.16 for the elimination strategy, as is a reduction in the peak-to-peak torque pulsations and speed ripple.

The behaviour of the drive when using a type B strategy is illustrated by figures 7.7 to 7.10. The number of switching angles is increased for each mode, using the equality constraints of section 7.3.2, so that the PWM voltage pattern ends up with the same pulse number as the elimination strategy. Figure 7.7(a) shows that the line voltage waveform for four switching angles per half-cycle has five pulses per half-cycle and does not display quarter-wave symmetry. Figure 7.7(b) illustrates the stator current waveform and its spectrum, with the 5th-and 7th-harmonic components clearly visible. Figure 7.7(c) shows the acceleration torque waveform, with its harmonic spectrum, which demonstrates a lower 6th-harmonic torque component than the QSW mode of figure 5.12(c), and a better distribution of higher order harmonic components than the elimination case of figure 5.13(c) for the same number of pulses per half-cycle. The peak-to-peak speed ripple in figure 7.7(d) is significantly reduced in comparison with that of figure 5.13(d). Figures 7.8 to 7.10 show that, as the pulse number increases and further torque components are considered for cancellation, a better distribution of the harmonic current magnitudes is obtained and lower torque pulsations and speed ripple are achieved. This confirms the practical implementation of this strategy and demonstrates the reduction in speed ripple with increasing PWM pulse number.

Observations of the speed harmonic spectra of figures 7.3 to 7.10 show that, in all cases, the 6th-harmonic component still exists and does not experience the same reduction as does the 6th-harmonic torque component. This is because

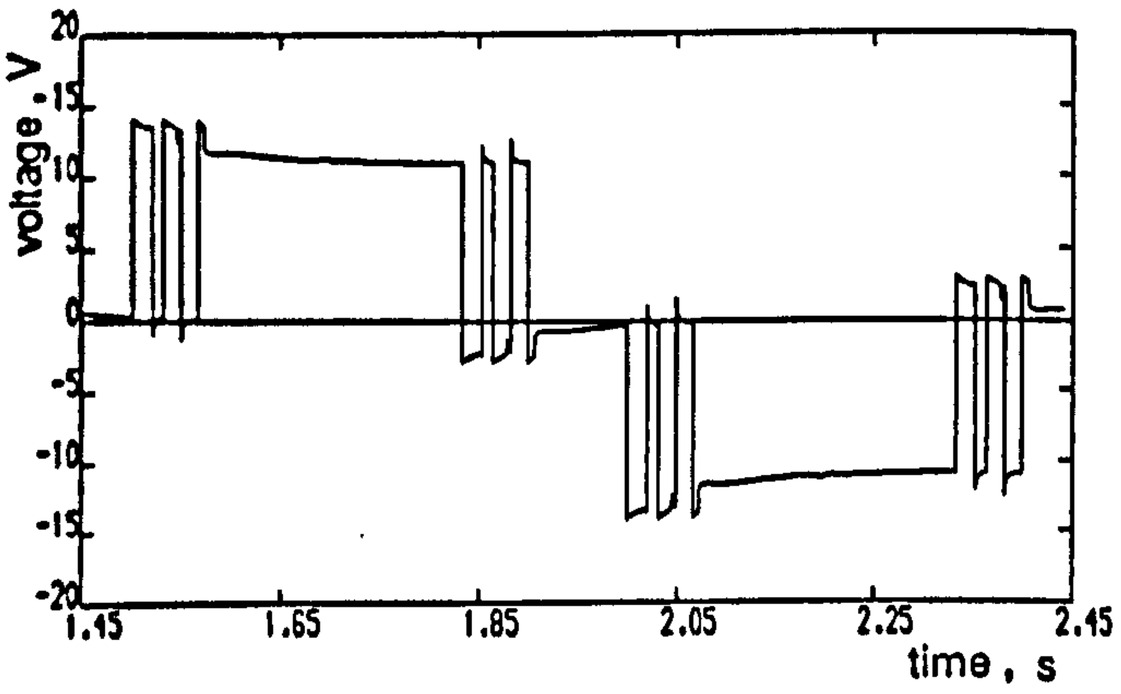

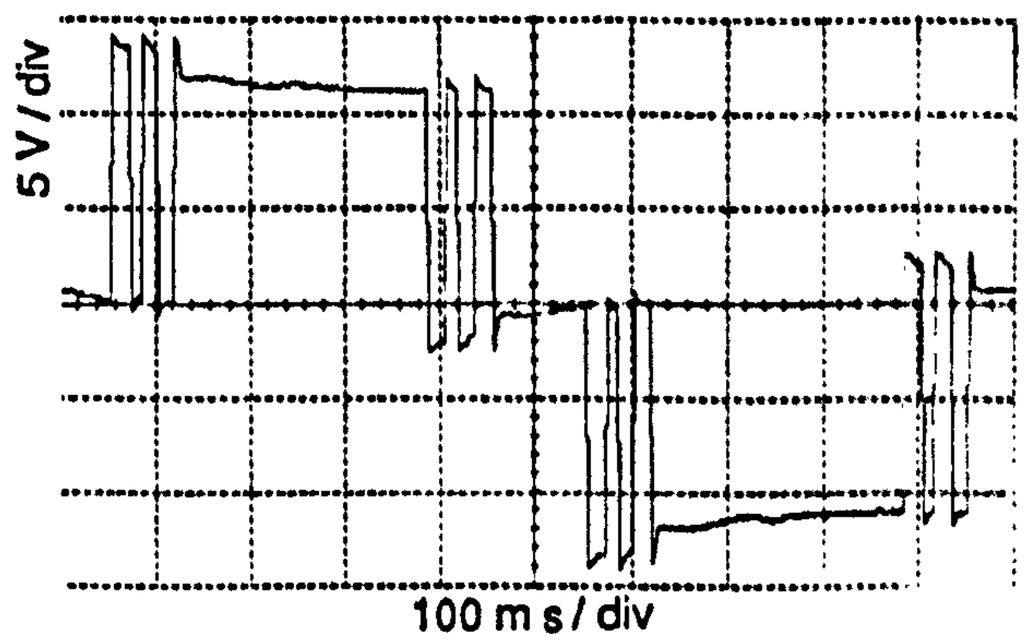

(a)

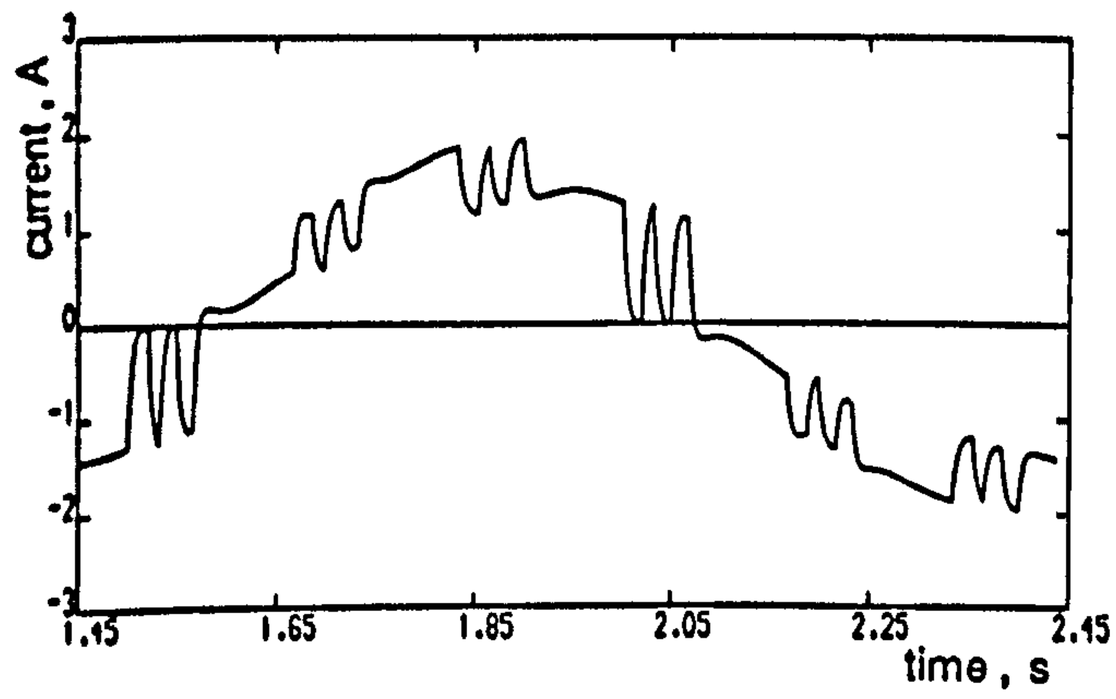

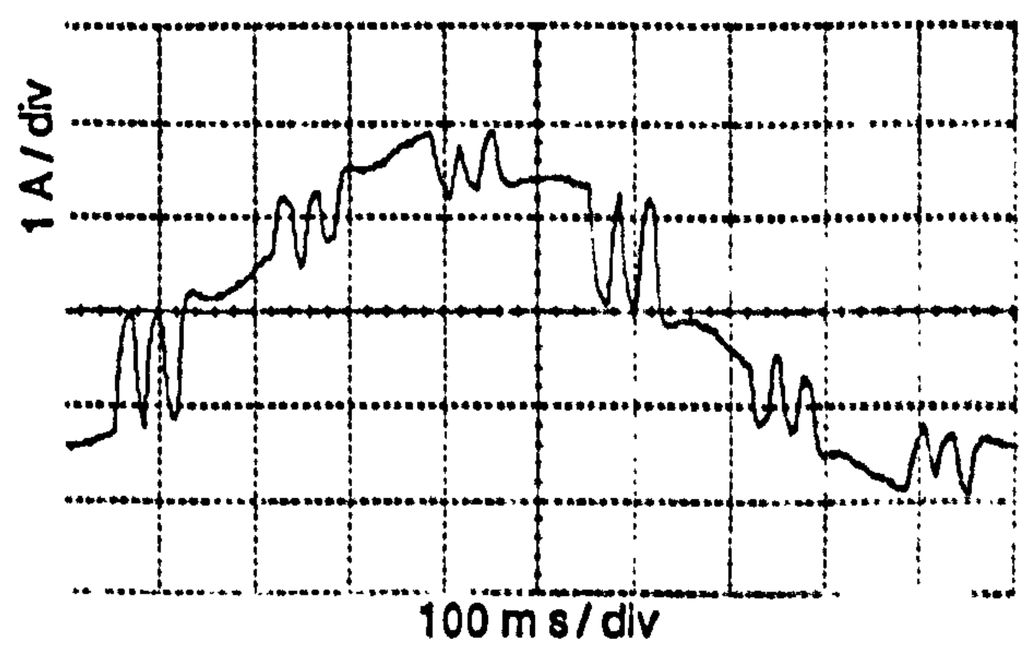

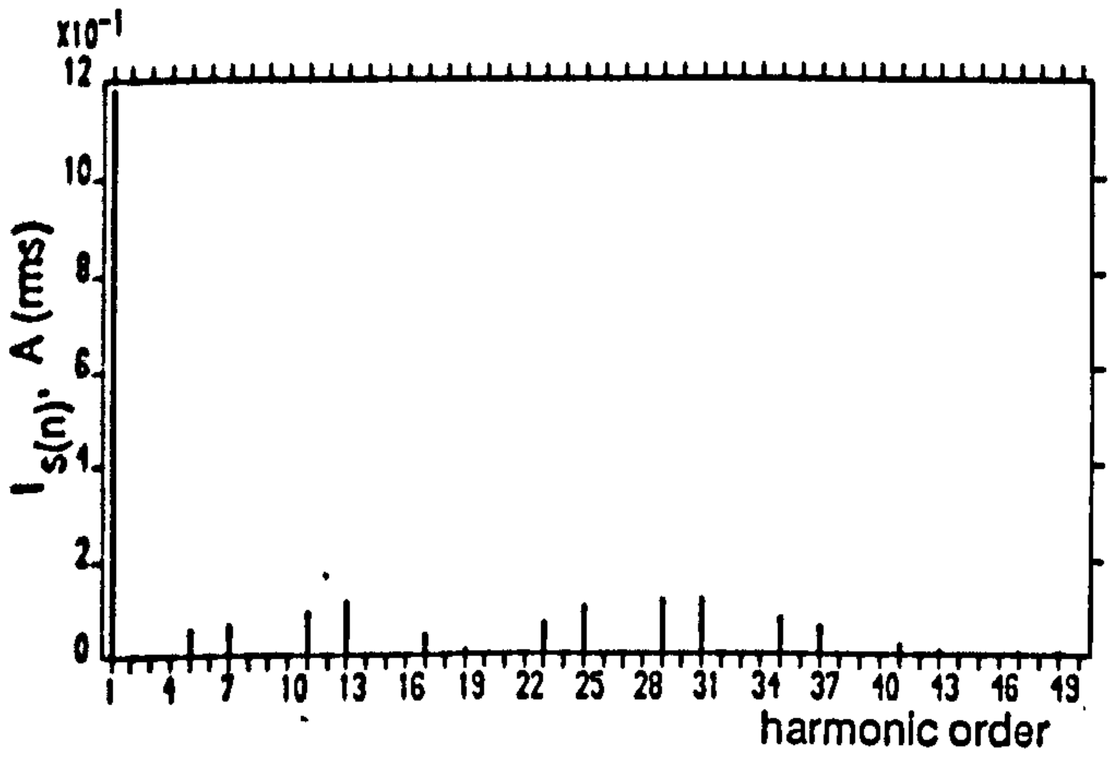

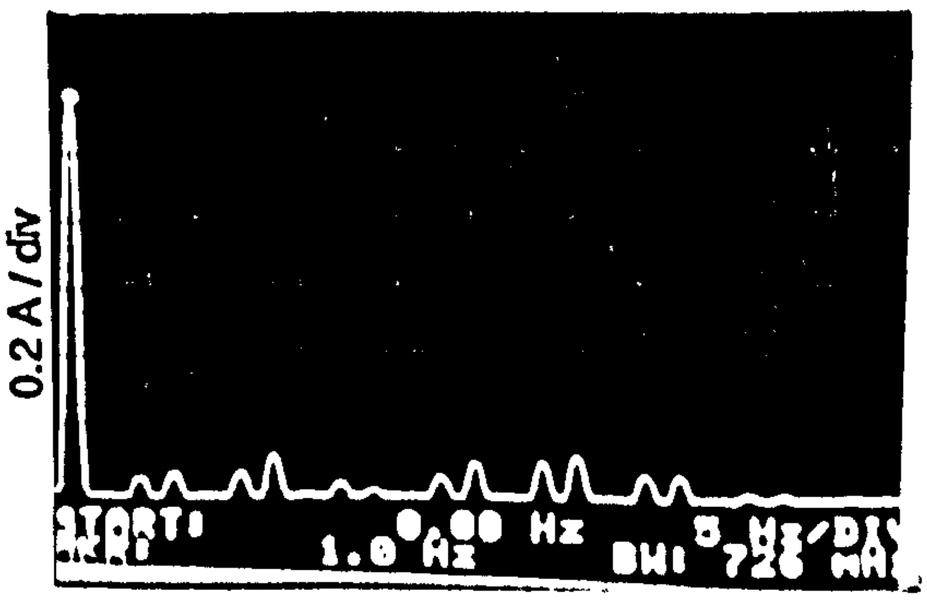

(b)

Figure 7.7 Computed and experimental results for type B PWMT4 half-wave symmetrical strategy at 1Hz stator frequency no-load operating condition
(a) Line voltage
(b) Stator current and spectrum

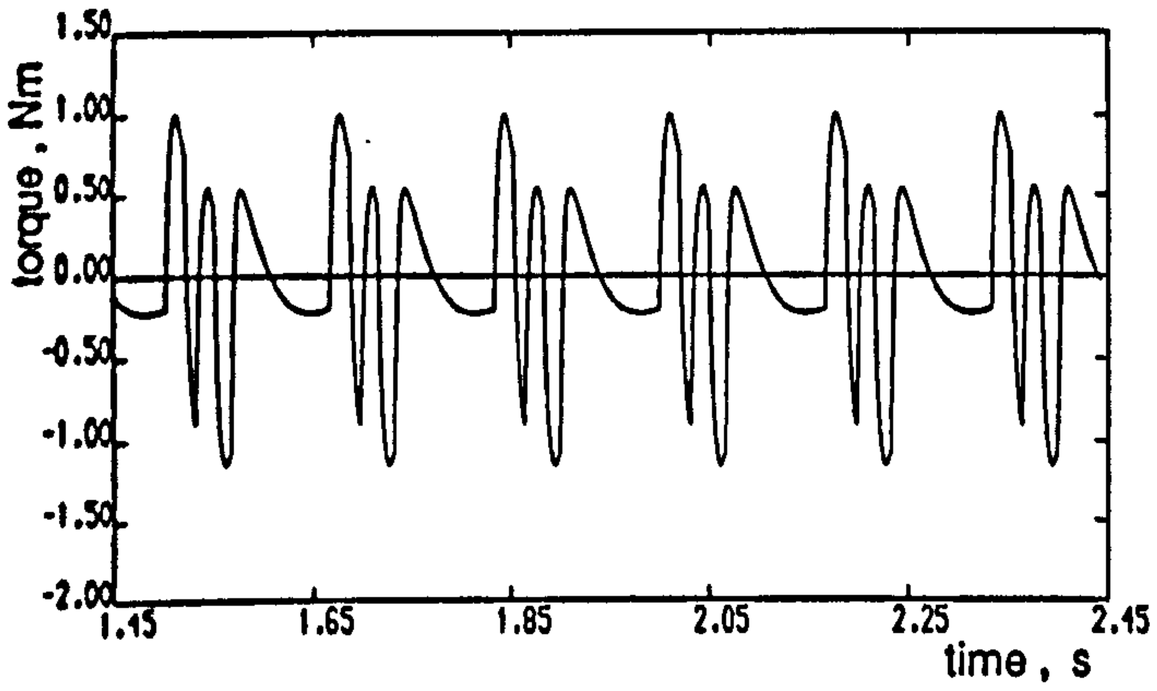

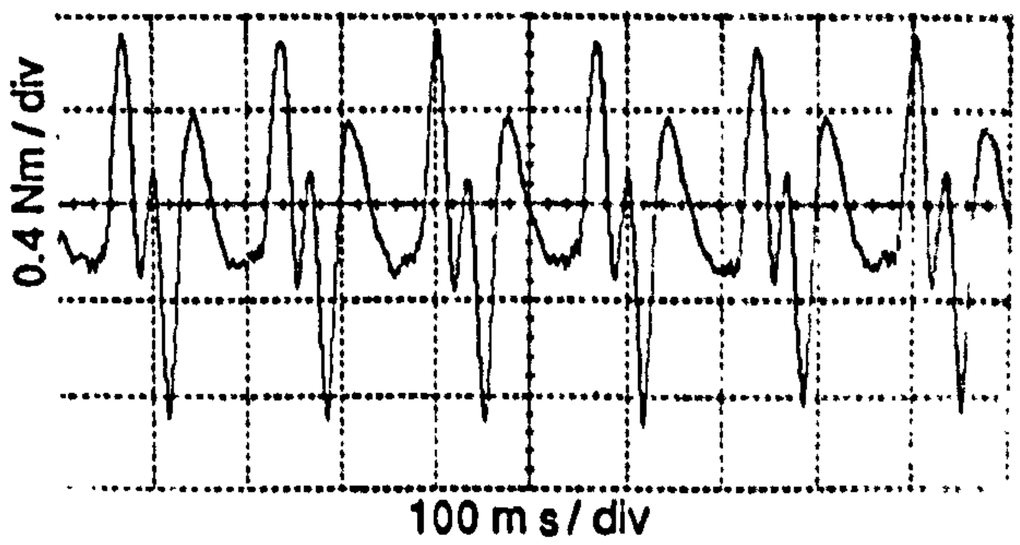

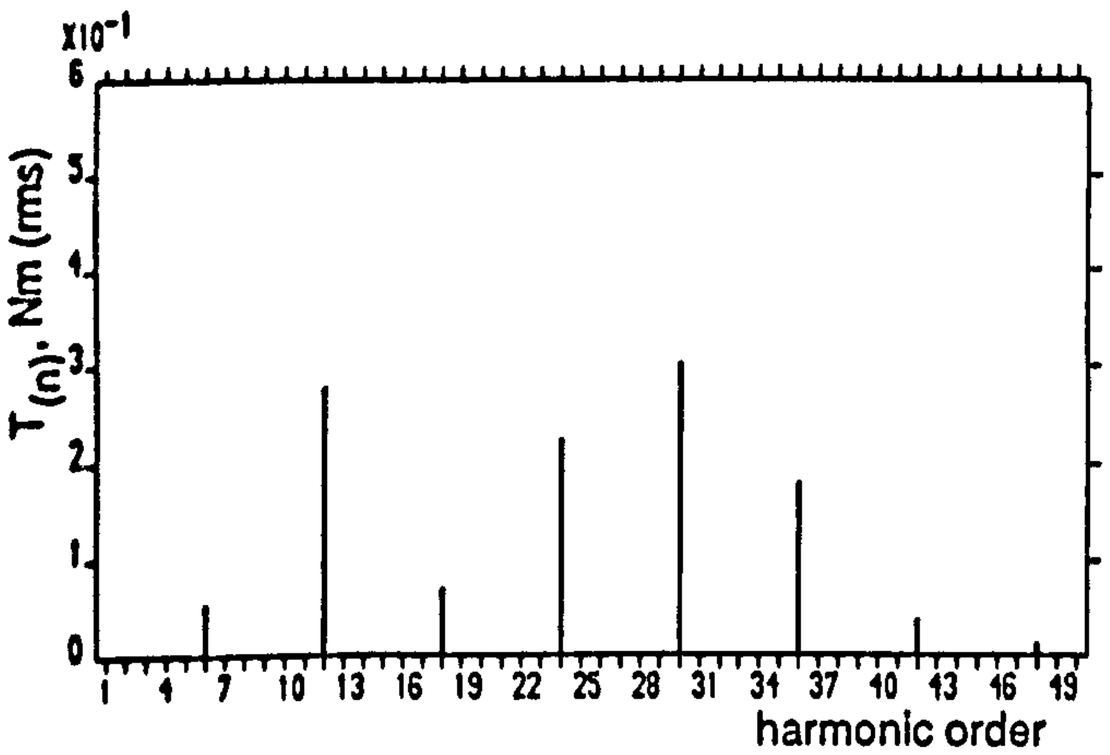

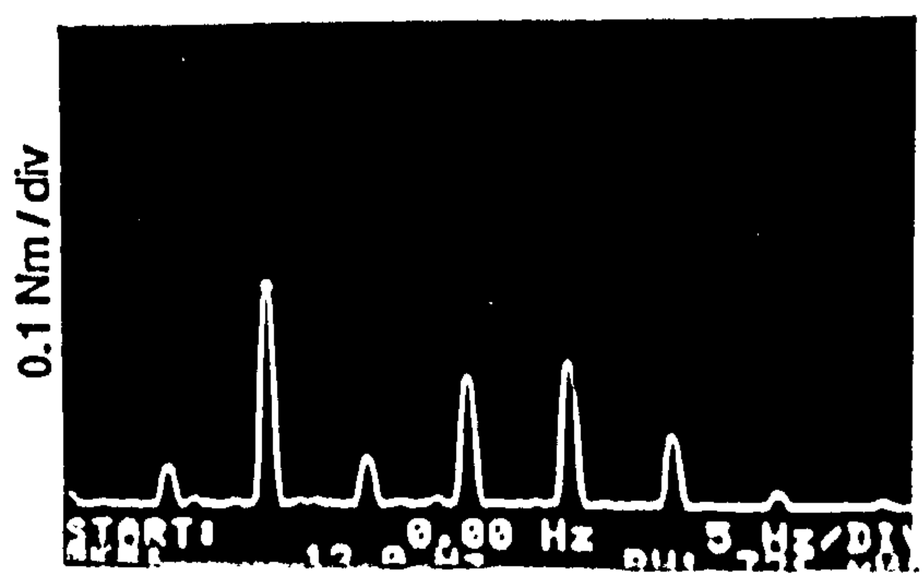

(c)

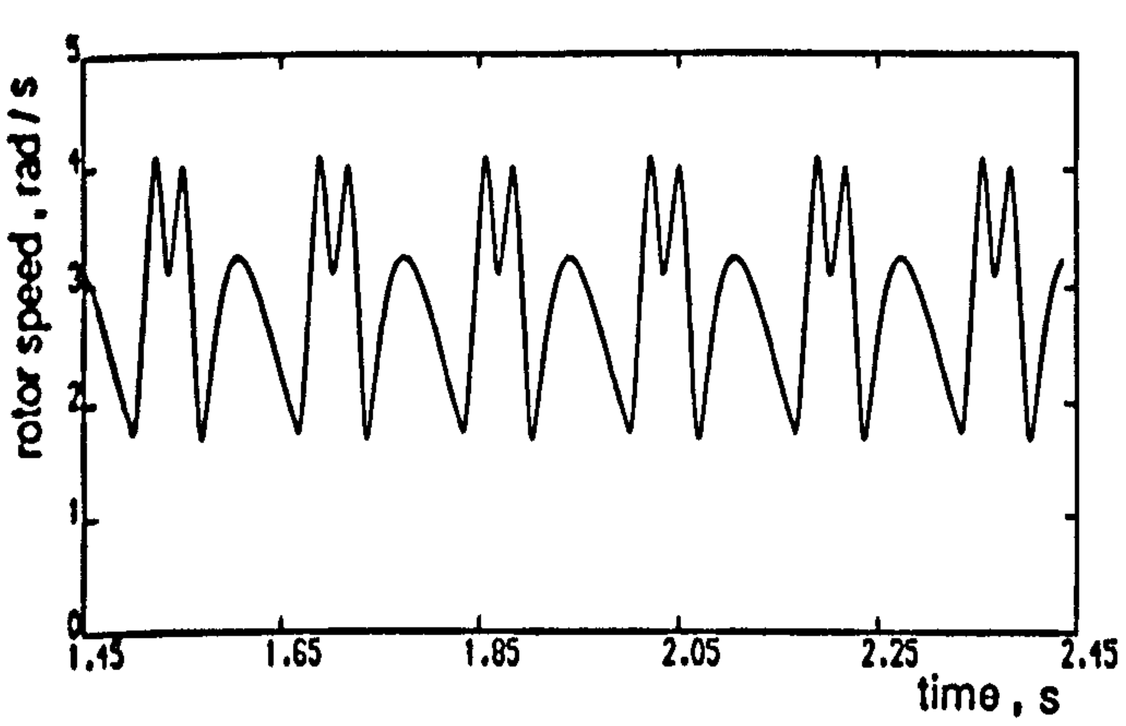

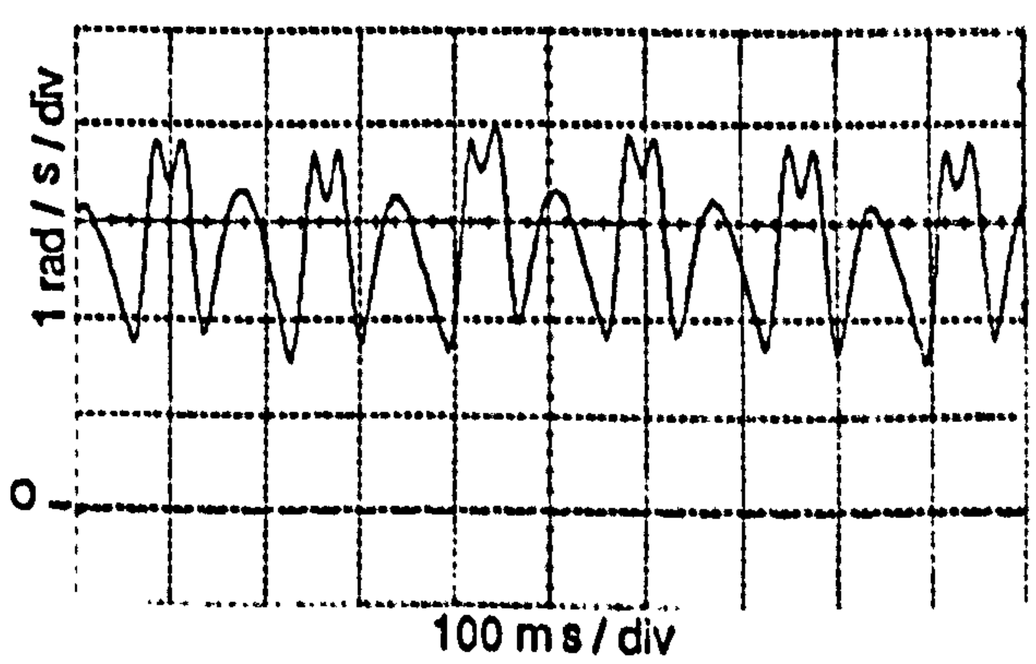

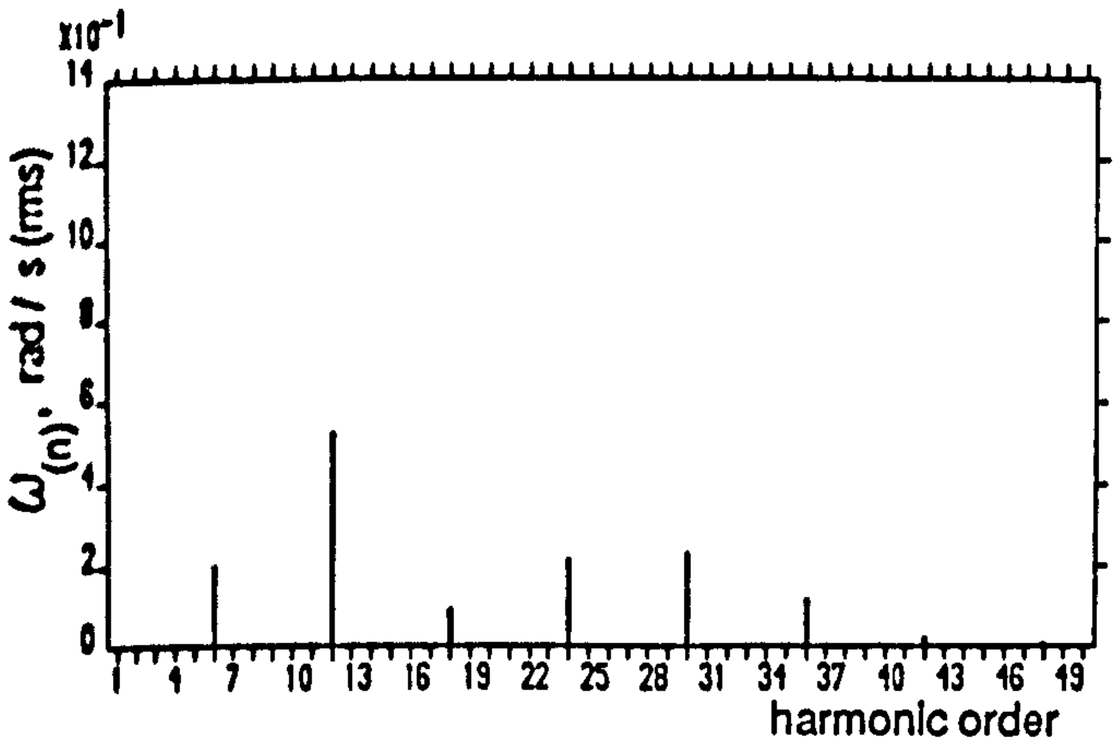

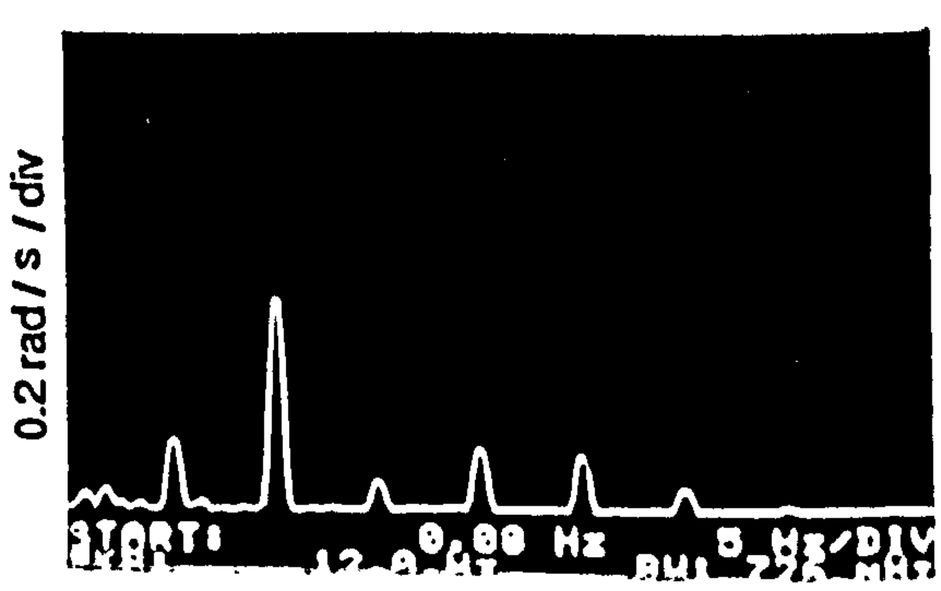

(d)

Figure 7.7 continued (c) Acceleration torque and spectrum
(d) Rotor speed and spectrum

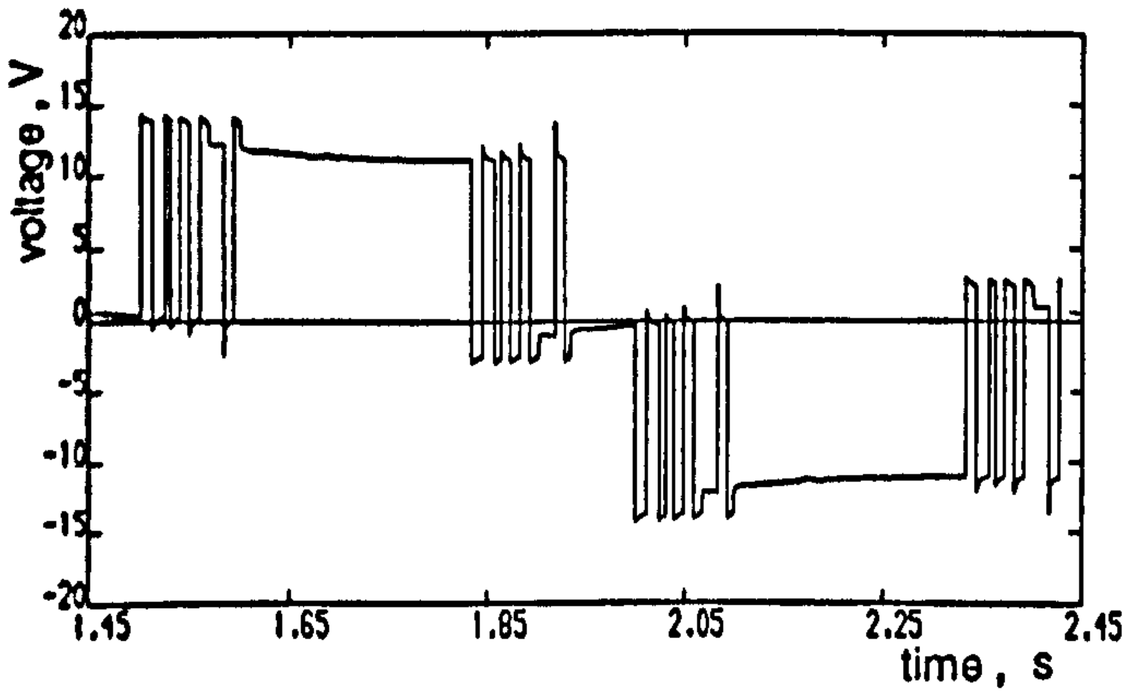

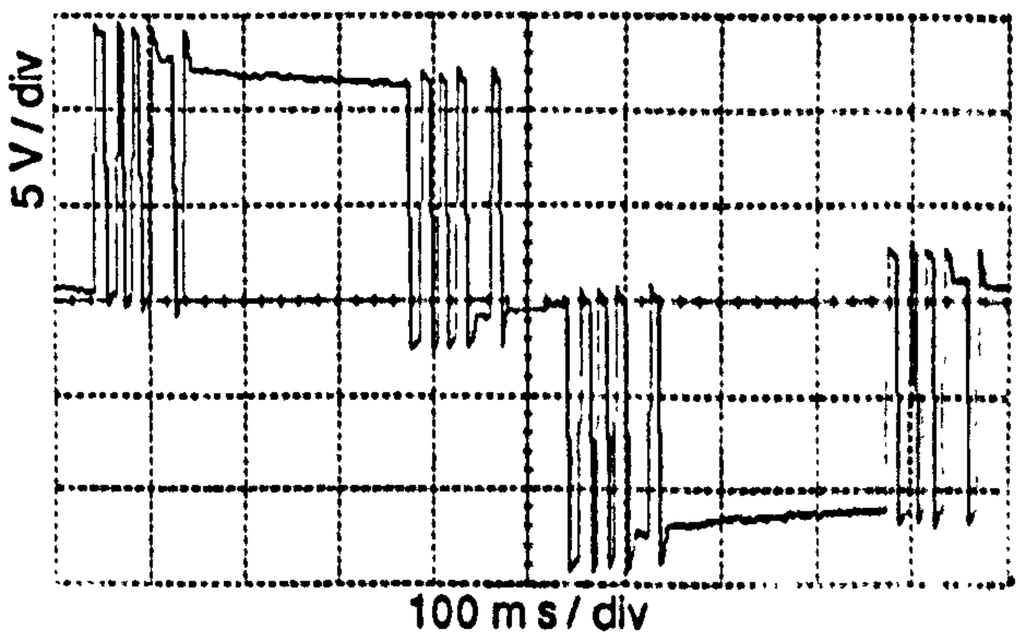

(a)

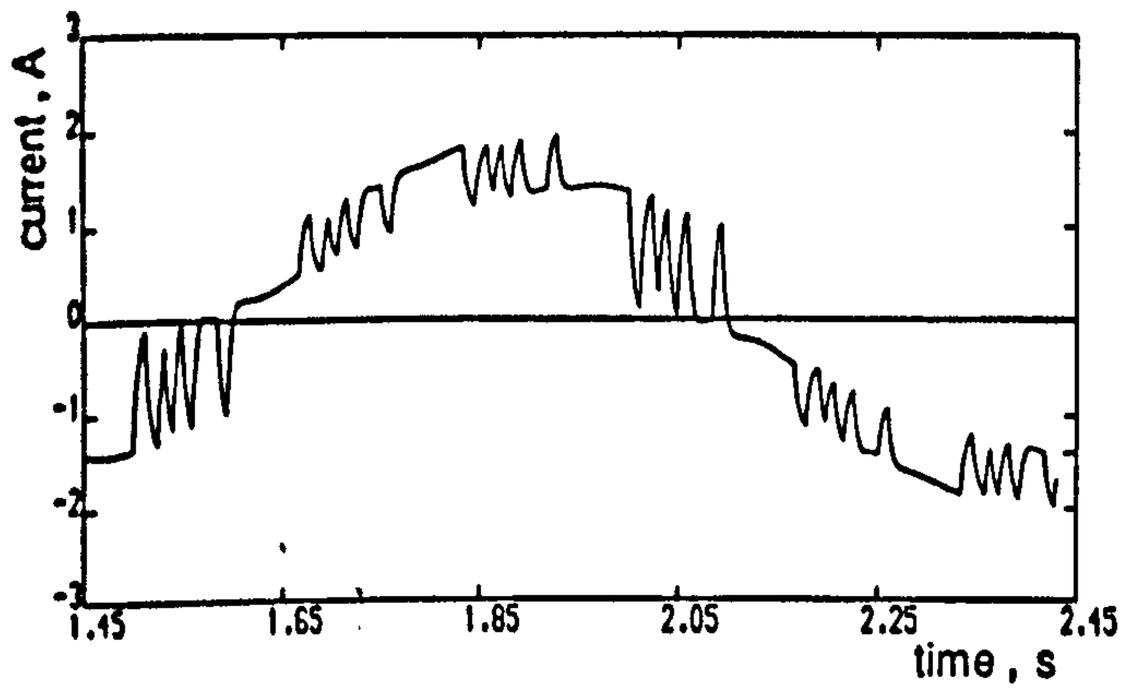

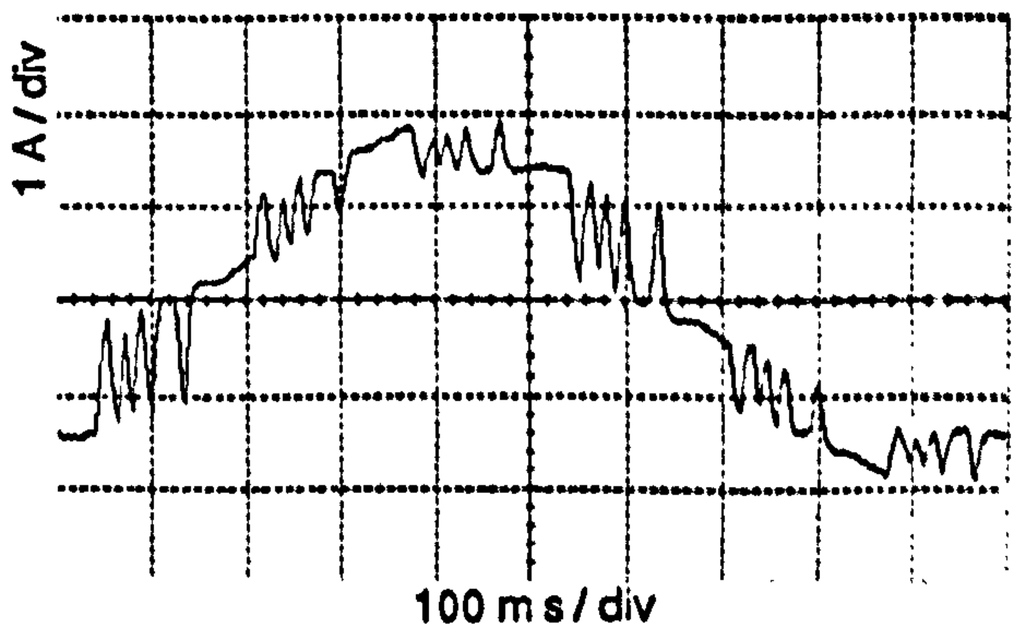

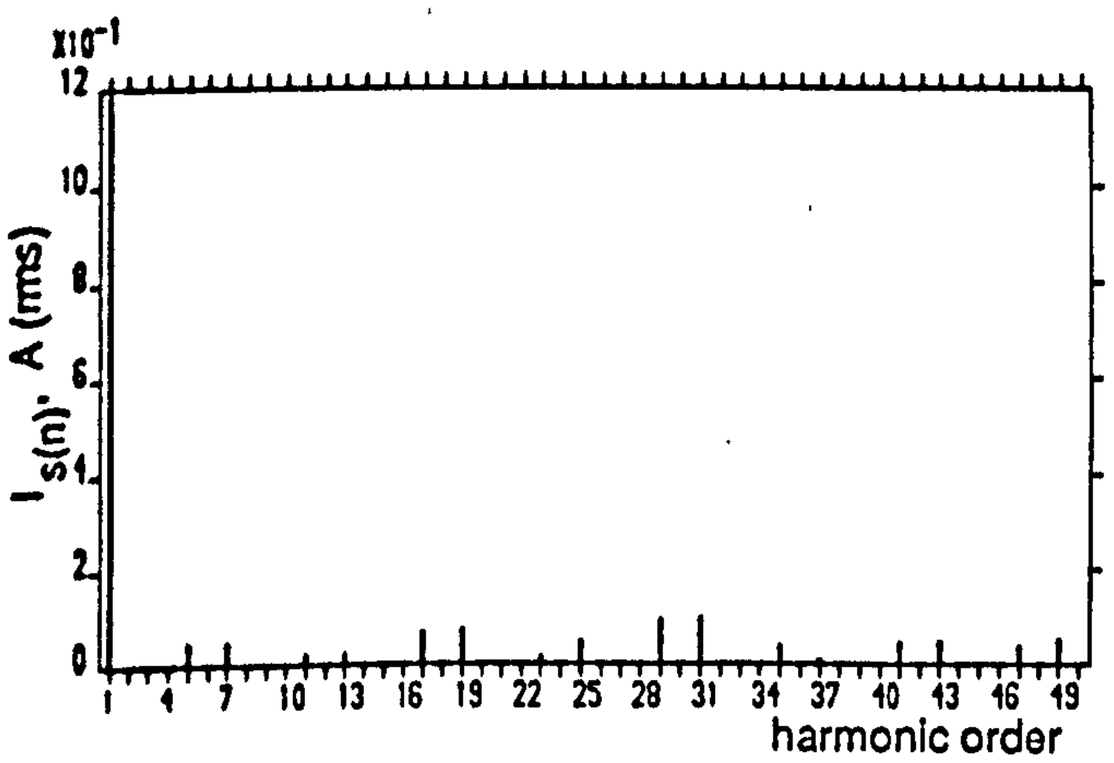

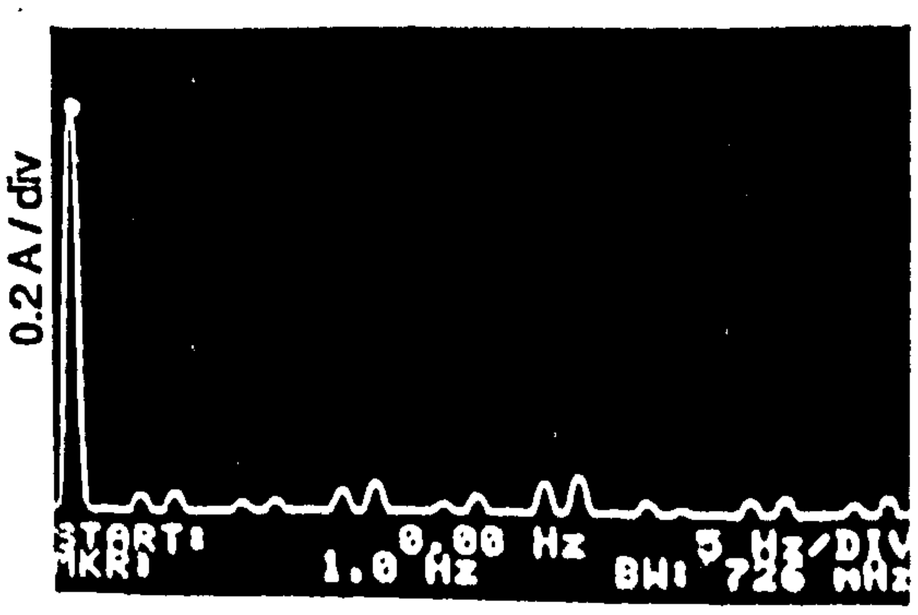

(b)

Figure 7.8 Computed and experimental results for type B PWMT8 half-wave symmetrical strategy at 1Hz stator frequency no-load operating condition
(a) Line voltage
(b) Stator current and spectrum

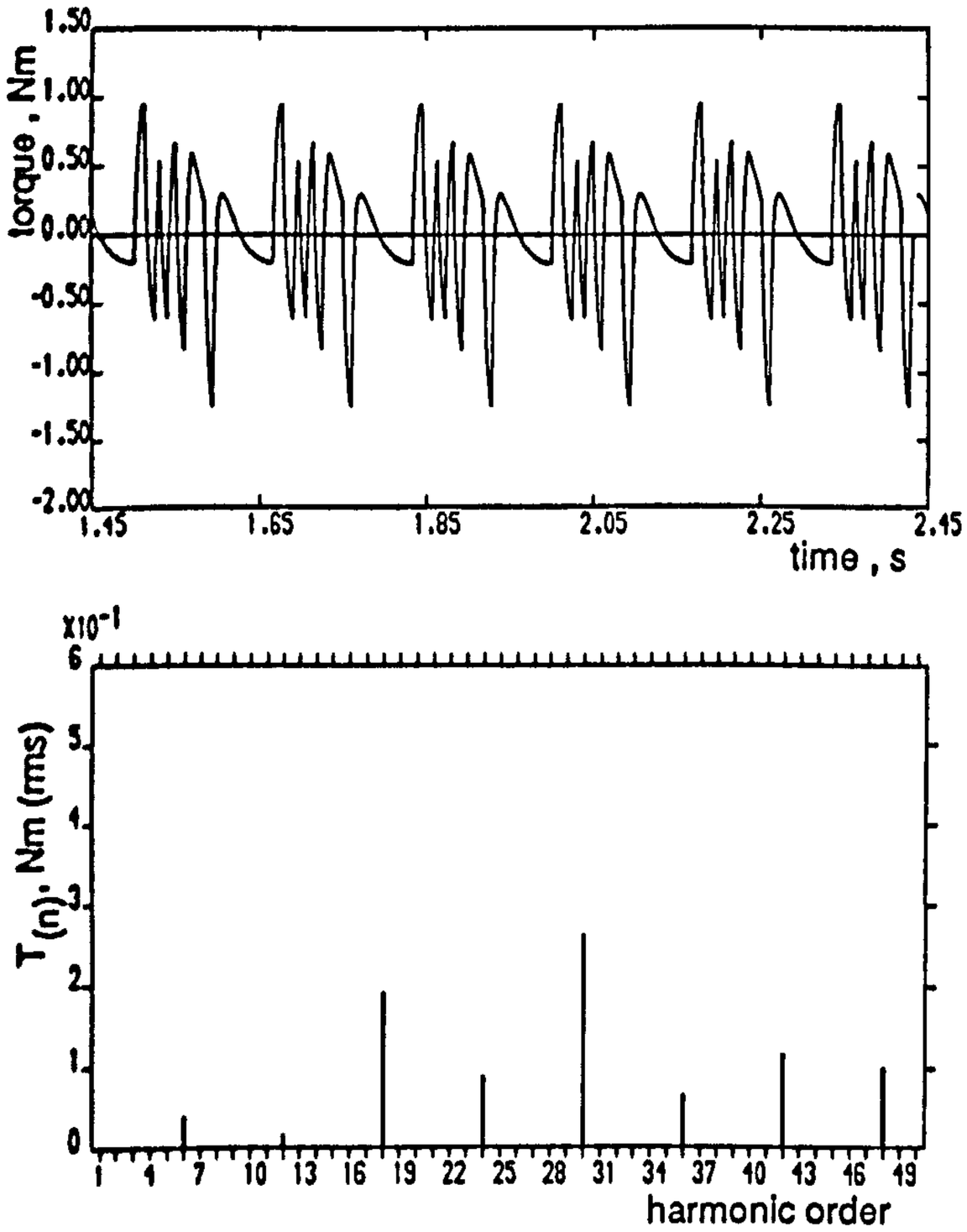

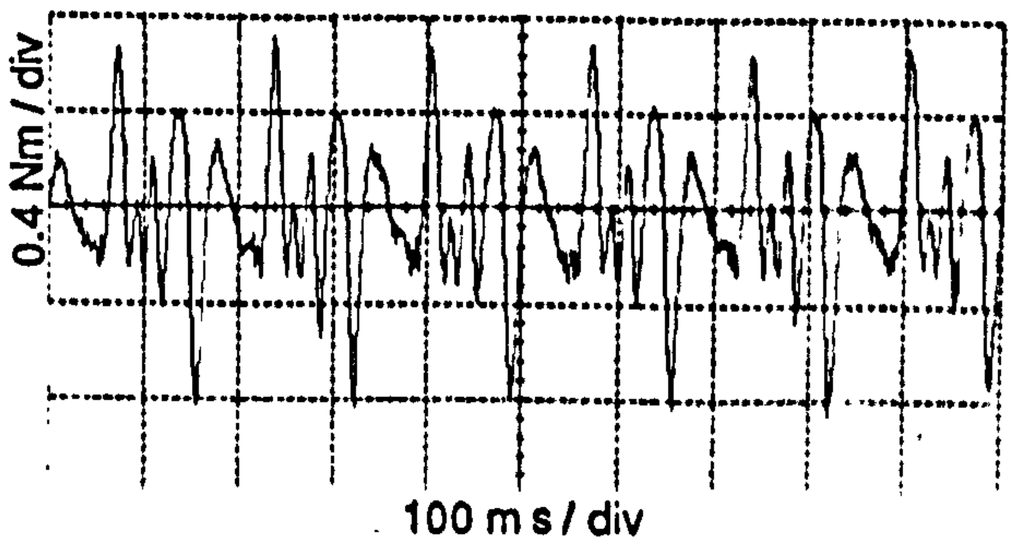

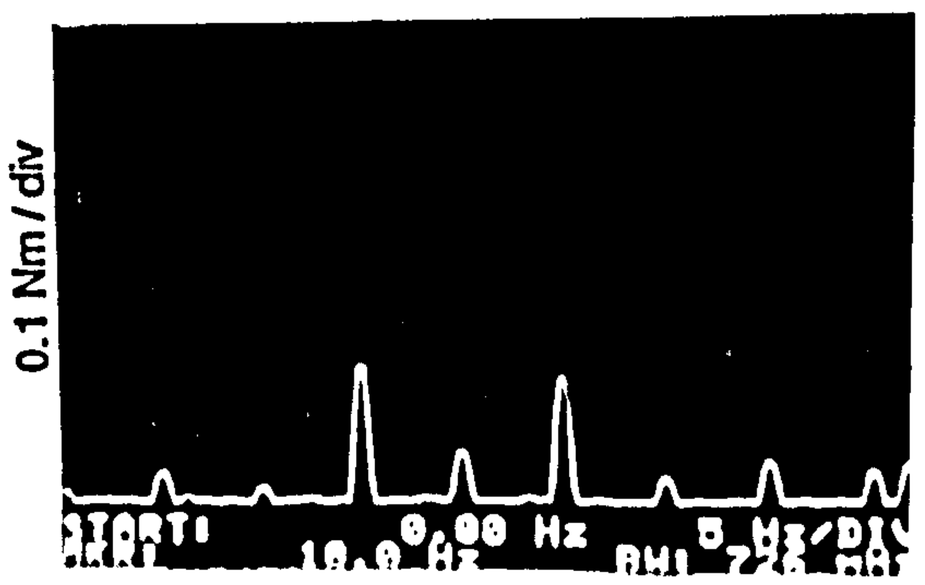

(c)

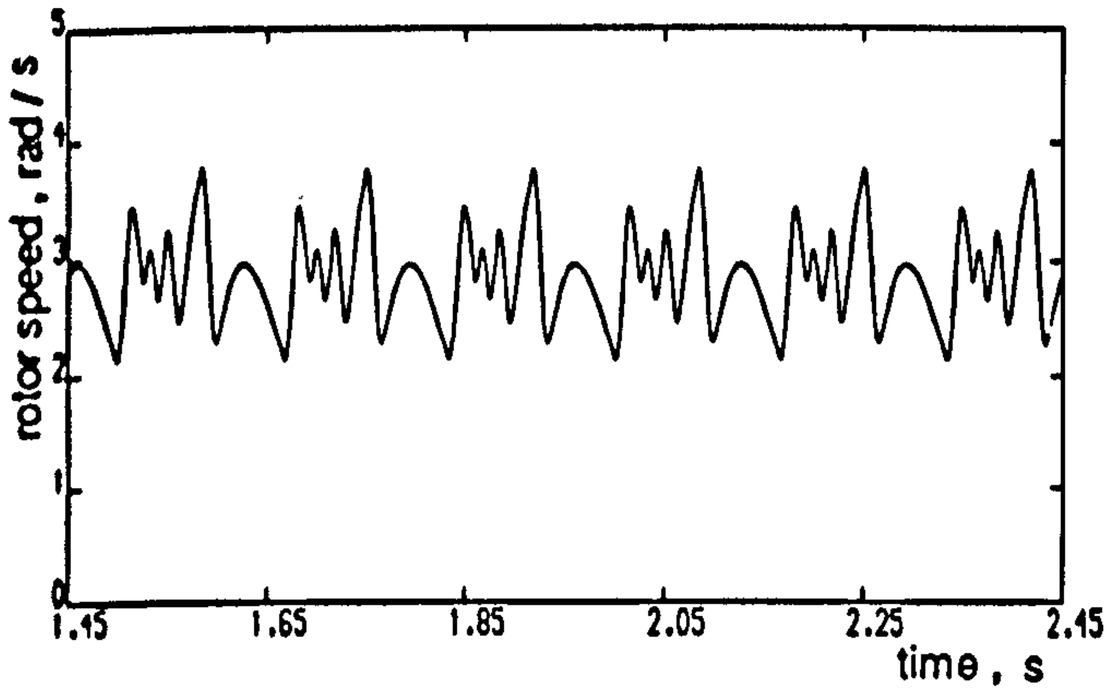

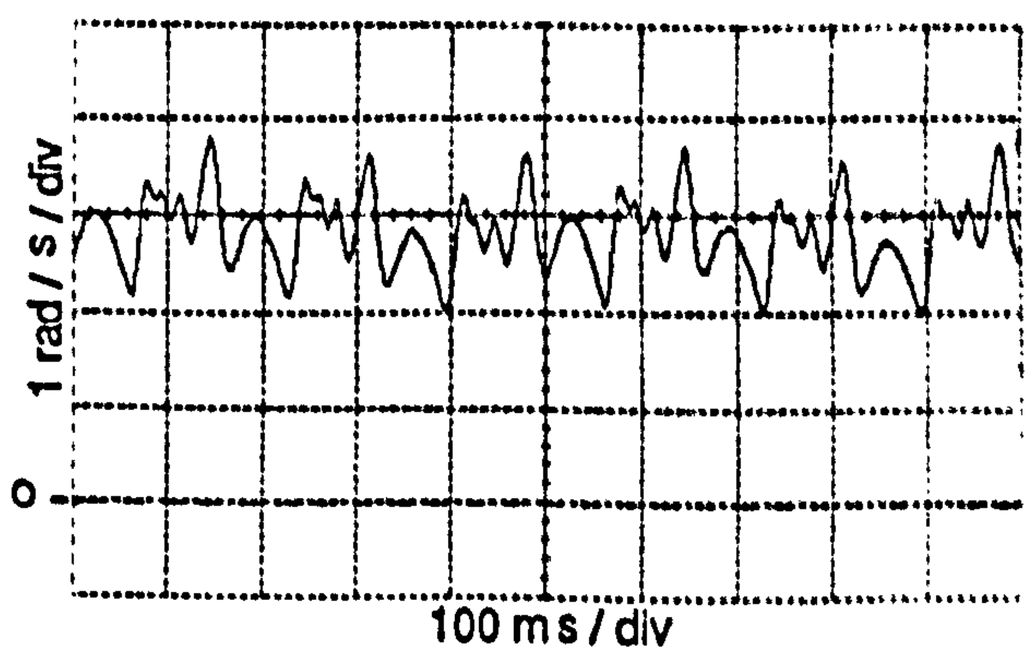

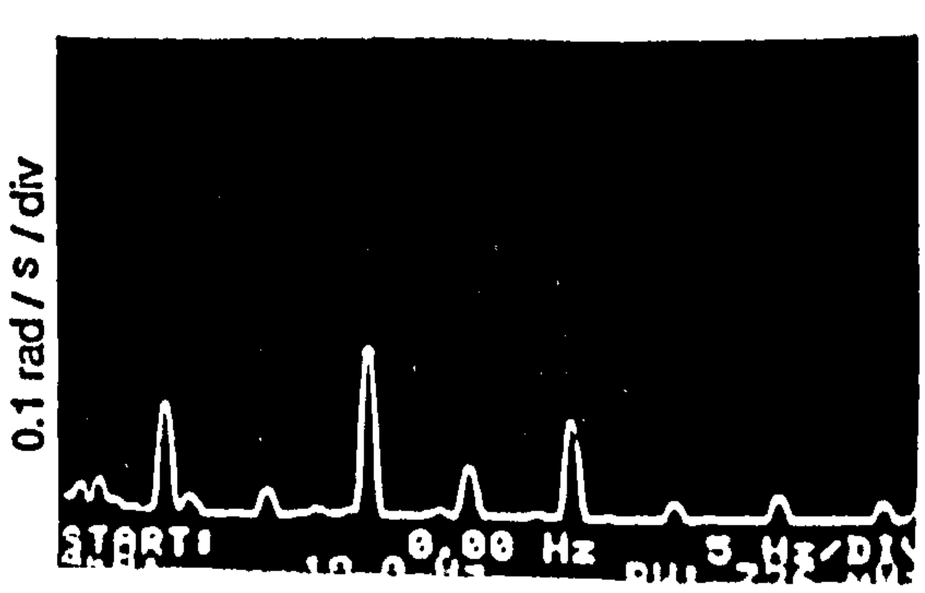

(d)

Figure 7.8 continued (c) Acceleration torque and spectrum
(d) Rotor speed and spectrum

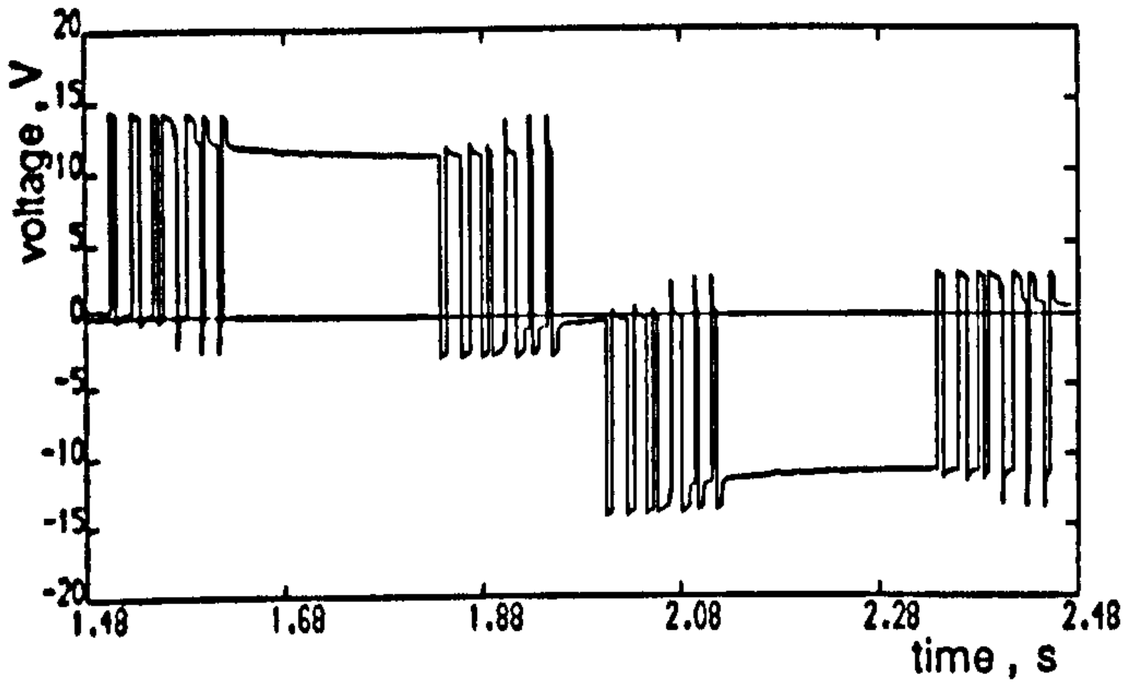

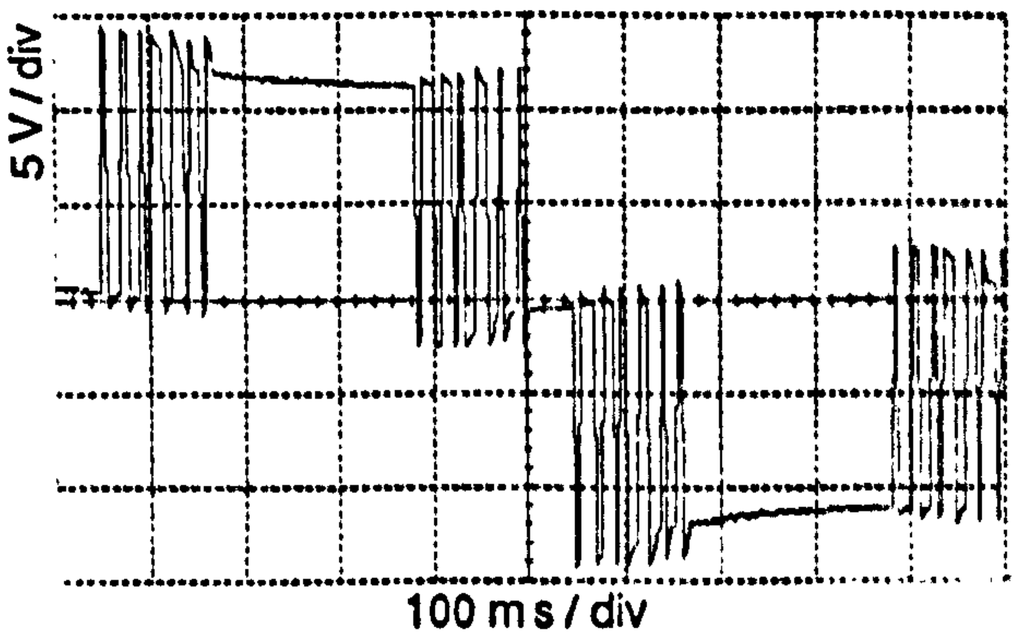

(a)

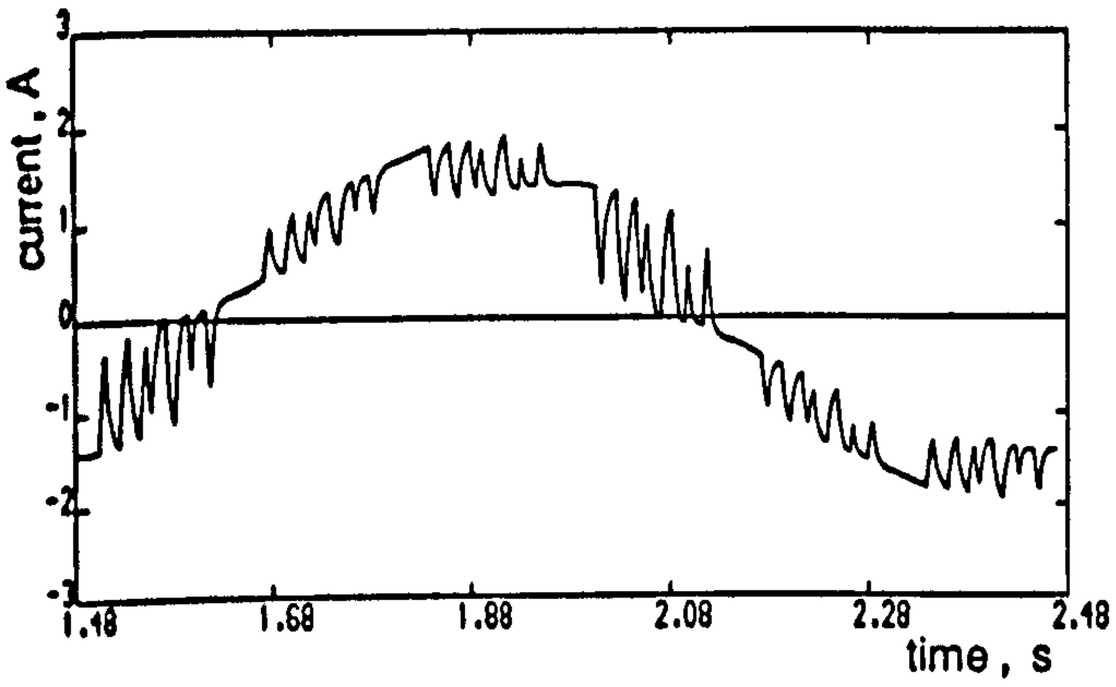

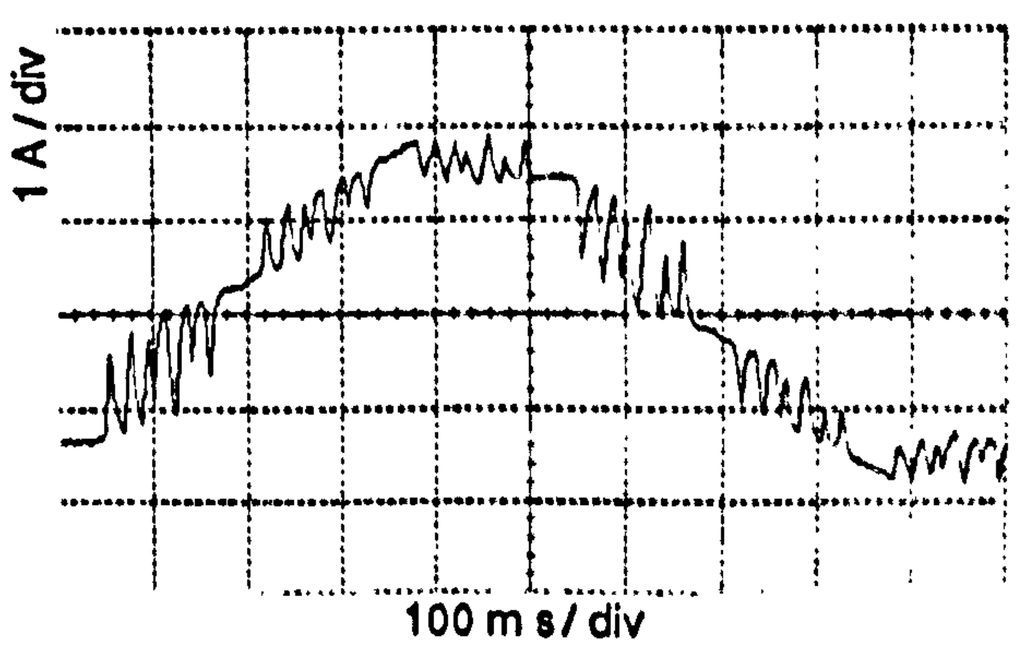

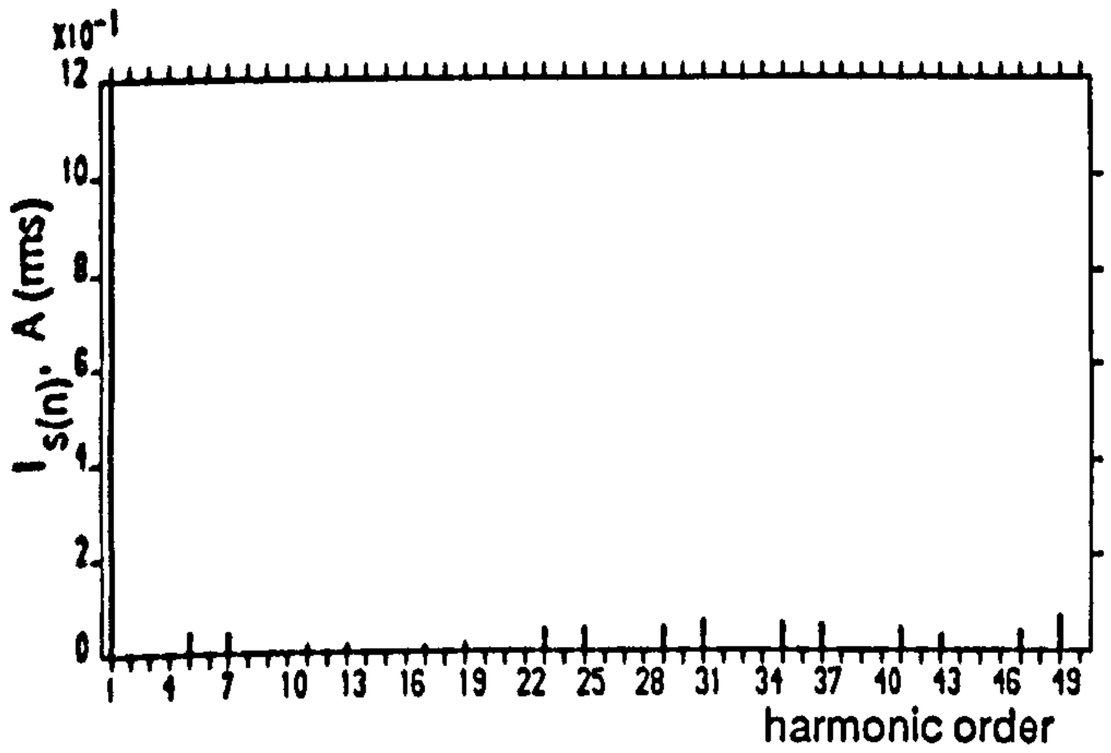

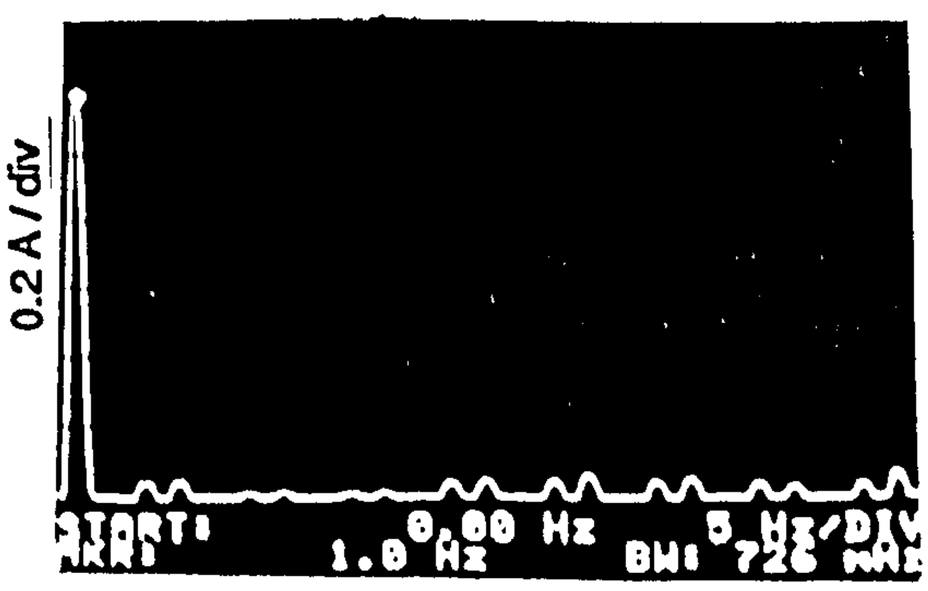

(b)

Figure 7.9 Computed and experimental results for type B PWMT12 half-wave symmetrical strategy at 1Hz stator frequency no-load operating condition
(a) Line voltage
(b) Stator current and spectrum

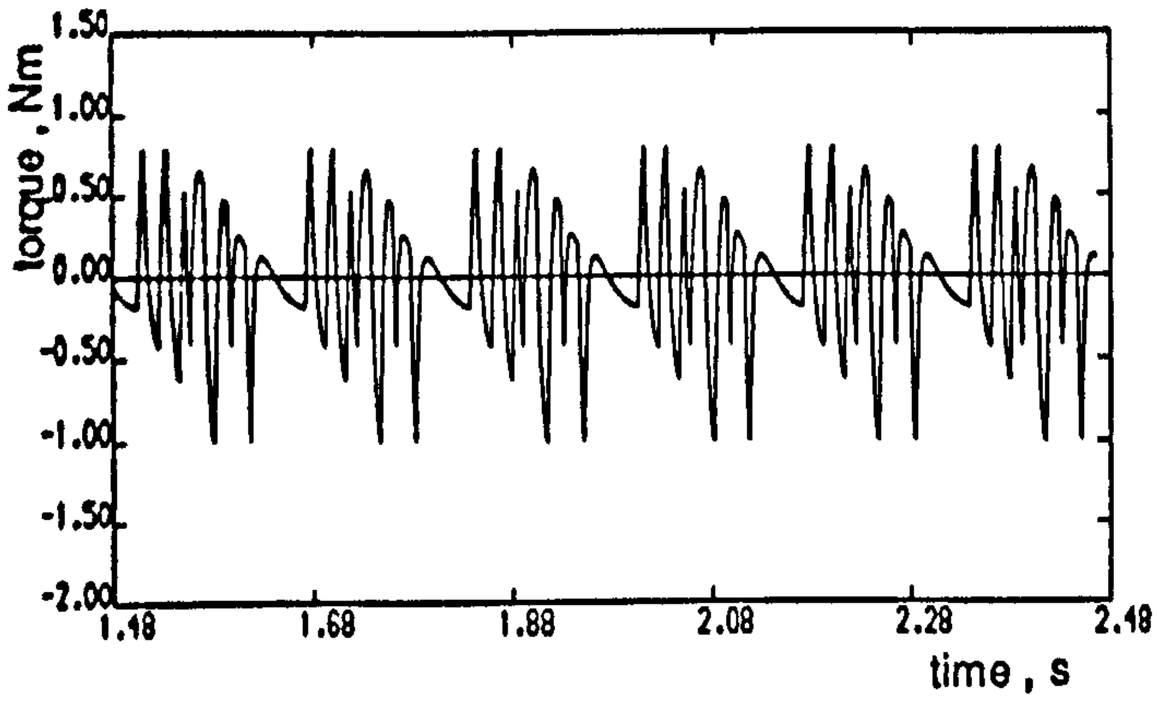

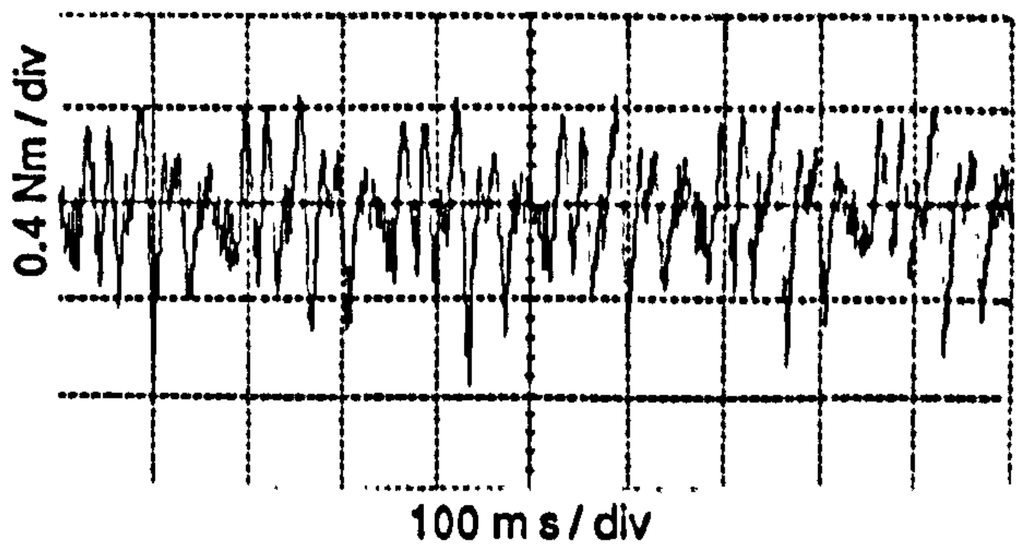

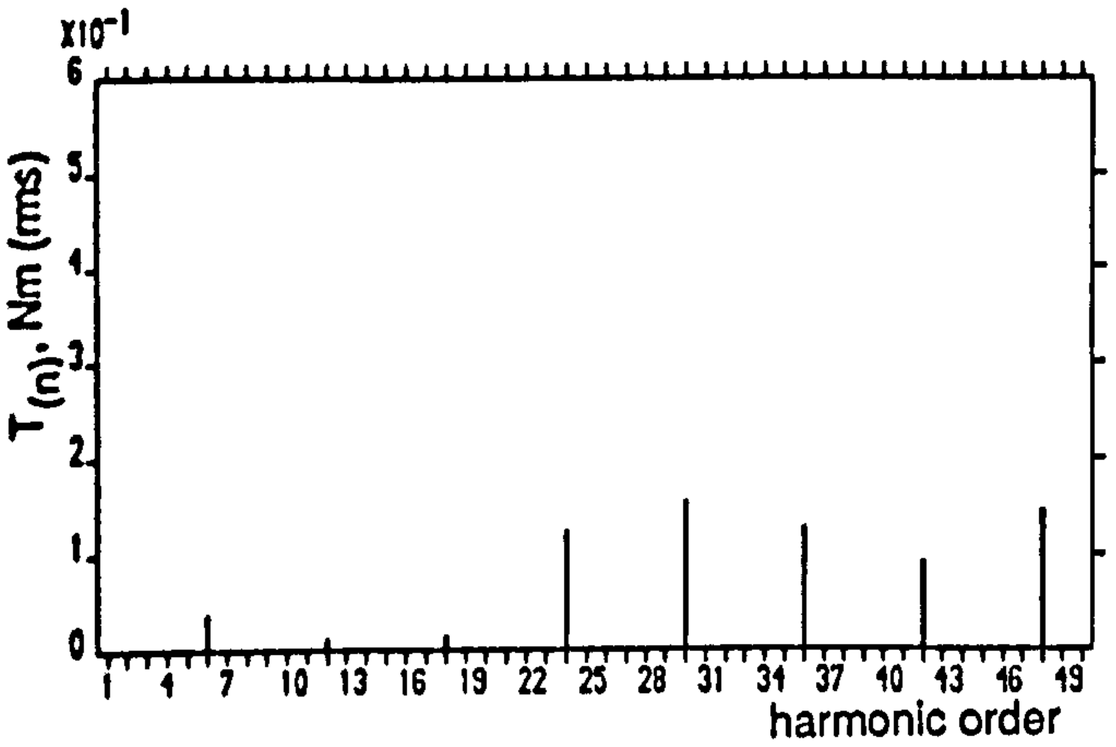

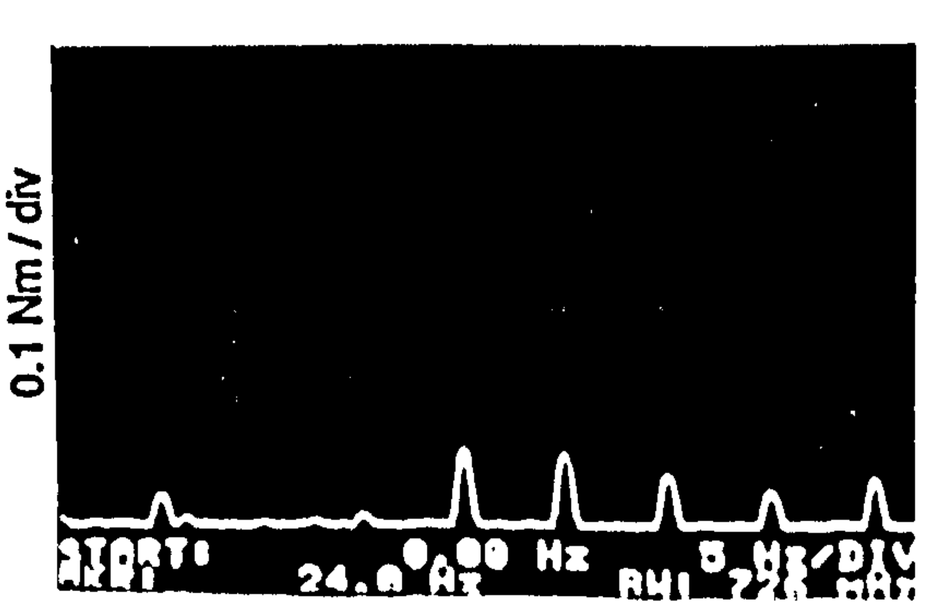

(c)

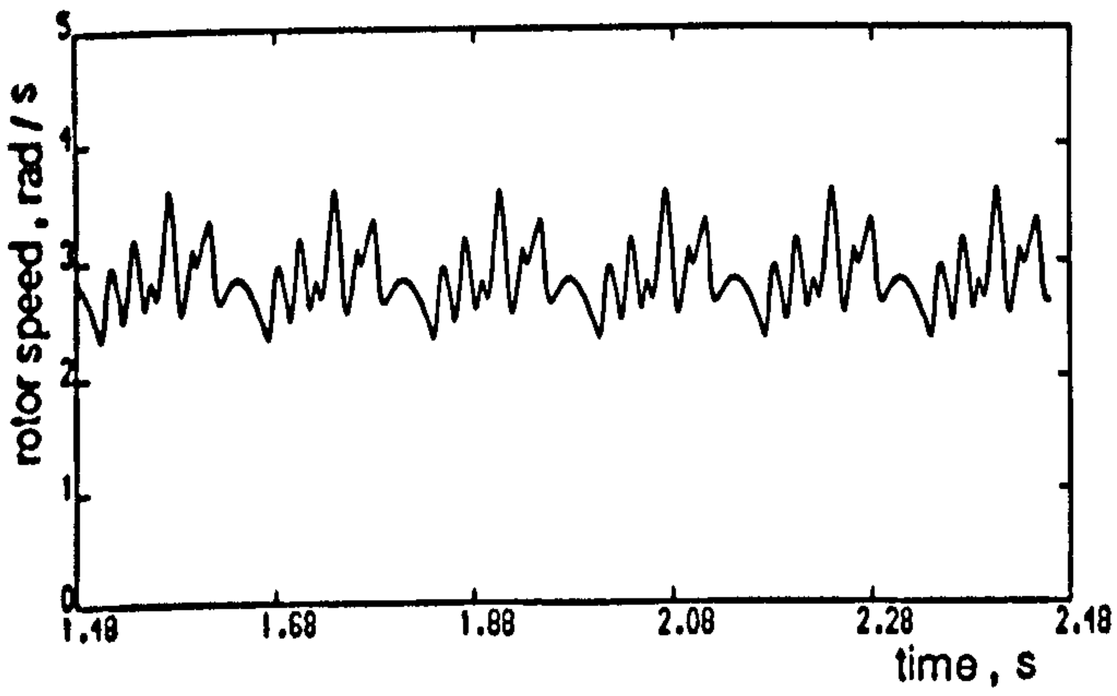

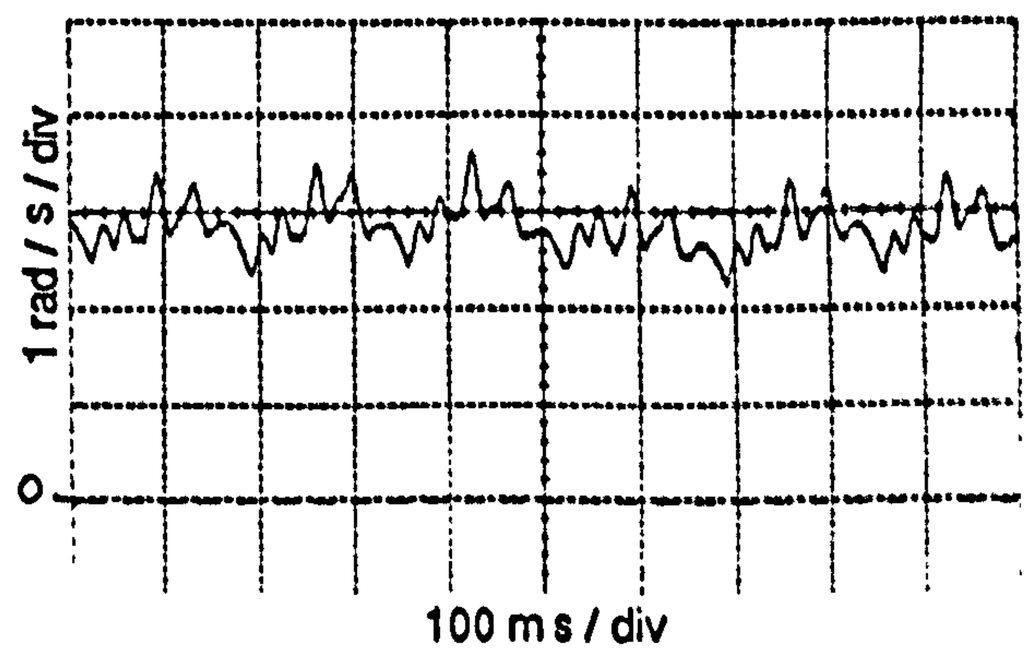

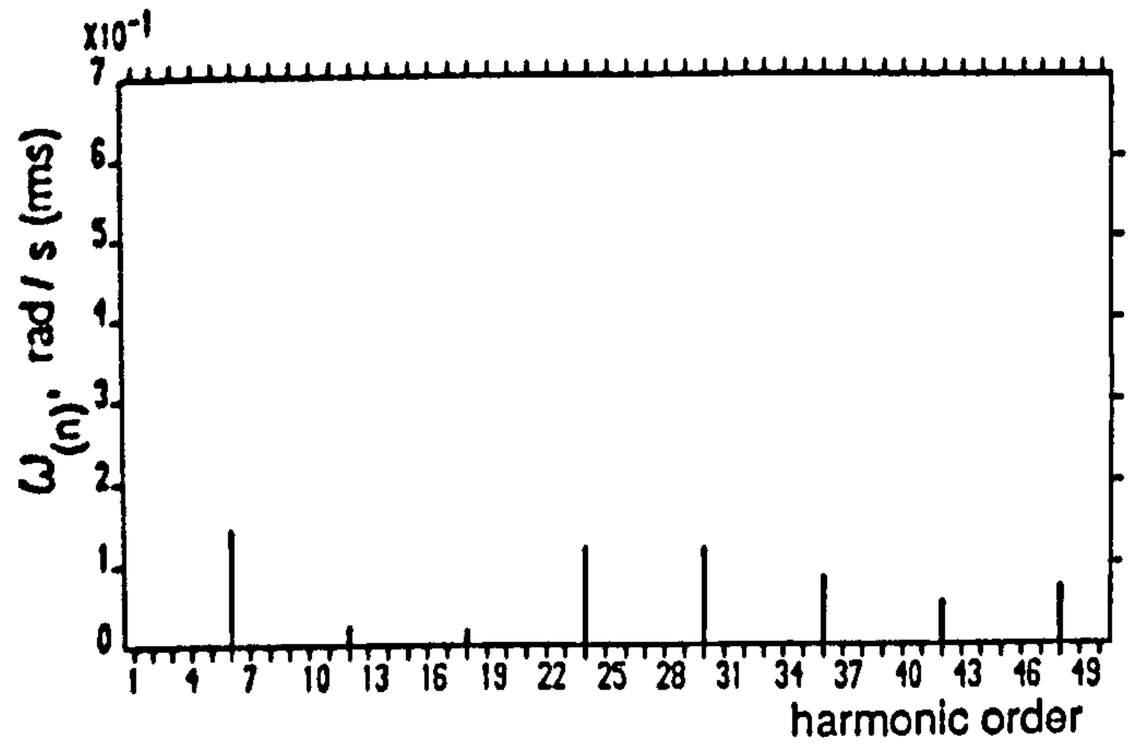

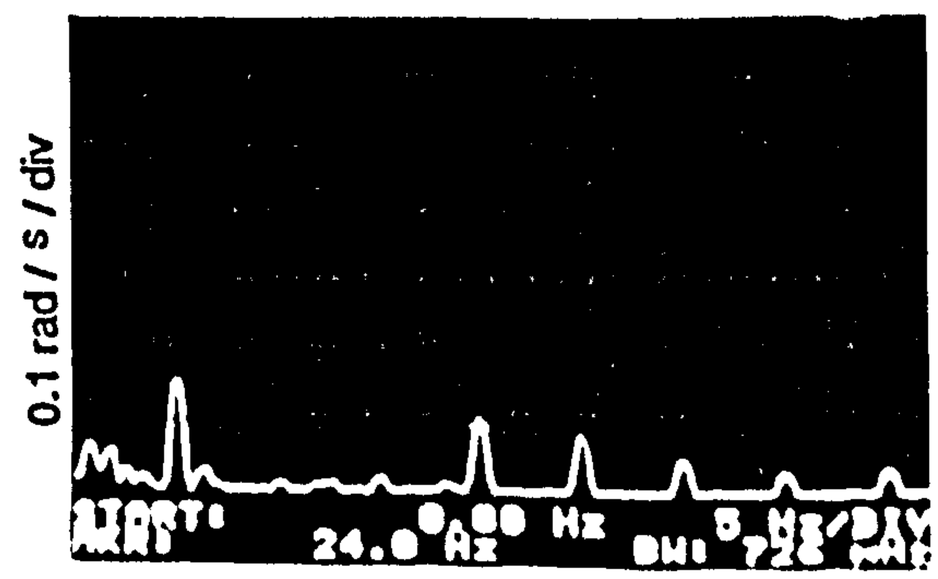

(d)

Figure 7.9 continued (c) Acceleration torque and spectrum
(d) Rotor speed and spectrum

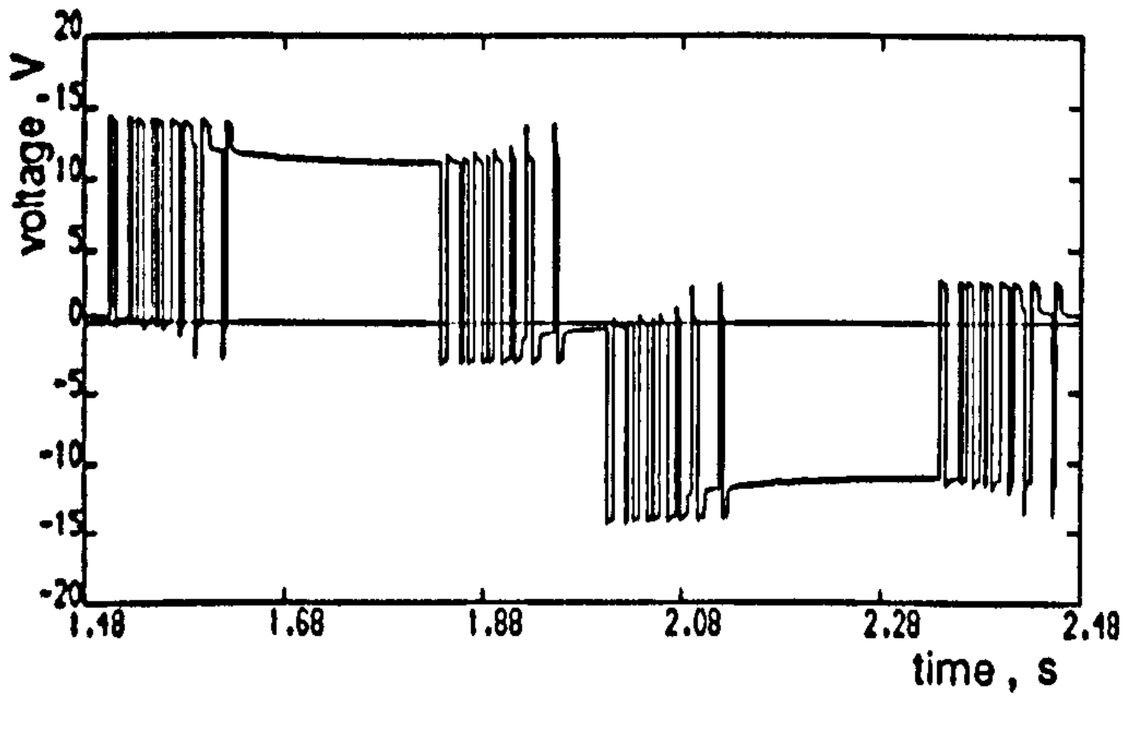

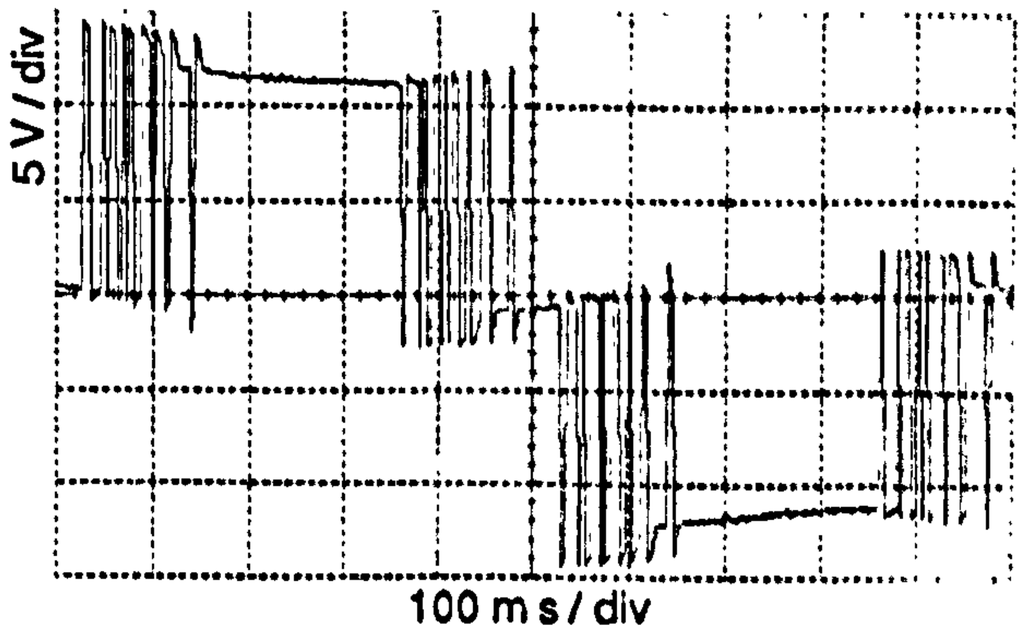

(a)

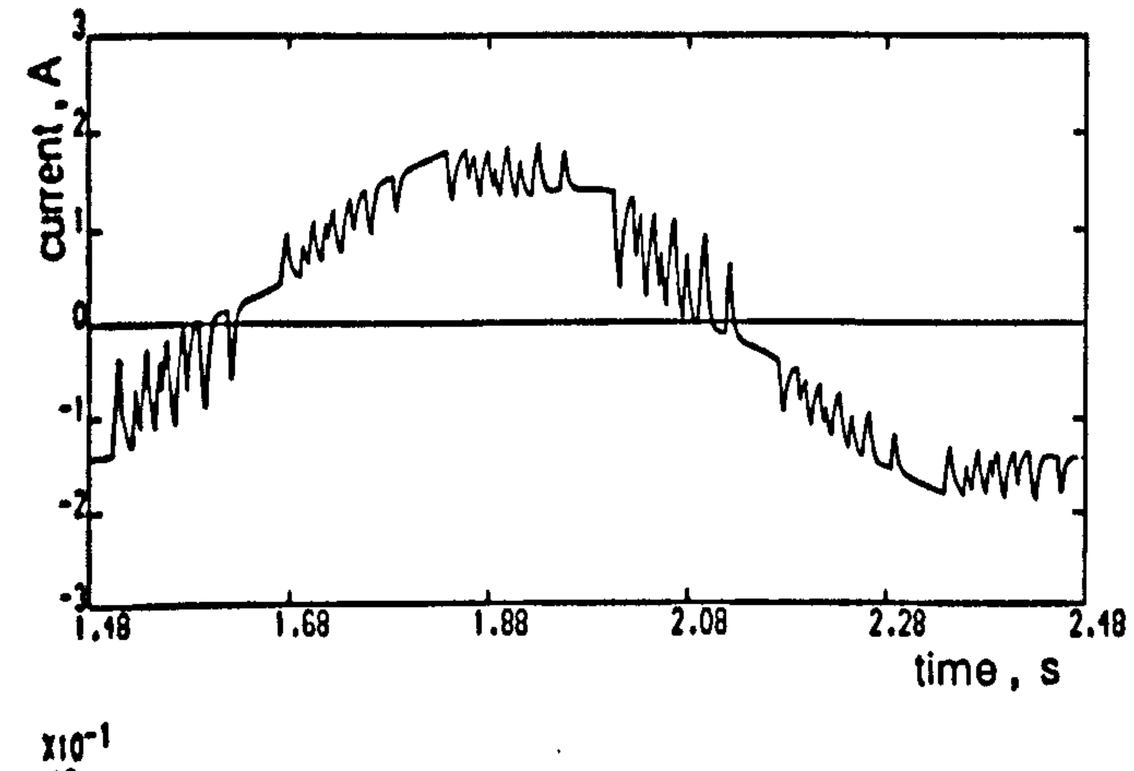

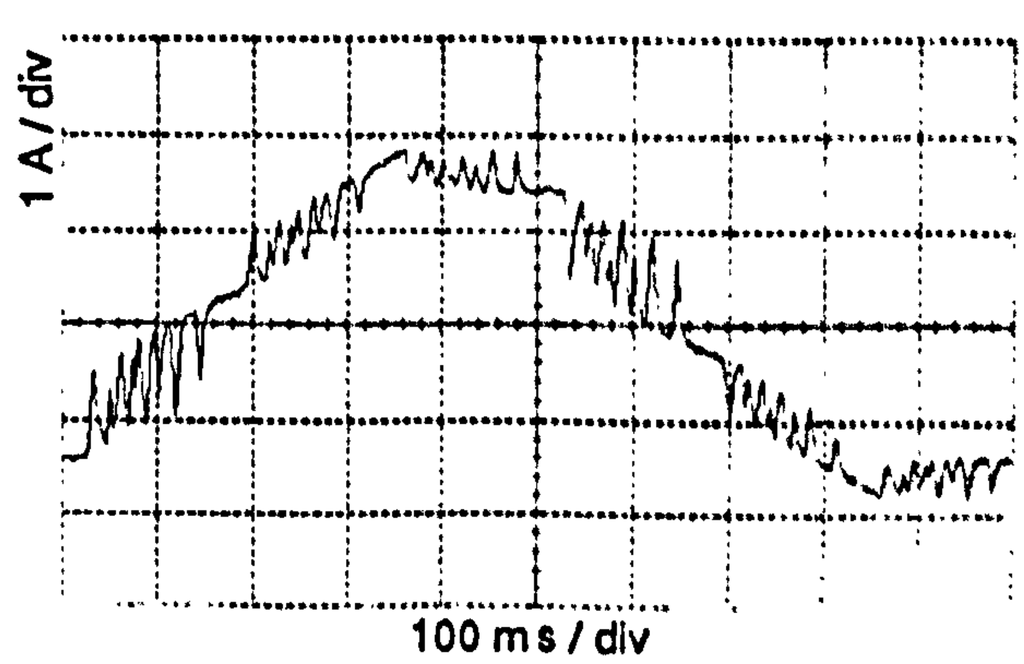

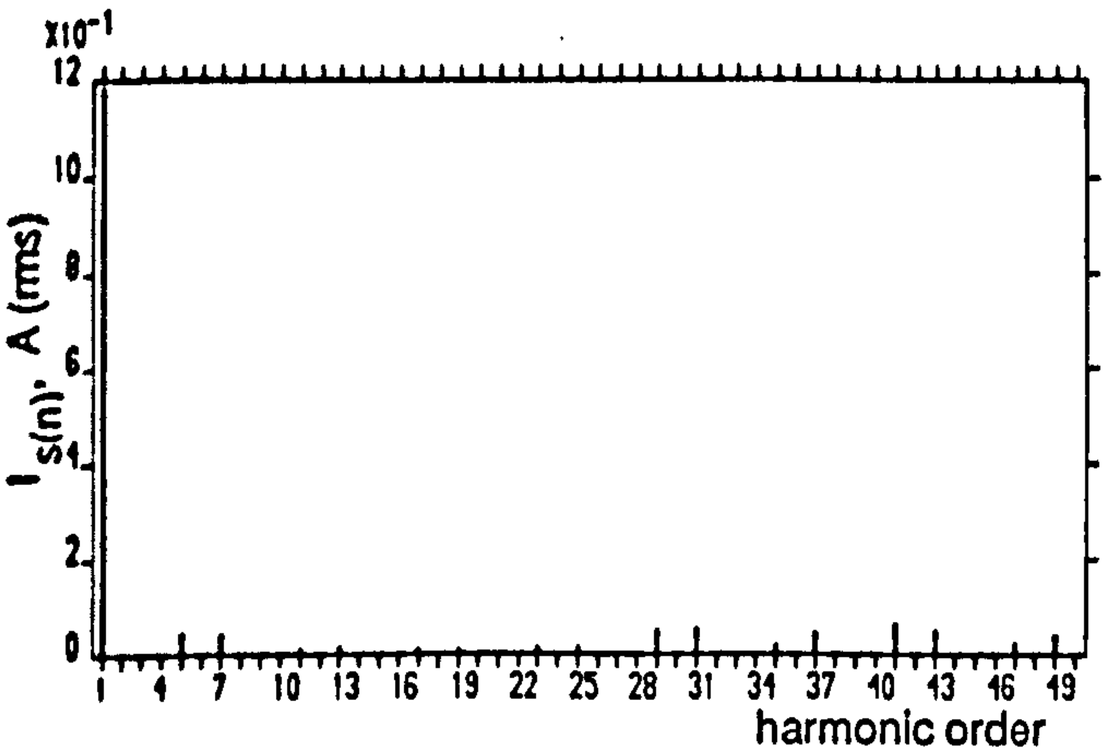

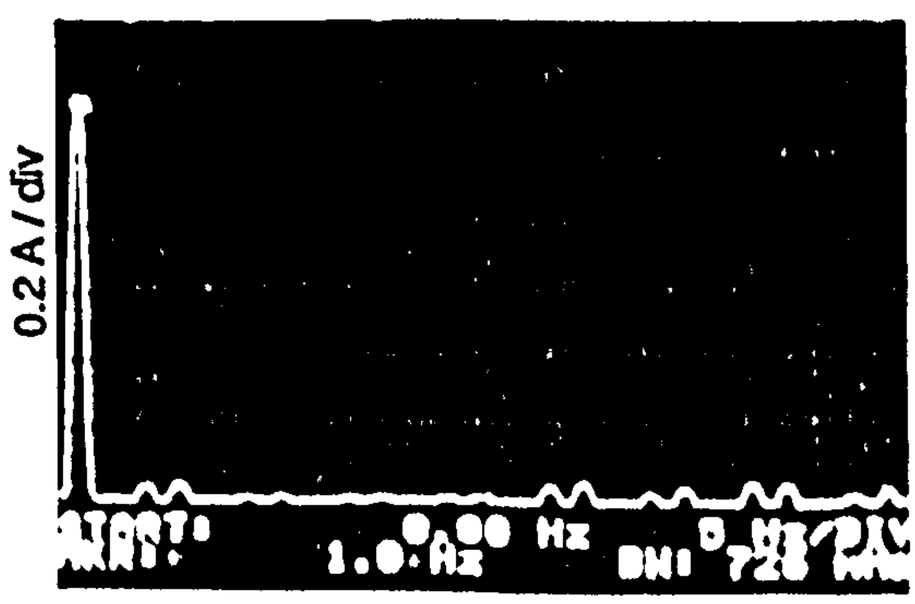

(b)

Figure 7.10 Computed and experimental results for type B' PWMT16 half-wave symmetrical strategy at 1Hz stator frequency no-load operating condition
(a) Line voltage
(b) Stator current and spectrum

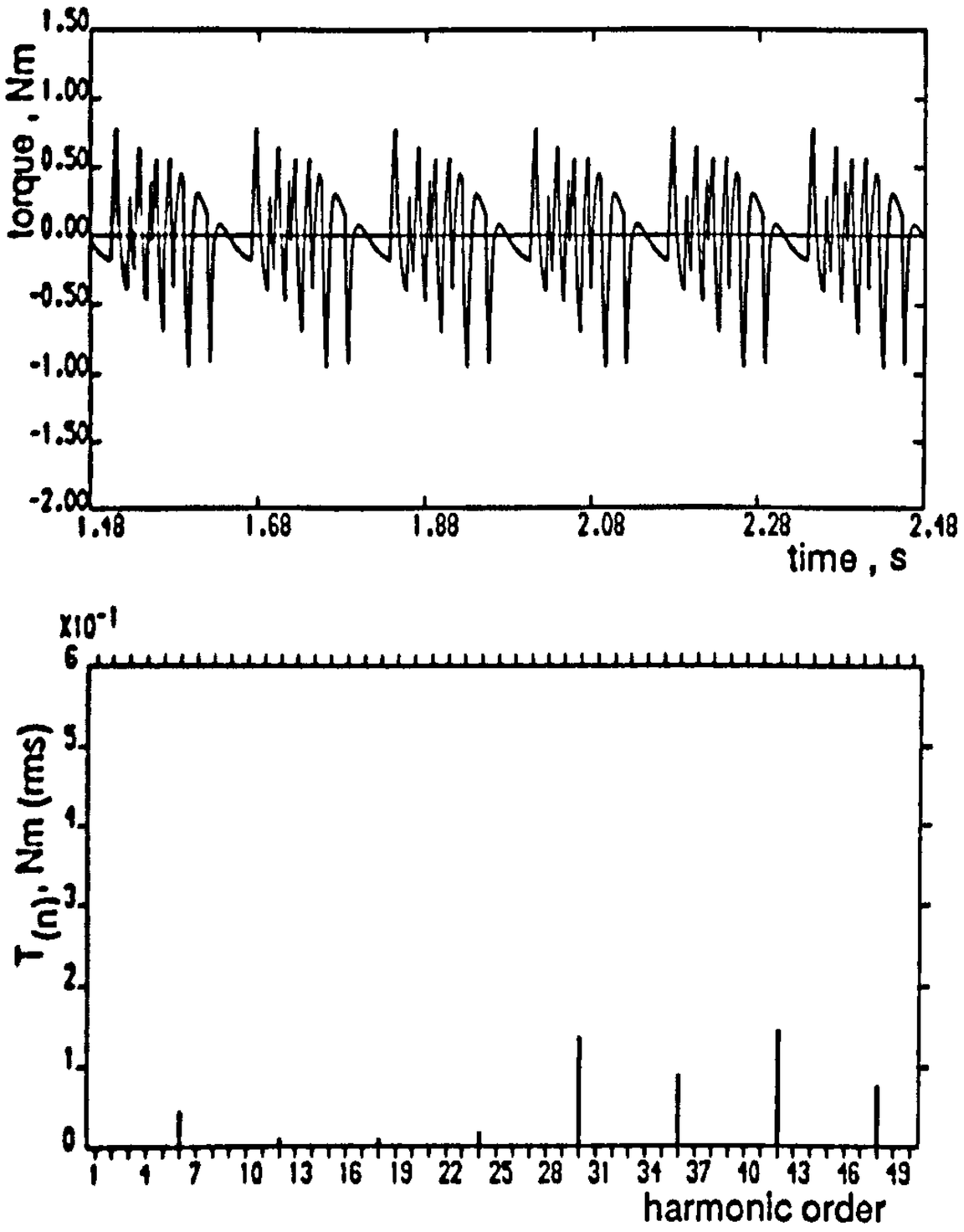

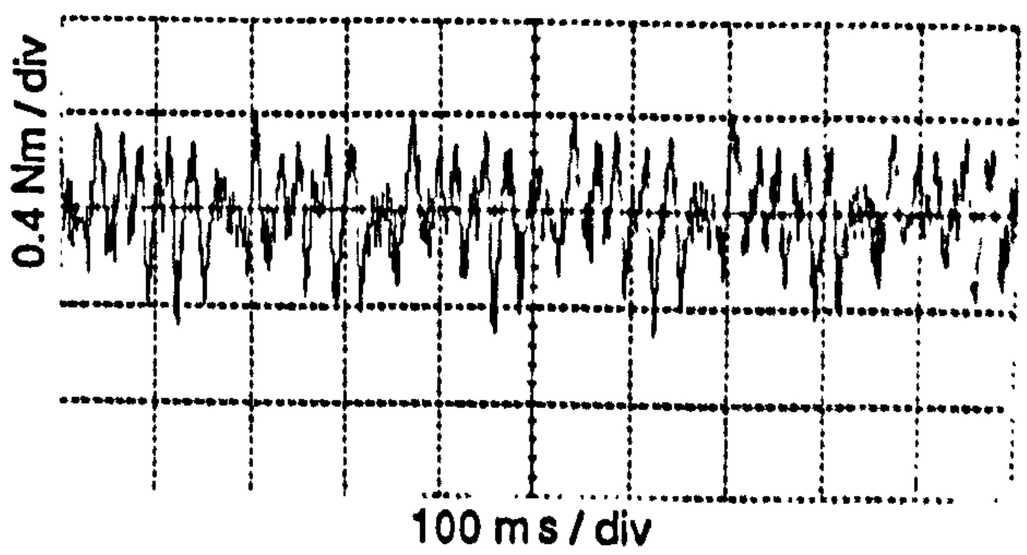

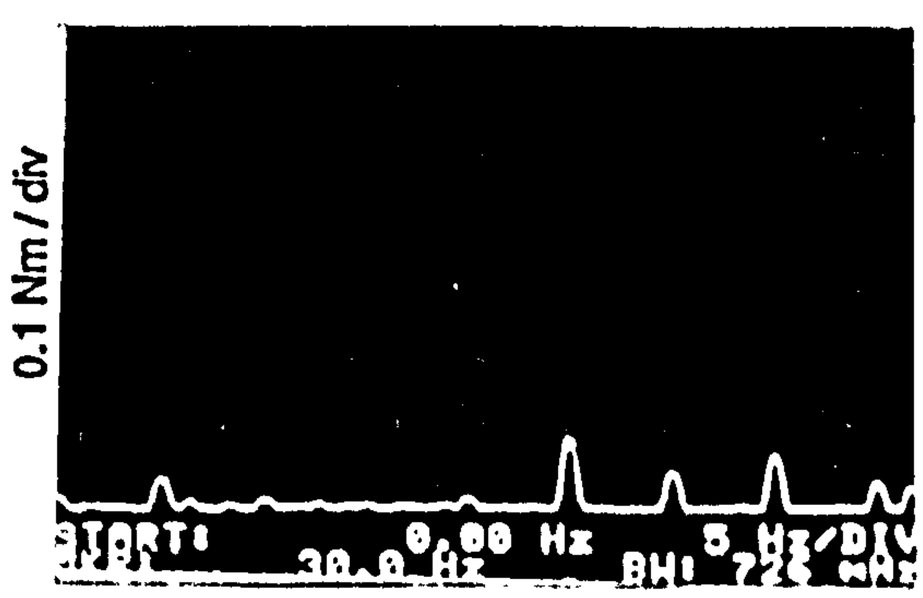

(c)

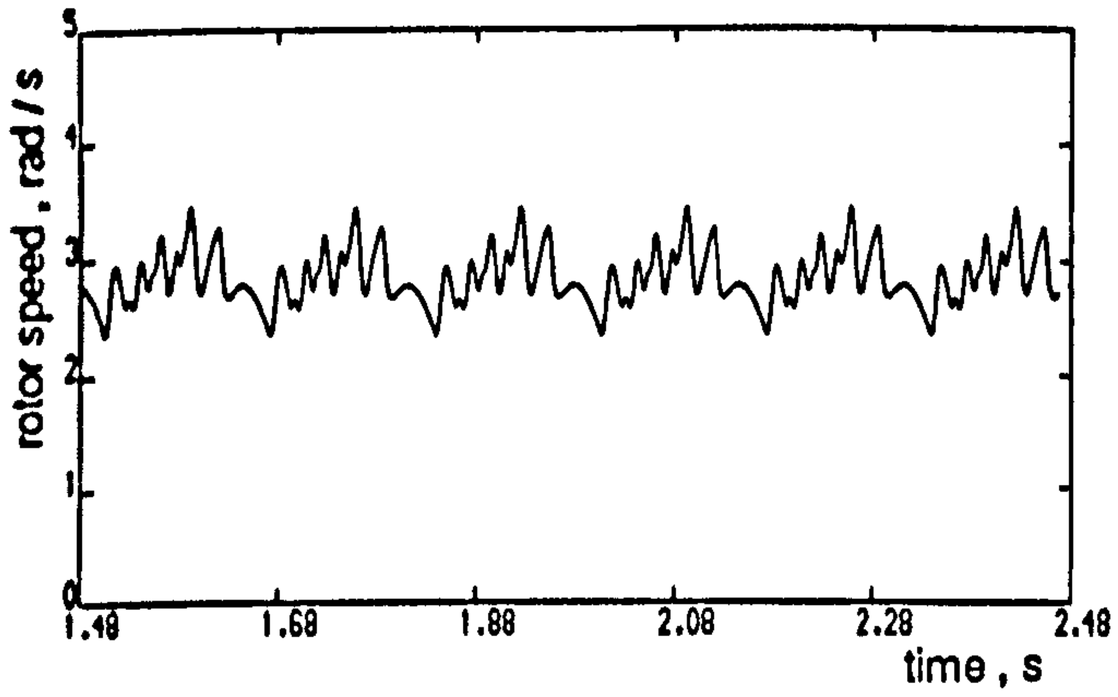

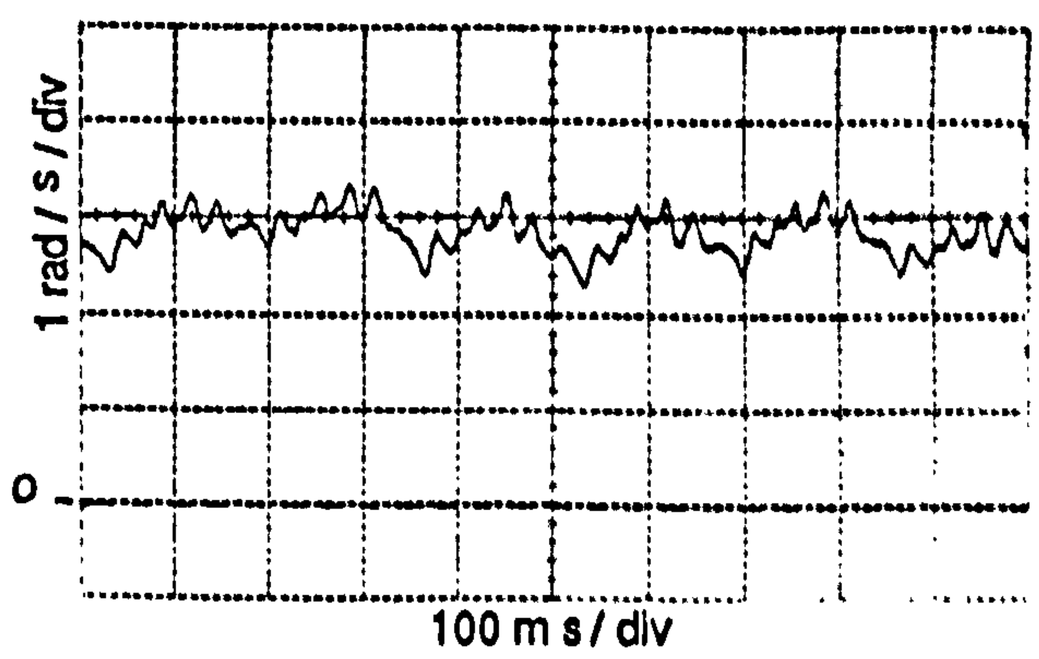

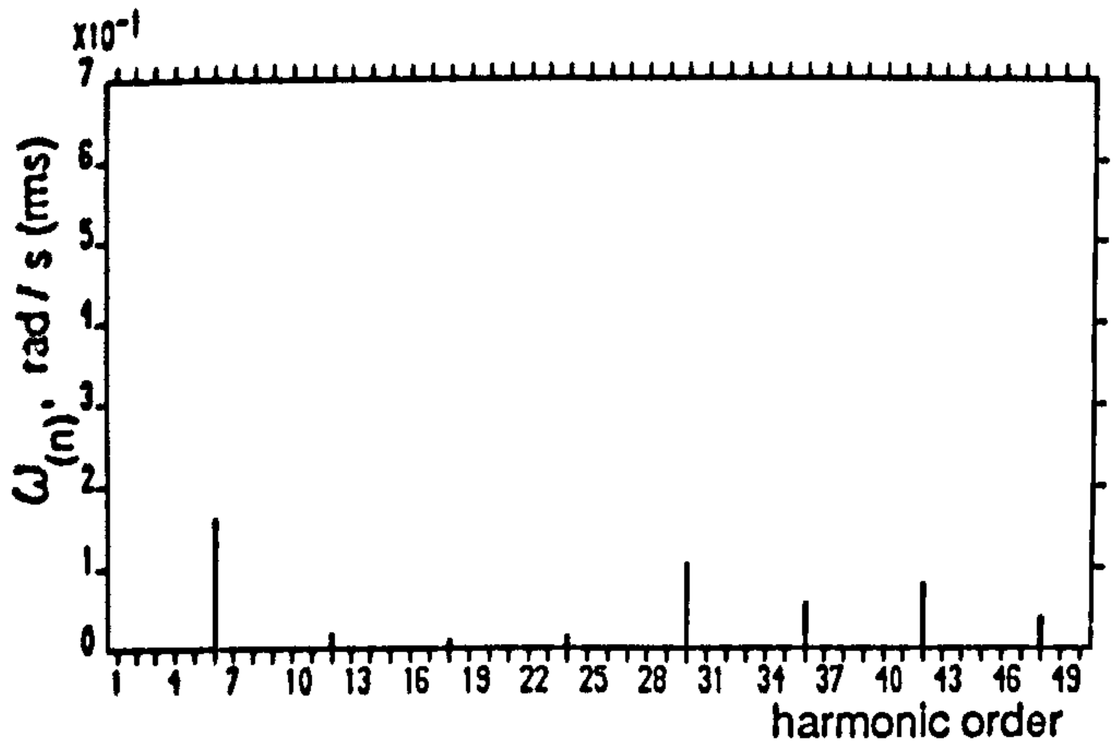

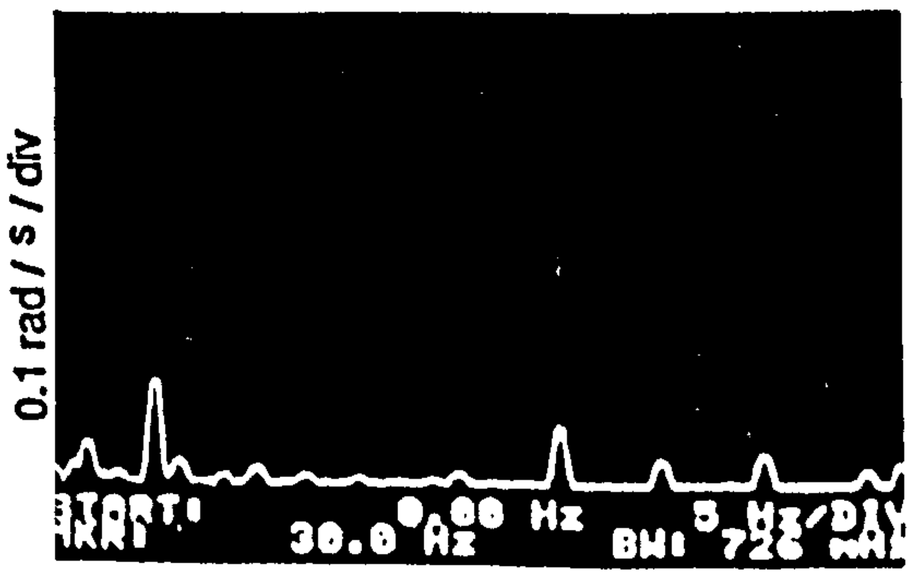

(d)

Figure 7.10 continued (c) Acceleration torque and spectrum
(d) Rotor speed and spectrum

cancellation of the torque components was based on equation 6.19 for the magnitudes of the torque pulsations, and not equation 6.25 for the peak-to-peak speed ripple.

Table 7.3 summarises the drive performance for all modes of operation, in terms of the different indices described in chapter 6. As verified earlier, the QSW mode has the lowest harmonic current distortion at low operating frequencies. Both strategies have a lower harmonic current content than the conventional elimination PWM strategy, due to a better distribution of the harmonic magnitudes. In terms of the torque waveform, the QSW mode has the lowest peak-to-peak torque pulsations, with the elimination and type A strategy having approximately similar values. The type B strategy shows an improved performance and reduced torque pulsations as the number of pulses is increased. The speed ripple is greatest in the QSW mode, with both the elimination and type A strategies showing lower and more or less similar ripple magnitudes. However the type B strategy produced a significant reduction. Moreover, the table shows that the new strategies have a higher fundamental component factor K than the elimination strategy, which results in a lower DC-link voltage to provide the required fundamental voltage component.

TABLE 7.3
COMPARISON OF THE DRIVE PERFORMANCE
AT 1Hz FREQUENCY, NO-LOAD CONDITION

MODE	K	THD	ΔT_e Nm	$\Delta\omega_m$ rad/sec
QSW	1.0000	17.25	1.47	4.15
PWM2	0.9330	29.39	2.48	3.46
TYPE A PWMT2	0.9680	25.50	2.26	3.63
TYPE B PWMT4	0.9659	23.10	2.14	2.41
PWM4	0.9200	28.30	2.26	2.46
TYPE A PWMT4	0.9593	24.92	2.26	2.35
TYPE B PWMT8	0.9577	17.56	2.19	1.61
PWM6	0.9140	25.78	2.20	1.83
TYPE A PWMT6	0.9557	22.85	2.13	1.79
TYPE B PWMT12	0.9543	14.05	1.78	1.24
PWM8	0.9116	19.68	2.04	1.36
TYPE A PWMT8	0.9540	19.06	1.91	1.30
TYPE B PWMT16	0.9535	11.60	1.72	0.95

7.5 Quarter-Wave Symmetrical Strategy

Complete cancellation between torque components of the same order cannot be achieved by the magnitude adjustment of individual harmonic current components. However, figure 7.1 suggests that, above a certain operating frequency, considerable reduction of the resultant harmonic torque components is obtainable, especially at high operating frequencies, if the magnitudes of similar order components are equal and are approximately opposed to one-another. Equation 6.19 provides the mathematical basis for the minimisation mechanism using quarter-wave symmetrical PWM switching patterns similar to those of the elimination strategy.

7.5.1 Solution Organization

The Fourier-series representing the voltage waveform of a quarter-wave symmetrical PWM pattern contains only $\alpha_{(n)}$ coefficients, which may be used to determine the magnitudes of the nth-harmonic voltage components given by equation 6.3. All of these components are either in-phase or in anti-phase at $t = 0$, which allows the analysis of section 6.3 to be used to determine the magnitudes and phase angles of the individual stator and rotor harmonic current components.

7.5.2 Mathematical Techniques and Optimization Approach

Equations 7.8, 7.9, 7.12 and 7.13 show that the magnitudes of the harmonic torque components produced by interaction between current components of orders (1,6n-1) and (1,6n+1) are respectively

$$T_e(1,6n-1) = \sqrt{(\Re T_e(1,6n-1))^2 + (\Im T_e(1,6n-1))^2} \qquad 7.19$$

and

$$T_e(1,6n+1) = \sqrt{(\Re T_e(1,6n+1))^2 + (\Im T_e(1,6n+1))^2} \qquad 7.20$$

Minimisation of the T_{e_n} component is achieved if

$$T_e(1,6n-1) = -T_e(1,6n+1)$$

with the negative sign ensuring that the two components are mutually opposed. Substituting equations 7.8, 7.9, 7.12 and 7.13 into this relationship, and re-arranging, results in

$$cc(n) = T_e(1,6n-1) + T_e(1,6n+1) = 0 \qquad 7.21$$

The inequality constraints which satisfies the minimum pulse-width requirements and the upper boundary for a quarter-wave symmetrical PWM pattern is

$$t_{min} < \alpha_1 < \alpha_2 < \alpha_3 < \ldots < \alpha_m < \frac{\pi}{2}$$

7.5.3 Optimization Results

Consideration of only one torque component involves two equations; an objective function needed to set the fundamental component factor and an equality constraint to equate torque component magnitudes of the same order. Following the same consideration as section 3.2.3 for a variable DC-link voltage, the solution requires at least one switching angle to minimise the 6th-harmonic torque component. With quarter-wave symmetry this produces three instead of five pulses per half-cycle of the line voltage needed to eliminate the 5th- and 7th-harmonic voltage components. Similarly, minimisation of the first four low order harmonic torque components requires at least four switching angles, producing nine pulses per half-cycle in the line voltage. An example is given in appendix A.5 for the reduction of the magnitude of the 6th-harmonic torque component using two switching angles per half-cycle. However, since the comparison is restricted to the drive performance, additional switching angles may be introduced with the same objective function and constraints to provide a fair comparison with the elimination strategy.

Tables 7.4 and 7.5 show respectively, sets of 1,2,3,4 and 2,4,6,8 switching angles per quarter-cycle, corresponding to 3,5,7,9 and 5,9,13,17 pulses per half-cycle in the line voltage waveform. Each set is designed to minimize successively the 6th, 12th, 18th, and 24th torque components at 10Hz operating frequency for full-load torque and an average speed of 3.95Nm and 7.85rad/s respectively. They are designated as types C and D PWMM strategies.

TABLE 7.4
OPTIMIZATION SUBROUTINE SETS OF 1,2,3,4 SWITCHING ANGLES PER QUARTER-CYCLE , TYPE C

MODE	K	α_1	α_2	α_3	α_4
PWMM1	0.9538	1.548			
PWMM2	0.9412	0.3190	0.4024		
PWMM3	0.9097	0.2013	0.3628	0.4276	
PWMM4	0.9284	0.1957	0.2641	0.3984	0.4477

TABLE 7.5
OPTIMIZATION SUBROUTINE SETS OF 2,4,6,8 SWITCHING ANGLES PER QUARTER-CYCLE , TYPE D

MODE	K	α_1	α_2	α_3	α_4	α_5	α_6	α_7	α_8
PWMM2	0.9371	0.2996	0.3920						
PWMM4	0.9300	0.2096	0.2766	0.4072	0.4524				
PWMM6	0.9134	0.0947	0.1880	0.3118	0.3715	0.5264	0.5464		
PWMM8	0.9247	0.0242	0.0497	0.1865	0.2524	0.3509	0.3738	0.4271	0.4604

7.5.4 Switching Pattern Generation

The procedure described in section 5.2.5 may be used to define the switching instants of the inverter GTOs for any number of switching angles per quarter-cycle.

7.6 Computed and Experimental Results

This section presents results which verify the strategy developed in section 7.5. Computed results were obtained using the direct-phase model, which has been extensively verified for different operating modes. In all cases the machine was fully loaded and the supply frequency 10Hz.

Figure 7.11(a) shows the line voltage waveform for QSW operation. For constant airgap flux, the fundamental component is 53.25V. Using equation 5.40, the DC-link voltage required is 71.8V, including compensation for the inverter voltage drop. The stator current waveform and its harmonic spectrum are shown in figure 7.11(b). The fundamental component is 2.30A, and all other odd non-triplen harmonics exist with decreasing magnitudes, which is a unique characteristic of the QSW mode. The harmonic distortion factor of this waveform is 27.67% .

Figures 7.12(a) and (b) show voltage and current waveforms for the PWM8 strategy, whose switching angles are given in table 3.1. The line voltage waveform has seventeen pulses per half-cycle, with the fundamental component of 53.25V obtained for a DC-link voltage of 74.9V. The current spectrum has a fundamental component of 2.30A, with elimination of the first four pairs of odd non-triple harmonics taking place to result in a distortion factor of 9.15% .

Results for types C and D strategies are illustrated for similar operating conditions in figures 7.13(a) and (b) and 7.14(a) and (b). Their respective switching patterns are generated using the switching angles of type C PWMM4 and type D PWMM8 sets given in tables 7.4 and 7.5. Figures 7.13(a) and 7.14(a) show respectively line voltage waveforms with nine and seventeen pulses per half-cycle, with switching pattern profiles clearly maintaining the property of quarter-wave symmetry. The fundamental voltages of 53.25V are obtained with DC-link voltages of 73.6V and 73.8V, including compensation. Figures 7.13(b) and 7.14(b) show the stator currents for the two modes, with their spectra containing a fundamental component of 2.30A and all odd non-triplen harmonics. A comparison of both spectra with that of figure 7.12(b) for the elimination strategy, reveals significant low order harmonics, resulting in a higher harmonic distortion factor of 13.8% for type C and 11.39% for type D strategies. This arises since, at high operating frequencies, high order components are more attenuated by the machine harmonic impedance, even if the voltage components are increased due

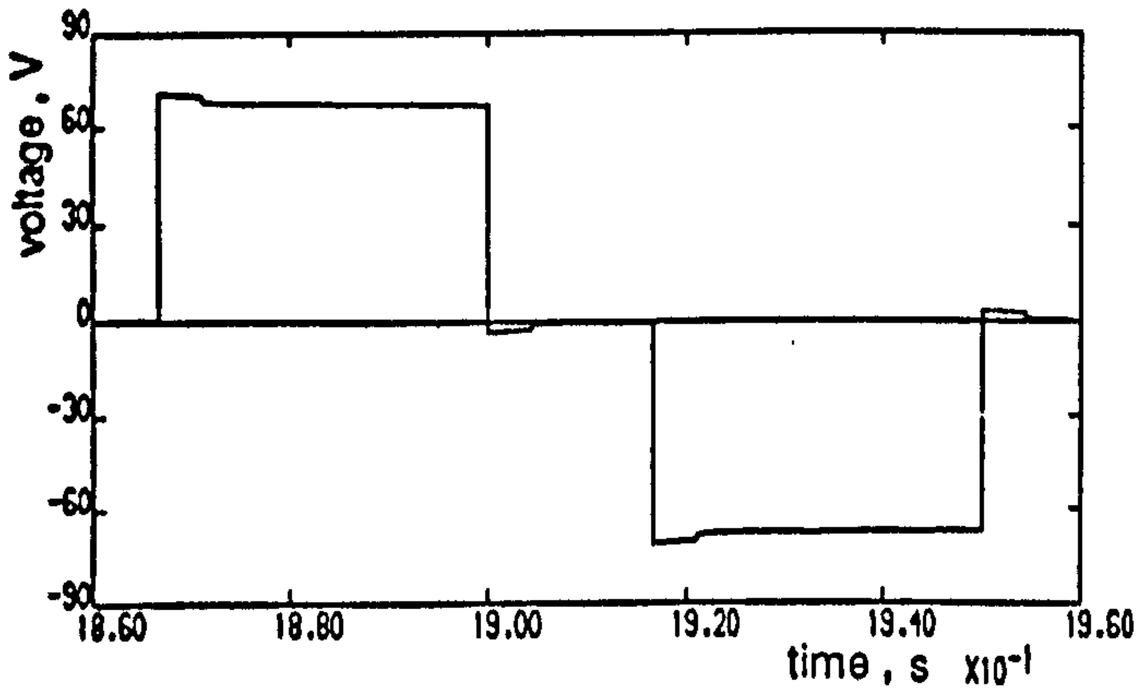

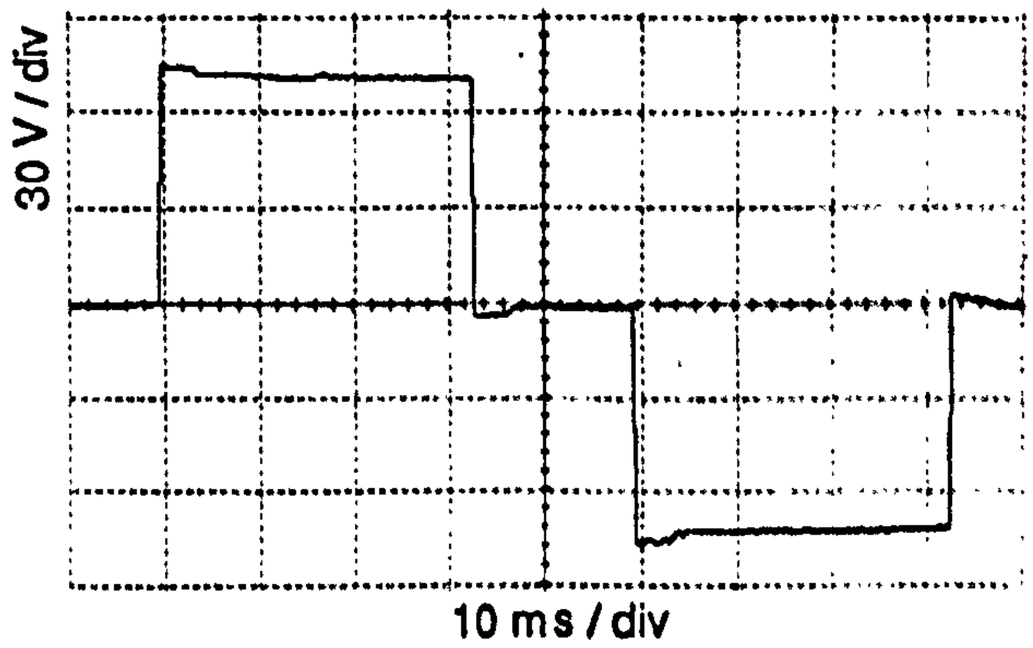

(a)

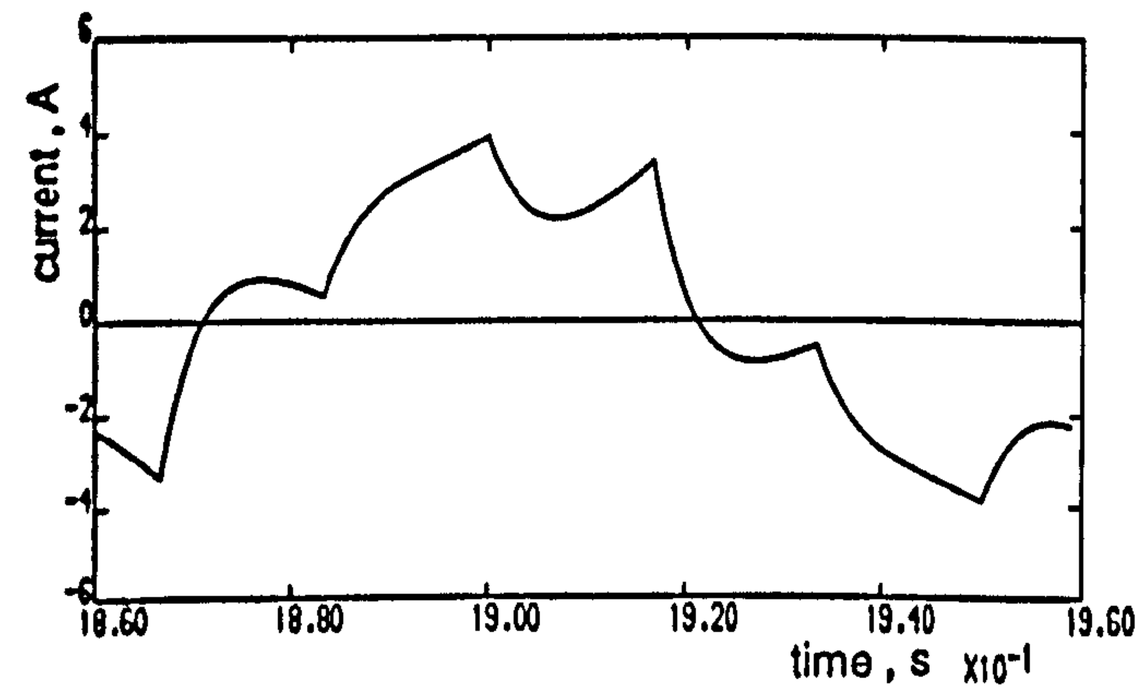

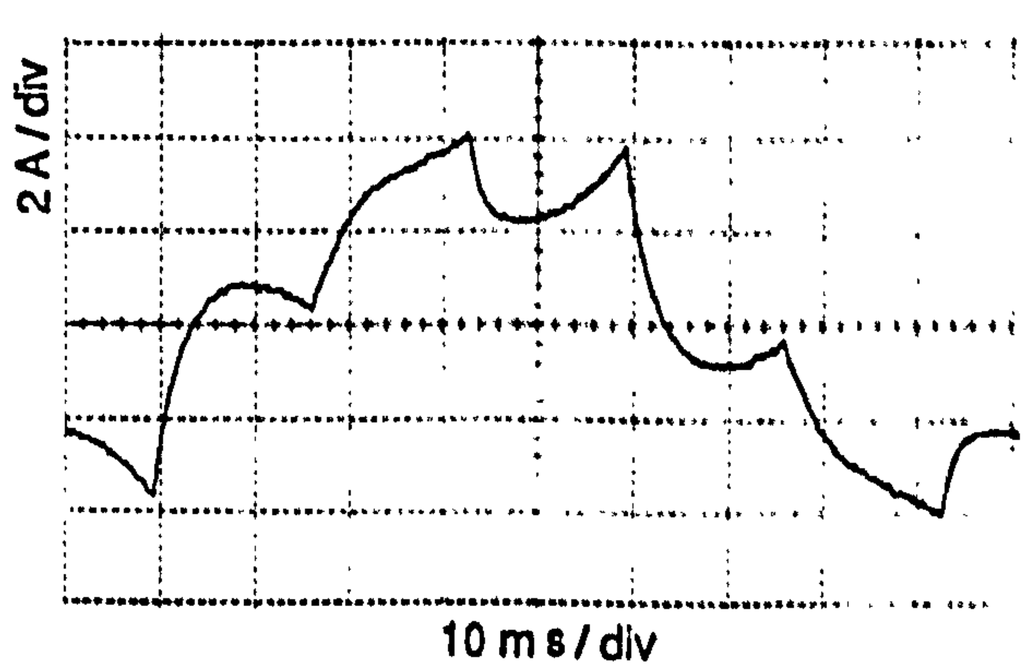

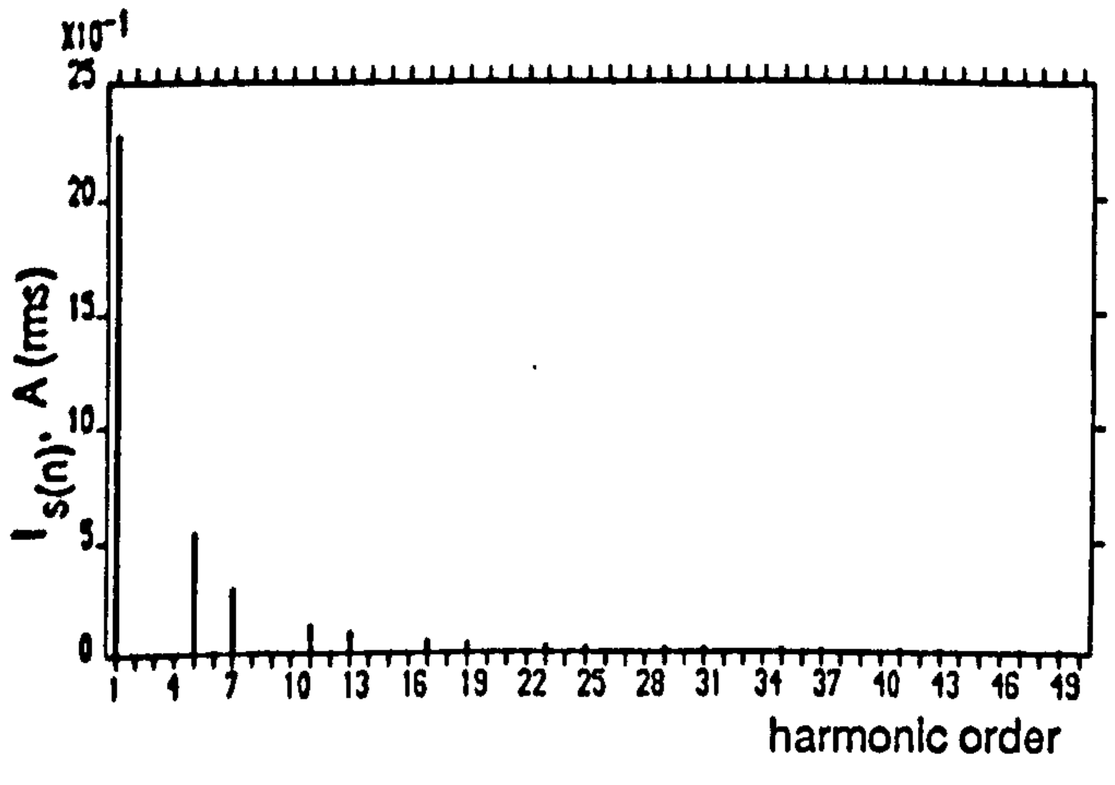

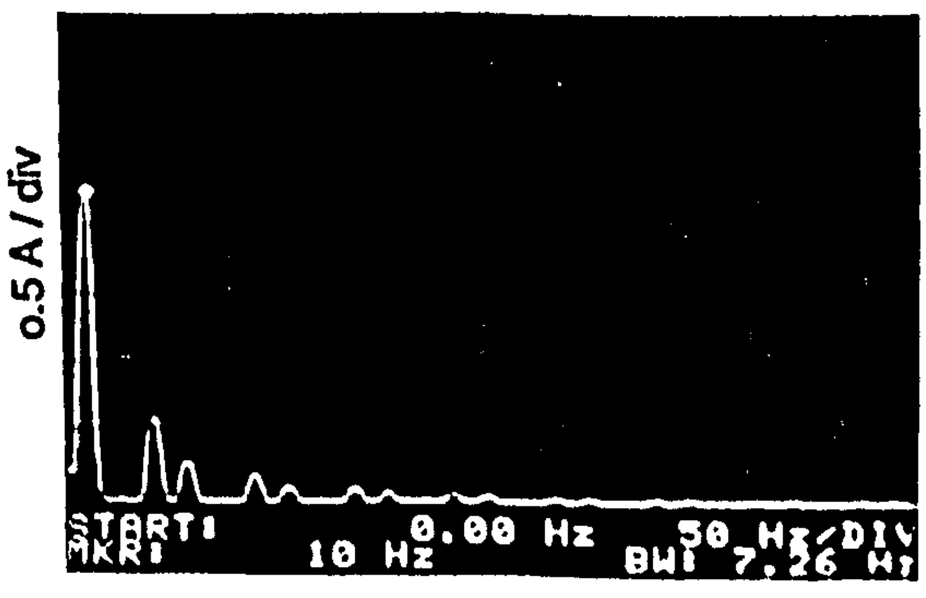

(b)

Figure 7.11 Computed and experimental results for QSW mode at 10Hz stator frequency , full-load operating condition

(a) Line voltage
(b) Stator current and spectrum

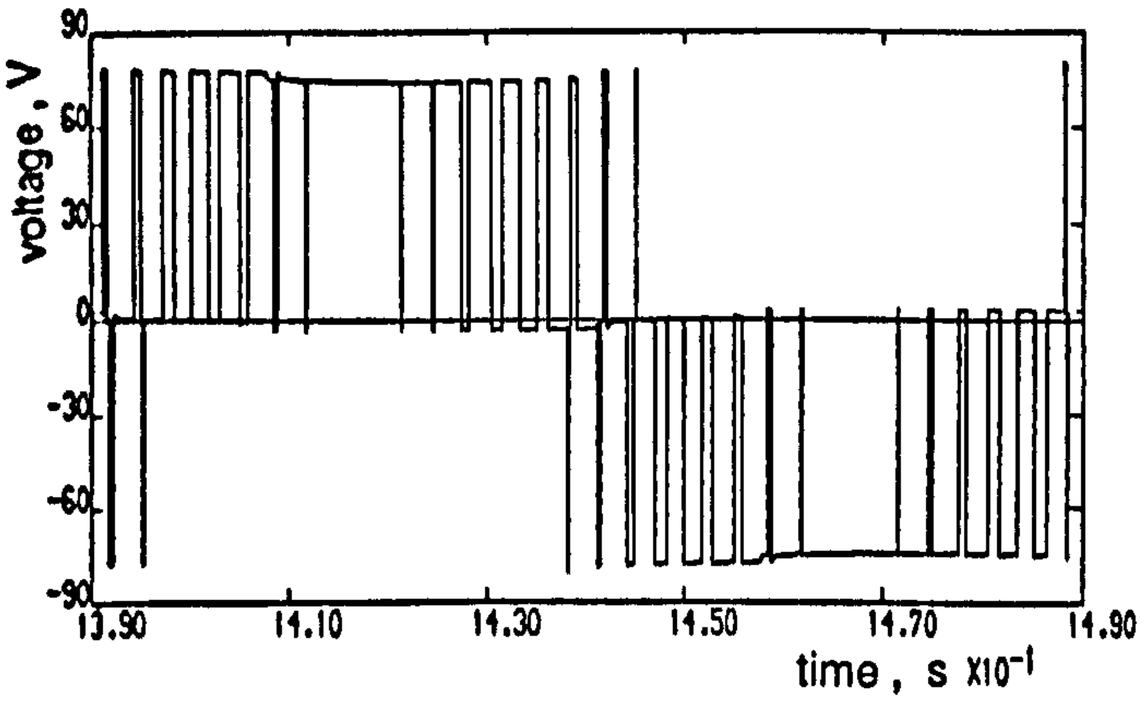

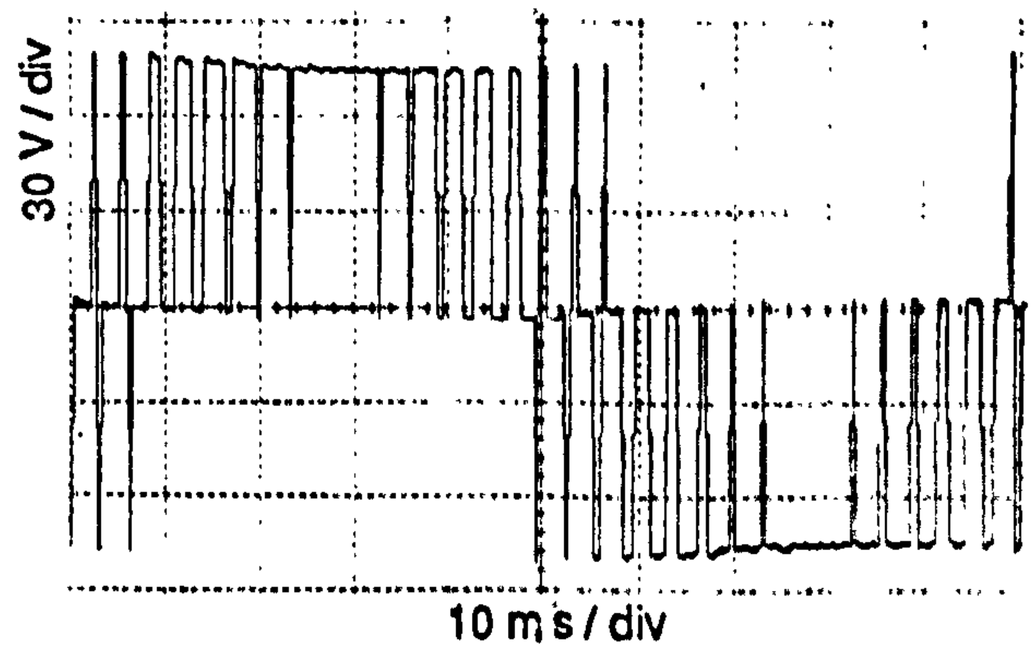

(a)

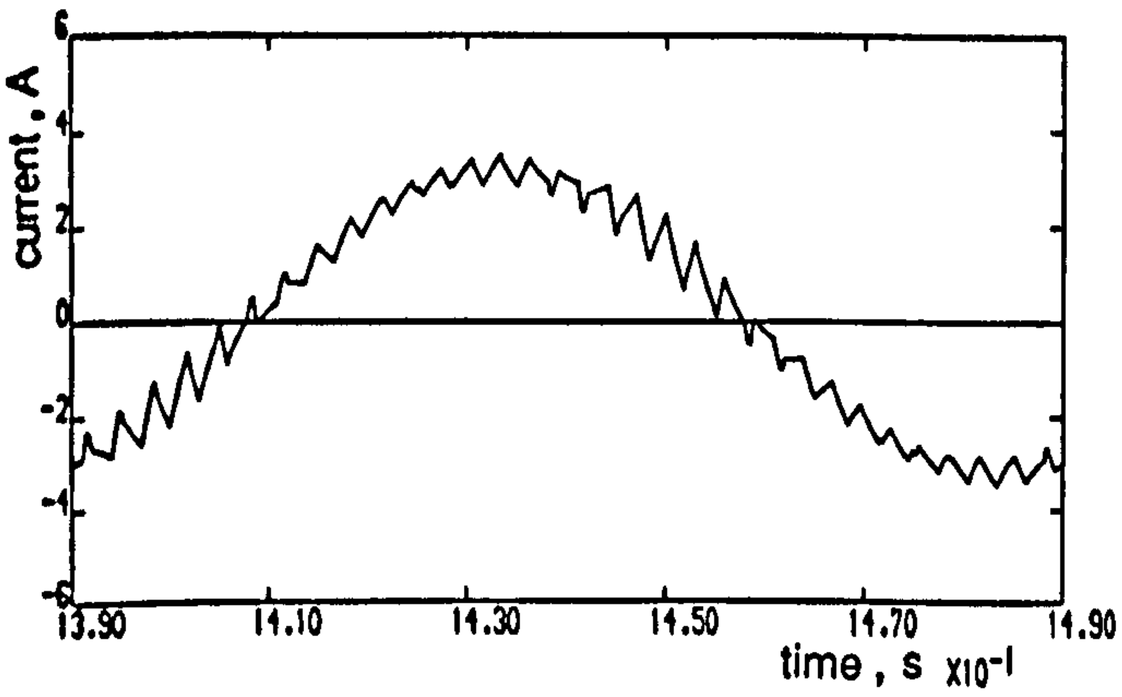

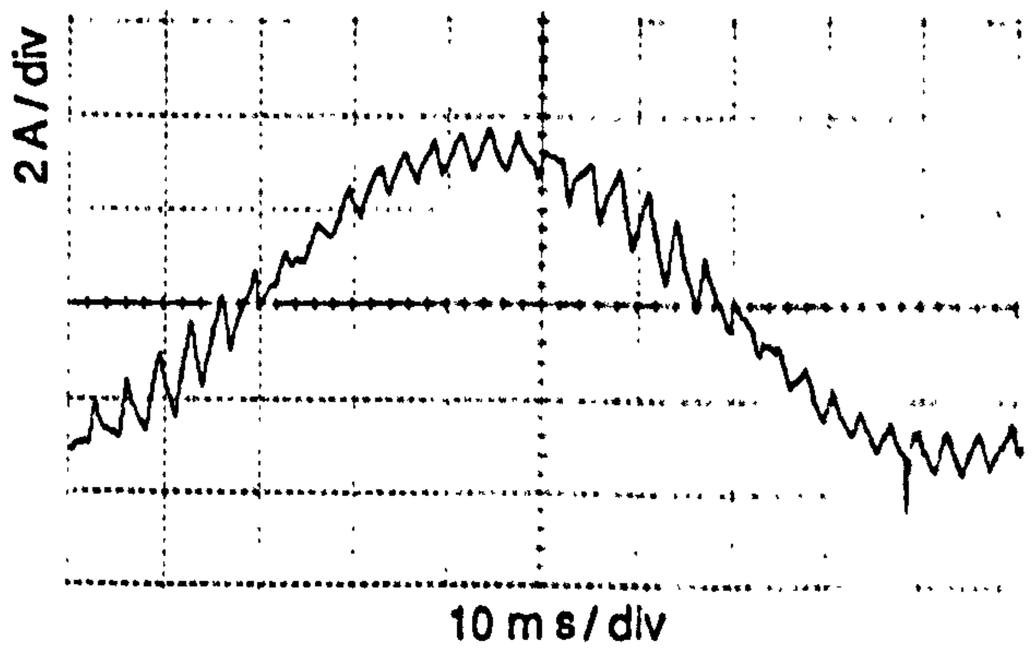

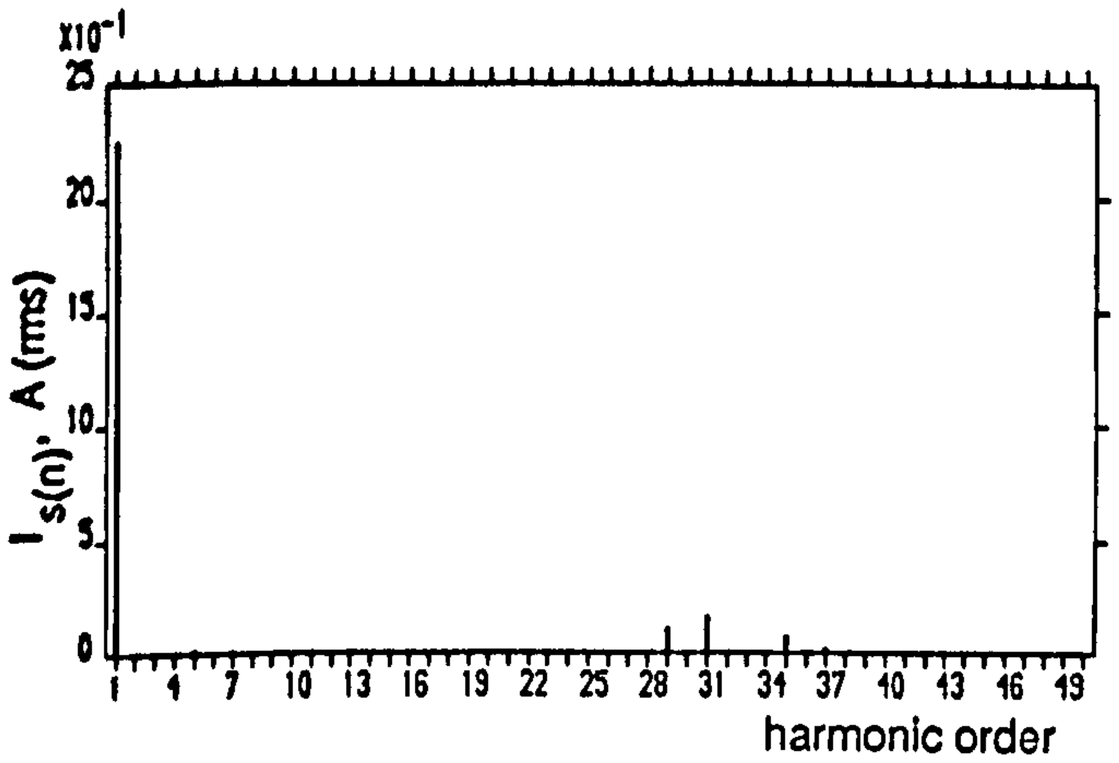

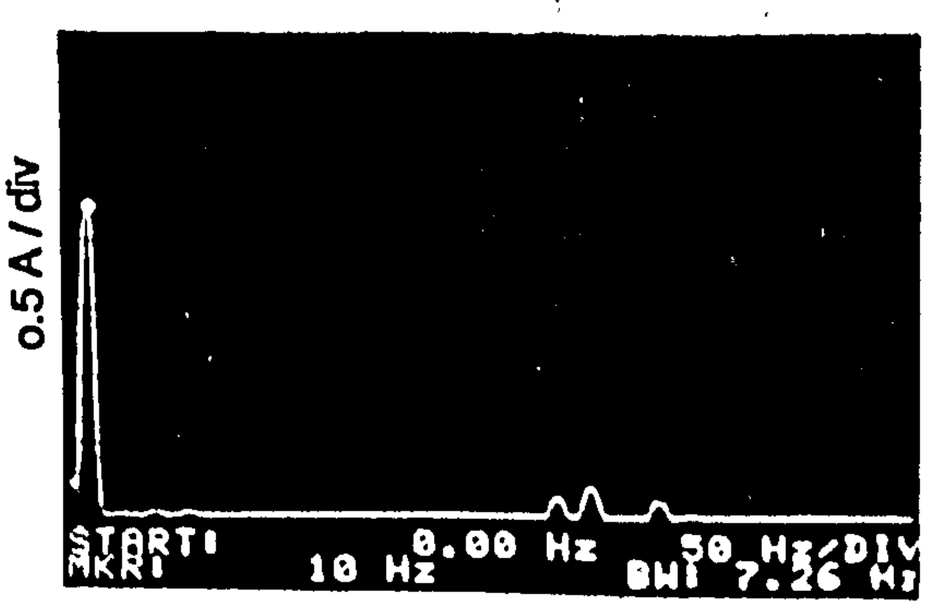

(b)

Figure 7.12 Computed and experimental results for PWM8 elimination strategy at 10Hz stator frequency , full-load operating condition

(a) Line voltage
(b) Stator current and spectrum

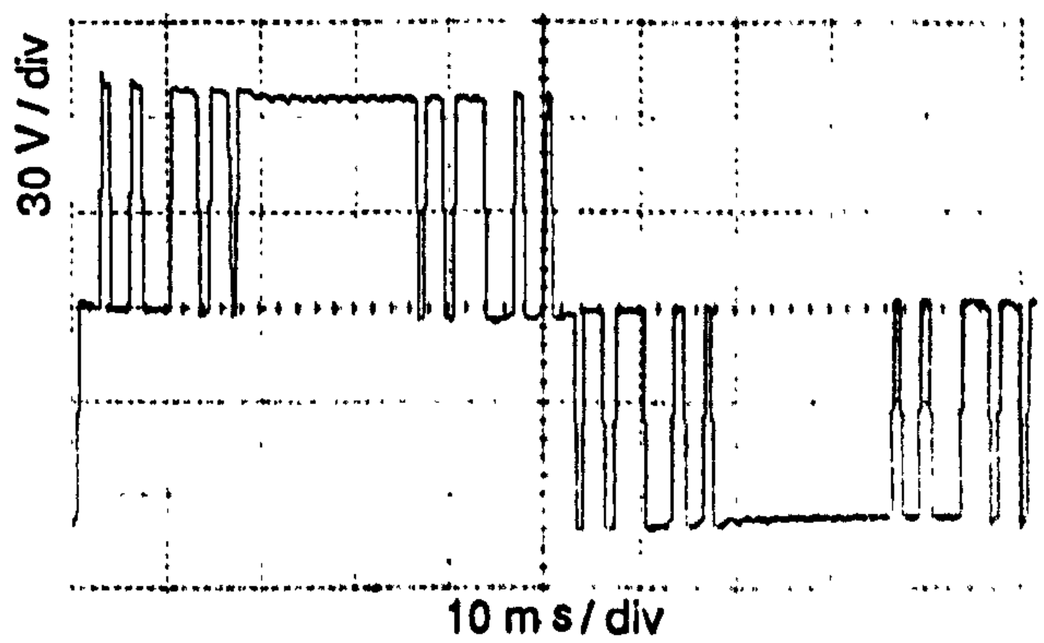

(a)

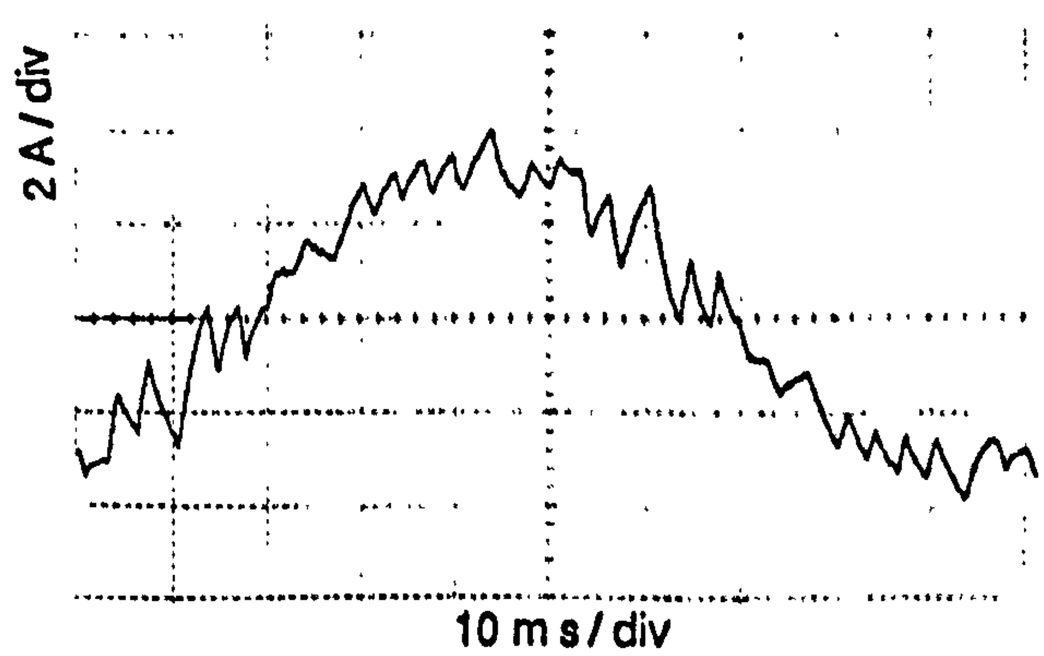

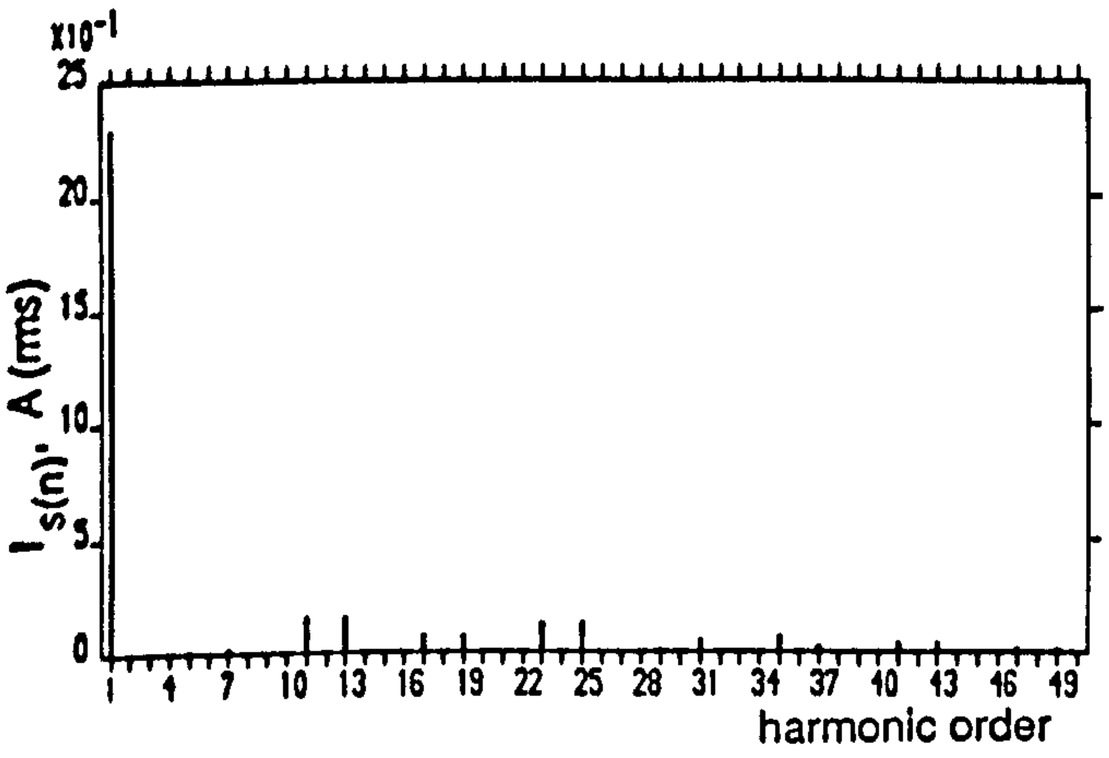

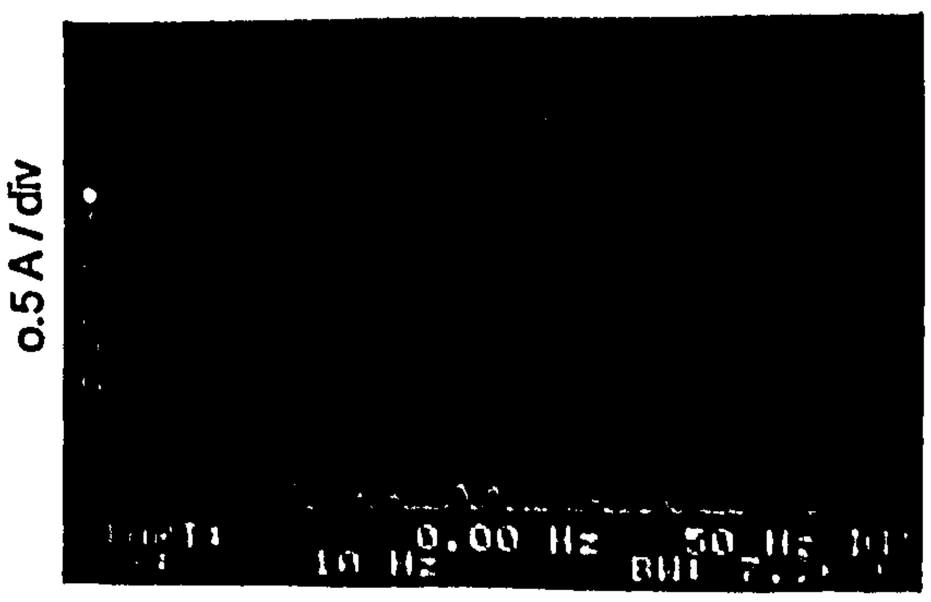

(b)

Figure 7.13 Computed and experimental results for type C PWMM4 quarter-wave symmetrical strategy at 10Hz stator frequency , full-load operation

(a) Line voltage
(b) Stator current and spectrum

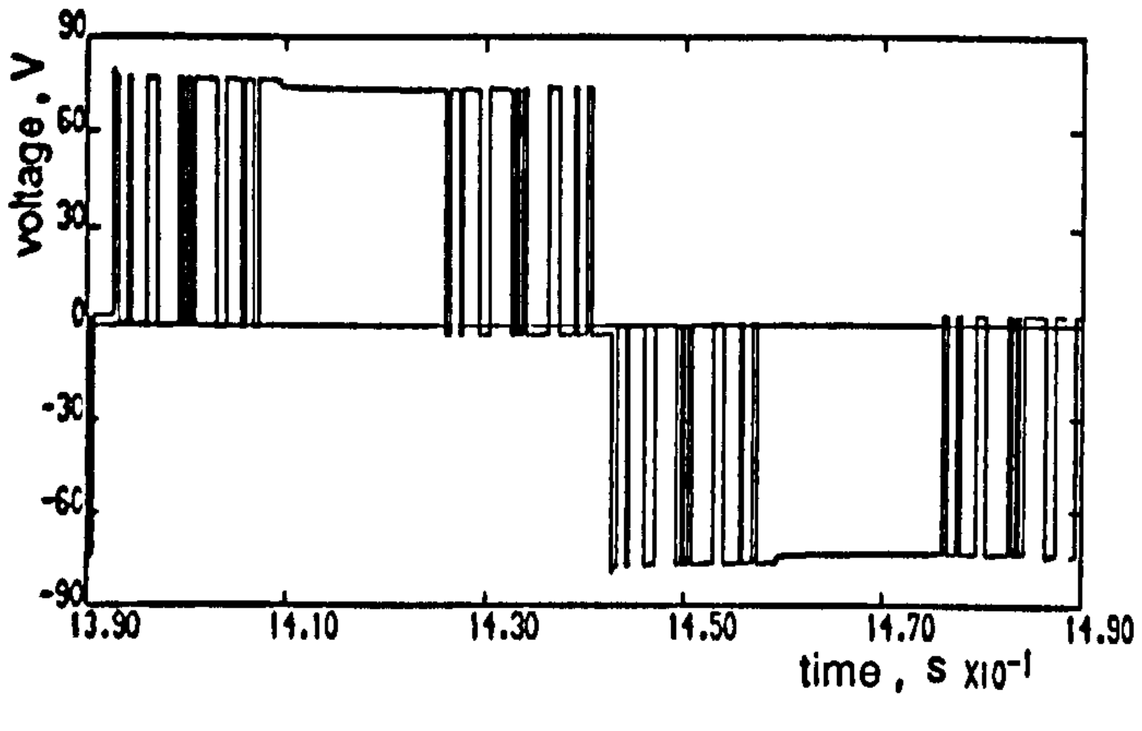

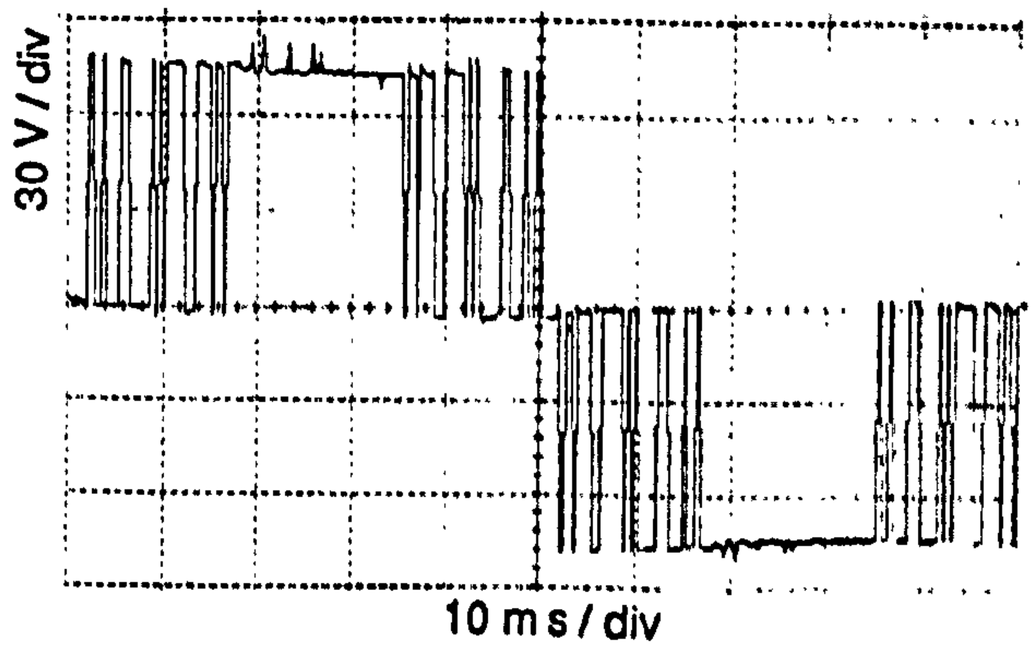

(a)

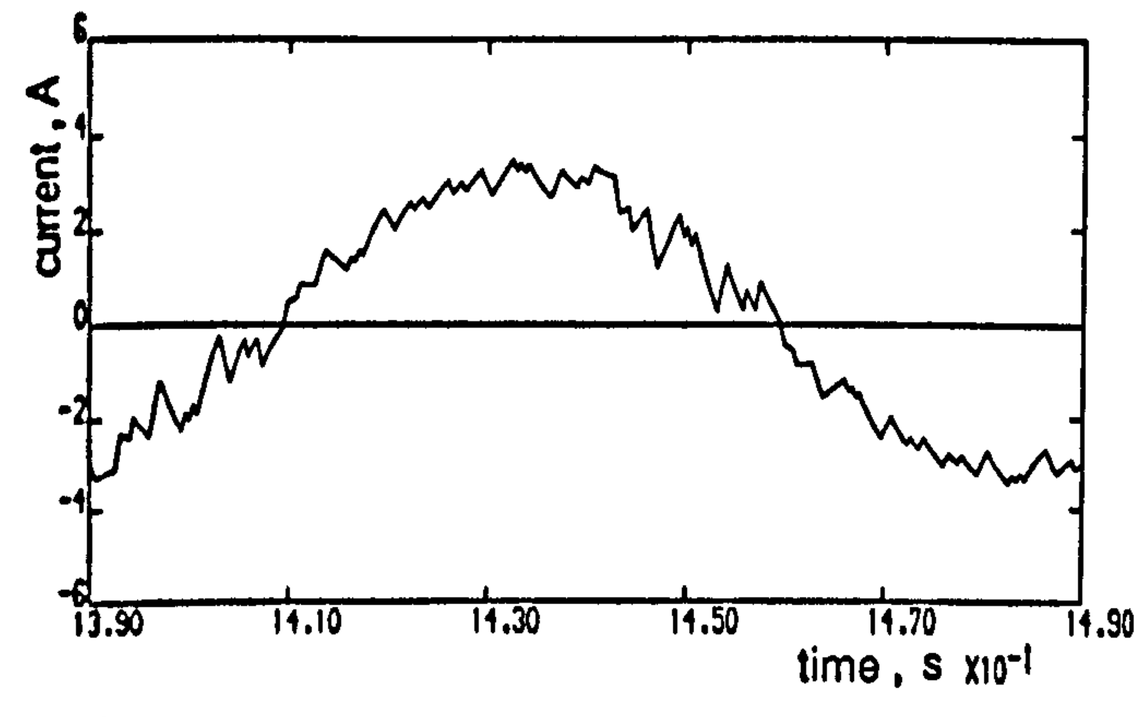

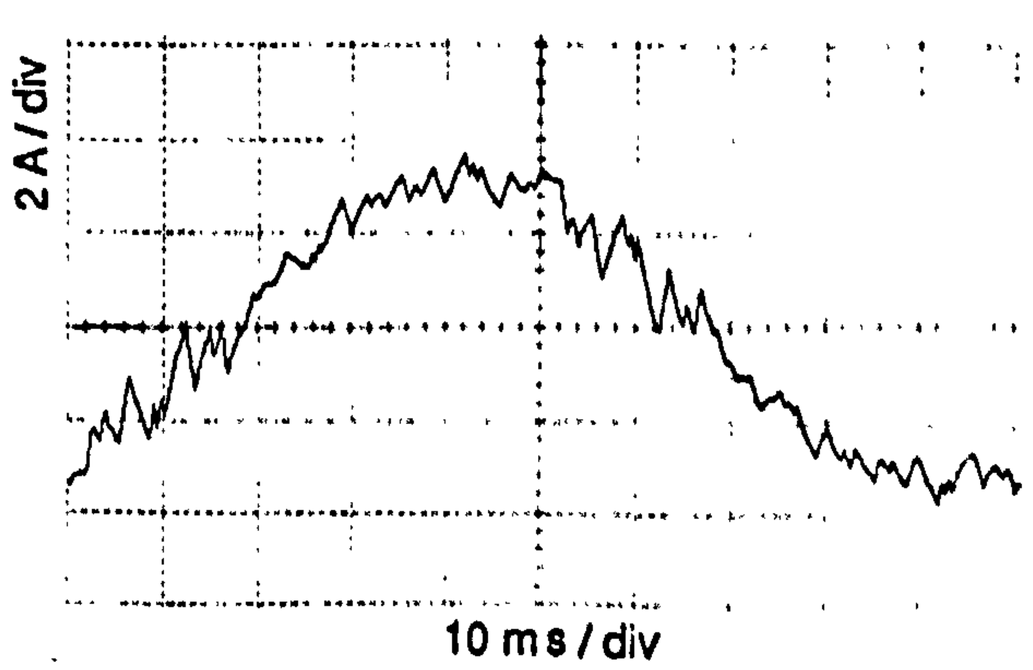

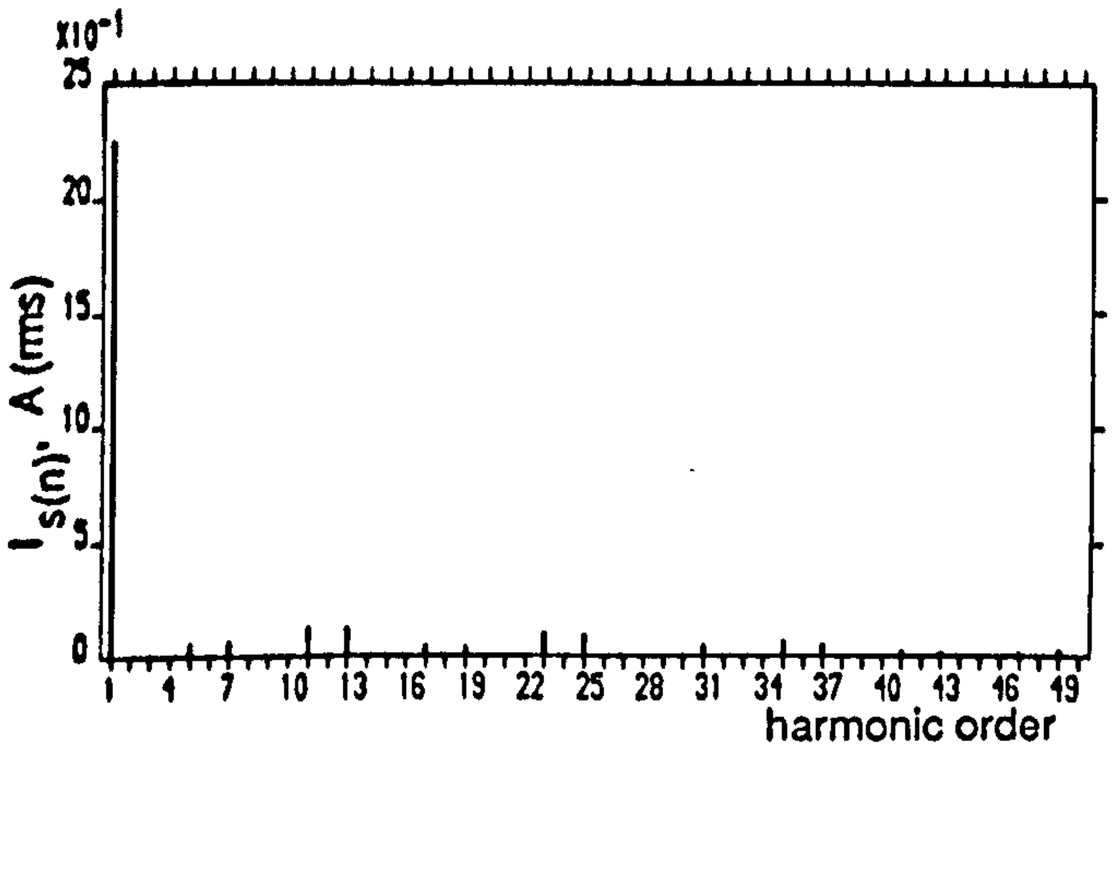

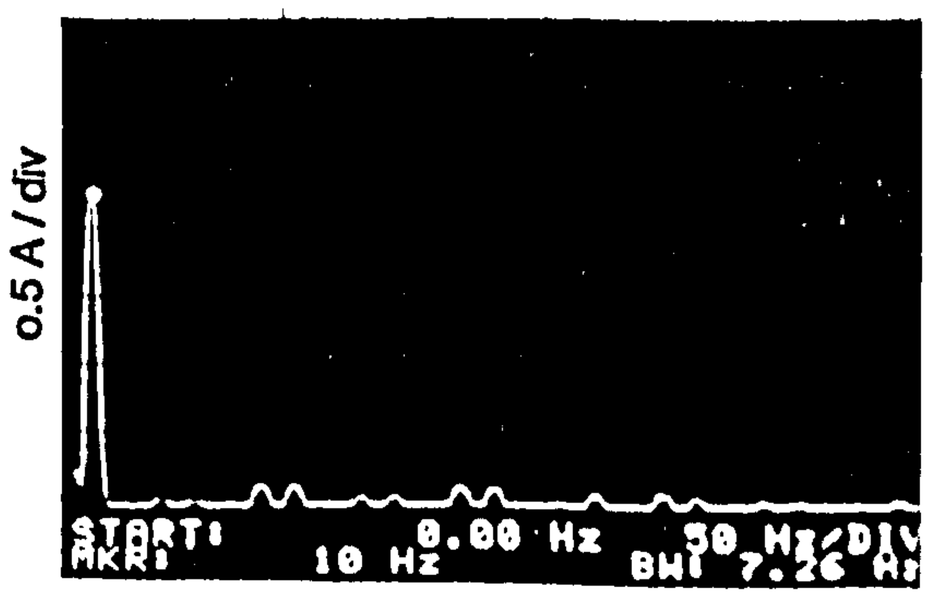

(b)

Figure 7.14 Computed and experimental results for type D PWMM8 quarter-wave symmetrical strategy at 10Hz stator frequency , full-load operation

(a) Line voltage
(b) Stator current and spectrum

to elimination of the low order ones. However, in the new strategy, low order harmonics are not eliminated and their magnitudes are not attenuated to the same extent as the higher order ones. Their contribution to the harmonic distortion factor is consequently significant.

The electromagnetic torque waveforms and their harmonic spectra shown in figure 7.15(a) to (d), indicate an average torque in all cases of 3.95Nm. For the QSW mode, a superimposed peak-to-peak pulsation of 0.92Nm exists, with the harmonic spectrum having a predominant 6th-harmonic component and decreasing higher order harmonics. The torque waveform for the elimination strategy shown in figure 7.15(b) has a superimposed pulsation of 0.6Nm, and the harmonic spectrum illustrates that the low order components are reduced while the 30th and 36th order components are increased. Figure 7.15(c) and (d) shows the torque waveforms and their harmonic spectra for the new switching strategies of figures 7.13 and 7.14 respectively. These demonstrate a significant reduction in the magnitudes of the 6th, 12th, 18th- and 24th-harmonic torque components. Peak-to-peak torque pulsations of 0.54Nm and 0.51Nm are achieved respectively, which represent a 10% and 15% reduction relative to the elimination strategy.

Experimental results for the torque waveforms could not be obtained at high operating frequencies, due to the limited sensitivity of the incremental encoder to the small speed ripple. Figure 7.16(a) and (b) shows respectively, for the QSW mode, the computed and experimental rotor speed for 1Hz no-load operation and 10Hz no-load and full-load operations. At 10Hz the speed ripple for both no-load and full-load conditions is insignificant, and the average speed drops from 30.0rad/s at no-load to 23.45rad/s at full-load operation.

Table 7.6 summarizes the drive performance in terms of different indices at 10Hz full-load operation. It demonstrates that the harmonic distortion for any mode in the type C strategy is higher than its counterpart in the elimination mode. However,

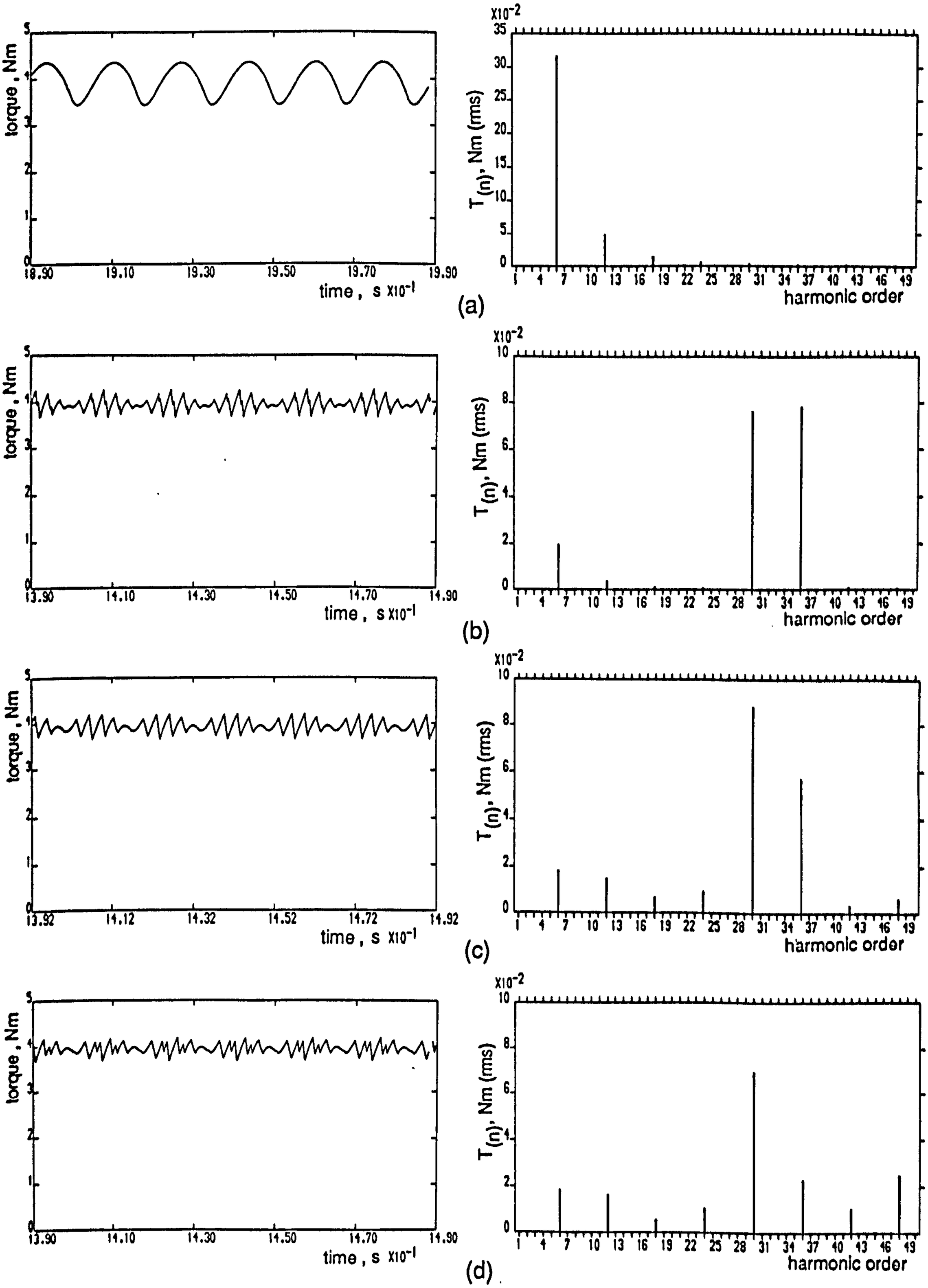

Figure 7.15 Computed electromagnetic torque and harmonic spectra at 10Hz stator frequency , full-load operation for
(a) QSW (b) PWM8 elimination strategy
(c)Type C PWMM4 strategy (d)Type D PWMM8 strategy

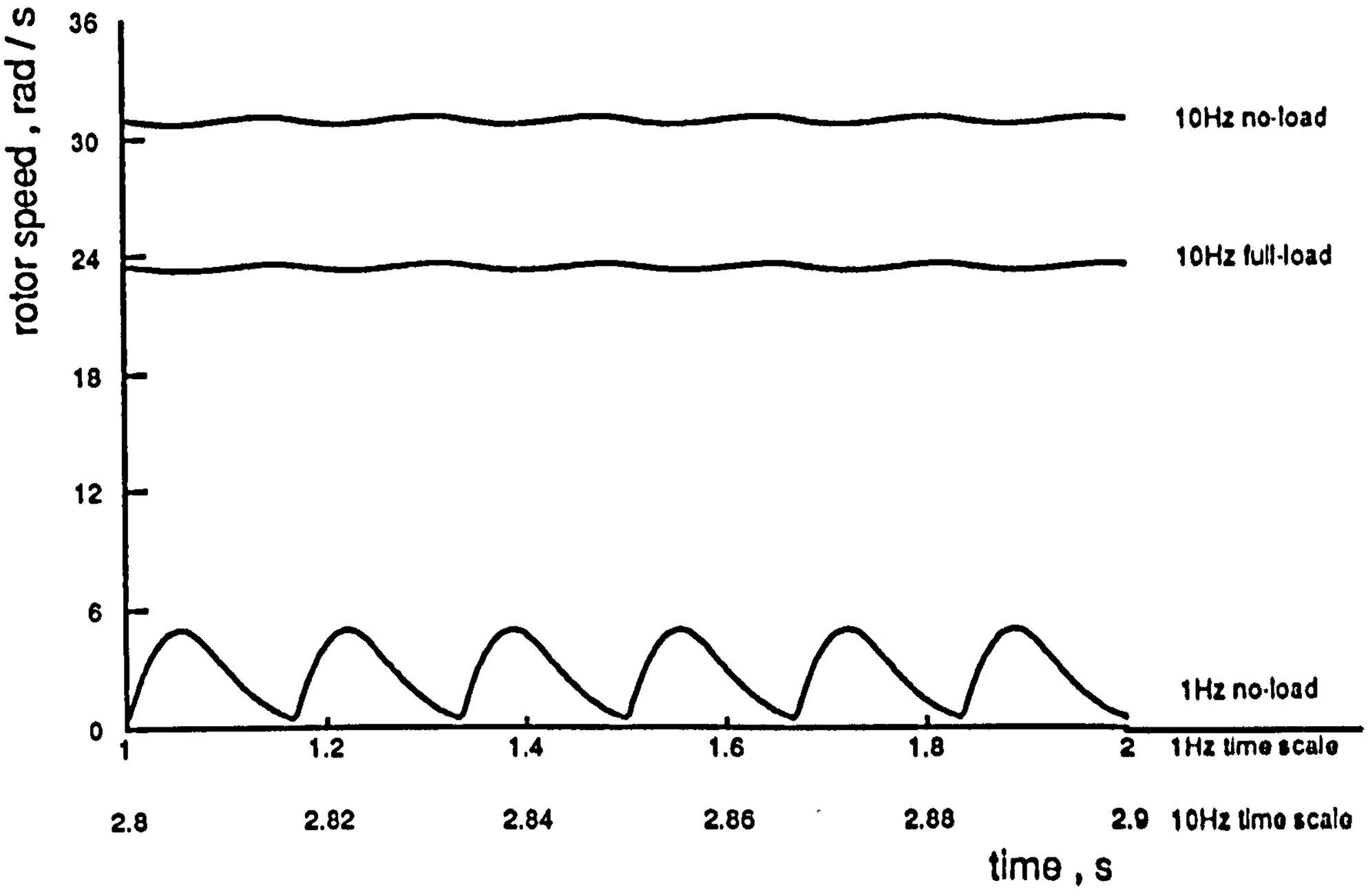

(a)

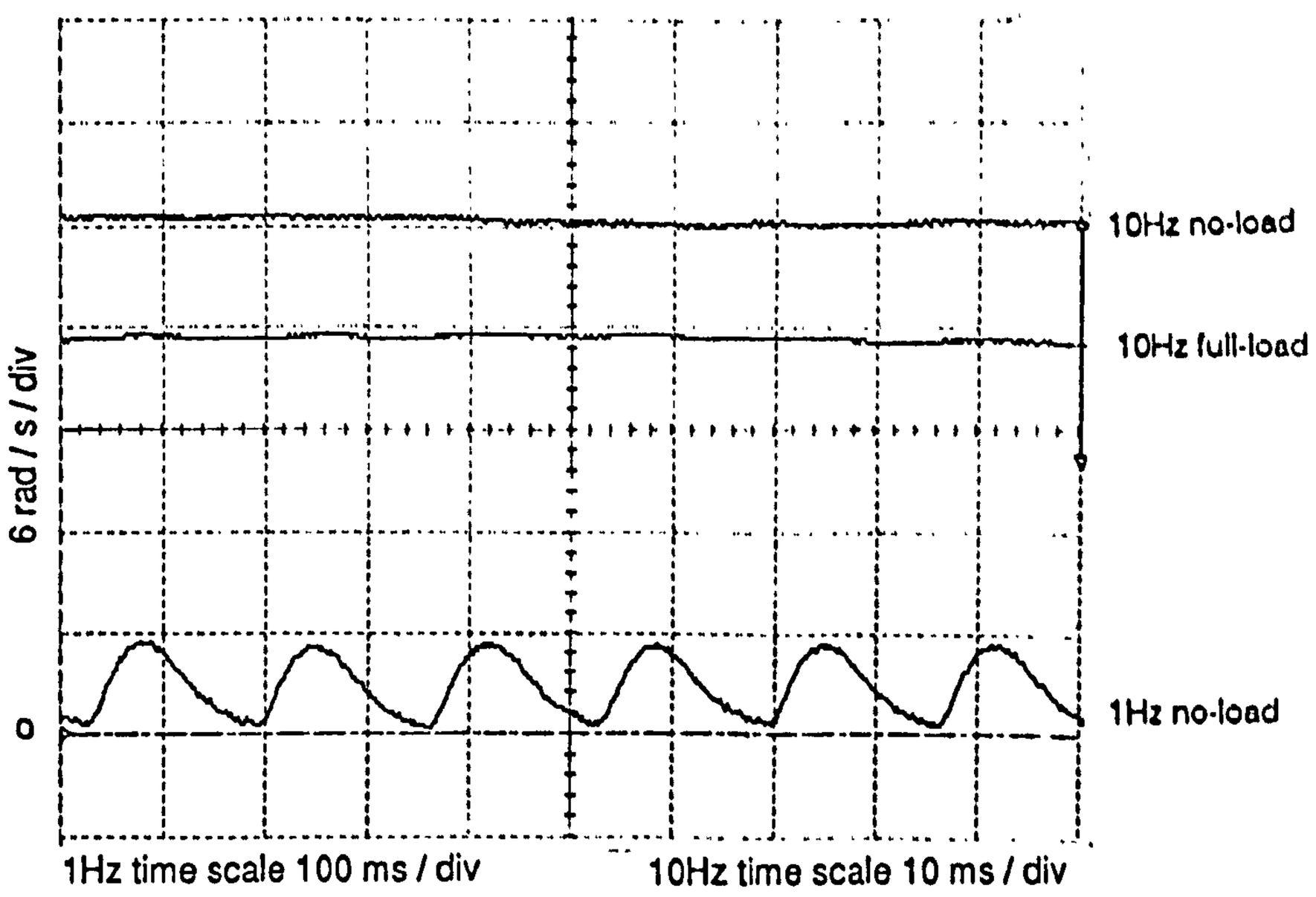

(b)

Figure 7.16 Induction motor rotor speed with a QSW inverter operating at 1Hz no-load , and , 10Hz no-load and full-load conditions
(a)Computed (b)Experimental

by increasing the pulse number, type D modes reduce the distortion factor to values similar to those of the elimination strategy. It is clear that, except for type C with one switching angle mode, both new strategies cause lower torque pulsations than the elimination modes. Although the speed ripple is insignificant at this frequency, it is listed to demonstrate that lower torque pulsations do not necessarily imply a lower speed ripple. This fact is well illustrated in the type C modes, where the speed ripples exceed those for the elimination strategy, even though lower torque pulsations are obtained. However, when matching the elimination strategy pulse numbers, the type D strategy modes result in lower speed ripple than the elimination modes. The fundamental component factor magnitudes are approximately the same in both strategies.

TABLE 7.6
COMPARISON OF THE DRIVE PERFORMANCE
AT 10Hz FREQUENCY , FULL-LOAD CONDITION

MODE	K	THD	ΔT_e Nm	$\Delta\omega_m$ rad/sec
QSW	1.0000	27.67	0.92	0.34
PWM2	0.9330	21.14	0.97	0.11
TYPE C PWMM1	0.9538	27.28	1.35	0.22
TYPE D PWMM2	0.9371	20.83	0.88	0.09
PWM4	0.9200	15.47	0.75	0.07
TYPE C PWMM2	0.9412	20.59	0.77	0.09
TYPE D PWMM4	0.9300	14.79	0.55	0.05
PWM6	0.9140	11.65	0.71	0.06
TYPE C PWMM3	0.9100	24.98	0.68	0.09
TYPE D PWMM6	0.9134	13.22	0.56	0.05
PWM8	0.9116	9.15	0.54	0.04
TYPE C PWMM4	0.9284	13.8	0.54	0.04
TYPE D PWMM8	0.9247	11.39	0.50	0.039

7.7 Conclusion

New optimal PWM strategies are proposed which do not completely eliminate low order harmonics. They do however manipulate the phase angles and/or magnitudes of pairs of low order current components such that their contribution to the harmonic torque production is cancelled or reduced. At 1Hz inverter frequency, the half-wave symmetrical strategy distributes the harmonic current magnitudes and phase angles in a way which promises to be beneficial to the drive performance. At 10Hz inverter frequency, a quarter-wave symmetrical strategy which controls the magnitudes only of harmonic components reduces the magnitudes of selective low order torque components and redistributes the remaining high order ones. Their results demonstrate a better performance in terms of reduced torque pulsations. Both strategies are dependent on the operating conditions of the machine and consequently any implementation is likely to require a closed-loop control system. In the next chapter, a more detailed evaluation and comparison of these strategies is made with respect to the elimination strategy, and a study is performed on their dependency on the operating conditions.

CHAPTER 8

COMPARATIVE EVALUATION OF THE DEVELOPED STRATEGIES

The optimization process for both strategies developed in chapter 7 requires, in addition to an initial estimate of the switching angles, the definition of the stator operating frequency and the machine load. Although both strategies were verified in terms of the cancellation or minimisation of low order harmonic torque components, the results presented were for the specific machine condition at which the optimization process has been normalised. Any change, either in the load condition or stator frequency, alters the distribution of the switching angles and therefore the harmonic currents and torques. The present chapter is concerned with exploring the merits of the two strategies, and assessing their effects on the machine performance when compared with those of the conventional optimal elimination strategy.

8.1 Half-Wave Symmetrical Strategy

8.1.1 Computation of Switching Angles for Different Load Conditions

Following the optimization process of chapter 7, switching angles for types A and B PWM strategies, defining 3,5,7,9 and 5,9,13,17 pulses per half-cycle and computed for different loads at 1Hz stator frequency, are plotted against load torque in figures 8.1(a) to (d) and 8.2(a) to (d). The variations of switching angles $\alpha_{(m)}$ with applied load are linear for all m values. Simple linear functions may be fitted to these variations, enabling the approximate switching angles to be calculated on-line using a microprocessor.

Computed results obtained from the direct-phase model for 1.5Nm load are shown in figures 8.3 and 8.4, for a nine pulse type A PWMT8 mode and a seventeen pulse type B PWMT16 mode respectively. These results demonstrate the ability of both

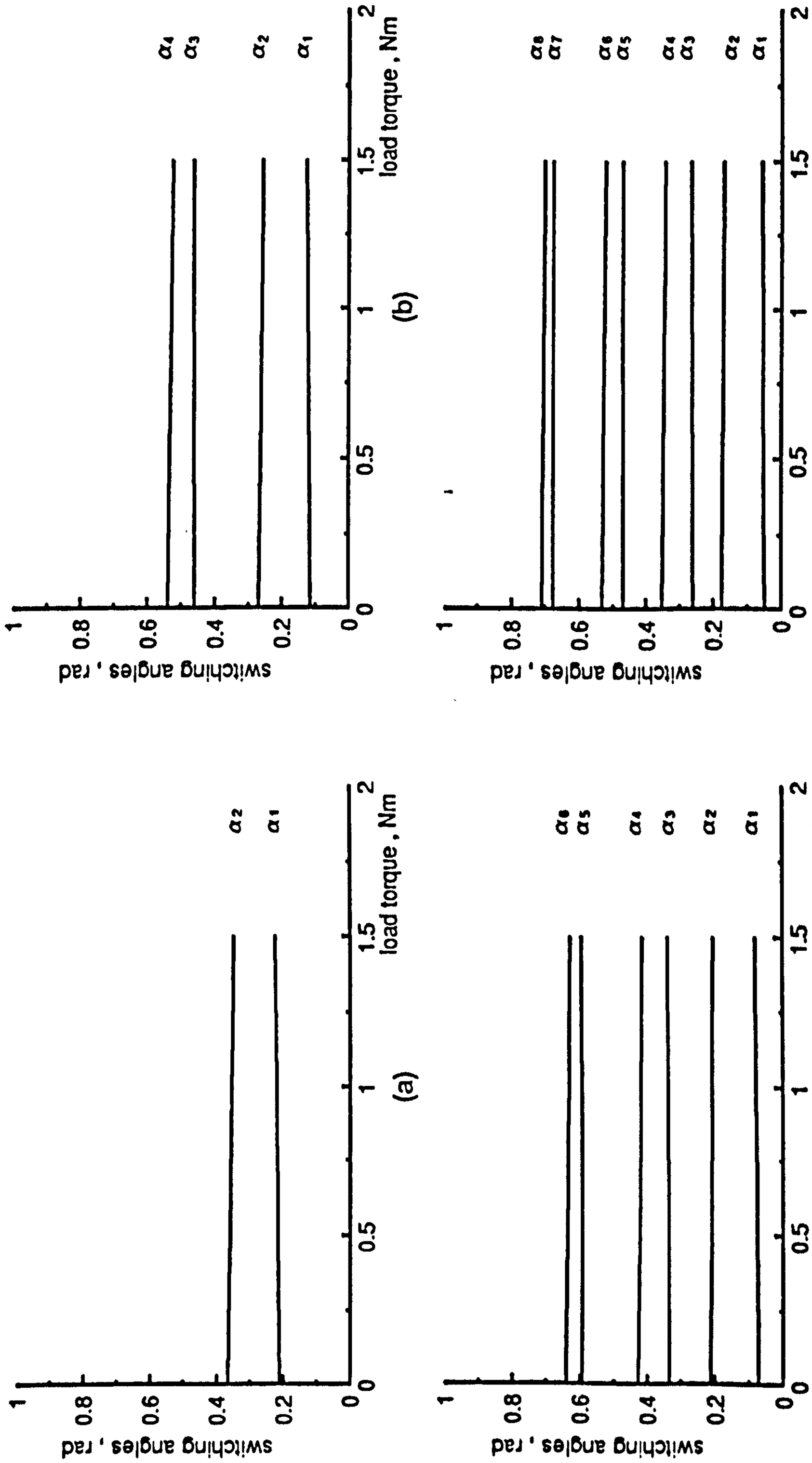

Figure 8.1 Variation of switching angles with load at 1Hz frequency for type A half-wave strategy

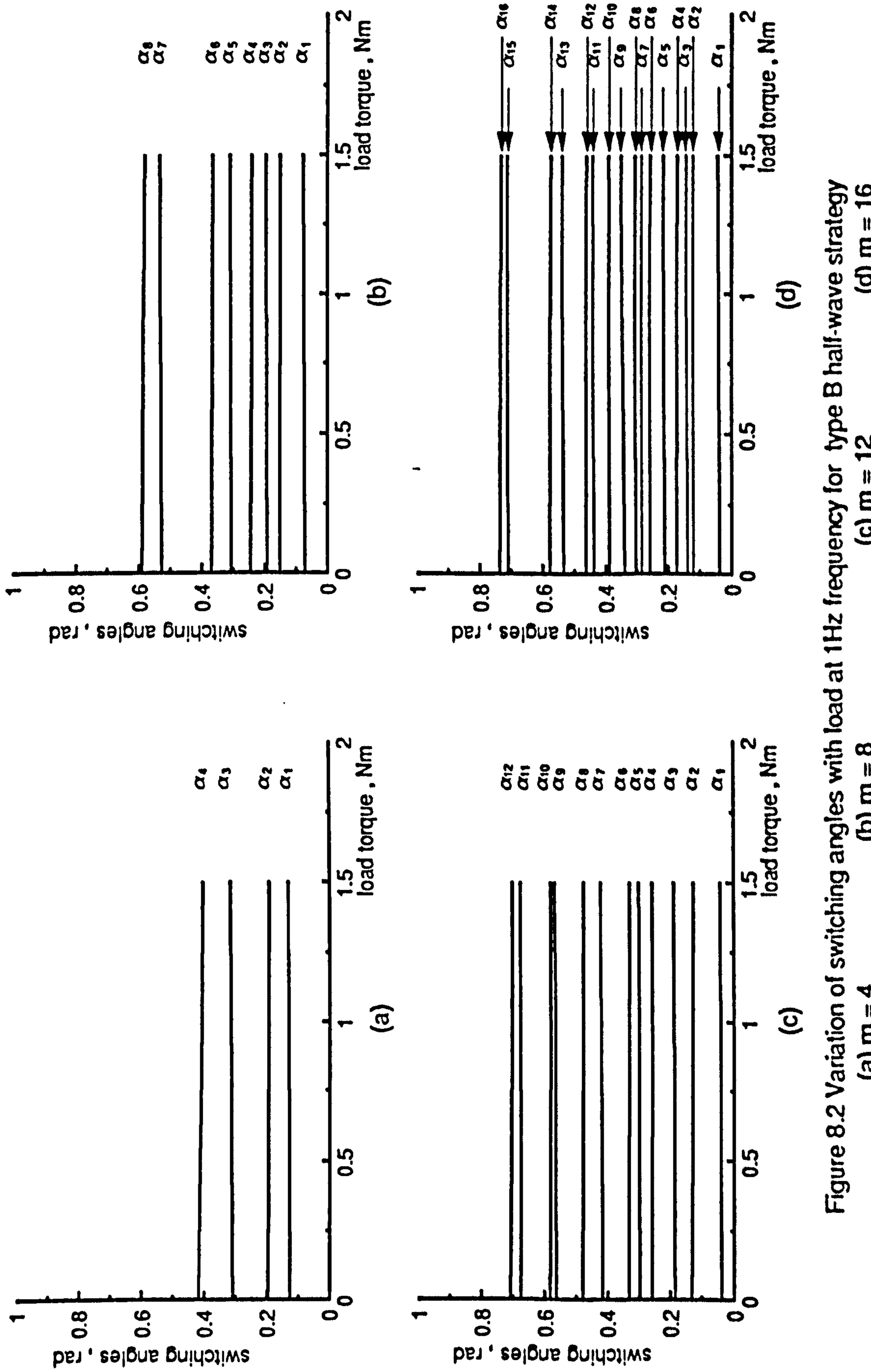

Figure 8.2 Variation of switching angles with load at 1Hz frequency for type B half-wave strategy
(a) m = 4 (b) m = 8
(c) m = 12 (d) m = 16

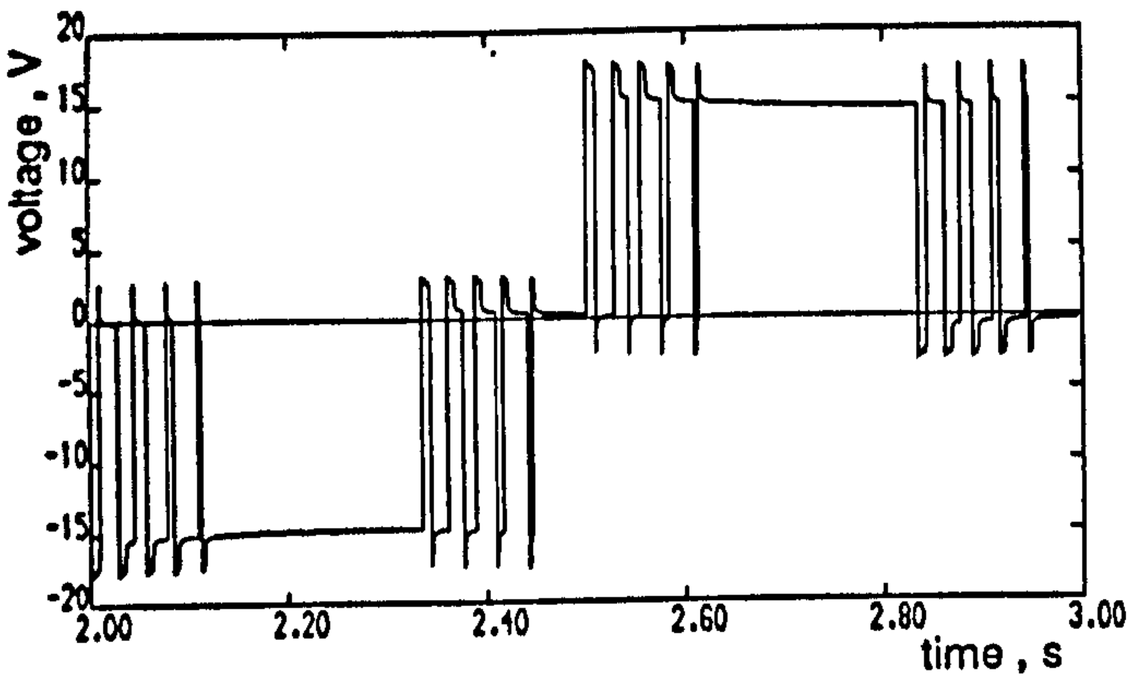

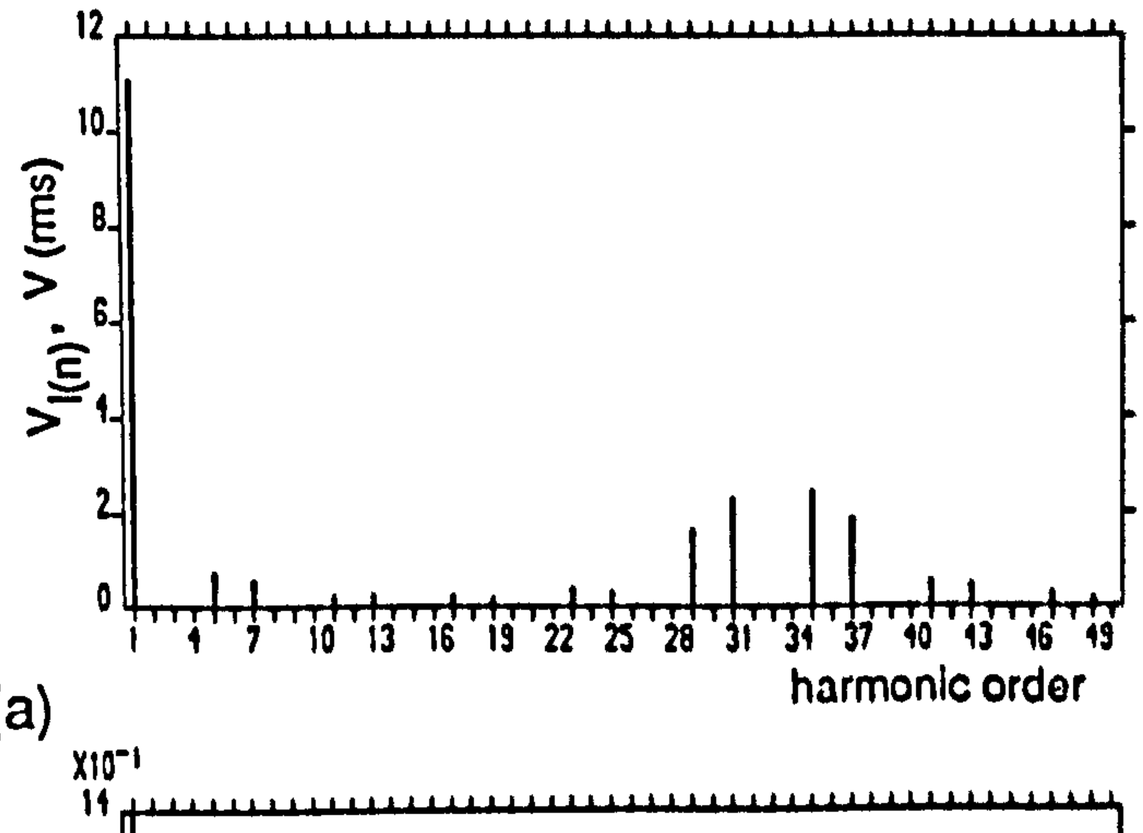

(a)

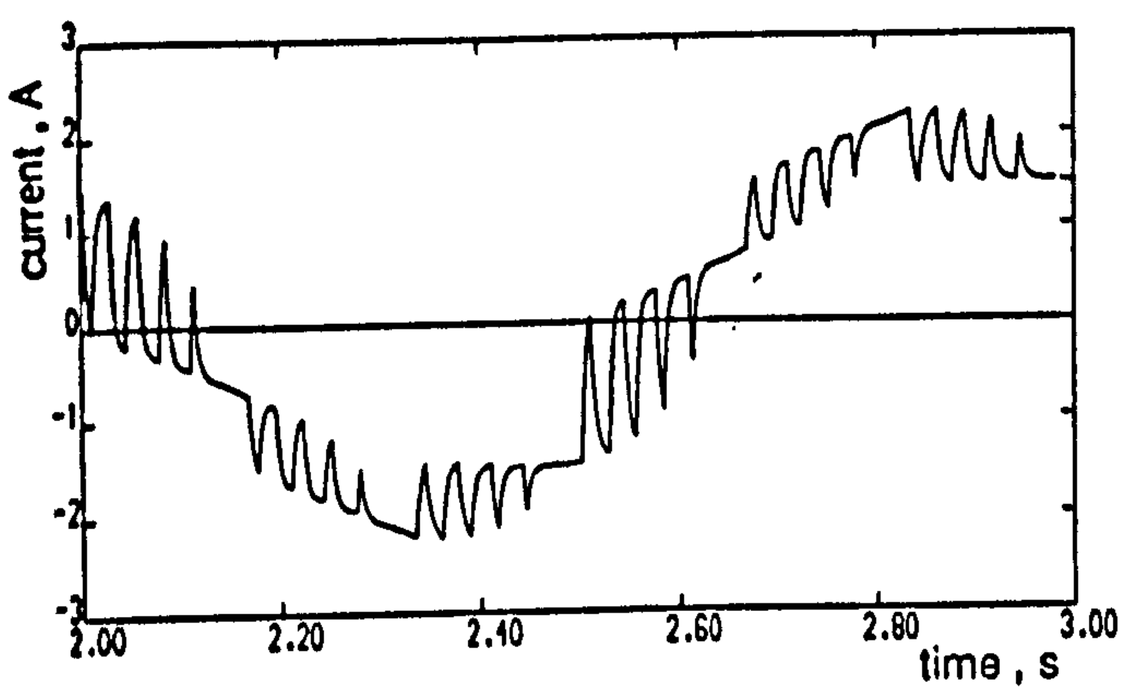

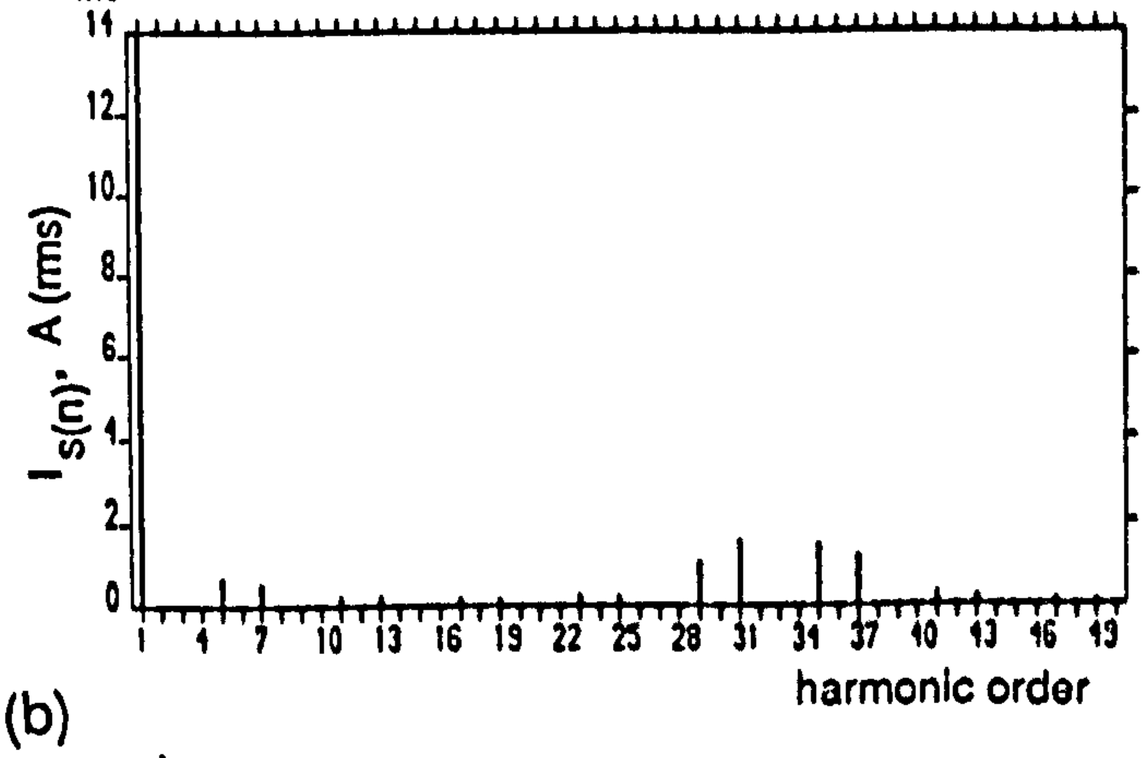

(b)

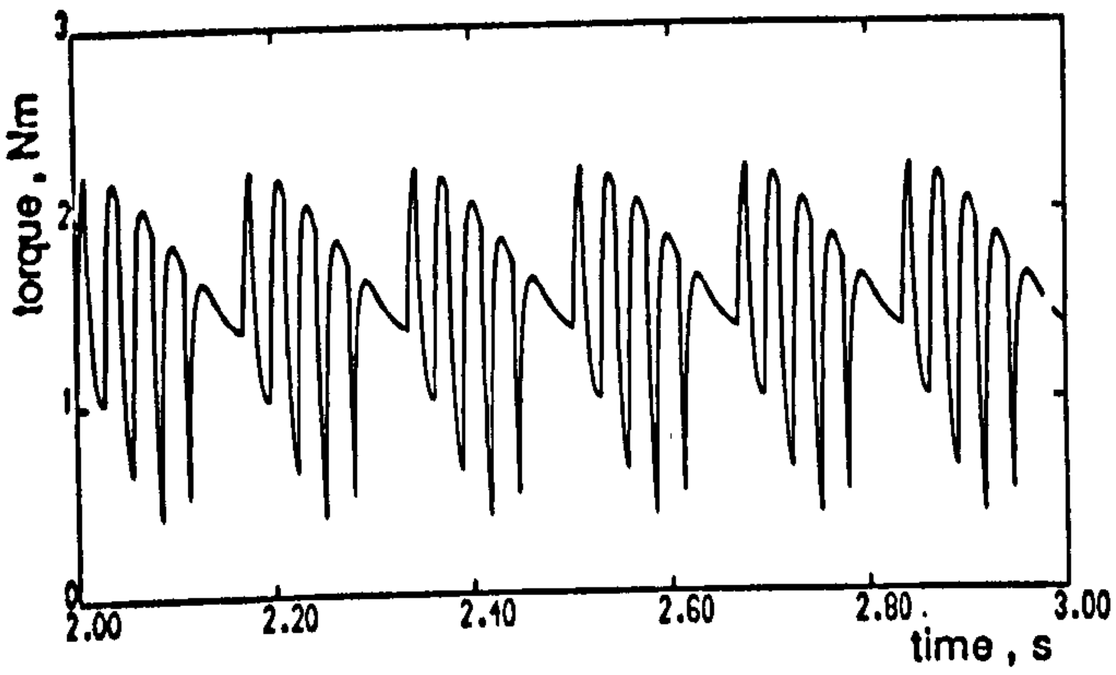

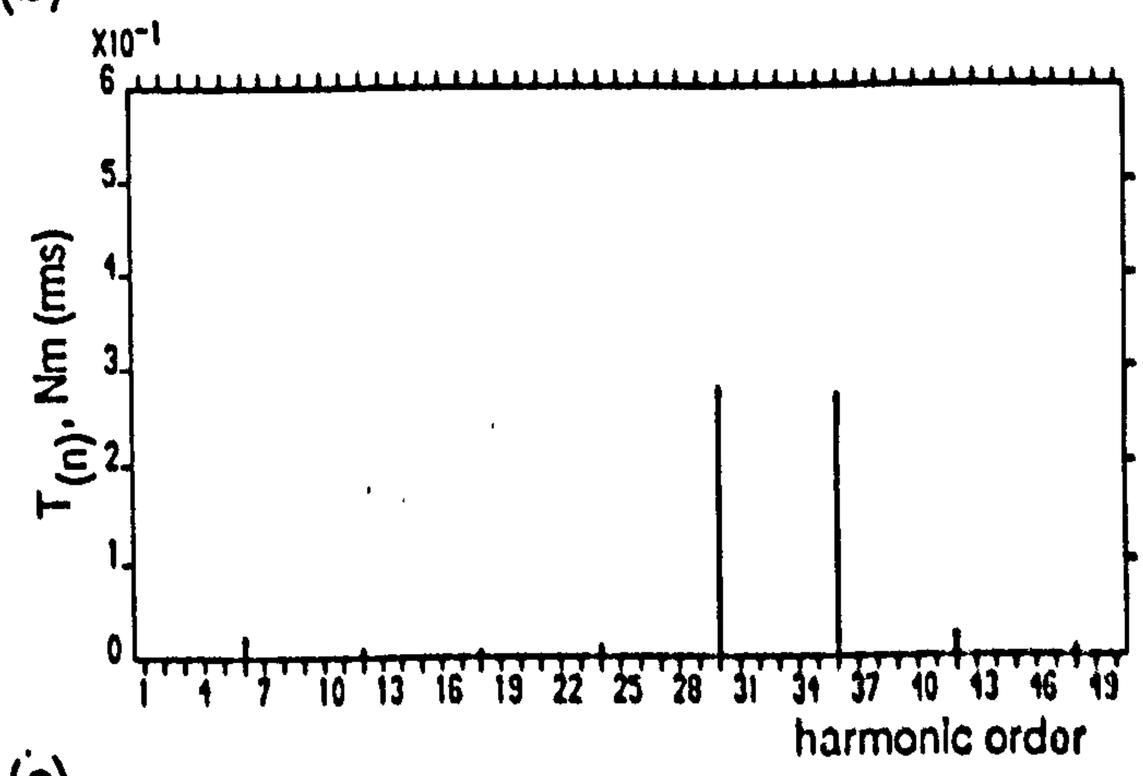

(c)

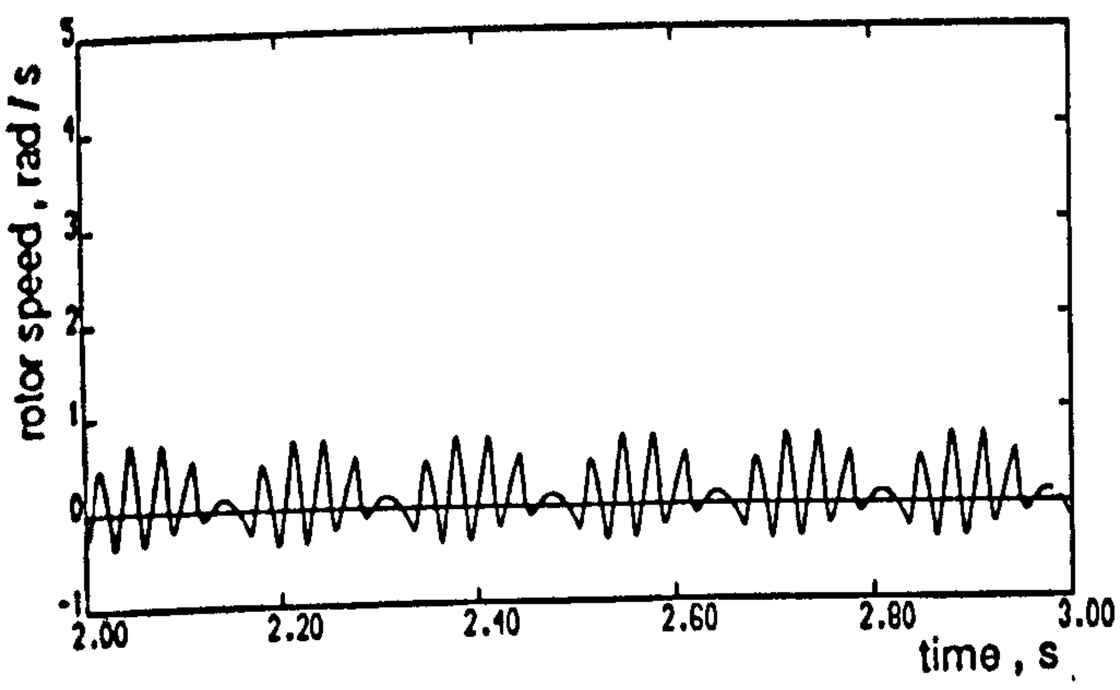

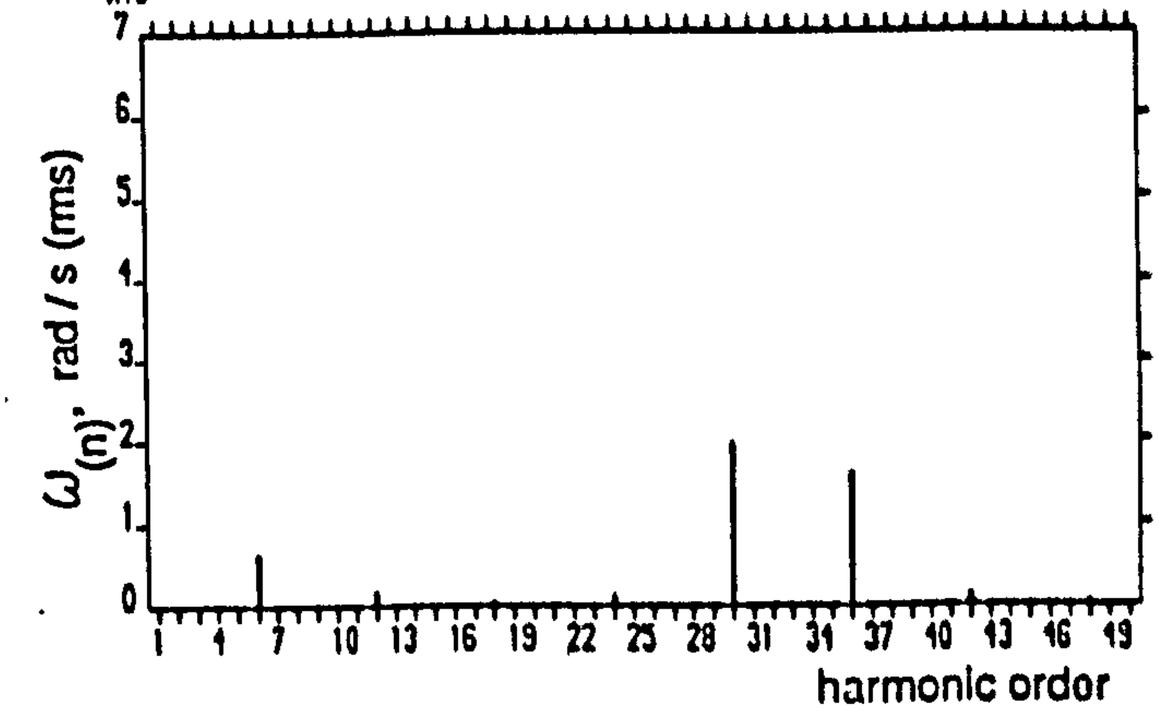

(d)

Figure 8.3 Computed results for type A PWMT8 half-wave strategy for 1Hz frequency , 1.5Nm load

(a) Line voltage and spectrum (b) Stator current and spectrum

(c) Electromagnetic torque and spectrum (d) Rotor speed and spectrum

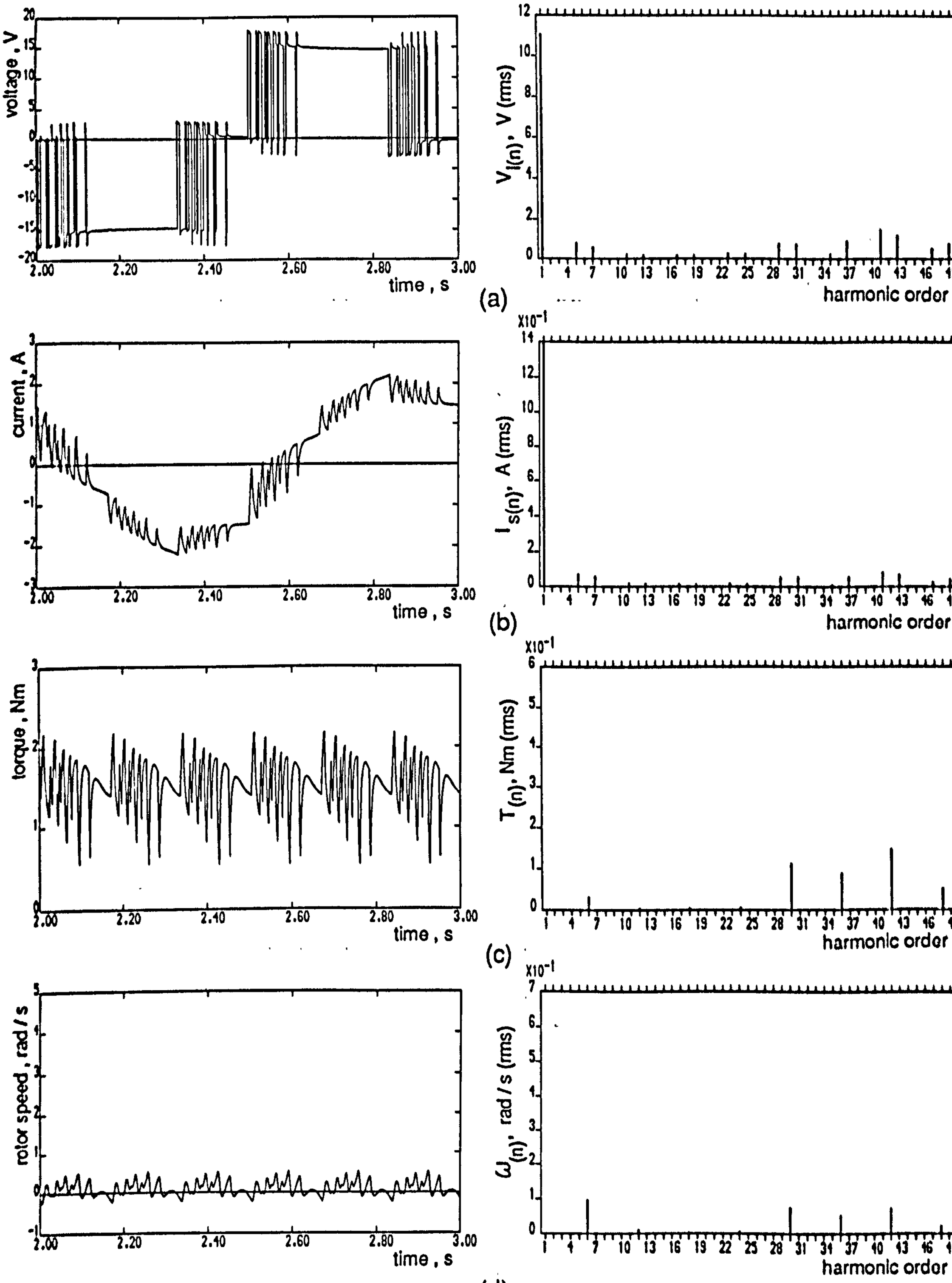

Figure 8.4 Computed results for type B PWMT16 half-wave strategy for 1Hz frequency , 1.5Nm load

(a) Line voltage and spectrum (b) Stator current and spectrum

(c) Electromagnetic torque and spectrum (d) Rotor speed and spectrum

types to achieve cancellation of torque components with different pulse numbers and load. The results are for a fundamental line voltage of 11.2V, obtained from DC-link voltages of 18.56V and 18.60V respectively, and produce a stator current of 1.4A. The average electromagnetic torque is about 1.5Nm and the rotor is almost stationary, with part of the superimposed speed ripple being in the reversed direction of rotation.

8.1.1.1 Effect on Harmonic Torque Components

To simplify the implementation of the two strategies, it is convenient to choose a switching pattern normalised at a certain load, and for this to remain unchanged for all other loads. Since the frequency-domain model reflects the efficiency of the optimization process in determining the optimal positions of the switching angles, both the frequency-domain and direct-phase models were used to investigate the sensitivity of the new strategies to load variations. Figures 8.5(a) to (d) show respectively, for 1Hz operation, the magnitudes of the 6th, 12th, 18th- and 24th-harmonic torque components for QSW, elimination PWM8, type A PWMT8 and type B PWMT16 modes, all obtained using the frequency-domain model. The effect of normalising the optimization process for both new strategies at no-load and on-load is evident, with the harmonic torque components under consideration being a minimum at the load for which the strategy was normalised. As the applied load is changed the harmonic torque components increase, although both strategies maintain lower magnitudes than the QSW case. Figures 8.5(e) to (h) show the magnitudes of the remaining higher order harmonic torque components to be load independent, and the 30th- and 36th-harmonic components can be seen to be increased for all PWM strategies. The 30th-harmonic component in the elimination mode is approximately 8.0 times that in the QSW mode, whereas for type A normalised at no-load and on-load its values are respectively 5.6 and 5.1 times the QSW values. For type B normalised at no-load and on-load the corresponding figures are 2.5 and 2.0 times.

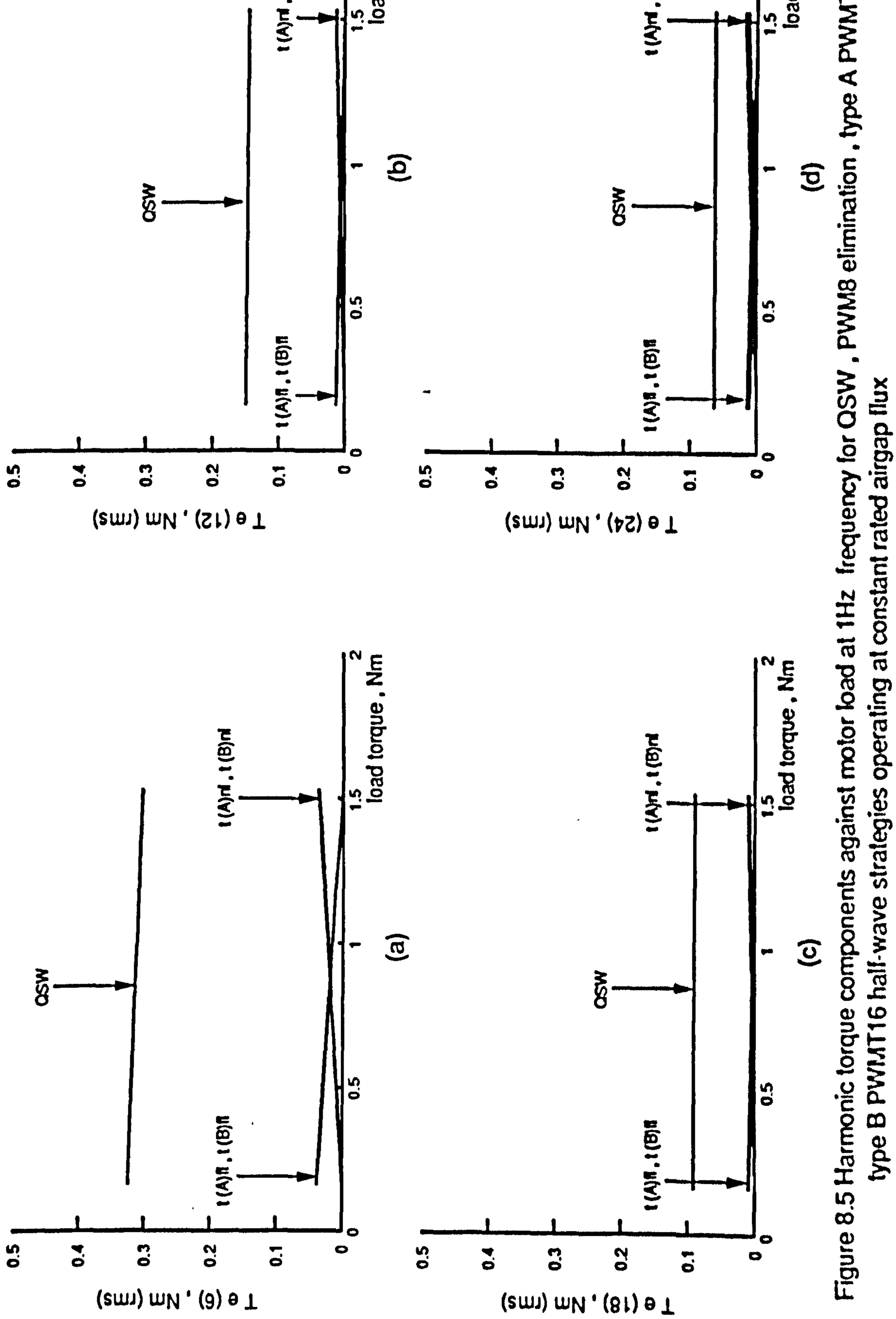

Figure 8.5 Harmonic torque components against motor load at 1 Hz frequency for QSW , PWM8 elimination , type A PWMT8 and type B PWMT16 half-wave strategies operating at constant rated airgap flux

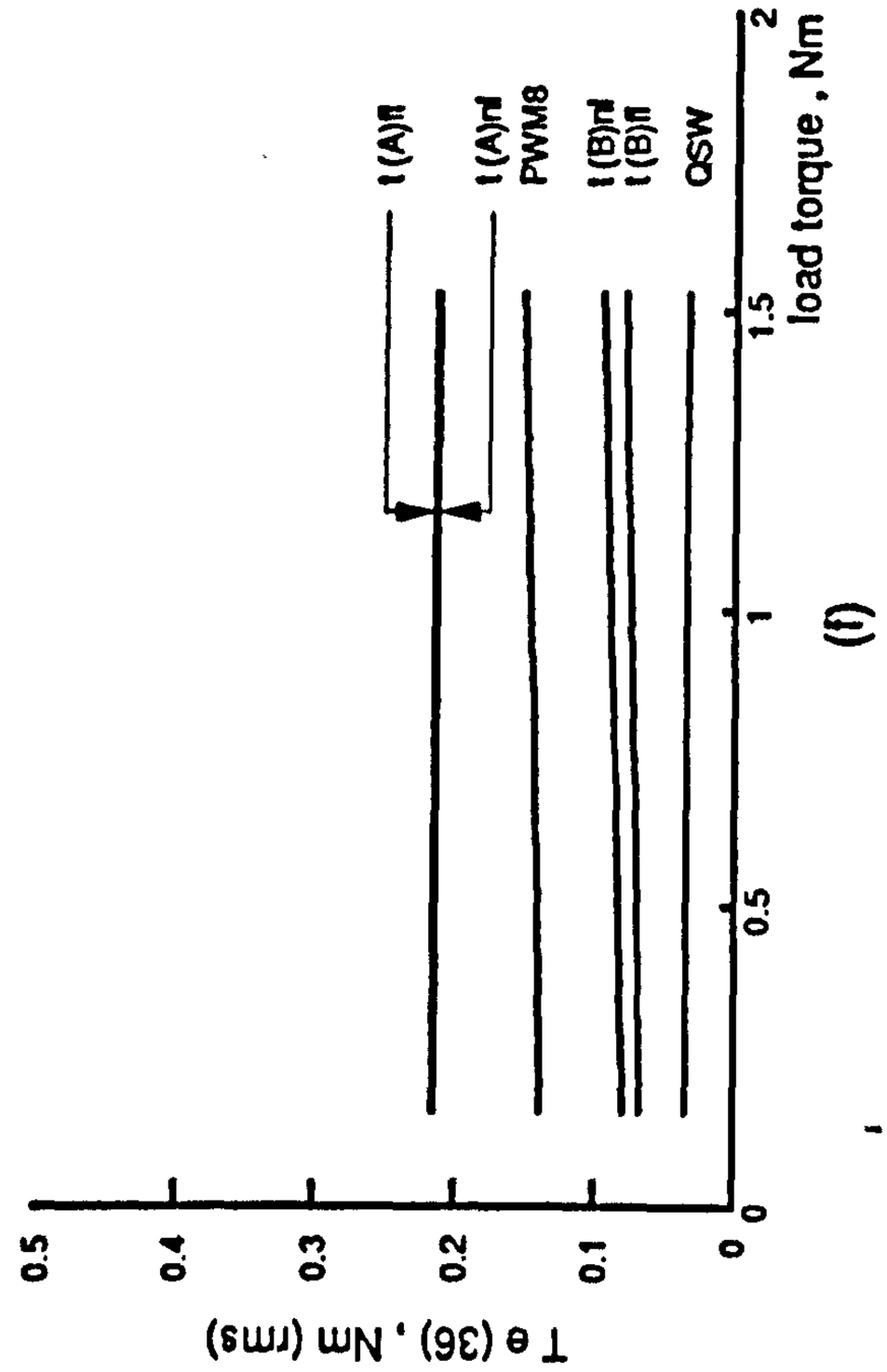

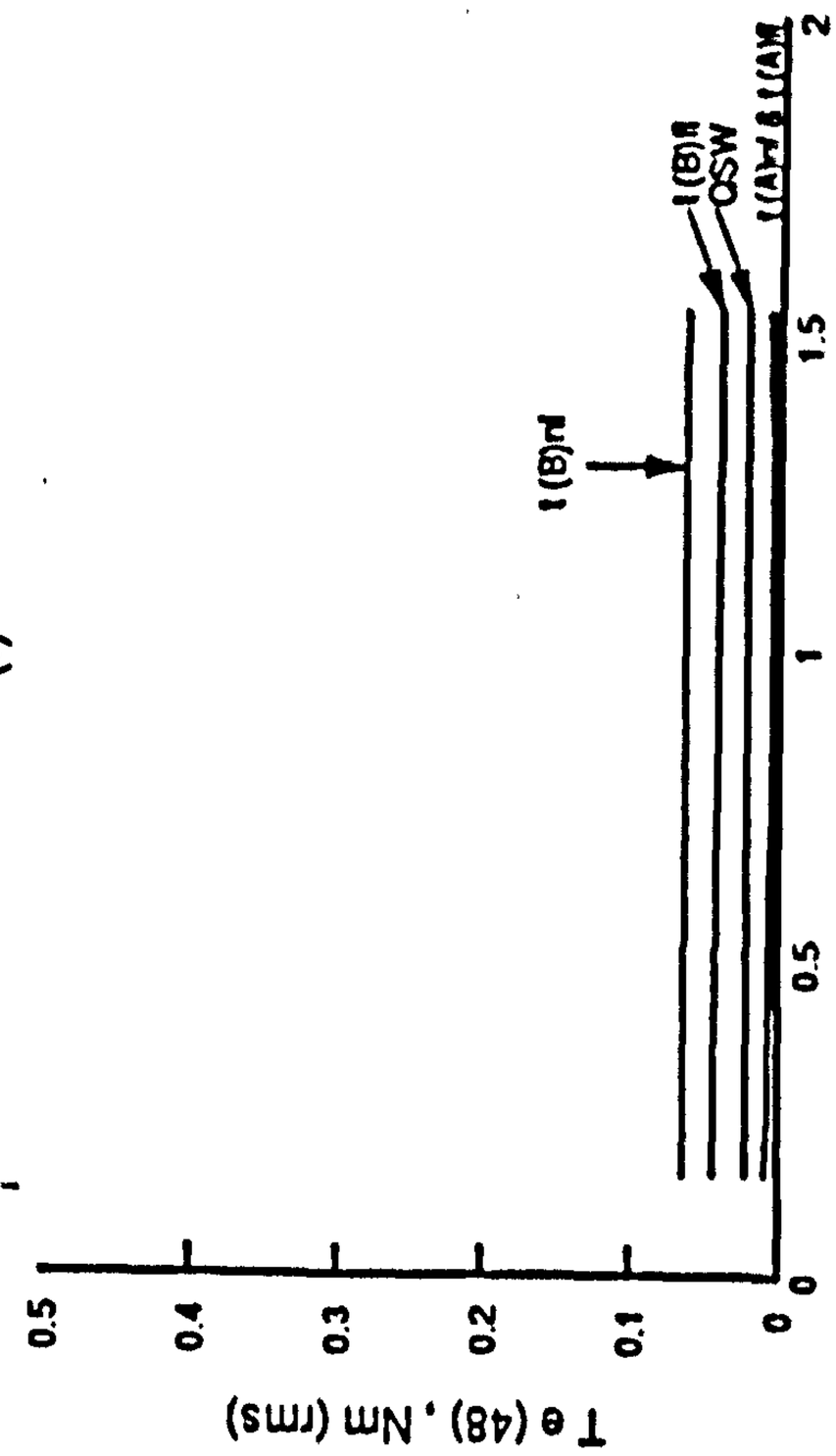

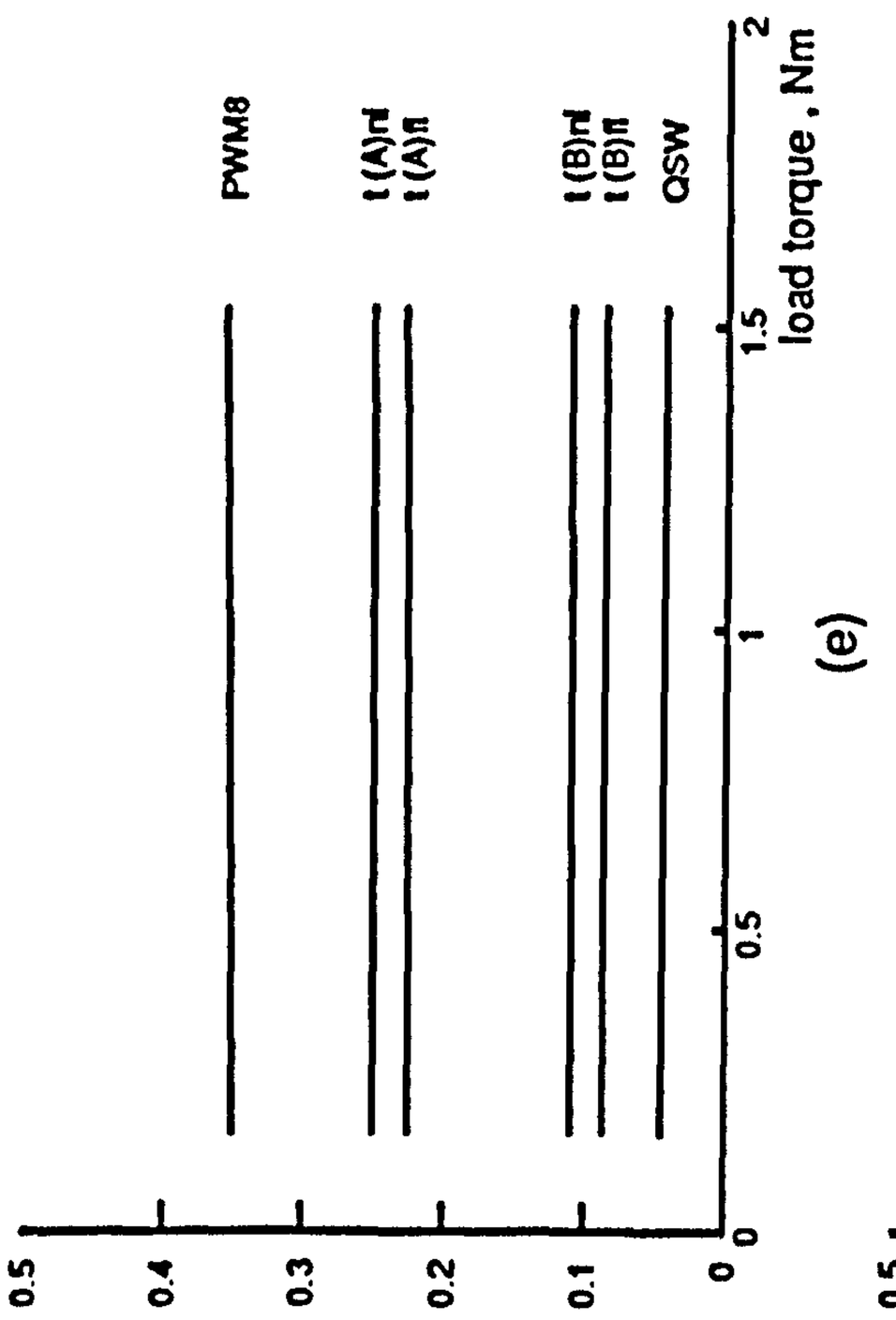

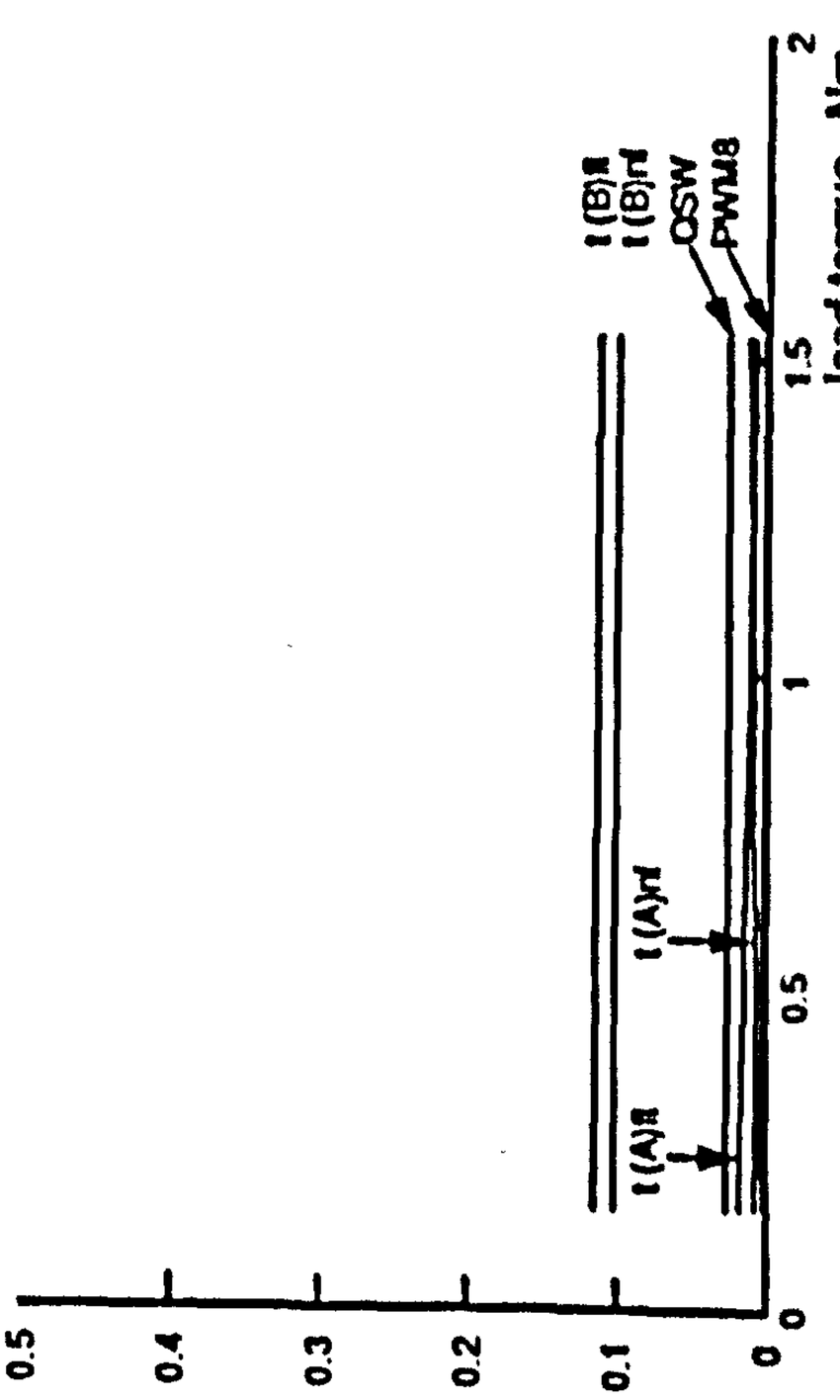

Figure 8.5 Continued

A similar comparison for the 36th-harmonic component also shows an increase for all PWM strategies when compared with the QSW mode. Type A shows the highest increase, followed by the elimination strategy, with the type B strategy showing the smallest increase. The 42nd and 48th-harmonic components are shown in figures 8.5(g) and (h) respectively. Generally speaking, these higher order components may produce dangerous stresses if their magnitudes are significant and their frequencies are close to the resonant frequency of the rotating system.

Figures 8.6(a) and (b) show the variation of the peak-to-peak torque pulsations on load and on no-load, as obtained from the frequency-domain and the direct-phase models. Despite small discrepancies both models show that, relative to the QSW mode, all other modes have higher torque pulsations. However, the direct-phase model results of figure 8.6(b) show the elimination PWM8 mode to have the highest increase of 44.5%, while the traces for no-load and on-load normalised half-wave symmetrical strategies show respectively increases of 35% and 28% for the type A strategy but only 21% and 16% for the type B strategy.

8.1.1.2 Effect on Harmonic Current Distortion Factor

As a direct result of the optimization process in controlling, rather than eliminating, particular low order harmonics, the half-wave symmetrical strategy achieved a uniform distribution of current harmonics with reduced magnitudes. Figures 8.7(a) and (b) present comparisons of the harmonic current distortion factor *THD* against load condition at 1Hz operation, for the operating modes of the previous section, as obtained from the frequency-domain and direct-phase models respectively. Figure 8.7(b) shows that, relative to the QSW mode, the harmonic current distortion is increased by approximately 18.5% for the elimination PWM8 mode, while for the type A strategy normalised at no-load and on-load, the

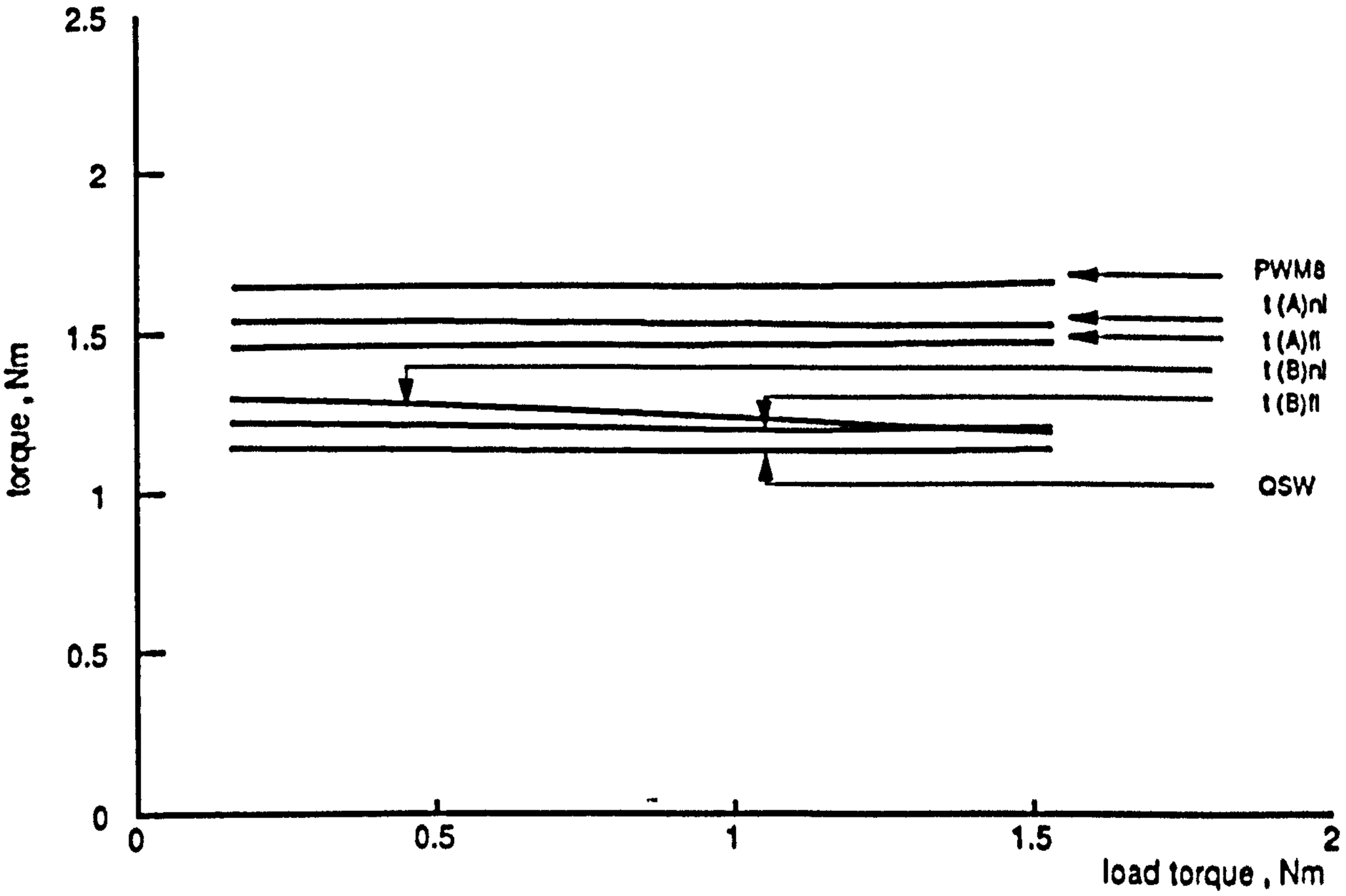

(a)

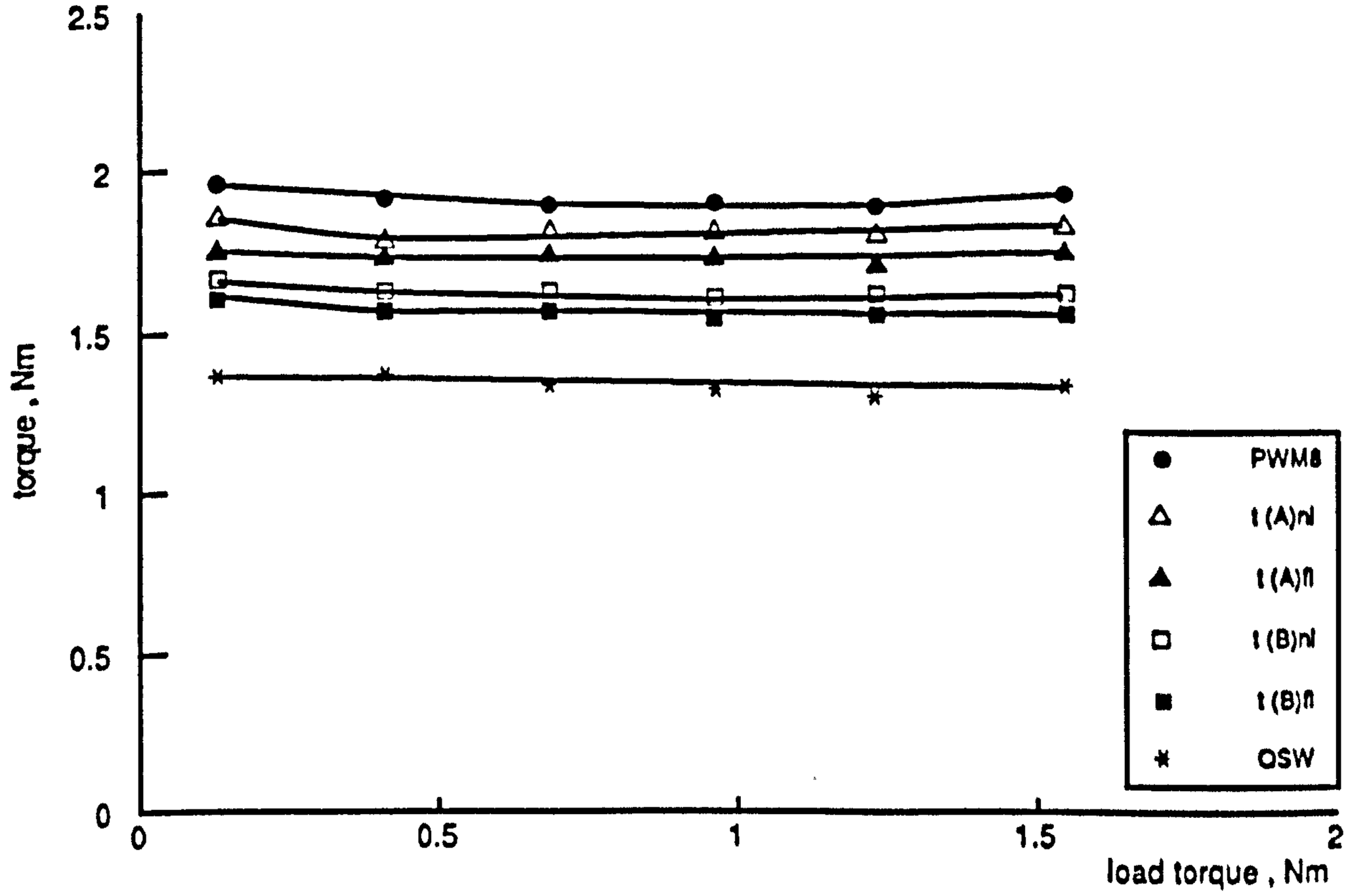

(b)

Figure 8.6 Peak-to-peak torque pulsation against load at 1Hz frequency for QSW , PWM8 elimination , type A PWMT8 and type B PWMT16 half-wave strategy operating at constant rated airgap flux condition
(a) Frequency-domain model (b) Direct-phase model

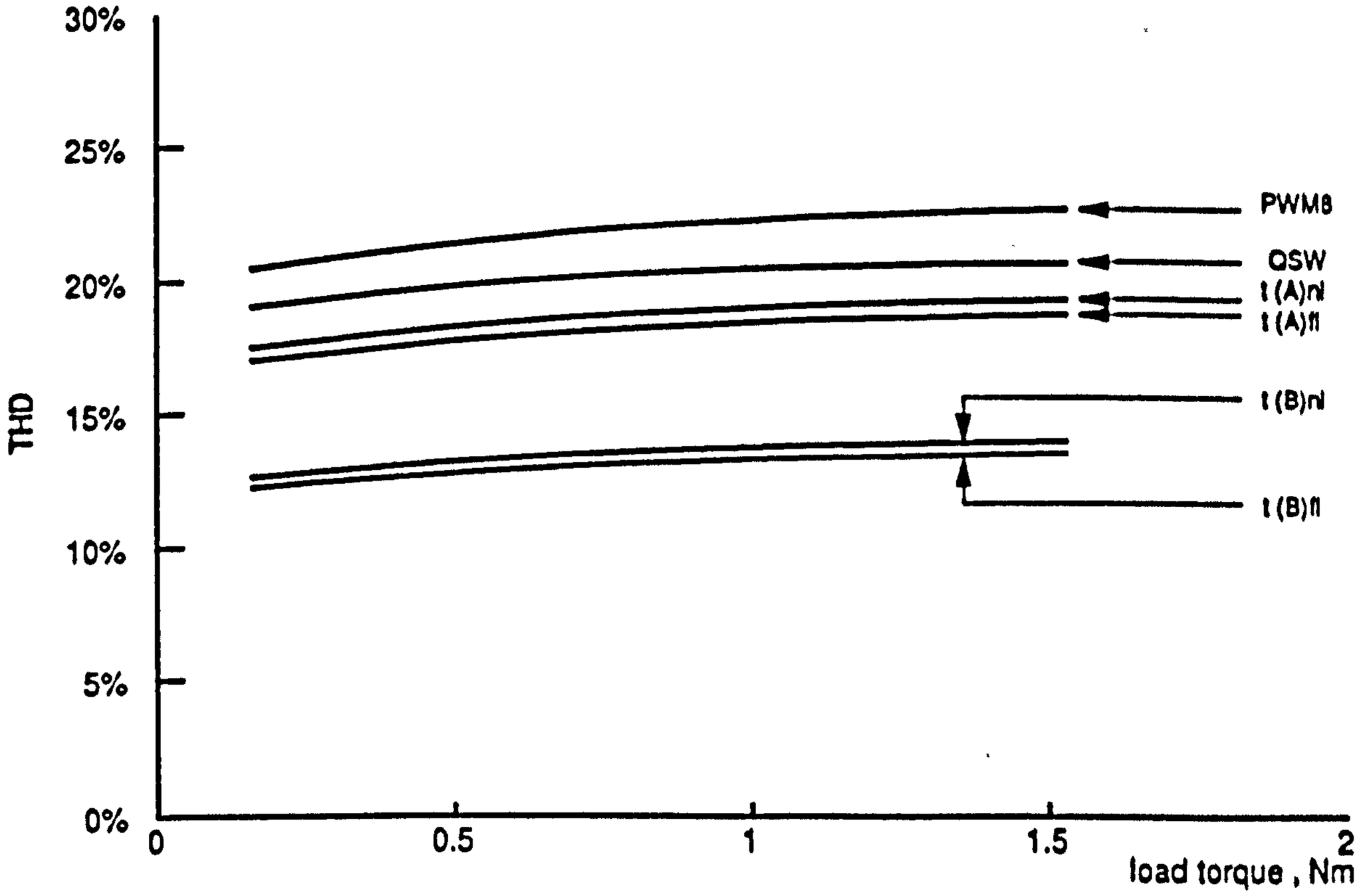

(a)

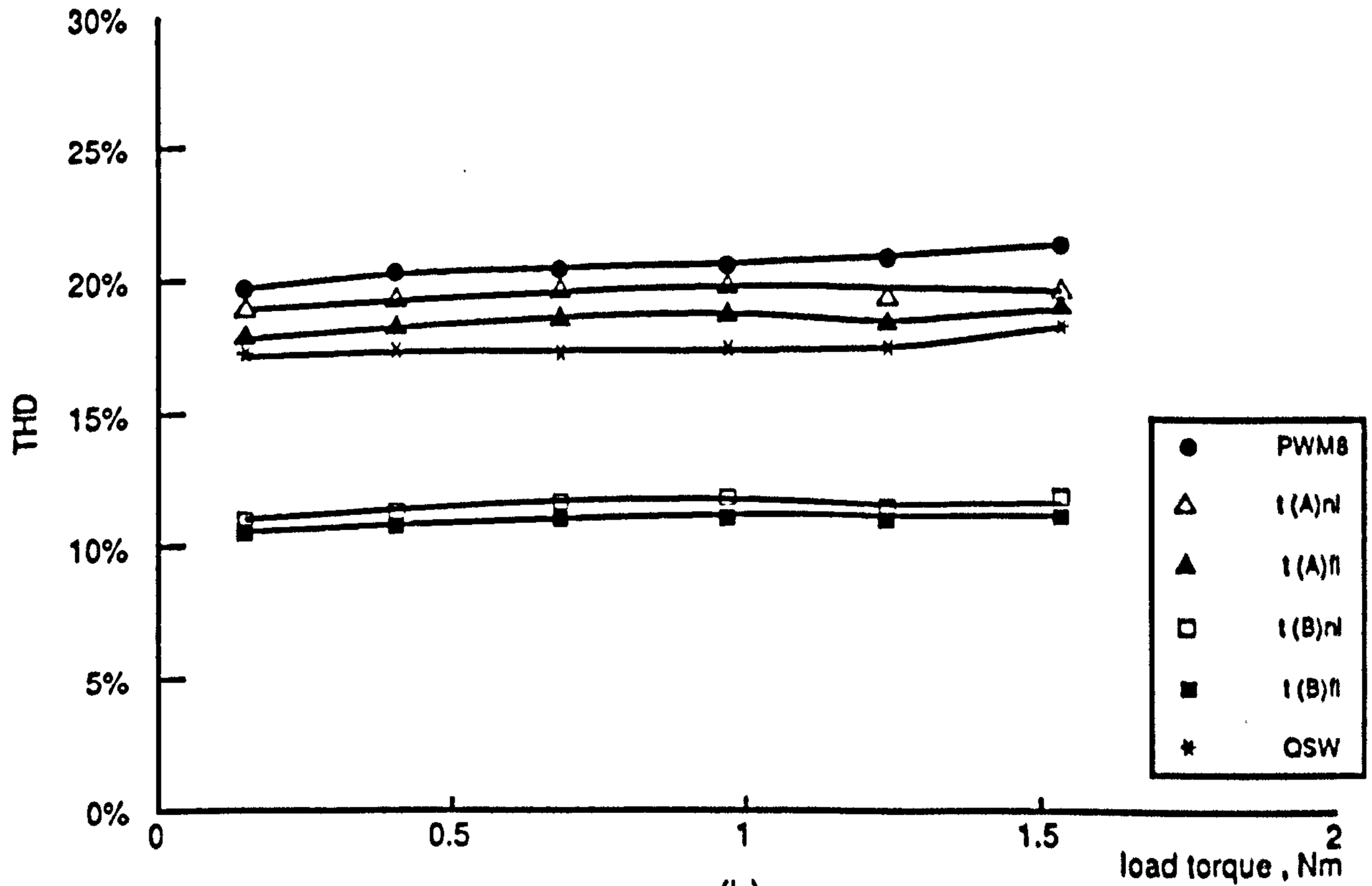

(b)

Figure 8.7 Harmonic distortion factor against load at 1Hz frequency for QSW , PWM8 elimination , type A PWMT8 and type B PWMT16 half-wave strategy operating at constant rated airgap flux condition
(a) Frequency-domain model (b) Direct-phase model

increases are respectively 5% and 10% . The type B strategy produces approximately similar magnitudes but with a 36.0% reduction compared with the QSW mode.

The conclusion is that, at this particular frequency, type A with nine pulses per half-cycle produces lower harmonic distortion than the elimination strategy with seventeen pulses, while type B with seventeen pulses reduces the harmonic distortion to below that of the QSW mode. The type B strategy consequently produces reduced harmonic copper losses, which is particularly important at low frequency where reduced cooling aggravates the heating problems.

8.1.1.3 Effect on Speed Ripple and Positional Error

The QSW mode represents the worst operating mode in terms of both speed ripple and positional error, especially at low operating frequencies. It is not however included in the comparisons of figure 8.8 as this would increase the vertical scale unnecessarily and make the comparison between the other strategies unclear.

Although the conventional elimination PWM strategy reduces the effect of harmonic torque components, it has been demonstrated that elimination of specific low order components is accompanied by an increase in the remaining high order ones. These are however increasingly attenuated as their order increases, resulting in a reduced speed ripple and positional error as the pulse-number is increased. However, due to the improved harmonic distribution of the remaining torque components, the new strategies produce lower speed ripple than does the elimination strategy.

Figure 8.8 shows that, compared with the PWM8 elimination mode, both strategies provide a reduced speed ripple and are most effective near their normalisation point. The direct-phase model results of figure 8.8(b) illustrates that the most significant reduction is achieved by the type B strategy.

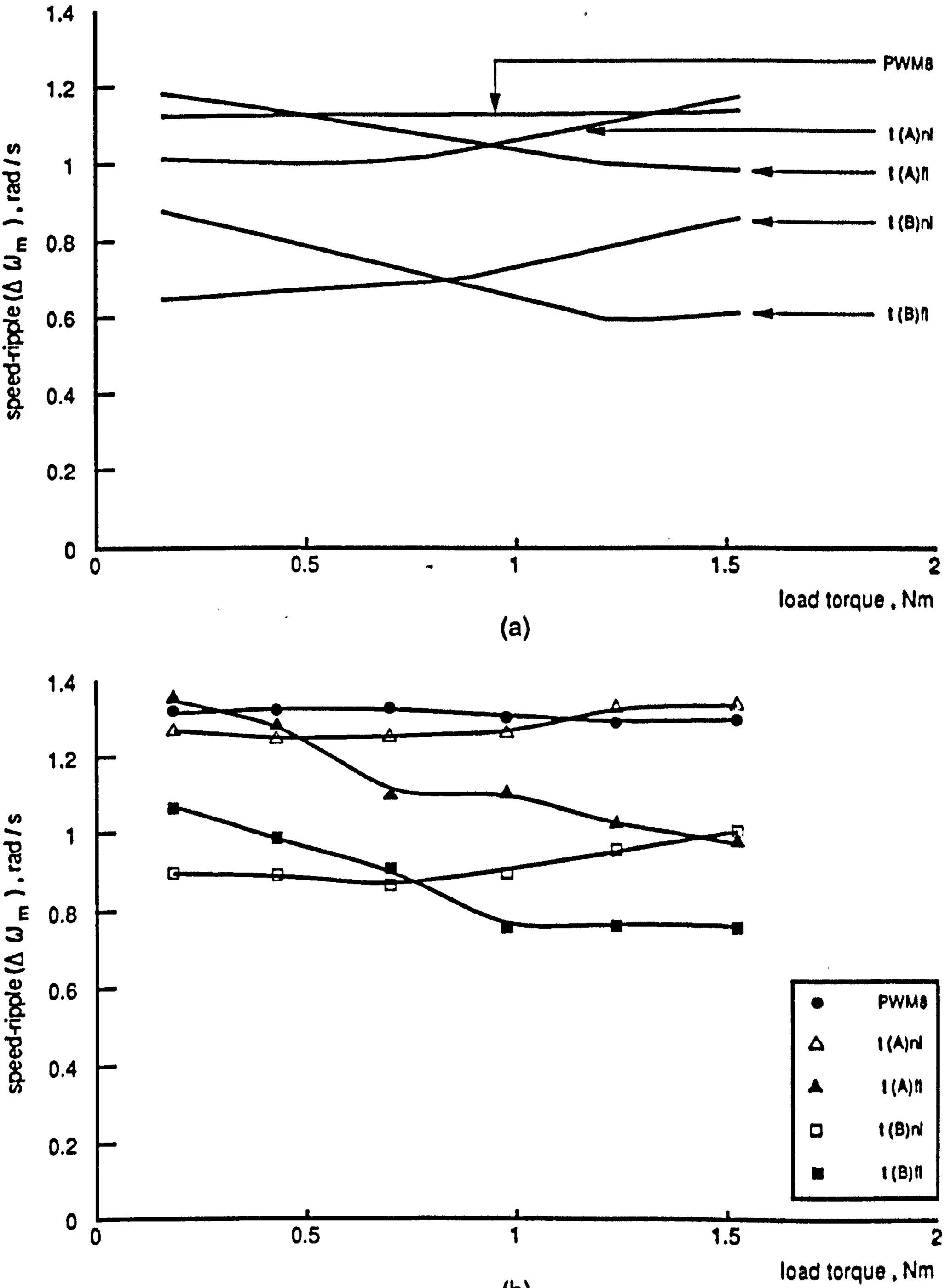

Figure 8.8 Peak-to-peak speed ripple against load at 1Hz frequency for PWM8 elimination , type A PWMT8 and type B PWMT16 half-wave strategy operating at constant rated airgap flux condition
(a) Frequency-domain model (b) Direct-phase model

For example, the type B strategy normalised at no-load produced 30% less speed ripple at no-load and 19.5% less at 1.5Nm than does the elimination strategy. When normalised at 1.5Nm, the corresponding reductions are 23% and 42%.

Figure 8.9(b) shows that the reduction in speed ripple does not necessarily imply a reduction in the positional error, since an appreciable deviation in the rotor speed from its average value will have little effect on either the rotor position or the smoothness of the rotor motion if it persists only for a comparatively short time. Alternatively, should the deviation of rotor speed be sufficient to appreciably deflect the rotor position from its linear variation with time, the effect on the rotor motion will become quite noticeable.

Figures 8.10 and 8.11 respectively show the electromagnetic torque, speed ripple and positional error waveforms for the type B strategy normalised at no-load, and the PWM8 elimination strategy, both with seventeen pulses per half-cycle. As illustrated in figure 8.8(b), the type B strategy produces a 23% reduction in speed ripple at 1.5Nm load compared with the elimination strategy. The net area enclosed by the speed ripple waveform between points a and b of figure 8.10(b) is large, and the corresponding large change in rotor position results in a positional error waveform with a predominant 6th-harmonic component. In contrast, figure 8.11 shows the effect of the elimination strategy with the same number of pulses and a higher speed ripple. The net area enclosed by the speed ripple waveform between points a and b is now small and the positional error is also small. From these results, it follows that the positional error is a more appropriate optimal performance criterion than speed ripple when assessing the quality of the rotor motion.

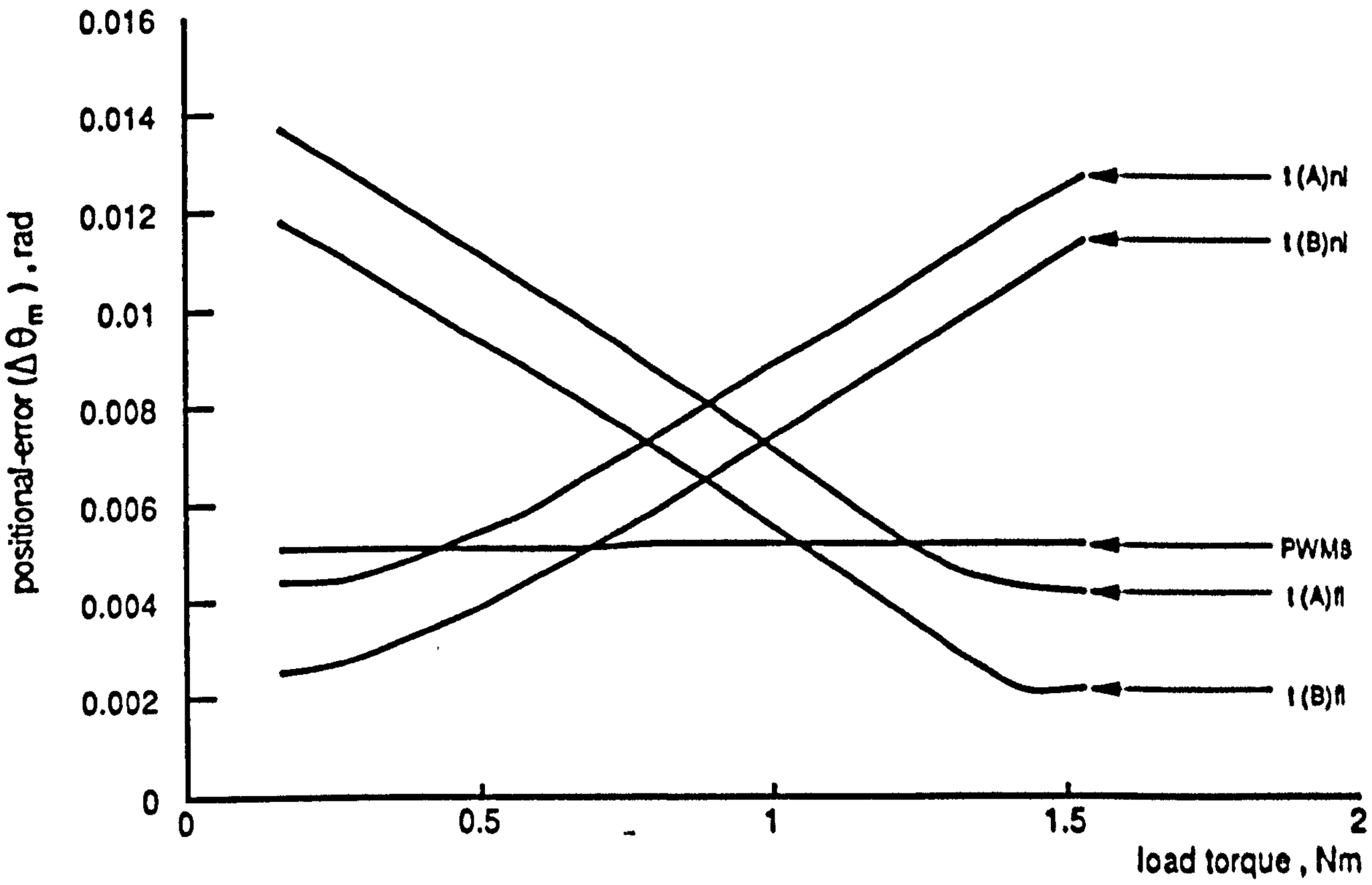

(a)

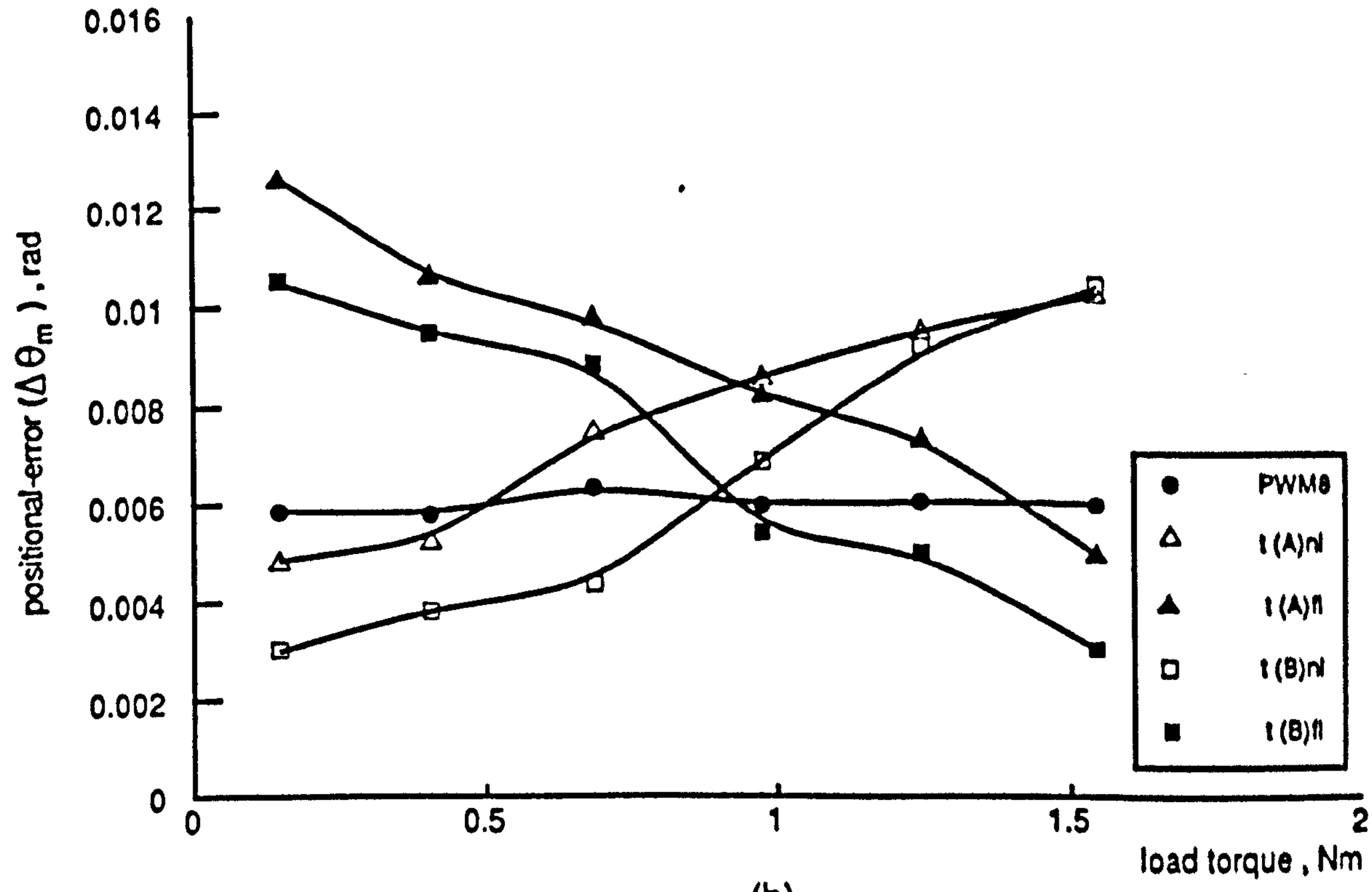

(b)

Figure 8.9 Peak-to-peak positional-error against load at 1Hz frequency for PWM8 elimination , type A PWMT8 and type B PWMT16 half-wave strategy operating at constant rated airgap flux condition
(a) Frequency-domain model (b) Direct-phase model

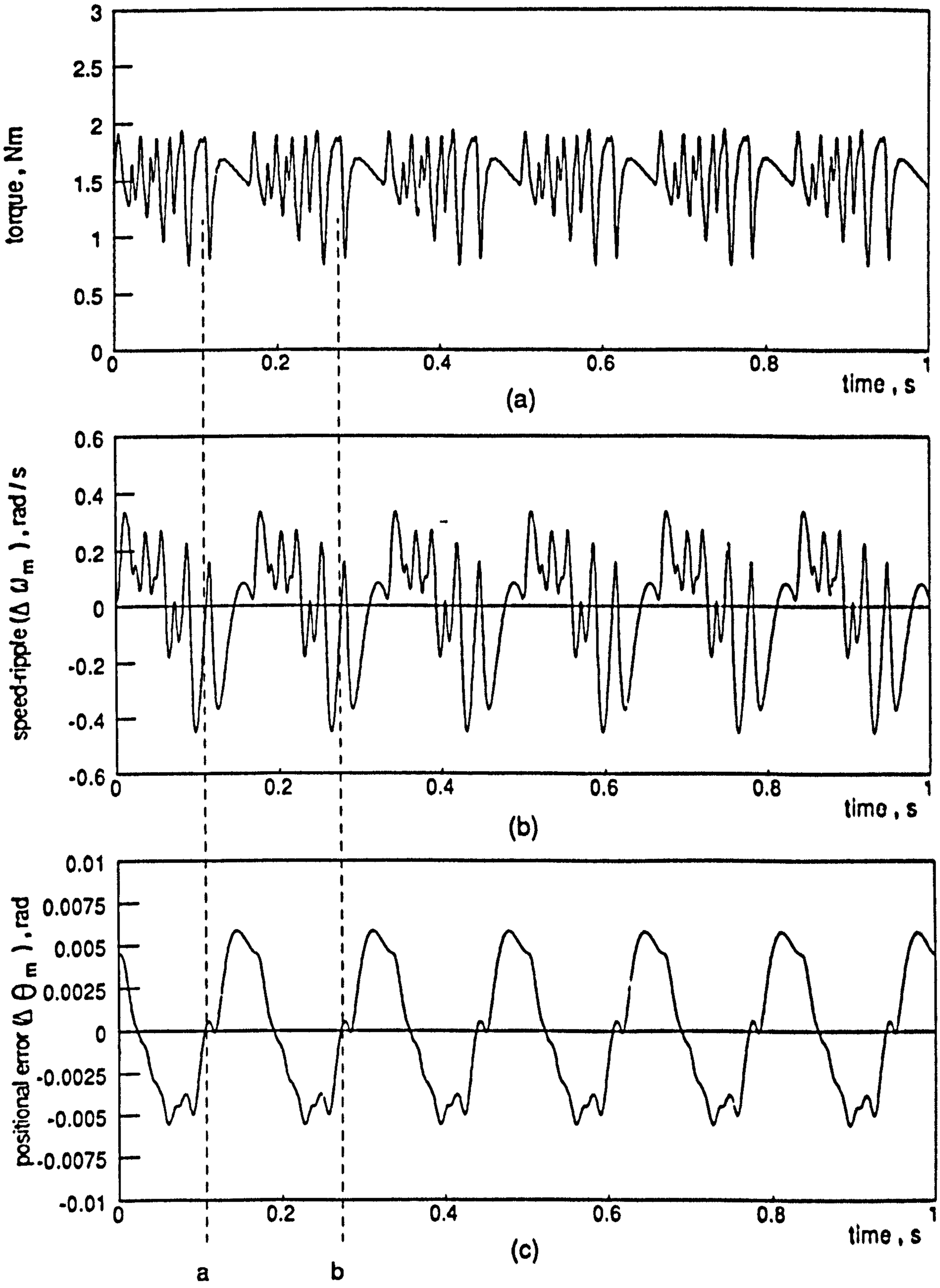

Figure 8.10 Motor dynamics with type B PWMT16 strategy at 1Hz , 1.5Nm load
(a) Electromagnetic torque
(b) Speed ripple
(c) Positional error

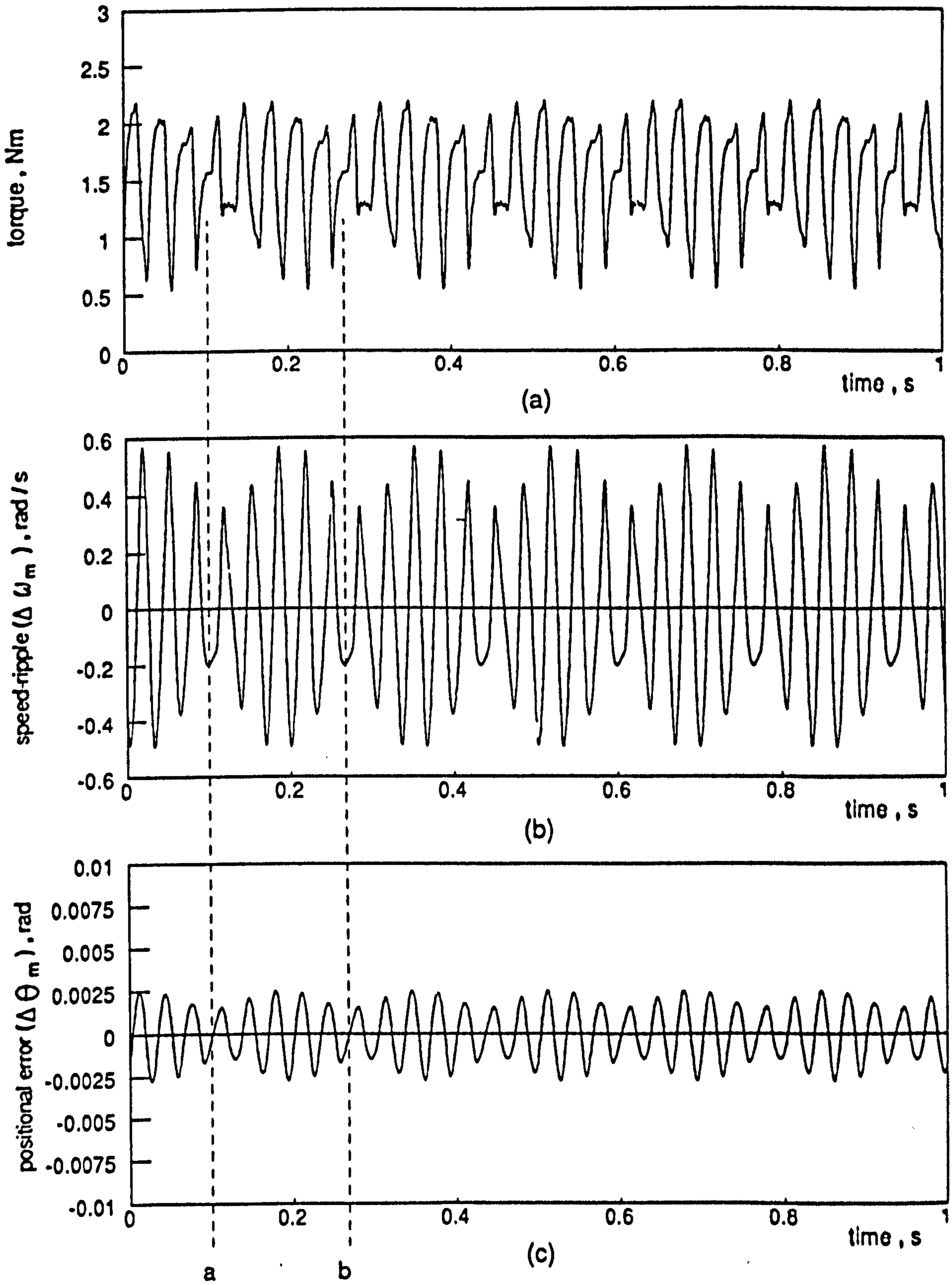

Figure 8.11 Motor dynamics with PWM8 elimination strategy at 1Hz , 1.5Nm load
(a) Electromagnetic torque
(b) Speed ripple
(c) Positional error

8.1.2 Computation of Switching Angles for Different Frequencies

At higher operating frequencies, the solution of the optimization problem becomes increasingly difficult as the pulse-number and load torque are increased. This difficulty is illustrated in figures 8.12(a) to (d), which show no-load and full-load normalised switching angle trajectories for type A half-wave symmetrical strategy as a function of the operating frequency. Figure 8.12(a) shows the trajectories for two switching angles per half-cycle to demonstrate a continuous response throughout the frequency range for no-load operation. On loading the machine, the problem of detecting local optimal solutions becomes more difficult and requires more iterations to converge as the frequency increases, until at 20Hz it become intractable. On searching the entire region from t_{min} to π for possible solutions, a step discontinuity was detected. A microprocessor implementation of this mode will require linearizing the switching angles characteristics up to the discontinuity, and to automatically re-adjust the subsequent linearization process. Figure 8.12(b) shows that, when the number of switching angles is increased to four, the solution becomes even more tedious, with the maximum frequency at which a solution was possible being decreased to 20Hz and 10Hz for no-load and full-load respectively. Figure 8.12(c) and (d) illustrates that for six and eight switching angles the maximum frequency at which a solution is achieved is respectively 7Hz and 5Hz for the same two conditions. Several problems may however jeopardise the optimization process, some of which are described below.

(1) Figure 7.1 demonstrated that, with a quarter-wave symmetrical strategy, harmonic torque components of the same order are approximately in antiphase as the operating frequency is increased. However, by constraining the optimization search of the PWM voltage pattern to half-wave symmetry, the switching angles produce a PWM pattern approaching quarter-wave symmetry, which contradicts the half-wave symmetry constraint.

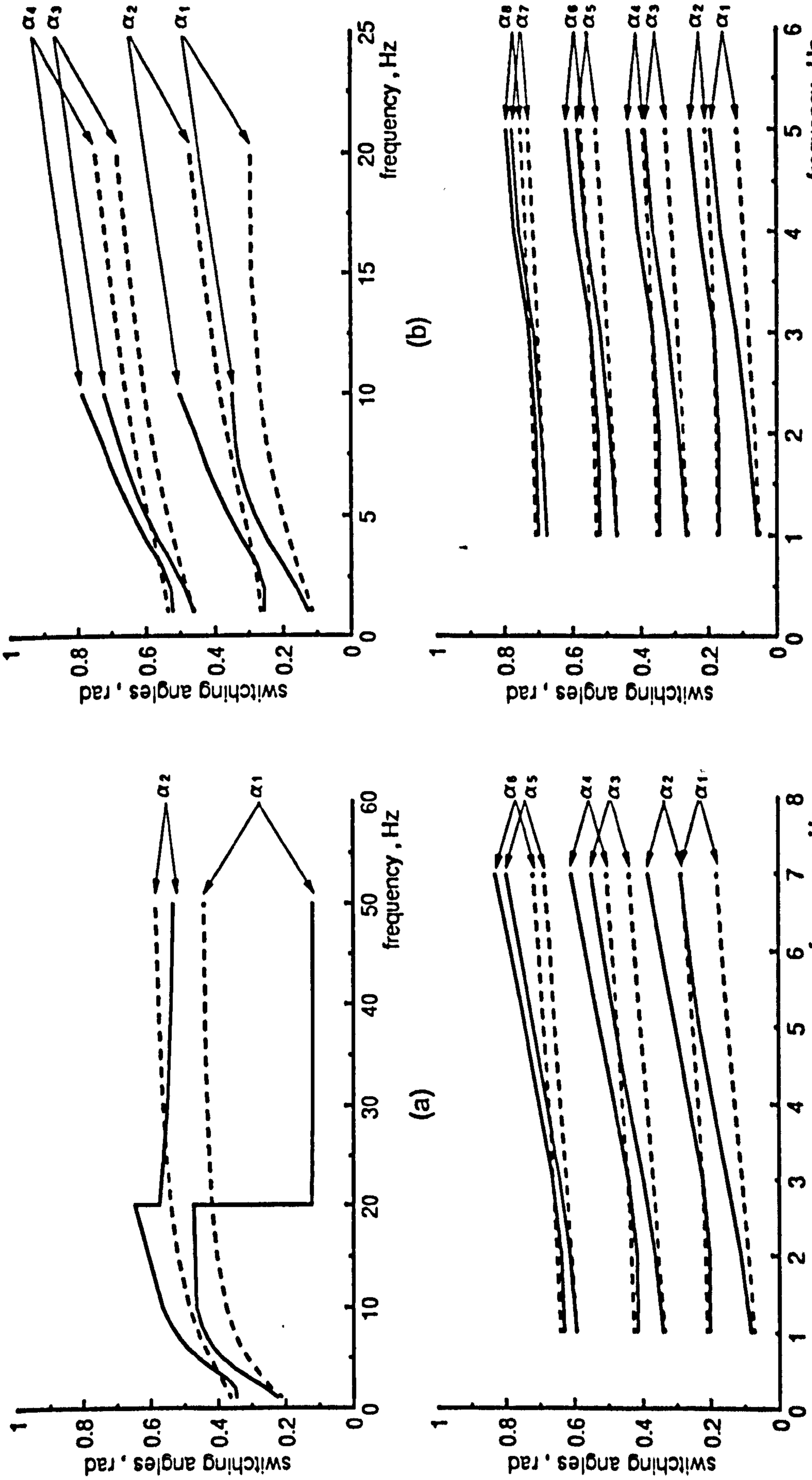

Figure 8.12 Variation of switching angles with frequency for type A half-wave strategy
(a) m = 2 (b) m = 4 (c) m = 6 (d) m = 8

(2) Figure 7.1 also illustrated that, when the machine is loaded, the above argument will start taking place at a lower operating frequency.
(3) A higher pulse-number involves more constraints for the optimization process to converge, and more variables (switching angles) have therefore to be determined.
(4) An optimization program which uses Lagrange multipliers [84] to perform the minimisation search may be inefficient for this particular problem. An alternative technique [85] employing the least-square method may be more efficient.

Figures 8.13(a) and (b) show respectively the trajectories for the type B strategy, with twelve and sixteen switching angles, normalised at no-load and full-load conditions for a frequency range of 1Hz to 5Hz. This range of low operating frequencies requires a high pulse-number, so that the elimination PWM8 mode producing seventeen pulses per half-cycle is used as a basis for comparison, together with the type B PWMT16 mode producing the same pulse-number and the type A PWMT8 mode which produces nine pulses per half-cycle. The QSW mode is excluded from the comparison of speed ripple and positional error for the reason outlined in section 8.1.1.3.

8.1.2.1 Effect on Harmonic Torque Components

Figure 8.14(a) to (d) shows computed variations of the harmonic torque components with operating frequency for the unloaded machine, obtained using the frequency-domain model. The figure demonstrates that, in all PWM modes, the 6th, 12th, 18th- and 24th-harmonic torque components are either eliminated or cancelled. Relative to the QSW mode, the 30th- and 36th-harmonic components are increased significantly by the elimination strategy, particularly at low frequencies. However, relative to the elimination strategy, the type A strategy mode produces lower 30th- and higher 36th-components, while the type B strategy mode demonstrates a significant reduction in both components especially at low frequencies.

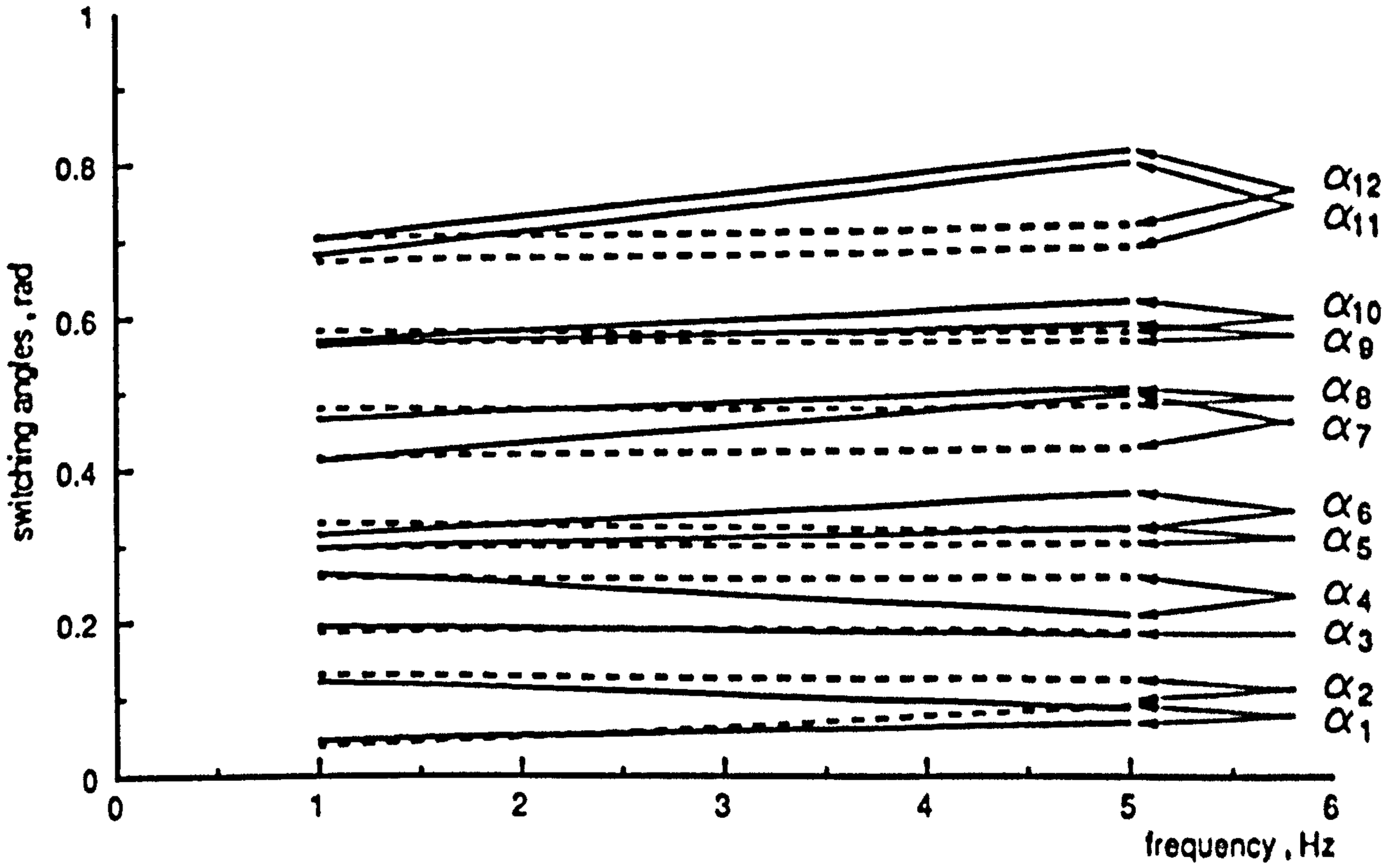

(a)

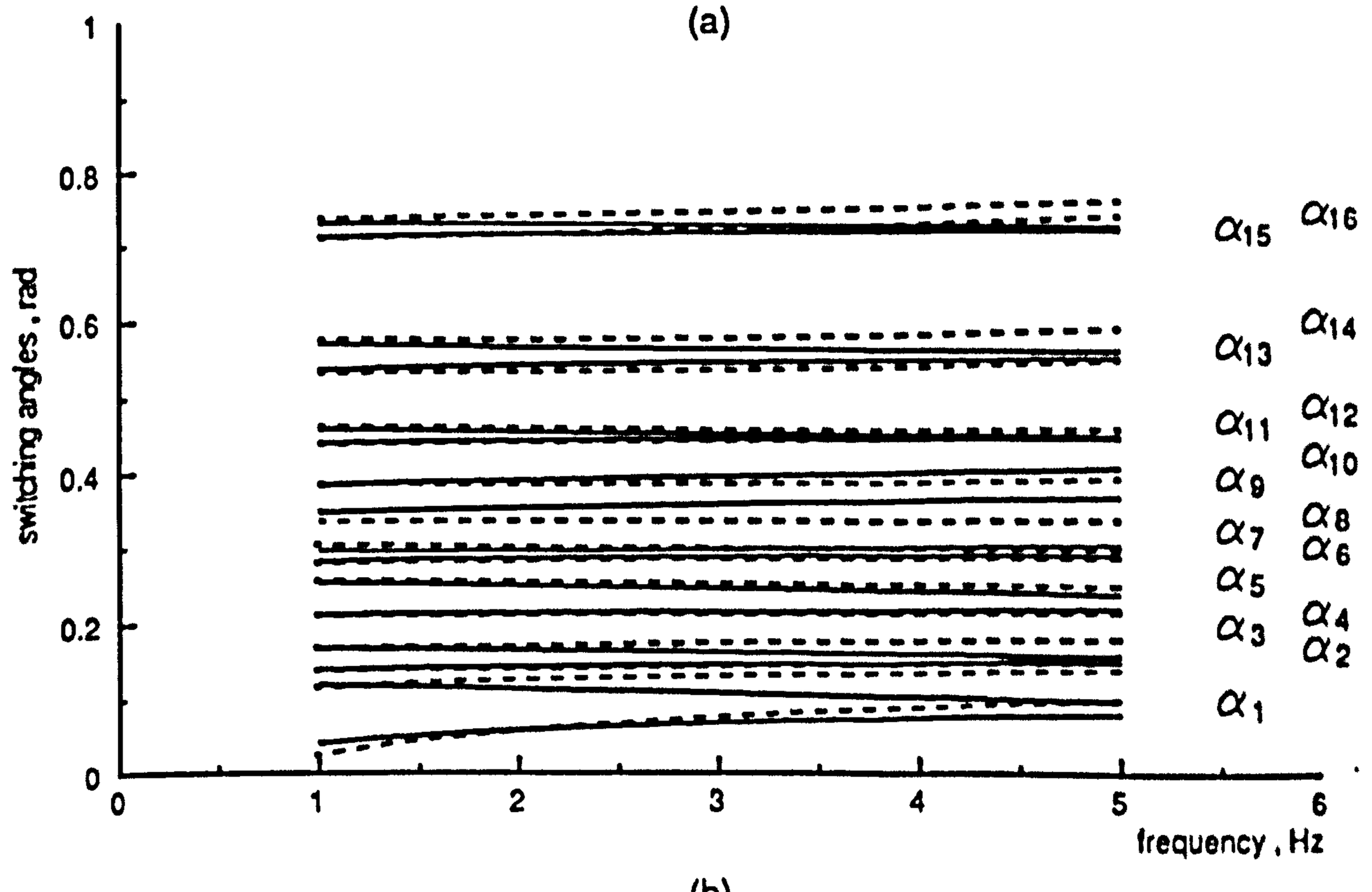

(b)

No-load ------ Full-load ——————

Figure 8.13 Variation of switching angles with frequency for :
(a) Type B PWMT12 mode half-wave strategy
(b) Type B PWMT16 mode half-wave strategy

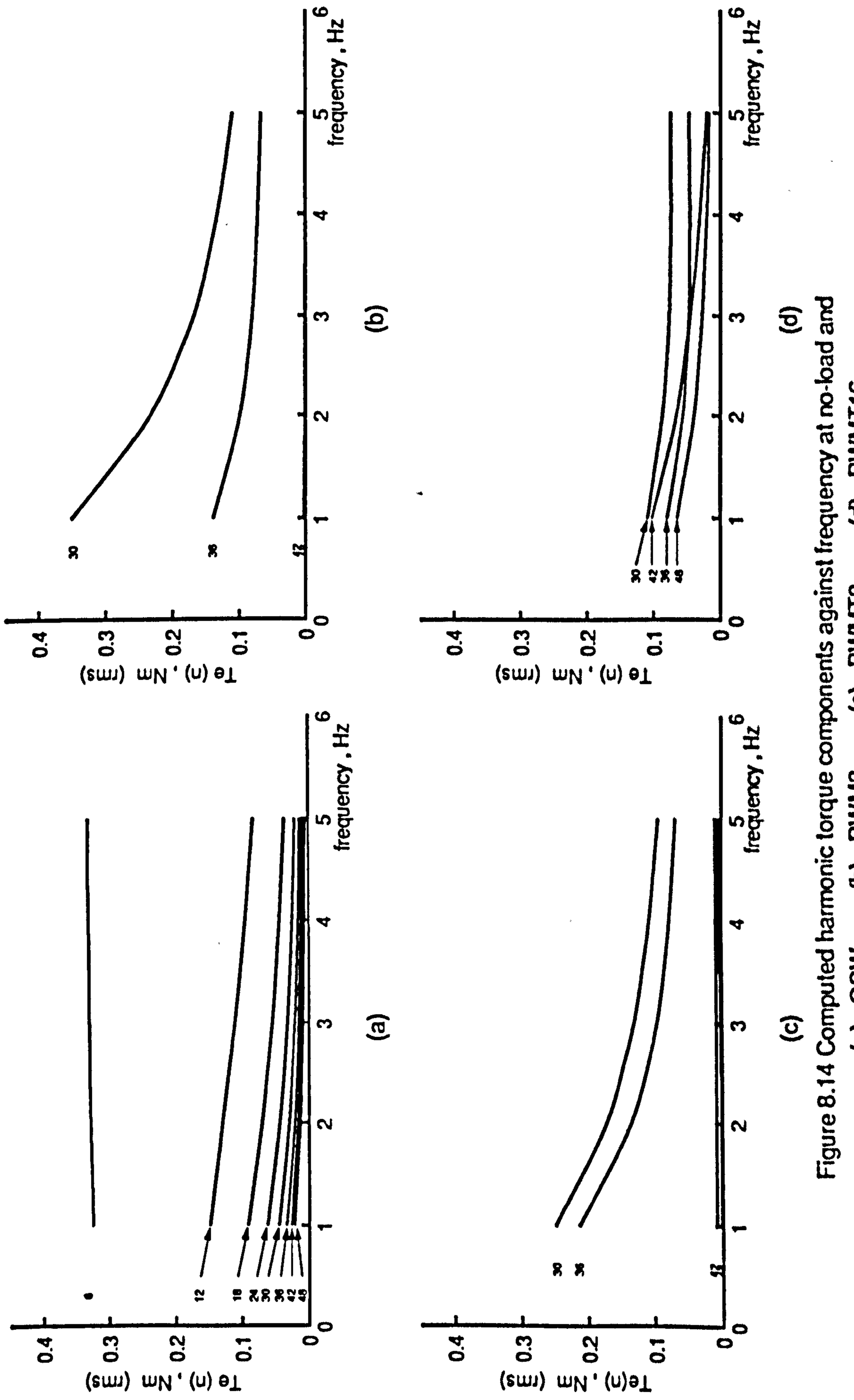

Figure 8.14 Computed harmonic torque components against frequency at no-load and
(a) QSW (b) PWM8 (c) PWMT8 (d) PWMT16

The 42nd- and 48th-harmonic components are insignificant in the elimination and type A modes, although they are slightly increased in type B.

Figure 8.15(a) to (d) shows results for full-load conditions. The above comments on harmonic behaviour apply again, with the type B strategy having a better distribution of the remaining high order harmonics than the other PWM modes.

Figures 8.16(a) and (b) compare respectively computed no-load and full-load torque pulsations over a 5Hz frequency range, obtained using the direct-phase model. For no-load operation, figure 8.16(a) shows that, although the type A PWMT8 mode has fewer pulses per half-cycle, it produces lower torque pulsations than the elimination mode. The type B PWMT16 mode with the same pulse-number however produces even lower pulsations. At 1Hz frequency, all PWM patterns produce higher torque pulsations than the QSW mode. This is due mainly to the increased magnitudes of the remaining high order harmonics for the PWM strategies compared with the QSW mode illustrated earlier in figure 8.5(e) to (h). However, as the frequency increases, types A and B strategies both produce lower pulsations than QSW operation at lower frequencies than the elimination strategy, due to the improved distribution of the high order harmonics remaining.

The better behaviour of the type A and B strategies is more significant when the machine is fully-loaded, as demonstrated in figure 8.16(b). This shows that, at 1Hz operation, both types produce torque pulsations higher than the QSW mode and lower than the elimination PWM8 mode. The torque pulsations for the PWM8 mode continue to be greater than the QSW mode up to 4Hz frequency. However, types A and B traces cross the QSW trace prior to 2Hz and maintain lower trends thereafter.

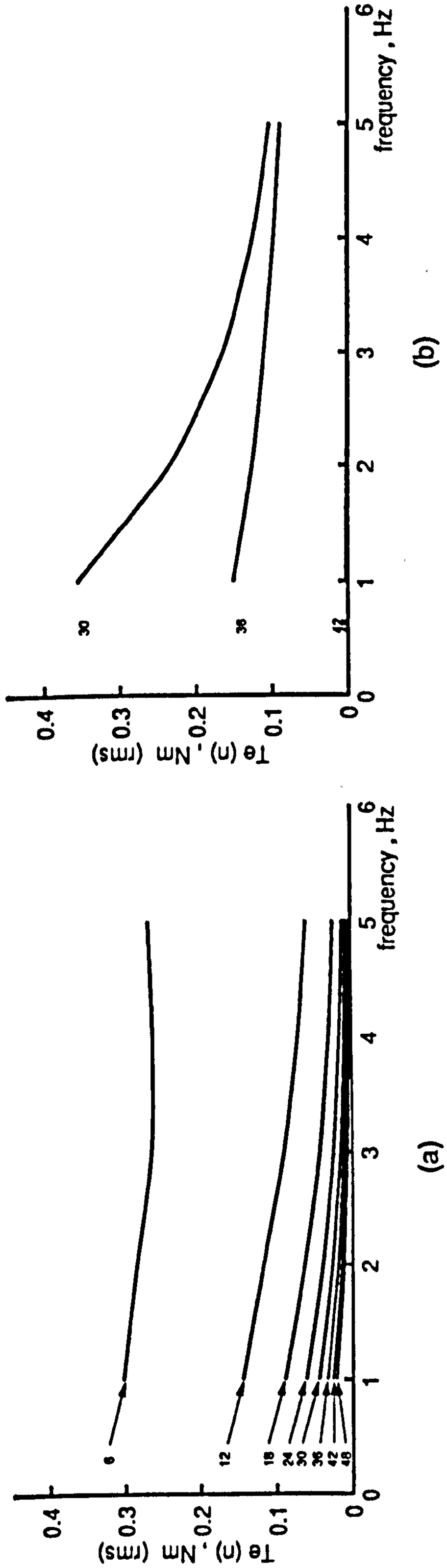

Figure 8.15 Computed harmonic torque components against frequency at full-load and

(a) QSW (b) PWM8 (c) PWMT8 (d) PWMT16

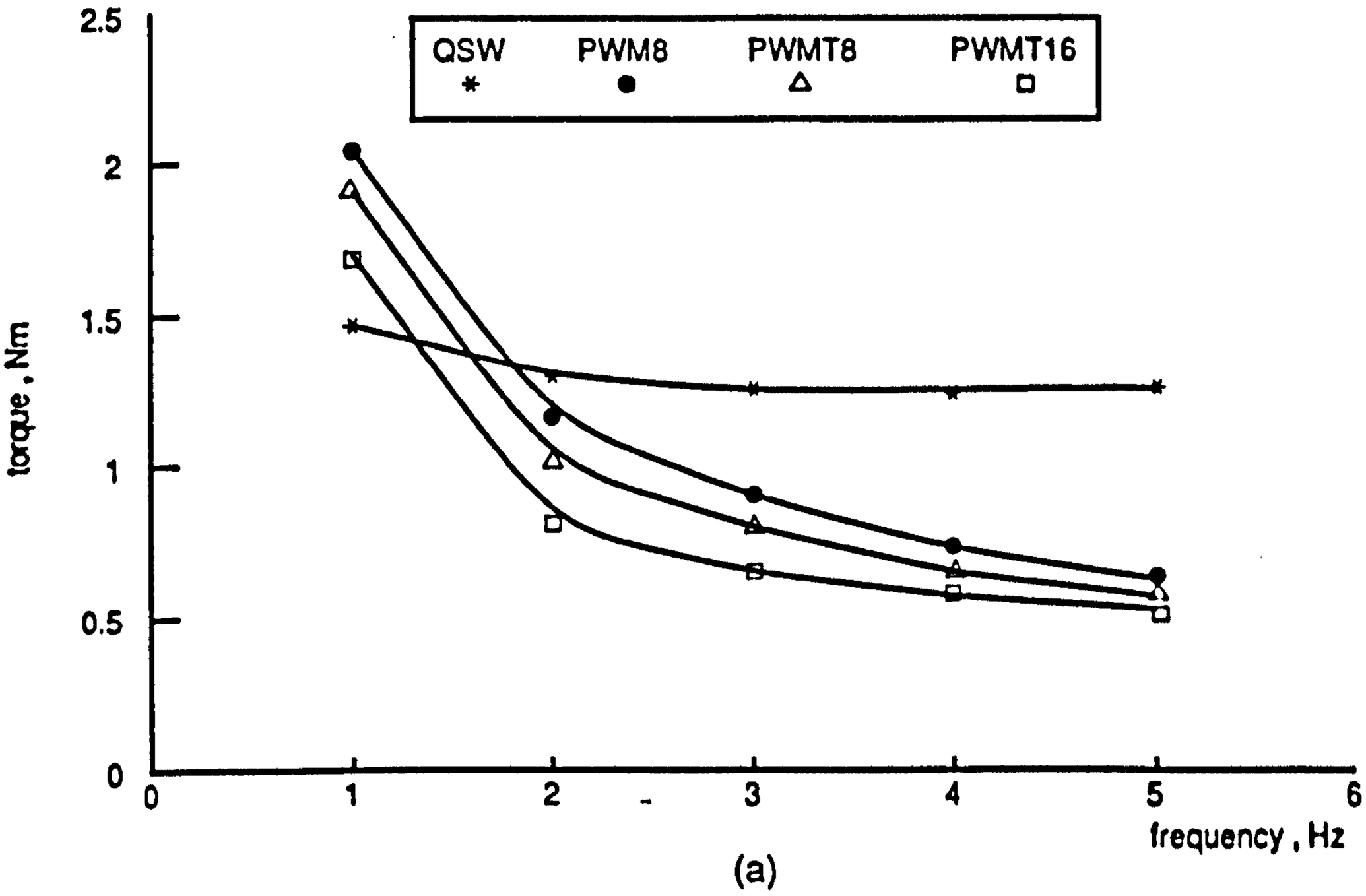

(a)

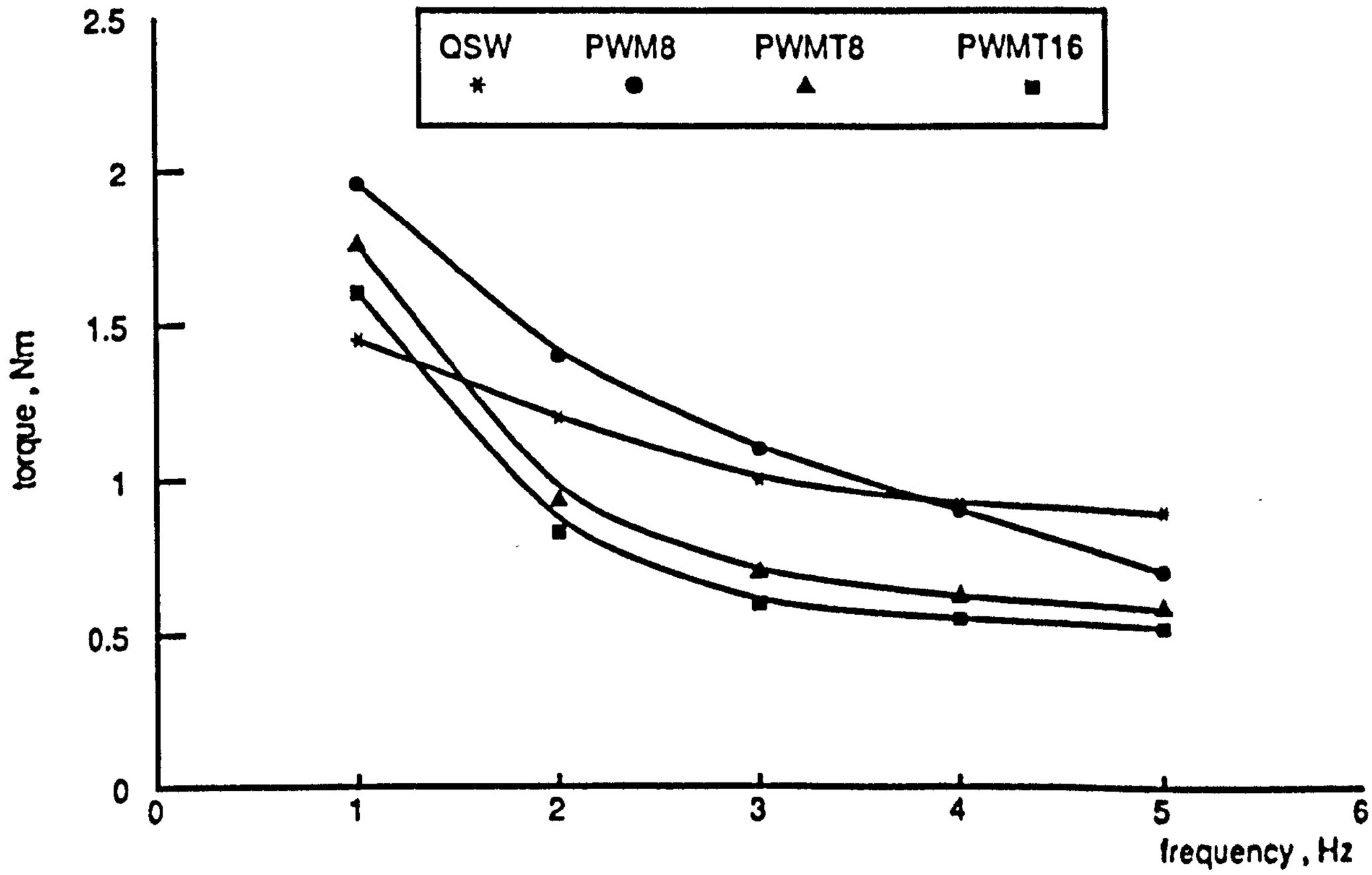

(b)

Figure 8.16 Computed peak-to-peak torque pulsation against operating frequency using the direct-phase model for QSW , PWM8 elimination , type A PWMT8 and type B PWMT16 half-wave strategies
(a) No-load (b) Full-load

8.1.2.2 Effect on Harmonic Current Distortion Factor

Figures 8.17(a) and (b) respectively compare the QSW and PWM modes in terms of the harmonic distortion factor, as a measure of the machine harmonic losses over the frequency range 1Hz to 5Hz for no-load and full-load conditions. Evidently, the type B PWMT16 mode is better than the elimination PWM8 mode below 4Hz, while the type A PWMT8 mode is better up to 2.5Hz. However, as the frequency increases, the elimination PWM8 mode benefits from the increased attenuation of the remaining high order harmonic components which results in a distortion factor lower than that with both developed strategies. In terms of the machine harmonic losses, the developed half-wave symmetrical strategies are clearly best suited for low frequency operation.

8.1.2.3 Effect on Speed Ripple and Positional Error

Figures 8.18(a) and (b) present the variation of speed ripple with frequency for no-load and full-load conditions, and figures 8.19(a) and (b) the positional error for the same conditions. The elimination PWM8 mode, type A PWMT8 and type B PWMT16 modes are included in the comparison. The QSW mode is excluded since it produces inferior results to those produced by any PWM operating mode, as demonstrated in chapter 5. Both figures demonstrate that the half-wave symmetrical strategies produce lower speed ripple and positional error than the elimination PWM8 mode. The advantageous of these strategies becomes increasingly significant as the operating frequency is reduced.

8.2 Quarter-Wave Symmetrical Strategy

The viable range of frequency for this strategy depends on the fact that, at high frequency, the harmonic torque components of the same order are approximately in antiphase. In addition, the half-wave symmetrical strategy of section 8.1 produces a superior performance between 1Hz and 5Hz operation. All

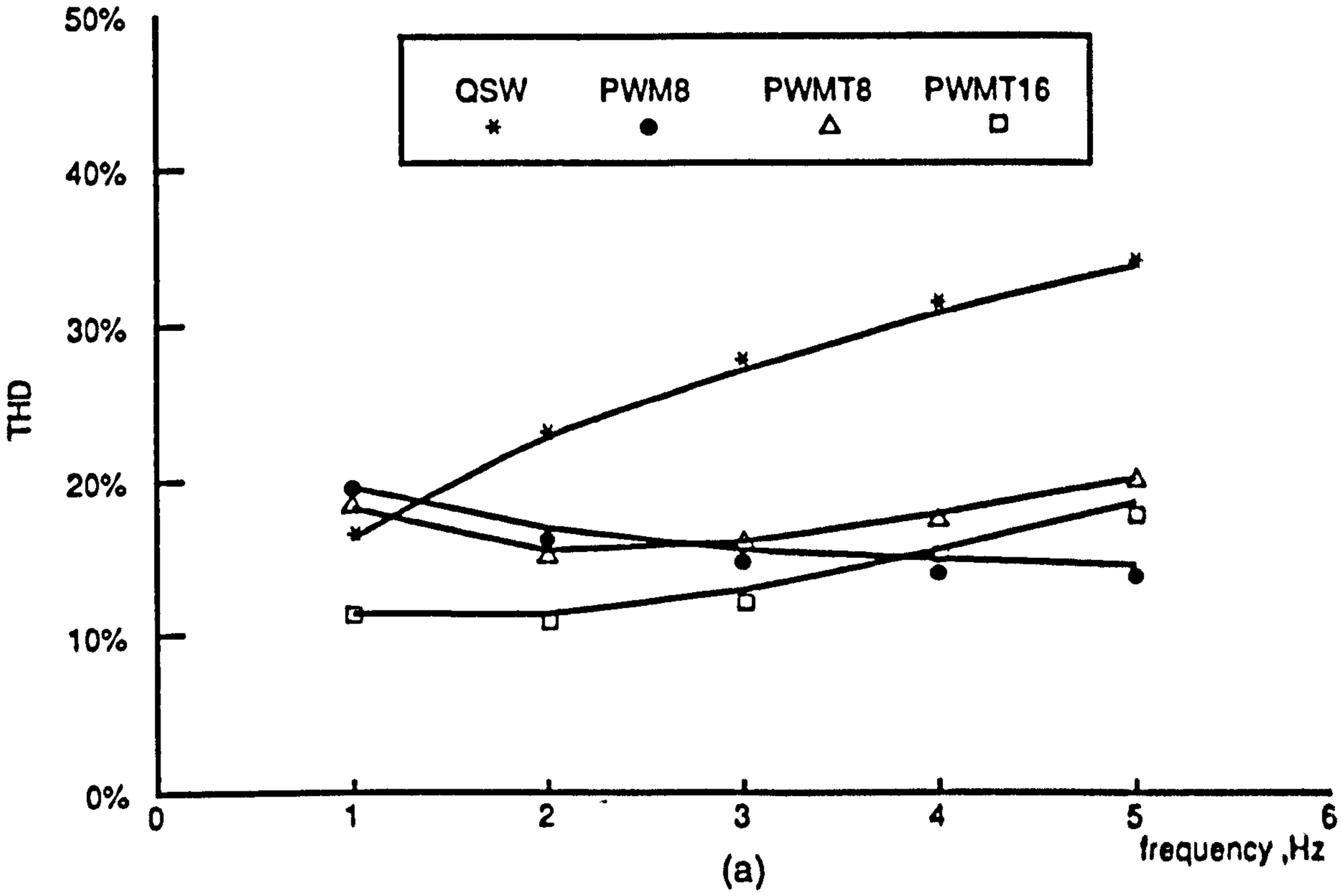

(a)

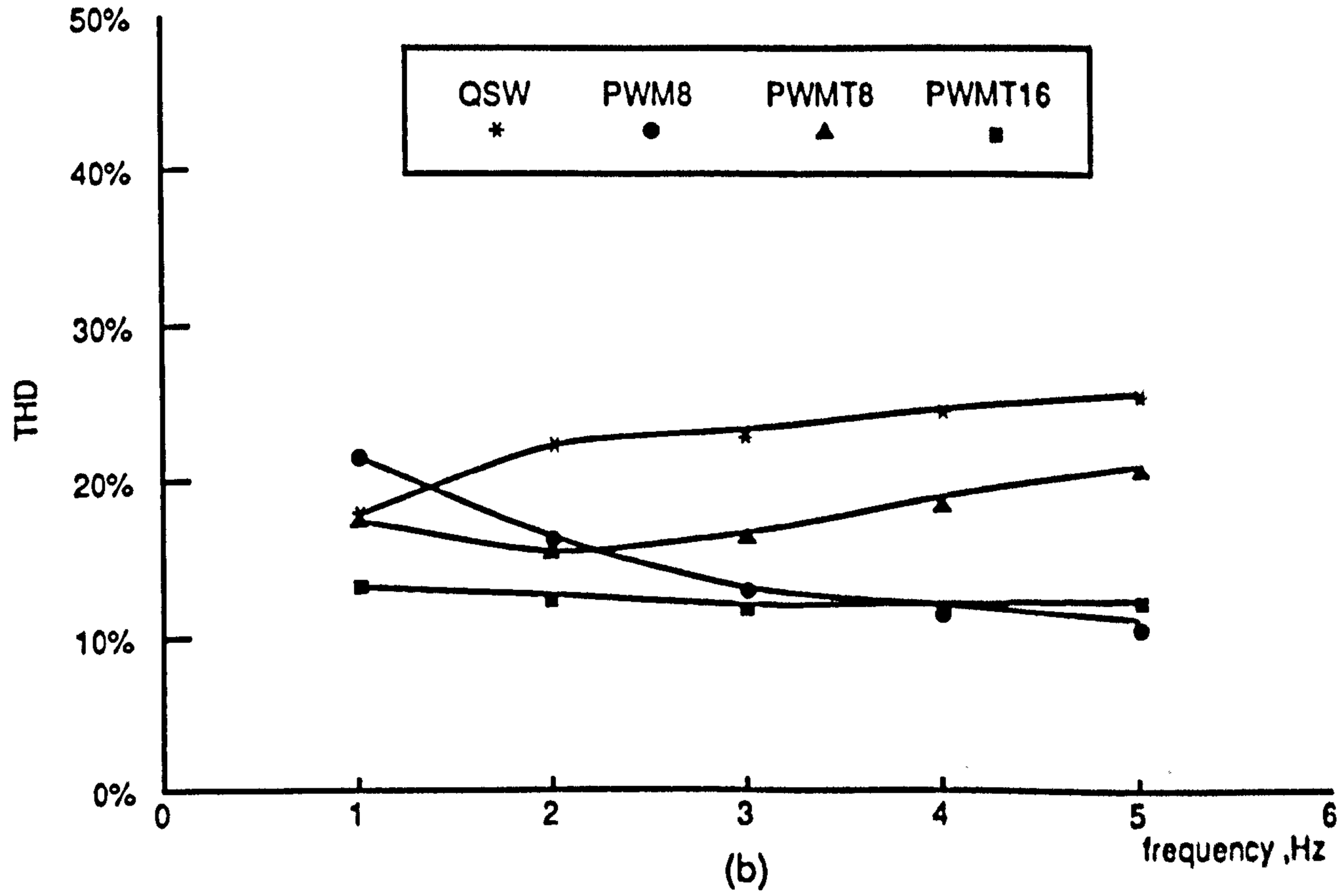

(b)

Figure 8.17 Computed harmonic distortion factor against operating frequency using the direct-phase model for QSW , PWM8 elimination , type A PWMT8 and type B PWMT16 half-wave strategies
(a) No-load (b) Full-load

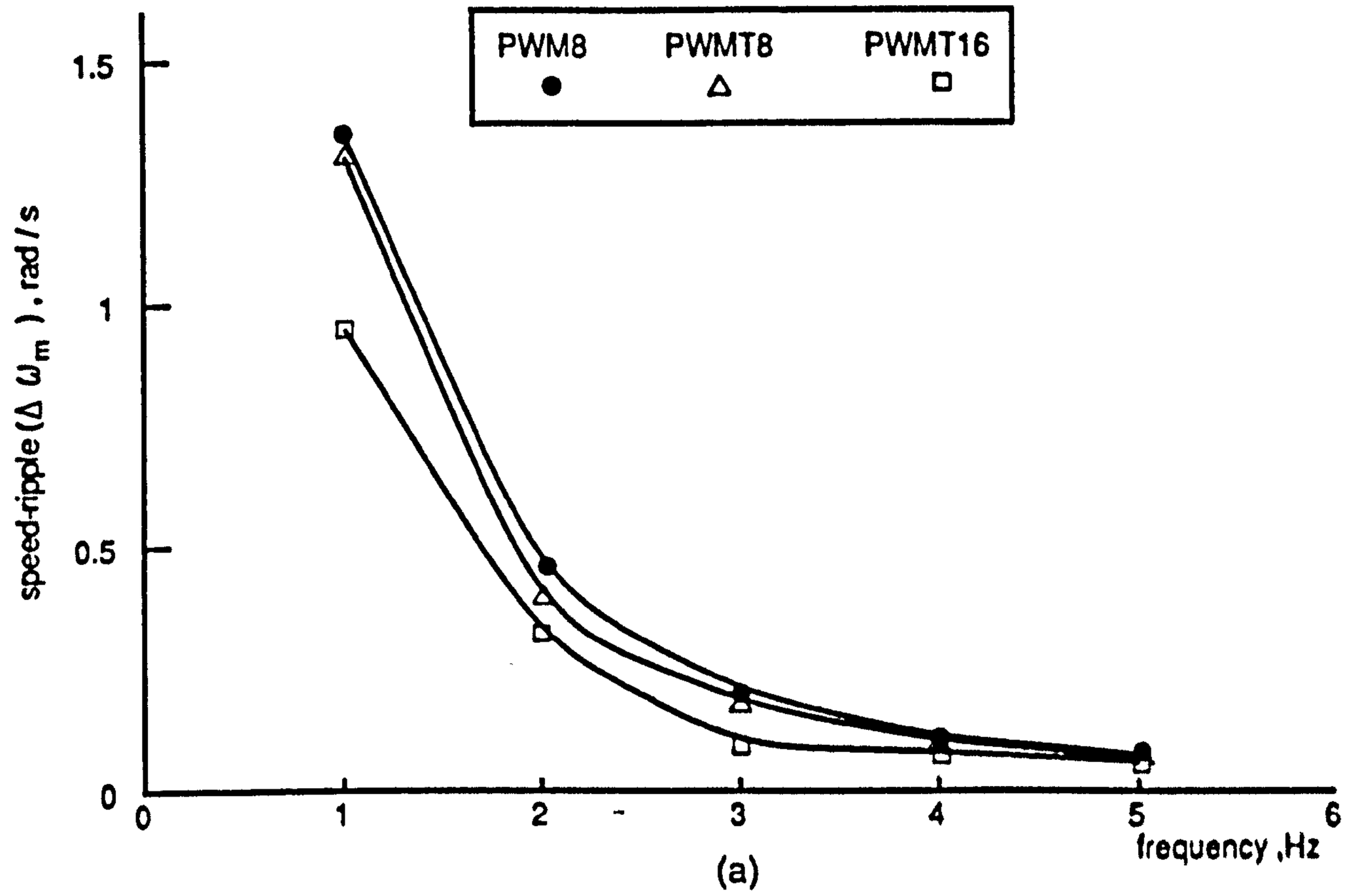

(a)

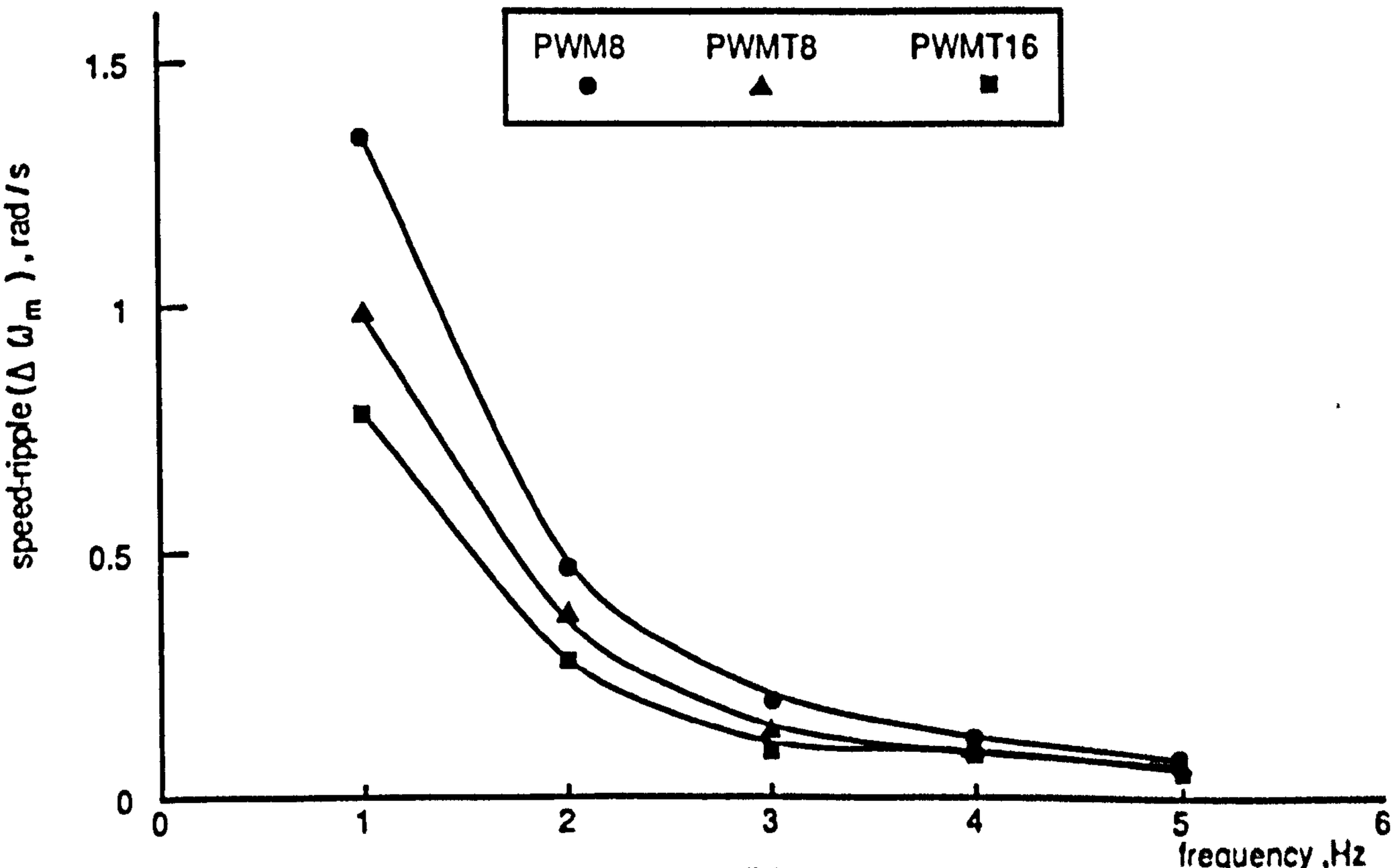

(b)

Figure 8.18 Computed peak-to-peak speed ripple against operating frequency using the direct-phase model for PWM8 elimination , type A PWMT8 and type B PWMT16 half-wave strategies
(a) No-load (b) Full-load

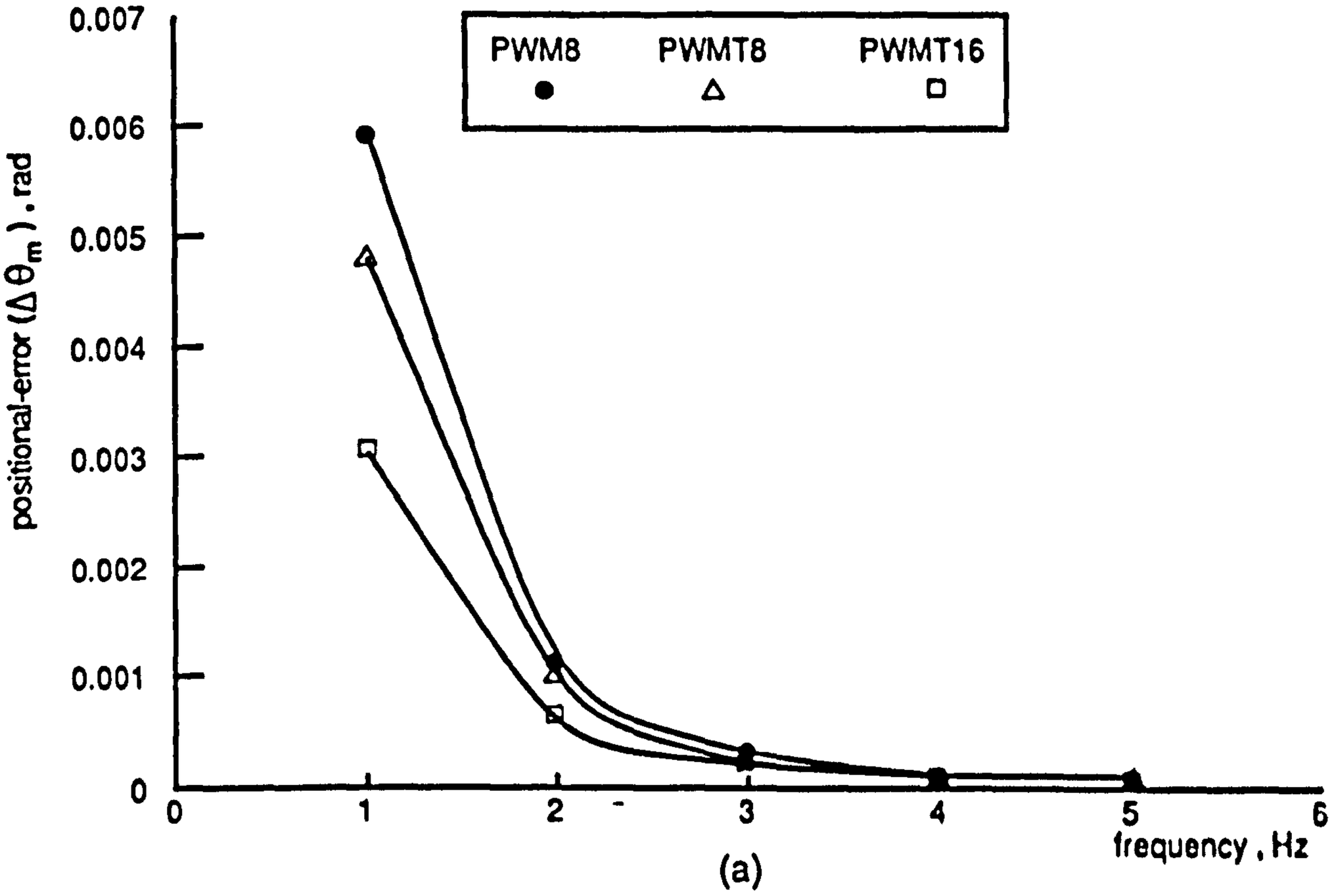

(a)

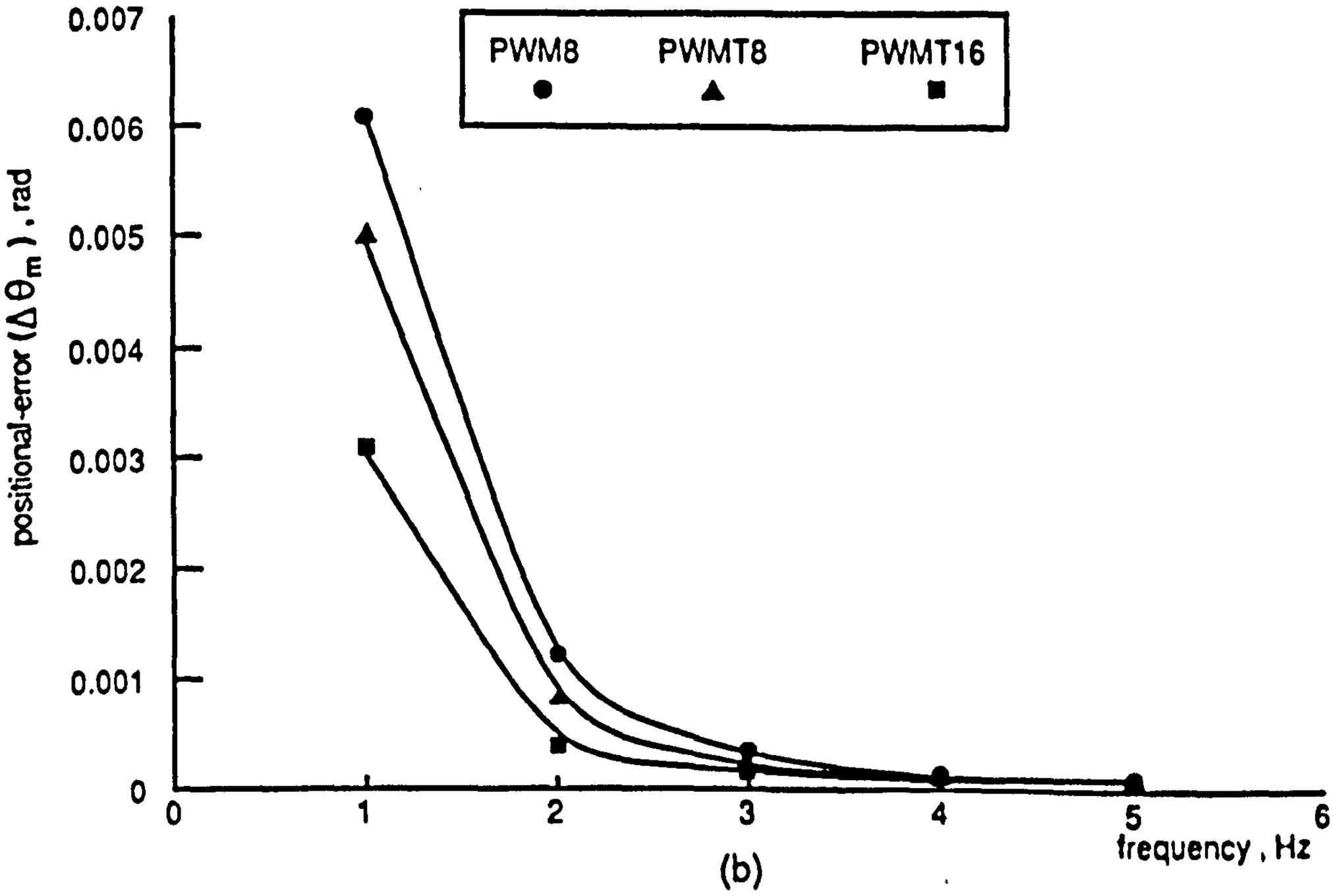

(b)

Figure 8.19 Computed peak-to-peak positional error against operating frequency using the direct-phase model for PWM8 elimination , type A PWMT8 and type B PWMT16 half-wave strategies
(a) No-load (b) Full-load

All investigations of the drive performance with this new quarter-wave symmetrical strategy are therefore restricted to the frequency range 5Hz to 50Hz.

8.2.1 Computation of Switching Angles

Unlike the half-wave symmetrical strategy, the solution to this optimization problem is possible for the full frequency range and all load conditions. This may be attributed to the less stringent constraints imposed on the optimization process.

Figures 8.20(a) and (b) show respectively the switching angle trajectories for type C PWMM4 and type D PWMM8 modes, defining nine and seventeen pulses per half-cycle for no-load and full-load operation. Switching angle trajectories for both types demonstrate nearly constant trends over the complete frequency range, as well as insignificant differences between no-load and full-load for much of the frequency range.

8.2.1.1 Effect on Harmonic Torque Components

The low frequency effect of torque pulsations may be assessed by the level of speed ripple and positional error, since these are both significant and measurable. As the frequency increases, they both become insignificant, due to the attenuation effects of the drive inertia. High frequency harmonic torques of significant magnitudes still however remain, and these may effect the life of the motor. Moreover, they may excite dangerous mechanical vibrations. There is no general solution to this problem, since every system has a different mechanical arrangement and must be investigated individually. In this thesis, the quality of the torque waveform at high operating frequencies is assessed in terms of the magnitudes of the harmonic torque components and the resultant torque pulsations.

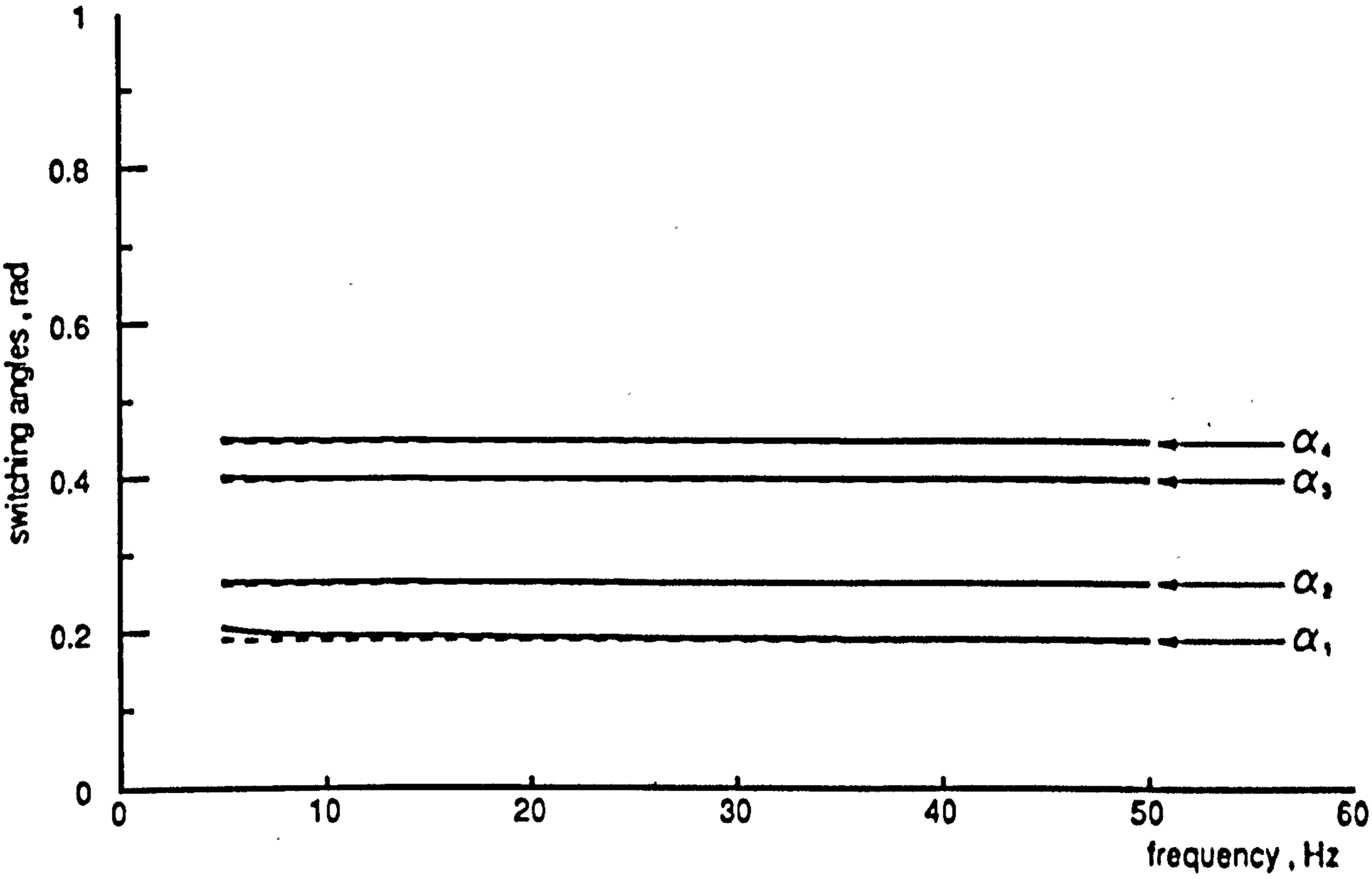

(a)

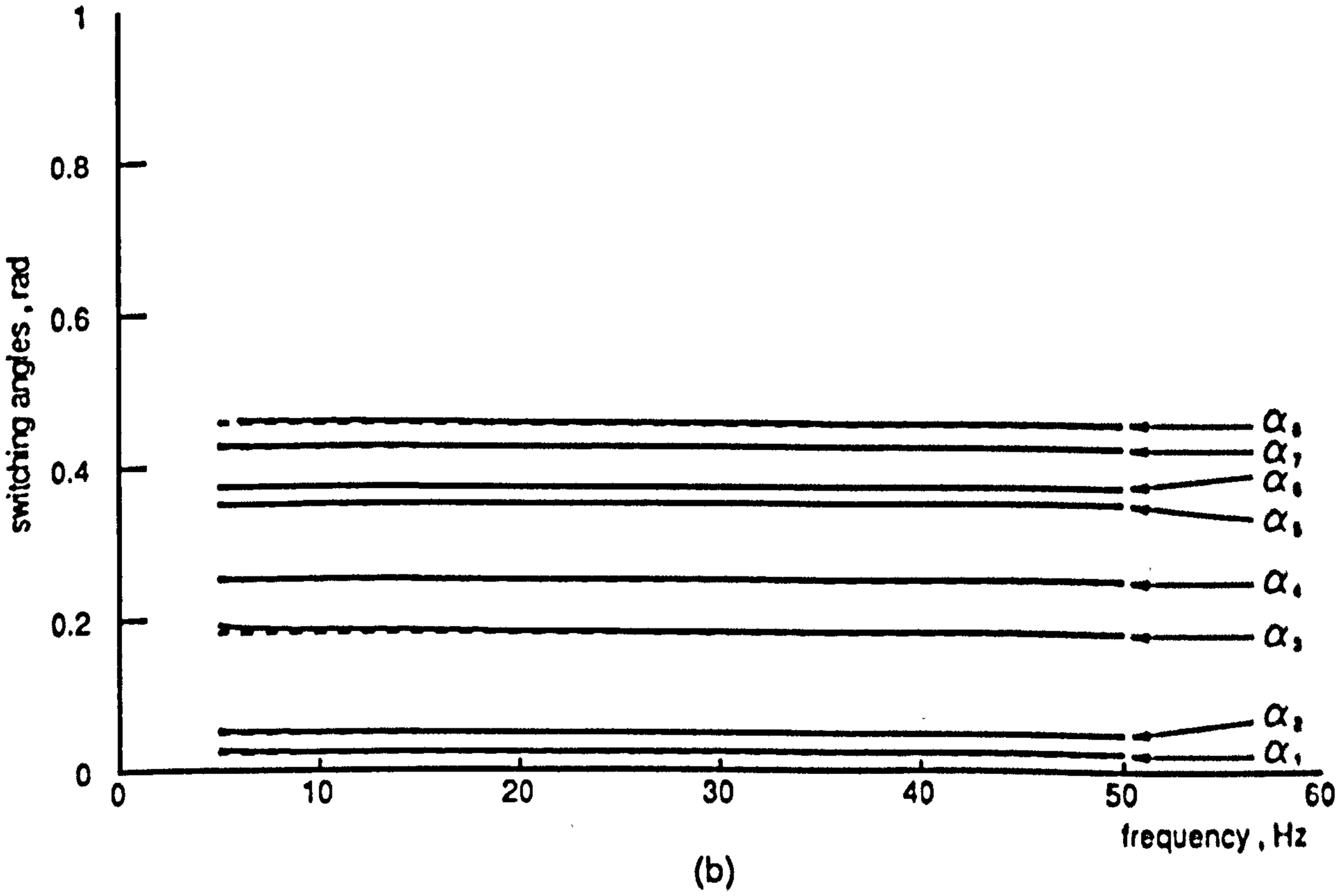

(b)

No-load ------ Full-load ——————

Figure 8.20 Variation of switching angles with frequency for :
(a) Type C PWMM4 mode quarter-wave strategy
(b) Type D PWMM8 mode quarter-wave strategy

Figures 8.21(a) and (b) show the torque components as a function of the operating frequency, obtained using the frequency-domain model, for the elimination PWM8 mode and type D PWMM8 mode respectively and an unloaded machine. Figure 8.21(a) shows that the 30th- and 36th-harmonic components are both significant, due to the elimination of the lower order components. The 30th-harmonic component decreases from 0.112Nm at 5Hz to 0.062Nm at 20Hz, after which it remains almost constant. The 36th-harmonic component is almost constant with a value of 0.071Nm over the full range of frequency considered. Figure 8.21(b) shows that all harmonics are present and decrease with frequency, except for the 30th which remain constant at 0.053Nm.

Figure 8.22(a) shows that, in the elimination strategy, the 30th- and 36th-harmonic components do not change their behaviour or magnitudes significantly when the machine is fully-loaded. Figure 8.22(b) shows however that, for the type D strategy, the magnitudes of the 6th, 12th, 18th- and 24th-components reflect to a greater extent the behaviour of the phase-angles between their relative torque components shown in figure 6.1. As the operating frequency approaches 10Hz, these components all experience a significant reduction. Above 10Hz they increase, but their trends remain below that of the 30th-harmonic component, whose magnitude varies between 0.075Nm at 5Hz and 0.055Nm at 50Hz.

To reduce the inverter switching losses and achieve a smooth transition to the QSW mode of operation, lower pulse-number PWM patterns are usually recommended as the rated frequency is approached. The elimination strategy PWM4 mode eliminates only the 6th- and 12th-harmonic components, and produces nine pulses per half-cycle in the line voltage waveform. For comparison the type C PWMM4 mode is also considered, which provides minimisation of the first four low order harmonic torque components for the same number of pulses per half-cycle as the PWM4 mode. Figure 8.23(a) and (b) shows respectively the harmonic torque components for these two modes for the

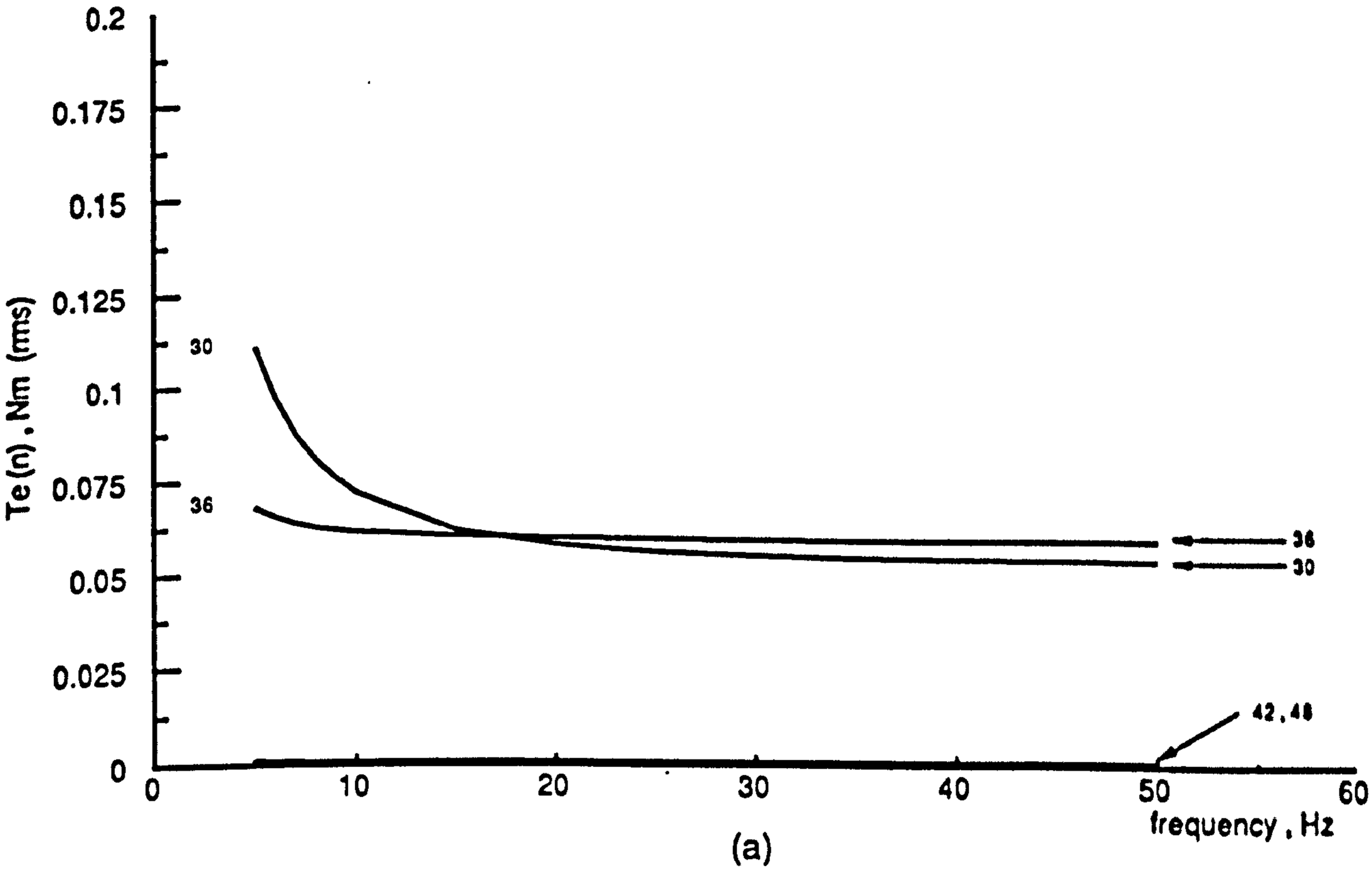

(a)

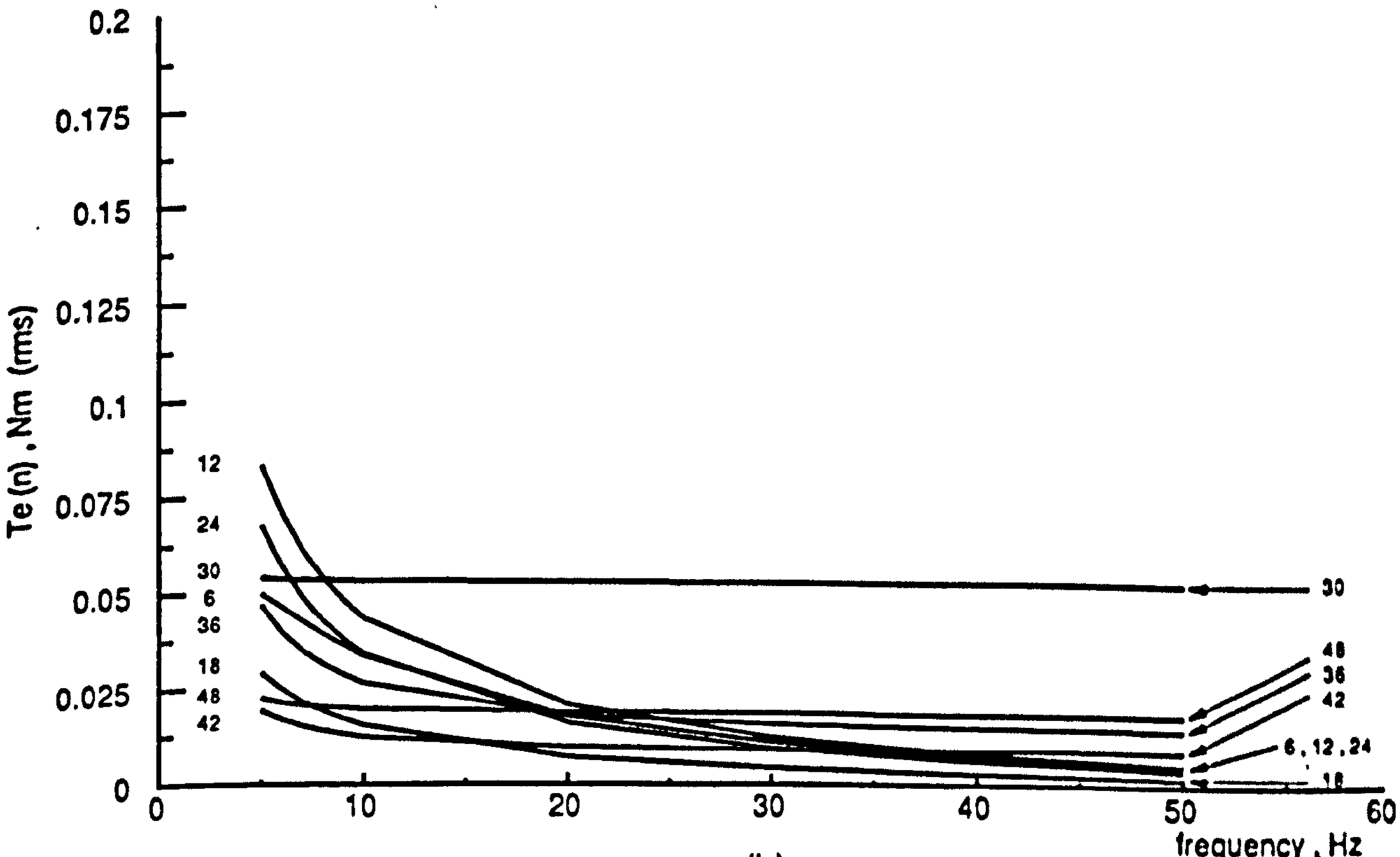

(b)

Figure 8.21 Computed harmonic torque components against frequency at no-load

(a) PWM8 elimination strategy mode

(b) PWMM8 type D strategy mode

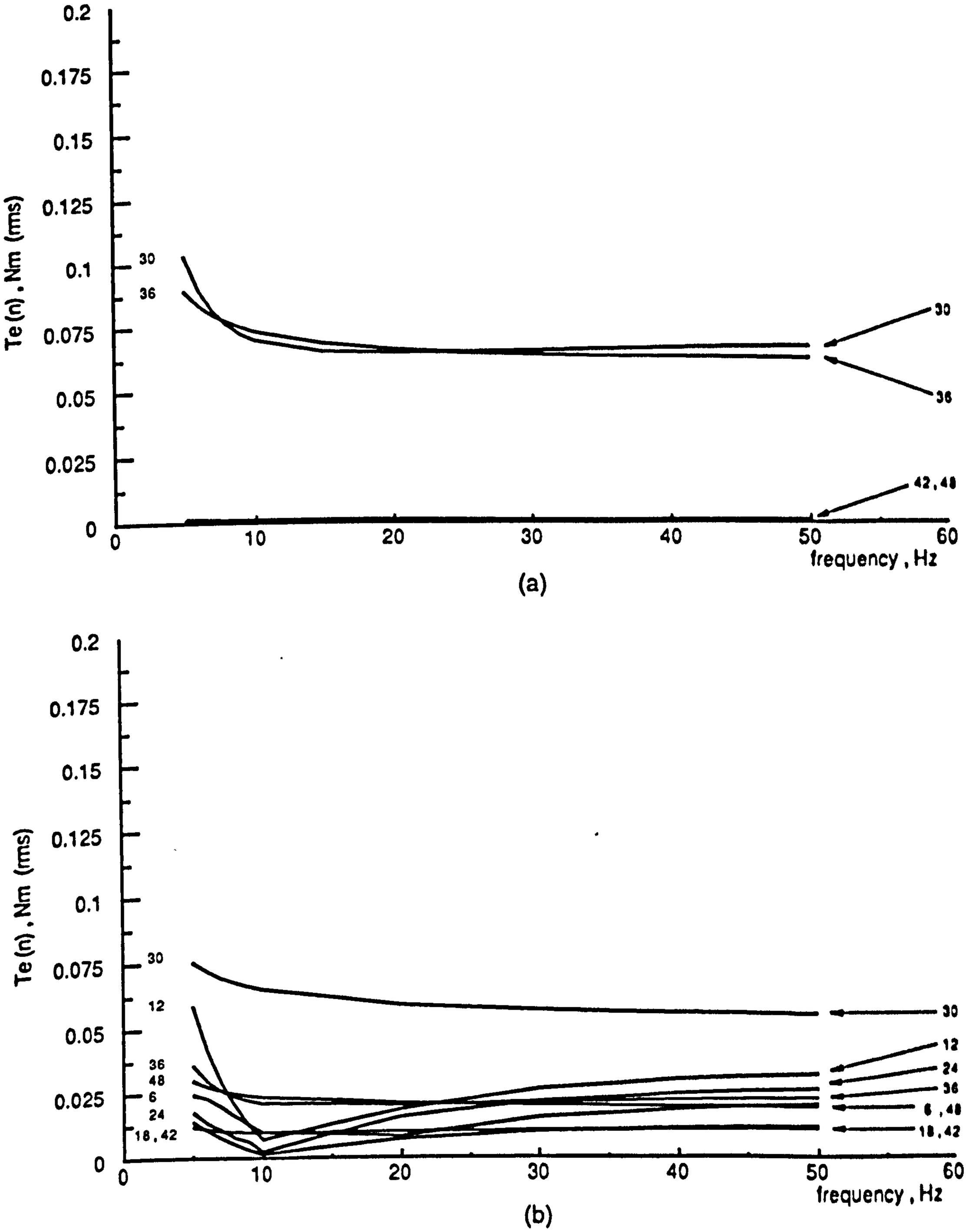

Figure 8.22 Computed harmonic torque components against frequency at full-load

(a) PWM8 elimination strategy mode

(b) PWMM8 type D strategy mode

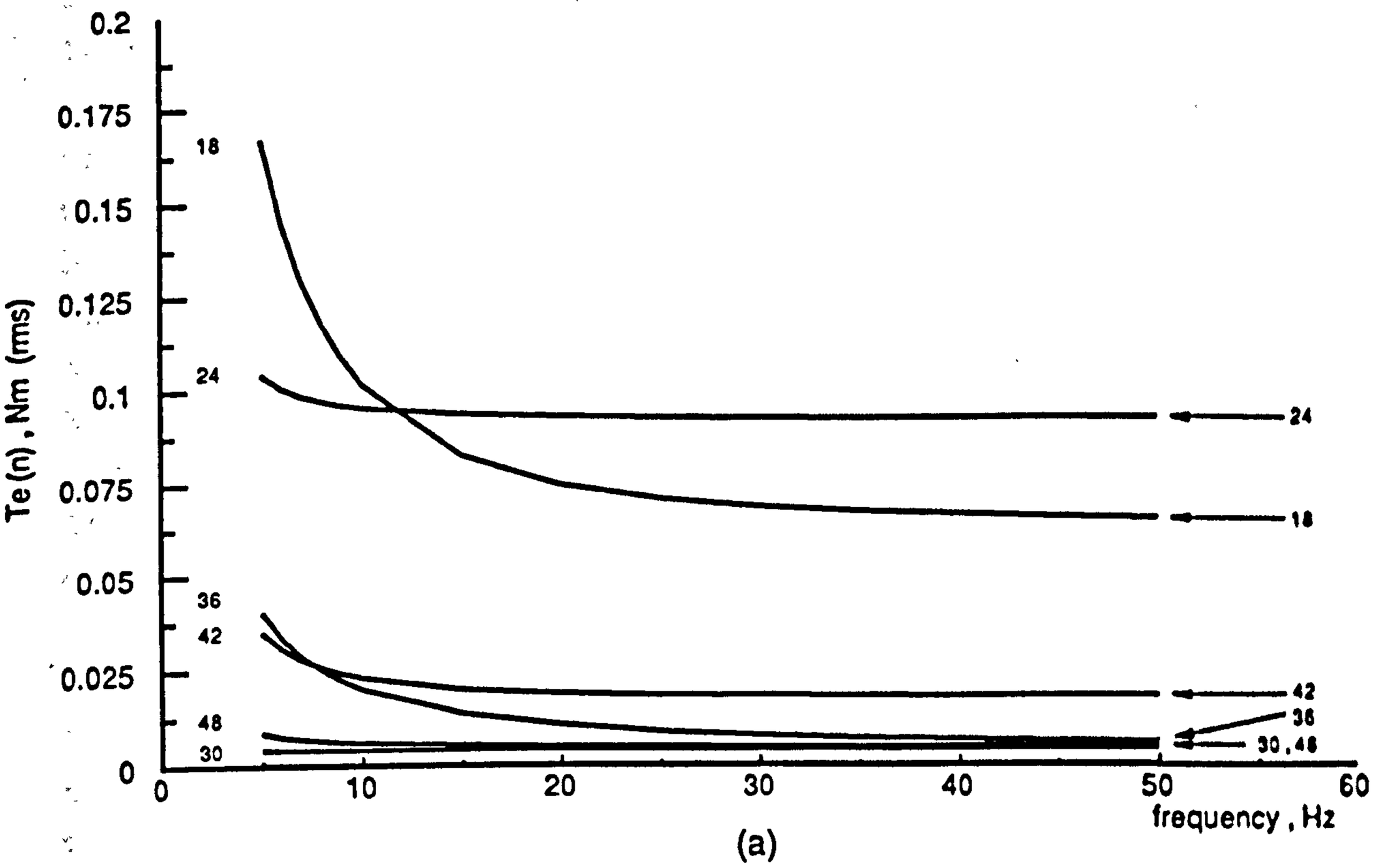

(a)

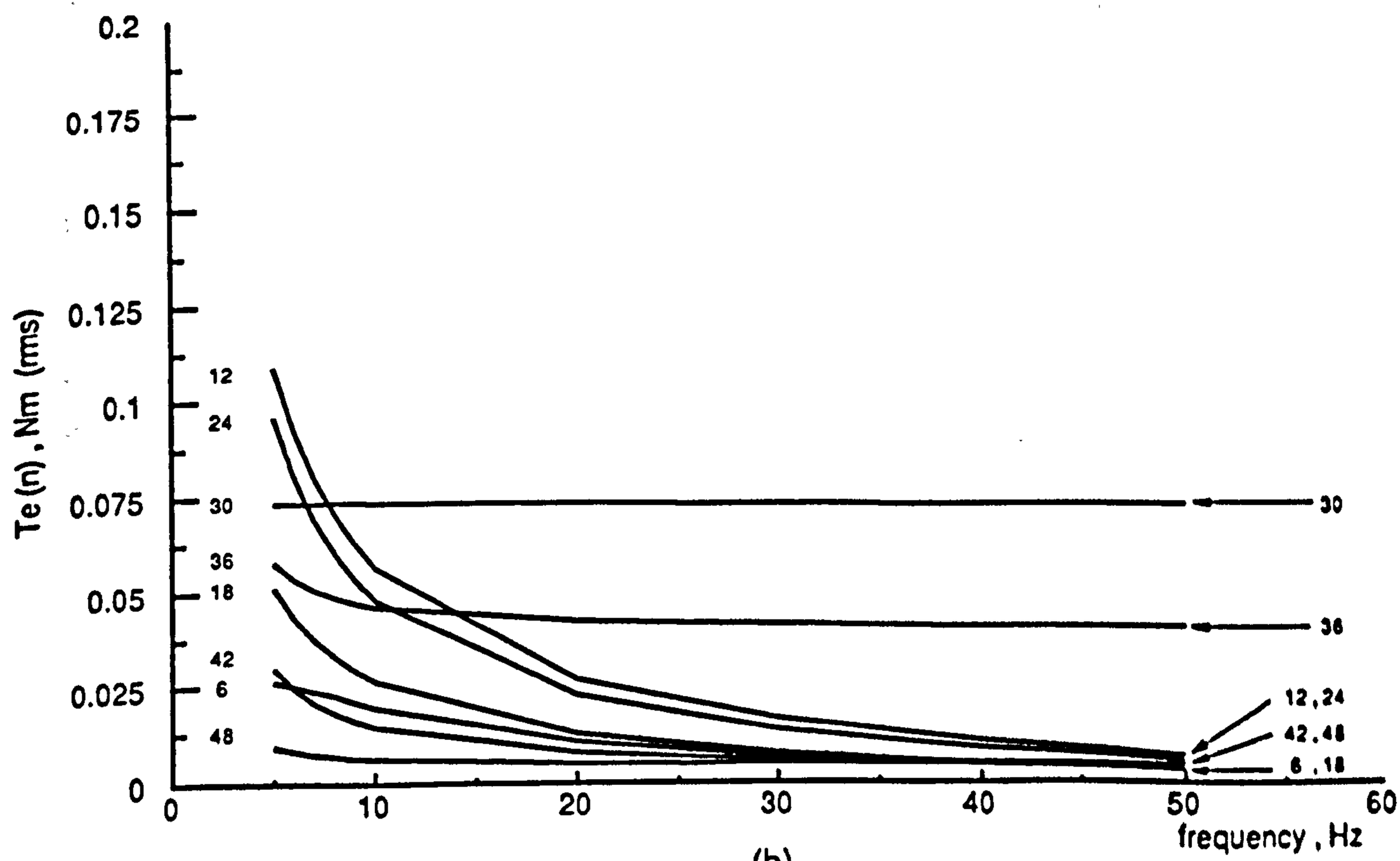

(b)

Figure 8.23 Computed harmonic torque components against frequency at no-load

(a) PWM4 elimination strategy mode

(b) PWMM4 type C strategy mode

unloaded motor. Figure 8.23(a) shows a significant 18th-harmonic component of 0.168Nm at 5Hz, decreasing to 0.066Nm at 50Hz, and an approximately constant 24th-harmonic component of 0.1Nm. The 6th- and 12th-harmonic components are eliminated, while other components exist with magnitudes below 0.043Nm over the full frequency range. Figure 8.23(b) shows however that the type C strategy increases the order of the most significant harmonic torque components, and produces a constant 30th-harmonic component of 0.073Nm and a 36th-harmonic component of 0.058Nm at 5Hz decreasing to 0.041Nm at 50Hz. Other harmonics exist with varying magnitudes, and all decreasing with increasing frequency.

Figure 8.24(a) shows that, for the elimination strategy, the application of full-load increases the 24th-harmonic component to 0.135Nm and reduces the 18th-harmonic component to 0.147Nm at 5Hz. The other components do not however vary significantly. Figure 8.24(b) shows that, with the type C strategy, the 30th- and 36th-harmonics on full-load are still the most significant torque components for the full frequency range, while the first four low order components display a pronounced dip around 10Hz.

The variation of the resultant torque pulsations for all these operating modes are shown in figures 8.25(a) and (b), for no-load and full-load operation respectively. The results were obtained using the direct-phase model. Figure 8.25(a) shows that, for no-load operation below 20Hz, the elimination PWM8 mode produces the least torque pulsations. Above 20Hz, the type D PWMM8 mode improves, and produces smaller torque pulsations up to rated frequency. For a lower pulse-number, the type C PWMM4 mode produces a reduced torque pulsations compared with the elimination PWM4 mode, particularly as the operating frequency approaches its rated value. This improved performance for a low pulse-number mode persists, even at full-load operation, as illustrated by figure 8.25(b). Here the most significant reduction in torque pulsations occurs around 10Hz, where the effect of the minimisation process is

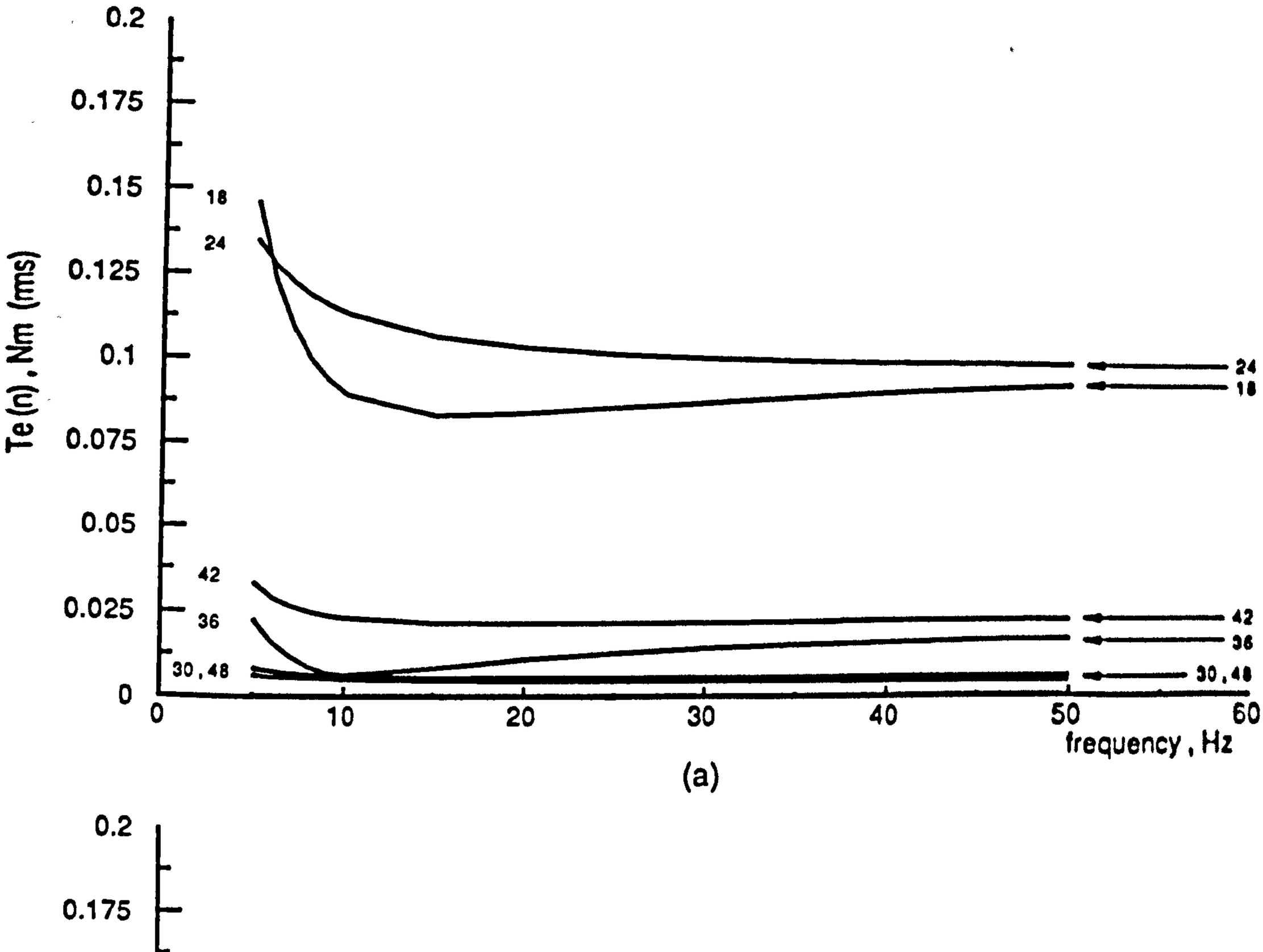

Figure 8.24 Computed harmonic torque components against frequency at full-load

(a) PWM4 elimination strategy mode

(b) PWMM4 type C strategy mode

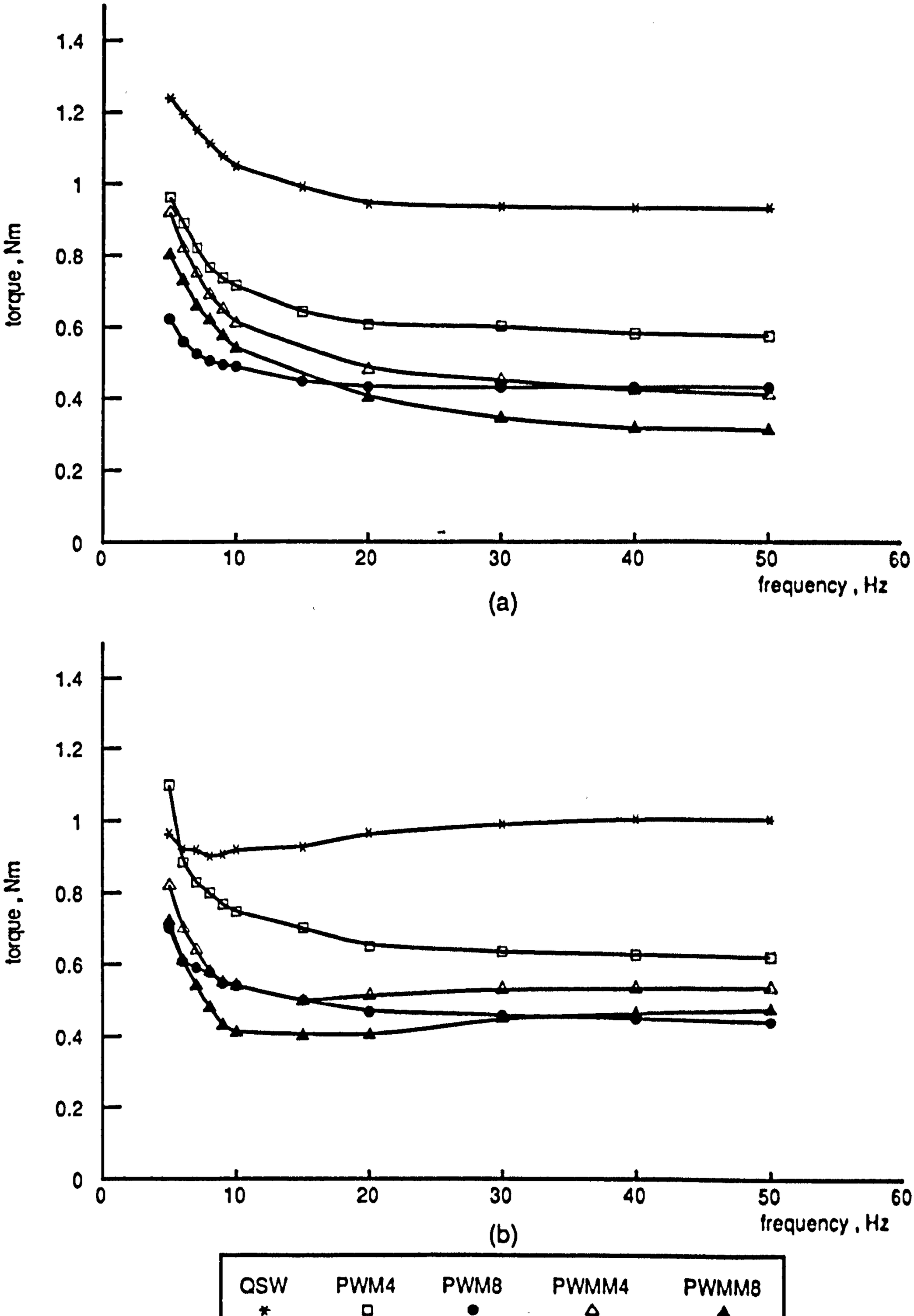

Figure 8.25 Computed variation of peak-to-peak torque pulsation with frequency for (a) No-load (b) Full-load

most effective. For a higher pulse number, the PWMM8 mode type D strategy produces smaller torque pulsations than the elimination PWM8 mode, especially around 10Hz. However, as the operating frequency increases, both modes show more or less similar performance.

It follows that, if a low pulse number strategy is required, the type C PWMM4 mode produces an improved performance for all load conditions over the frequency range 5Hz to 50Hz. A higher pulse-number strategy further reduces the torque pulsations, although careful considerations must be given in terms of its usefulness to a particular portion of the frequency range and load condition.

8.2.1.2 Effect on Harmonic Current Distortion Factor

The effect of significant high order harmonic voltage components in the elimination strategy is reduced at high operating frequencies, due to the increased attenuation effect of the higher input impedance. Since low order harmonics are still present in both strategies, and their effects are less attenuated by the input impedance, these strategies will have a higher harmonic distortion factor which will result in increased heat losses. This behaviour was evident at frequencies below 5Hz when the drive performance was investigated in section 8.1.2.2. The arbitrary re-distribution of harmonic components that the new strategy achieves, if accompanied by the minimisation of some harmonics, may result in a similar, if not lower, harmonic current content than the elimination strategy.

Figures 8.26(a) and (b) compare the harmonic distortion produced by the QSW and various PWM operation modes for no-load and full-load conditions. Both figures show the QSW mode to have the highest harmonic distortion factor for the full frequency range considered. For the same pulse-number, the type C PWMM4 mode and the elimination PWM4 mode both produce very similar results for both no-load and full-load conditions.

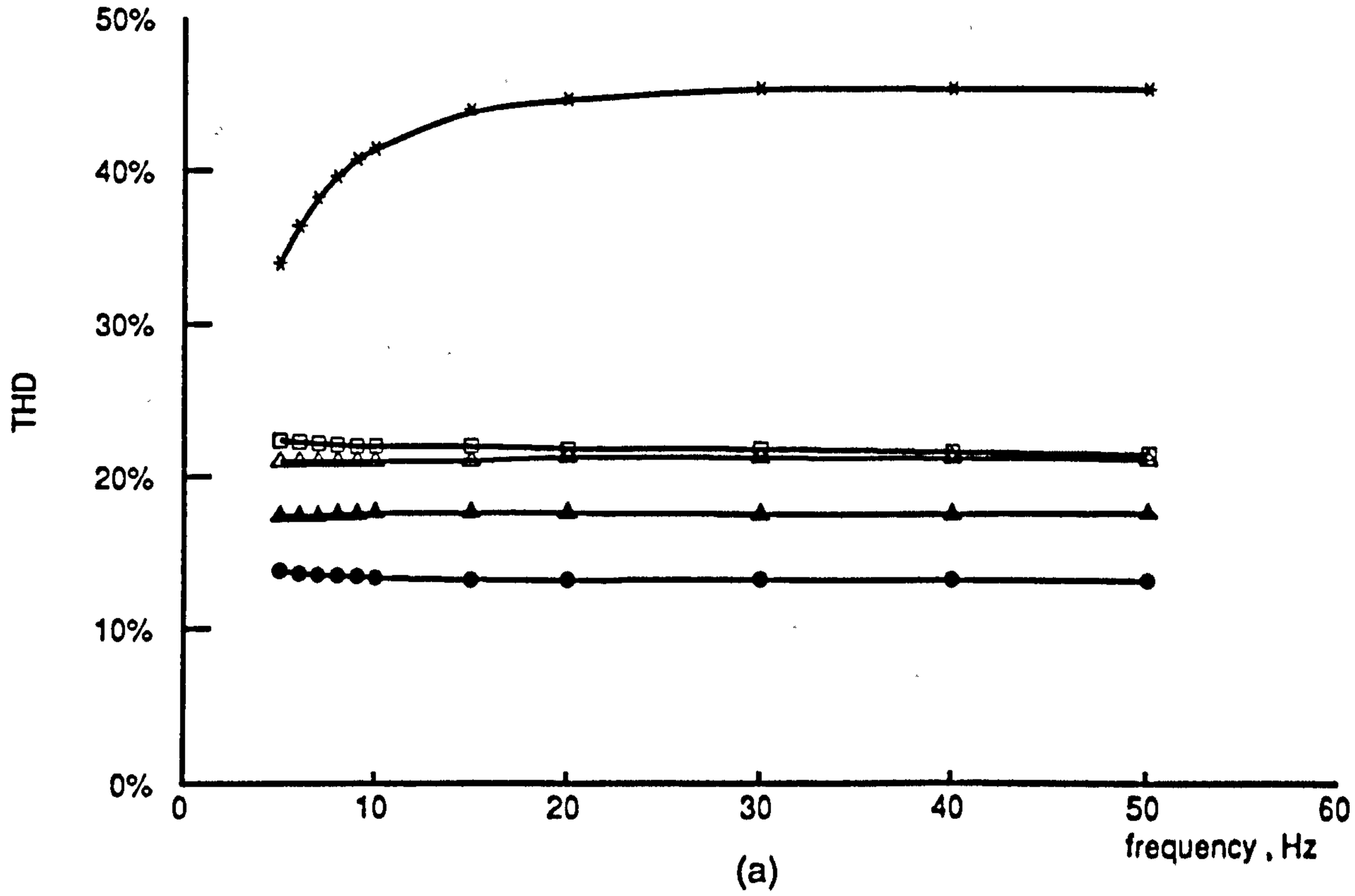

(a)

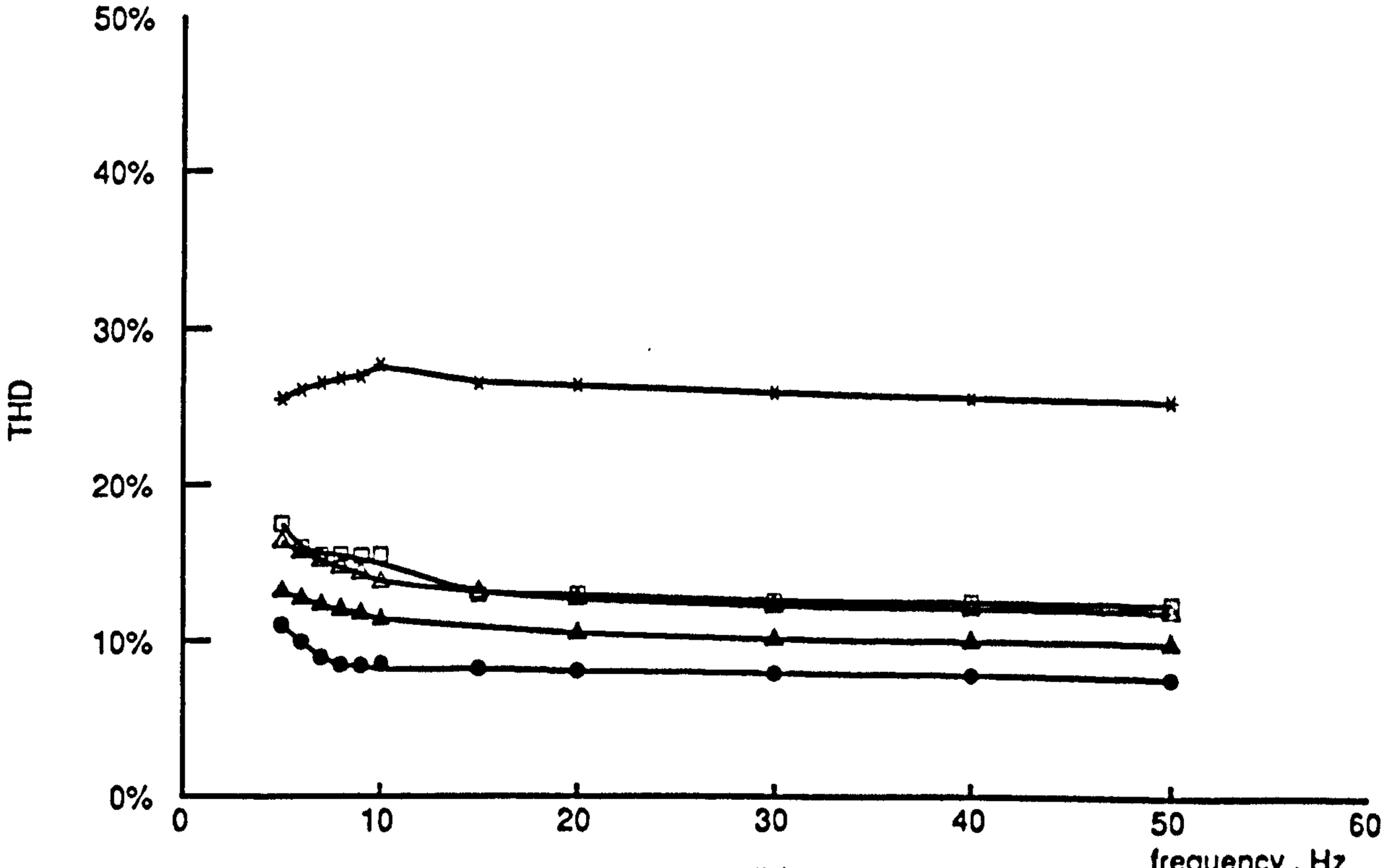

(b)

Figure 8.26 Computed variation of harmonic distortion factor with frequency
(a) No-load (b) Full-load

The type D PWMM8 mode produces respectively a 32.5% and 25.8% increase for no-load and full-load compared with the elimination PWM8 mode.

8.3 Conclusions

The new PWM strategies presented in this chapter were all designed to improve the quality of the torque waveform and so reduce the possibility of mechanical resonance effects. During low frequency operation, the half-wave symmetrical strategy achieved this objective, and even provided smoother rotor motion and lower harmonic losses than the elimination strategy if careful considerations was paid to the operating conditions. Above 5Hz, the quarter-wave symmetrical strategy proved to be more advantageous, by improving the quality of the torque waveform. However, its implementation may introduce additional heat losses in the machine, although this problem becomes less severe as the operating frequency is increased due to the more efficient cooling.

CHAPTER 9

CONCLUSIONS AND SUGGESTIONS FOR FURTHER WORK

This chapter presents concluding comments on the work described in the thesis. The principles of harmonic torque production in VSI/induction motor drives were stated and explained and, based upon these, studies were performed to minimize the undesirable effects of torque pulsations on the drive performance.

9.1 Conclusions and Remarks

A thorough investigation of the performance of a motor drive was undertaken using a comprehensive mathematical model. The investigation was based on the solution of the direct-phase reference frame machine equations, using tensor techniques, which provided an elegant and efficient method of dealing with varying inverter circuit topologies. The model predicts accurately both the steady-state and the transient system characteristics, although the results in the thesis relate particularly to torque pulsation problems during low speed steady-state operation. These results were verified experimentally using a laboratory-scale prototype, able to provide both QSW and any other PWM modes of operation by storing the relevant switching pattern in the form of a look-up table (see chapter 4).

Experimental and simulated results for the drive performance, in particular those in chapters 5 and 7, show close correlation and verify the modelling techniques of chapter 5. Chapter 5 also demonstrated the ability of the direct-phase model to accommodate the effects of unbalanced machine winding parameters, and to account in a straightforward manner for the voltage and current constraints of the inverter switching devices. After studying the QSW and the elimination optimal PWM strategy modes it may be concluded that;

(1) Eliminating low order voltage harmonics using the PWM strategy may increase the remaining high order harmonics above their values for the QSW mode.
(2) High order current and torque harmonics may experience a similar increase, although the high order current components are increasingly attenuated by the harmonic input impedance of the machine.
(3) At low operating frequencies, and due to the greater magnitudes of the remaining torque components, the peak-to-peak torque pulsations with the elimination optimal PWM strategy exceed those of the QSW mode, whose torque ripple contains a predominant 6th-harmonic component.
(4) The effect of high order torque components in producing speed ripple is attenuated by the drive inertia. This causes the speed ripple to be reduced as the operating frequency and the PWM pulse-number are increased.

Chapter 6 described a simple and efficient model based on the equivalent circuit for the motor. Using this model, the correlation between harmonic current and torque components was investigated, and an analytical expression for the instantaneous electromagnetic torque was derived in terms of its harmonic current components. The expression was generalized to account for all possible interactions between harmonic current components which produce steady-state and pulsating torques.

Results for torque pulsations provided by this expression were compared with those obtained using the direct-phase model. The comparison revealed that, during low frequency operation, the neglect of steady-state speed ripple has a first-order effect on the accuracy of prediction, particularly with the QSW mode where the speed ripple is significant. However, the constant speed assumption becomes closer to reality as either the operating frequency or the PWM pulse-number is increased, and the discrepancy between results from the two models

correspondingly diminishes. The new analytical model provides further insight into the relationship between harmonic current and torque components, from which it may be concluded that:

(1) Harmonic torque components produced by interaction between harmonic current components of different orders (excluding the fundamental) are insignificant. Only the interaction between the fundamental component on one side of the airgap with harmonics on the other side of the airgap produces significant harmonic torque components.
(2) Neighbouring pairs of harmonic voltage and/or current components must be treated together. The harmonic torque components produced may be re-arranged such that they are minimized or cancelled, even though the current harmonics are not completely eliminated.
(3) The magnitudes and phase angles of harmonic current components play an important role in the minimization of the harmonic torque components.

Based on these conclusions, two novel techniques for reducing harmonic torque components were developed in chapter 7. At low operating frequencies it is necessary to control the phase angles, as well as the magnitudes of the individual harmonic current components, to achieve cancellation between torque components produced by their interaction. This requires a half-wave symmetrical PWM voltage waveform, whose switching angles are determined relative to the frequency and load conditions. At higher frequencies, a quarter-wave symmetrical PWM voltage waveform may be used to control only the magnitudes of the harmonic current components, and thereby to reduce specific low order harmonic torque components. Both techniques were explored and two new optimal PWM strategies were proposed. Practical implementation of these strategies verified the analytical techniques and revealed significant improvements in the dynamic performance.

In chapter 8, a comparison between the new strategies and the conventional elimination optimal PWM strategy, over the full frequency range, demonstrated that:

(1) Between 1Hz to 5Hz, the half-wave symmetrical strategy achieved cancellation of low order harmonic torque components and introduced an improved distribution of those which remain. This resulted in lower peak-to-peak torque pulsations, even when a lower pulse-number is used, than the elimination strategy. Between 5Hz to 50Hz, the quarter-wave symmetrical strategy may increase the order of the most significant harmonic torque components above that with an elimination strategy for the same pulse-number, and may also maintain reduced magnitudes for the low order harmonics. Careful consideration of the resonant frequency of the torque transmission system must clearly be made before the quarter-wave symmetrical strategy is used in preference to the elimination strategy.

(2) During low frequency operation, the half-wave symmetrical strategy produced lower speed ripple and positional error than the elimination strategy, particularly towards the lower end of the frequency range.

(3) At 1Hz operation, the half-wave symmetrical strategy introduced a better distribution of the harmonic current components than the elimination strategy, even though it did not completely eliminate low order harmonics. A lower harmonic distortion factor and lower harmonic losses were consequently produced. As the operating frequency increases, the remaining harmonic components (whose magnitudes increase due to the elimination of the low order components) are more highly attenuated by the input impedance of the machine. This will counterbalance the better harmonic distribution of the half-wave symmetrical strategy, and reduce the distortion factor produced by

the elimination strategy. This applies also to the quarter-wave strategy, which controls only the magnitudes of specific low-order harmonic components.

(4) Since the new strategies depend on the operating conditions of the machine, they require a closed-loop control system to achieve the best performance.

9.2 Suggestions for Further Work

The investigations undertaken in this thesis have highlighted several areas for further work.

(1) The techniques developed to minimize the torque pulsations may be used in further studies aimed at improving the machine performance to achieve smoother rotor motion and minimum positional error. Equations 6.25 and 6.27 provide a basis for these studies.

(2) Control of the fundamental voltage component may be achieved within the PWM process by introducing one more degree of freedom into the optimization process [18]. Thus, for each strategy, a further switching angle is added to the problem of maximizing the fundamental component and satisfying the constraints related to the required performance index. The process begins with the minimum fundamental component value, which is then incremented in steps up to the maximum value. At each step, values of the switching angles from the previous step are used as an initial estimate.

(3) The determination of switching angles for the half-wave symmetrical strategy, using an optimization technique based on the minimization of the objective function by a quasi-Newton method, proved to be inefficient. Alternative method based on solving for the least squares of the objective function may be more effective.

(4) At low operating frequencies and constant airgap flux operation, the on-state voltage drop of the inverter switching devices is a significant proportion of the required DC-link voltage. Simply compensating for this by a constant voltage boost of 3.5V to the DC-link at all operating conditions will either slightly over-saturate the machine at light loads, or result in field weakening when the machine is fully loaded. For a precise prediction of the required DC-link voltage for all conditions, the input-output transfer relationships for the fundamental voltage and current components must be obtained. Due to the reactive power properties of the inverter, and the voltage and current constraints of the switching devices, the direct-phase model and the analysis described in [86] may be used for consideration of this problem.

REFERENCES

(1) Jones, B.L. : "*Electrical Variable Speed Drives*", IEE Proc., Pt. A, Vol. 131, No. 7, Sep. 1984, PP. 516-558.

(2) Murphy, J.M.D. and Turnbull, F.G. : "*Power Electronic Control of AC Motors*", Pergamon Press, 1988.

(3) Novotny, D.W. : "*Steady State Performance of Inverter Fed Induction Machines by Means of Time Domain Complex Variables*", IEEE Trans., Power App. Syst., Vol. PAS-95, No. 3, May/June 1976, PP. 927-935.

(4) Skogsholm, E.A. : "*Efficiency and Power Factor for a Square Wave Inverter Drive*", IEEE Conference Record, IAS, 1978, PP. 463-469.

(5) Lipo, T.A. and Turnbull, F.G. : "*Analysis and Comparison of Two Types of Square Wave Inverter Drives*", IEEE Trans., Ind. App., Vol.IA-11, No. 2, Mar./Apr. 1975, PP. 137-147.

(6) Schonung, A. and Stemmler, H. : "*Static Frequency Changers with Subharmonic Control in Conjunction with Reversible Variable Speed AC Drives*", Brown Boveri Review, Aug./Sep. 1964, PP. 555-577.

(7) Mokrytzki, B. : "*Pulse-Width-Modulated Inverters for AC Motor Drives*", IEEE Trans., Ind. Gen. App., Vol. IGA-3, No. 6, Nov./Dec. 1967, PP. 493-503.

(8) Bowes, S.R. and Bird, B.M. : "*Novel Approach to the Analysis and Synthesis of Modulation Processes in Power Converters*", Proc. IEE, Vol. 122, No. 5, May 1975, PP. 507-513.

(9) Kliman, G.B. and Plunkett, A.B. : "*Development of a Modulation Strategy for PWM Inverter Drive*", IEEE Trans., Ind. App., Vol. IA-15, No. 1, Jan./Feb. 1979, PP. 72-79.

(10) Bowes, S.R. and Clements, R.R. : "*Computer-Aided Design of PWM Inverter Systems*", IEE Proc., Pt. B, Vol. 129, No. 1, Jan. 1982, PP. 1-17.

(11) Bowes, S.R. : "*New Sinusoidal Pulsewidth-Modulated Inverter*", Proc. IEE, Vol. 122, No. 11, Nov. 1975, PP. 1279-1285.

(12) Mazzucchelli, M., Puglisi, L. and Sciutto, G., : "*PWM Systems in Power Converters: an Extensions of the Sub-harmonic Method*", IEEE Trans., Ind. Electron. Contr. Instrum., Vol. IECI-28, Nov. 1981, PP. 315-322.

(13) Bowes, S.R. and Davis, T. : "*Microprocessor-Based Development System for PWM Variable-Speed Drives*", IEE Proc., Pt. B, Vol. 132, No. 1, Jan. 1985, PP. 18-45.

(14) Franzo, G., Mazzucchelli, M., Puglisi, L. and Sciutto, G. : "*Analysis of PWM Techniques using Uniform Sampling in Variable-Speed Electrical Drives with Large Speed Range*", IEEE Trans., Ind. Appl., Vol. IA-21, No. 4, Jul./Aug. 1985, PP. 966-974.

(15) Balestrino, A., DE Maria, G. and Sciavicco, L. : "*Analysis of Modulation Processes in Power Converters*", Proc. IEE, Vol. 125, No. 5, 1978, PP. 411-412

(16) Turnbull, G.F. : "*Selected Harmonic Reduction in Static DC-AC Inverters*", IEEE Trans., Commun. Electron., Vol. 83, 1964, PP. 374-378.

(17) Patel, H.S. and Hoft, R.F. : "*Generalized Techniques of Harmonic Elimination and Voltage Control in Thyristor Inverters : Part 1- Harmonic Elimination*", IEEE Trans., Ind. Appl., Vol. IA-9, No. 3, May/June 1973, PP. 310-317.

(18) Patel, H.S. and Hoft, R.F. : "*Generalized Techniques of Harmonic Elimination and Voltage Control in Thyristor Inverters : Part 2- Voltage Control Techniques*", IEEE Trans., Ind. Appl., Vol. IA-10, No. 5, Sep./Oct. 1974, PP. 666-673.

(19) Nayak, P.H. and Hoft, R.G. : "*Optimizing the PWM Waveforms of a Thyristor Inverter*", IEEE Trans., Ind. Appl., Vol. IA-11, 1975, PP. 526-530.

(20) Buja, G.S. and Indri, G.B., : "*Optimal Pulse-Width-Modulation for Feeding AC Motors*", IEEE Trans., Ind. Appl., Vol. IA-13, No. 1, Jan./Feb. 1977, PP. 38-44.

(21) Creighton, G.K., Smith, I.R. and Mergen, A.F. : "*Loss Minimisation in 3-Phase Induction Motors with PWM Inverter Supplies*", IEEJ, Electr. Power Appl., 2, (5), 1979, PP. 167-173.

(22) Zach, F.C. and Ertl, H. : "*Efficiency Optimal Control for AC Drives with PWM Inverters*", IEEE Trans., Ind. Appl., Vol. IA-21, No. 4, Jul./Aug. 1985, PP. 987-1000.

(23) Zach, F.C., Martinez, R., Keplinger, S. and Seister, A. : "*Dynamically Optimal Switching Patterns for PWM Inverter Drives (for-Minimization of the Torque and Speed Ripples)*", IEEE Trans., Ind. Appl., Vol. IA-21, No. 4, Jul./Aug. 1985, PP. 975-986.

(24) Zubek, J. : "*Evaluation of Techniques for Reducing Shaft Cogging in Current-Fed AC Drives*", IEEE, IAS Conference Record, 1978, PP. 517-524.

(25) Lipo, T.A. : "*Analysis and Control of Torque Pulsations in Current-Fed Induction Motor Drives*", IEEE, Power Elect. Spec. Conference Record, 1978, PP. 89-96.

(26) Chin, T.H. and Tomita, H. : "*The Principles of Eliminating Pulsating Torque in Current Source Invertor Induction Motor Systems*", IEEE Trans., Ind. Appl., Vol. IA-17, No. 2, Mar./Apr. 1981, PP. 160-166.

(27) Lienau, W. : "*Torque Oscillations in Traction Drives with Current-Fed Asynchronous Machines*", IEE, Electrical Variable-Speed Drives, Conf. Publ., 179, 1979, PP. 102-107.

(28) Bowes, S.R. and Bullough, R. : "*PWM Switching Strategies for Current-Fed Inverter Drives*", IEE Proc., Pt. B, Vol. 131, No. 5, Sep. 1984, PP. 195-202.

(29) Walker, L.H. and Espelage, P.M. : "*A High Performance Controlled-Current Inverter Drive*", IEEE Trans., Ind. Appl., Vol. IA-16, Mar./Apr. 1980, PP. 193-202

(30) Bowes, S.R. and Bullough, R. : "*Steady-State Performance of Current-Fed Pulse-Width-Modulated Inverter Drives*", IEE Proc., Pt. B, Vol. 131, No. 3, May 1984, PP. 113-132.

(31) Bowes, S.R. and Bullough, R. : "*Harmonic Minimization in Microprocessor Controlled Current Fed PWM Inverter Drives*", ibid, Vol. 134, No. 1, Jan. 1987, PP. 25-41.

(32) Bowes, S.R. and Bullough, R. : "*Fast Modelling Techniques for Microprocessor-Based Optimal Pulse-Width-Modulated Control of Current-Fed Inverter Drives*", ibid, Vol. 131, No. 4, Jul. 1984, PP. 149-158.

(33) Bowes, S.R. and Bullough, R. : "*Optimal PWM Microprocessor-Controlled Current-Source Inverter Drives*", ibid, Vol. 135, No. 2, Mar. 1988, PP. 59-75.

(34) Namduri, C. and Sen, P.C. : "*Optimal Pulsowidth Modulation for Current Source Inverters*", IEEE Trans., Ind. Appl., Vol. IA-22, No. 6, Nov./Dec. 1986, pp. 1052-1072.

(35) Taufiq, J.A., Goodman, C.J. and Mellit, B. : "*Railway Signalling Compatibility of Inverter Fed Induction Motor Drives for Rapid Transit*", IEE Proc., Pt. B, Vol. 133, No. 2, Mar. 1986, PP. 71-84.

(36) Taufiq, J.A., Mellit, B. and Goodman, C.J. : "*Novel Algorithm for Generating Near Optimal PWM Waveforms for AC Traction Drives*", ibid, Vol. 133, No. 2, Mar. 1986, PP. 85-94.

(37) Stanly, H.C. : "*An Analysis of Induction Motor Transients*", AIEE Trans., 1938, Vol. 57, PP. 751-757.

(38) Smith, I.R. and Sriharan, S. : "*Transient Performance of the Induction Motor*", Proc. IEE, Vol. 133, No. 7, Jul. 1966, PP. 1173-1881.

(39) Krause, P.C. : "*Method of Multiple Reference Frames Applied to the Analysis of Symmetrical Induction Machinery*", IEEE Trans., Power App. Sys., Vol. PAS-87, No. 1, Jan. 1968, PP. 218-227.

(40) Krause, P.C. and Lipo, T.A. : "*Analysis and Simplified Representation of a Rectifier-Inverter Induction Motor Drive*", ibid, Vol. PAS-88, May 1969, PP. 588-569.

(41) Bowes, S.R. and Clements, R.R. : "*Digital Computer Simulation of Variable-Speed PWM Inverter-Machine Drives*", IEE Proc., Pt. B, Vol. 130, No. 3, May 1983, PP. 149-160.

(42) Krause, P.C. : "*Electromechanical Motion Devices*", McGraw-Hill, 1989.

(43) Robertson, S.D.T. and Hebber, K.M. : "*A Digital Model for Three-Phase Induction Machines*", IEEE Trans., Power App. Sys., Vol. PAS-88, No. 11, Nov. 1969, pp. 1624-1632.

(44) Desarkar, A.K. and Berg, G.J. : "*Digital Simulation of Three-Phase Induction Motors*", ibid, Vol. PAS-89, No. 6, Jul./Aug. 1970, PP. 1031-1037.

(45) Rahman, S. and Shepherd, W. : "*Thyristor and Diode Controlled Variable Voltage Drives for 3-Phase Induction Motors*", Proc. IEE, Vol. 124, No. 9, Sep. 1977, pp. 784-790.

(46) Nath, G. and Berg, G.J. : "*Transient Analysis of Three-Phase SCR Controlled Induction Motors*", IEEE Trans., Ind. Appl., Vol. IA-17, No. 2, Mar./Apr. 1981, PP. 133-142.

(47) Le, L.X. and Berg, G.J. : "*Steady-State Performance Analysis of SCR Controlled Induction Motors : A Closed Form Solution*", IEEE Trans., Power App. Sys., Vol. PAS-103, 1984, pp. 601-611.

(48) Murphy, J.M.D. and Egan, M.G. : "*A Comparison of PWM Strategies for Inverter-Fed Induction Motors*", IEEE Trans., Ind. Appl., Vol. IA-19, No. 3, May/June 1983, PP. 363-369.

(49) Jain, G.C. : "*The Effect of Voltage Waveshape on the Performance of a 3-Phase Induction Motor*", ibid, Vol. PAS-83, June 1964, PP. 561-566.

(50) Klingshrin, E.A. and Jordan, H.E. : "*Polyphase Induction Motor Performance and Losses on Nonsinusoidal Voltage Supplies*", ibid, Vol. PAS-87, Mar. 1968, PP. 624-631.

(51) Chalmers, B.J. and Sarkar, B.R. : "*Induction Motor Losses Due to nonsinusoidal supply waveforms*", Proc. IEE, Vol. 115, Dec. 1968, PP. 1777-1782.

(52) Robertson, S.D.T. and Hebber, K.M. : "*Torque Pulsations in Induction Motors with Inverter Drives*", IEEE Trans., Ind. Gen. Appl., Vol. IGA-7, Mar./Apr. 1971, PP. 318-323.

(53) Jacovides, L.J. : "*Analysis of Induction Motor Drives with Nonsinusoidal Supply Voltages using Fourier Analysis*", IEEE Trans., Ind. Appl., Vol. IA-9, Nov./Dec. 1973, PP. 741-747.

(54) Venkatesan, K. and Lindsay, J.F. : "*Comparative Study of Losses in Voltage and Current Source Inverter Fed Induction Motors*", ibid, Vol. IA-18, May/June 1982, PP. 240-246.

(55) Rawcliffe, G.H., Burbidge, R.F. and Fong, W. : "*Induction-Motor Speed Changing by Pole-Amplitude Modulation*", The Institution of Electrical Engineers, Paper No. 2597u, Aug. 1958, PP. 411-419.

(56) Abbondanti, A. : "*Method of Flux Control in Induction Motors Driven by Variable Frequency, Variable Voltage Supplies*", IEEE Int. Semicond. Power Converter Conf., 1977, PP. 177-184.

(57) Bose, B.K. : "*Power Electronics and AC Drives*", Prentice-Hall, 1987.

(58) Grant, D. and Seidner, R. : "*Technique for Pulse Elimination in Pulsewidth-Modulation Inverters with no Waveform Discontinuity*", IEE Proc., Pt. B, Vol. 129, No. 4, July 1982, PP. 205-210.

(59) Bowes, S.R. and Mount, M.J. : "*Microprocessor Control of PWM Inverters*", ibid, Vol. 128, No. 6, Nov. 1981, PP. 293-305.

(60) Rajashekara, K.S. and Vithayathil, J. : "*Microprocessor Based Sinusoidal PWM Inverter by DMA Transfer*", IEEE Trans., Ind. Electron., Vol. IE-29, No. 1, Feb. 1982, PP. 46-51.

(61) Grant, D.A. and Seidner, R. : "*Ratio Changing in Pulse-Width-Modulated Inverters*", IEE Proc., Pt. B, Vol. 128, No. 5, Sep. 1981, PP. 243-248.

(62) Houldsworth, J.A. and Rosink, W.B. : "*Introduction to PWM Speed Control System For 3-Phase AC Motors*", Electronic Components and Applications, Vol. 2, No. 2, Feb. 1980, PP.

(63) Dwyer, E. and Ooi, B.T. : "*A Look-up Table Based Microprocessor Controller for a Three Phase PWM Inverter*", IECI 79, Proc. Ind. and Control Appl. of Microprocessors, March (19-21) 1979, PP. 19-22.

(64) Buja, G.S. and Fiorini, P. : "*Microcomputer Control of PWM Inverters*", IEEE Trans., Ind. Electron., Vol. IE-29, No. 3, Aug. 1982, PP. 212-216.

(65) Mishriky, A.H., Girgis, G.A. and Selim, H. : "*Microcomputer Implemented PWM Inverter Using a Unique Pattern of Switching Angles*", IEEE Trans., Ind. Appl., Vol. IA-23, No. 1, Jan./Feb. 1987, PP. 85-89.

(66) Alger, P.L. : "*Induction Machines, their Behaviour and Uses*", Gordon and Breach, 1970.

(67) Wong, Y.C. : "*Optimal Pulse Width Modulated Inverter for Induction Motor*", L.U.T Final Year Project Report, 1988.

(68) Burjam, F.J. : "*Basic GTO Drive Circuits*", Electrinic Components and Applications, Vol. 3, No. 4, Aug. 1981, PP. 232-237.

(69) Rosink, W.B. : "*Analogue Control System for A.C. Motor with PWM Variable Speed Drive*", ibid, Vol. 3, No. 1, Nov. 1980, PP. 6-15.

(70) "*Voltage to Frequency and Frequency to Voltage Converter TSC9400*", RS Data Library, No. 7764, Jul. 1987.

(71) Hoffman de Visme, G. : "*Digital Processing Unit for Evaluating Angular Acceleration*", Electronic Eng., Apr. 1968, PP. 183-188.

(72) Kron, G. , "*Tensors for Circuits*", Dover, 1959.

(73) Williams, S. and Smith, I.R. : "*Fast Digital Computation of 3-Phase Thyristor Bridge Circuits*", Proc. IEE, Vol. 120, No. 7, July 1973, PP. 1-6.

(74) Kettleborough, J.G. ,, Smith, I.R. and Fanthom, B.A. : "*Simulation of a Dedicated Aircraft Generator Supplying a Heavy Rectified Load*", IEE Proc., Pt. B, Vol. 130, No. 6, Nov. 1983, PP. 431-435.

(75) Happ, H.H. : "*Diakoptics and Networks*", Academic Press, 1971.

(76) Hancock, N.N. : "*Matrix Analysis of Electrical Machinery*", Pergamon Press, 1971.

(77) Hindmarsh, J. : "*Electrical Machines and Drives, Worked Examples*", Pergamon Press, 1985.

(78) Dewan, S.B., Slemon, G.R. and Straughen, A. : "*Power Semiconductor Drives*", John Wiley & Sons, 1984.

(79) Kettleborough, J.G., Smith, I.R. and Fanthome, B.A. : "*Simulation of a Transformer/Rectifier Unit for Aircraft Power-Supply System*", IEE Proc., Pt. B, Vol. 129, No. 6, 1982, PP. 323-329.

(80) Gerald, C.F. : "*Applied Numerical Analysis*", Addison-Wesley, 1978.

(81) Pillai, S.K. : "*A First Course on Electrical Drives*", Wiley Eastern Ltd., 1982.

(82) Gray, C.B. : "*Electrical Machines and Drive Systems*", Longman Scientific & Technical, 1989.

(83) Bowes, S.R. and Midoun, A. : "*Suboptimal Switching Strategies for Microprocessor-Controlled PWM Inverter Drives*", IEE Proc., Pt. B, Vol. 132, No. 3, May 1985, PP. 133-148.

(84) "*E04 Minimizing or Maximizing a Function*", NAG-Fortran Library, Mark 11, Vol. 3.

(85) "*E04 Minimizing or Maximizing a Function*", NAG-Fortran Library, Mark 14, Vol. 3.

(86) Novotny, D.W. : "*Equivalent Circuit Steady State Analysis of Inverter Driven Electric Machines*", University of Wisconsin-Madison, Department of Electrical and Computer Engineering, Report ECE-80-19, June 1980.

APPENDIX A.1

1. Induction Motor Parameters

The experimental cage-rotor induction motor was rated at 380/220V 0.56kW 4-pole 50Hz, and the stator winding could be either star or delta connected. Due to supply constraints, the machine was delta connected throughout the experimental work, although its parameters were defined in terms of an equivalent star connection. The per-phase parameters for the equivalent circuit of figure 2.1(b) are

Stator resistance	$R_s = 3.5\ \Omega$
Rotor resistance (referred)	$R_r' = 3.1\ \Omega$
Stator leakage inductance	$l_s = 0.0169\ H$
Rotor leakage inductance (referred)	$l_r' = 0.0165\ H$
Magnetizing inductance	$l_m = 0.3056\ H$

with the phase parameters in equation 5.1 being obtained from these by

Stator phase self inductance	$L_{ss} = l_s + \frac{2}{3}l_m = 0.2206\ H$
Rotor phase self inductance	$L_{rr} = l_r' + \frac{2}{3}l_m = 0.2202\ H$
Mutual inductance between stator phases	$M_s = -\frac{1}{3}l_m = -0.1020\ H$
Mutual inductance between rotor phases	$M_r = -\frac{1}{3}l_m = -0.1020\ H$
stator/rotor mutual inductance	$M_{sr} = \frac{2}{3}l_m = 0.2040\ H$

2. DC Dynamometer

The dynamometer used was a 240V 0.25kW separately-excited DC machine. The electromagnetic torque T_m of the machine is proportional to the product of the airgap flux Φ and the

armature current I_a . For constant excitation, as in this case, T_m is controlled solely by the armature current I_a , when

$$T_m = K_\phi I_a \qquad A.1.1$$

where the excitation constant K_ϕ was measured as 1.98 for a field current of 0.15A. From the conventions adopted in figure A.1.1, the armature current I_a is

$$I_a = \frac{V_T - E}{R_1 + R_a} \qquad A.1.2$$

where R_a and R_1 are respectively the armature resistance and an external series resistance, which may be combined as $R = R_a + R_1$. V_T is the motor supply voltage and the back emf E is a function of speed given by

$$E = K_\phi \omega_m \qquad A.1.3$$

If $E < V_T$, the machine is motoring and I_a and T_m are positive. If $E > V_T$, the machine is generating and I_a and T_m are negative. There is a further operating mode when V_T is reversed, so that V_T and E are additive and equation A.1.2 become

$$I_a = \frac{V_T + K_\phi \omega_m}{R} \qquad A.1.4$$

In this mode I_a and T_m are both negative and the machine is attempting to reverse its direction of rotation. This mode was chosen for loading the machine, since it was found to be the most stable method for low speed operation. Substituting I_a from equation A.1.4 in equation A.1.1 gives the generated torque as

$$T_m = \frac{K_\phi V_T + K_\phi^2 \omega_m}{R} \qquad A.1.5$$

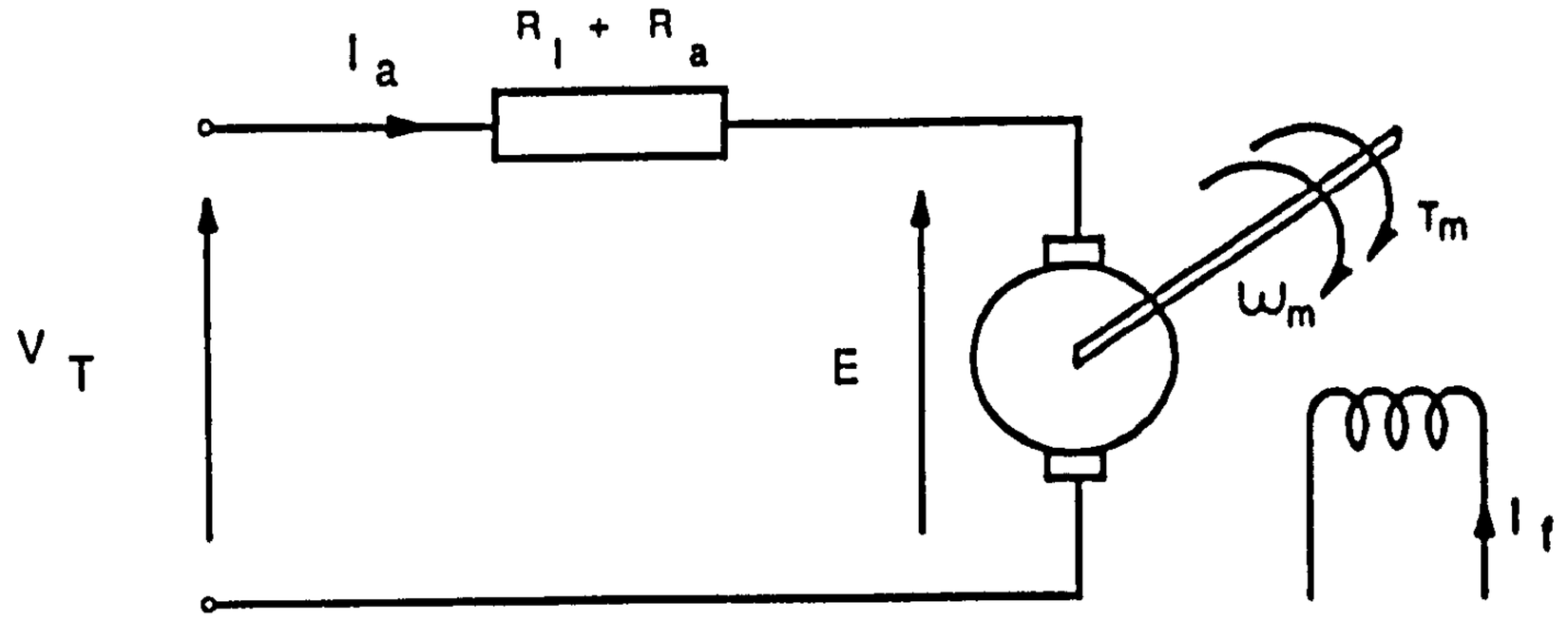

Figure A.1.1 Separately excited DC motor

3. Mechanical Loss

The mechanical losses were determined with the DC machine driving the un-excited induction motor. The copper and iron losses were subtracted from the DC power input, and the variation of no-load output power or mechanical losses were obtained with speed. The resulting torque/speed characteristic is shown in figure A.1.2, and fitting a second-order polynomial to this gives

$$T_f = 0.1341 + 2.2\ 10^{-3}\omega_m + 3.1\ 10^{-7}\omega_m^2 \qquad A.1.6$$

Comparing equation A.1.6 with equation 5.20 yields

$T_c = 0.1341\,Nm$.

$K_v = 2.2\ 10^{-3}$.

$K_\omega = 3.1\ 10^{-7}$.

The very small windage constant K_ω is due to the removal of the induction motor cooling fan to allow coupling to the incremental encoder.

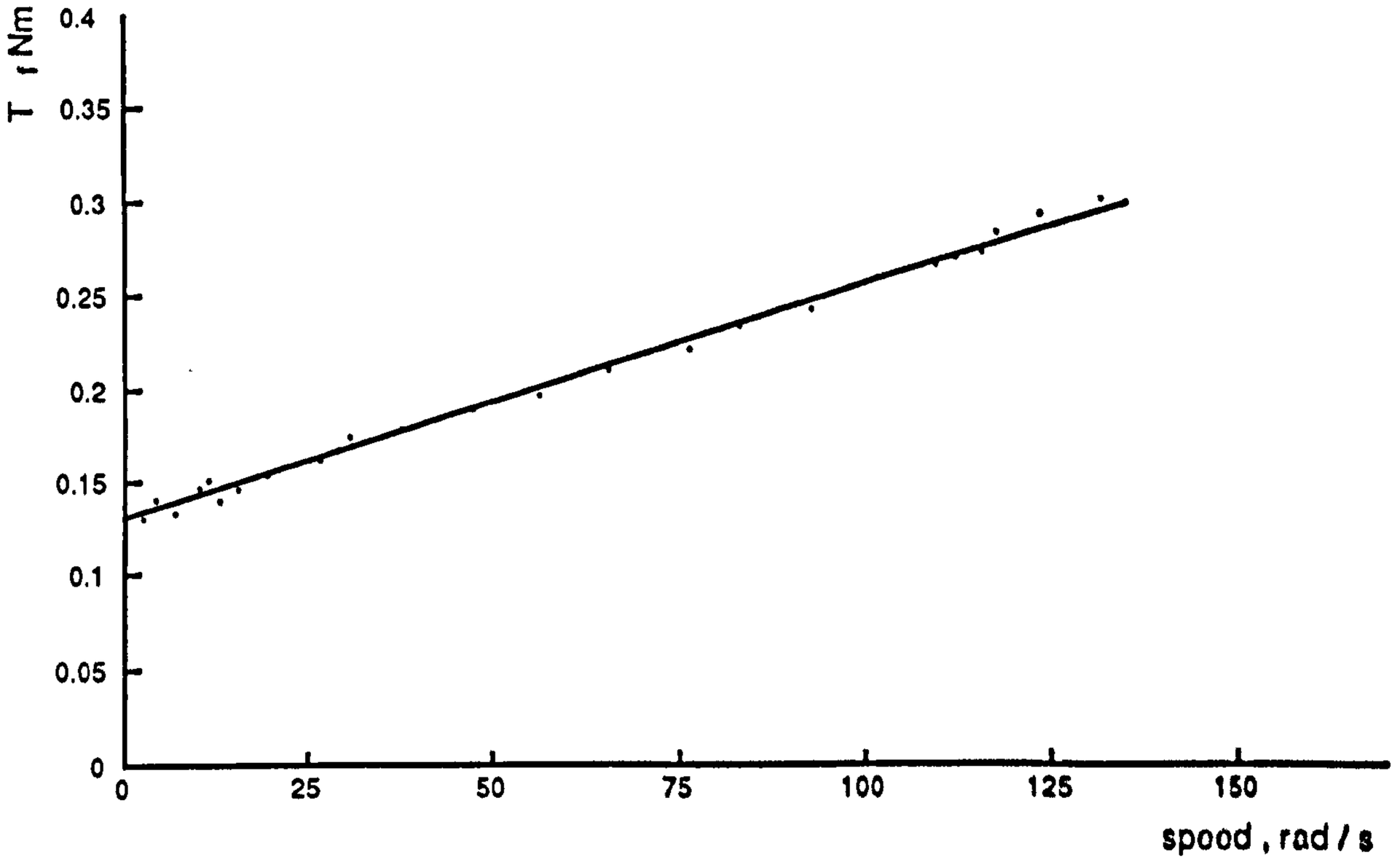

Figure A.1.2 Mechanical loss / speed curve

4. Moment of Inertia

The moments of inertia of the two machines were measured using run-down tests [A.1-1] and were found to be

J_m = 0.0032$kg.m^2$ for the induction motor.

J_g = 0.0035$kg.m^2$ for the DC machine.

References.

(A.1-1) Pillai, S.K. : "*A First Course on Electrical Drives*", Wiley Eastern Ltd., 1982.

APPENDIX A.2

SAMPLE OPTIMIZATION PROCESS FOR THE ELIMINATION STRATEGY

The general non-linear optimization problem to be solved for m switching angles per quarter-cycle, is to maximize the fundamental component

$$\alpha_1 = \frac{\sqrt{2}}{\pi} V_{dc} \left(1 + 2 \sum_{i=1}^{m} (-1)^i \cos\alpha_i \right) \qquad A.2.1$$

and to eliminate m harmonic components with magnitudes

$$\alpha_n = \frac{\sqrt{2}}{n\pi} V_{dc} \left(1 + 2 \sum_{i=1}^{m} (-1)^i \cos n\alpha_i \right) \qquad A.2.2$$

such that $\alpha_{min} < \alpha_1 < \alpha_2 < \alpha_3 < \ldots < \alpha_m < \pi/2$, where α_{min} and $\pi/2$ are the lower and upper bounds imposed on the switching angles.

The problem was solved using NAG-Library subroutine E04UAF, which attempts to find the minimum of a function of several variables subject to fixed bounds and general equality and/or inequality constraints. It was necessary to re-arrange equation A.2.1, whose second term is

$$f_1 = 2 \sum_{i=1}^{m} (-1)^i \cos\alpha_i \qquad A.2.3$$

This trigonometric equation is periodic with a maxima of f_1 and minima of $-f_1$, so that minimizing $-f_1$ maximizes f_1 .

The optimization problem for 8 switching angles per quarter-cycle can be summarised as :

Minimize

$$-f_1 = -2 \sum_{i=1}^{8}(-1)^i \cos\alpha_i \qquad A.2.4$$

subject to the elimination of all existing harmonic components up to the 25th, expressed as the equality constraints

$$cc(1) = 1 + 2 \sum_{i=1}^{8}(-1)^i \cos 5\alpha_i = 0$$

$$cc(2) = 1 + 2 \sum_{i=1}^{8}(-1)^i \cos 7\alpha_i = 0$$

$$cc(3) = 1 + 2 \sum_{i=1}^{8}(-1)^i \cos 11\alpha_i = 0$$

$$cc(4) = 1 + 2 \sum_{i=1}^{8}(-1)^i \cos 13\alpha_i = 0$$

$$cc(5) = 1 + 2 \sum_{i=1}^{8}(-1)^i \cos 17\alpha_i = 0 \qquad A.2.5$$

$$cc(6) = 1 + 2 \sum_{i=1}^{8}(-1)^i \cos 19\alpha_i = 0$$

$$cc(7) = 1 + 2 \sum_{i=1}^{8}(-1)^i \cos 23\alpha_i = 0$$

$$cc(8) = 1 + 2 \sum_{i=1}^{8}(-1)^i \cos 25\alpha_i = 0$$

and the inequality constraints

$$cc(9) = \alpha_2 - \alpha_1 - t_{min} \geq 0$$

$$cc(10) = \alpha_3 - \alpha_2 - t_{min} \geq 0$$

$$cc(11) = \alpha_4 - \alpha_3 - t_{min} \geq 0$$

$$cc(12) = \alpha_5 - \alpha_4 - t_{min} \geq 0 \qquad A.2.6$$

$$cc(13) = \alpha_6 - \alpha_5 - t_{min} \geq 0$$

$$cc(14) = \alpha_7 - \alpha_6 - t_{min} \geq 0$$

$$cc(15) = \alpha_8 - \alpha_7 - t_{min} \geq 0$$

The solution of equation A.2.4 converged to a minima of $-f_1 = 0.0885$, which led to the maximum magnitude of the fundamental component as

$$a_1 = \frac{\sqrt{2}}{\pi} V_{dc} \ (K) \qquad A.2.7$$

where $K = 1 - f_1$ is the fundamental component factor given in table 3.1.

There are various combinations of switching angles which comply with the above constraints, and it is necessary to search the entire region $(t_{min} - \frac{\pi}{2})$ for possible solutions of a_1. Several different initial estimates were therefore used with each solution being tested in terms of its effect on the dynamic performance of the drive to select the optimum set.

APPENDIX A.3

TORQUE EQUATION DERIVATION

Equation 6.18 expresses the electromagnetic torque of the motor in terms of the instantaneous stator and rotor currents given in equations 6.5 and 6.6. The equation correlates the interaction between harmonic currents in producing harmonic torques. Equation 6.19, which expresses this correlation mathematically, is derived as follows :

Substituting for $I_{s(1)}$ and $I_{r(7)}$ from equations 6.5 and 6.6 into equation 6.18 yields, for the 1st term

$$2I_{s(1)}I_{r(7)}\sin(p\omega_m t)\ [\sin(\omega_s t+\theta_{s(1)})\sin(7\omega_s t-p\omega_m t+\theta_{r(7)})$$
$$+\sin\left(\omega_s t+\theta_{s(1)}-\frac{2\pi}{3}\right)\sin\left(7\omega_s t-p\omega_m t+\theta_{r(7)}-\frac{2\pi}{3}\right)$$
$$+\sin\left(\omega_s t+\theta_{s(1)}+\frac{2\pi}{3}\right)\sin\left(7\omega_s t-p\omega_m t+\theta_{r(7)}-\frac{2\pi}{3}\right)]$$

Using trigonometric manipulations and simplifying results in

$$\frac{3}{2}I_{s(1)}I_{r(7)}[\sin(2p\omega_m t-6\omega_s t+\theta_{s(1)}-\theta_{r(7)})$$
$$+\sin(6\omega_s t-\theta_{s(1)}+\theta_{r(7)})] \qquad A.3.1$$

Similarly, the second and third terms of equation 6.18 yield the following expressions

$$\frac{3}{2}I_{s(1)}I_{r(7)}[\sin\left(2p\omega_m t-6\omega_s t+\theta_{s(1)}-\theta_{r(7)}+4\frac{\pi}{3}\right)$$
$$+\sin(6\omega_s t-\theta_{s(1)}+\theta_{r(7)})] \qquad A.3.2$$

and

$$\frac{3}{2}I_{s(1)}I_{r(7)}\left[\sin\left(2p\omega_m t-6\omega_s t+\theta_{s(1)}-\theta_{r(7)}-4\frac{\pi}{3}\right)\right.$$

$$\left.+\sin(6\omega_s t-\theta_{s(1)}+\theta_{r(7)})\right] \qquad A.3.3$$

Combining expressions A.3.1, A.3.2 and A.3.3 reduces to

$$\frac{9}{2}I_{s(1)}I_{r(7)}\sin(6\omega_s t-\theta_{s(1)}+\theta_{r(7)}) \qquad A.3.4$$

Thus, the harmonic torque component produced by the interaction of $I_{s(1)}$ and $I_{r(7)}$ is

$$T_e(I_{s(1)},I_{r(7)}) = -3pl_mI_{s(1)}I_{r(7)}\sin(6\omega_s t-\theta_{s(1)}+\theta_{r(7)}) \qquad A.3.5$$

$$= +3pl_mI_{s(1)}I_{r(7)}\sin(-6\omega_s t+\theta_{s(1)}-\theta_{r(7)}) \qquad A.3.6$$

which is a harmonic torque time phasor rotating in a clockwise direction at six times the supply frequency. Similarly, the interaction between $I_{s(7)}$ and $I_{r(1)}$ produces a harmonic torque time phasor rotating in an anti-clockwise direction at six times the fundamental frequency, and given by

$$T_e(I_{s(7)},I_{r(1)}) = +3pl_mI_{s(7)}I_{r(1)}\sin(6\omega_s t+\theta_{s(1)}-\theta_{r(7)}) \qquad A.3.7$$

Equations A.3.6 and A.3.7 may be generalized for the harmonic torque time phasor produced by the interaction of two forward rotating stator and rotor current components

$$T_e(I_{ksf},I_{krf})=+3pl_mI_{s(ksf)}I_{r(krf)}\sin((ksf-krf)\omega_s t+\theta_{s(ksf)}-\theta_{r(krf)}) \qquad A.3.8$$

In a similar manner, a general expression for the harmonic torque time phasor produced by two backward rotating components is

$$T_e(I_{ksb},I_{krb})=-3pl_mI_{s(ksb)}I_{r(krb)}\sin((ksb-krb)\omega_s t+\theta_{s(ksb)}-\theta_{r(krb)}) \qquad A.3.9$$

Finally, the interaction between forward and a backward rotating stator and rotor current components yields

$$T_e(I_{ksf}, I_{krb}) = -3pl_m I_{s(ksf)} I_{r(krb)} \sin((ksf + krb)\omega_s t + \theta_{s(ksf)} + \theta_{r(krb)}) \qquad A.3.10$$

and

$$T_e(I_{ksb}, I_{krf}) = +3pl_m I_{s(ksb)} I_{r(krf)} \sin((ksb + krf)\omega_s t + \theta_{s(ksb)} + \theta_{r(krf)}) \qquad A.3.11$$

APPENDIX A.4

EXAMPLE OF THE HALF-WAVE SYMMETRICAL OPTIMIZATION PROCESS

This example shows how mutual cancellation between the 6th-harmonic torque components produced by current components of orders (1,5) and (1,7) is achieved, using two switching angles per half-cycle (corresponding to type A PWMT2 mode). After specifying the frequency, load condition and an initial estimate of the two switching angles, the solution continues as follows using the procedure described in section 6.5:

(1) The initial information permits determination of the DC-link voltage, together with the fundamental, 5th- and 7th-harmonic terminal voltage components using equations 7.1 to 7.3, which are written as

$$a_{(n)} = \frac{\sqrt{2}}{n\pi} V_{dc} \ (1 - \cos n\alpha_1 + \cos n\alpha_2) \qquad A.4.1$$

$$b_{(n)} = -\frac{\sqrt{2}}{n\pi} V_{dc} \ (\sin n\alpha_1 - \sin n\alpha_2) \qquad A.4.2$$

$$V_{(n)} = \sqrt{a_{(n)}^2 + b_{(n)}^2} \qquad A.4.3$$

The phase angle for $V_{(n)}$ is obtained using equation 7.4.

(2) Equation A.4.3 is re-arranged as

$$f_1 = \frac{1}{\sqrt{a_{(1)}^2 + b_{(1)}^2}} \qquad A.4.4$$

and NAG-library subroutine E04UAF, which finds a minimum of a function, may be used to solve for a minimum f_1, which corresponds to a maximum of $V_{(1)}$.

(3) The stator and rotor currents $I_{s(n)}$, $I_{r(n)}$ and their phase angles $\theta_{s(n)}$, $\theta_{r(n)}$ are calculated for the fundamental, 5th- and 7th-harmonic components using equations 6.7, 6.10, 7.5 and 6.11 respectively. The values are substituted into the equality constraint equations defining the relationships between the harmonic torque components, which are then re-arranged as

$$\begin{aligned} cc(1) = 3pl_m[& .I_{s(5)}I_{r(1)}\cos(\theta_{s(5)}+\theta_{r(1)}) \\ & -I_{s(1)}I_{r(5)}\cos(\theta_{s(1)}+\theta_{r(5)}) \\ & +I_{s(7)}I_{r(1)}\cos(\theta_{s(7)}-\theta_{r(1)}) \\ & -I_{s(1)}I_{r(7)}\cos(-\theta_{s(1)}+\theta_{r(7)})] = 0 \end{aligned} \qquad A.4.5$$

$$\begin{aligned} cc(2) = 3pl_m[& .I_{s(5)}I_{r(1)}\sin(\theta_{s(5)}+\theta_{r(1)}) \\ & -I_{s(1)}I_{r(5)}\sin(\theta_{s(1)}+\theta_{r(5)}) \\ & +I_{s(7)}I_{r(1)}\sin(\theta_{s(7)}-\theta_{r(1)}) \\ & -I_{s(1)}I_{r(7)}\sin(-\theta_{s(1)}+\theta_{r(7)})] = 0 \end{aligned} \qquad A.4.6$$

while the minimum pulse-width limit is re-arranged as the inequality constraint

$$cc(3) = \alpha_2 - \alpha_1 - t_{min} \geq 0$$

For each iteration made by the optimization subroutine in searching for a local optima, the values of the switching angles will remain within the boundary limits of t_{min} and π . This requires the repetition of steps 1-3 for the new set of switching angles until a solution of equation A.4.4 converges to a minimum value of f_1 .

APPENDIX A.5

EXAMPLE OF THE QUARTER-WAVE SYMMETRICAL OPTIMIZATION PROCESS

This example shows how the resultant 6th-harmonic torque component is minimized, by imposing the same magnitudes on the components produced by the (1,5) and (1,7) current components using two switching angles per quarter-cycle (corresponding to type D PWMM2 mode). After specifying the frequency and load condition, and an initial estimate of the two switching angles, the procedure of section 6.5 is used as follows :

(1) The initial information permits determination of the DC-link voltage together with the fundamental, 5th- and 7th-harmonic terminal voltage components which using equation 6.3, may be rewritten as

$$V_{(n)} = \frac{\sqrt{2}}{n\pi} V_{dc} \left(1 - 2(\cos n\alpha_1 - \cos n\alpha_2)\right) \qquad A.5.1$$

The phase angles for the harmonics are either 0 or 180° , due to the quarter-wave symmetry of the voltage waveform.

(2) Equation A.5.1 may be re-arranged to define the function

$$-f_1 = 2(\cos\alpha_1 - \cos\alpha_2) \qquad A.5.2$$

which, using NAG-Library subroutine E04UAF, is solved for a minimum $-f_1$ corresponding to a maximum of $V_{(1)}$.

(3) The stator and rotor currents $I_{s(n)}$, $I_{r(n)}$, and their phase angles $\theta_{s(n)}$, $\theta_{r(n)}$, are calculated for the fundamental, 5th- and 7th-harmonic components, using equations 6.7, 6.10, 7.5 and 6.11 respectively. Their values are substituted in equations 7.8, 7.9, 7.12 and 7.13 to determine the corresponding 6th-harmonic torque components from

$$T_e(1,5) = \sqrt{(\Re T_e(1,5))^2 + (\Im T_e(1,5))^2} \qquad A.5.3$$

$$T_e(1,7) = \sqrt{(\Re T_e(1,7))^2 + (\Im T_e(1,7))^2} \qquad A.5.4$$

These two components are substituted into the equality constraint equation, which defines the required relationship as

$$cc(1) = T_e(1,5) + T_e(1,7) = 0 \qquad A.5.5$$

while the minimum pulse-width limit is re-arranged as the inequality constraints

$$cc(2) = \alpha_2 - \alpha_1 - t_{min} \geq 0$$

At each iteration of the optimization subroutine, when searching for a convergence of the solution to a local optima, the values of the switching angles will remain within the boundary limits of t_{min} and $\pi/2$. This requires the repetition of steps 1-3 for the new set of switching angles until a solution of equation A.5.2 converges to a minimum value of $-f_1$.